University of Bath

UNIVERSITY OF BATH

PHD

Microstructural, mechanical and electrical characterisation of piezoelectric particulate composites with dielectric modelling

Panteny, Simon Robert

Award date:
2003

Awarding institution:
University of Bath

[Link to publication](#)

Alternative formats

If you require this document in an alternative format, please contact:
openaccess@bath.ac.uk

Microstructural, Mechanical and Electrical Characterisation of Piezoelectric Particulate Composites with Dielectric Modelling

Submitted by Simon Robert Panteny

for degree of Doctor of Philosophy

of the University of Bath

2003

UMI Number: U208564

UMI

Dissertation Publishing

ProQuest

ACKNOWLEDGEMENTS

ABSTRACT

This thesis examines the influence of particulate addition on the mechanical and dielectric properties of barium titanate. Initial composites were manufactured with nano-sized silicon carbide particles in barium titanate. The effect of these particles on the sintering kinetics and final density were studied, suggesting that densification was inhibited. X-ray analysis indicated a reaction phase, barium titanate silicate, between the silicon carbide and barium titanate. The formation of this reaction phase and a reducing atmosphere during sintering increased the conductivity and was detrimental to the dielectric loss. Domains were observed by electron microscopy in the silicon carbide composites. Hot pressed barium titanate-silicon carbide composites had an improved density but were mechanically weak due to the presence of cracks from thermal residual stresses.

Silver particulate composites were formed from thermal decomposition of metallic compounds. The silver based composites fabricated from silver nitrate were characterised in terms of mechanical, dielectric and piezoelectric properties. No reaction phases were detected and a significant increase in the relative permittivity and fracture strength were recorded. Transmission electron microscopy showed the interaction of domains with silver particles. A linear decrease in the piezoelectric coefficient was recorded with the addition of silver to barium titanate. The platinum compound used for composite fabrication was determined to be ineffective due to an inhibited densification and the formation of an unknown reaction phase.

In order to model the influence of particle addition on barium titanate the dielectric behaviour of two and, for the first time, three-dimensional random resistor-capacitor networks were modelled. The models allowed the simulation of permittivity, conductivity and phase angle as a function of frequency, composition and component values. The simulated results were in agreement with the observed increase in the permittivity measured in the barium titanate-silver composites fabricated in this study. An unexpected change in the conductivity below 1 MHz is proposed to be due to a conductive "skin" on the barium titanate grains.

CONTENTS

Contents

LIST OF FIGURES

LIST OF TABLES

LIST OF SYMBOLS

List of symbols and their units

Symbol	Meaning	SI-Unit
a	Half indent dimension	m
A	Area	m^2
Ag	Silver (Element)	
$BaTiO_3$	Barium titanate	
c	Half crack length/ flaw size	m
C	Capacitance	F
C^E	Constant electric field elastic stiffness	N/m^2
C_m	Speed of sound in material, m	m/s
C_0	Free cell capacitance	F
d	Grain diameter	m
d_s	Domain size	m
d_{33}	Piezoelectric charge (strain) coefficient, parallel to poled direction	C/N or m/V
d_{31}	Piezoelectric charge (strain) coefficient, perpendicular to poled direction	C/N or m/V
D	Dielectric displacement	C/m^2
e	Piezoelectric modulus	C/m^2
E	Electric field strength	V/m
E_{Young}	Young's modulus	N/m^2
E_0	Zero porosity Young's modulus	N/m^2
f	Frequency	Hz
$f_{acoustic}$	Acoustic resonant frequency	Hz
f_m	Frequency of minimum impedance	Hz
f_n	Frequency of maximum impedance	Hz
f_p	Parallel resonance frequency	Hz
f_s	Series resonance frequency	Hz
F	Force	N
h	Distance between capacitance plates	m
H_v	Vickers hardness	N/m^2
k	Hall-Petch constant	$N/m^{1.5}$
K_{eff}	Effective electromechanical coupling coefficient	
K_p	Planar coupling coefficient	
K_{1c}	Mode one fracture toughness	$N/m^{1.5}$

l_s	Shielding zone size	m
l	Disk radius	m
L	Acoustic length	m
m	Weibull modulus	
n	Diffusion variable (3 for lattice and 4 for grain boundary)	
p	Fractional porosity	
P	Polarisation	C/m^2
P_0	Single crystal polarisation	C/m^2
P_f	Load	N
P_{grain}	Average grain polarisation	C/m^2
P_r	Remnant polarisation	C/m^2
P_s	Saturation polarisation	C/m^2
Pt	Platinum (Element)	
Q	Storage charge	C
Q_m	Mechanical quality factor	
r	Particle radius	m
R	Resistance	Ω
SiC	Silicon carbide	
S_{11}^E	Constant electric field compliance in 1-direction	m^2/N
t	Thickness	M
T	Temperature	°C
V	Voltage	V
V_f	Volume fraction	
wt%	Percent weight fraction	%
x	Radial distance from particle surface	m
Y	Geometric constant	
Y	Admittance	Ω^{-1}
Z	Impedance	Ω
Z_m	Resonant impedance	Ω
Z'	Real impedance	Ω
Z''	Imaginary impedance	Ω
α	Coefficient of thermal expansion, CTE	°C^{-1}
β	Strength-porosity constant	
ϵ_t	Strain tensor	
ϵ	Absolute permittivity	Fm^{-1}
ϵ_H	High frequency permittivity	Fm^{-1}

ε_b	Bulk permittivity	Fm^{-1}
ε_{gb}	Grain boundary permittivity	Fm^{-1}
ε_r	Relative permittivity	
ε_t	Strain	
ε_0	Permittivity of free space	Fm^{-1}
γ	Surface energy	J/m^2
ν	Poisson's ratio	
π	Pi	
θ	Diffraction angle	$^\circ$
ρ	Density	Mg/m^3
ρ_r	Resistivity	$\Omega.m$
σ	Conductivity	$\Omega^{-1}.m^{-1}$
σ_f	Fracture stress	N/m^2
σ_m	Fracture initiating stress	N/m^2
σ_s	Shielding stress	N/m^2
σ_T	Stress tensor	N/m^2
σ_0	Characteristic material strength/Zero porosity strength value	N/m^2
$\sigma_{thermal}$	Thermal residual stress	N/m^2
τ	Resistor-capacitor parallel circuit time constant	s^{-1}
ω	Angular frequency	$Rad\ s^{-1}$

1 GENERAL INTRODUCTION

The ability of a material to generate electrical surface charge under the application of stress was discovered by Pierre Curie in 1880 when working with quartz. This type of material is termed piezoelectric and the class of materials to which it belongs is now used to produce a broad range of actuators and transducers for use in a variety of applications from optical physics to the automotive industry. Piezoelectric technology has advanced by the discovery of new materials with improved properties, such as barium titanate and lead zirconate titanate. These materials traditionally have not functioned as part of the load bearing structure, however, the modern requirement for miniaturisation is a driving force for research into improving the mechanical properties of these materials.

In the past decade considerable interest has been shown in the improvement of ceramic properties by the addition of particles to the ceramic matrix. Structural ceramics, such as alumina, have had particles of silicon carbide added, with reported benefits to mechanical properties. Electroceramic materials, such as barium titanate, have also had improved mechanical properties reported with particle addition. However, electroceramic materials are utilised primarily for their dielectric or piezoelectric characteristics. Limited research has been focused on the characterisation of both the mechanical and electrical properties of electroceramic particulate composites.

This thesis presents the structural, mechanical and electrical characterisation of an electroceramic material with incorporated non-metallic and metallic particles. The aim is to investigate manufacturing methods for these composites and characterise their microstructural, mechanical and electrical properties. In addition, it describes attempts to develop models to understand the relationship between composite structure and the type of particle. A search of the literature indicates a dearth of information on the processing and properties, mechanical and electrical, of particulate-based barium titanate composites. Barium titanate was chosen as a model system due to the extensive literature. Methods of composite manufacture, ball milling and attrition milling, are detailed for both the monolith and composites. The composites chosen were barium titanate with silicon carbide or silver particles. Both systems are referred to the limited data available and have differing electrical properties. Fabrication of barium titanate-platinum composites was also attempted in order to produce nano-sized metallic particles that would not evaporate under the sintering conditions of barium titanate.

The microstructural (XRD, SEM, TEM), mechanical (hardness, strength, toughness) and electrical (relative permittivity, resistivity, piezoelectric coefficient, dielectric breakdown, polarisation-field) parameters used to characterise the fabricated samples are described.

In addition, modelling was conducted in order to construct a reference resistor-capacitor network that would simulate a dielectric material. The modelling allowed the simulation of permittivity, conductivity and phase angle with frequency. The effect of low resistance resistor addition to the reference random resistor-capacitor network was modelled. This is to simulate the addition of a low resistance particle to a dielectric matrix as conducted experimentally. The results for both the monolith and composite are given. The modelling results are compared, where appropriate, to data from experimental characterisation of samples. A general discussion, in terms of the properties characterised, is given for each of the composites manufactured before stating the conclusions and suggestions for future work.

2 LITERATURE REVIEW

2.1 INTRODUCTION

This chapter presents a literature review regarding the properties of ceramic matrix composite systems containing either electrically insulating or metallic particles. The following chapter is concerned with the fabrication of composites for this research and Chapter Four describes the microstructural, mechanical and electrical techniques used to characterise the composites. Appendix II gives extra detail on some of the information presented in this chapter and this is stated where relevant.

This chapter is divided into sections starting with background information on the physical properties of composites, barium titanate (which is the matrix material used in this work) and the types of particle inclusion that have been used in similar composite systems. The subsequent sections relate to the effect of these particles on the microstructure, mechanical properties and finally the electrical properties. To conclude this chapter, there is a section on the current and possible future applications of these materials.

The development of composite materials has been driven by the miniaturisation of electrical devices and the need for improved mechanical and electrical properties[1]. Improved materials will allow new uses and devices that make better use of the ceramic properties. Recent research has focused on the incorporation of particles, with dimensions typically in the nanometre range, in electroceramics and to characterise their effect on the mechanical and electrical properties of the electroceramic.

2.2 PHYSICAL PROPERTIES OF COMPOSITES

This section gives an introduction to composites, after which details are given of the materials used in this research project.

2.2.a COMPOSITE TYPES

A large percentage of both organic and non-organic structures, whether natural or man-made, are formed from composites. Examples include wood and rocks, whilst man-made synthetic composites can be found, for example, from the Space Shuttle (epoxy composite payload doors) to the bicycle tyre. The matrix can be metallic such as aluminium, in aluminium-silicon carbide; ceramic, such as in ceramic matrix composites or organic as in bone, while the filler can be of a similar or dissimilar material. The matrix is the part of the composite that holds the other part, the filler, in the required position. Composites can have properties that are superior to the separate individual constituents. The volume fraction and size of the filler addition can be varied to tailor the composite properties for a particular use.

The research for this thesis is primarily concerned with developing recent work on the mechanical and electrical properties of nano-composites systems. An introduction to nano-particle systems is first given, while the following sections are concerned with systems in which particles have been added and mechanical and electrical properties characterised.

2.2.a.i   *Nano-composite*

The term nano-composite was originally defined in 1986 by Roy[2] in relation to ceramic-metal materials. The definition is:

"a composite of more than one Gibbsian solid phase where at least one of the phases shows dimensions in the nanometre range"[3]

Most nano-composite work has concentrated on structural ceramics[4], such as reinforcement of alumina with silicon carbide, while other areas, for example have produced photosensitive glass by the incorporation of silver halide nano-particles[3]. Niihara documented the structural concept in the period 1980-91[5]. He proposed four possible nano-composite structures that can be obtained by the incorporation of nano-particles into a host matrix.

Figure 2.1 illustrates the potential structures, namely,

i.   **Intergranular**

Particles are situated on the grain boundaries so that grain sliding, even at high temperature, is reduced[6]. Possible benefits are increased high temperature creep resistance.

ii.   **Intragranular**

Particles are located within the matrix grains so that cracks passing though the grains may be deflected or pinned, improving the toughness.

iii.   **Intra/Inter-granular**

Toughness and creep resistance improvement.

iv.   **Nano/nano**

A mixture of two nano-phase materials can allow the possibility of superplasticity[7].
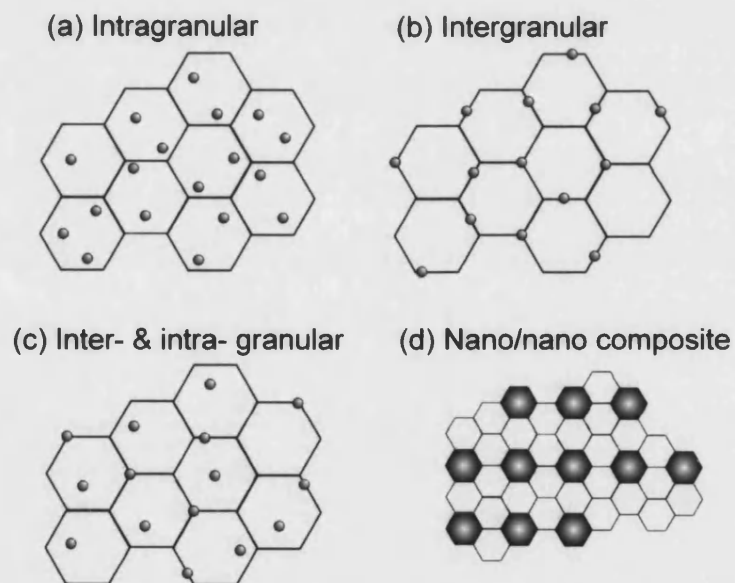
Figure 2.1: The types of nano-composites (a) intragranular, (b) intergranular,

(c) inter/intragranular and (d) nano/nano[5].

2.2.a.ii   The Matrix

A number of principal ceramic matrices, such as alumina[4, 6, 8-10], lead zirconate titanate (PZT)[11-15], and MgO[2, 6, 16] have had various micro- or nano-metre sized particles added to influence properties. This has been done with the intention to introduce ferroelectric properties into structural ceramics[16], or to enhance mechanical properties, such as strength or toughness[6, 17]. This study is concerned with the effects of particles on a matrix of barium titanate in relation to electrical and mechanical properties.

2.2.b   BARIUM TITANATE MATRIX

Barium titanate was chosen as the matrix to represent a model piezoelectric material. There are other piezoelectric materials available, such as PZT, but while these lead-based piezoelectric compounds have higher piezoelectric coefficients they are generally more difficult to process. An advantage in using barium titanate is that there has been considerable research into this traditional dielectric material, so that comparison can be made with reported properties. The general properties of barium titanate are now discussed, whilst Appendix I contains a summary of the properties and Appendix II information of the basis of piezoelectricity.

2.2.b.i   Crystal Structure

The dielectric properties of barium titanate were discovered independently around 1943 in the United States of America (Wainer & Saloman), Japan (Oqawa) and Russia (Wal & Goldman)[18]. The unit cell arrangement of barium titanate consists of a highly charged titanium ion (B-ion) situated in the centre of an oxygen octahedral cage that is surrounded by a cubic lattice of barium ions (A-ions), as shown in Figure 2.2.
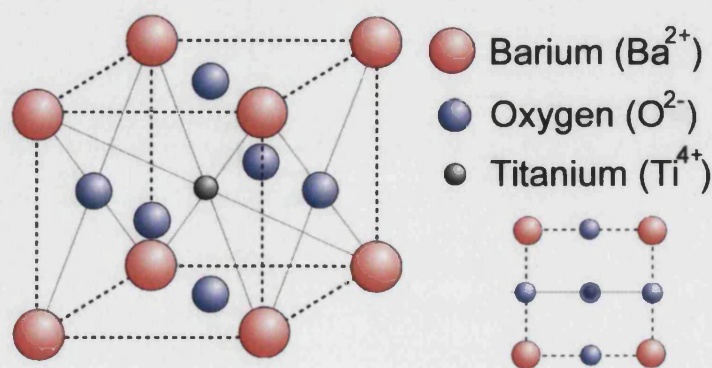
Figure 2.2: Structure of cubic barium titanate.

The ionic radii of the component ions determine the structure of the material. The tolerance factor indicates how far the ions are from ideal packing. In the perovskite structure, a tolerance factor above one signifies that the unit cell is governed by the A-site ion. As such the B-site ion (Ti^{4+}) has room to oscillate, as in barium titanate, the opposite being true for a tolerance factor below one. When tolerance factor equals one the structure is close packed[19].

The titanium ion has more than one minimum energy position, as thermal energy is sufficient to allow these ions to overcome electrostatic forces[20]. In one of these sites the oxygen cage moves in relation to the barium ion lattice creating a unit cell dipole, Figure 2.3.

This distortion of the crystal causes one cube edge to elongate and become the tetragonal c-axis, while the other two edges (a-axes) contract[18]. This transformation occurs below a material specific temperature, identified as the Curie temperature, T_c. For barium titanate, T_c has been reported to lie in the range 120-130°C [18].
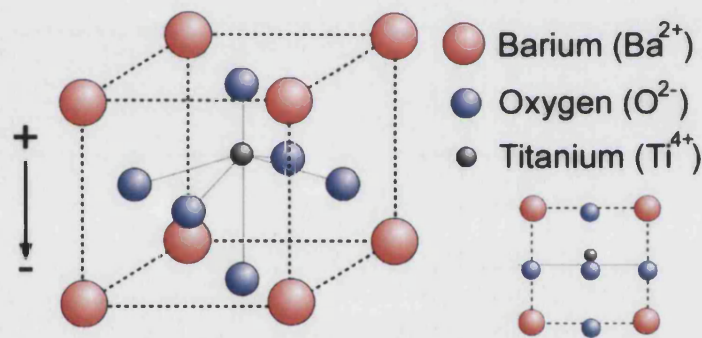
Figure 2.3: Tetragonal barium titanate unit cell dipole.

At the T_c the material is in a metastable cubic-tetragonal structure that allows the majority of dipoles to align with the field, aided by the nearly symmetrical structure. Below the T_c, in the tetragonal temperature range, the polar direction is along the c-axis[18]. Considerable strain occurs in the free crystal when cooled through the Curie temperature, due to the change in unit cell dimensions with temperature, as indicated in Figure 2.4 [21].
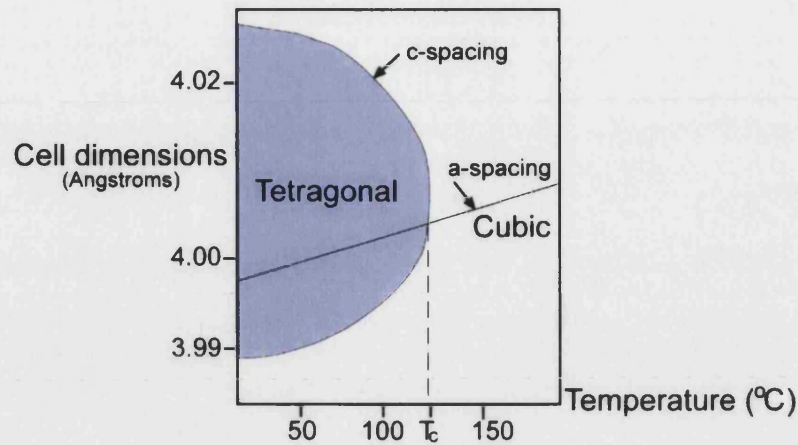
Figure 2.4: Variation of a-axis and c-axis dimensions with temperature for barium titanate[21].

The polarisation direction is determined by the unit cell structure. Polarisation changes are fixed for a specific structure, which restrict, under an applied driving force, the polarisation directions between these allowed crystallographic directions[21]. Figure 2.5 shows the polar directions in the different structural forms of the perovskite structure. A description of the properties at temperatures above or below the tetragonal structure is beyond the scope of this introduction, although a description is available[22].
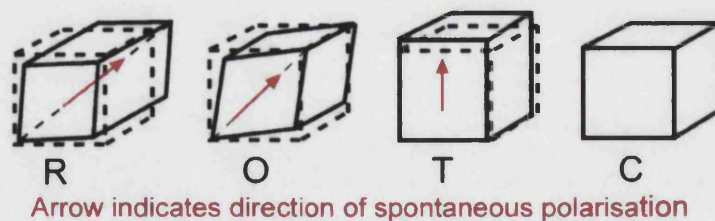
Figure 2.5: Direction of spontaneous polarisation in (R) rhombohedral, (O) orthorhombic,

(T) tetragonal and (C) cubic crystals of barium titanate[21, 23].

The greater the number of polar directions in a structure the more closely the dipole can align itself to an applied electric field. The tetragonal structure has six directions[22, 23], whilst there are none in the cubic structure. The macroscopic effect of these dipoles, piezoelectricity, is reported in Section 2.5.c and Appendix II, and the presence of dipoles in barium titanate affects the dielectric properties, Section 2.5. The chemistry of this compound affects the formation of reaction phases, Section 2.3.d.

2.2.c   INFLUENCE OF PARTICULATE INCLUSIONS ON THE PHYSICAL PROPERTIES OF COMPOSITES

A wide range of inclusions in a ceramic matrix have been studied in order to examine their effects on the microstructure (Section 2.3), mechanical properties (Section 2.4) and electrical properties (Section 2.5). This section gives details on silicon carbide and silver, the inclusions used in this research, and in some cases the effect of other inclusions for comparison.

As the sintering of the barium titanate matrix requires a high temperature, typically greater than 1100°C, the inclusions will be required to survive this fabrication process. Table 2.1 gives the melting points of traditional secondary phase particles used in ceramics. The maximum temperature under oxidising conditions can be much lower than the melting point of the inclusion.

An additional requirement, at the commencement of this research, was that the particles are of nano-size. This limited the available secondary phases at the time, but more recently nano-sized particles of different metals have been manufactured[24].

Table 2.1: Inclusion melting points and maximum application temperatures[25, 26].

Material	Melting point (°C)	Maximum application temperature under oxidising conditions (°C)
Al_2O_3	2053	1600
SiC	2300	>1000
Si_3N_4	1900 (sublimes)	1100
TiC	3140	2000
TiN	2950	500
ZrO_2	2700	1900

2.2.c.i   Semiconducting / insulating inclusions

A number of non-metallic secondary phase particles have been used to change ceramic properties, such as PZT[27, 28], TiC[29, 30] and $BaTiO_3$[16, 31, 32], however by far the greatest amount of research has been conducted using silicon carbide, SiC. Silicon carbide has a low expansion coefficient, high thermal conductivity and is semiconducting[23, 33]. Investigation has principally been in respect to microstructure/mechanical property modification of structural ceramics[3, 34, 10, 35-39]. Silicon carbide has been added to barium titanate[40, 41] but only the mechanical properties were reported.

The silicon carbide used to form the nano-composites has predominately been based on α-SiC, with a surface area of 45 m^2/g, and is commercially referred to as UF45. The average particle diameter of this silicon carbide has been reported by the researchers to fall in the range 90-240 nm[*].

Other researchers have used silicon carbide of sizes 0.6 μm[39], 0.51 μm[42], 0.3 μm[10] and 30 nm[43]. It has been reported that α-SiC produced via Achesion carbothermal reduction and milling, produces an irregular particle morphology that becomes spherical on sintering[3]. This morphology change could affect the mechanical properties as localised stress concentrations, due to the angular shapes, are reduced. An additional concern is the packing efficiency of these irregular powders in the unsintered "green" state.

It is appropriate to mention, at this stage, that the reported silicon carbide particles have a surface layer of silicon dioxide (silica), SiO_2, formed by oxidation. It has been reported that this oxidation has two modes, active and passive[44]. Under high partial pressures of oxygen there is a mass gain by oxide film formation. The diffusion of oxygen through the silica layer is slow and its formation increases the particles' resistance to oxidation[45]. This protective oxide layer has been reported to be stable up to 1650°C in air[23]. The layer thickness has been described to be proportional to the square root of the oxidation time. This diffusion controlled oxidation in nano-sized SiC has been reported at 650°C[46]. The presence of a thin oxide layer, 1.7vol%[39], has consequences for the formation of reaction phases, see Section 2.3.d. In atmospheres with a low oxygen concentration active loss of the silicon carbide via oxidation occurs by the vaporisation of the silica layer[45]. The temperature of passive to active oxidation transition decreases as the oxygen partial pressure, PO_2, is reduced. For example at a PO_2 of 2.5 Pa and 123 Pa the transition temperature changes from 1350°C to 1550°C[44].

In summary silicon carbide can form conventional nano-particles that have been used frequently in structural nano-composites. An added benefit in choosing this material as an inclusion is that comparison can be made with properties that have been reported in the literature. The general properties of silicon carbide are given in Appendix I.

---

[*] 90 nm[17], 120 nm[37], 200 nm[36, 38] and 240 nm[42]

2.2.c.ii   *Metallic inclusions*

Metallic particles consisting of silver have been extensively studied[46-51], in many cases to understand possible reactions that occur in silver electrode multi-layer capacitors. Other metals that have been researched include, copper[9, 52], nickel[8, 53, 54] and platinum[15]. Research has generally been concentrated on structural matrix ceramics, such as alumina[8, 9, 54], but electroceramics, such as PZT-silver[50, 55] and PZT-platinum[15], have also been used. These composites are fabricated by addition of the metal oxide[9, 48] or metal nitrate[47] to the matrix, which is subsequently processed by traditional wet ceramic processing methods (for details see Appendix III). The oxide, or nitrate, is either reduced (as with the use of a hydrogen atmosphere for copper oxide) or decomposes during the calcination process.

It is worth mentioning, at this stage, that in general the melting point of the secondary phase is below the sintering temperature of the ceramic matrix, and can be further reduced by the presence of impurities. In the case of silver the melting point is 961°C[56]. This may have consequences for the formation of reaction phases, final grain size (Section 2.3.b) or residual stresses (Section 2.4.d) and surface metal loss. A silver surface free layer of 100-300μm has been directly observed in ceramic-silver composites[47]. This layer is formed due to the high partial pressure of the silver at the ceramic sintering temperature[46, 47, 49]. Table 2.2 gives the partial pressures for a number of metals that have been used in ceramic composites. At a certain temperature the higher the metal vapour pressure the greater the extent of the depletion layer. It can be observed that at the typical barium titanate sintering temperature of 1300°C, silver has a much higher vapour pressure than copper. Using a lower sintering temperature or a metal with a higher melting point can reduce the loss of metal, through evaporation, from the composite.

Table 2.2: Temperatures (°C) required to produce a certain metal vapour pressure[57].

Metal/Vapour pressure (Pa)	0.01	0.13	1.33	13.3	133
Silver, Ag	832	922	1027	1162	1322
Copper, Cu	1027	1132	1257	1417	1617
Nickel, Ni	1262	1382	1527	1697	1907
Platinum, Pt	1747	1907	2097	2317	2587
Tungsten, W	2757	2977	3227	3537	3917

As the silver is molten at the sintering temperature studies have been conducted to determine the solubility of the metal in the composite matrix. A degree of solubility indicates that the ionic radii of the matrix and second phase ions are similar and doping of the host is occurring. Silver has a greater ionic radius (0.149 nm) in comparison to both the barium ion (0.135 nm) and titanium ion (0.061 nm) so replacement is expected to be negligible. In fact the solubility of silver in barium titanate has been reported to be less than 300 ppm[49].

In summary silver has been chosen as a particulate inclusion, as it is chemically stable, with negligible solubility in the matrix, barium titanate, and provides an electrical contrast to the insulating matrix. It has also been reported to have benefits to the mechanical properties of ceramic matrices (see Section 2.4).

2.3 EFFECT OF INCLUSIONS ON MICROSTRUCTURE

The basic microstructure of a particulate composite, Figure 2.6, consists of the matrix grains separated by internal interfaces. There are homophase interfaces, that is, boundaries between the same phase, such as the grain boundaries, twin boundaries and domain walls, and also hetero-interfaces, which separate different phases[58].
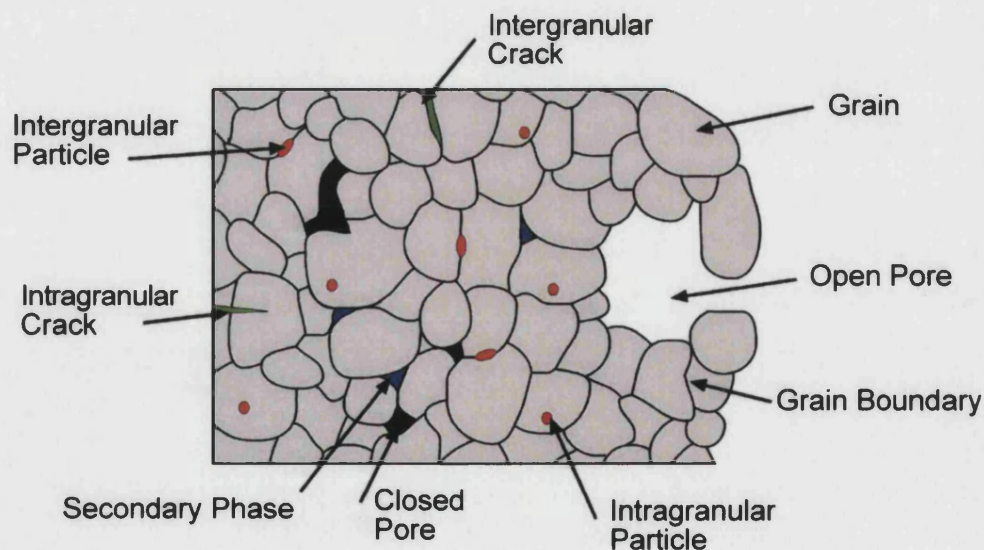
Figure 2.6: Schematic microstructure of a particulate composite.

There are three main additives used in the modification of electroceramics[40];

1. **Dopants** – These are ions that substitute for the Ba^{2+} and Ti^{4+} ions in barium titanate with little effect on the mechanical properties, but they modify the electrical properties.

2. **Oxide additives** – These have a low melting point and good wetting, such as glasses[59] that improve sintering at lower temperature. The grain boundary and microstructural modifications caused by these oxide additives can affect mechanical and electrical properties.

3. **Second phase** – The intention is to incorporate a material of different composition in to the matrix. Reactions, however, may occur between the matrix and the secondary phase so affecting the mechanical (Section 2.4) and electrical properties (Section 2.5).

The work contained within this thesis is concerned with this third type, namely the addition of a particulate secondary phase. This section begins with the influence of inclusions on the sintering characteristics of the matrix and the final density achieved. Information is then presented on the modification of grain size, inclusion size and location. This section finishes with the possible effects on the tetragonal crystal structure and reaction phases that may occur between the matrix and particles.

2.3.a   DENSITY

The density of the final sintered ceramic composite depends on the powder fabrication, powder consolidation, liquid phases, inclusions, temperature and time. Uniform powder pressing is important, as density variation can cause warping of samples[33]. Processing methods are discussed in Appendix III, while that used in this research are detailed in Chapter 3. In general a process called solid state sintering occurs to densify ceramic powders. This requires the transport of atomic species of the matrix to reduce the proportion of voids present. To aid this process it is beneficial to produce a green compact of the highest density possible so that the solid particles are in intimate contact. Powder consolidation is generally undertaken by pressing the powder particles together. In some cases the particles, especially second phase metallics, may undergo plastic deformation during the consolidation process. The morphology and size of both the matrix and the second phase powder particles can affect this densification. A greater green density is achieved by a broad particle size distribution as the smaller particles can fit in the interstices of the large particles. General background information on the densification of powders during sintering is given in Appendix II.

Barium titanate can be fabricated by reacting mixtures of barium oxide, BaO, and titania, TiO_2. For barium titanate the effects of titania or barium oxide excesses on the final composition density have been reported[60, 61]. The results indicate that an excess of titania enhances sintering, while barium oxide excess hinders densification. The explanation for the sintering improvement with excess TiO_2 has been attributed to the pronounced solid-state reaction formation of $Ba_6Ti_{17}O_{40}$. The lowest eutectic in the $BaO-TiO_2$ system is the $BaTiO_3-Ba_6Ti_{17}O_{40}$ boundary at 1332°C. Above this temperature densification is assisted by liquid phase sintering[23, 41, 49]. The temperature of liquid formation may be reduced by the presence of impurities[60]. It has been proposed that the presence of a low viscosity liquid leads to a faster equilibrium and the disappearance between homogenous and less homogeneous additive distributions[62]. Sintering below the eutectic to avoid liquid-phase sintering may be compounded by the formation of platelet-like grains[60]. Figure 2.7 is the results reported by M-H. Lim *et al*[60], showing the effect of stoichiometry and sintering temperature on the density of barium titanate.
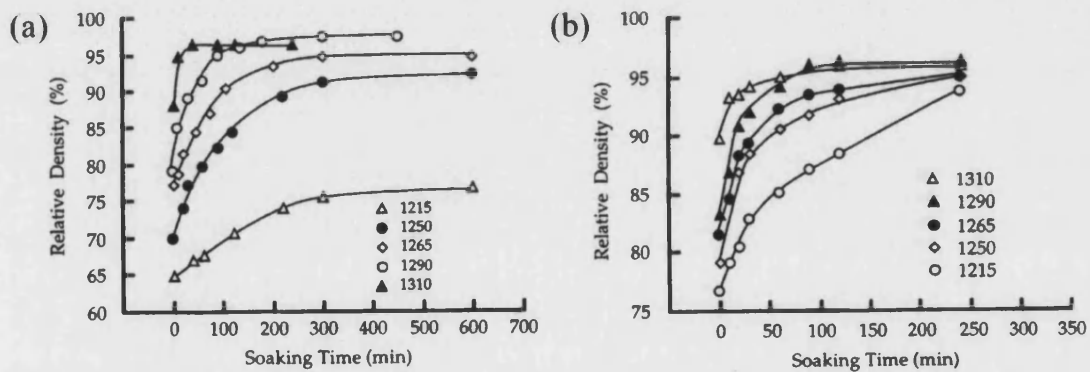
Figure 2.7: Relative densities for samples sintered at different temperatures with

(a) Ba:Ti=0.997 (TiO_2-excess) and (b) Ba:Ti=1.03 (BaO-excess)[60].

It was reported for the titania excess samples that $Ba_6Ti_{17}O_{40}$ was observed after sintering at 1265°C for 20 hours. A bimodal grain distribution was present, with the small grains exhibiting a rounded surface that is characteristic of liquid phase sintering. In contrast the barium oxide excess samples had a microstructure of a typical polycrystalline ceramic, with the grain size increasing with sintering temperature. It was noted however, that there were many residual pores and intragranular Ba_2TiO_4 inclusions. It was concluded from this study that barium vacancies appeared to be the rate-determining species for the solid-state sintering of barium titanate.

With the incorporation of a secondary phase the significant factor during sintering is the minimisation of interfacial energy between matrix and particles. This causes the mutual attraction of particles and grain boundaries by the removal of a grain boundary section[34], as shown in Figure 2.8.
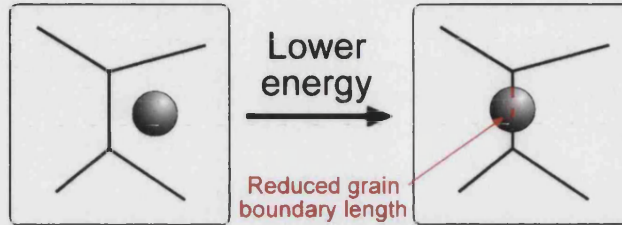
Figure 2.8: Lowering of system energy by grain boundary passing though a particle.

Thus grain growth will depend on particle mobility and the thermodynamic driving forces present during the sintering process, as shown in Figure 2.9.
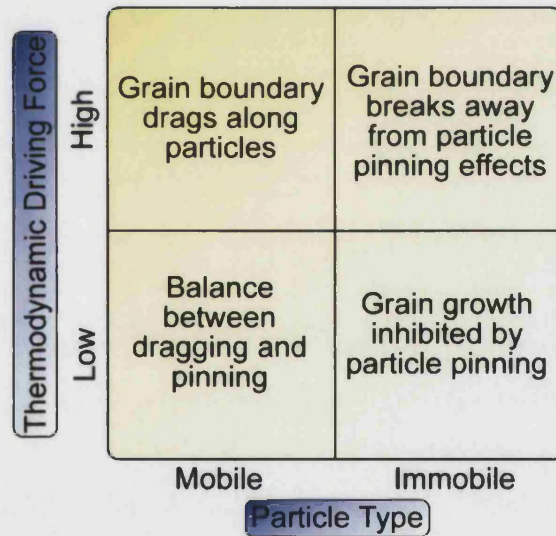
Figure 2.9: Effect of thermodynamic driving force and particle

mobility on grain boundary mobility.

As nano-composites are fabricated from small particle sized powders there is an initial high driving force that can allow grain growth by grain boundary breakaway. Grain development ceases once the driving force falls below the particle pinning force, producing grain size stagnation. The pinning force of an intergranular inclusion, on a moving grain boundary, is assumed to be proportional to its size[37]. Small particles detached easily from the advancing grain boundary during grain growth, becoming entrapped within the matrix grain, while larger particles pin the boundaries by removal of a larger grain boundary section. The mobility of the grain boundary surface can be

limited by solute drag, which is affected by the bonding between the matrix and particle. Strong bonding will make transport of material from one side of the particle to another, as is required for the grain boundary to move, more difficult[63]. Thus the particle can pin the grain boundary even if it is of small size. It has been reported that the degree of densification hindrance increases with the increased volume fraction of particles, and a decrease in particle size[64].

Particles situated intergranularly can lower the final sintered density by inhibiting diffusion along the grain boundaries. This means that hot fabrication processes, such as hot pressing or hot-isostatic pressing, are required to generate a desirable density[6, 65]. For example in the alumina-silicon carbide system an increase in sintering temperature of at least 200°C is required to approach full density with 17vol% silicon carbide particles present[6]. It is important that these particles are uniformly distributed since agglomerates will act as flaws and adversely affect the mechanical properties[66]. In some cases the predominant flaw is where a void is formed by particle agglomeration[3], Figure 2.10.
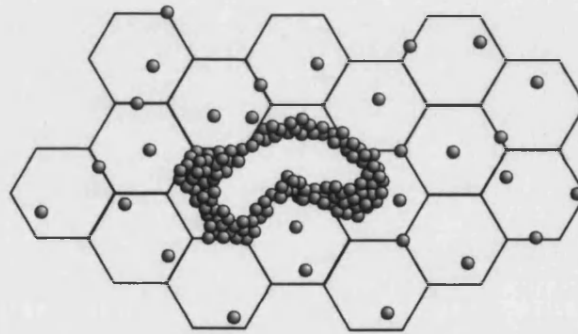
Figure 2.10: Particle agglomeration generating a flaw[3].

A pore surrounded by particles, as shown schematically in Figure 2.10, is thermodynamically stable and can be filled with a glassy phase or gas[37] and once formed is difficult to remove. To reduce the likelihood of agglomerate formation the volume fraction of particles should be kept as low as possible[17]. The degree of agglomeration may be greater with nano-particles due their high inter-particle adhesion in comparison to conventional powders[67].

From the above discussion it is clear that the incorporation of inert particles is likely to reduce the final density of the composite. In the case of nano-particles, the large surface area to volume ratio makes them highly susceptible to impurity uptake and oxide layer formation[67]. Table 2.3 gives an indication of the density reduction by different particle volume fractions principally for silicon carbide and silver; others are presented for comparison. It has generally been reported that a higher

sintering temperature is required to achieve the same composite density in order to overcome the inhibition in densification with silicon carbide[39, 68].

Table 2.3: Reported densities for various ceramic-inclusion systems.

The values in parentheses indicate the reported monolithic density for that system.

Comments	Density achieved (% Theoretical)	Reference
Barium titanate		
BaTiO$_3$ Hot pressed 1300°C	99.5	1, 69
Silicon Carbide		
BaTiO$_3$-5vol% SiC at 1300°C Hot pressed	96	1, 40, 41
Al$_2$O$_3$-5vol% SiC/ 1600°C, 11vol% SiC/ 1700°C	~100	6
Al$_2$O$_3$-10vol% SiC/ 1700°C	96.1	37
Al$_2$O$_3$-10vol% SiC/ 1800°C	[98] 85	36
MgO-10vol% SiC/ 1700°C, 20vol% SiC/ 1800°C	~100	6
Silver		
Al$_2$O$_3$-10vol% Ag/ 1700°C, 14vol% Ag/ 1700°C	[98.6] 97.4, 93.7	46
BaTiO$_3$-10vol% Ag/ 1290°C	91.5	70
PZT-10vol% Ag/ 900°C	[89], 93	50
Platinum		
PZT/1150°C	98.5	15
PZT-1vol% Pt/ 1150°C	97.2	15

For metal systems, sintering above the melting point has been reported both as prohibiting[8] and enhancing[14, 50, 71] densification. A reduction in densification can be explained if the wetting of the matrix by the molten second phase is poor and the matrix-particle solubility is negligible. Molten metal is therefore not an effective liquid phase sintering aid[8] or there is an increase in diffusion distance[47, 70]. Benefits have been suggested, however, from the reduction of grain boundary movement, allowing a refined microstructure[71].

Densification can be adversely affected by gas production and entrapment in closed pores[38]. In addition to gas formation from the generation of reaction phases, gaseous products can also arise from poor sintering regimes. A binder, incorporated to aid specimen consolidation, is normally burnt out at low temperatures (150-300°C). If carbonaceous material becomes sealed off from the

air before oxidation is complete it can act as a reducing agent at high temperatures. High heating rates can cause blistering and bloating of the sample as the gas pressure increases with temperature[33].

2.3.b   GRAIN SIZE

The final grain size of the composite is an important parameter as it has consequences for the mechanical and electrical properties, see Sections 2.4 and 2.5, respectively. Immobile particles make mass transport from the front of the particle to its rear difficult, due to high matrix-particle bond strength. If the particles are immobile they are unaffected by grain boundary movement and will retain their initial distribution within the matrix. Strong directional covalent bonding, such as in Al_2O_3-SiC, inhibits sintering by hindering grain boundary diffusion[34].

The driving force for grain growth changes during the sintering process and the rate of sintering is often related to the rate of shrinkage with temperature. This information is collected from dilatometry, Chapter 4 and Appendix IV, and indicates two sintering maxima for barium titanate at 1250°C and 1320°C [72]. The high temperature peak belongs to liquid phase sintering at the eutectic[72].

In addition to influencing the sintering rate, a non-uniform second phase distribution can result in the formation of a bimodal matrix grain size distribution[72]. Pure barium titanate has been reported to produce a bimodal grain structure above 1300°C with normally sized 2-4 μm grains and abnormal grains larger than 100 μm [41]. This is likely to be due to the presence of a liquid phase, especially for barium oxide excess above 1250°C [73]. With the addition of silicon carbide the small particles may act as nuclei, in the presence of a liquid phase, for abnormal grain growth[41]. It has been reported that a small amount of silver (0.3wt%) can increase both the size and number of abnormal grains in barium titanate[47], whilst another report suggests a decrease occurs for higher silver contents, Table 2.4. This may be as the distribution of the secondary phase at low volume fractions can be non-uniform resulting in abnormal grains[49]. Abnormal grain growth has been reported to worsen the mechanical properties[68].

Table 2.4: Percentage of abnormal grains in barium titanate-silver composites[70]

Vol% silver	0	0.5	5	10
Area % abnormal grains	76	78	55	30

The reported average grain size for the barium titanate matrix varies depending on the processing conditions. In some cases longer dwell times have been used to produce composites of a desired grain size[69]. The grain size is an important factor for the determination of properties and restricting grain growth can be undertaken to enhance these properties. Methods of reducing grain growth include[25];

    i.   insoluble element doping,

    ii.   grain boundary contamination,

    iii.   composite formation at grain boundary,

    iv.   sintering under pressure,

    v.   adding a growth inhibitor, such as Nb_2O_5, ZnO, Nd_2O_3[74].

As considerable research has been focused on structural ceramics, these have been included for information in Table 2.5, which shows the change in grain size with the addition of a secondary phase. It has been suggested that the inhibition of grain growth in the silver systems (Al_2O_3-Ag and $BaTiO_3$-Ag) is due to poor matrix wetting by the metal phase[46].

Table 2.5: Effect of inclusions on the monolithic matrix grain size. HP = Hot Pressed.

Matrix	Inclusion	Monolithic grain size (μm)	Composite grain size (μm)/ vol% inclusion	Reference
Al_2O_3	SiC	3.2	5.4/ 5, HP=4.2/5	75
Al_2O_3	SiC	2.9, 2.64, 7.61	2.4/ 10, 1.45/ 10, 1.83/ 20	36,39, 68
MgO	$BaTiO_3$	10	<1/ 20	31
$BaTiO_3$	SiC	2, 1-2, 1-2, 1.35	0.4/ 5, 0.35/ 5, <0.32/ 10, 0.31/ 10	1, 40, 41, 76&77
Al_2O_3	Ag	5	2.5/ 18	46
PZT	Ag	1-1.5	No change/ 10	48
$BaTiO_3$	Ag	19.9	13.4/ 10	70
PZT	Pt	1.6	2/ 1	15

The location and size of the inclusions has also been studied. The barium titanate-silicon carbide system with a uniform second phase distribution has been observed with large particles at the grain boundaries[4, 40] and those of approximately 30 nm in the matrix grains[78]. It has generally been found in many different systems that the smaller particles are situated within the grains, whilst large inclusions are observed at the grain boundaries[1, 16, 31, 40, 41, 63, 77]. It has been proposed that the finer

particles have broken away from the grain boundary pinning force, like pores trapped in the matrix[41]. Some reports on alumina-silicon carbide state that most of the silicon carbide particles are intragranular[68, 79], and this is due to their small size (70 nm[79]). The size of the particles at each location varies and Table 2.6 presents some reported values.

Table 2.6: Comparison of intra- and inter-particle size in different composites.

Matrix	Inclusion	Intra-particle size (nm)	Inter-particle size (nm)	Reference
Al_2O_3	SiC	20, -	300, 20-150	3, 37
MgO	$BaTiO_3$	240	500	16, 32
Al_2O_3	Ni	80	118	80
PZT	Pt	<100	>100	15

In terms of the number of inclusions at each location a few studies, mainly with alumina-silicon carbide, have indicated that the percentage of silicon carbide particles at grain boundaries increases with content[31], Table 2.7. Winn *et al*[81] suggested that increasing the silicon carbide content increases the fraction of grain boundary particles. It has been proposed, however, that this depends on the initial silicon carbide size[37].

Table 2.7: Percentage of intergranular and intragranular particles for Al_2O_3-SiC[10].

Vol%SiC	% Intergranular	% Intergranular
5	11	89
10	28	72
20	63	37
30	60	40

Annealing or a higher sintering temperature of the composites has been observed to cause inclusions to agglomerate[12, 71]. The silver inclusion size has been observed, in general, to increase in size with increasing inclusion content, Table 2.8. This is expected to be due to the molten state of the silver at the sintering temperature that enhances diffusion. The larger silver particles grow in size as they have a lower overall energy (lower surface area to volume ratio) than the smaller particles.

Table 2.8: Silver inclusion size at low and high silver volume contents.

Matrix	Low silver content	High silver content	Reference
Al_2O_3	2.7 μm (5vol% silver)	3.1 μm (18vol% silver)	46
PZT	0.7 μm (1vol% silver)	1.4 μm (10vol% silver)	48
$BaTiO_3$	3.3 μm (0.5vol% silver)	1.5 μm (10vol% silver)	70
$BaTiO_3$	1 μm (0.05vol% silver)	3 μm (1vol% silver)	49

In summary, it appears that the grain size may be reduced by the incorporation of a second phase, which causes pinning of the grain boundaries during densification. Silicon carbide is a good grain boundary controller and microstructural modifier[23]. The metallic particles are generally uniformly dispersed within the material, rather than forming a thin elongated metal foil[51]. Larger inclusions are located at the grain boundaries and grain junctions with smaller particles situated inside the grains. The size of low melting point particles is affected by agglomeration at elevated temperature[49, 82] and the particle content present (possibly only in metallic systems).

2.3.c   CRYSTAL STRUCTURE

In order that electroceramics, such as barium titanate, can show piezoelectric behaviour the crystal structure of the grains must be non-centro-symmetric. For barium titanate a change in crystal structure from the normal tetragonal configuration to paraelectric cubic has been observed to occur with:

i.   a reducing atmosphere during sintering, such as argon[40],

ii.   inclusion incorporation, such as silicon carbide[1, 41, 76, 77, 83],

iii.   ion substitution[53],

iv.   grain size reduction[32, 84].

The first has been explained by an increase in the number of oxygen vacancies that result in crystal structure disorder. The proposed explanation for the role of inclusions is the reduction in grain size, Section 2.3.b. A change to a pseudo-cubic structure has been reported to occur above 3vol% silicon carbide[1, 77, 83]. Reactions between the matrix and particles are undesirable but some solubility may lead to a crystal structure change through ion substitution, as reported for nickel[53]. This is often the case if the ionic radii are similar, for example nickel, Ni^{2+}(0.70 A); can substitute for Ti^{4+}(0.61 A)[53].

Arlt[84] observed a decrease in the c/a ratio with a reduction in grain size that may be due to unrelieved internal stresses. For the barium titanate system the crystal structure is influenced by the grain size and this can be observed in the X-ray diffraction pattern, Figure 2.11, where decreasing the grain size reduces the tetragonality. A non-tetragonal crystal structure will inhibit the formation of domains, due to fewer polarisation directions, and therefore the piezoelectric response.
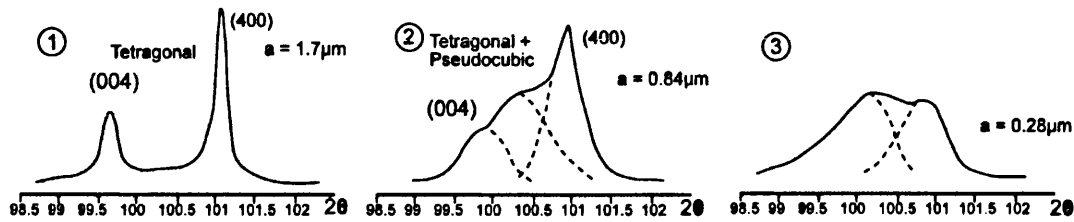
Figure 2.11: X-ray diffraction peak modification for barium titanate indicating a change in crystal structure for different grain sizes, (1) 1.7 μm, (2) 0.84 μm and (3) 0.28 μm[84].

2.3.d   REACTION PHASES

Many composite systems have been studied, such as MgO-$BaTiO_3$[16, 31, 32], MgO-PZT[85], PZT-Ag[12, 48, 50], $BaTiO_3$-SiC[1, 40, 77], Si_3N_4-SiC[35], Al_2O_3-Ag[46], Al_2O_3-Ni[54], $BaTiO_3$-Ag[70], PZT-Pt[15], and in general no reactions have been reported for low inclusion contents. In spite of this, reactions may still occur, as X-ray diffraction analysis cannot resolve contents below 5vol% due to background noise. While the inertness of silver is suitable for composite production, silicon carbide may react to form an undesirable glassy phase. The formation of a glassy phase during the sintering of even pure barium titanate would cause major problems during the sintering of a nano-composite as the liquid phase can act as a medium for reaction phases and even be one itself. A liquid phase is possible in the TiO_2-BaO system due to the eutectic at 1312°C. Sintering above this temperature causes discontinuous grain growth[41] by increased diffusion in the liquid phase. A number of different compounds can be formed with either excess of TiO_2 or BaO, as shown in Figure 2.12.
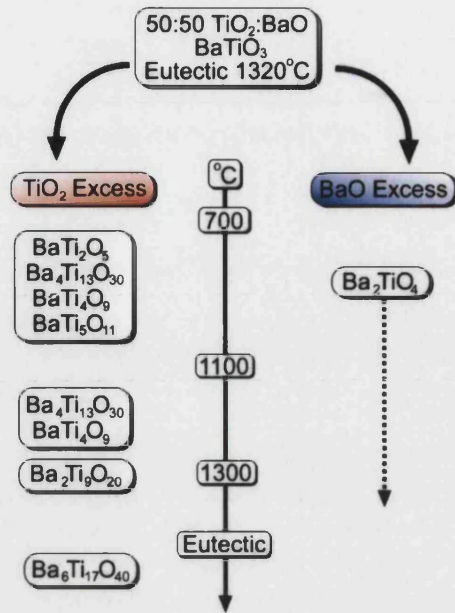
Figure 2.12: Possible non-ferroelectric reaction phases generated with

a non-stoichiometric BaO-TiO$_2$ composition[23, 41, 60, 62].

With the incorporation of silicon carbide into the matrix, there is further potential for phases to be generated. The silicon carbide may be oxidised to silicon dioxide, silica, during the processing of barium titanate in an oxygen containing atmosphere[76]. The silica layer is considered to be protective and reduces the rate of silicon carbide particle oxidation[86]. Figure 2.13 shows, however, that at about 1400°C the silica becomes more thermodynamically stable in comparison to the silicon carbide particles so sintering should be carried out below this temperature to hinder silica formation.
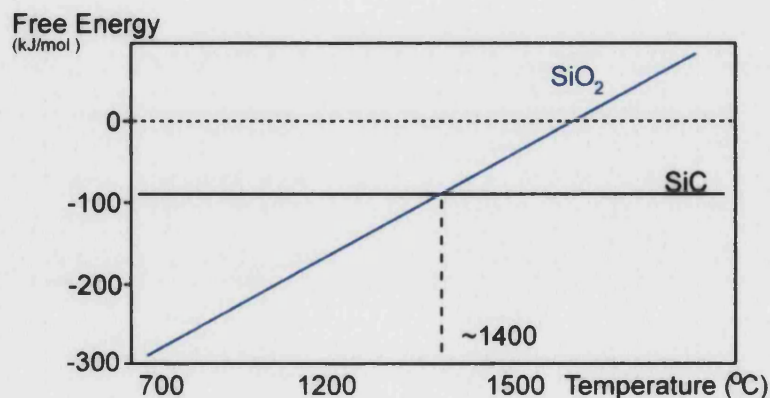
Figure 2.13: Representation of the free energy versus temperature for silica and silicon carbide[86].

It has been reported that a 0.3-0.4 μm silica coating is effective in suppressing thermal decomposition of silicon carbide[87]. Due to the small size of the nano-particles, however, it is

possible that they will be completely transformed to silica during processing. Particle oxidation may occur by reaction of the thin oxide layer, of approximately 1 nm thickness, under slow heating rates, via equation 2.1.

$$SiC_{(s)} + 2SiO_{2(l)} \rightarrow 3SiO_{(g)} + CO_{(g)} \qquad \{2.1\}^{37}$$

In this way the silicon carbide can be completely lost by continual oxidation of the silicon carbide surface. This reaction causes the production of a gaseous product, carbon monoxide, which can cause the sample to become bloated, when the gas effusion from the sample is poor, decreasing the density. The presence of this oxide layer on the silicon carbide may be removed by etching the particles in 20vol% HF for 24 hours. However, re-oxidation will occur in the presence of an oxidising sintering atmosphere[42]. It appears that silica will always be present when processing barium titanate-silicon carbide composites. The formation of excess silica via such reactions will modify the mechanical properties, as it will tend to be located at triple point pockets forming glassy flaws[37]. A thin glassy phase can be beneficial by bonding adjacent matrix grains, however, liquid phase sintering will give a wider range of grain sizes[23].

The use of a protective atmosphere has been proposed to prevent silicon carbide oxidation. Reports suggest that a suitable atmosphere is difficult to attain as even an inert atmosphere may allow the carbide to react with residual oxygen in the specimen, whilst a vacuum may cause silicon carbide leaching by active oxidation by the low oxygen partial pressure[36]. Hot pressing is a likely candidate due to lower processing temperatures[3], but difficulties arise from the possibility of barium titanate reduction by the graphite die.

In barium titanate it has been reported by Hwang that no unwanted phases are generated with less than three volume percent of silicon carbide[1]. The formation of $Ba_2TiSi_2O_8$ above 800°C [62], however, has been reported with the addition of 5vol% silicon carbide to barium titanate[40, 41]. Fresnoite, $Ba_2TiSi_2O_8$ is a constituent of the $BaO\text{-}SiO_2\text{-}TiO_2$ (46-24-30 at%) eutectic at 1245°C [62], with a melting point of 1440°C [88]. This compound has a density of 4.43 g/cm³, is greenish/yellow[89] and is formed from the silica reacting with barium titanate, equation 2.2.

$$2BaTiO_{3(s)} + 2SiO_{2(l)} \rightarrow Ba_2TiSi_2O_{8(s)} + TiO_{2(s)} \qquad \{2.2\}$$
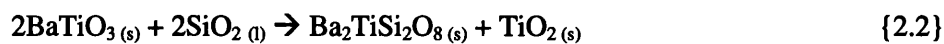
A ternary eutectic exists containing fresnoite, barium titanate and $Ba_6Ti_{17}O_{40}$ at approximately 1260°C [90] or 1195°C [91]. The temperature for liquid phase sintering can thus be reduced, in the presence of silica, from, the barium titanate eutectic temperature (~1320°C), to that required to form the ternary eutectic[90].

Some reactions have been reported for metal inclusions in barium titanate, such as tungsten, which may produce a $BaWO_4$ reaction phase above 1250°C [53].

2.3.e   SUMMARY OF PARTICLE EFFECTS ON MICROSTRUCTURE

The addition of non-metallic inclusions, such as silicon carbide, and metallic inclusions, such as silver, to a ceramic matrix is reported to decrease the density of the monolithic ceramic. The grain size is typically reduced by the presence of the inclusions as strong particle-matrix interface bonding can hinder grain boundary movement. The addition of nano-particles could cause the generation of agglomerates due to their high surface to volume ratio. A transformation from the tetragonal to pseudo-cubic structure has been reported, but is considered undesirable for functional piezoelectric materials as it reduces the number of domains available to contribute to sample polarisation. Formation of reaction phases is also possible, especially with silicon carbide, however, their formation has not been heavily reported.

2.4 MECHANICAL PROPERTIES OF PARTICULATE-BASED COMPOSITES

This section presents information concerning the strength, toughness, residual stresses, hardness and elastic modulus. In general the manufacture of structural ceramics is concerned with improving their reliability by toughening processes or flaw control. In service, flaws cause premature failure when greater than 50 μm in length[92], depending on the application. The optimisation of toughness (the presence of many energy dissipation methods) and strength (the reduction of weak points) typically involve different microstructures[93]. Strong and tough ceramics have been proposed with the use of hybrid nano-metre/micro-metre reinforcement[25].

The majority of the materials studied concerned the modification of structural ceramics, such as alumina, with considerably less research on the mechanical properties of the electroceramics, such

as barium titanate. Thus the collated information is mainly in regard to structural ceramics, which is in general transferable to electroceramics. It has been reported, however, that the actual property improvements depend on the composite system[94]. Results for electroceramics are given where possible, in conjunction with structural ceramic values for comparison.

Ferroelectric ceramics are generally developed from considerations of electrical response. Consequently many display poor mechanical properties. In some respects the mechanical failure strength is irrelevant, as by the time the component experiences stresses approaching the failure stress it has long since lost any useful piezoelectric properties. There may, however, be regions of high stress, particularly at edges and surfaces, and piezoelectrics are known to be generally weak in shear. It has been reported that stresses of magnitude 30-50 MPa can be generated in a capacitor during end termination and soldering[70]. Many of these issues have been surmounted in the field of structural ceramics, whilst the requirement in electroceramics is to improve piezoelectric and dielectric performance[95]. The electrical-mechanical coupling in piezoelectric materials complicates the situation as hard electrical loading over long periods can cause cracking by the accumulation of mechanical damage. The presence of cracks can cause local electric field concentrations that subsequently seriously degrade electrical performance[96].

The first subsection relates to the modification of strength by the addition of particles, while the second focuses on the change of toughness with particle additions. Residual stresses influence both the strength and toughness properties and as such have been considered in more detail in the third subsection.

2.4.a   STRENGTH

Ultimate strength is the maximum load attained per unit original cross-sectional of the sample. The theoretical strength of materials is discussed in Appendix II and indicates that flaws in the material determine the practical strength. A considerable number of composite systems have been examined, such as Al_2O_3-Si_3N_4[94] and MgO-SiC[4] and strength improvements reported with non-metallic (Table 2.9) and metallic inclusions (Table 2.10).

Table 2.9: Monolithic and composite strengths for various ceramic-non-metallic systems
(HP=Hot pressed).

Matrix	Inclusion material/ vol%	Monolithic strength (MPa)	Composite strength (MPa)	Reference
Al_2O_3	SiC/ 5	350	1520 (annealed)	4, 34
Al_2O_3	SiC/ 5, 10	350	467, 415	68
Al_2O_3	SiC/ 10, 33	355	1017, 870	6
Al_2O_3	Si_3N_4/ NP	350	850	4, 94
MgO	SiC/ NP	348	700	4, 94
MgO	$BaTiO_3$/ 20	410 (HP)	600 (HP)	16
Si_3N_4	SiC/ 10	850	990	35
PZT	Al_2O_3/ 0.1	69	103	11
PZT	Al_2O_3/ 1	93	106	13
$BaTiO_3$	SiC/ 5	174	305	1, 41
$BaTiO_3$	SiC/ 3, 10	145	350, 303	77

The strength of structural ceramics (alumina) and electroceramics (PZT and $BaTiO_3$) can be enhanced with the addition of non-metallic particles. Improvements are generally in the range of a 10-100% increase in strength. With the addition of metallic particles, Table 2.10, the measured strength also increases, however, in some cases such as the alumina-nickel composite and barium titanate-silver, the improvement is considerably smaller.

Table 2.10: Monolithic and composite strengths for various ceramic-metal systems.

Matrix	Inclusion material/ vol%	Monolithic strength (MPa)	Composite Strength (MPa)	Reference
Al_2O_3	W/ 5	350	1105	4
Al_2O_3	Mo/ 5	350	920	4
Al_2O_3	Ni/ 5	350, 390	1090, 526	4, 71
Al_2O_3	Ni/ 5, 20	425	400, 150	8
Al_2O_3	Ti/ 5	350	813	4
Al_2O_3	Cu/ 5	370	583	9
Al_2O_3	Ag/ 9, 18	300	450, 400	46
PZT	Ag/ 10	96	169	12, 48
PZT	Ag/ 5, 10	111	167, 179	14
$BaTiO_3$	Ag/ 0.5, 10	53	64, 42	70

The variability in strength is taken into account by the Weibull modulus, m (see Appendix II). A Weibull modulus corresponds to a more homogeneous set of flaws. An increase in m from 6.5 in monolithic alumina to 13.5 with the addition 5%vol silicon carbide has been reported[4]. For PZT-Ag, the monolithic PZT has a Weibull modulus of 9.6, which decreased to 8.7 for 5vol% silver but improved to 11.8 for the 10vol%[14]. This change is not conclusive as it is within experimental error.

2.4.a.i   *Influence of non-metallic inclusions on strength*

Niihara describes the processing of alumina by ball-milling with the addition of silicon carbide, SiC, of particle diameter below 300 nm[34]. He observed that the microstructure contained intragranular and intergranular silicon carbide particles and a reduced grain size. It was reported that 5vol% silicon carbide increased the strength by three times in comparison to the monolithic alumina and could be increased to 1500 MPa by annealing (see Table 2.9). Other researchers have also observed improvements in strength but of considerably lower values than those reported by Niihara. It has also been noted that the strength begins to decrease at high contents of non-metallic particles[6, 68, 77], possibly due to a build up of residual stress[97] or an increase in porosity. A peak in the strength is observed with increasing sintering temperature that indicates a balance between improved density at higher temperatures and the grain coarsening that effectively increases the critical flaw size, Figure 2.14. This is assuming there are no effects from reaction phases formed at the higher temperature.
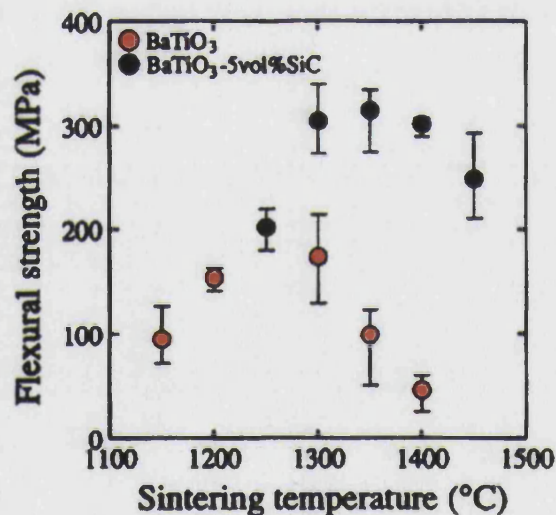
Figure 2.14: Flexural strength of monolithic $BaTiO_3$ and $BaTiO_3$-5vol% silicon carbide as

a function of sintering temperature[1].

28

2.4.a.ii   Annealing

Annealing (elevated temperature soak) has been reported to further improve the strength[71] with healing of near-surface cracks as the proposed mechanism[6]. A ~50% increase in strength has been reported with the annealing of Al_2O_3-5vol% silicon carbide (see Table 2.9). Observation using Transmission Electron Microscopy (TEM) indicates dislocation pinning and pile-up by intragranular particles[4]. These dislocations are generated during the cooling part of the sintering cycle. It has also been suggested that annealing develops these dislocation networks into sub-grain boundaries[4, 6, 34] and that these dislocation networks have a minor role[3]. In the metallic Al_2O_3-Ni and Al_2O_3-Ag systems a reduction in strength on annealing is suggested to be due to particle agglomeration at grain boundaries and the effect of the softer metal at high volume contents. This is particularly the case for low melting point metals due to their rapid diffusion[9].

2.4.a.iii   Influence of metallic inclusions on strength

The addition of silver particles has been reported to increase the strength of PZT due to reduction of internal stress[50]. Ductile particles can accommodate strain by plastic deformation and so reduce the internal stresses that are present[82]. A strength decrease of 40% has been reported for the incorporation of silver in a zirconia toughened Al_2O_3[51]. This disparity in results has been assigned to the existence of a critical particle size. Above a certain particle size (2 μm [8], 2.7 μm [51]) the stress generated by the differences in thermal expansion coefficient of the matrix and the inclusion is sufficient to generate cracks. A large amount of particle strain before fracture, coupled with good interface bonding is desirable. The maximum strength value depends on the particle yield strength[97].

2.4.a.iv   Porosity

Hindrance of densification by particles increases the importance of porosity, which can act as a critical flaw. Equation 2.3 is a simple relationship between the porosity fraction, p, and strength, σ.

$$\sigma = \sigma_0 e^{-(\beta\, p)}$$ {2.3}[66],

where σ_0 is the zero porosity strength value and β is a constant. Continuous pore channels are generally present above 10%vol porosity and isolated pores below this value[98]. Porosity acts as a

stress concentrator, but can prevent crack propagation by increasing the crack tip radius[33], effectively blunting it.

The addition of isolated inclusions reduces the porosity, as the small inclusions take up positions in the interstices of the matrix particles in the green state. If the particles are not effectively dispersed the porosity can be increased due to the formation of agglomerates. Rigid agglomerates of particles resist consolidation and result in open pores that can fill with glassy phases and gases creating flaws[37], Figure 2.10.

2.4.a.v   Grain refinement

Grain refinement to reduce the critical flaw size has been reported by many researchers, such as with the addition of silicon carbide particles[1, 4, 6, 16, 40, 65, 72, 76]. A grain size reduction of ten times has been reported for alumina-5%vol silicon carbide in comparison to monolithic alumina[4]. The retardation of grain growth by particles hinges on their interaction with grain boundaries. After powder pressing the nano-sized silicon carbide particles are situated randomly in the green matrix compact. As sintering progresses the grains will grow unaffected until the grain boundaries impinge on the particles. At this stage the interface bonding between the matrix and particle is critical and a strong bond, as in the alumina-silicon carbide system, will mean that that the particles are immobile and retain their initial distribution[34]. This is due to the high bond strength making it thermodynamically unfavourable for matter to be transported from one side of the particle to the other. The rapid diffusion along the grain boundaries becomes impeded by the particles that are now situated intergranularly, and sintering rests with the slower bulk diffusion. The interface between the particles and matrix becomes more important with regard to the strength as the particle volume fraction increases. The upper strength limit occurs when there is perfect bonding at the interface, with the lower limit being when there is no interface bonding[99].

To produce a nano-scale grain size would require manufacturing methods that hinder grain coarsening. Grain coarsening has a high thermodynamic driving force at this scale, as the small grains are metastable due to their high surface area to volume ratio. Fortunately, in this case, it has been observed that a second phase can inhibit coarsening[93]. The Zener relationship, where grain boundaries become pinned by particles, has been proposed to account for this outcome. The Hall-Petch equation relates the Zener grain size, d, to the ceramic strength, as in equation 2.4.

$$\sigma = \sigma_0 + kd^{-0.5}$$ {2.4}[3, 66]

σ_0 is the monolithic strength and k a constant. The strength is determined by the critical flaw size, and this may not be the grain size, but due to pores and particle agglomerates.

A reduction in grain size can lower the internal stresses that are associated with anisotropic thermal expansion, as these can be relieved more easily by small changes in many grains[100]. It is suggested that this internal stress reduces the strength and is discussed in more detail in Section 2.4.d, with a basis of residual stresses given in Appendix II.

The incorporation of a nano-scale second phase has been reported to be a more effective method for improvement of the mechanical properties than elemental doping[101]. While doping may affect the dimensions of the unit cell, it is unsuitable for producing a microstructure capable of affecting crack propagation.

2.4.a.vi   Surface condition

It has been proposed that the ceramic strength is largely determined by its surface condition[102]. Machining induced surface stresses have attracted considerable analysis, but it has been reported that the residual stresses induced are not a major contributor to strength modification. The improvement in strength, in these studies, may in some part come from the improved processing that reduces the size and density of defects[3]. The sample preparation conducted in the literature is given in Appendix III.

2.4.a.vii   Grain keying

While grain size is an important factor it has been proposed that inclusions can aid grain keying[92]. This is where particles, of sufficient strength, inhibit grains from sliding over each other. This process is more important at elevated temperatures where creep may be reduced.

2.4.a.viii   Effect of poling

The effect of applying a dc voltage, across the sample, in the poling direction has been observed to marginally improve the strength in that direction[95, 103]. This may be due to the closure of cracks that are perpendicular to the electric field. Crack closure can result from domain switching due to the applied electric field in the local crack vicinity, so that their c-axis is perpendicular to the crack

direction. Internal stress that may have previously prevented the formation or movement of domains is then relieved by the presence of the crack. No difference was observed between open and short circuit configurations[95].

In summary the main improvements in strength, afforded by inclusion addition, are due to grain refinement and flaw size reduction. As the volume content of particles increases the strength can decrease due to increased agglomeration and production of flaws.

2.4.b   TOUGHNESS

Toughness is the material's resistance to fracture from a pre-existing defect, such as a crack. Appendix II gives an outline of the primary and secondary toughening mechanisms possible in composites. This subsection presents tables that summarise published results with non-metallic and metallic inclusions. The influence of these particles on the toughness is then discussed.

The reported toughening results for inclusions incorporated in to a ceramic matrix are given for non-metallic particles in Table 2.11, and for metallic particles in Table 2.12. Toughness improvements are observed with the addition of non-metallic and metallic particles in structural and electroceramic matrices. A considerable increase in toughness has been reported for many of the structural ceramics, whilst the improvement for the electroceramics is moderate. Experimental errors in the range of 0.1-0.3 $MPa.m^{0.5}$ have been reported[75, 79].

Table 2.11: Toughness of ceramic monoliths and ceramic-non-metallic particle composites.

Matrix	Inclusion / Vol%	Monolithic toughness $(MPa.m^{0.5})$	Composite toughness $(MPa.m^{0.5})$	Reference
Al_2O_3	SiC/ 5	3.25, 3.5	4.7, 4.8	6, 4
Al_2O_3	SiC/ 5	3.5	3.8	79
Al_2O_3	SiC/ 5	2.9	2.7, (3.6 Hot pressed)	75
Al_2O_3	SiC/ 5, 10	3.25	4.7, 3.8	68
MgO	SiC/ 5	1.2	4.5	4
Si_3N_4	SiC/ 5, 10	7.2	7, 6.2	35
$BaTiO_3$	SiC/ 5	0.86	1.2	1, 77

Table 2.12: Toughness of ceramic monoliths and ceramic-metallic particle composites.

Matrix	Inclusion / Vol%	Monolithic toughness $(MPa.m^{0.5})$	Composite toughness $(MPa.m^{0.5})$	Reference
Al_2O_3	W/ 5	3.5	4	4
Al_2O_3	Mo/ 5	3.5	7.2	4
Al_2O_3	Ni/ 5	3.5, 3.6	4.5, 4.2	4, 71
Al_2O_3	Ti/ 5	3.5	4.3	4
PZT	Pt/ 1	1.23	1.31	15
PZT	Ag/ 10	0.7, 1	1.1, 1.5	12, 50

The addition of particles can generate, or improve, existing toughening mechanisms. The issues given below have been discussed in the literature.

Crack bridging

The addition of ductile particles can improve fracture toughness and is most likely to be due to the plastic deformation of particles after the crack has passed, producing crack bridging. Bridging has been observed in PZT-5vol% silver[50] and plastic deformation has been proposed in $BaTiO_3$-Ag[70]. In order to activate this process the inclusions need to be firmly bonded to the matrix, otherwise the crack propagates along the weak particle-matrix interface. Large ductile particles are required as generally no significant toughening effect is provided by sub-micrometre inclusions[97]. For inclusions greater than the critical size (2 μm), which have a higher expansion coefficient than the matrix, the induced stress can generate micro-cracking. These micro-cracks can deflect cracks, but reduce the quantity of particle plastic deformation[8], possibly reducing toughness[3]. It has been reported that the contribution to toughness from plastic deformation is related to the square root of the product of inclusion volume fraction and inclusion size and there is a linear increase in the toughness change with this function[46].

The toughness variation with particle addition by particle bridging has been reported by Ohji[94], with the residual stress effects neglected, and are shown in Figure 2.15(a) and (b). The steep gradient below a volume fraction of 0.1 is suggested to be due to the crack propagating through nearest neighbour particles. Practical measurements are typically lower than those predicted as the model assumes that all particles participate.
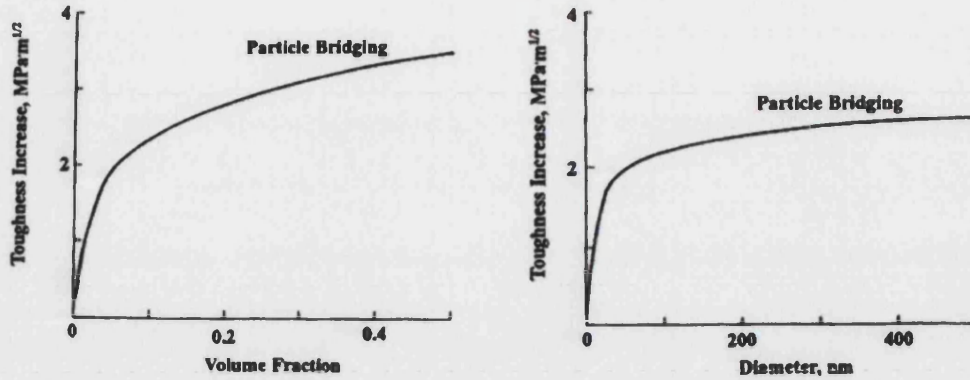
Figure 2.15: (a) Volume fraction dependence of bridging-induced toughness with a particle diameter of 50 nm and (b) particle diameter dependence of bridging-induced toughness with a volume fraction of 0.05[94].

Grain boundary strengthening

Grain boundary strengthening is progressive with particle content as a greater number of boundaries can be strengthened with more particles, especially for creep resistance[35]. A reduction in grain pull-out in Al_2O_3-SiC in comparison to monolithic alumina suggests grain boundary strengthening may occur to some extent in this system[3].

Residual stresses

Residual stress from thermal mismatch of composites constituents may have a negative effect with the crack selecting interfaces that are under residual tension. This negative effect has been observed in alumina where incorporation of silicon carbide causes a change in fracture mode from intergranular to transgranular, however, this could also be due to grain boundary strengthening or the local stress system, Figure 2.16.
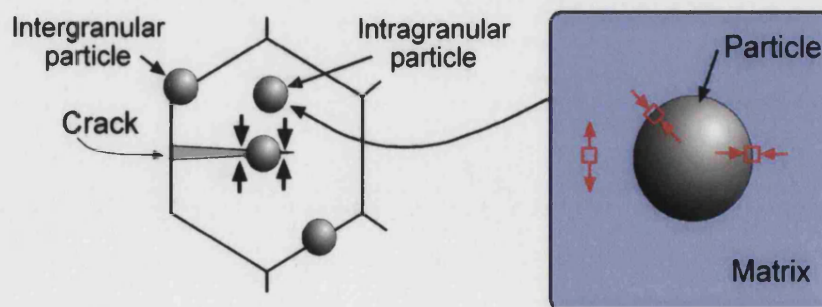
Figure 2.16: Schematic of internal stress, generated by the particle having a lower thermal expansion coefficient to the matrix, surrounding an intragranular particle[94].

The local tangential tension surrounding the intragranular particle (see Section 2.4.d) causes cracks to converge on the particle. Due to the superior diffusion along grain boundaries rather than in the bulk, at lower temperatures, stresses are relieved around intergranular particles more than intragranular particles.

Micro-cracking

An important contribution is expected with the generation of micro-cracks, even though these can reduce mechanical strength[8]. In the alumina-silicon carbide system micro-cracks have been observed to originate from particles greater than 100nm, which suggests that there is a critical particle size[37]. Above this critical size sufficient stress is induced for micro-cracking to occur. The proportion of these particles should be controlled to optimise the toughness. In ferroelectrics, micro-cracks, originating from grain boundaries and propagating into grains, can be caused by the application of high electric fields, which increases internal stress by domain reorientation. Durability may be improved by increasing the coercive field on the material, reducing domain switching, or improving the fracture strength[13]. Micro-cracks have also been reported to extend along grain boundaries, and particle dispersion at grain boundaries can pin these micro-cracks[13, 104]. Although micro-cracking has been proposed, in some cases, crack deflection has been considered the primary mechanism[4].

Crack deflection

Crack deflection can be caused by low fracture energy interfaces[93], either matrix-particle or matrix-matrix. For the alumina-silicon carbide system the particle-matrix interface strength has been reported to be twice that of the matrix-matrix[3]. For particles situated along the grain boundaries the crack may be deflected into the grains[36, 81] or impeded by the high interface strength. Deflection occurs as the crack selects the weakest path through the material. Reaction phases that may be present at interfaces, such as oxides, are therefore important[105]. Metallic inclusions, with an elastic modulus less than the ceramic matrix, that are sufficiently small and strongly bonded to matrix will attract the propagating crack and contribute approximately 0.3 $MPa.m^{0.5}$ to the toughness[9].

Particle shielding

The general concept for the effect of brittle particles on the toughness is that the primary crack is impeded by particles, be they intragranular for transgranular fracture or intergranular for intergranular fracture. This crack then proceeds to bow out between the particles, with no relative crack extension, Figure 2.17. In this case there is crack-tip shielding by the particles, as the primary crack front has not propagated. This shielding occurs until either the particle or matrix-particle interface fractures[94].
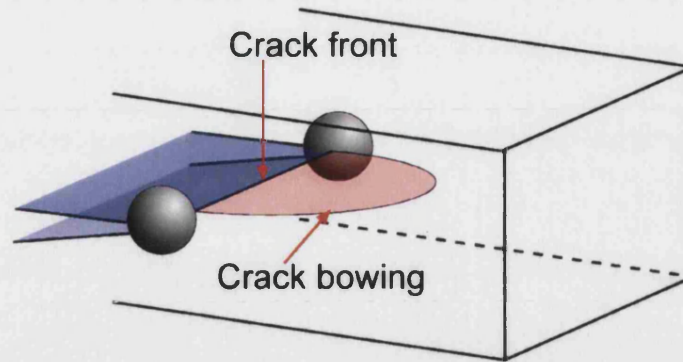
Figure 2.17: Crack bowing with an immobile primary crack front produces a shielded zone.

If the matrix-particle interface bond is strong the shielding zone length can be large. The shielding zone length is short, typically a few hundred nanometres, for small particles. This produces a system where fracture resistance increases rapidly for small crack growth distances[94] and is possible with brittle nano-particles. This resistance can be either via intergranular or transgranular fracture modes.

Due to the number of possible toughening mechanisms an improvement or reduction in toughness can be difficult to assign to a particular type. In a particular composite there may be a balance between mechanisms that decrease toughness, such as matrix average tensile internal stress, and those that improve toughness, for example crack deflection and grain boundary strengthening[3]. The effectiveness of each mechanism can be affected by the size and volume fraction of the incorporated particles.

2.4.c   FRACTURE MODE

The change of fracture mode has already been mentioned in regard to strength (Section 2.4.a) and toughness (Section 2.4.b). Table 2.13 indicates the reported fracture modes for ceramic-inclusion systems indicating changes can occur with non-metallic inclusions, whereas metallic particles do not appear to have any affect. The intergranular to intragranular fracture mode change has been proposed to be from grain boundary strengthening[3, 13, 34, 39]. The change in fracture mode for alumina has been suggested to be from interfacial particles firmly bonding the matrix interfaces[94].

Table 2.13: Fracture modes in ceramic-inclusion systems.

Matrix	Inclusion material	Fracture mode of composite (monolithic)	Reference
Al_2O_3	SiC	Intragranular (intergranular)	6, 34, 39, 68, 75, 81
MgO	$BaTiO_3$	Intragranular & intergranular	31
$BaTiO_3$	SiC	Intragranular (Intragranular, but with an intergranular origin)	41 (69, 104)
PZT	Al_2O_3	Intragranular (Intergranular)	13
Al_2O_3	Ni	No change (Intergranular)	71
PZT	Ag	No change (Intergranular)	12

However, composites also have particles situated in the grains and these could generate residual stress in the grains to cause a change in fracture mode[94]. The crack propagates from one particle to the next, whereas in the monolith it travels along the weaker grain boundaries. There is a modification of the fracture resistance with crack bridging for an assumed equal flaw size, Figure 2.18[94]. This mode change does not equate to a toughness reduction as the transgranular path absorbs more energy[17, 36].
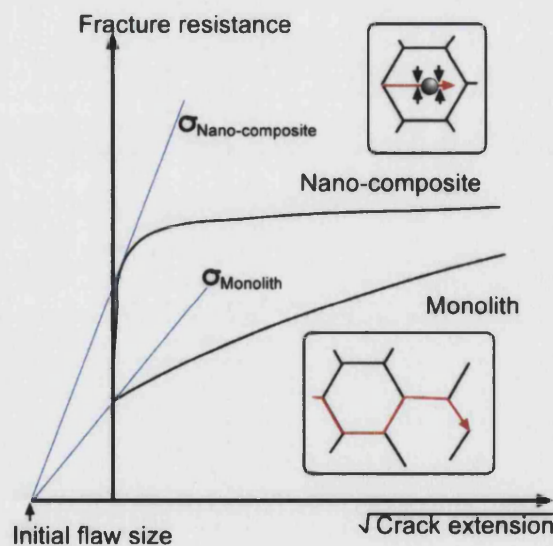
Figure 2.18: Change to intragranular fracture in the composite can improve toughness due to crack bridging. Curve tangent gives material strength[94].

Another possibility for this fracture mode change proposes that the particles strengthen the grain boundaries by forcing the crack to propagate through the grains[36, 106]. This may indeed be the case as transgranular fracture still occurs at elevated temperatures where residual stresses are relieved.

Both these mechanisms may occur simultaneously and the intragranular particles may aid crack pinning[17]. Deflection of cracks to the transgranular mode by intergranular silicon carbide has also been reported in barium titanate[83].

A detailed study of particle location has been reported for the alumina-silicon carbide system and results of the fracture mode are reproduced in Table 2.14. It is apparent that as the volume content of particles increases the proportion at intergranular sites also increases, giving weaker grain boundaries[10].

Table 2.14: Fracture mode and inclusion location in various Al_2O_3-SiC composites[10].

Al_2O_3 %SiC	Fracture Mode (%)		Inclusion location (%)	
	Intergranular	Intragranular	Intergranular	Intragranular
0	89	11	-	-
5	15	85	11	89
10	18	82	28	72
20	43	57	63	37
30	46	54	60	40

With metallic particles no fracture mode change is observed. This suggests that grain boundary strengthening and matrix weakening by residual stresses are not present[39, 71].

2.4.d   RESIDUAL STRESS

An understanding of residual stresses is important as these stresses can influence toughness and strength. Considerable stresses are predicted in the Al_2O_3-SiC and $BaTiO_3$-SiC systems as illustrated in Table 2.15. The equation for the residual stress calculation and a detailed discussion of residual stresses is given in Appendix II.

The predicted values for structural nano-composites, such as in Al_2O_3-SiC, are comparable to the $BaTiO_3$-SiC system, so that any benefits should also be achieved. Examination of these residual stresses shows that in a system where the matrix has the greater CTE a general tensile stress is set-up in the matrix[3, 34, 92, 108] and the particles are compressed. These stresses can be used to control the fracturing of the material as discussed in Section 2.4.c. The high stress that might be developed in the ceramic-metal systems, such as BaTiO3-Ag, are unlikely to occur as the ductile metal will deform relieving some or all of the stress[54].

Table 2.15: Calculated thermal residual stresses for various composite systems.

Composite system		CTE (x10^{-6} m/°C)		Calculated thermal residual stress (MPa)
Al$_2$O$_3$	SiC	8.8^{107}	4^{40}	1400
PZT	Al$_2$O$_3$	13$^{48, 82}$	8.8^{107}	400
PZT	MgO	13$^{48, 82}$	13.5^{107}	40
PZT	SiC	13$^{48, 82}$	4^{40}	900
PZT	Ag	13$^{48, 82}$	28$^{40, 48}$	1300
BaTiO$_3$	SiC	14^{40}	4^{40}	1000
BaTiO$_3$	Ag	14^{40}	28^{40}	1400

Values for E$_{Young}$ and ν can be found in Appendix I, ΔT was taken as 1500 for Al$_2$O$_3$, 1000 for PZT and 1300 for BaTiO$_3$.

2.4.e   HARDNESS

The hardness of a material is a measure of its resistance to indentation. Measurements are typically conducted by applying a predetermined load, through a shaped indentor, onto the sample. A traditional shape is the Vickers indentor that uses a diamond tip. Under sufficient load an indent is made in the sample, the size for a given load being a measure of the hardness. Typically cracks propagate from the indent corners that allow calculation of the materials' toughness (Appendix IV), Figure 2.19. This geometry has the advantage that the indent shape remains constant with changing load.
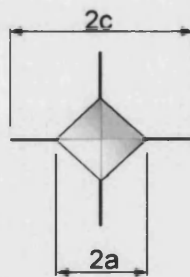
Figure 2.19: Vickers indent diagonal, 2a, and cracks of 2c length.

The Vickers hardness, H$_v$, can be calculated (in GPa) from the indent diagonal, 2a, and applied load, P$_f$, via equation 2.5.

$$H_V = \frac{P_f}{2a^2} \hspace{4cm} \{2.5\}^{109}$$

An increase in hardness with particle additions has been reported in the Si_3N_4-SiC^{66} and hot pressed Al_2O_3-SiC^{75} systems. In particular, addition of 5vol% silicon carbide increased the Vickers hardness of $BaTiO_3$ from 7 GPa in the monolithic form to 9 GPa[41, 77]. The increase is reported to be due to the incorporation of a secondary phase with a higher hardness[17], or a matrix crystal structure variation[41]. For metallic inclusions it is concluded that a decrease in hardness occurs[9, 50, 51], as expected from addition of a softer second phase. A peak in hardness has been reported with 5vol% silver for a PZT-Ag composite, and explained as the incorporation of the silver into the perovskite structure[50].

2.4.f   ELASTIC MODULUS

The elastic modulus is the ratio of stress to strain in the elastic range, where Young's modulus refers to a tensile loading. Increasing porosity, at constant grain size, reduces the materials modulus value[38, 110, 111] and equation 2.6 is a suggested relationship between the Young's modulus, E_{Young}, and porosity volume fraction, p[33, 112]. E_0 is the zero porosity modulus value.

$$E_{Young} = E_0\left(1 - 1.9p + 0.9p^2\right) \hspace{2cm} \{2.6\}$$

The incorporation of non-metallic particles that have a higher stiffness than the matrix increases the Young's modulus of the monolith[17, 105]. The addition of 5vol% silicon carbide in barium titanate has been reported to increase the Young's modulus from 94 GPa to 141 GPa[1, 41]. It was concluded that the enhancement was greater than the rule-of-mixtures estimate due to crystal structure variation[41]. In PZT an increase from the monolithic value of 78 GPa to 91 GPa with 10vol% silver particles has been reported[48], although another report suggested that there is a decrease in the modulus value above 5vol% silver[50]. The addition of nickel to alumina has also been observed to reduce the modulus, with a reduction to 326 GPa for 25vol% nickel from the 392 GPa monolithic value[112]. These decreases are expected from the addition of a lower stiffness second phase.

2.4.g   SUMMARY OF THE MECHANICAL PROPERTIES OF PARTICLE-BASED COMPOSITES

Strength, toughness, hardness and modulus are observed to change with the addition of particles for both non-metallic and metallic dispersants. Benefits have been reported for particle additions of 1-2vol%, however, above this value inferior materials result. It is suggested that the particles cause grain refinement, which improved the mechanical properties. At high particle contents the

presence of the inclusions significantly reduces densification and significant porosity occurs. While recent research has focused on incorporating nano-particles into ferroelectric materials to improve poor mechanical properties, limited work has been undertaken to observe the effect of particle addition on electrical properties of these materials.

2.5 ELECTRICAL PROPERTIES OF PARTICLE-BASED COMPOSITES

This section is concerned with the electrical properties of a dielectric matrix and the modification of these properties with particle addition. In the presence of an electric field a dielectric material experiences no net flow of electric charge, only charge displacement.

2.5.a RELATIVE PERMITTIVITY

2.5.a.i Introduction

The relative permittivity, or dielectric constant, of a material describes the dielectric displacement induced when it is excited by an electric field[23, 18, 33]. Ferroelectrics are generally characterised by a high relative permittivity of 200-10,000, while typical insulators have values of 5-100[22]. Relative permittivity is a measure of the electric dipoles present within the material and their ability to realign in response to an electric field[113]. The relative permittivity is given by equation 2.7, while its definition and contributing factors are discussed in Appendix II.

$$\varepsilon_r = \frac{C\,h}{A\,\varepsilon_0}$$
{2.7}

A is the cross-sectional area of the dielectric medium and h the distance between the plates. The relative permittivity can be calculated by measuring the capacitance, C, of a sample of known dimensions.

2.5.a.ii   *Crystal structure and relative permittivity*

The change in relative permittivity for barium titanate with temperature follows characteristic peaks that correspond to crystal structural changes. Figure 2.20 gives the relative permittivity profile with temperature along both the a and c-axes for barium titanate[114].
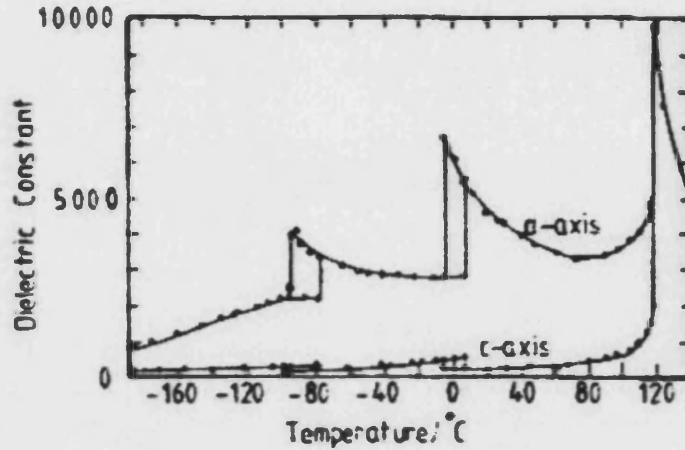
Figure 2.20: Variation of dielectric constant (relative permittivity) for

barium titanate with temperature[114].

A peak in relative permittivity is observed at the Curie temperature, $T_c \sim 120°C$, and at other phase transition temperatures. The highest relative permittivity peak is caused by a maximum in the domain orientation at the cubic-tetragonal phase transition temperature, which is at approximately 130°C in barium titanate[115]. Domains are discussed in more detail in Section 2.5.a.vii. The relative permittivity of single crystal barium titanate is anisotropic with c-axis values of about 400[84] and 230[23] reported, while the a-axis value is considerably greater at 4000[84] and 4770[23]. Polycrystalline materials can have an average relative permittivity calculated due to the random orientation of the grains. The room temperature value for barium titanate has been reported to be in the range of 1500 (or 950-1200[84], 1740[23], ~1600[18]), which is an average of the single crystal constants[116], similar to those given in Figure 2.20. This value has been reported to be composed of a volume effect ($\varepsilon_{r,vol}$) and a domain wall vibration component ($\varepsilon_{r,dom}$), and is described by equation 2.8[84]. The calculated volume contribution is a constant 1000, while the remaining domain wall vibration term increases with poling[117].

$$\varepsilon_r(T) = \varepsilon_{r,vol}(T) + \varepsilon_{r,dom}(T) \qquad \{2.8\}^{84}$$

For grains sizes above 10 μm the domain contribution has been reported to be approximately 700[84], but increases as the grain size is reduced. This is discussed in more detail in Appendix II.

The relative permittivity is affected by variables such as porosity, reaction phases, grain size[118], measurement frequency, impurities and processing conditions[115].

2.5.a.iii   *Porosity and relative permittivity*

An increase in porosity causes a reduction in the relative permittivity[25, 80, 110, 119]. The actual value is a function of the number, shape and relative permittivity of the pore filling substance[18]. A 30% decrease in relative permittivity has been reported for 10% porosity in PZT[110], while another study suggests that porosity has a minimal effect below this value[80]. The relationship between relative permittivity and porosity over a wide temperature range for barium titanate is given by Figure 2.21.
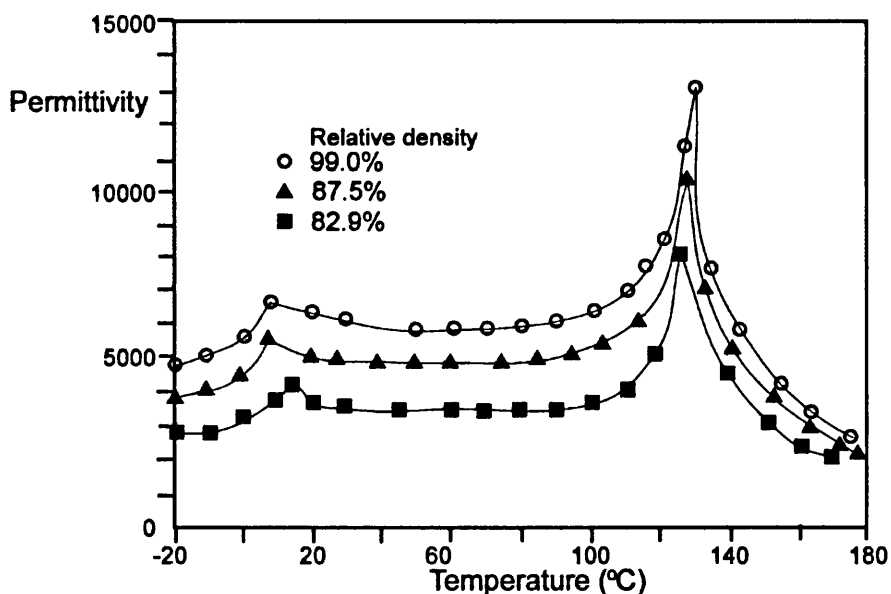
Figure 2.21: Effect of porosity on the relative permittivity of barium titanate[98].

To account for the reduction in relative permittivity with increasing porosity, a lowering of the potential polarisation per unit volume and an increase in the depolarising field have been proposed[110].

2.5.a.iv   *Effect of the inclusion of particles on relative permittivity*

Two different particle types can be added to the dielectric matrix, either non-metallic or metallic.

2.5.a.iv.a   Non-metallic inclusions

Incorporation of non-metallic particles into barium titanate, such as zirconia, can increase the relative permittivity[11, 72], while it diminishes with silicon carbide, Table 2.16[1]. A decrease is expected as the volume fraction of dielectric material has been reduced. The improvement with zirconia addition to $BaTiO_3$ is considered to be due to a substitution of the highly charged titanium ion by a zirconium ion. This produces a shell of modified matrix around each grain that generates internal stress in the pure $BaTiO_3$ core. This doping process has been has been heavily researched[20].

Table 2.16: The effect of silicon carbide addition on the room

temperature relative permittivity of barium titanate at 1 kHz[1].

Vol% silicon carbide	Room temperature relative permittivity (1 kHz)
0	6000
1	3000
5	2000

Piezoelectric particles have also been added to a non-piezoelectric matrix[16, 27, 31, 120] in an attempt to introduce ferroelectric properties. For dispersions of PZT in MgO, as shown in Figure 2.22, a non-linear change in relative permittivity was observed[27]. The relative permittivity increase with PZT addition is greater than that expected from the logarithmic mixture model.
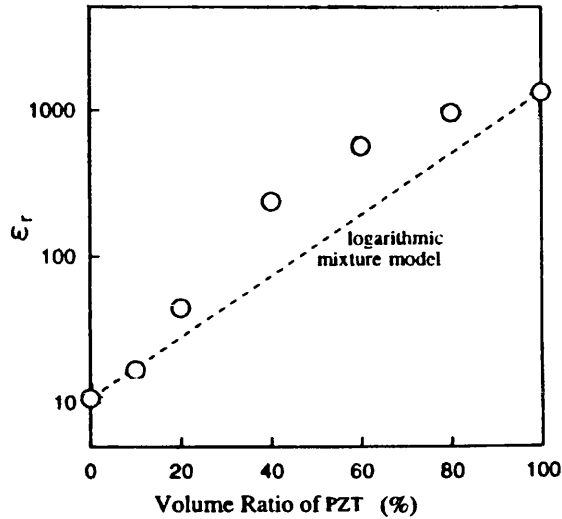
Figure 2.22: Relative permittivity variation in the MgO-PZT system[27].

2.5.a.iv.b   Metallic inclusions

With the incorporation of a metallic phase a decrease in the relative permittivity would be expected from the rule-of-mixtures[12] and equation 2.19. However, the addition of metallic particles, such as nickel, is expected to improve the dielectric response of the composite due to "internal electrode" and effective dielectric field effects[101]. This increase may be due to effective electric fields being developed around the conducting phases[48], or by the apparent shortening of the electrode spacing[121]. This increase follows from a modification of Maxwell's equations for a non-continuous metallic phase[12], equation 2.9.

$$\varepsilon_r = \frac{\varepsilon_{rm}}{\left(1 - V_f\right)^3} \qquad \{2.9\}^{[121, 122]},$$

where ε_{rm} is the relative permittivity for the monolith and V_f the volume fraction of metal inclusions. In the dielectric regime the relative permittivity increases with metal volume fraction[123]. The presence of metallic particles increases the localised field, hence enhancing the charge displacement processes. However, the volume fraction of metallic particles must be kept low or the material will become ineffective as a dielectric. The conductivity is increased, as expected, with the addition of a conductor. Polymer-metallic composites are widely used for electromagnetic shielding and to eliminate the build up of electrostatic charge. When the material transforms from an insulating to a conducting behaviour there is a change in electrical properties of many orders of magnitude within a narrow composition range. This change is termed the percolation phenomenon[124] and is caused by the formation of metallic clusters as the volume approaches a critical value, termed the percolation threshold.

A relative permittivity improvement has also been observed for silica-tungsten, above a composition of 0.2vol% tungsten[125]. The presence of a non-continuous metallic phase of 10vol% silver in PZT has been reported to enhance the relative permittivity;

    i.   to 3000 against the monolithic relative permittivity of 2700[12],

    ii.   to 2560 from the monolithic relative permittivity of 2540[48],

    iii.   at room temperature as shown in Figure 2.23[82].
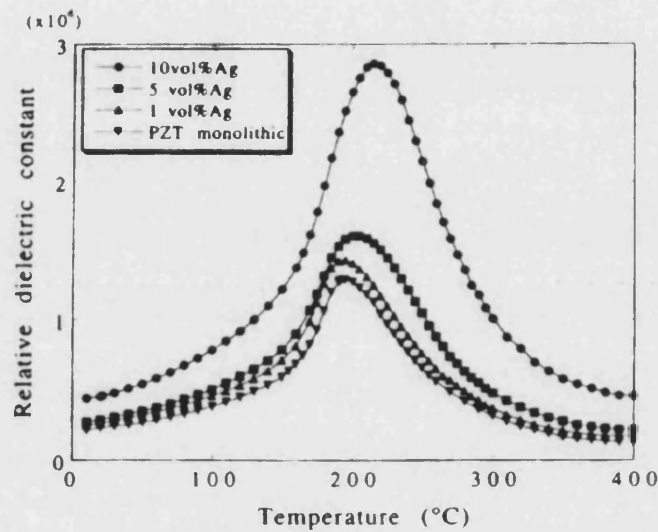
Figure 2.23: Change in the relative permittivity-temperature response

of PZT with the addition of silver particles[82]

In Figure 2.23 the greatest change has occurred near the Curie temperature, with a doubling of the relative permittivity. However, relative permittivity decreases have also been reported, such as the reduction from 1830 to 1784 observed for PZT-1vol% platinum[15]. It has also been reported that in PZT-Ag (produced from Ag_2O) the relative permittivity is decreased, Figure 2.24[14]. In the $BaTiO_3$-Ag system a decrease in relative permittivity[70, 49] has been reported and attributed to interaction of the metallic particles and the ferroelectric domains[106]. With nickel inclusions at 10vol% in barium titanate, a relative permittivity decrease was observed, but at 40vol% a four-fold increase was measured[121].
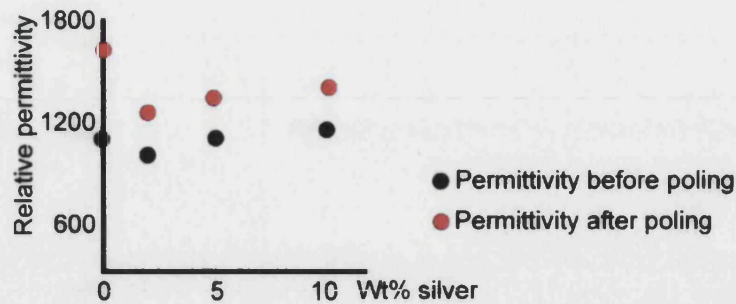
Figure 2.24: Relative permittivity for PZT-Ag (from Ag_2O) before and after poling[14].

2.5.a.v   *Reaction phases and relative permittivity*

Any chemical reactions that could occur between the matrix and the particles are undesirable as they are liable to generate non-ferroelectric phases with a reduced relative permittivity. This factor has limited the production of ferroelectric composites since perovskites react easily with both oxides and non-oxides, generating non-ferroelectric phases[16].

2.5.a.vi   *Grain size and relative permittivity*

A marked change in the relative permittivity with grain size has been reported by many researchers[23, 32, 73, 80, 84, 98, 114, 126, 127]. As early as 1954[99] a relative permittivity value of 3500 was reported for an average grain size of $1\mu m$[84], whilst others have reported nearer 6000[80, 114, 116]. This is in comparison to a value between 1500 and 2000 for grains in the range 20-50 μm [80, 84, 116, 127]. The general trend is shown in Figure 2.25, whereby a peak is present around a grain size of 1 μm [127].
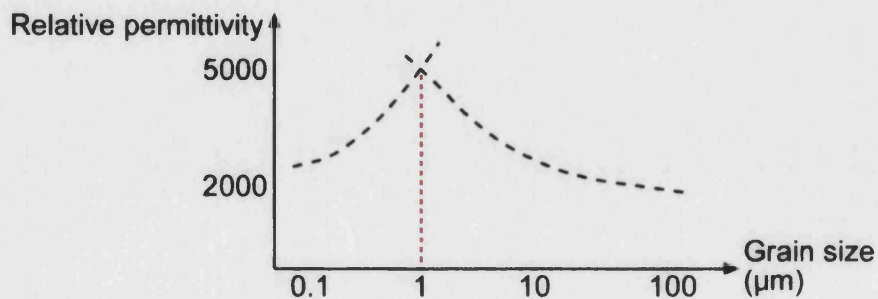
Figure 2.25: Grain size effect on the relative permittivity of barium titanate.

These measured results cannot be explained by averaging the single crystal values[143]. The form of this response and the temperature behaviour is discussed in Appendix II.

2.5.a.vii   Other influences on relative permittivity

Other effects that have been reported to influence the relative permittivity include:

i. Relative permittivity increases of 10-15% have been reported for piezoelectric samples with poling[11, 14, 18], as shown in Figure 2.24. This increase would not be expected if the effect of the poling process were merely an alignment of further 180° domains parallel to the field, but if it is assumed that the poling field relieves part of the clamping stress, by reversal of 180° domains, then an increase is expected[18].

ii. Barium titanate becomes semi-conducting when sintered in a reducing atmosphere, such as argon, and this substantially increases the relative permittivity. Processing of barium titanate-silicon carbide in a reducing atmosphere increases the relative permittivity, which can then be decreased with sample oxidation, Table 2.17[76]. At first glance these results are significant, however, the reducing atmosphere has also increased the conductivity (see Section 2.5.e), which makes them more difficult to pole and of little use in piezoelectric applications.

Table 2.17: Relative permittivity of BaTiO$_3$-SiC before and after an oxidation treatment[76].

Vol% silicon carbide	Reduced atmosphere relative permittivity	Relative permittivity after 3 hours at 1000°C in air (estimated)
0	5465	5400
1	35963	2500
3	26664	2400
5	14382	2400

iii. A distinct change in relative permittivity has been observed between low and high electric field levels in BaTiO$_3$, Figure 2.26. Above a certain threshold field value (200-300 V/cm [128], 56 V/cm [129]) the relative permittivity increases significantly with increasing field. It has been proposed that this behaviour is caused by hysteretic domain wall motion that results in the reorientation of domains[128, 130].

Relative Permittivity
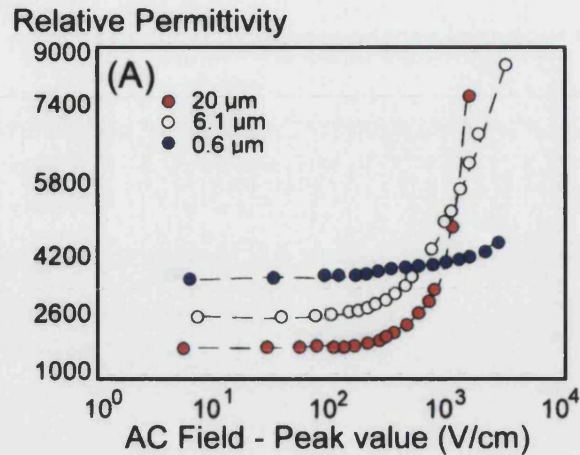
Figure 2.26: Dielectric response of barium titanate as

a function of applied field and grain size[128].

Domain wall motion is suggested to take place over many unit cell distances at high fields in comparison to a fraction of a cell at low fields[128]. Above the Rayleigh threshold, E_t, the relative permittivity is approximately linear with field, and this is known as the Rayleigh region[129]. Most active piezoelectric transducers are used in this region[130]. The behaviour over a large electric field range is shown in Figure 2.27.
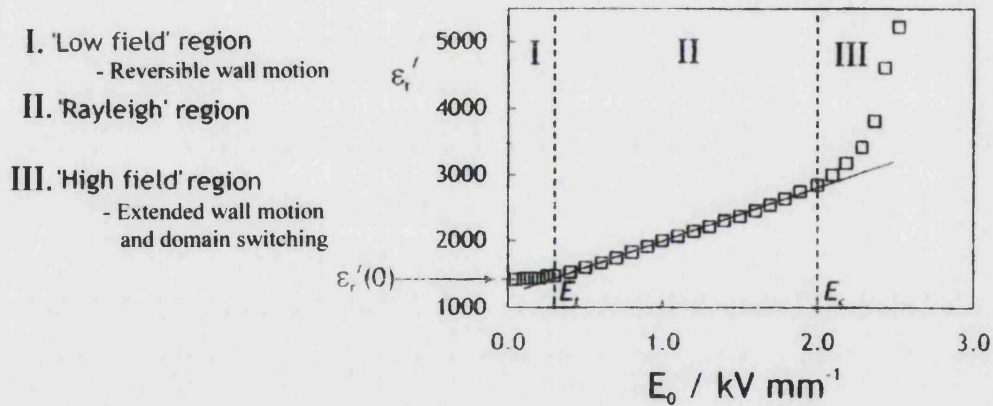
Figure 2.27: The three relative permittivity regimes with applied electric field,

showing the Rayleigh threshold, E_t, and coercive field, E_c. $\varepsilon_r'(0)$ is the

relative permittivity under zero field conditions[130].

The linear response is a reasonable approximation of the functional characteristics of piezoelectric ceramics at low electric field levels, but this approximation becomes increasingly inappropriate as the field and stress levels increase. Typically, a field level of approximately 0.5 kV/mm is necessary for a useful actuation response[131]. Above the

coercive field, E_c, the piezoelectric behaviour is invariably non-linear and strongly hysteretic. In this region the remanant polarisation, coercive field and hysteresis loss are more appropriate to describe the dielectric behaviour than the relative permittivity[130]. Polarisation-field analysis is discussed in Section 2.5.h and background in Appendix II. Above the critical coercive field, domain wall switching occurs and the wall translation contribution is saturated.

iv. There are relative permittivity changes with frequency from the relative contribution of the bulk and grain boundary regions at elevated temperature. The results, Figure 2.28, indicate the presence of two plateaus as the real relative permittivity decreases with increasing frequency.
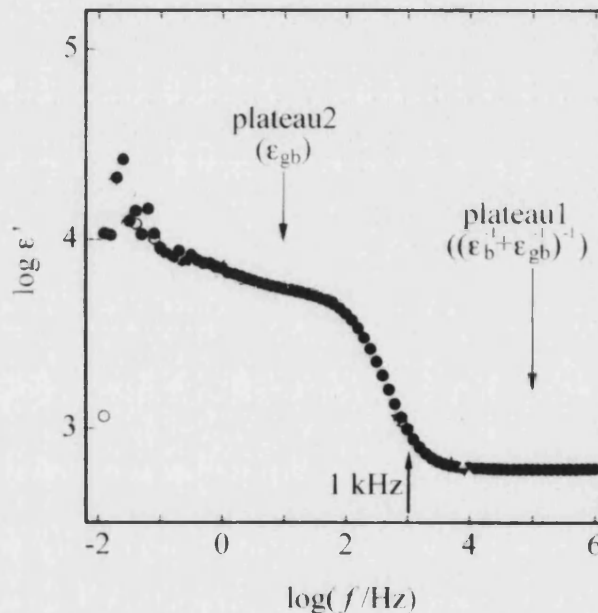
Figure 2.28: Log real part of relative permittivity versus log frequency

showing a sharp decrease between two permittivity plateaux for barium titanate[132].

The low frequency plateau is reported to correspond to the relative permittivity of the grain boundary, and the high frequency plateau is ascribed to this and the bulk relative permittivity, via equation 2.10.

$$\varepsilon_H = (\varepsilon_b^{-1} + \varepsilon_{gb}^{-1})^{-1} \qquad\qquad \{2.10\}^{132}$$

For most ceramics the grain boundary relative permittivity is much larger than that of the bulk, and ε_H is approximated to the bulk value.

v. Humid conditions promote a higher relative permittivity, Figure 2.29, since water molecules can be adsorbed onto the surfaces[133] and act as an additional dielectric.
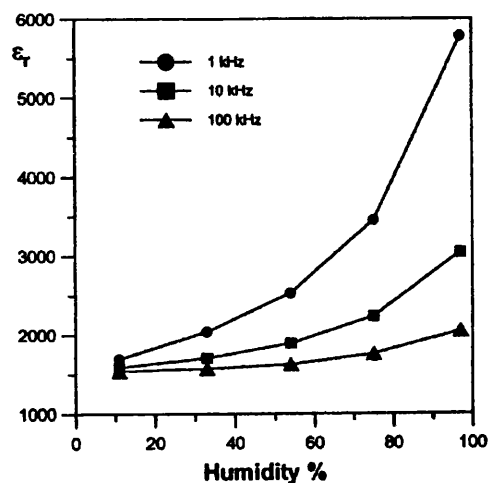
Figure 2.29: Relative permittivity increase with humidity and decrease with higher frequency[133].
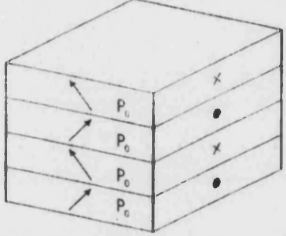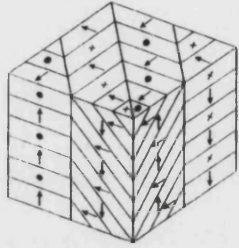
vi. The stoichiometry of barium titanate has been reported to influence the relative permittivity. A barium oxide excess composition increases the relative permittivity[61].

vii. A decrease in relative permittivity is expected at a frequency corresponding to the piezoelectric resonance. Below this resonant frequency the relative permittivity is that of the free crystal, whilst above this frequency it becomes the clamped value[18]. The effect of resonance is discussed in more detail in Appendix II and important parameters in Section 2.5.g.

2.5.a.viii   Domains

In 1907 Pierre Weiss postulated the presence of domains in magnetic materials[134] and similar assumptions can be applied to postulate ferroelectric domains. A full discussion of domains is given in Appendix II. In barium titanate the domain structure is formed during the cubic to tetragonal crystal transformation[135]. Domains are regions of "homogenous" polarisation[136]. Polarisation in the same direction occurs if the resulting polarisation from neighbouring dipoles exerts a sufficiently large force on a dipole[33]. As a ferroelectric ceramic cools from above its Curie temperature it will contract. Since all the crystal orientations within the polycrystalline ceramic are randomly aligned this contraction will be isotropic. However, individual crystals will favour anisotropic contraction according to their domain orientation.

These two systems lead to the ferroelectric material forming many, seemingly randomly oriented domains. Twinning is the formation of these domains to balance the domain wall energy, elastic and electric field energy. It has been suggested that the domain pattern is different in coarse grains in comparison to fine grains. This can affect the average polarisation of the grain, P_{grain}, as highlighted in Table 2.18, P_0 is the polarisation of the single crystal[131]. It appears that the average grain polarisation is reduced for the coarse grained structure, suggesting a reduced relative permittivity value.

Table 2.18: Reduction of the single crystal polarisation value, P_0, with grain size[131].

Fine grain domain pattern		**Coarse grain domain pattern**	
	$P_{grain} = \dfrac{P_0}{\sqrt{2}}$		$P_{grain} = \dfrac{P_0 \sqrt{2}}{3}$

There are two types of domain, known as 90° and 180° domains[127, 136], and these are shown in Figure 2.30. For the 90° domains the c-axis of each twin is mutually perpendicular, whilst they are parallel and have opposite polarity in the 180° domains[137, 138].
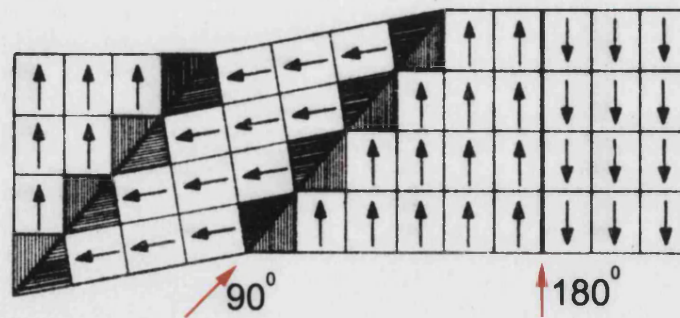
Figure 2.30: Physical representation of 90° domains and thinner 180° domains[18].

Clamping by adjacent grains, however, can hinder the formation of a domain configuration. The complex domain structure in large grains is a disadvantage in cases where it is required to drive a domain boundary through a grain using an external field[127]. Deformation of the dielectric material can influence the domain structure as cooperative twinning in adjacent grains can relieve stress.

The presence of the domains influences the relative permittivity and the piezoelectric coupling factors[139].

Domains may be manipulated by a number of methods, such as;

i.   Reversible domain motion occurs under small electric fields and the displacement contributes to the dielectric constant[127]. Higher fields cause reorientation[104].

ii. Electrical and mechanical cycling can cause domain reorientations. This is reversible by re-application of the poling field[140].

iii. The domain pattern increases complexity on annealing of the piezoelectric[114].

iv. 90° domain twins have been reported to disappear in barium titanate with the addition of silicon carbide. No domains were observed with 5vol% silicon carbide[1, 77]. This could be due the modification of the grain size.

v.   At room temperature only 1% of the sample is tetragonal as clamping inhibits the cubic to tetragonal transformation. Tetragonality develops by a twinning mechanism in large grains[136].

vi. Close crystallographically orientated adjacent grains can act as a single large grain, with little impairment of 90° domain motion by the grain boundary[136].

vii. Application of stress can rotate domains by 90° only, whilst an electric field can rotate 90° and 180° domains. 90° domain switching results in a strain change, whereas switching of 180° domains does not[22, 141].

2.5.a.ix   *Poling and domain orientation*

A ferroelectric polycrystalline material has no overall polarisation, as the domains are randomly orientated. A process termed "poling" is necessary to align the unit cell dipoles within the material and is discussed in Appendix II. The poling procedure is considered essential as the piezoelectric coefficients, such as d_{33}, are related to the poling state of ferroelectric materials[118]. According to equation 2.11 the d_{33} term is a function of polarisation, P_3, and stress in the 3-direction (poled direction), σ_3.

$$d_{33} = \frac{P_3}{\sigma_3}$$
{2.11}[118]

Rearrangement shows that under stress the sample produces a useful polarisation, which is used in spark ignitors. The inverse is also possible whereby application of electric field produces an anisotropic strain[142]. Figure 2.31 shows the dimensional changes of the poled sample under an electric field. Application of an electric field in the poling direction reinforces the domain extension so increasing the length of the sample parallel to the field, as the c-axis is greater than the a-axis. If the field is reversed the opposite occurs and the sample contracts as the dipoles shorten and at a sufficiently high field switch occurs with an associated extension in the opposite direction.
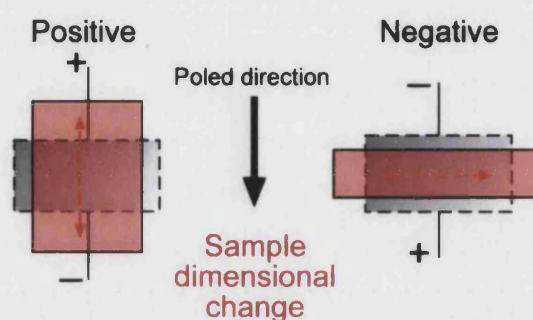
Figure 2.31: Effect of electric field application on the

dimensions of a poled piezoelectric sample.

In summary, piezoelectric ceramics can contain many domains and poling, causing domain reorientation is necessary to achieve functional properties, such as a dimensional change on application of an electric field.

2.5.a.x   *Domain Pinning*

Domain mobility leads to difficulties in producing uniform and consistent materials[33] as the motion is energetically lossy, leading to a non-linear response with field application[131]. Pinning of ferroelectric domains is analogous to the restraining of magnetic domains. Wall motion, required for a domain to grow, can be influenced by the presence of entities that make such movement more difficult. This is discussed in Appendix II.

The intention of the present research work is to use the presence of inclusions to improve the relative permittivity and decrease the dielectric loss, by reducing domain wall motion, and enable the material to be used at higher electric fields.

2.5.b   DIELECTRIC LOSS

Dielectric loss is related to non-instantaneous polarisation due to the inertia of charges and absorption of electrical energy by the dielectric[107]. Background information to dielectric loss is given in Appendix II, while a rapid rise in the dielectric loss, as occurs for relative permittivity, is observed at high fields[128, 143], Figure 2.32.
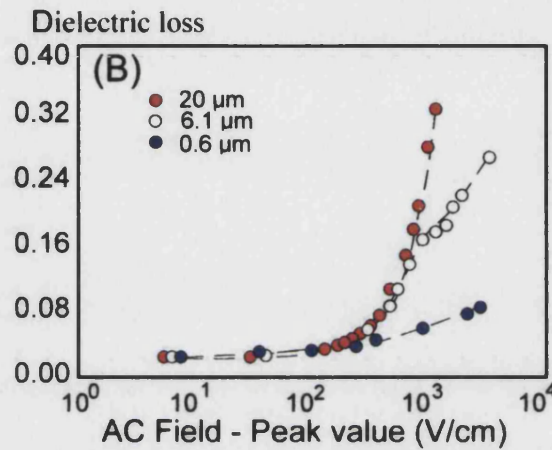
Figure 2.32: Behaviour of dielectric loss with field and grain size[128].

It has been proposed that the increase in loss with higher fields is the result of lossy ferroelectric domain wall motion[130]. To improve the range and usefulness for high field applications it would be beneficial to delay or eliminate this rapid increase in loss at high electric fields, which in this case can be achieved by a reduced grain size. Low loss at the device utilisation frequency is required for device efficiency and reliability[107].

It has been reported that internal stress can increase the dielectric loss[144]. With the additions of particles, such as silver into PZT, an increase in loss has been reported[14, 48]. Table 2.19, shows the change in dielectric loss for the addition of silver into barium titanate.

Table 2.19: Dielectric loss for various barium titanate-silver composites[70].

Vol% silver	Dielectric loss (%)
0	2.4
5	2.9
10	3.2

A number of additional observations have been made;

i.   A more homogeneous microstructure and fewer reaction phases reduce the losses[145].

ii.   Dielectric loss increases in high humidity environments[198, 133].

iii.   Loss is reduced at higher temperatures as the thermal energy reduces the barrier to dipole rotation[80], however, the heat generated by loss mechanisms needs to be dissipated by the sample surface area in order that breakdown and degradation of properties is avoided. The actual heat generation is proportional to the frequency and the amount of loss per cycle. The area of the hysteresis loop[146] is the loss of energy per cycle, see Section 2.5.h.

iv.   Reducing atmospheres generate higher concentrations of oxygen vacancies that increase the loss[121].

v.   The loss increases with excess barium oxide in the composition[61].

In summary, it is important that the dielectric loss is minimised wherever possible in order that applications convert energy efficiently and do not become degraded by heat generated by the loss mechanisms. If the dielectric loss can be reduced then it may be possible to use the material under higher fields and increase the performance range.

2.5.c   PIEZOELECTRICITY

Piezoelectricity was discovered in Rochelle salt (Potassium Sodium Tartrate, $KNa(C_2H_4O_6).4H_2O$) in 1880 by Jacques and Pierre Curie[22]. Piezoelectricity is one property of a group of dielectric materials called ferroelectrics. These materials are characterised by having a domain structure that can be modified by an electric field. The piezoelectric effect is manifest as a spontaneous electric polarisation across the opposite faces of a volume of material when under an applied stress. The magnitude of the polarity is directly proportional to the mechanical stress applied to it. The converse is also true, i.e. the application of an electric field causes strain in a volume of piezoelectric material. Application of pressure to an electroded piezoelectric crystal causes charge to flow in a specific direction, the direction being reversed on pressure inversion[18]. The illustration, Figure 2.33, demonstrates the piezoelectric effect. This explains the origin of the word piezoelectricity as "piezin" is Greek for "to press".
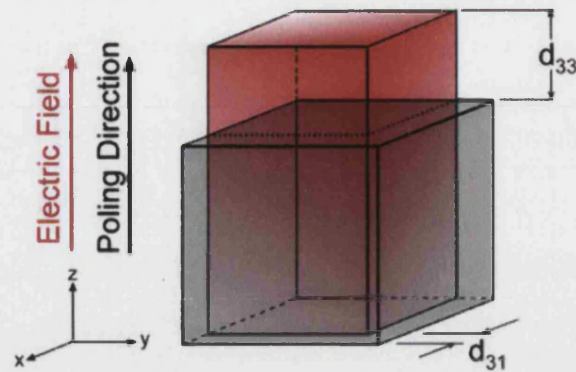
Figure 2.33: Effect of electric field on a poled piezoelectric cube (grey is before

field application, red is during electric field application).

The original poled volume of material, in grey, experiences the electric field and transforms into the red shaded volume. This has created the extension in the z-direction (poled direction), while contraction occurs in both the x- and y-axis directions, due to constant sample volume. Additional information on piezoelectricity and its notation is given in Appendix II. The piezoelectric coefficients, d_{33} and d_{31}, are now discussed.

2.5.c.i   *Piezoelectric Coefficients*

The dimensions of the piezoelectric coefficient, d, are charge per unit force, or strain per unit field. Measurement consists of applying a known force to a piezoelectric specimen and recording the induced charge across the poled sample. For d_{33} the stress is applied parallel to the poling direction, while it is perpendicular for d_{31} measurement, Figure 2.34. The force probes must be appropriate to reduce sample surface traction as strain can occur in plane, due to the Poisson's ratio effect.
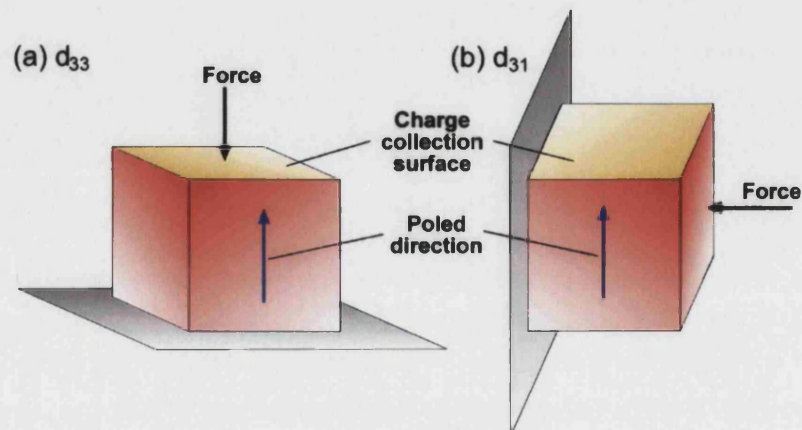
Figure 2.34: Force application during measurement of (a) d_{33} and (b) d_{31}.

An ideal piezoelectric material would have a response that is linear in an electric or stress field. Common materials, however, show a non-linear response that depends on the rate of field application, equation 2.12[147].

$$d_{33} = \frac{\partial Q}{\partial F} = C\frac{\partial V}{\partial F}$$

{2.12}[147],

where Q is the induced charge, F the force applied, V the applied voltage and C the sample capacitance. This time-dependent and non-linear behaviour is associated with 90° domains, as their motion is thermally activated[147]. A better piezoelectric response is achieved by applying the stimulus (stress or field) at a lower frequency as this allows more domains the time to re-align[147].

The section on mechanical properties, Section 2.4, highlights that particles are typically added to improve the strength and toughness. A number of studies have been carried out to study the effect of dispersing piezoelectric particles in polymer systems[118, 148, 149]. Experiments indicated that increasing the piezoelectric particle size causes an improvement of the d_{33}. While ceramics have had piezoelectric particles added[16, 27, 28, 32, 120] very few results have been published in regard to the modification of a piezoelectric matrix by particle addition. Table 2.20 summarizes the systems and results reported, which show a decrease in the piezoelectric coefficient with non-metallic particles, but an improvement with metallic particles. The change, however, is minimal and is within the experimental error range. Table 2.20 highlights the lack of data concerning the effect of particle additions on the piezoelectric properties of a piezoelectric matrix.

Table 2.20: Effect of alumina or platinum addition on the piezoelectric coefficient, d_{33},

of PZT. Monolithic values in parentheses.

Matrix	Particle/ vol%	d_{33} (10^{-12} m/V)	d_{31} (10^{-12} m/V)	Reference
PZT	Al_2O_3/ 1	-	79 (72)	13
PZT	Pt/ 1	-	133 (137)	15

2.5.d   REPORTED ELECTRICAL PROPERTIES

Although improved mechanical properties have been reported for ferroelectric materials with particle inclusions, there is a lack of information concerning the effect of particle incorporation on the dielectric and piezoelectric properties. This deficiency is highlighted in Table 2.21.

Table 2.21: Outline of electrical properties for some piezoelectric particulate composites.

The figures in parentheses denote the monolithic values.

Matrix/ Particle	Reference	Relative permittivity (25°C, 1 kHz)	Dielectric Loss	Piezoelectric coefficient, d_{33} (x10^{-12} C/N)
Monolithic PZT	142	1725	0.01	380
Monolithic $BaTiO_3$	12, 114	1500-5000	-	190
PZT/ 0.5vol% Al_2O_3	11	1660 (1420)	0.08 (0.06)	-
$BaTiO_3$/ 5vol% SiC	1	2000 (6000)	-	-
PZT/ 10vol% Ag	12, 82	2900 (2500)	0.032	-
$BaTiO_3$/ Ni	101	2500 (1000)	-	-

2.5.e   RESISTIVITY

2.5.e.i   Introduction

Resistivity, ρ, is a geometrically independent value of the materials resistance to the flow of electrons. It is related to the electrical resistance of the material, R, the sample thickness, l, and the sample cross-sectional area, A, as shown in equation 2.13.

$$\rho = \frac{RA}{l} \qquad \{2.13\}$$

The resistivity is equal to the reciprocal of the conductivity, σ, and is discussed in Appendix II with some important influences now given.

2.5.e.ii   Oxygen vacancies

The electrons generated from the formation of an oxygen vacancy are a major charge carrier in barium titanate. Mobile electrons lead to increased conductivity and higher dielectric loss[150]. The electrons created can be captured by the highly positive Ti^{4+} ion, which is then converted to Ti^{3+}, a requirement effort to keep charge neutrality[76, 143, 150, 151]. An excess of oxygen vacancies can turn barium titanate into an n-type semiconductor with composition of $BaTiO_{2.997}$ [31]. This has been reported to occur when sintering is undertaken in reducing conditions, such as in argon[1, 23, 101]. The sample turns from the cream/yellow colour in the oxidised form to a blue-black colour[1, 32, 76]. It has been reported that by reducing the barium titanate a high relative permittivity around 100,000 can be achieved, but as it is semi-conducting it is limited to low voltage applications[20]. Barium titanate can also be made conductive by substitutions that increase the carrier content[23], however, substitutions, such as manganese, can also trap electrons and so reduce the conductivity[150]. Oxidation by annealing in air of the reduced barium titanate has been reported to increase the resistivity from $1.1 \times 10^{-3}\,\Omega.m$ to $7.8 \times 10^{9}\,\Omega.m$ [1]. Ferroelectric materials are commonly characterised by a resistivity greater than $1 \times 10^{11}\,\Omega.m$ [22].

2.5.e.iii   Effect of particles on resistivity

The incorporation of metallic particles is expected to decrease the resistivity, due to the easy electron transport through the second phase, if present as a continuum. Before this stage is reached, however, it has been reported that there is a narrow compositional transition stage over which the electrical conductivity changes by orders of magnitude[124]. This transitional behaviour is discussed in Appendix II. Table 2.22 indicates the decrease in resistivity for a number of ceramics with the addition of metallic inclusions. A rapid decrease in the resistivity is observed on addition of 15vol% nickel in alumina, suggesting that the percolation threshold has been exceeded. With non-metallic particles (silicon carbide), Table 2.22, the resistivity decrease is due to the chemical reduction of the matrix. Oxidation of the barium titanate-silicon carbide composite increases the resistivity to a suitable value for use as a dielectric.

Table 2.22: Change in resistivity of a dielectric matrix with metallic and

non-metallic inclusions. Parenthesis indicate the reduced value.

Matrix	Inclusion / Vol%	Monolithic resistivity (Ω.m)	Composite resistivity (Ω.m)	Reference
Al_2O_3	Ni/ 7.5, 15, 35	4.5×10^9	1.97×10^9, 2.6×10^{-4}, 3.97×10^{-6}	112
PZT	Ag	Above 10vol% silver too conductive to be poled		14
$BaTiO_3$	Ni	Insulating below 30vol% Conducting above 40vol%		101
$BaTiO_3$	SiC/ 5	4.7×10^{10}	5.5×10^8	76
$BaTiO_3$	SiC/ 5	(1.1×10^{-3}) 7.82×10^9	(1.3×10^{-4}) 2.54×10^8	1

2.5.e.iv   *Effect of grain boundaries*

Grain boundary conduction is reduced when the number of grain boundary intersections increases, such as with fine grains[76]. The grain boundary effect is related to the mean-free path of charge carriers between collisions. A fine grain size equates to a high probability of grain boundary interaction and collisions[33], as demonstrated by Figure 2.35.
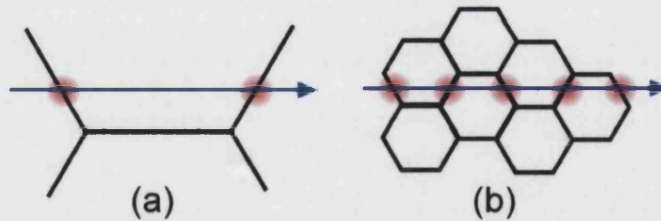
Figure 2.35: Schematic showing the increase in charge carrier interaction with grain

boundaries for a material of (a) large grain size and (b) small grain size.

2.5.e.v   *Other influences on resistivity*

Other parameters that can affect the resistivity are;

i.   the resistivity is reduced in humid conditions as the water molecules can contribute to the conduction process[133].

ii.   vitreous solids, such as glassy phases, have a substantially greater ionic mobility than normal solids, due to the disordered structure[33].

iii.   impurities can reduce the resistivity by introducing new energy levels that may allow the formation of electron-hole pairs more readily[33].

iv.   DC conductivity, relating to electronic and ionic imperfections, increases as the field is increased, until breakdown occurs[33], Section 2.5.f.

v.   conduction in a dielectric is thermally activated so resistivity decreases with temperature[123].

2.5.f   DIELECTRIC STRENGTH

The dielectric strength of a substance is the magnitude of the electric field required to produce an electrical breakdown[113, 107]. Breakdown in an insulator can be caused by one or more mechanisms, especially in sintered ceramics that can be dominated by residual porosity or surface asperities[95]. These mechanisms and factors that influence the dielectric strength are discussed in Appendix II. Knowledge of breakdown characteristics is important for efficient poling of the material.

Ferroelectric materials are generally characterised by a dielectric breakdown strength of 10-12 kV/mm [22]. It is observed that low dielectric strength is associated with a high relative permittivity material, due to the large amount of stored charge. Dielectrics having a relative permittivity of 4000-6000 may have a breakdown strength of only 2.5 kV/mm in comparison to 15 kV/mm for those with a relative permittivity nearer 30 [20]. Barium titanate has been reported to have a dielectric strength of 13.5 kV/mm (with a Weibull modulus of 3.9 [59]) and 7.4 kV/mm [152]. It is noted that the breakdown strength and Weibull modulus are very dependent of the quality of sample processing.

2.5.g   IMPEDANCE ANALYSIS

An introduction to impedance analysis is given in Appendix II, while the coupling coefficient and mechanical quality factor are now mentioned.

2.5.g.i   *Coupling coefficient*

The coupling coefficient is the efficiency with which energy is converted from the mechanical to the electrical form or vice versa, and is given by equation 2.14.

$$K_{eff} = \sqrt{\frac{f_p^2 - f_s^2}{f_p^2}} \approx \sqrt{\frac{f_n^2 - f_m^2}{f_n^2}} \qquad \{2.14\}^{153,\,154}$$

The planar coupling factor can be obtained from this equation[110, 155] and is a direct measurement of the overall strength of the electromechanical effect[22]. This coupling factor for a thin disc represents coupling between the electric field parallel to the disc axis (3-direction) and simultaneous mechanical effects in the 1- and 2-directions that result in radial vibrations[153], Figure 2.36. Conversion is always incomplete as there are losses in real materials, see Section 2.5.b, so k_p is less than one. Barium titanate has been reported to have a $k_p \approx 0.35$ [22].
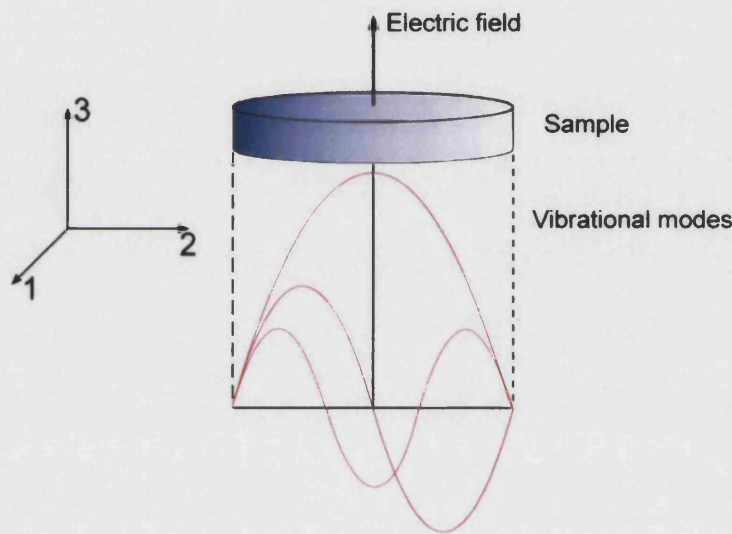
Figure 2.36: Radial vibration modes for a disc with electric field in the 3-direction.

2.5.g.ii   *Mechanical quality factor*

The mechanical quality factor, Q_m, can also be determined from impedance analysis, equation 2.15 [23, 154]. The mechanical quality factor is a dimensionless measure of mechanical losses and describes the sharpness of the resonant peak[154].

$$\frac{1}{Q_m} = 2\pi f_s |Z_m| (C_0 + C) K_{eff}^2 \qquad \{2.15\}$$

Here $|Z_m|$ is the impedance value at resonance and C_0 the free cell capacitance, usually taken as the capacitance at 1 kHz[181]. An estimate for the primary radial resonant frequency, f_{radial}, is given by equation 2.16 for an unconstrained disc shaped sample.

$$f_{radial} = \frac{1}{\sqrt{4\rho\ r^2 S_{11}^E}}$$

{2.16}[157]

Here ρ is the sample density (kg.m^{-3}), r the sample radius (m) and S_{11}^E the compliance at constant electric field strength (m^{2}N^{-1}).

2.5.g.iii   Reported impedance analysis results

Piezoelectric inclusions have been added to structural ceramics in an attempt to introduce piezoelectric properties[27]. The results indicate an increase in k_p as the volume fraction of piezoelectric phases is increased. As expected, from the better piezoelectric properties, PZT was found to be superior to BaTiO$_3$ [27]. The addition of non-piezoelectric particles to a piezoelectric matrix, which is more relevant to the research reported here, has also been studied, Table 2.23. The change in the mechanical quality factor is more significant than that in the coupling coefficient.

Table 2.23: Effect of alumina and platinum addition on the planar coupling coefficient and mechanical quality factor for PZT. Parentheses indicate the monolithic value.

Matrix	Inclusion/ Vol%	K_p	Q_m	Reference
PZT	Al$_2$O$_3$/ 1	0.61 (0.62)	1240 (1550)	13
PZT	Pt/ 1	0.68 (0.66)	59 (84)	15

It should be noted that the sample dimensions, geometry, density, elastic, dielectric and piezoelectric constants affect the impedance spectra for a piezoelectric material[156].

2.5.h   POLARISATION-FIELD ANALYSIS

2.5.h.i   Introduction

Hysteresis in the broad sense is the retardation of an effect behind the cause of the effect. For piezoelectric materials hysteresis is typically attributed to the impediment of domain wall movement by pinning centres, Section 2.5.a.x, inherent in the material[158]. A detailed description of

the polarisation-electric field loop for a piezoelectric is given in Appendix II. There are three reference points used to describe the polarisation-electric field loop. These are the coercive field, E_c, saturation polarisation, P_s and remanant polarisation, P_r. In addition other information can be obtained from the polarisation-field loop, such as;

i.   a degree of 'squareness' of the loop can indicate better homogeneity and grain size uniformity[18, 22]. The shape of the loop is also affected by the rate at which the loop is traversed. At slow rates the dipoles have sufficient time to reverse the polarisation so nearly complete alignment occurs long before the peak voltage is reached. At faster rates the time is insufficient for the reversal process and the coercive field increases[18],

ii. a high electrical resistivity ($>1\times10^7$ Ω.m) is signified by the sharpness of the loop tips[22],

iii. the slope of the low polarisation-electric field sub-loops gives the relative permittivity[18, 22, 33].

For barium titanate a polarisation of 1.5 C/m^2 is reported for a field of 2 kV/mm [72]

2.5.h.ii   *Particle incorporation and polarisation-field behaviour*

The incorporation of a non-piezoelectric phase (MgO) into a piezoelectric matrix (PZT) indicates that the loop area is reduced[27]. This is the expected response from a reduction in the proportion of piezoelectric content. The saturation polarisation in barium titanate can be reduced by the presence of a non-ferroelectric phase, such as $Ba_6Ti_{17}O_{40}$ [72]. It has been suggested that these composites may have a reduced hysteresis as the matrix provides a consistent restoring force for domain wall motion[72]. No significant change in the coercive field was observed with the incorporation of 1vol% Al_2O_3 into PZT[13].

The effect of hysteresis can be reduced in practical applications by restricting the input field/stress to the linear region. However, this limits the use of the material. Feedback mechanisms can be used to correct for non-linearity, but the phase lag means this technique is not amenable for high accuracy processes, such as micro-positioning[158].

2.5.i   SUMMARY OF ELECTRICAL PROPERTIES OF PARTICLE-BASED COMPOSITES

Limited information has been reported on the effect of particles on the dielectric and piezoelectric properties in an electroceramic matrix. Literature suggests that the addition of non-metallic particles that cause grain refinement will increase the relative permittivity. The addition of metallic particles has been proposed to increase the relative permittivity by increasing the local electric field surrounding the particles. The electrical properties are sensitive to processing parameters, such as the sintering atmosphere, formation of reaction phases, and this limits the particles that can be added to electroceramics. The piezoelectric properties have decreased with particle addition due to a reduction in the volume of piezoelectric material, and problems in poling compositions with high metal contents. The polarisation-field behaviour of electroceramic particulate composites suggests the loop area may become reduced, however, the results reported are limited.

2.6   APPLICATIONS

Piezoelectric materials have widespread applications as transducers and actuators. Transducers are used to convert energy from one form to another, such as in sensors that give accurate measurement of force or acceleration, or large structures such as passive sonars and hydrophones[21]. Actuators use the controllable deformation by the piezoelectric effect to achieve high precision and accuracy for positioning, which is necessary, for example, in laser optics. Applications for ceramic actuators are increasing due to their high reliability and chemical stability, for example as valves in fuel injection systems. The intention behind the incorporation of piezoelectric particles into structural ceramics has been the prospect of "intelligent" functions[120];

    i.   Sensing of crack propagation by electromotive force generation.

    ii.   Improving fracture toughness by electric field application.

This is interesting for applications that use brittle material, such as ceramics, in order that warning of crack growth and failure may be predicted.

The performance of piezo-ceramics, however, commonly reduces under high electric fields and frequencies due to mechanical and electrical degradation. This has promoted research into the fabrication of piezoelectric ceramics that have high field applications, such as active sonars and ultrasonic baths.

In the present research, barium titanate has been chosen as the piezoelectric matrix into which particles will be added. Barium titanate is commonly used as a capacitor material due to its high relative permittivity. It also has reasonable piezoelectric properties and will allow the effect, of particle addition, on a broad range of electrical properties to be studied. The particles to be incorporated will consist of silicon carbide and silver. Silicon carbide has previously been used to enhance the mechanical properties of structural ceramics and silver has traditionally been used as an electrode material in actuators. The differing electrical and mechanical properties of these particles will indicate the affect of differing particle types. This research is intended to discover how the addition of inclusions influences the electrical and mechanical properties of the electroceramic barium titanate.

3 COMPOSITE FABRICATION

3.1 INTRODUCTION

A review of the literature has indicated that there is a lack of information concerning the electrical and piezoelectric properties of electroceramics with the addition of inclusions. The aim has been to fabricate a range of barium titanate composites with different particle weight fractions in order to study their effect. This section discusses the methods used to produce the samples used in this work.

3.2 EXPERIMENTAL PROCEDURES

The precise methods used to fabricate the samples in this research are now given, while background literature on the techniques used is located in Appendix III.

3.2.a   POWDER PROCESSING

3.2.a.i   Ball milling

The silicon carbide and silver oxide composites were produced by ball-milling the required formulations. The milling parameters are shown in Table 3.1, and the compositions for the powder mixes are given in Table 3.2.

Table 3.1: Ball milling parameters for barium titanate-silicon carbide composites.

Parameter	Ball-milling	
	Dry	Wet
Media type	10 mm zirconia	10 mm zirconia
Time (hours)	24	24
Medium	-	Distilled water

The binder, PEG, was added to improve the handling strength of green compacts and to enhance lubrication of particles during pressing. It was found that pressing with the binder added produced delamination free green compacts.

Table 3.2: Ball milling compositions for barium titanate-silicon carbide,

silver (oxide) and platinum composites.

Material	Percentage (wt%)
Barium titanate	99, 98, 96, 94, 84
Polyethylene glycol (PEG) binder	1
Silicon Carbide (Stark UF45)	0, 1, 3, 5 and 15

Material	Percentage (wt%)
Barium titanate	97, 89, 84 and 79
Polyethylene glycol (PEG) binder	1
Silver Oxide (Ag_2O)	2, 10, 15 and 20

Material	Percentage (wt%)
Barium titanate	84 (~93.5wt% after calcination)
Polyethylene glycol (PEG) binder	1
Platinum compound ($H_2PtCl_6.xH_2O$)[#]	15 (~5.7wt%Pt after calcination)

[#] The platinum compound contains 38-41wt%Pt

3.2.a.ii   Attrition milling

Attrition milling was chosen as the method for the preparation of the barium titanate-silver nitrate composites in order to break up the silver nitrate crystals. For the silicon carbide system attrition milling is not required as the inclusions are already in the nano-size range. The attrition milling parameters and powder compositions are given in Table 3.3 and Table 3.4 respectively.

Table 3.3: Attrition milling parameters.

Parameter	Attrition milling
Media amount & type	1 part powder plus ethanol to 3 parts 5 mm zirconia balls
Time (hours)	2
Other	300 rpm, 60-70% solids

Table 3.4: Attrition milling compositions for barium titanate-silver (nitrate) composites.

Material	Percentage (wt%)
Barium titanate	99, 97, 94, 89, 84, 79, 74, 69, 64 and 59
Polyethylene glycol (PEG) binder	1
Silver Nitrate	0, 2, 5, 10, 15, 20, 25, 30, 35 and 40

3.2.a.iii   Powder drying

Once the powder had been mixed it was dried under an infrared lamp at a temperature of approximately 50°C. The ceramic-composites solution was stirred during drying to prevent undesirable sedimentation of the second phase particles. A small quantity of freeze-dried powder was manufactured for comparison with the conventional ball-milled and attrition milled powders, Table 3.5.

Table 3.5: Freeze-dried barium titanate-silicon carbide powder compositions.

Material	Percentage (wt%)
Barium titanate	98 and 97
Polyethylene glycol (PEG) binder	2
Silicon Carbide (Stark UF45)	0 and 1

3.2.a.iv   Powder sieving

Once dried, the powder was broken up with a pestle and mortar to reduce hard agglomerates before passing through a 150 μm sieve.

3.2.a.v   Calcination procedure

The barium titanate-silicon carbide composites were not calcined in order to prevent undue oxidation of the silicon carbide. Calcination was carried out using a temperature of 300°C for three hours in an atmosphere of air for the silver composite samples. This was necessary to ensure that the starting silver nitrate had decomposed to silver and that any gaseous products would not interfere with densification during sintering. Silver nitrate decomposes to silver oxide, which has

been reported to breakdown at 200°C[14]. A higher temperature of 600°C was used for the calcination of the barium titanate-platinum powder. Calcination was carried out with the powder in an alumina crucible with a loose fitting alumina lid. A Vecstar furnace using $MoSi_2$ heating elements was used for calcination and subsequent sintering. The mass of the silver containing samples was measured before and after calcination to assess the degree of decomposition of the silver compound.

3.2.a.vi   *Green compact manufacture - Uni-axial pressing*

Preliminary green compacts were manufactured by uni-axial pressing of a quantity of powder to form:

i.   12 mm diameter discs of up to 5 mm thickness.

ii.   five millimetre diameter cylinders of up to 15 mm in length. These high aspect ratio samples were fabricated for dilatometry testing (Chapter 4).

All samples were produced using a pressure of 32-50 MPa applied for two minutes. The effect of the pressing pressure on the final density was determined. The pressure used corresponds to that used in the literature and produced samples of the correct shape with sufficient green strength to be handled in the following cold isostatic pressing stage.

3.2.a.vii   *Green compact manufacture – cold isostatic pressing*

A number of samples were isostatically pressed for comparative studies. Samples that were isostatically pressed followed the procedure outlined below.

i.   Pre-pressed compacts were placed in 2.5 cm colostomy tubing, evacuated and sealed. Colostomy tubing was used due to its convenient size and flexibility; it easily conforms to the shape of the sample when evacuated. Knots were tied at each end to seal the ends of the tubing.

ii.   The package was inserted into larger tubing (3.75 cm) then again evacuated and sealed. This second tube was to provide additional protection from fluid penetration through the thin tubing.

iii.   To aid removal from the pressure chamber the packaged sample was placed within an aluminium cylinder and then submerged in the pressurising fluid.

iv.   The pressure chamber was closed and the green compacted sample subjected to 150 MPa for one minute using a Stansted cold iso-static press (Stansted Fluid Power Ltd, England).

v.   The samples were subsequently removed from the tubing and required no additional processing before sintering.

3.2.b   SINTERING PROCEDURE

Samples have been pressureless sintered as it is simple, cheap and has the ability to process a large numbers of samples simultaneously.

3.2.b.i   *Barium titanate-silicon carbide composites*

Sintering of the composite samples in a tube furnace, Pyro Therm 3.5 kW, was conducted with a flowing stream of argon (1 l/min) above 600°C to minimise silicon carbide oxidation and loss. The sintering profile is given in Figure 3.1. Both silicon carbide and barium titanate powder beds were investigated. An α-SiC powder was used with an atmosphere of argon for the freeze-dried powders and wet milled $BaTiO_3$-2.5wt% silicon carbide.
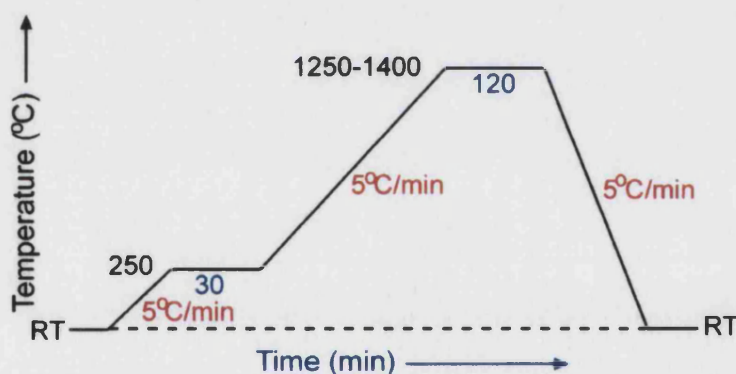
Figure 3.1: Sintering profile for barium titanate-silicon carbide composites.

3.2.b.ii   *Barium titanate-metal composites*

A protective atmosphere was not required for the sintering of the metallic particle composites and a normal furnace (Vecstar Furnace) was employed. Previously sintered coarse barium titanate particles were used as a sintering bed on an alumina base plate. The furnace elements were in the line of sight of the samples so the samples were shielded, by another alumina plate supported on zirconia spacers, to minimise direct heating effects, Figure 3.2.
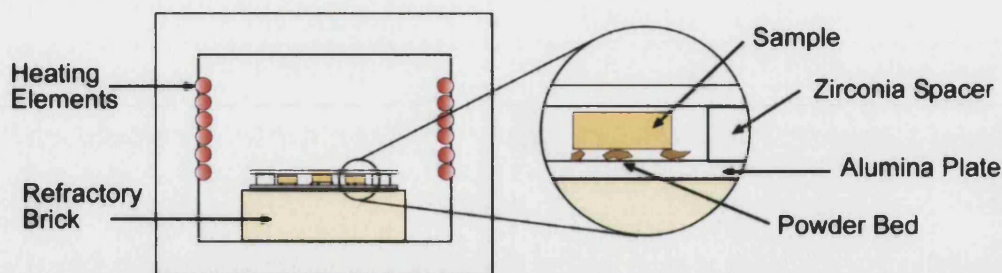
Figure 3.2: Pressureless ceramic-metal composites furnace sintering set-up.

The sintering profile consisted of a ramped temperature rise to 1300°C at 5 °C/minute from room temperature. A low temperature dwell was not required, as the calcination process had removed the decomposition gases. The samples were held at 1300°C for two hours to sinter before natural cooling was used (no faster than 5 °C/minute). The mass of individual specimens was measured before and after sintering to assess the degree of silver loss.

3.2.c   HOT PRESSING

One sample of each silicon carbide content (0, 1, 3, 5wt%) was hot pressed in order to compare the composite results with those published by Hwang[40]. The conditions used were 1300°C, 1hr, 30 MPa, with a ramp rate of 15 °C/min and carbon paper to separate the ceramic material from the die wall.

3.2.d   ANNEALING

Annealing of the samples was generally not conducted in this work. A few samples, however, were heated below the sintering temperature in an attempt to oxidise the material. This is described in more detail in Chapter 5.

3.2.e   PROCEDURES FOR SAMPLE FINISHING

3.2.e.i   Surface finishing for optical and electron microscopy

A high degree of flatness is required when using the optical microscope due to the poor depth of field in comparison to the electron microscope. The polishing conditions in Table 3.7 were used on a Motopol 12 (Buehler UK Ltd., England) for the preparation of specimens for microscopy and for

thermal or chemical etching. The samples were mounted in an epoxide resin (Buehler UK Ltd., England) to assist surface preparation.

Table 3.7: Surface preparation for microscopy and etched specimens.

Stage	Surface	Particle size (μm) /type	Wheel speed (rpm)	Load (lb/sample)	Time (min)	Lubricant
Grinding	Paper	46/ SiC	150	6	Until plane	Water
Sample integrity	Paper	15/ SiC	150	6	0.5	Water
	Ultrapad	9/ diamond	200	6	5	Oil-based
	Texmet 1000	3/ diamond	250	10	5	Oil-based
Polishing	Texmet	1/ diamond	250	5	2	Water

3.2.e.i.a   Etching

Once polished using the procedures in Table 3.7, samples for microstructural analysis were etched.

Thermal Etching

Samples for thermal etching were removed from the epoxide mounting resin using a microwave oven (600 W Sharp carousel convection-microwave oven) to heat and soften the polymer and allow extraction. These samples were then placed on an alumina plate before being heated to 1200°C (600 °C/hour) in air for 10 minutes.

Chemical Etching

These samples were left within the mounting compound to ease handling. A solution of nitric acid and hydrofluoric acid ($H_2O+4\%HNO_3+2\%HF$) was used for 20-60 seconds. The samples were gently agitated so that the reaction products did not settle on the surface and to remove any air bubbles that may impede the chemical reaction. After etching the sample was washed free of any residue and subsequently dried.

3.2.e.ii   Surface finishing for mechanical testing

Samples for mechanical testing were first ground flat with 1200 grit (15 μm) on both sides using a Knuth rotor (Struers, Denmark) with water lubrication, down to a thickness near 2 mm. These samples were then mounted in an epoxide resin (Buehler UK Ltd., England) and polished down to

three microns surface finish using the procedures in Table 3.7, but without the final polishing stage, on a Motopol 12 (Buehler UK Ltd., England).

The individual specimens were then carefully removed from the epoxide mount. This procedure was aided by heating the mounted samples in a microwave oven (600 W Sharp carousel convection-microwave oven) at full power for 30 seconds. The opposite specimen face was then delicately polished to remove any excess polymer that could obstruct the testing equipment. The samples were mounted in the test equipment with the tensile surface having the 3 μm surface finish.

3.2.e.iii   Surface finishing for electrical testing

The upper and lower surfaces of the discs were ground with 320 grit, and then 1200 grit, paper, in order to produce comparatively flat parallel surfaces. This process was carried out using a Knuth rotor (Struers, Denmark) with water lubrication. The amount of material removed was sufficient to eliminate the surface layers, which are more likely to contain reaction phases and low melting point metal depletion layers. After polishing the specimens were dried using a Gallenkamp hot plate at 100°C for 30 minutes, to remove excess moisture before electroding.

3.2.f   ELECTRODING PROCEDURE

The ground surfaces were manually coated with a silver paste (RS-1015621) and left to dry at room temperature. To reduce errors from short circuits the edges of the disc were then briefly sanded (1200 grit) to remove any silver that had spread over the edge. The samples thus produced had a structure as shown schematically in Figure 3.3.
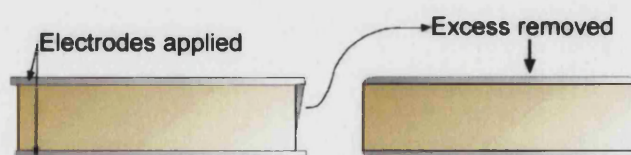
Figure 3.3: Sample preparation by surface layer removal and electroding.

The electrode was removed if samples underwent an oxidation treatment, and then reapplied for electrical property determination.

For the dielectric breakdown test samples (to be discussed in Chapter 4) the electrode was not applied to the edge of the sample, as shown in Figure 3.4. This was to reduce the possibility of

discharge across the sample edge instead of through the sample. Masks were created from adhesive paper and holes of 9 mm diameter punched in. The paper mask was then placed symmetrically on both sides of the sample before the silver electrode paint was applied. Once the paint had dried the mask was peeled off, the sample checked, and any undesirable electrode sections cleaned.

Figure 3.4: Silver electrode applied to a dielectric breakdown test sample.

3.2.g   POLING PROCEDURE

Corona poling was chosen in preference to the oil bath method as the equipment required is less complicated and the health and safety aspects more acceptable. The use of an oil bath would also require cleaning of the samples post-poling and involve higher field strengths. A corona poling rig was, therefore designed and constructed, and is show in Figure 3.5.
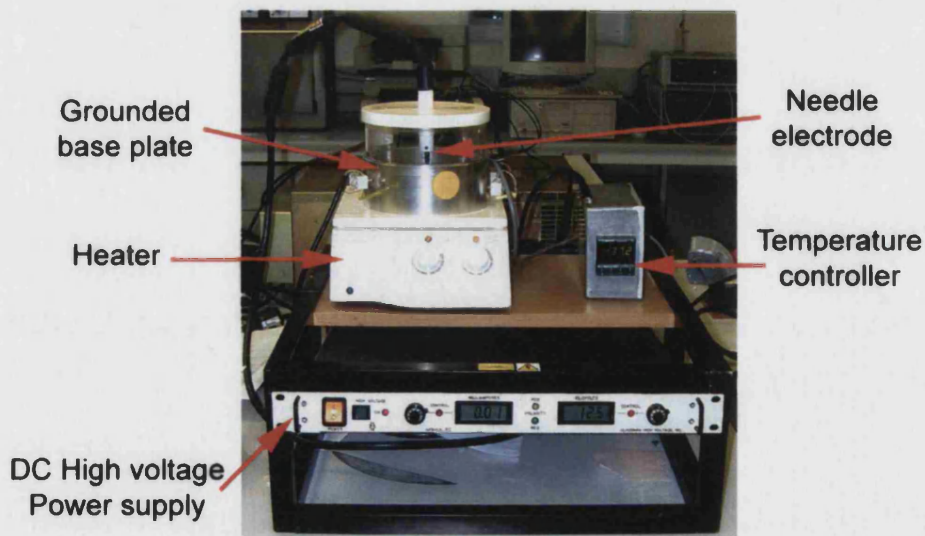
Figure 3.5: The corona poling rig used for sample poling.

The basic poling characteristics of the rig were tested by:

i.   Poling the same samples, under different electric field strengths, at constant temperature and with a needle-base distance of 3.5 cm. In all tests the time under the trial voltage and

temperature was held for 30 minutes. While it is possible that a similar result might be possible with shorter poling times this period was used to ensure equilibrium has been established.

ii. Electric field, temperature and needle-base distance were kept constant while the dwell time was varied.

iii. The temperature of the specimen during the dwell period was varied whilst keeping all other parameters constant.

Once the dwell period was completed the heater was switched off and the sample allowed to cool under the electric field. The electric field was not turned off until the sample had reached a temperature below 50°C. After cooling, samples were discharged as a residual charge was typically present on the upper electrode surface. The presence of this charge indicated that a sample was reasonably resistive, as the charge did not leak to earth.

To reduce any thermal shock effects the samples were placed in the equipment at room temperature. A heating rate sufficient to reach the poling temperature in 30-40 minutes was used. The temperature was controlled via a thermocouple placed in the ground plate and a feedback loop connected to a plate heater (Bibby HB502, Bibby Sterlin Ltd, UK). The corona current supplied was kept to a minimum to limit the thermal breakdown generated by ionisation of air.

De-poling

As mentioned above the testing of the equipment required the same sample to be tested more than once. The samples were thermally de-poled between test runs by heating the samples above their Curie temperature. The thermal energy supplied is sufficient to remove the aligned domain structure, and a random domain pattern is formed during the cooling stage. De-poling was carried out at 200°C (180 °C/hr) for 1 hour and the piezoelectric coefficient (d_{33}) checked to be negligible before further testing.

3.3 SUMMARY

In summary the samples that have been fabricated for this work are:

i. Ball and attrition milled pure barium titanate to produce reference samples.

ii. Ball milled barium titanate with silicon carbide to produce 1, 3, 5 and 15wt% silicon carbide samples.

iii. Ball milled barium titanate with silver oxide to produce 1.9, 4.7, 9.3, 14.0 and 18.6wt% silver containing samples.

iv. Ball milled barium titanate with ~6.5wt% platinum.

v. Attrition milled barium titanate with silver nitrate to produce 1.3, 3.2, 6.4, 9.5, 12.7, 15.9 and 19.1wt% silver containing samples.

The barium titanate powders containing silver nitrate and platinum were calcined to decompose the metallic compounds to metal. Samples were initially uni-axially pressed at 50 MPa and then consolidated using a cold isostatic press at 150 MPa. Samples were generally sintered at 1300°C, with a binder burn-out dwell if required. The surfaces of the samples were polished to 1 μm for optical/electron microscope observation and 3 μm for the mechanical testing while a 1200 grit finish was used for the electrical samples. These electrical samples were subsequently electroded with silver paste. The fabricated samples were then characterised by the methods discussed in the next chapter.

4 CHARACTERISATION TECHNIQUES

4.1 INTRODUCTION

The samples fabricated using the methods and formulations outlined in the previous chapter have been analysed in terms of microstructure, mechanical and electrical properties using a number of techniques that are now discussed.

4.2 MICROSTRUCTURAL CHARACTERISATION

4.2.a X-RAY ANALYSIS

Background information on XRD analysis is given in Appendix IV. XRD analysis of the relevant specimens was performed on a Philips PW1710 Diffractometer with a generator voltage of 40 kV and current of 25 mA. Monochromatic $Cu_{k\alpha}$ radiation of wavelength, λ, equal to 0.154 nm was employed. X-ray scans were made between 2θ angles of $10°$ and $90°$ degrees in general, but the range was modified in specific cases, with data acquisition occurring for one second at intervals of $0.02°$. The acquired X-ray intensities were recorded using a computer before being processed.

Crystalline phases were identified by comparison with standard reference patterns from the Powder Diffraction File, PDF-2, database sets 1-45 maintained by the International Centre for Diffraction Data (ICDD). XRD is a standard technique used extensively to determine qualitatively the presence of any reaction phases in ceramics. There are three methods for quantitative analysis:

i. **External standard**

In binary systems the proportion of a component can be calculated by using a pure sample of that component as a reference.

ii. **Internal standard**

The internal standard must have peak intensities that do not interfere with peaks in the compound being analysed. This separate compound is added to each sample in the same mass proportion. The quantities of the respective constituents are then calculated using the internal standard reference peak at a specific angle. A calibration curve is

typically required if the mass absorption coefficients of the constituents are dissimilar. If the mass absorption coefficients are similar then compositional changes will have proportional intensity changes.

iii.   Theoretical

An estimate of the amount of a compound in a mixture can be calculated from the XRD diffraction pattern and knowledge of the chemical compositions of the phases present in the material.

The internal standard method was used to determine the amount of silver present in barium titanate-silver (nitrate) samples. Sintered specimens were ground with a pestle and mortar and a constant mass proportion of an internal standard compound added. High purity anatase (TiO_2), or alumina (Al_2O_3), are typical internal standards and Figure 4.1, shows the primary diffraction peaks for $BaTiO_3$, silver, alumina and anatase using data from the PDF-2 database.
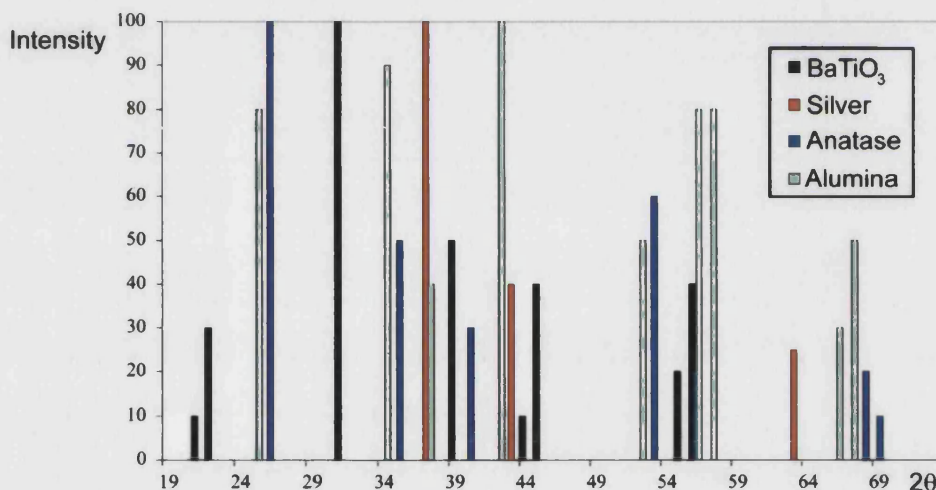
Figure 4.1: Intensity versus 2θ for barium titanate, silver, alumina and anatase.

Alumina was not chosen as the internal standard in this work since the diffraction peaks (2θ=37°, 42°) overlap with those diffraction peaks produced by silver (2θ=37°, 43°). Anatase was therefore chosen as the internal standard, due to no peak overlaps, and 20wt% was added to each ground sintered sample. This quantity was used as it produced an anatase peak height that gave nearly a full scale. The internal standard should not react with the barium titanate or silver at room temperature.

4.2.b   PARTICLE SIZE CHARACTERISATION

There are a number of techniques for determining particle size including sedimentation, laser diffraction, microscopy and X-ray diffraction. Each method measures a different particle parameter (length, volume, surface area etc) and can result in different measured values, which are not comparable. The following methods are extensively used and the particles are assumed to be of spherical geometry.

i.   **Microscopy** – Particles are observed via optical or electron microscopy and the diameter directly determined.

ii.   **Image analysis** – Using images obtained from microscopy, the area of the particle and other parameters are obtained with the use of computer software.

iii.   **Laser diffraction** – The volume of the particles is measured from the dispersion of a laser beam.

The laser diffraction method involves the scattering and dispersion of a light source by the particles. The particle size is then inferred from the light intensity pattern produced[159, 160]. This is an extensively used technique as it can analyse a large particle size range and is easy to use.

Particle size analysis was carried out using a Malvern Mastersizer 2000 system that uses laser diffraction. The powder to be measured was dispersed in distilled water and a particle distribution recorded three times for each sample. The results are given in terms of the parameters, D_{10}, D_{50} and D_{90}. D_{50} is the volume median particle diameter and is defined as the particle size that exactly divides the particle distribution in half.

Transmission and scanning electron microscopy were also used to determine the particle size and geometry of the starting materials. The particulate size, within the sintered composite, was measured from optical and scanning electron microscope images.

4.2.c   THERMOGRAVIMETRIC ANALYSIS

Thermogravimetric analysis, TGA, is commonly used to investigate the decomposition or oxidation of materials, such as polymers, and basic information is given in Appendix IV. For barium titanate two maxima in the sintering rate have been reported, at 1250°C and 1320°C [72]. The formation of a eutectic liquid may account for the higher temperature peak; the lower peak has been suggested to relate to grain boundary solid-state diffusion. This lower peak can be shifted to a higher

temperature by the presence of inclusions at the grain boundaries that increase the grain boundary diffusion activation energy[72].

Thermogravimetric analysis of powders was undertaken at a heating rate of 10 °C/min and with an air atmosphere on a Pelkin Elmer TGA 7 with a thermal analysis controller TAC 7/DX. These tests were carried out to determine the decomposition of the silver oxide and silver nitrate and the oxidation of the silicon carbide.

4.2.d   SINTERING RATE DETERMINATION

The heating profile used to measure sample shrinkage was identical to the sintering profile discussed in Chapter 3. The general method used for the determination of the sintering rate is given in Appendix IV. The dilatometer (Netzsch Dil 402C) and controller (Netzsch Tasc 414/4) used in this study were temperature calibrated with a gold sample. The surfaces of the dilatometer were protected from the sample by alumina spacers and the 5000 μm full-scale range used. Monolithic barium titanate and composite samples underwent dilatometry to investigate the influence of particle additions on the sintering behaviour.

4.2.e   DENSITY MEASUREMENT

The green density was calculated using the geometric method. The density of sintered samples was determined by the Archimedes techniques using distilled water as the liquid medium. The density of some sintered samples were measured, however, by the geometric method so that a comparison, with the geometrically obtained values, could be made. The equations and method of density determination are given in Appendix IV.

4.2.f   LIGHT MICROSCOPY

Microstructural analysis has traditionally used the optical microscope to examine reflection and transmission sections of materials. The depth of field decreases in an optical microscope as the magnification increases. For this reason very flat surfaces are required at high magnifications. The optical microscope may be used up to a magnification of one thousand times.

Grain size, fracture mode and phase distribution can be determined by optical microscopy. The proportion of silver, with a reported accuracy of ~1wt%, in a barium titanate-silver composite may

be determined using image analysis and calculating the area fraction of silver from microscope images[49]. This is possible as the silver particles have sufficient contrast with respect to the barium titanate matrix that they are easy to differentiate using image analysis software.

In this study optical photographs were taken of the samples to show the distribution of phases. The micrographs were subsequently digitised as 24-bit greyscale images. Two techniques were used to analyse the grain size, particle size, porosity and phase content. The first technique consisted of using a threshold greyscale value (between 1 and 255) to highlight the region of interest. In the barium titanate-silver composites, pores showed up as black regions and the silver particles were lighter than the matrix, see Figure 4.2.
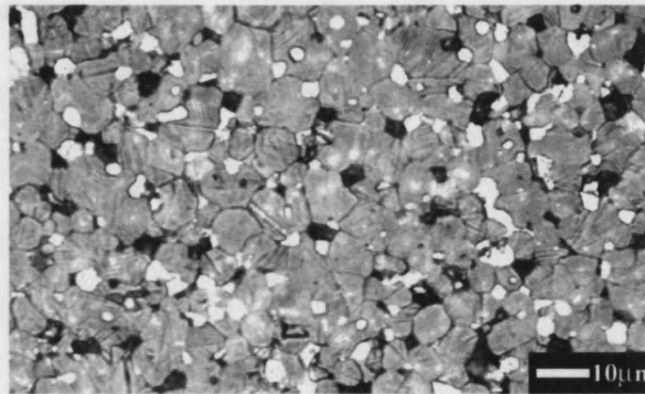
Figure 4.2: Optical microscope image of barium titanate-silver composite

showing bright silver particles, dark pores and grey barium titanate matrix.

Image analysis was performed with Optimas 6.2 software on the highlighted regions and the results (major and minor axis lengths, particle area and particle orientation) recorded. This technique, however, suffered difficulties in defining the threshold required to differentiate the boundary between two phases over the whole image. For this reason a second, more time consuming, technique was used where digitised images had the boundaries of grains and particles manually traced. This is a more accurate method and produces the same parameter types. The circularity of the particles was calculated in the second technique to determine any change in particle shape with change in silver inclusion content. In each case the image was spatially calibrated so that results were given in absolute terms. Frequency distributions of the particle sizes recorded were generated to discover if more than one mode of particle size existed.

4.2.g   SCANNING ELECTRON MICROSCOPY

Basic information pertaining to Scanning Electron Microscopy, SEM, is given in Appendix IV. Samples in this study were either coated in gold, for microstructural and fracture surface observation, or carbon for elemental mapping. Gold coatings were applied for 4-6 minutes using a Sputter coater, S150B model (Edwards High Vacuum Ltd. England). When required a thin carbon coating was applied with a Carbon coating machine model 12E6 (Edwards High Vacuum Ltd. England). The general microstructure, particle size and measurement of the hardness and toughness properties were determined from images taken using a JEOL T330 SEM. X-ray analysis and elemental mapping was undertaken using a JEOL JSM-6310 Analytical SEM fitted with an Oxford Instruments AN 10/85 Link microanalysis system.

4.2.h   TRANSMISSION ELECTRON MICROSCOPY

Transmission Electron Microscopy, TEM, has been used to determine the powder particle size[40, 161], but can also be used to observe domains[136] and examine sample composition. Sample preparation for TEM observation and information relating to TEM can be found in Appendix IV. The prepared sample was mounted in a beryllium holder and analysed using a JEM 2010 200 kV TEM. The formulations analysed were monolithic barium titanate, barium titanate-1wt% silicon carbide and barium titanate-3.2wt% silver.

4.3 DETERMINATION OF MECHANICAL PROPERTIES

4.3.a   STRENGTH DETERMINATION

A popular method for the determination of fracture strength is the three-point bend test and this is described in Appendix IV. The ball-on-ring method, used in this work, is suitable for testing the ceramic strength with axi-symmetric bending of the disk and requires minimal alignment[162]. The values obtained for strength were analysed using Weibull statistics.

In this research mechanical testing was conducted on the monolithic and composite samples prepared by the method described in Chapter 3. Sample radius and thickness were recorded before testing the samples to failure in an Instron Universal Tester Model 1122 (Instron, Massachusetts,

USA). The load being recorded on chart paper at 50 mm/min and a crosshead speed of 0.5mm/min. Unpoled samples were tested under open circuit conditions.

4.3.b   TOUGHNESS DETERMINATION

Many techniques have been devised to estimate the resistance of a material to crack propagation, such as Vickers indentation, Knoop indentation and Controlled Surface Flaw[2, 12, 41]. The Vickers indentation method is described in Appendix IV and was the technique used in this research for toughness determination. In this study polished samples were indented using a Zwick Vickers hardness tester 3212 (Zwick Materialprüfung, Zwick GmbH & Co., Germany). Initially the variation of toughness with load was investigated before other tests were carried out with a load of 9.8 N for 30 seconds. The crack lengths were evaluated in both orthogonal directions. The magnification factors of the eyepiece and objective were 10 and 20 times respectively.

In addition to observing the cracks optically the samples were sputter coated with gold for three minutes (Edwards sputter coater S150B) and images of the indent and cracks taken using the JEOL T330 Scanning Electron Microscope, within three hours of indentation. The crack lengths were calculated from the images taken.

4.3.c   HARDNESS DETERMINATION

The Vickers indentor technique has been used by previous researchers for the determination of the hardness of a material[41, 109]. The deformation of the material under a constant load will vary depending on the hardness of the material. As with the toughness, both dimensions of the orthogonal diagonals, a, for the indent are used to calculate the Vickers hardness, H_v, from equation 4.1.

$$H_v = \frac{P_v}{2a^2} \qquad \{4.1\}^{109}$$

It should be noted that the material is assumed to deform at constant volume. However, in practice this may not be the case, especially in highly porous materials where densification may occur. In addition to observing the indents optically the samples were sputter coated with gold for three minutes (Edwards sputter coater S150B) and images of the indent taken using the JEOL T330 Scanning Electron Microscope, within three hours of indentation. The indent diagonals were then measured from the recorded images and the hardness calculated using equation 4.1.

Hardness was measured for the monolith and composites to evaluate the influence of particle addition on barium titanate.

4.3.d   STIFFNESS DETERMINATION

The stiffness of a material can be determined by the slope of the stress-strain plot, or calculated using an ultrasonic method[12]. The small discs produced in this study are unsuitable, however, for the ultrasonic method and the load-displacement plots from the biaxial testing are too variable for comparison between compositions. A stiffness value was determined from the resonance behaviour, during impedance analysis, of the disc shaped samples. This is the elastic stiffness in the 1-direction, which is parallel to the poling direction, under constant electric field conditions. The calculation uses the radial resonant mode of a disc, where 1 is the disc radius (in metres). Equation 4.2 was used, where ρ is the sample density (in $Mgcm^{-3}$) and f_s (in Hz) is the radial resonant frequency.

$$Elastic\ stiffness,\ 1/s_{11}^E\ =\ \frac{4\ \rho\ \pi^2 l^2 f_s^2 (1-v^2)}{2.05^2}\qquad\{4.2\}^{154}$$

4.4   ELECTRICAL PROPERTIES DETERMINATION

4.4.a   DETERMINATION OF RELATIVE PERMITTIVITY

The relative permittivity is determined from the capacitance of the sample at room temperature, using a voltage of 1 V at a frequency of 1 kHz. The relative permittivity, ε_r, was given by equation 2.17. Measurements of sample capacitance were recorded using a Hewlett Packard 4263B LCR meter with six centimetre diameter top and bottom metal plates. The device was calibrated by testing reference capacitors (10 pF, 1 nF). The sample surface was prepared as mentioned in Chapter 3, as surface roughness introduces air gaps between the dielectric and the electrode and this induces error[113]. The dielectric loss was directly recorded using the Hewlett Packard 4263B LCR meter.

Additional relative permittivity measurements were made using a Solartron 1296 Dielectric Interface and a S11260 Impedance/Gain phase analyser. The relative permittivity of the monolithic and composite materials was recorded over a frequency range of 1 Hz to 1 MHz, using an applied

voltage of 1 V. The conductivity of the barium titanate was increased by heating the sample, so that the frequency range of the Solartron overlapped the change between two relative permittivity trends. The two trends have been discussed in Chapter 2 and are related to the bulk and grain boundary contributions. The different temperatures used were 186°C, 242°C and 310°C in order to compare with reported results[115]. These results can then be compared to the data produced by the computational modelling, which is discussed in Chapter 6.

4.4.b   MEASUREMENT OF PIEZOELECTRIC COEFFICIENTS

The piezoelectric coefficient, d_{33}, is the charge per unit force (C/N) measured in the poled direction of the sample. The disc samples are suitable for measurement as the lateral dimensions are at least twice the sample thickness[163]. The d_{31} coefficient is the charge per unit force in the orthogonal directions for a disc.

In this work the charge per unit force was measured with a Take Control Piezometer System PM25, which is described in Appendix IV. The calibration of the PM25 piezometer was undertaken using the PZT reference sample supplied with the device that is reported to have a d_{33} of 330 pC/N. The measurements of the monolithic and composite d_{33} and d_{31} piezoelectric coefficients were carried out at least 24 hours after poling to enable the rapid ageing in this time period to stabilise[21, 118].

The d_{33} coefficient was also used to characterise the poling rig that was constructed for this research and determine the effect of time, temperature and voltage on the degree of poling. In order to characterise the extent of the poling field, small disks (5 mm diameter and 5 mm thickness) were fabricated from barium titanate. These were then positioned in the poling chamber in the pattern shown by Figure 4.3. A thermocouple (type K) was connected to a Digitron 20981 Thermometer in order to measure the temperature below and above a sample centred in the poling rig. This was used to determine the difference between the temperature set on the thermostatic controller and the actual temperature experienced by the specimen. The d_{33} values of the samples were recorded and plotted to determine the optimum poling area of the rig.

d_{33} measurements were also recorded at the edge of the samples as a five percent increase has been reported for this region[163]. This effect was investigated by recording the piezoelectric coefficient at different positions across three large 30 mm diameter PZT discs (4 mm thickness), Figure 4.4. The measurements were taken in each cell marked out on the discs, which were poled under the same conditions.
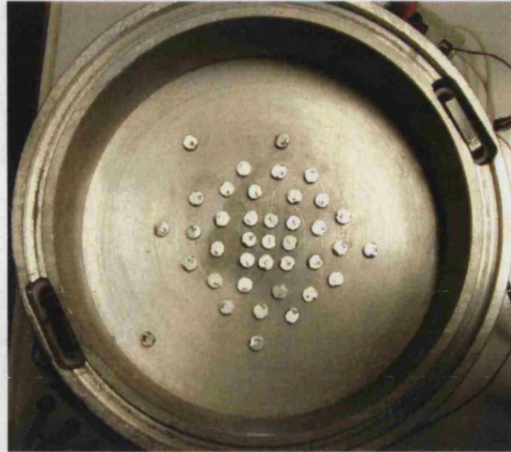
Figure 4.3: Position of the small discs used in the characterisation of the poling rig.
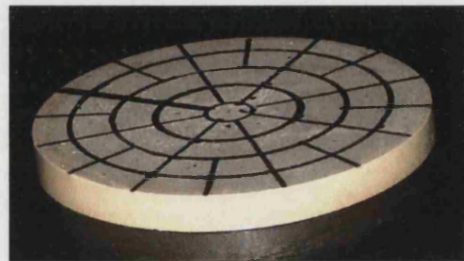
Figure 4.4: PZT sample of 30 mm diameter used for sample edge effect analysis.

4.4.c   RESISTIVITY DETERMINATION

The sample resistance, R_p, in Ohms, was directly recorded using the Hewlett Packard 4263B LCR meter for the monolithic and composite materials. This was then converted to a resistivity value (Ω.m), ρ_r, using equation 4.3, where t is the sample thickness (m) and A the cross-sectional area (m^2).

$$\rho_r = \frac{R_p A}{t} \qquad \{4.3\}$$

R_p is the effective resistance of a resistor in parallel with the sample. The device was checked for calibration with reference resistors (100 Ω, 1 kΩ, 1 MΩ).

4.4.d   DIELECTRIC BREAKDOWN MEASUREMENT

Dielectric breakdown was conducted to examine the influence of metallic particle addition on the dielectric strength of barium titanate. Samples had an electrode of reduced area to promote breakdown of the bulk material, rather than surface shorting of the sample. The investigation was carried out using a Sefelec breakdown system (Sefelec SA, France) at the National Physical Laboratory (NPL). Each sample was placed between spring loaded steel electrodes in a jig that is subsequently immersed in Shell Diala transformer oil, Figure 4.5. The jig was vibrated to remove air bubbles from the sample and electrode prior to testing.
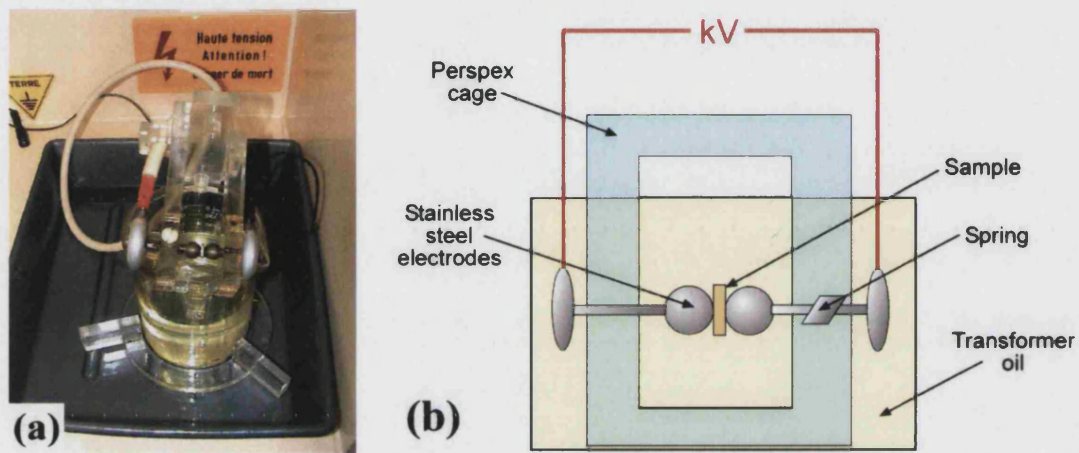
Figure 4.5: Dielectric breakdown (a) sample test fixture and (b) schematic of test fixture.

Stainless steel spherical electrodes were used to reduce the risk of discharge between electrode surfaces and the spring provided a constant force for both mechanical and electrical contact. The rate of voltage rise was set such that dielectric breakdown occurred within 10-20 seconds under DC conditions. Dielectric breakdown was considered to have occurred when a rate of current change greater than 3 mA/s was detected across the sample. The full-scale deflection was 50 kV for the monolith and 20 kV for the composites. Testing was carried out at a temperature of 22.6°C. After breakdown the samples were removed and subsequently analysed to determine where breakdown occurred and the breakdown sites were observed using the SEM.

4.4.e   IMPEDANCE ANALYSIS

The effective coupling coefficient, K_{eff}, and the mechanical quality factor, Q_m, of the materials were calculated from data obtained using a Solartron 1296 Dielectric Interface and S11260 Impedance/Gain phase analyser. The data was logged using a PC installed with Solartron Impedance Measurement software version two.

The primary resonant frequency, f_{radial}, was estimated as approximately 209 kHz from equation 2.33 (ρ=5950 kgm^{-3}, r=0.0053 m, S_{11}^E=8.55x10^{-12} m^{2}N^{-1} [156]). A frequency range of 100 kHz to 1 MHz with 500 steps was therefore used. Once the impedance peak had been located an additional sweep, typically over 100 kHz with 270 steps was undertaken to determine the sample behaviour more accurately. The data of real impedance (Z') and imaginary impedance (Z'') were then analysed in Microsoft Excel.

During measurement care was taken not to place objects close to the sample and electrode, as spectra can be affected by interference[164]. Open and short compensation was carried out to minimise effects from the testing equipment during measurement of an actual specimen. Samples were placed on a flat brass bottom electrode.

Spurious results can occur for samples that are not perfectly circular, have defects or are not held correctly. However, the calculated material parameters are not greatly affected as they depend on the resonant and anti-resonant frequencies[156]. An electric voltage of 1 V was applied over the sample (typically 2-3 mm in thickness). In the literature a field around 1 V/mm is a recommend maximum[156].

4.4.f   POLARISATION-FIELD ANALYSIS

Polarisation-Field, PE, analysis requires the application of an electric field to a sample while measuring the current response of the material. These measurements were carried out at the National Physical Laboratory, NPL, using a modular Polarisation-Strain-Electric Field (PSE) system. A schematic diagram of the system, basic information and a device listing are given in Appendix IV.

In this research monolithic and composite samples were analysed to determine the change in polarisation-field loop, coercive field and remanant polarisation as a function of particle addition. 1200 points were captured for each run over the applied stimulus field voltages (in kV) 0.05, 0.1, 0.2, 0.3, 0.4, 0.5. Above a field of 0.5 kV the voltage was increased in steps of 0.5 kV until a broad polarisation-field loop was produced or it was felt that sample breakdown might occur. As each sample was of different thickness the actual field (kV/mm) varied.

5 RESULTS OF MICROSTRUCTURAL, MECHANICAL AND ELECTRICAL PROPERTIES ANALYSIS

5.1 MICROSTRUCTURAL ANALYSIS

5.1.a   X-RAY DIFFRACTION ANALYSIS

X-ray diffraction (XRD) has been utilised to determine the phase content of the raw starting materials, manufactured powders and fabricated sintered samples.   It has allowed the decomposition of the starting components and formation of any reaction phases to be observed. Appendix VI contains the reference XRD data of the compounds analysed.

5.1.a.i   XRD analysis of as-received starting materials

5.1.a.i.a   XRD analysis of barium titanate starting powder

The XRD trace of 'as received' barium titanate powder is shown in Figure 5.1.
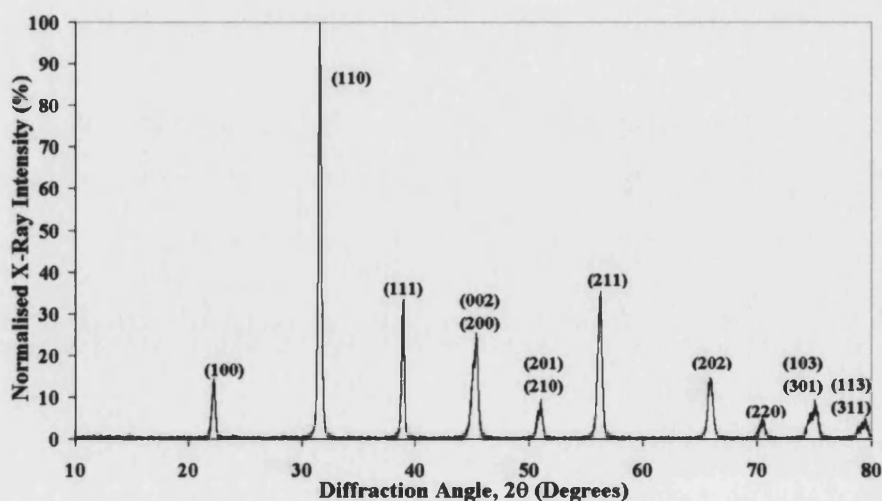
Figure 5.1: X-ray diffraction pattern of barium titanate powder showing that all intensity

peaks are associated with tetragonal barium titanate.

Comparing the principle peaks given in the reference data (Appendix VI) confirms that there are no major impurity phases with intensity peaks above ~2%. The diffraction pattern indicates that the powder supplied has been previously calcined as there are no peaks at 28.7° and 35.7°, which correspond to barium oxide (BaO) and titania (TiO_2), respectively.

5.1.a.i.b   XRD analysis of silicon carbide starting powder

Figure 5.2 shows the XRD analysis of the silicon carbide powder before any heat-treatment. The peaks of the silicon carbide correspond well to the major peaks of the alpha silicon carbide standard reference. No other significant peaks were observed.
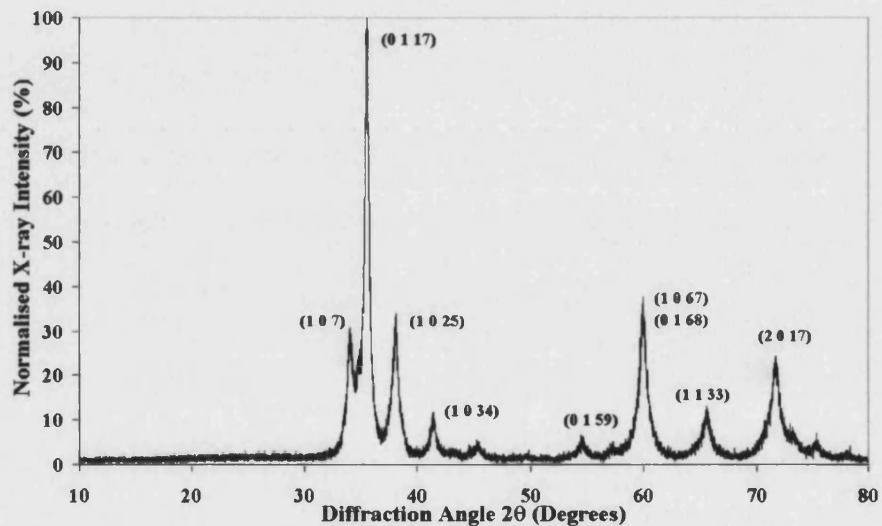
Figure 5.2: X-ray diffraction pattern of as received silicon carbide.

To examine the extent of silicon carbide particle oxidation in an argon atmosphere the powder was heat-treated in flowing argon at 1300°C for two hours to represent a standard sintering schedule. Figure 5.3 shows the XRD trace of the powder after heat treatment. The peaks of the heat-treated silicon carbide correspond well to the major peaks of the alpha silicon carbide standard reference. It appears that sintering in argon at 1300°C has little affect on the silicon carbide except for a slight sharpening of the peaks, compared to Figure 5.2, indicating a higher degree of crystallinity. Silica (Appendix VI) has not been formed, as a peak at 28.8° is not observed.
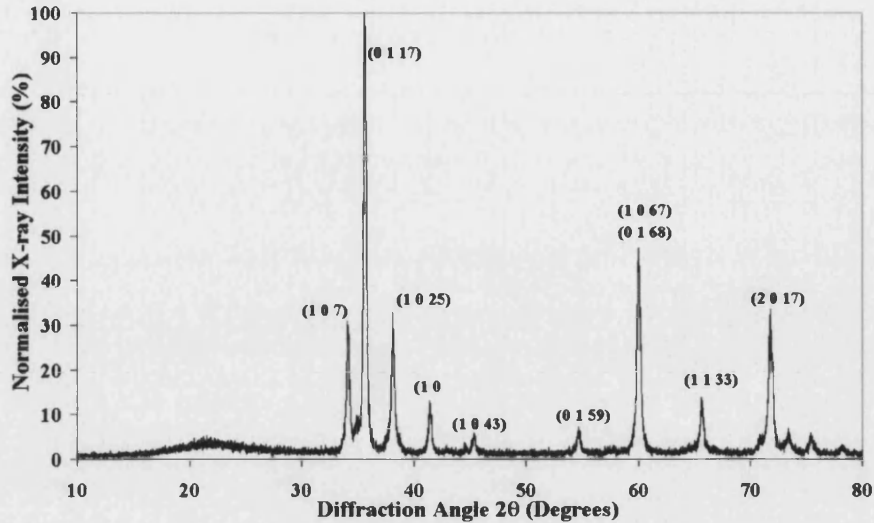
Figure 5.3: XRD result for heat-treated silicon carbide.

5.1.a.i.c   XRD analysis of silver oxide and silver nitrate starting compounds

Figures 5.4 and 5.5 show the XRD diffraction patterns of the silver oxide and silver nitrate powders, respectively. These compounds were used in the manufacture of the barium titanate-silver composites. Silver carbonate peaks are represented by AC, silver oxide by AO and silver nitrate is assigned AN.
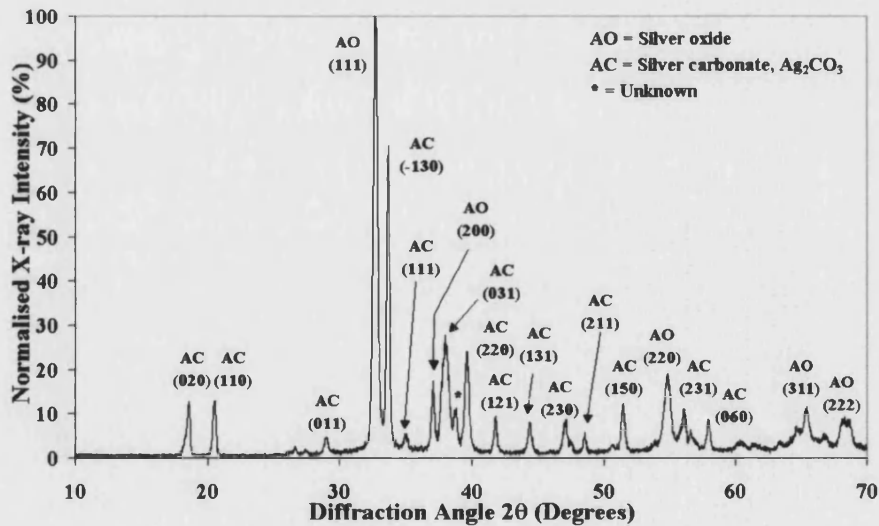
Figure 5.4: Silver oxide powder X-ray diffraction pattern showing the

presence of silver oxide and silver carbonate.
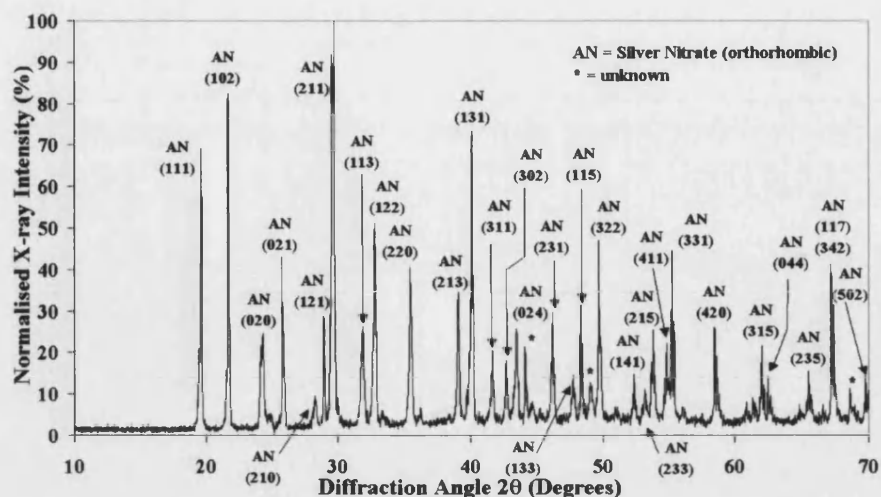
Figure 5.5: Silver nitrate powder X-ray diffraction pattern with minor unknown peaks.

The silver oxide powder contains a considerable amount of the impurity silver carbonate. Silver carbonate is the starting material, which is decomposed, for silver oxide production; in this case incompletely. Complete decomposition is expected during the sintering of silver (oxide) composite powder. The majority of the diffraction peaks for silver nitrate were associated with the orthorhombic phase. A number of minor peaks (44.1°, 49.1°, and 68.6°) could not be assigned to any expected compound. The actual measured intensities do not correspond closely with the reference standard. This is most likely due to the silver nitrate being in the form of large crystals of a few millimetres in diameter. Although these crystals were ground before X-ray analysis was performed their morphology may have produced preferential alignment.

5.1.a.i.d   XRD analysis of platinum compound

Analysis of the starting compound hydrogen hexachloroplatinate(IV) was not possible due to its ease of hydration in the presence of atmospheric moisture and insufficient powder being available for analysis. X-ray diffraction analysis was carried out on the calcined composite powder.

5.1.a.ii   XRD analysis of composite powders

5.1.a.ii.a   XRD analysis of calcined barium titanate-silver (nitrate) powder

Figures 5.6 and 5.7 are the XRD results of non-calcined and 300°C calcined barium titanate-silver nitrate powders respectively. All major peaks were assigned to barium titanate and silver nitrate for the non-calcined powders and the peaks corresponding to silver nitrate increased with increasing silver nitrate weight fraction. Two minor peaks were unassigned and no peaks observed

due to silver nitrate decomposition to silver or silver oxide during the milling process (2θ values for possible compounds are Ag 38.1°, Ag_2O_2 37.3° [*], Ag_2O 37.9° [*], AgO 37.2° [*]).

Figure 5.7 shows that silver nitrate was still present, after calcination at 300°C, in the 19.1wt% and 25.4wt% samples, but to a lesser degree than before the heat treatment. Of significance is the presence of four new peaks (38.2°, 44.6°, 64.5° and 77.5°) that correspond to metallic silver. These results indicate that the sintering of calcined silver nitrate powders will not be inhibited by the nitrous oxide gases formed during silver nitrate decomposition.
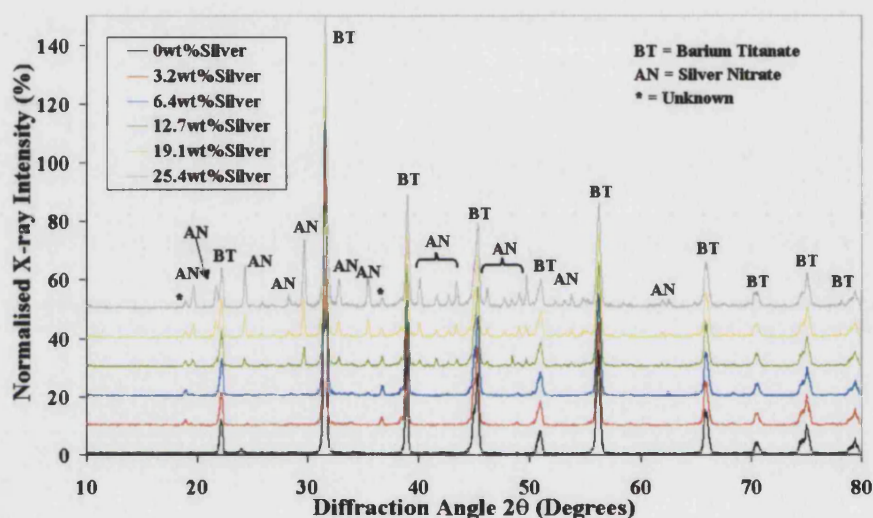
Figure 5.6: X-ray diffraction patterns for non-calcined barium titanate-silver powders

showing peaks associated with silver nitrate (AN) and barium titanate (BT).

---

[*] These peaks are not the 100% peak for that compound as they are overshadowed by the proximity of the barium titanate 100%.
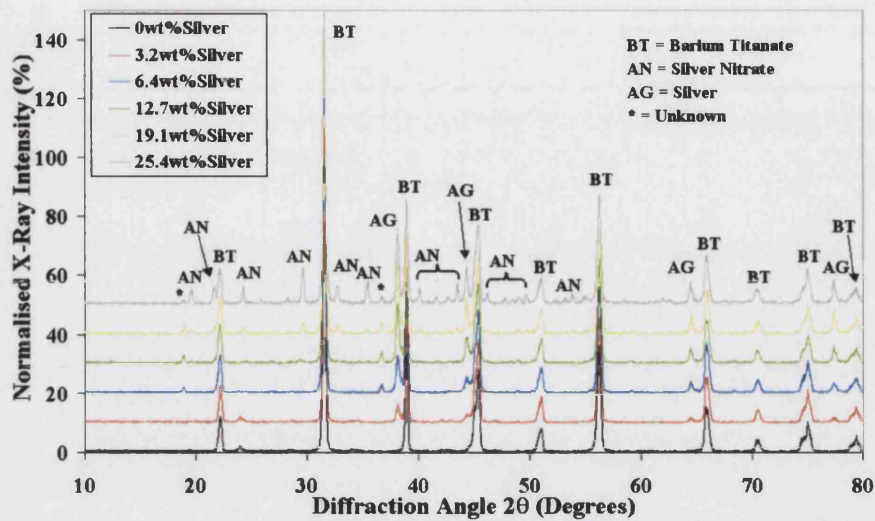
Figure 5.7: X-ray diffraction patterns of barium titanate-silver powders calcined at 300°C showing peaks associated with silver (AG) and barium titanate (BT). Silver nitrate (AN) was observed in the 19.1wt% and 25.4wt% composites.

5.1.a.ii.b XRD analysis of calcined barium titanate-platinum

XRD analysis of the calcined barium titanate-platinum powder, Figure 5.8, revealed the presence of major peaks for barium titanate and platinum, however, a number of additional unknown peaks were observed. These may be due to the incomplete breakdown of the complex platinum compound ($H_2PtCl_6.xH_2O$), impurities or a reaction product.
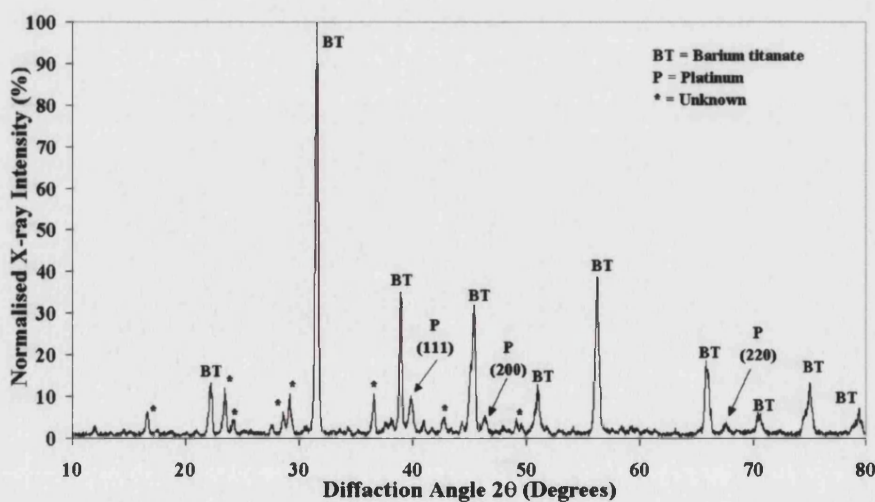
Figure 5.8: X-ray diffraction pattern of barium titanate-5.7wt% platinum calcined at 600°C showing a number of unassigned minor peaks.

5.1.a.ii.c   XRD analysis of sintered barium titanate

The XRD pattern, Figure 5.9, of the monolithic barium titanate, sintered in air showed no secondary phases. One sample was sintered at 1400°C to observe the generation of any eutectic liquid phase. No unknown peaks were discovered indicating that the quantity of any liquid phase must be less than the resolution of the equipment, which is taken to be ~2wt%. Figure 5.9 is taken as the reference for the sintered composite samples. The absence of additional phases at 1400°C indicates that none will be present at the monolithic sintering temperature of 1300°C.
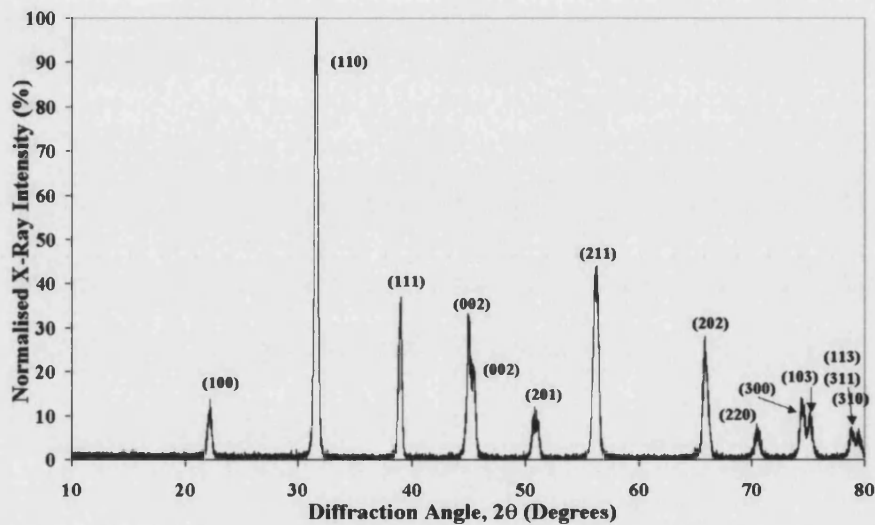
Figure 5.9: X-ray diffraction pattern of sintered barium titanate with all peaks

assigned to the tetragonal structure of barium titanate.

5.1.a.ii.d   XRD analysis of sintered barium titanate-silicon carbide composites

XRD analysis was not conducted on a sintered barium titanate composite with 1wt% silicon carbide as the resolution of the diffraction equipment would be insufficient to pick out the silicon carbide or any reaction phases due to background noise. Figures 5.10 and 5.11 show the XRD patterns of $BaTiO_3$-2wt% silicon carbide and $BaTiO_3$-5wt% silicon carbide respectively.
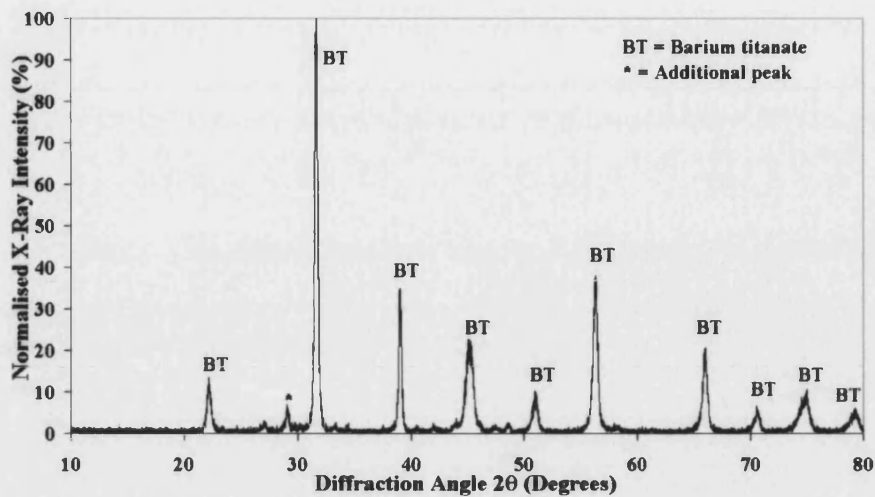
Figure 5.10: X-ray diffraction pattern of barium titanate-2wt% silicon carbide.
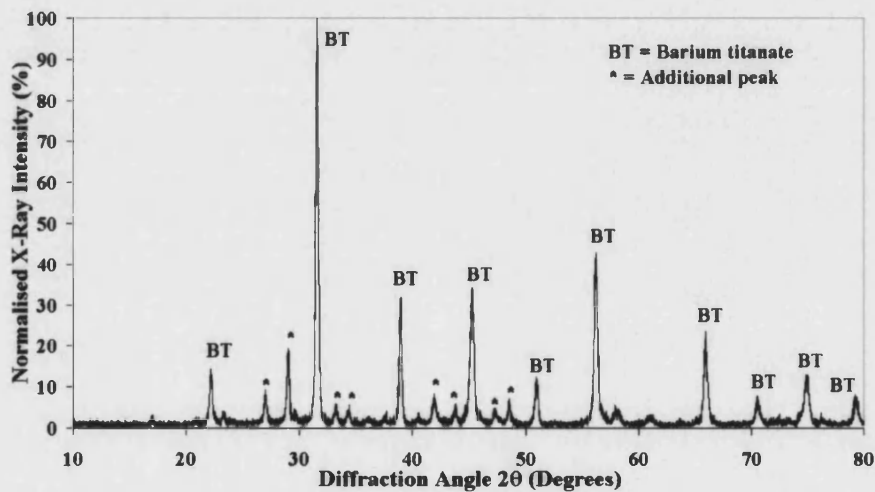
Figure 5.11: X-ray diffraction pattern of barium titanate-5wt% silicon carbide showing

the increase in additional peak intensity in comparison to the barium

titanate-2wt% silicon carbide diffraction pattern.

Formation of a secondary phase is observed as the composite silicon carbide weight percentage is increased, as indicated by the unassigned peaks in Figures 5.10 and 5.11. The peaks at 27° and 29° suggest the formation of the reaction compound $Ba_2TiSi_2O_8$ (Appendix VI) from the reaction of the barium titanate with the silica layer on the silicon carbide particles, equation 5.1.

$$BaTiO_{3\,(s)} + 2SiO_{2\,(l)} \rightarrow Ba_2TiSi_2O_{8\,(s)} + TiO_{2\,(s)} \qquad \{5.1\}$$
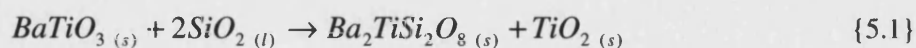
The silica is formed by the oxidation of the silicon carbide particle, equation 5.2.

$$SiC_{(s)} + 2O_{2\ (g)} \rightarrow SiO_{2\ (l)} + CO_{2\ (g)} \qquad\qquad \{5.2\}$$
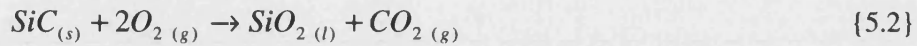
There are no peaks corresponding to the pure silicon carbide indicating that, at least on the surface of the sample, all the silicon carbide has reacted. The presence of silica, which is not observed, would be expected if the silicon carbide has been oxidised. It may have completely reacted, however, to form the $Ba_2TiSi_2O_8$ compound. Niihara[41] has reported the presence of this reaction phase in hot pressed barium titanate-5vol% silicon carbide composites sintered above 1300°C.

Samples with 15wt% silicon carbide were fabricated to determine the composition of the reaction phase. The compositional differences were examined, by XRD analysis, of the sample surface and interior. Figure 5.12 shows the XRD pattern for the surface of the barium titanate-15wt% silicon carbide, while the composite interior is shown in Figure 5.13.
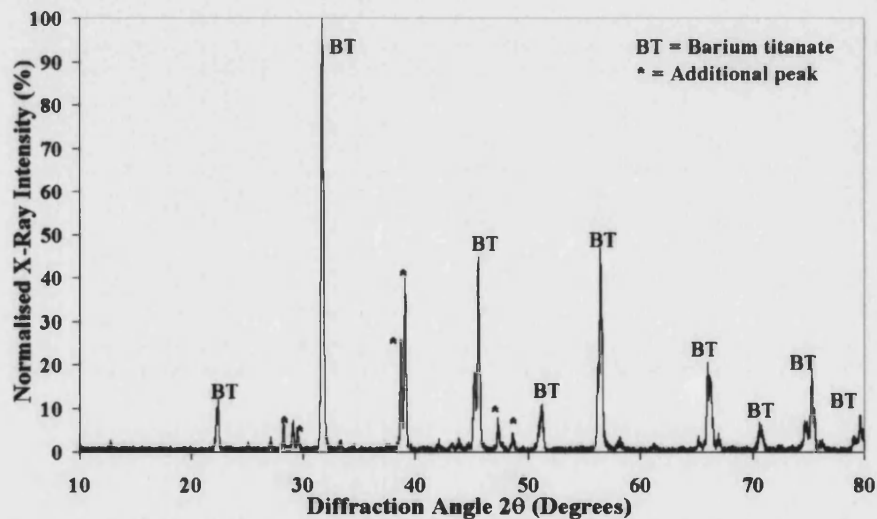
Figure 5.12: X-ray diffraction pattern for the surface of barium titanate-15wt% silicon carbide indicating additional peaks associated with a reaction phase.
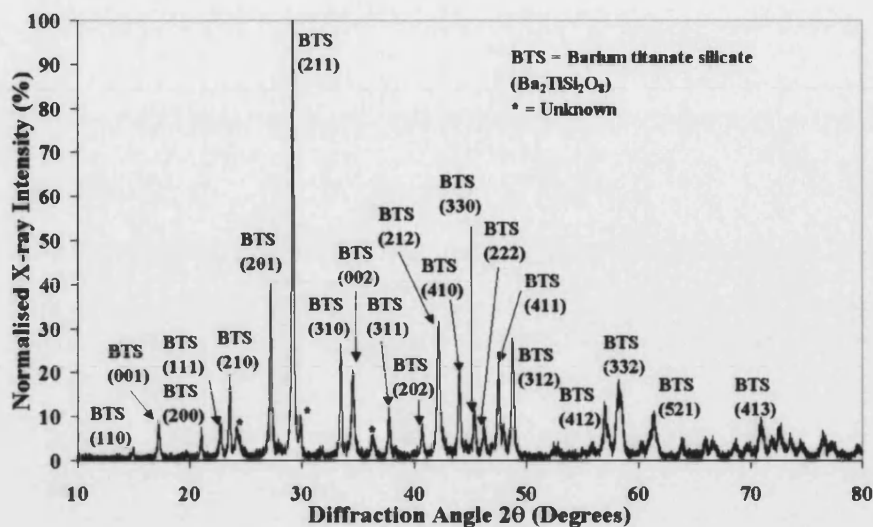
Figure 5.13: X-ray diffraction pattern for sample interior of barium titanate-15wt% silicon carbide, indicating the presence of the reaction phase $Ba_2TiSi_2O_8$.

At the surface there are a few unknown minor peaks and the diffraction pattern suggests a depletion of silicon carbide and the presence of a reaction phase. The core of the sample appears to be completely $Ba_2TiSi_2O_8$ with the surface being barium titanate. The silicon carbide has been lost from the surface and subsequent sample finishing needs to remove this layer to ensure that the properties of the actual "reacted" composite are measured.

Comparing Figures 5.9 and 5.11 shows that as the silicon carbide content is increased the crystallography of the barium titanate samples has changed from tetragonal to a more cubic structure as the (002) and (200) peaks have merged (~45°). This change is likely to affect the formation of domains, as they are not formed in the cubic system. The extent of this modification, however, is unknown and the presence of the secondary phase increases the complexity. In the barium titanate-15wt% silicon carbide the structure has been completely changed into the non-piezoelectric reaction phase. Niihara reported that the addition of silicon carbide to barium titanate changed the monolithic tetragonal crystal structure to pseudo-cubic[41].

For the hot pressed samples, Figure 5.14, $Ba_2TiSi_2O_8$ was discovered to be present. A few peaks remain unassigned, with the rest relating to barium titanate.
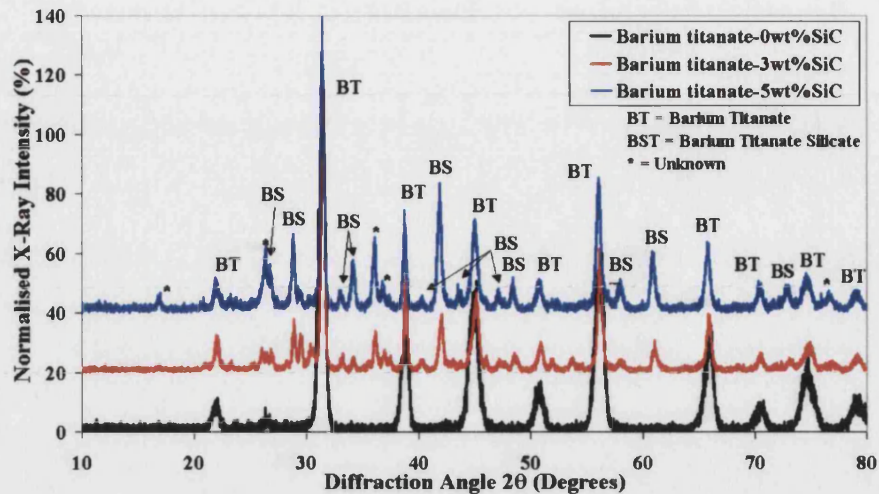
Figure 5.14: X-ray diffraction pattern of hot pressed barium titanate with varying amounts of silicon carbide showing the presence of the reaction phase barium titanate silicate.

5.1.a.ii.e   XRD analysis of sintered barium titanate-silver (oxide) composites

Composites with silver inclusions were fabricated by decomposing silver oxide. Silver oxide was not observed in the sintered composites and complete decomposition to silver had occurred, Figure 5.15. X-ray analysis of these composites indicated a depletion of silver at the surface of the specimens, see Figure 5.15. The surface of the $BaTiO_3$-18.6wt% silver sample shows no silver due to loss by evaporation, while in samples that have been polished to remove the depletion layer the presence of silver (peaks at 38.2°, 44.6° and 64.5°) is observed. Evaporation of silver occurs due to the high vapour pressure of ~130 Pa at the sintering temperature. Silver is not seen with a barium titanate sample containing 4.7wt% silver due to the resolution limit of the equipment. The intensity of the silver peaks for the $BaTiO_3$-14wt% silver and the $BaTiO_3$-18.6wt% silver composites are similar, which may imply that silver evaporation is greater in the higher weight fraction composites. No reaction phases between the components were observed.
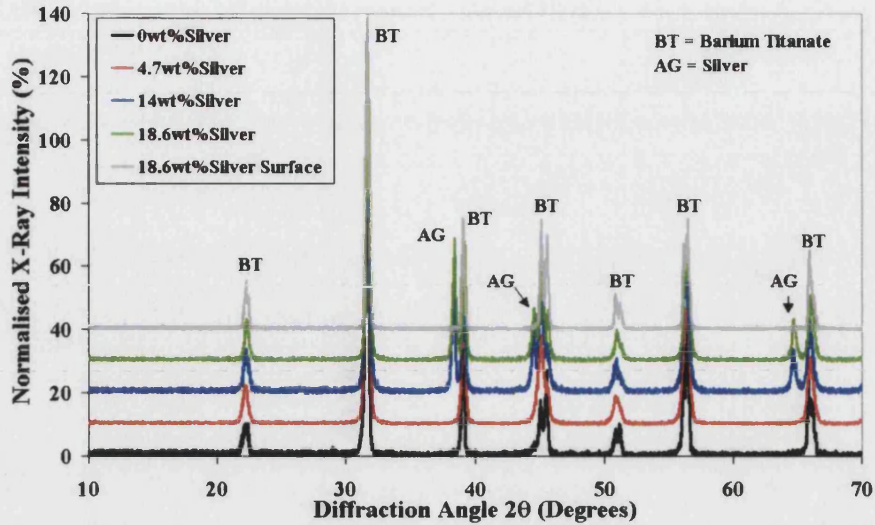
Figure 5.15: X-ray diffraction patterns of sintered barium titanate-silver (oxide)

showing silver peaks due to the decomposition of silver oxide. A depletion

of silver at the composite surface is also observed.

5.1.a.ii.f   XRD analysis of sintered barium titanate-silver (nitrate) composites

A solution-based method of producing $BaTiO_3$-silver composites using silver nitrate was employed to improve the dispersion of silver in the barium titanate matrix. XRD examination of the sintered, and polished, samples revealed that the proportion of silver increases with silver (nitrate) weight fraction, see Figures 5.16 and 5.17. No reaction phases were observed, even at the high silver fractions.
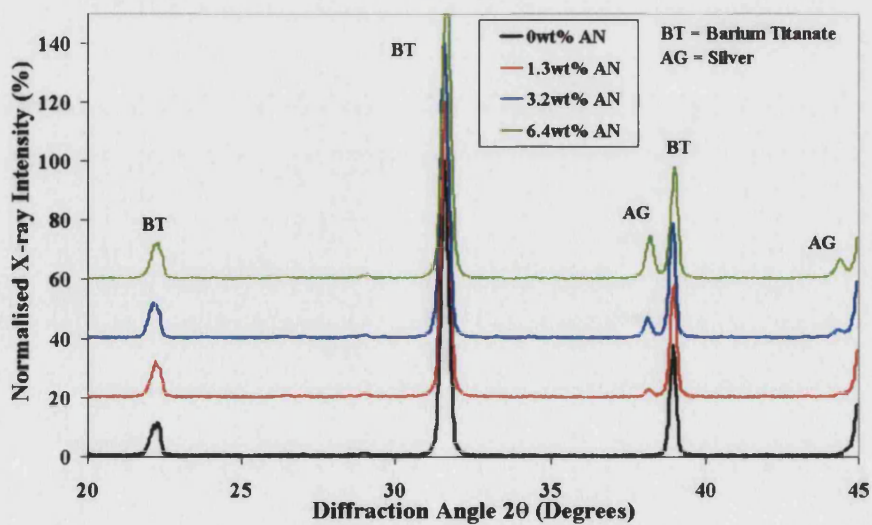
Figure 5.16: X-ray diffraction patterns of sintered barium titanate-silver (nitrate)

(0, 1.3, 3.2, 6.4wt% silver) composites indicating no unassigned peaks.
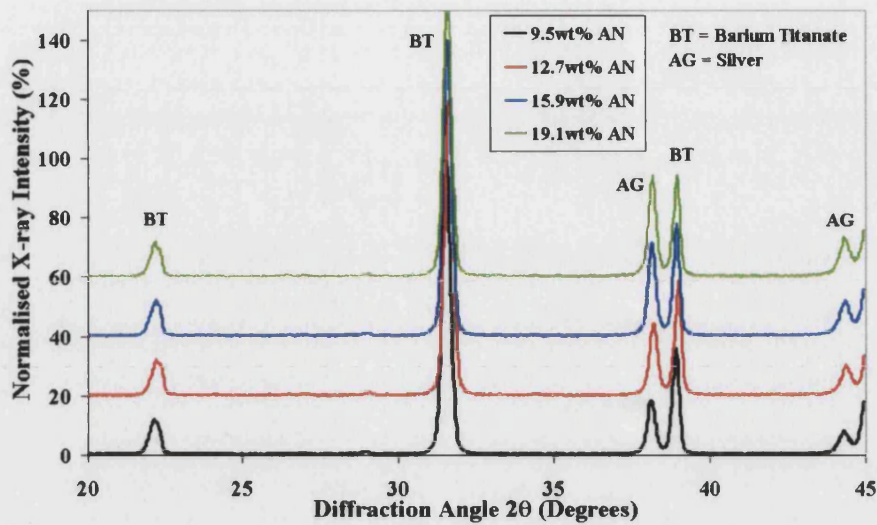
Figure 5.17: X-ray diffraction patterns of sintered barium titanate-silver (nitrate) (9.5, 12.7,

15.9, 19.1wt% silver) composites indicating no unassigned peaks.

The proportion of silver may decrease from the value added in the original powder due to evaporation. Silver has a melting point of 961°C and a vapour pressure of ~130 Pa at 1300°C. The internal standard method was employed to determine the fraction of silver within the samples. The compound used as the internal reference was anatase, which is a form of titania, TiO_2. Figure 5.18 is the anatase reference diffraction pattern. The procedure has been previously mentioned in Chapter 4, but involves mixing anatase with the ground powders of the sintered composites.
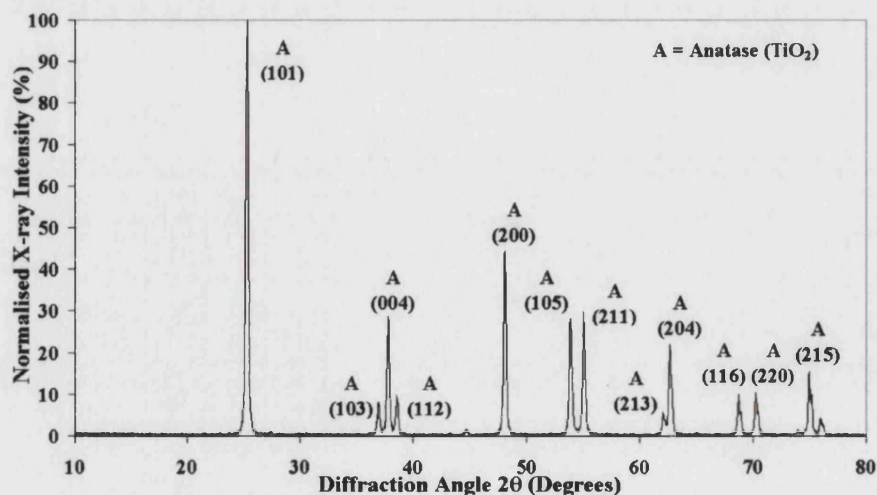
Figure 5.18: X-ray diffraction pattern of anatase used as the internal standard

indicating no unknown phases.

Figures 5.19 and 5.20 show the X-ray diffraction results of ground sintered barium titanate-silver (nitrate) samples mixed with the internal standard, anatase.
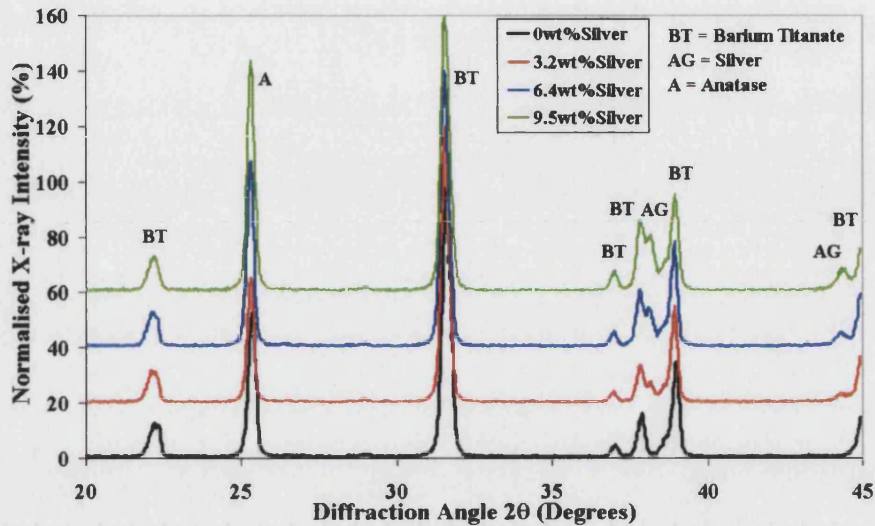
Figure 5.19: X-ray diffraction patterns used for the calculation of silver content in

the barium titanate-0, 3.2, 6.4, 9.5wt% silver composites.
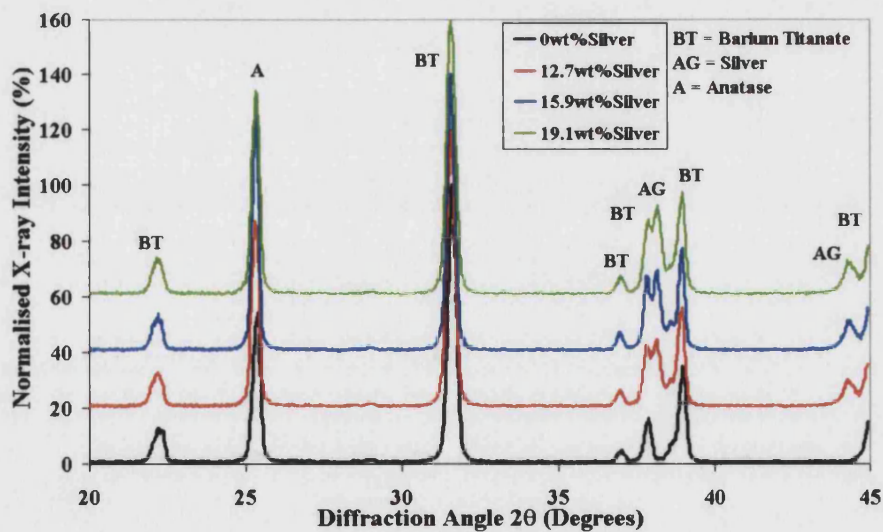
Figure 5.20: X-ray diffraction patterns used for the calculation of silver content in

the barium titanate-0, 12.7, 15.9, 19.1wt% silver composites.

The primary silver peak (38.1°) is in close proximity to the 37.8° barium titanate peak, but is sufficiently different for a calculation of the silver content to be made. Using the silver primary peak the silver contents were determined and are given in Figure 5.21.
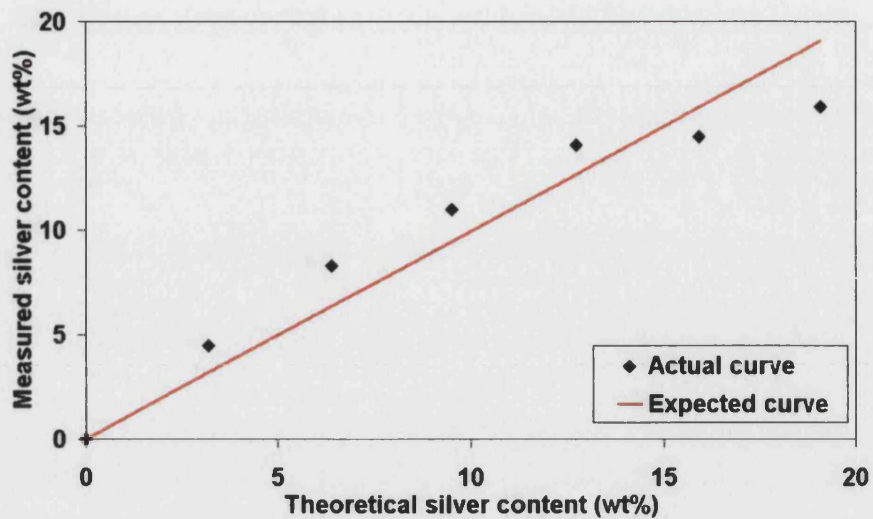
Figure 5.21: Silver content as determined by X-ray diffraction analysis using

an internal standard of anatase.

At low silver contents the results from XRD analysis give higher than expected values but a change occurs in the higher silver content samples. This suggests that there could possibly be some loss of silver from the core of these samples. However, accurate determination is limited to the ~2wt% resolution of the equipment. It can be concluded, however, that silver loss from the sample interior was not a significant occurrence in these composites.

5.1.a.ii.g   XRD analysis of sintered barium titanate-5.7wt% platinum

A single weight fraction of barium titanate with platinum was fabricated due to the high cost of the platinum compound. XRD analysis of the sintered sample is given in Figure 5.22. A reduced diffraction angle range of 20-45° was used in order to analyse the unknown peaks more accurately. The presence of these additional peaks suggests that the unknown compound is present in a high proportion, as the peak intensity is comparable to that of the platinum metal. The amount of platinum present in the composite is expected to be the 5.7wt% added, as the high melting point of platinum (1768°C) should prevent loss through evaporation (vapour pressure <0.01 Pa).
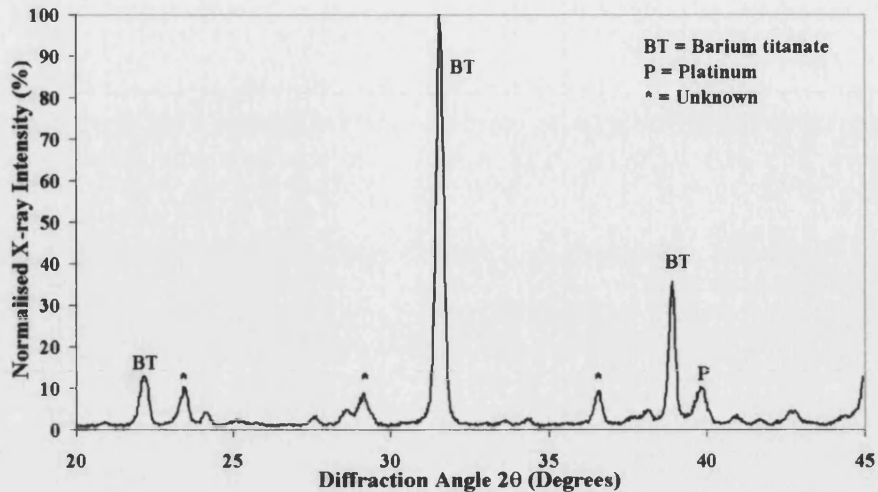
Figure 5.22: X-ray diffraction pattern of barium titanate-5.7wt% platinum

showing the presence of a secondary phase.

5.1.b   PARTICLE SIZE MEASUREMENT

The particle size of the original powders was determined by using a particle size analyser and by analysing scanning electron microscope, SEM, images. SEM images of polished cross-sections were also analysed to examine the grain size and particle size in the sintered materials.

5.1.b.i   Particle size of barium titanate and silicon carbide powders

Barium titanate and Lonza UF45 silicon carbide, used for composite manufacture, were tested on a Malvern Mastersizer 2000. Results are given in Table 5.1 and suggest that the silicon carbide particles are larger than would be expected (<100 nm) from a surface area of 45 m^2/g.

Table 5.1: Particle size results for barium titanate and silicon carbide (UF45).

Material	D_{10} (µm)	D_{50} (µm)	D_{90} (µm)
Barium titanate	0.76	1.85	4.76
Silicon carbide (UF45)	0.31	10.9	42.0

Two peaks in the silicon carbide particle size distribution were present at 0.4 µm and 30 µm, see Figure 5.23. This suggests that the particle size is approximately 0.4 µm, while agglomerates of these particles have a stable size of 30 µm. Break-up of these agglomerates is important to reduce inhomogeneities in the sintered composite.
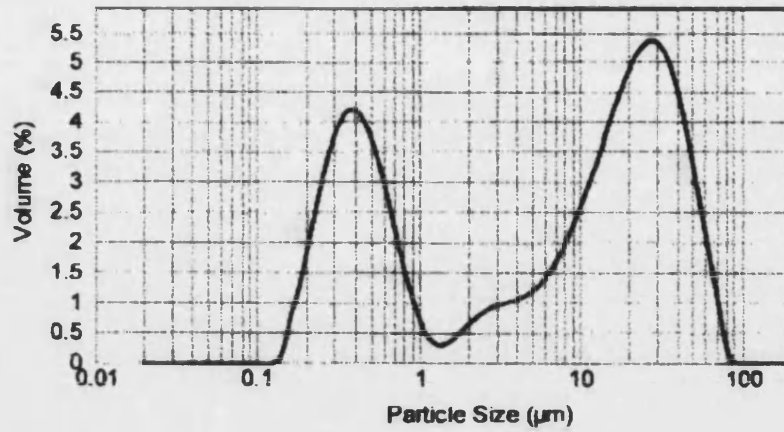
Figure 5.23: Particle size distribution for silicon carbide (UF45).

Scanning electron microscope examination of the barium titanate (Figure 5.24) and silicon carbide (Figure 5.25) powders revealed the agglomerated nature of the materials.
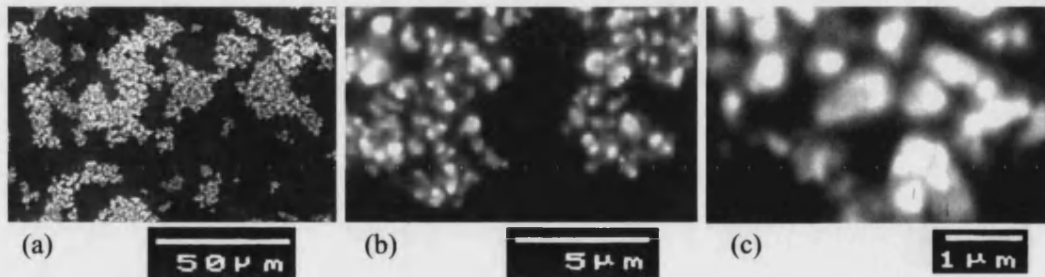
Figure 5.24: (a), (b) and (c) barium titanate starting powder as observed with the scanning

electron microscope, SEM.

The agglomerated barium titanate particles form groups about 25 μm in diameter, while the actual particles are ~1 μm in size. This particle size agrees well with that measured in the particle size analyser. The particles appear to have a rounded shape.
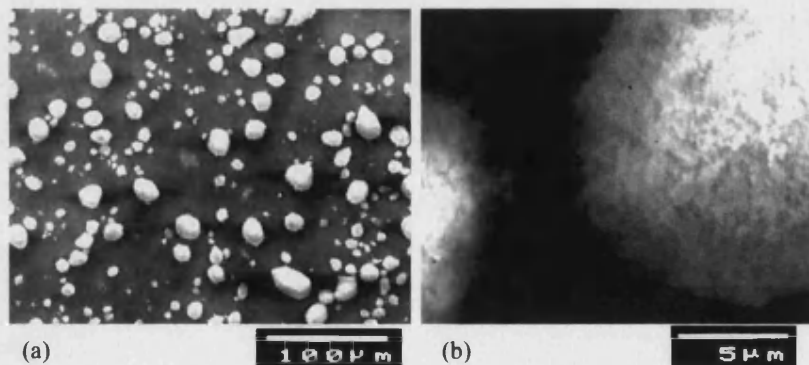
Figure 5.25: Silicon carbide powder (UF45) as observed with the SEM.

The silicon carbide powder formed agglomerates in the range 10-50 μm. The actual particle size was difficult to determine, but appeared to be less than one micron, Figure 5.25. This confirms the results of the particle size analyser, which gave two particle peaks at 0.4 μm and 30 μm. The particle size calculated from Transmission Electron Microscope, TEM, images of UF45 was 204 nm with a standard deviation of 110 nm. This corresponds well with literature values for the same powder that give a 100-300 nm range[37, 42, 75, 81]. Figure 5.26 shows some of the particles imaged and used for the particle size measurements.
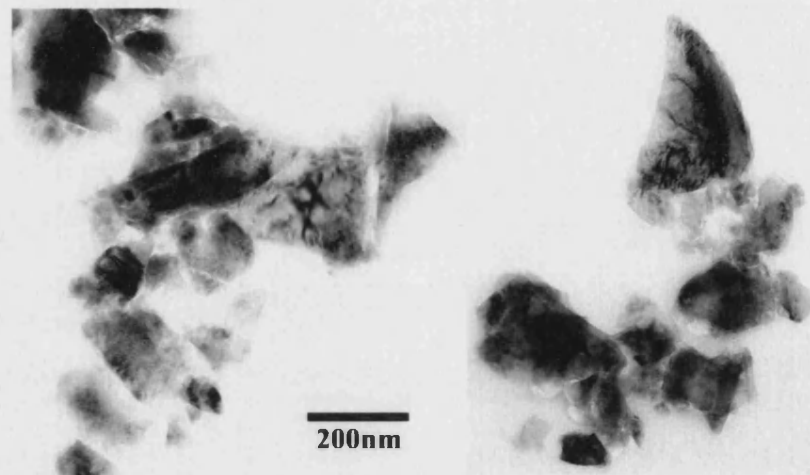
Figure 5.26: TEM images of silicon carbide particles (UF45) showing their angular shape.

The results of the TEM analysis are subject to inaccuracy as only those particles that could be observed were included. This method does not take into account the three-dimensional nature of the particles and the actual particle edge was difficult to resolve. It was found that some particle agglomeration occurred even though a dispersing agent (Dispex A40) and ultrasonic energy was used to disperse them. This strengthens the suggestion, as from the particle size analysis, that agglomerates are present. TEM observation of the particles highlighted their non-spherical morphology. While the majority of the particles approximated to spheres a number had high aspect ratios and a few appeared cubic in shape. The irregular shape suggests the particles were formed by the Achesion Carbothermal reduction process[3].

5.1.b.ii   *Particle size of silver oxide starting powder*

As silver oxide powder did not disperse easily in water, cyclohexane was used instead. A monomodal particle size distribution is observed, see Figure 5.27, with a $D_{50} = 16$ μm. This indicates that the silver particle size within the composites will be of similar starting size, unless the particles are all present as agglomerates, which coalesce on sintering.
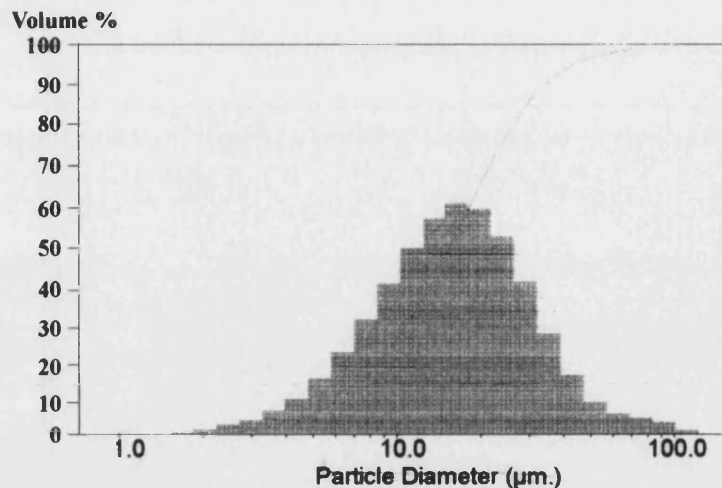
Figure 5.27: Particle size distribution for silver oxide powder dispersed in cyclohexane.

Observation of the silver oxide powder in the scanning electron microscope, see Figure 5.28, revealed the agglomerated nature of the material. The agglomerates are >>10 μm in size, confirming the particle size analysis above. The individual crystals, however, are smaller, ≈1 μm, and are angular in shape.
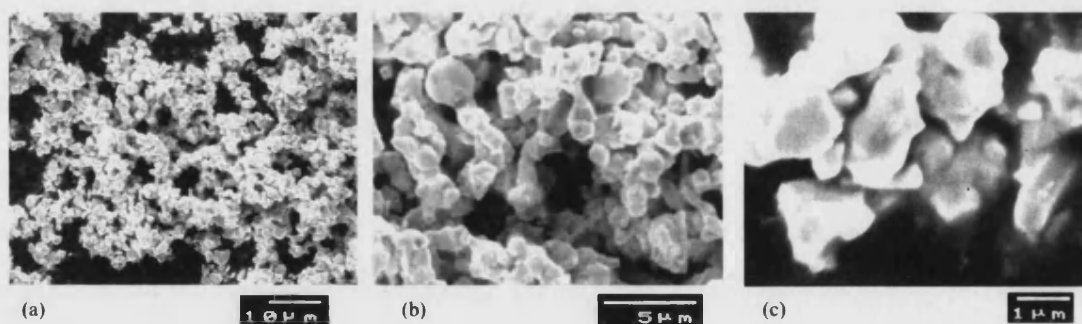
Figure 5.28: SEM images of the silver oxide starting powder showing the agglomerated

nature of the individual angular crystals.

5.1.b.iii   *Particle size of silver nitrate and platinum compounds*

The silver nitrate and the platinum compound were not analysed using the particle size analyser due to their solubility in water and ethanol. The calcined powders, however, were observed under the electron microscope, the results are given below.

5.1.b.iii.a   Calcined barium titanate-silver (nitrate) powder

Analysis of the calcined silver (nitrate) composite powder indicated the agglomerated nature of the material with the actual particles of ~1 μm in size.
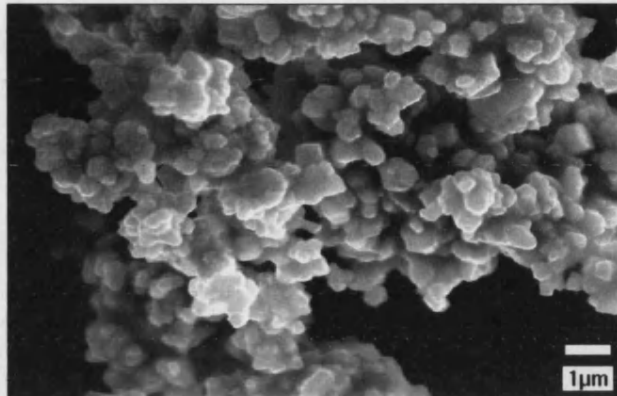
Figure 5.29: SEM of calcined barium titanate-silver (nitrate) composite

powder indicating heavy agglomeration of 1 μm particles.

5.1.b.iii.b   Calcined barium titanate-platinum powder

The calcined platinum composite powder is composed of agglomerates of about 20 μm in diameter that consist of individual barium titanate particles ~1 μm. Back-scattered imaging mode indicates bright regions dispersed within the agglomerates. These bright regions are expected to be platinum particles and are less than 200 nm in size.
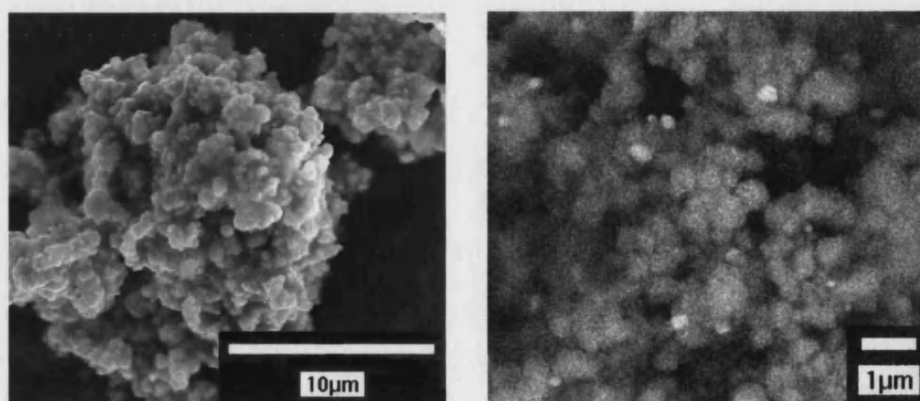
Figure 5.30: Calcined barium titanate-platinum powder (a) secondary electron

image and (b) back-scattered image.

5.1.c   THERMOGRAVIMETRIC ANALYSIS (TGA)

5.1.c.i   TGA of barium titanate starting powder

No significant change occurred on the heating of barium titanate powder to 900°C.

5.1.c.ii   TGA of silicon carbide starting powder

In order to investigate the oxidation of silicon carbide, thermogravimetric analysis was undertaken. The results for the oxidation of silicon carbide are given in Figure 5.31, which shows the weight change of the material as a function of temperature.
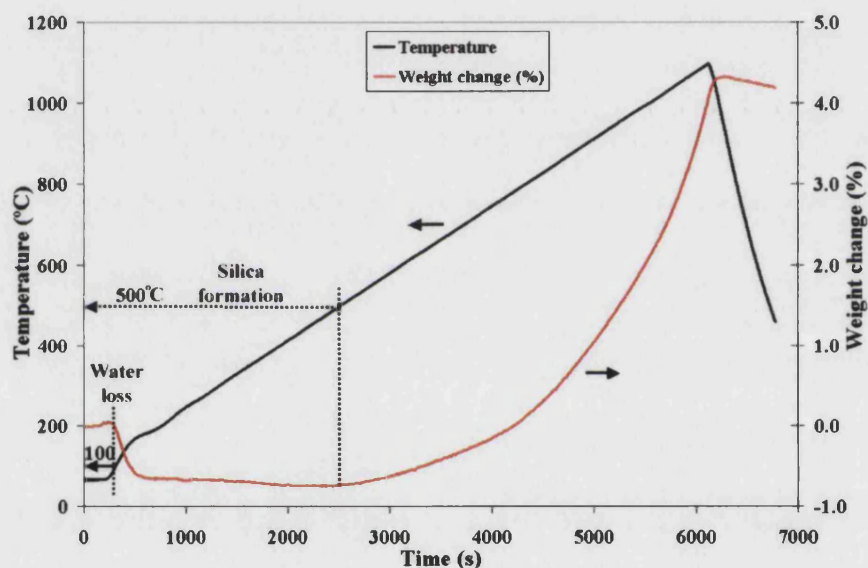
Figure 5.31: Weight change with temperature for silicon carbide heated in air.

The result shows the loss of moisture from the sample at 100°C and a weight gain above a temperature of approximately 500°C. This increase in weight with time appears to have a power law relationship and by extrapolation a weight gain of 8.6% for a 1300°C sinter temperature is predicted. This weight gain is due to silicon carbide oxidation, to silica, which would indicate that 17.2wt% of the silicon carbide had oxidised (molar mass SiC=40, SiO_2=60). The presence of the resultant glassy silica phase will influence the sintering kinetics of the barium titanate-silicon carbide composite and hence the microstructure achieved.

111

5.1.c.iii   TGA of silver oxide starting powder

Figure 5.32 demonstrates that the silver oxide will decompose during the sintering cycle. The total weight change corresponding to the decomposition, as taken from Figure 5.32 is 7.2wt%, which is in agreement with the theoretical loss of 6.9% calculated for the complete decomposition of silver oxide to silver, equation 5.3. The initial weight loss around 200°C is due to loss of water and organic impurities. Decomposition of the silver oxide begins at ~500°C and is complete by 650°C.

$$2Ag_2O_{(s)} \rightarrow 4Ag_{(s)} + O_{2(g)} \qquad \{5.3\}$$
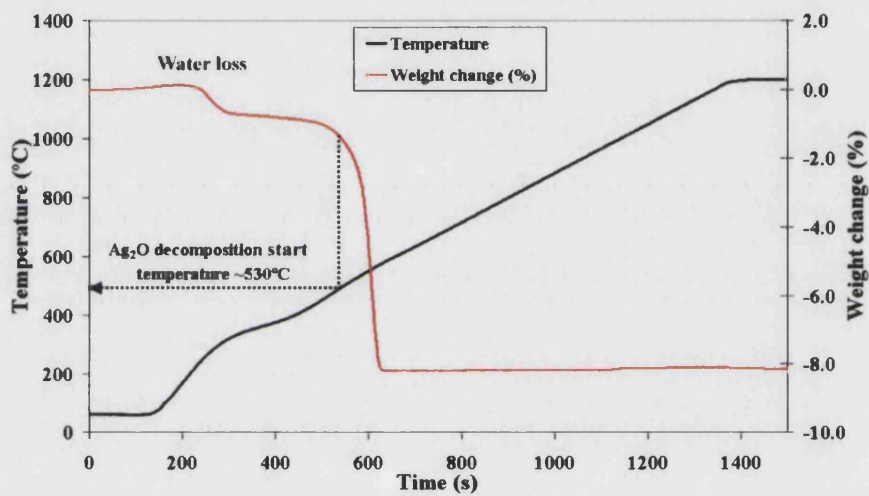
Figure 5.32: Weight change with temperature for silver oxide indicating that

decomposition to silver occurs at ~500°C and is complete at 650°C.

5.1.c.iv   TGA of silver nitrate starting material

A single decomposition event occurred during TGA of silver nitrate but the temperature at which this happened was higher than expected. The calcination temperature of 300°C, mentioned in the literature[47, 49], suggests that nitrate breakdown should occur within this heating range but this was not borne out by the results, see Figure 5.33. The X-ray analysis does indicate, however, that silver is formed during the calcination at 300°C. This would appear to imply that the TGA result for silver nitrate is suspect. The TGA heating rate (10 °C/min) may have been sufficiently high that the sample was actually at a lower temperature than that recorded. The single decomposition event is substantiated by the lack of observed intermediate decomposition compounds from X-ray analysis.

112
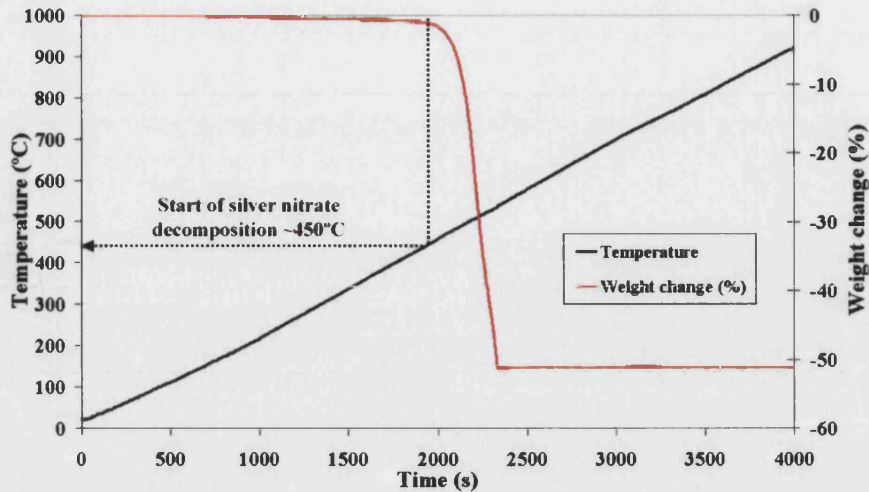
Figure 5.33: Weight change with temperature for silver nitrate.

The final mass loss recorded is just under 50%, which is significantly greater than expected from theory (29.4%), calculated using equation 5.4. This difference is not explained as no major impurities or water were observed in the starting materials.

$$AgNO_{3(s)} \rightarrow Ag_{(s)} + NO_{3(g)} \qquad \{5.4\}$$

5.1.c.v   TGA of platinum compound

Heating the platinum compound up to 600°C indicated that the compound was completely decomposed to the 38-40wt% platinum as expected from the Aldrich catalogue[165], Figure 5.34.
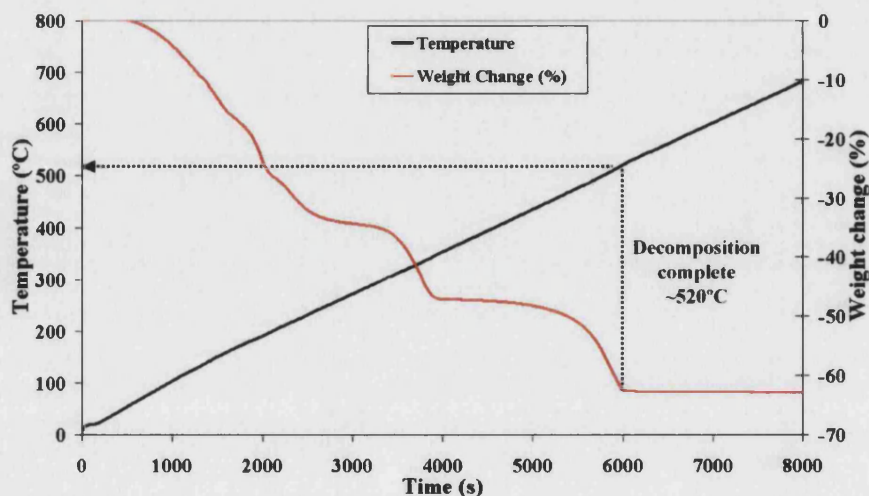
Figure 5.34: Weight change with temperature for dihydrogen hexachloroplatinate (IV).

The steady weight loss below 200°C corresponds to the loss of moisture from the sample, including the water of hydration. The two additional drops in weight at 300°C and 500°C are likely to correspond to the decomposition of the remaining compound to lower molecular weight compounds, in the last instance to platinum. One of these could conceivably be the loss of hydrogen chloride. The reported melting and boiling points of dihydrogen hexachloroplatinate (IV) are reported as 60°C and 115°C, respectively[165]. There appears to be no significant mass changes at these temperatures, suggesting these events may have occurred over a range of temperatures.

5.1.d   SINTERING RATE

The dilatometer was calibrated with a gold sample before testing green compacted monolithic barium titanate and composite samples. The gold sample melted at 1064°C, close to the reported temperature of 1063°C [166]. The sintering rate is obtained from the gradient at each temperature for the percentage change in sample length.

5.1.d.i   Sintering rate of barium titanate

Figure 5.35 displays the normalised sintering rate-temperature results for monolithic barium titanate.
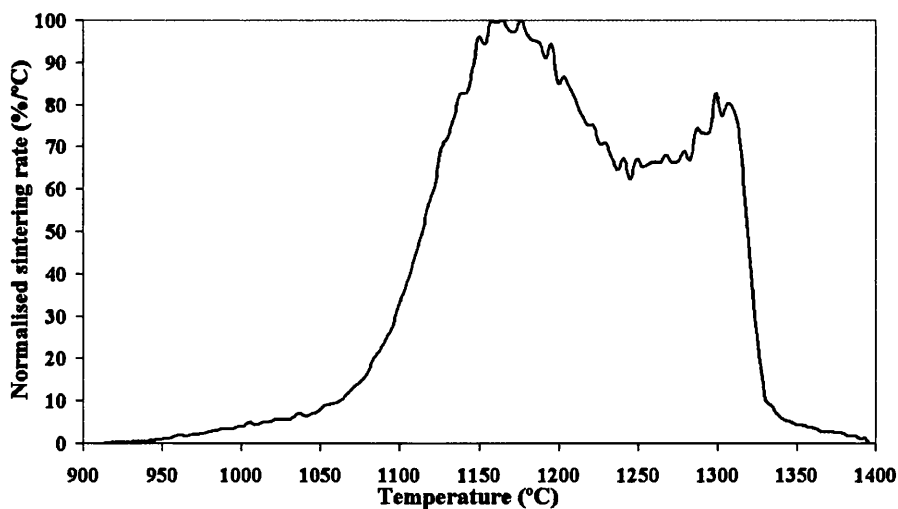
Figure 5.35: Normalised sintering rate as a function of temperature for

monolithic barium titanate.

Figure 5.35 indicates that densification of pure barium titanate does not start until the sample reaches a temperature above 900°C. Two peaks in the sintering rate are observed at around 1170°C and 1300°C. This result has been previously reported in the literature, but for slightly higher temperatures of 1250°C and 1320°C respectively[72]. The higher temperature peak may be due to the formation of a liquid eutectic, with a formation temperature that may be lowered by the presence of impurities.

5.1.d.ii   *Sintering rate of barium titanate-silicon carbide composite*

The shrinkage-temperature relationships obtained from dilatometer data are shown in Figure 5.36 for both the monolithic barium titanate and a composite sample containing 1wt% silicon carbide. Figure 5.36 indicates that incorporation of silicon carbide inhibits the densification of barium titanate as the final density is reduced. However, the composite appears to begin sintering at a lower temperature (~1050°C) than the monolithic barium titanate (~1100°C). This may be due to the generation of a liquid phase, such as silica, that could aid diffusion.
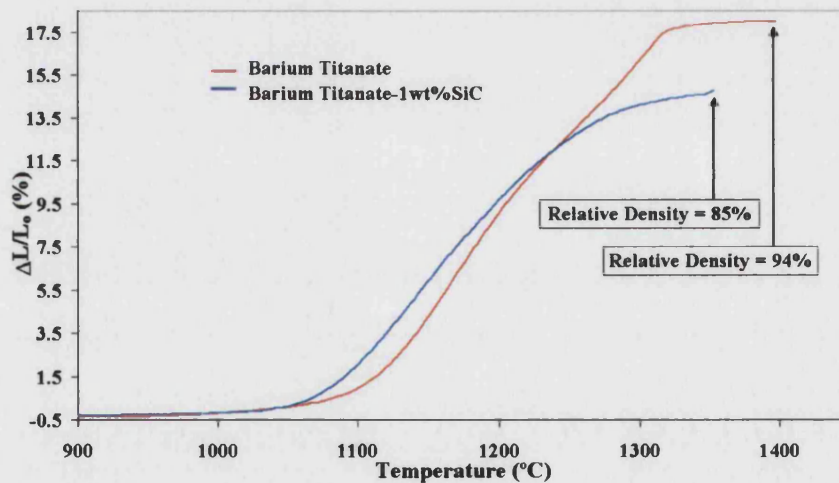
Figure 5.36: Shrinkage-temperature results for monolithic barium titanate and

barium titanate-1wt% silicon carbide composite sintered in argon.

Further examination of the data is achieved by plotting the sintering rate against the temperature as in Figure 5.37. The monolith has two temperatures at which the sintering rate peaks, while for the composite sample there is only a single maximum sintering rate peak at 1150°C. This peak is likely to correspond to the 1170°C peak of the monolithic sample. It appears that the silicon carbide inhibits the high temperature sintering rate peak at ~1300°C. This explains the lower density generated in the composite.
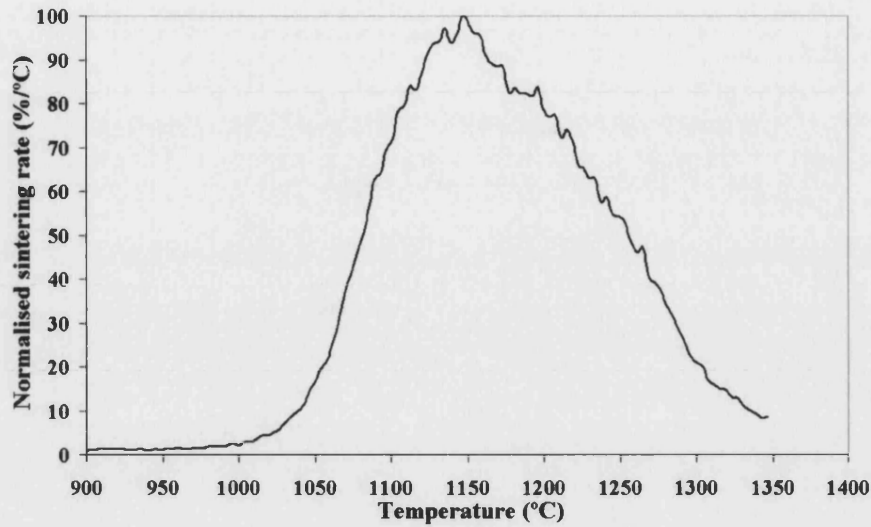
Figure 5.37: Sintering rate of barium titanate-1wt% silicon carbide composite

as a function of temperature.

5.1.d.iii   *Sintering rate of barium titanate-silver composites*

Sintering studies were conducted on the silver (nitrate) based composites. The normalised percent change in length with temperature and the normalised shrinkage rate with temperature are given by Figures 5.38 and 5.39, respectively. Table 5.2 lists the final percentage shrinkage for the composites. Each line represents the behaviour of a single sample.
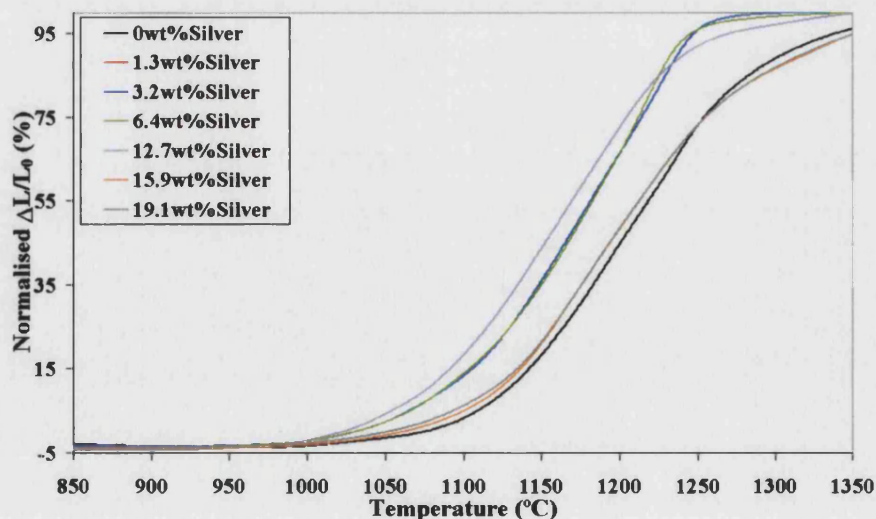
Figure 5.38: Normalised change in sample length with temperature for

barium titanate-silver composites.

With reference to Figure 5.38, sample length reduction only begins above a temperature of 950°C in the monolith and the composites. In the monolithic case one hundred percent of the final shrinkage value is obtained when the sample is held at 1350°C, while the composites (up to 6.4wt%) have obtained their final dimensions below this temperature. As the silver content increases above 12.7wt% the trend in sintering characteristics becomes more like the monolithic barium titanate. The curve gradients are similar in the 1150-1250°C temperature range, suggesting the same thermally activated process is present.

The rate of shrinkage, Figure 5.39, indicates that the temperature of maximum shrinkage rate decreases as the proportion of silver increases. The monolithic sintering peak is at a temperature of 1240°C, while the barium titanate-6.4wt% silver is at 1220°C and those samples with higher silver contents are around 1180°C. The broadness of the peak has also increased indicating a broad range of temperatures over which the sample is sintering.
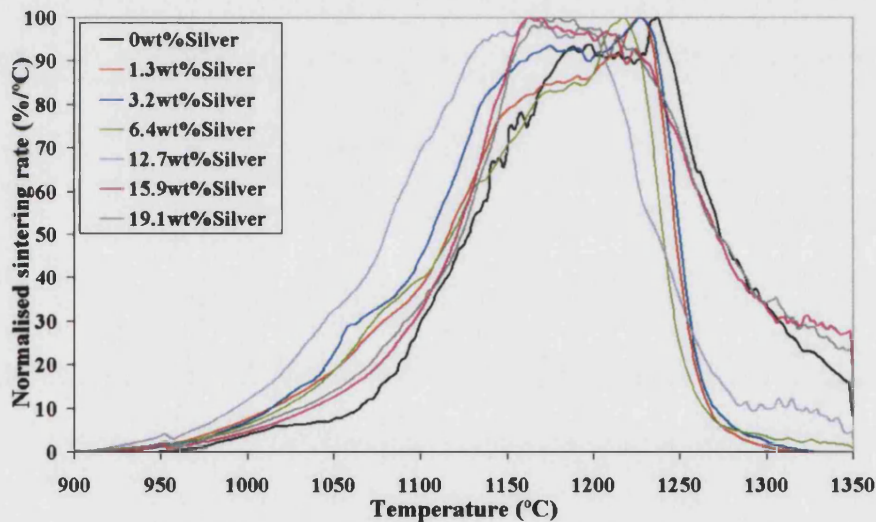
Figure 5.39: Normalised shrinkage rate with temperature for barium

titanate-silver (nitrate) composites.

The final percentage shrinkage, Table 5.2, varies between 14.8-17.9% and a reduction in shrinkage is observed with the incorporation of low silver contents (1.3-6.4wt%) in comparison to the monolith. At high silver contents the original shrinkage is observed, suggesting that the larger amount of silver does not affect densification. The melting point of silver is 961°C and is therefore molten at the sintering temperature of barium titanate. When a large fraction of silver is present its connectivity can be sufficiently high that capillary pressure and surface tension continue to contract the specimen. This must balance the poor diffusion of sintering species in silver that cause the

reduced density at low silver content. A greater degree of bonding between the alumina spacers, used to protect the ends of the dilatometer rod, and the sample was observed as the silver content increases, as seen in Figure 5.40.

Table 5.2: Percentage final shrinkage for barium titanate-silver (nitrate) composites.

Composite (wt% silver)	Final shrinkage (%)
0	17.0
1.3	15.4
3.2	15.4
6.4	15.7
12.7	14.8
15.9	17.3
19.1	17.9

%Ag   0   1.3   3.2   6.4   9.5   12.7   15.9   19.1
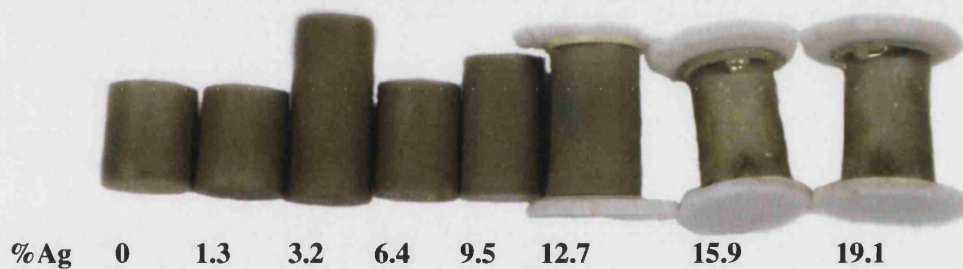
Figure 5.40: Dilatometer samples post-measurement showing silver on the composite surface and bonding between the alumina spacer and composite. Sample diameter is ~5 mm.

5.1.d.iv   *Sintering rate of barium titanate-platinum composite*

Dilatometry was conducted on the barium titanate-5.7wt% platinum composite manufactured for comparison with the monolithic barium titanate. However, the total shrinkage of the composite was only 4.4% in comparison to the 17.0% for the monolith. The presence of the platinum appears to inhibit the sintering of barium titanate. Even though the powder was calcined, glassy reaction products were formed at the high temperature (1300°C) that began to interact with the equipment. The glassy material appeared to diffuse over or through the alumina supports and caused them to become attached to the dilatometer chamber. The liquid phase may form at the specimen surface, due to the higher oxygen content when compared to the bulk, causing differential sintering. Dilatometer testing was discontinued because of these issues. The sample was also observed to sag

under its own weight and crack, Figure 5.41, which may be caused by the presence of the glassy phase.

Figure 5.41: Barium titanate-5.7wt% platinum sample after dilatometry testing.

Sample diameter is ~5 mm.

5.1.e   DENSITY MEASUREMENT

5.1.e.i   Green density measurement

5.1.e.i.a   <u>Green density of barium titanate and barium titanate-silicon carbide composites</u>

The green compact density was determined using the geometric method and the composite densities were modified to take account of the difference in density between the silicon carbide and barium titanate (the method is given in Appendix VI). As expected, the green density is improved with a higher pressing pressure. There is a significant increase in green density of ~4% by the use of the 150 MPa cold isostatic press in comparison to uni-axial pressing at 50 MPa (57% theoretical). The freeze-dried powder has a notably lower density of 52% theoretical compared to the ball-milled powders, when both types are pressed at 50 MPa. This may be explained if the powder agglomerates have different particle shapes. Spherical particles (in ball-milled) will compact better than higher aspect ratio particles (in freeze-dried). Narrow 95% confidence intervals of ~1% theoretical suggest there is little density variation for the same sample type and pressure. The addition of silicon carbide had no significant effect on the green density. The observed silicon carbide particle shape is non-spherical and as such would be expected to reduce the packing efficiency, see sub-Section 5.1.b, however, the small particles will become located in between the larger barium titanate particles.

The incorporation of a binder was found to improve the green density by approximately 7% for monolithic and composite powders, suggesting lubrication. The Polyethylene Glycol, PEG, binder

is a soft polymer that coats the particles and reduces sliding friction between the particles, allowing better consolidation. However the final sintered density may be adversely affected if the binder does not burn out completely. Carbon deposits left behind when the binder fails to oxidise completely can inhibit diffusion and cause flaws in the final structure.

5.1.e.i.b Green density of barium titanate-silver and barium titanate-5.7wt% platinum composites

The variation of green density with silver content is given in Figure 5.42, after cold isostatic pressing at 150 MPa. The calculated densities have been modified to account for constituent density differences.
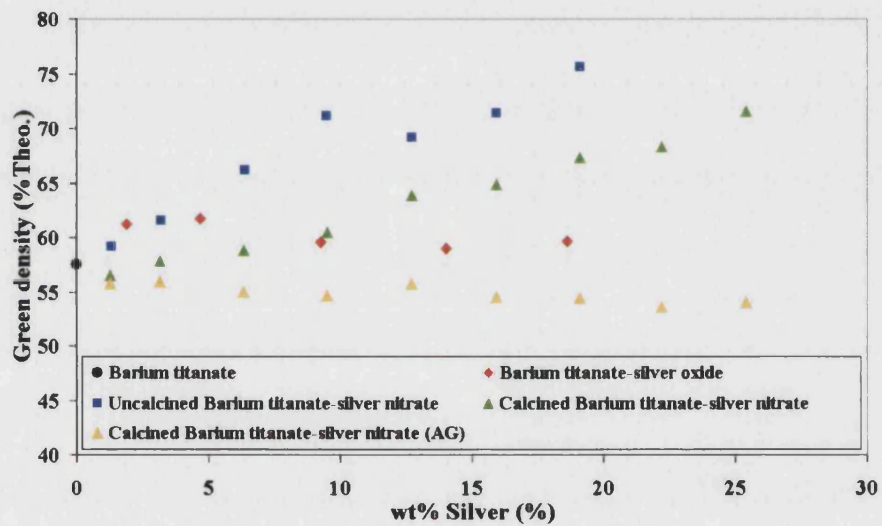
Figure 5.42: Variation of silver (oxide) and silver (nitrate) sample densities with silver content.

The addition of silver oxide had little effect on the compact green density but the addition of silver nitrate appears to increase the green density. This may be due to the silver nitrate having a particle size that allows it to fit in the voids between the larger barium titanate particles. Calcination of the powder reduces the green density as the decomposition of the silver nitrate may form silver oxide particles that inhibit particle sliding. The actual density is unknown since the composition is unknown as the level of silver nitrate decomposition could vary. If the silver nitrate is assumed to decompose completely to silver (designated as AG) the green density appears unaffected by increasing the amount of silver. This suggests that complete decomposition of the silver nitrate does not occur during calcination, confirming the XRD results. In all cases the 95% confidence interval was in the range ±1%.

The cold isostatically pressed platinum samples had a green density of 49.2% (95%Confidence interval=±0.5%), which is considerably lower than that observed for the pure barium titanate samples (~57% theoretical). It is thought that the platinum or any remaining platinum compound, after calcination, has hindered the consolidation of the barium titanate particles, possibly by reducing the ease of particle sliding.

5.1.e.ii   Density measurement of sintered materials

The densities measured for the composites have been modified to account for the change in the theoretical composite density by the addition of a second phase. For the silver composites it has been assumed that the silver compound has decomposed completely to silver. This is a reasonable assumption due to the sintering temperature used, evidence from XRD analysis and thermogravimetric analysis given in Section 5.1.a and 5.1.c, respectively.

5.1.e.ii.a   Density measurement of barium titanate-silicon carbide composites

Figure 5.43 shows the calculated volumetric densities for barium titanate sintered in air, under different temperatures, in relation to the pressing pressure.
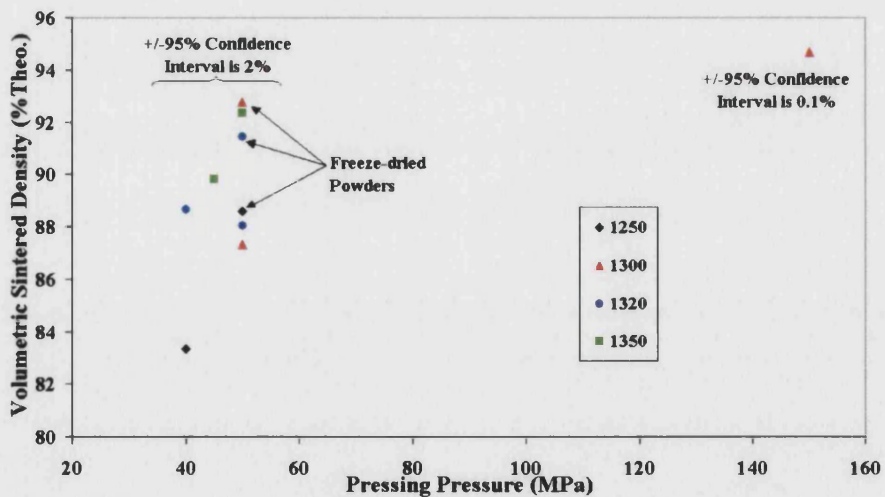
Figure 5.43: Volumetric sintered density for barium titanate sintered for various

temperatures in air and under different pressing conditions.

Increasing the pressing pressure to 150 MPa improves the final sintered density. This result is expected as the higher pressure gives higher green density and allows densification to occur more readily. The freeze-dried powders achieved a higher sintered density than those produced by

conventional ball milling. It is suggested that the particle size and shape may cause this difference, with the more spherical particles of the non-freeze-dried powders giving a higher green density and lower sintered density. The freeze-dried powders, with a more angular morphology, have a higher surface to volume ratio and thus sinter faster, even though their green density is slightly reduced. The 95% confidence intervals are greater than for the green density, typically in the range ±1-2%. This increased variation is due to local temperature fluctuations during sintering and powder in-homogeneities that become more important in relation to a sintered body. A higher sintering temperature is observed to improve the sintered density as the activation energy barrier for diffusion is reduced. A density improvement of 4.3% is obtained by increasing the sintering temperature from 1320°C to 1350°C. This is in comparison to 0.7% for the 1300°C to 1320°C sintering temperature increase. The density increase at a higher temperature is proposed to be due to the formation of a liquid eutectic phase that acts as a sintering aid above its melting temperature.

No significant difference was observed between the different pressing pressures when the barium titanate was sintered in an argon atmosphere. The density, however, is less than barium titanate sintered in an air atmosphere by ~4%.

An increase in density compared to the monolith is achieved with the addition of 1wt% silicon carbide, as shown in Figure 5.44. A decrease in density, however, is observed at higher silicon carbide addition. Overall, increasing the consolidation pressure from 50 MPa to 150 MPa does increase the density. The reduction in density with the addition of silicon carbide suggests that the densification processes for sintering, such as grain boundary diffusion, are inhibited. The improvement for the 1wt% silicon carbide does not follow the trend indicated by the inhibition of diffusion in the higher silicon carbide composites. The formation of a liquid phase at grain boundaries is also possible and could account for improved density in the barium titanate-1wt% silicon carbide composite due to liquid phase sintering.
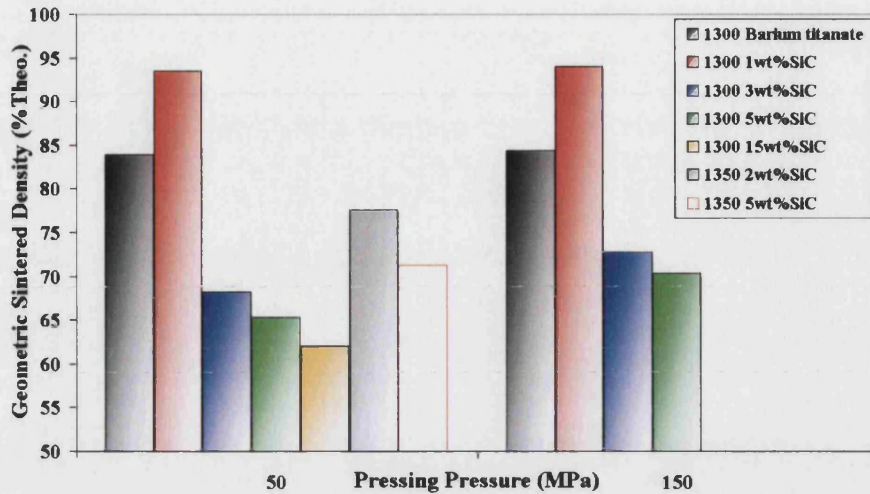
Figure 5.44: Geometric density for barium titanate-silicon carbide composites

sintered in an argon atmosphere.

The geometric density values, Figure 5.44, for the silicon carbide composites, sintered under argon, were similar to the volumetric density values, Figure 5.45. In general the volumetric densities, Figure 5.45, are higher than those based on the geometric measurement. This is thought to be due to non-uniform sample shapes, which caused an overestimation of the sample volume in the geometric method.
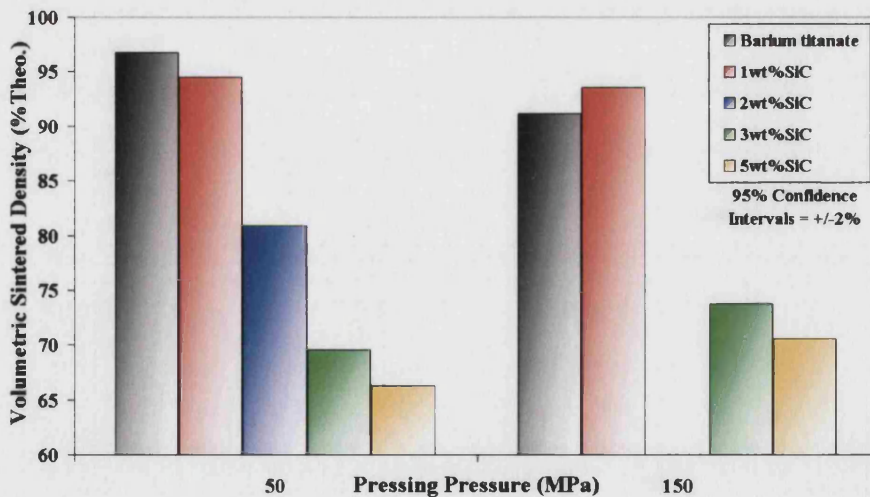
Figure 5.45: Composite volumetric sintered densities under argon atmosphere at 1300°C.

While three barium titanate-15wt% silicon carbide samples were sintered only one survived as the thermal stresses generated during cooling shattered the other two. A volumetric density was not measured.

In summary, the freeze-dried powder provides an improved sintered density compared to the conventional ball-milled powder, by approximately 4%. Results suggest that the addition of 1wt% silicon carbide improves the density, while raising the content to 5wt% silicon carbide hinders densification. This assumes that there is no loss of silicon carbide during the sintering process. Although an argon atmosphere is used, the presence of residual oxygen from this gas or the barium titanate could cause silica formation, which could be lost to the atmosphere as silicon monoxide or aid in liquid phase sintering. This is the explanation proposed for the expansion of some composites samples sintered at the highest temperature of 1350°C, see Figure 5.46.

1mm

Figure 5.46: Large void formation due to gas generation

in $BaTiO_3$-2wt% silicon carbide sintered at 1350°C.

In addition to pressureless sintering, hot pressing was also investigated for the barium titanate-silicon carbide system. The density of hot pressed barium titanate-silicon carbide composites was improved in comparison to the pressureless sintered samples, particularly for the higher percentage silicon carbide composites, as shown in Figure 5.47. An improved density is expected as the application of pressure and temperature during the sintering cycle allows enhanced diffusion and plastic deformation to occur.
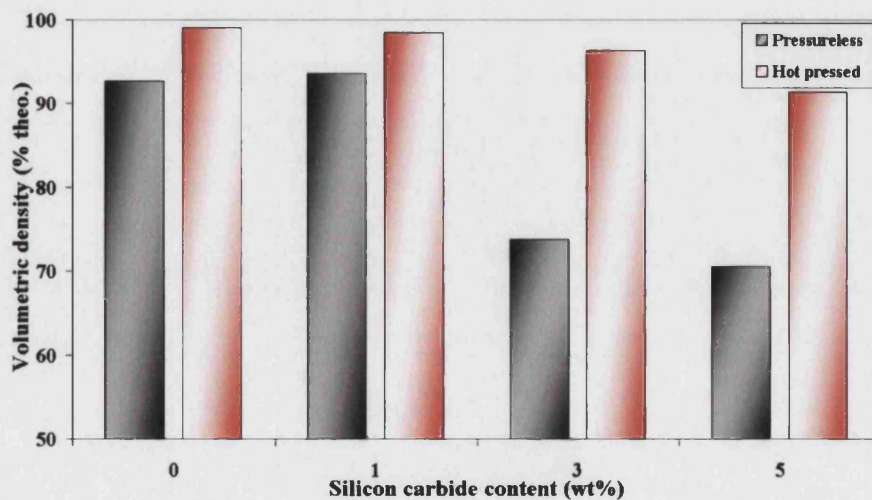
Figure 5.47: Comparison of pressureless sintered and hot pressed densities for

the barium titanate-silicon carbide composites.

5.1.e.ii.b   Density measurement of barium titanate-silver composites

The calculated modified sintered densities for the silver composites are shown in Figure 5.48. The addition of silver in the form of silver oxide powder has no significant effect on the composite density developed. However, the silver nitrate based composites have densities that decrease with increasing silver content. Calcination was shown to improve the density achieved, as expected, by removing gas formed during the decomposition of silver nitrate. The reduction in the calcined sample sinter density suggests that the presence of the silver had also inhibited the densification process. It is suggested that as the silver has a negligible solubility in barium titanate its existence at the barium titanate grain boundaries hinders diffusion by this route, so slower bulk diffusion is relied upon during sintering.
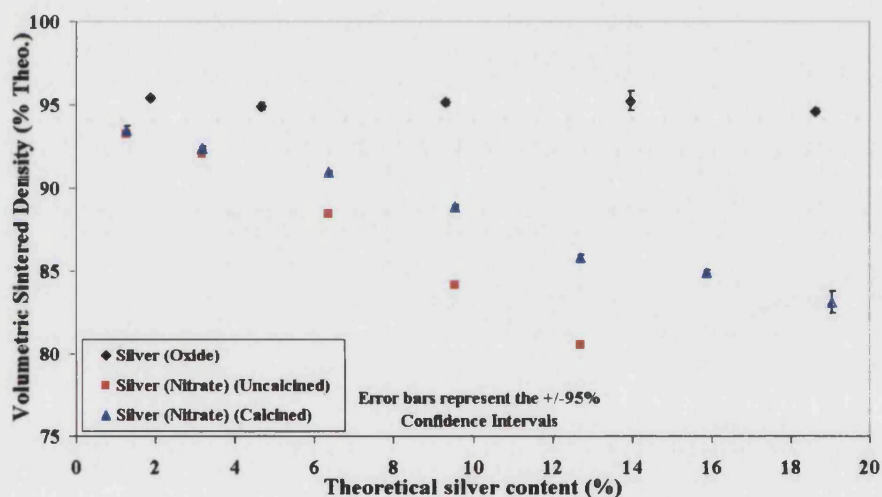
Figure 5.48: Modified volumetric sintered densities for barium titanate-silver composites.

The actual density for the silver composites may be slightly greater, as the calculated theoretical composite density assumes that no silver is lost during firing. As the sintering temperature is considerably higher than the melting point of silver, evaporation, due to a vapour pressure ~130 Pa, would be expected.

5.1.e.ii.c   Density measurement of barium titanate-5.7wt% platinum

The sintered density of the surviving platinum samples was calculated to be ~86%. The addition of platinum appears to have a greater effect on hindrance of the matrix densification than silver. The lower density may in part be due to the presence of impurity phases left over from the calcination stage if they inhibit diffusion. The low density achieved was not expected from the way in which the samples deformed during sintering, see Figure 5.49.

Figure 5.49: Barium titanate-5.7wt% platinum sintered at 1300°C

showing amber glassy phase and differential sintering.

The samples appeared to flow under their own weight and typically covered the sintered barium titanate supports. This behaviour would be expected in the presence of a low melting point liquid that allows the particles to move over each other. The remanants of a secondary phase were observed and X-ray diffraction analysis of this material was conducted, but the compound could not be identified.

5.1.e.iii   *Measurement of silver mass loss*

The percentage mass difference between the sintered and un-sintered calcined samples was calculated in order to quantify the loss of silver during sintering. Silver is observed to leave the sample forming a surface depletion layer, see Section 5.1.f.ii.e. Silver droplets are formed, by capillary action, on the surface of the specimen, Figure 5.50. This observation has been reported by Chen *et al*[47].
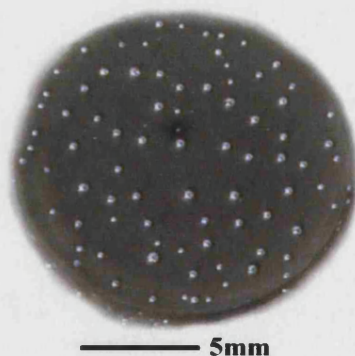
Figure 5.50: Silver droplets on the surface of a barium titanate-19.1wt% silver sample.

These silver droplets and depletion layer were removed before density determination was undertaken. The chart below, Figure 5.51, shows the mass loss for various silver (nitrate) composites.
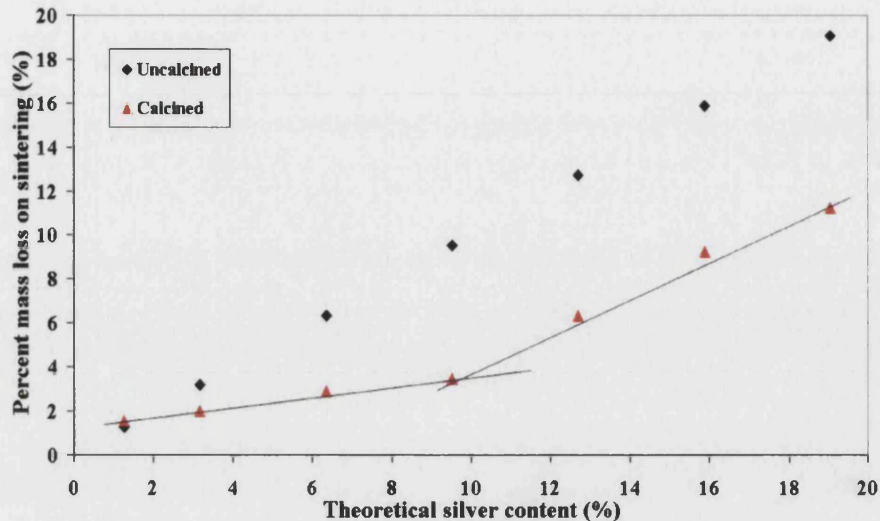
Figure 5.51: Percentage mass loss for the un-calcined and calcined sintered barium titanate-silver composite samples. Two trends are observed in the calcined mass loss.

As expected the samples fabricated from the un-calcined powders have a greater mass loss due to the decomposition of the silver nitrate during the sintering process. Examination of the calcined data in Figure 5.51 appears to have two trends for the mass loss. A low gradient line up to ~9wt% silver and a steeper one at higher silver contents is observed. It is suggested that the shallow gradient is due to silver loss, while that of the steeper gradient is due to both silver loss and the decomposition of the remaining silver nitrate going to completion. Undecomposed silver nitrate was observed by XRD analysis in calcined high silver content samples, as shown in Figure 5.7. This implies a silver mass loss of ~4wt% in the barium titanate-19wt% silver composite. This corresponds well to the observed depletion layer depth, which is shown in Section 5.1.f.ii.d. Fortunately this silver loss is non-uniform and removal of the surface depletion layer by grinding provides a specimen with minimal silver loss. The actual loss of silver for this part of the composite has been determined by X-ray analysis of the component phases, see subsection 5.1.a. The loss of silver was not found to decrease significantly in the sample core. This is unexpected as higher silver contents might be expected to lose a greater amount due to capillary action, where surface particles are more likely to be connected to other silver particles, Figure 5.52.

As the more rapid silver loss does not occur it suggests that the silver loss is only related to the proportion at the surface, which is approximately related to the silver volume fraction. Silver is not lost from the sample interior due to insufficient time above the melting point of silver.
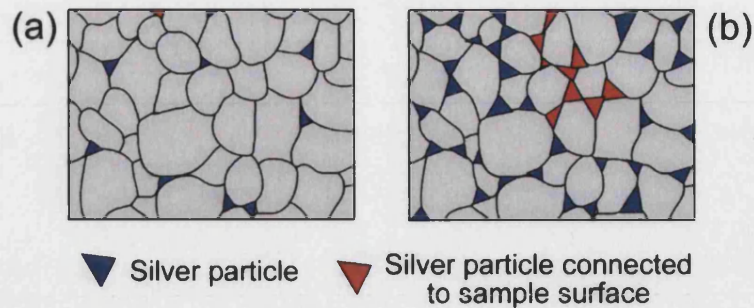
Figure 5.52: Silver connectivity variation with (a) low and (b) high silver content.

5.1.f   LIGHT MICROSCOPY

5.1.f.i   Observation of processed powders

Two colour changes were observed by visual inspection during powder processing, the first being the effect of moisture absorption. Samples of pure barium titanate, in particular, showed a surface colour change when left in the atmosphere either in powder or pressed form. The colour change to a pinky hue from the cream/white is highlighted in Figure 5.53. This change, reversible on heating the powder above 100°C, demonstrates the effect of moisture adsorption. The powder colour relates to the oxygen stoichiometry, which has consequences for the electrical properties, see Section 2.5.e.ii. Powder was kept sealed from the open atmosphere whenever possible to minimise moisture uptake.

Figure 5.53: Colour of barium titanate powder (a) before and (b) after 144 hours

open to the atmosphere at room temperature.

The second observed colour change was that of the silver (nitrate) composite powder before and after calcination, Figure 5.54. Prior to calcination all the composite samples were brown in colour, whereas after heat treatment the low silver containing composites were of a more red/purple hue. The composites with higher silver mass fractions were dark brown, which from X-ray diffraction analysis indicated the presence of both silver and silver nitrate.

128
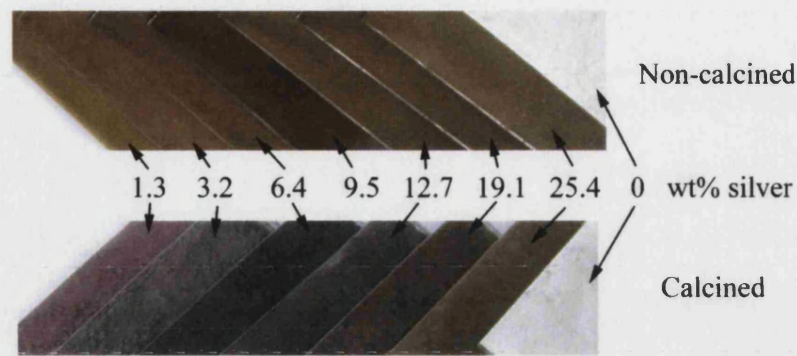
Figure 5.54: Change in colour of barium titanate-silver (nitrate) powder

before and after calcination.

5.1.f.ii   *Light microscopy of sintered samples*

5.1.f.ii.a   Light microscopy of sintered barium titanate

No depletion layer was present in the barium titanate but a colour difference was observed, Figure 5.55. This colour difference may be due to temperature variations within the furnace in relation to the position of the specimen, with a darker colour nearer the heating elements. A higher temperature was found to improve the sintered density and oxidise the material, giving a more yellow colour.
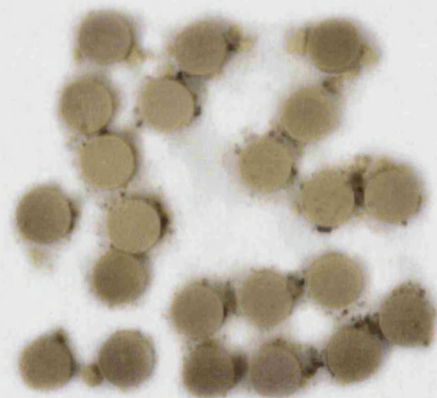
Figure 5.55: Sintered barium titanate showing colour differences between samples.

Each sample is approximately 12 mm in diameter.

5.1.f.ii.b   Light microscopy of barium titanate-silicon carbide composites

Figure 5.56 shows the surface and the internal colours of a barium titanate-15wt% silicon carbide sample, highlighting the oxidation of the surface layer. This sample contained internal stresses, as internal cracking could be observed, although the image fails to show the fractures. These images illustrate the loss of silicon carbide from the surface and that samples require removal of a 0.3 mm layer to ensure examination of the actual composite unaffected by a depletion layer. The production of a reaction phase in the core will affect the piezoelectric behaviour and will be discussed in Section 5.3.c.ii.
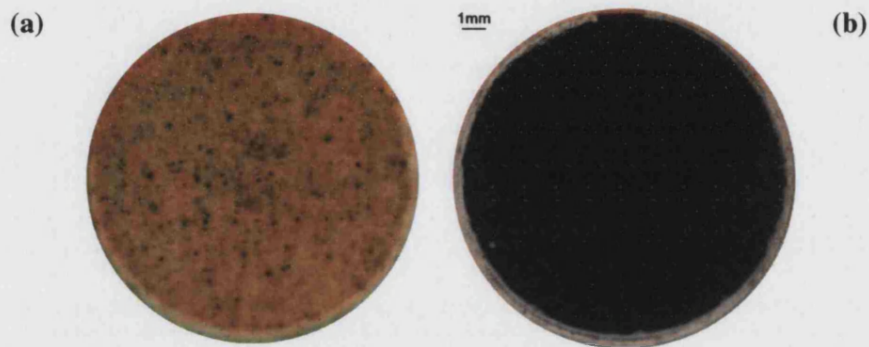
Figure 5.56: (a) Surface and (b) section through the BaTiO$_3$-15wt% silicon carbide

sample showing an oxidation layer of approximately 0.3 mm.

Similar differences in colour were observed for lower silicon carbide content composites, sintered at 1350°C, see Figure 5.57.

Figure 5.57: Barium titanate- (a) 2wt% and (b) 5wt% silicon carbide composites pressureless sintered at 1350°C showing chemical reduction of the barium titanate.

5.1.f.ii.c   Light microscopy of hot pressed barium titanate-silicon carbide composites

The hot pressed samples were completely black in colour indicating the material was chemically reduced. Cracking was observed in the barium titanate monolith, see Figure 5.58, although it remained in one piece. The other composites, however, broke-up during removal from the mould.

Figure 5.58: Appearance of the hot pressed monolithic barium titanate indicating a

reduced state (black) and cracking. Disc diameter is 68 mm.

The porosity of the hot pressed samples, as indicated in subsection 5.1.e, is lowered with the addition of silicon carbide. This is confirmed from light microscopy of the etched samples, Figure 5.59, where the black regions are pores. The reduction of grain size can be clearly observed in these etched samples, but the contrast is diminished.

(a) —— 25um (b) —— 50um (c) —— 50um
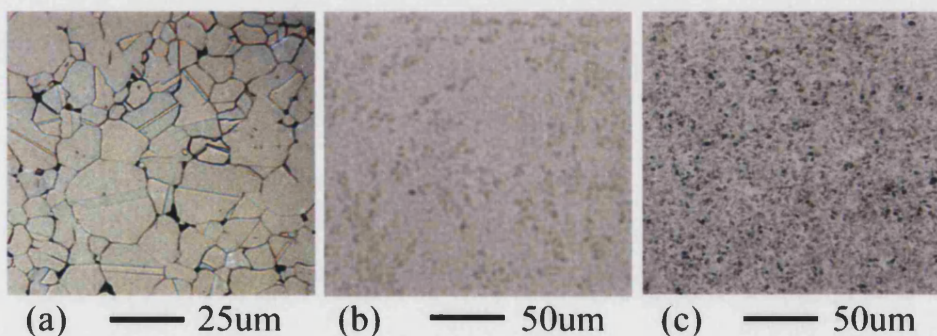
Figure 5.59: Etched hot pressed samples of (a) barium titanate, (b) barium titanate-1wt% silicon carbide, and (c) barium titanate-5wt% silicon carbide.

5.1.f.ii.d   Light microscopy of barium titanate-silver (oxide) composites

A surface depletion layer of silver was readily observed after the specimens were cross-sectioned, as shown in Figure 5.60. The light areas are silver particles and the barium titanate matrix is grey in colour. It is apparent that with the loss of silver by evaporation there is an increased porosity in the surface layer, Figure 5.60(c). The evaporation of silver from barium titanate has been reported by Chen *et al*[47] to produce a silver depletion layer of 100-300 μm. As shown in Figure 5.50 there is poor wetting between the liquid silver and barium titanate, and this limits capillary action. The depth of silver loss becomes dependent on the silver vapour pressure, silver connectivity and time[33].
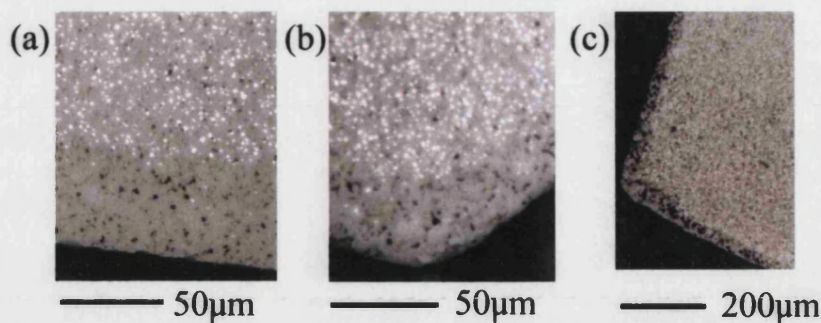
Figure 5.60: Light microscopy of barium titanate-silver composites showing

the extent of the silver depletion layer in barium titanate-(a) 9.3wt% silver,

(b) 14wt% silver and (c) 18.6wt% silver.

5.1.f.ii.e   Light microscopy of barium titanate-silver (nitrate) composites

A silver depletion layer was observed with the barium titanate-silver composite based on silver nitrate, as with the silver (oxide) composites, both before and after sample preparation, Figure 5.61. Marks on the underside of some samples, Figure 5.62, corresponded to the contact points of the sintered barium titanate support and suggests that the supports act as sinks for the transport of silver, increasing the degree of silver loss, as seen in Figure 5.63. The silver loss appeared to be a surface effect only, as it could be removed by grinding, but for the 19.1wt% silver even after polishing a variation in colour, hence composition, was observed.
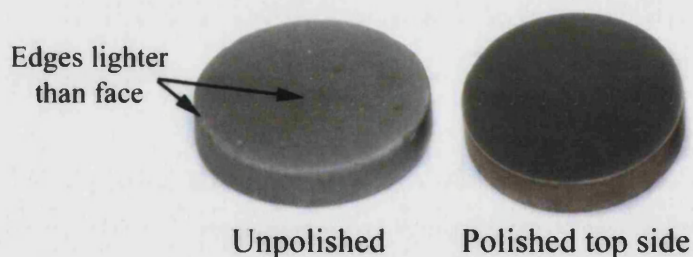
Figure 5.61: Unpolished and polished barium titanate-15.9wt% silver samples

indicating surface silver loss and a darker sample core.

Figure 5.62: Barium titanate-1.3wt% silver showing the contact points due to additional
silver loss. Sample at far right is the top surface shown for comparison.
Discs are approximately 12 mm in diameter.
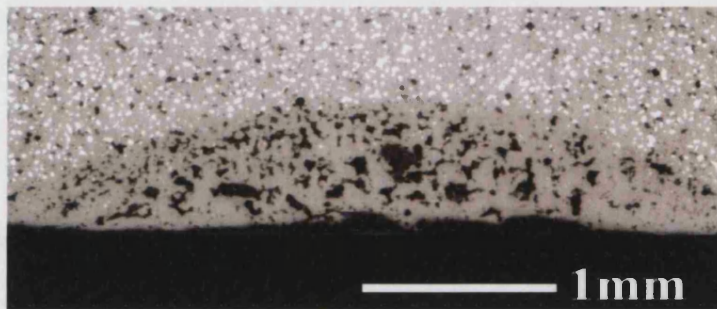
Figure 5.63: Increased silver depletion at a contact point in barium titanate-12.7wt% silver.

5.1.f.ii.f   Light microscopy of barium titanate-5.7wt% platinum

The alumina on which the barium titanate-5.7wt% platinum samples were sintered became
discoloured and the top surface of the samples developed a spotty yellow colour, as shown in
Figure 5.64. These observations indicate the presence of a secondary phase that could explain the
deformation of the samples over the barium titanate supports, so that the samples had direct contact
with the alumina base, Figure 5.65. When the composite came into contact with the alumina base it
became highly porous and white/grey in colour. No significant platinum depletion layer was
observed on polishing the samples.
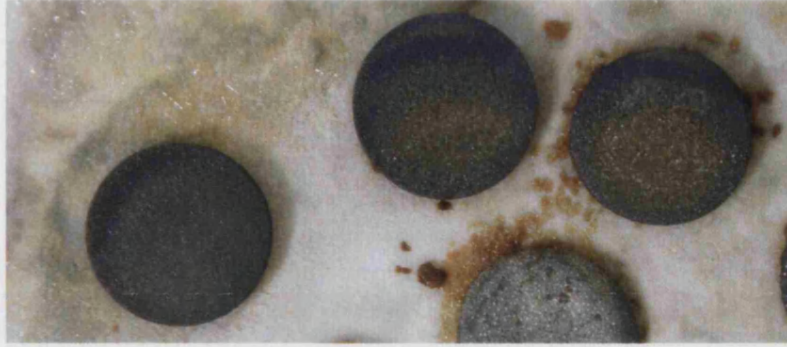
Figure 5.64: BaTiO₃-5.7wt% platinum showing the colour variation of the alumina base

(originally white) and a yellow phase on the top of samples. Discs are

approximately 12 mm in diameter.

Barium titanate supports

Figure 5.65: The under side of the BaTiO₃-5.7wt% platinum samples indicating the barium

titanate supports and the composite colour change to grey/white on contact

with the alumina base plate. Discs are approximately 12 mm in diameter.

5.1.f.iii   *Grain and particle size measurement*

The optical microscope was employed to obtain images of the polished, and in some cases etched, composite microstructures. These images were subsequently analysed to determine the grain size and, where possible, the second phase particle size, in order to establish the distribution of particle sizes. In each case the parameters recorded were area, perimeter, major axis length and minor axis length of the region of interest. The area and perimeter were used to calculate the circularity, equation 5.5, while the major axis length was taken to represent the grain/particle diameter.

$$Circularity \ = \ \frac{Perimeter^2}{Area} \qquad\qquad \{5.5\}$$

A circularity of 4π (~12.6) corresponds to a perfect circle, so grains with a higher value indicate a more convoluted sample shape, as illustrated in Figure 5.66.

(a) Circle
Area = πr^2
Perimeter = 2
Circularity = 4

(b) Freeform
Small area
Large perimeter
Circularity >> 4π

Figure 5.66: Variation of circularity with grain shape.

5.1.f.iii.a   Grain size of monolithic barium titanate

The pressureless sintered and hot pressed samples were both examined to determine the grain size and the results are presented in Table 5.3.

Table 5.3: Image analysis results of barium titanate (pressureless and hot pressed)

showing grain size parameters from images obtained optically.

Barium titanate sample fabrication type		Grain Area (μm^2)	Grain perimeter (μm)	Circularity	Major axis length (μm)	Minor axis length (μm)
Pressureless	Average	52.9	27.8	16.2	9.5	7.6
	95%CI	5.2	1.26	0.3	0.4	0.4
Hot pressed	Average	93.8	36.8	16.5	12.7	10.0
	95%CI	8.4	1.5	0.2	0.5	0.4

Contrary to the results obtained, a lower grain size would be expected for the hot pressed samples as this technique is reported to reduce grain growth due to the pressure, shorter times and lower sintering temperatures[75]. It is suggested that this disparity is due to the absence of re-crystallisation in the pressureless sintered samples, perhaps due to the high porosity (~6%) in these specimens. It is inferred from the major and minor axis lengths that the grains have equal aspect ratios and circularity. The 95% confidence intervals are similar for both samples and are small due to the large number of grains measured (typically >100).

5.1.f.iii.b   Grain and particle size of barium titanate-silicon carbide composites

Silicon carbide particles, if present, were not observed using the optical microscope. Analysis of scanning electron microscope, SEM, images is given in Section 5.1.g.

5.1.f.iii.c   Grain and particle size of barium titanate-silver (oxide) composites

Figure 5.67 shows the grain sizes obtained from analysing optical images of the barium titanate-silver (oxide) composites.
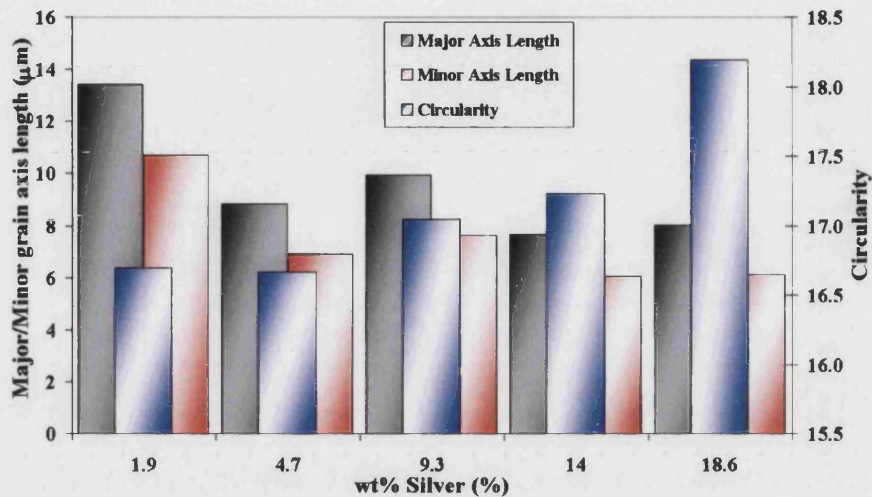
Figure 5.67: Silver (oxide) composite grain sizes showing decreasing grain size

and increased circularity with increasing silver content.

The grain size decreases as the silver content increases, suggesting that grain growth is inhibited by the presence of silver. The grain size aspect ratio is not significantly altered on addition of the silver. The circularity increases, suggesting that the grains become more complex with higher surface area to volume ratio. The 95% confidence intervals were below 0.5 µm for the axis lengths and approximately 0.3 for the circularity.

The silver particles, see Figure 5.68, appear to increase in size as the silver content rises, suggesting agglomeration is more prevalent with higher silver fractions. The circularity varied considerably but on average was greater than the circularity of the grains. This is expected as the silver is molten at the sintering temperature and will deform to fit in between the grains. The axis length and circularity for silver particles had 95% confidence intervals reduced to 0.2 µm and about 0.4, respectively, in comparison to the grains.
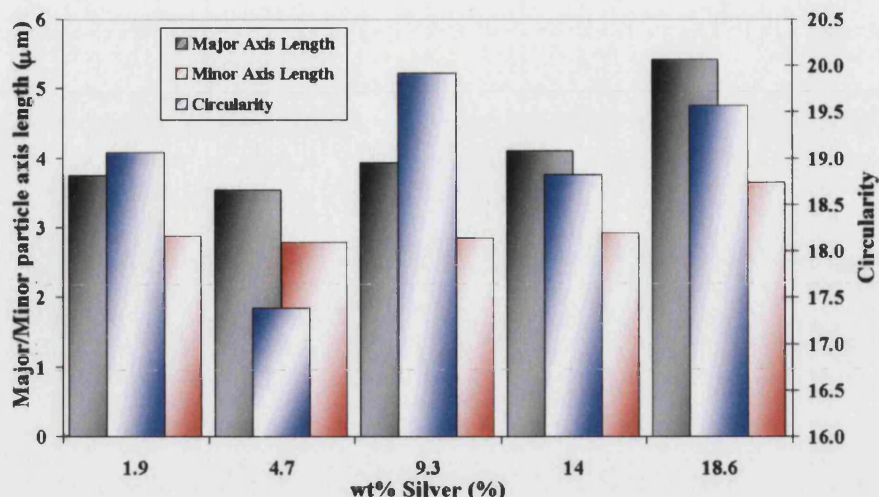
Figure 5.68: Particle size of silver in barium titanate-silver (oxide) composites

indicating increased silver particle size with silver content.

An estimation, based on area, of the silver content was made, from image analysis, by summing all the particle areas and calculating this as a percentage of the total image area. The results (assuming a 5% porosity value) are shown in Table 5.4, with the theoretical silver content.

Table 5.4: Comparison of calculated (from image analysis) and theoretical silver

contents for barium titanate-silver (oxide) composites.

Theoretical silver (wt%)	1.9	4.7	9.3	14.0	18.6
Area estimated silver (wt%)	2.6	3.4	8.7	7.7	15.5

In most cases the estimated value is similar, as close as could be expected from the method employed, to the theoretical value, suggesting that the majority of silver loss is restricted to the surface layer only, although a low value is observed for the barium titanate-14wt% silver sample. Estimated values of silver content from image analysis are expected to be lower than the theoretical value as only particles that can be seen optically are taken into account.

5.1.f.iii.d   Particle size of barium titanate-silver (nitrate) composites

Image analysis consisted of converting colour scans to 24-bit greyscale images and a threshold technique used to define the phase areas. This was facilitated by the high contrast between the different phases, as the pores were black, the matrix grey and silver was white. Spatial calibration

was carried out so that the results were obtained in micrometres. The results are shown in Figure 5.69 and indicate, as expected, that the silver content increases with silver (nitrate) content.
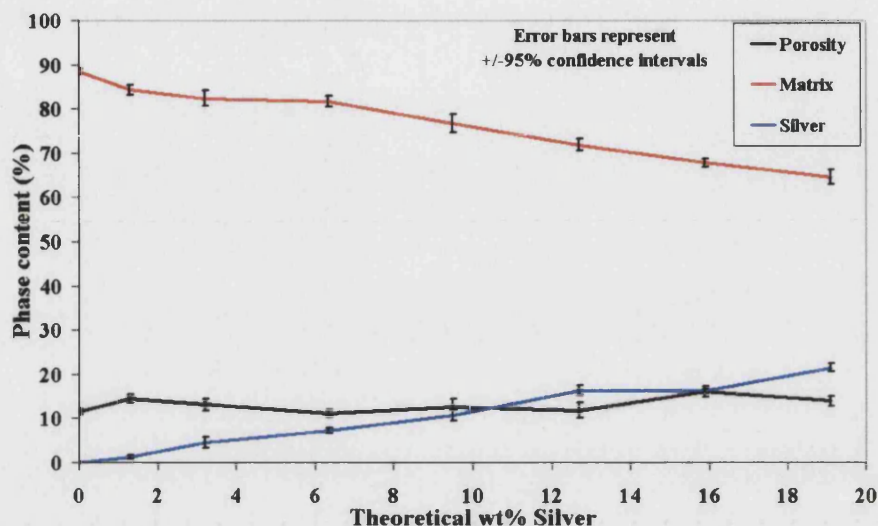
Figure 5.69: Phase content for silver (nitrate) composites from threshold image analysis.

The increase in silver content is linear and corresponds well with the theoretical amount anticipated. The proportion of porosity appears to be fairly constant for all composites, which is in contrast to the density measurements that suggest the porosity increases as the silver content increases. This discrepancy may be due to the threshold value chosen to define the boundary between the phases. For this reason a second method was used, in which grains and particle boundaries were traced and the dimensional properties given by the image analysis software. The results are given in subsection 5.1.g. as the analysis was conducted on images obtained from the scanning electron microscope, in order to take advantage of the increased brain boundary contrast.

Other properties obtained from the threshold method included silver particle orientation and major axis length. No preferred orientation was discovered, however, as with silver (oxide) composites the silver particle size was observed to increase with silver content, Figure 5.70, indicating particle agglomeration.
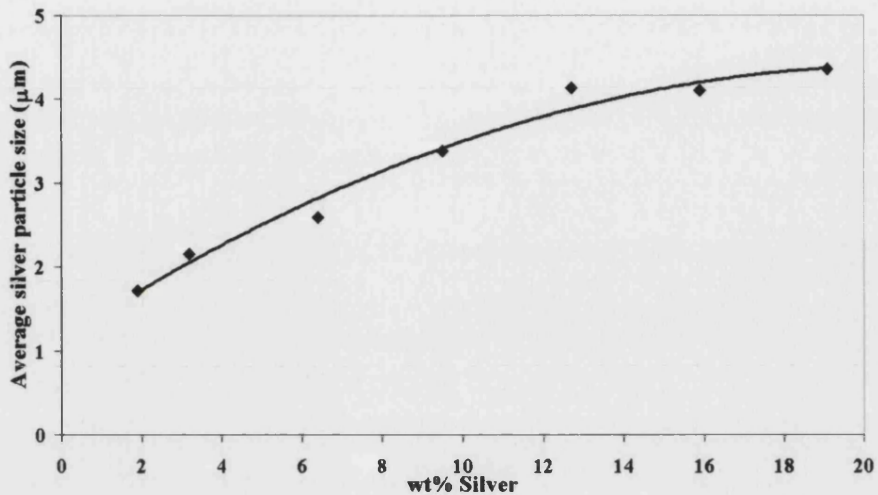
Figure 5.70: Average silver particle size from the threshold image analysis

of barium titanate-silver (nitrate) composites.

5.1.f.iv   *Particle location analysis*

5.1.f.iv.a   Particle location in barium titanate-silicon carbide composites

Silicon carbide particles were not expected to be observed due to the reactions characterised by X-ray diffraction. Figure 5.71 indicates the presence of a second phase, which may be silicon carbide, however, these "particles" are not nano-sized. Further SEM analysis on these samples showed that the phases were not silicon carbide, but contained barium and titanium. No particles or secondary phases were observed in the hot pressed samples.
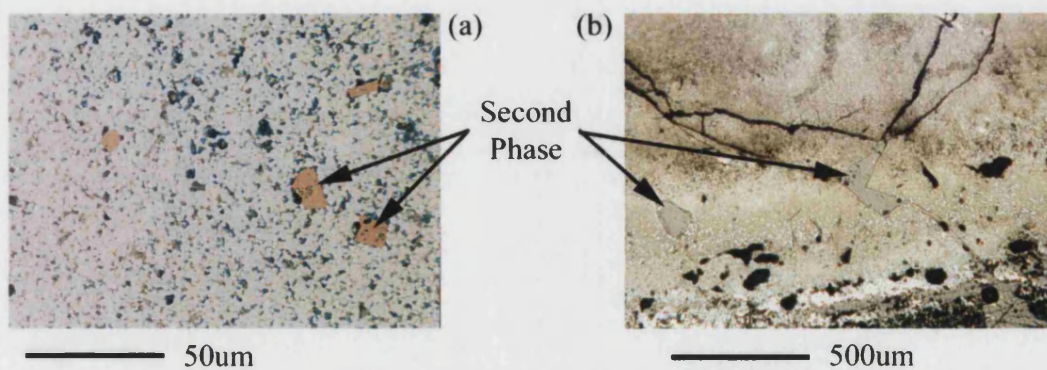
Figure 5.71: Barium titanate-silicon carbide composites with (a) 1wt% silicon carbide

and (b) 15wt% silicon carbide.

5.1.f.iv.b   Particle location in barium titanate-silver (oxide) composites

Silver particles were easily observed using the optical microscope; their position was seen to be mainly at the grain boundaries with a small percentage within the grains, Figure 5.72. In many cases circular "holes" were observed within grains, which might have contained silver particles that were subsequently lost during the polishing and etching process. In general the smaller particles, typically ~1 μm, were observed to be located within the grains rather than at the grain boundaries.
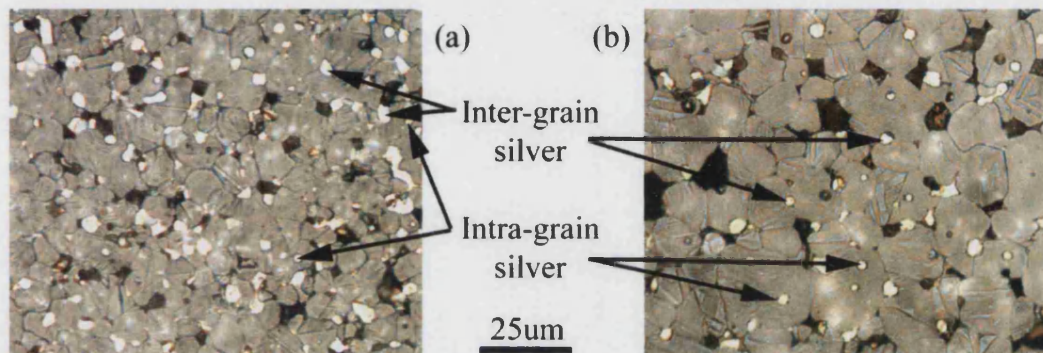
Figure 5.72: Silver particles within grains and at the grain boundaries in (a) barium titanate-14wt% silver and (b) barium titanate-4.7wt% silver (oxide) composites.

5.1.g   SCANNING ELECTRON MICROSCOPY

The SEM was used to examine the microstructure of the composites, undertake X-ray mapping of phase distributions, investigate powder morphology (5.1.b.) and to obtain images used for hardness and toughness calculations.

5.1.g.i   *Fracture mode determination*

5.1.g.i.a   Fracture mode of monolithic barium titanate

The barium titanate fracture mode was observed to be intragranular as shown in Figure 5.73. This fracture mode has been reported elsewhere for the monolithic barium titanate[144, 69].
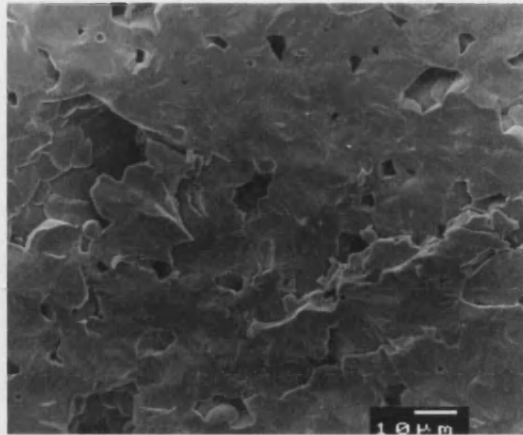
Figure 5.73: Intragranular fracture of monolithic barium titanate.

5.1.g.i.b   Fracture mode of barium titanate-silicon carbide composites

The incorporation of silicon carbide caused the fracture mode to change from the intragranular mode for the monolithic case to intergranular in the composite, see Figure 5.74. Individual matrix grain fracture was also observed, Figure 5.75, suggesting micro-cracking is possible in these composites due to residual stress generation by a secondary phase.
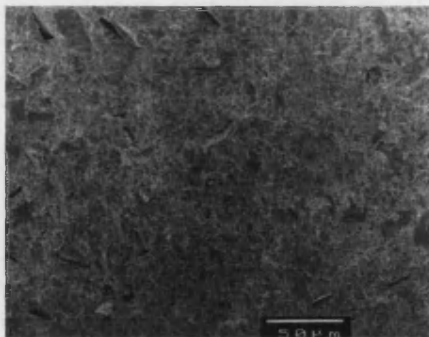
Figure 5.74: Intergranular fracture of barium titanate-5wt% silicon carbide composite.
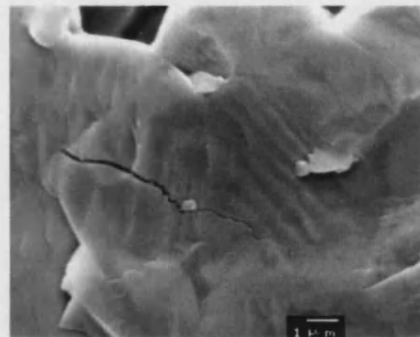
Figure 5.75: Individual grain fracture in barium titanate-5wt% silicon carbide composite.

This change in fracture mode has not been observed in hot pressed barium titanate-silicon carbide composites[41]. The difference may be related to the higher porosity in the pressureless sintered samples. Structural alumina with the incorporation of silicon carbide has been reported to change from an intergranular fracture mode to intragranular with silicon carbide addition[2, 34, 75, 81]. This alumina system has improved mechanical properties that may be possible in the barium titanate-silicon carbide system. The barium titanate-silicon carbide system, however, may suffer from the fracture mode change, if the silicon carbide particles, or secondary phase, weaken the grain

boundaries. However, the matrix grains may be strengthened and cause more energy to be expended by grain boundary fracture. More energy is required for intergranular fracture due to the larger amount of new surface area formed when compared to intragranular fracture.

5.1.g.i.c   Fracture mode of barium titanate-silver composites

Silver particles were easier to observe than silicon carbide due to their greater size and being less reactive at the sintering temperature. The fracture mode for the silver (nitrate) composites was determined to be intragranular, see Figure 5.76, with no change from the monolithic barium titanate. The ductile nature of the silver particles can allow relief of stress produced by the different thermal expansion coefficients of the particles and matrix. However, micro-cracking was still observed, Figure 5.76(d). The presence of the silver particles at the grain boundary and in the grain interior (see Section 5.1.g.iii) suggests that energy absorption by the ductile deformation of silver in both location is possible during intragranular fracture. However, it is likely that the small particles, less than 1 μm, within the grains will be pulled out (due to poor mechanical keying), during intragranular fracture, without undergoing deformation if the barium titanate-silver interface strength is low.
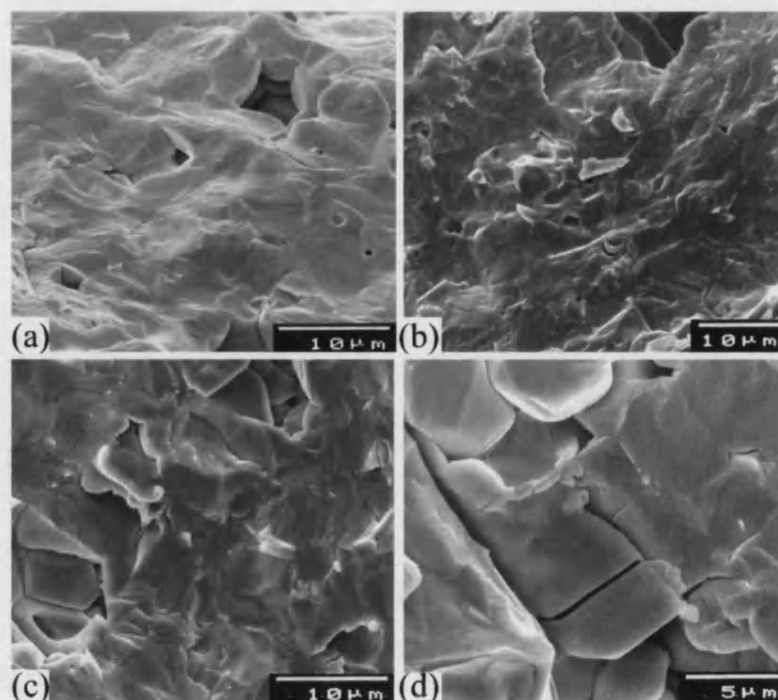
Figure 5.76: Barium titanate-(a) 6.4wt% silver, (b) 9.5wt% silver and (c) 12.7wt% silver.

(d) Micro-cracking in barium titanate-9.5wt% silver composite. Intragranular

fracture was observed in all barium titanate-silver composites. (Nitrate derived).

The silver particles, see Figure 5.77, were observed to be ductile in nature. The occurrence of this ductile behaviour was only detected for the silver particles of 1-2 μm or more in size that were located intergranularly.
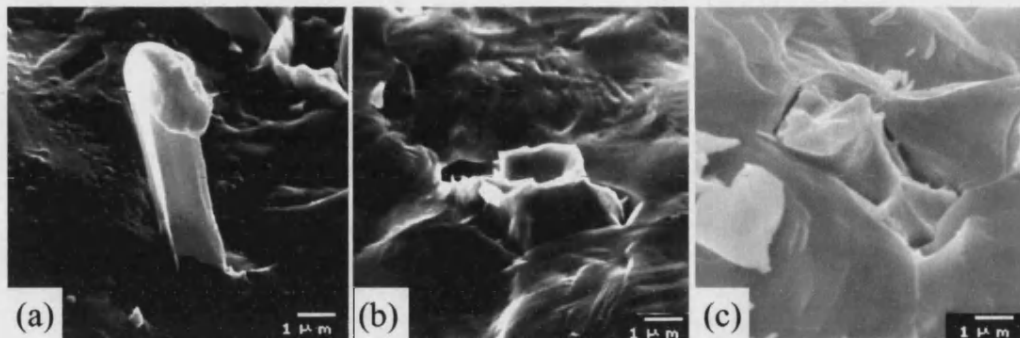
Figure 5.77: Barium titanate-6.4wt% silver indicating the ductile behaviour of the silver

particles by (a) pull-out and (b) and (c) cup-cone fracture zone.

5.1.g.ii *Grain and particle size*

5.1.g.ii.a <u>Grain size of monolithic barium titanate</u>

The measured grain size for the monolithic samples was in the range 5-50 μm, as shown in Figure 5.78. The average grain size has been measured as 9.5 μm using light microscopy, Section 5.1.f.iii.
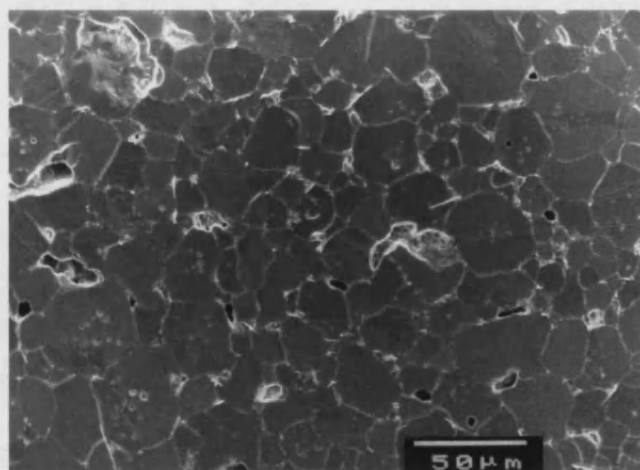
Figure 5.78: Micrograph of monolithic barium titanate showing a grain size range of 5-50 μm.

5.1.g.ii.b   **Grain and particle size of barium titanate-silicon carbide composites**

A significant reduction in grain size was observed with addition of the silicon carbide, see Figure 5.79, in comparison to the monolith, Figure 5.78.
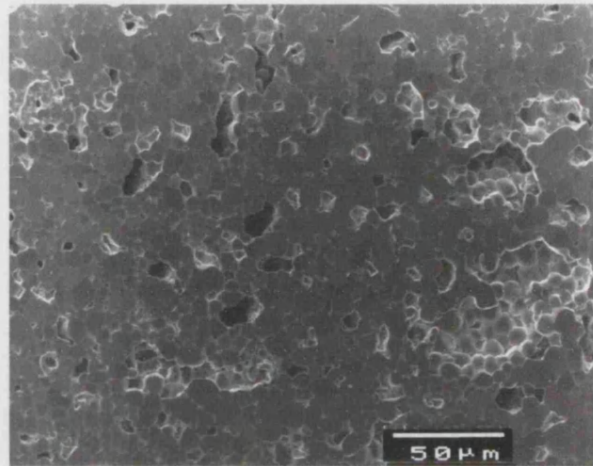
Figure 5.79: Reduced grain size and increased porosity of barium titanate-2wt% silicon

carbide composite in comparison to the monolith.

The detailed image analysis results for the grain size are shown in Figure 5.80. The 9.5 μm average grain size, of the monolith, was reduced to less than 2 μm in the barium titanate-5wt% silicon carbide composite. As the actual silicon carbide particles were not detected it is suspected that they may have been oxidised during thermal etching or formed a reaction phase. An argon atmosphere was supplied during etching with the intention to stop oxidation, however, the surface layer is more liable to oxidise than the bulk.
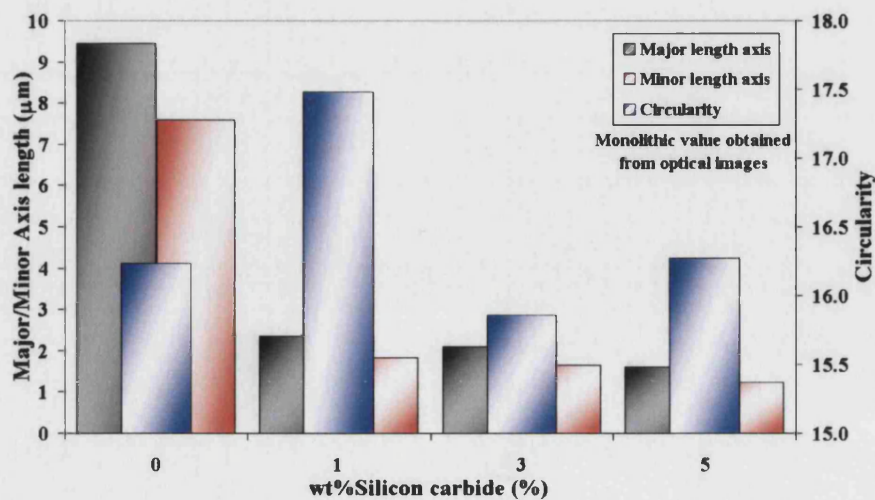
Figure 5.80: Monolithic and barium titanate-silicon carbide composite grain

sizes from analysis of SEM images.

The average grain size of the barium titanate-silicon carbide composites was about 25% that of the monolith and hardly varied with increased particle content. This confirms the view that silicon carbide particles or a reaction phase hinders grain growth during sintering. The circularity is relatively unchanged, suggesting that the grain shape is not affected by the addition of silicon carbide particles. The 95% confidence intervals were typically below 0.1 μm and 0.5 for the length measurements and circularity value, respectively.

For the hot pressed samples the addition of silicon carbide caused a grain size reduction that is greater than observed for the pressureless sintered samples, Figure 5.81. The grain shape is also modified and becomes more circular. This is proposed to be due to the presence of the pressure at the elevated sintering temperature that allows the grains to form a lower energy morphology than that in the pressureless sintered case. Additionally the shorter sintering time and lower temperature will reduce the formation of abnormal grain growth. Silicon carbide particles were not found using the SEM and this precluded measurement of their size.
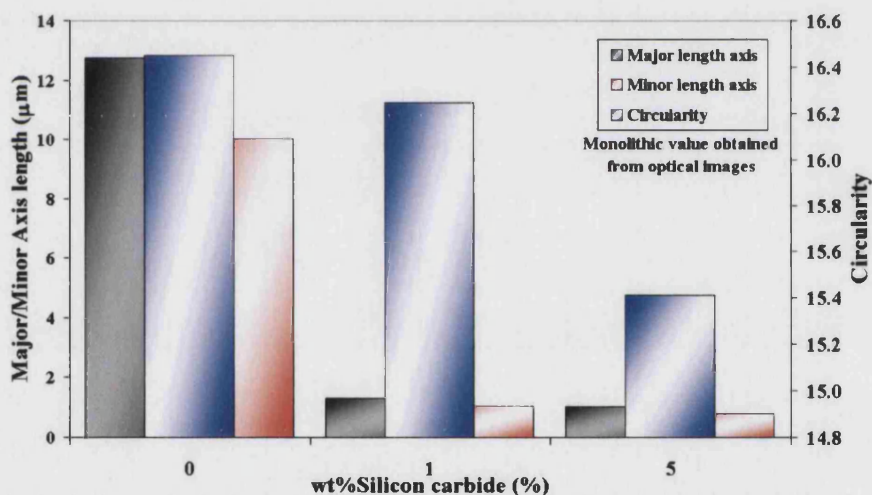
Figure 5.81: Hot pressed monolith and barium titanate-silicon carbide composite grain sizes.

5.1.g.ii.c   Grain and particle size of barium titanate-silver (nitrate) composites

A steady decrease in the grain size for increasing silver content in barium titanate-silver (nitrate) composites is revealed from the image analysis of SEM micrographs, Figure 5.82. This is thought to be due to the limited solubility of barium titanate in the silver that hinders diffusion during densification. The circularity of the grains decreases slightly, suggesting that the molten silver has a part to play in minimising the surface area of the grains. The 95% confidence intervals for the grain size and circularity were below 0.4 μm and 0.5, respectively.
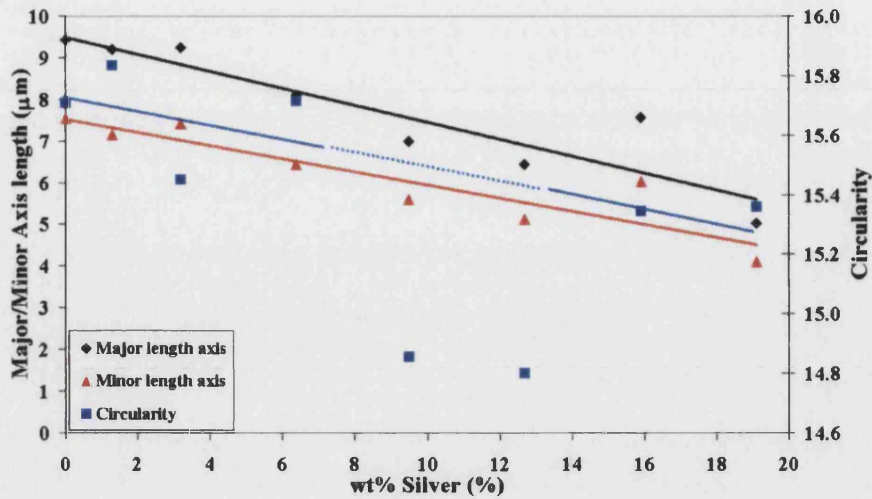
Figure 5.82: Decrease of barium titanate-silver (nitrate) grain size with the addition of silver.

5.1.g.ii.d   Grain and particle size distributions

The distribution of the grain sizes from optical and SEM image analysis was examined for changes in grain distribution with particle addition. A bimodal distribution could indicate the presence of exaggerated grain growth. Exaggerated grain growth occurs when certain grains grow in preference to other grains. The result is that the large grains sacrificially consume small grains. The results of the analysis using a polynomial trend line fitted to the grain size data is given in Table 5.5.

In most cases a bimodal distribution was not observed, Figure 5.83, except in the pressureless sintered monolithic case. The bimodal behaviour in both the 12.7wt% silver and 19.1wt% silver samples appear to be anomalous in comparison to the trend and is suspect. The lack of a bimodal distribution in the composites suggests that exaggerated grain growth has not occurred. It may, however, be present in the pressureless sintered monolithic material. It has been reported that silver addition caused abnormal grain growth[47]. However, this was not conclusively observed in this work.

Table 5.5: Grain size distributions for monolithic barium titanate

and composites from image analysis.

Composite	Particle content (wt%)	Comments
BaTiO$_3$	0	Possible bimodal due to peaks at 7.5 μm and 17.5 μm
BaTiO$_3$-HP	0	Single peak at 12 μm
BaTiO$_3$-SiC	1	Mono-modal with peak at approximately 2.4 μm
	3	Mono-modal with peak at approximately 1.8 μm, but skewed towards higher grain sizes
	5	Mono-modal with peak at approximately 1.5 μm, but skewed towards higher grain sizes
BaTiO$_3$-SiC (HP)	1	Narrow distribution, peak about 1 μm
	5	Narrow distribution, peak slightly less than 1 μm
BaTiO$_3$-Ag (Ag$_2$O)	1.9	Broad distribution with peak in range 8-15 μm
	4.7	Peak at about 8 μm, but strongly skewed to higher grain sizes, with possible additional peak at 11 μm.
	9.4	Single peak in range 9-10 μm
	14.0	Peak at 7 μm
	18.6	Peak at 7 μm, but distribution is narrower than for 14.0wt% silver
BaTiO$_3$-Ag (AgNO$_3$)	1.3	Possible bimodal, main peak at 7.5 μm, but smaller second peak in 10-20 μm region
	3.2	Bimodal not observed, peak at 8 μm
	6.4	No bimodal distribution, peak at 7.5 μm
	9.5	Single peak at 6 μm
	12.7	Bimodal with peaks at 6 μm and 14 μm
	15.9	Single peak 6.5 μm
	19.1	Bimodal with peaks at 4 μm and 12.5 μm
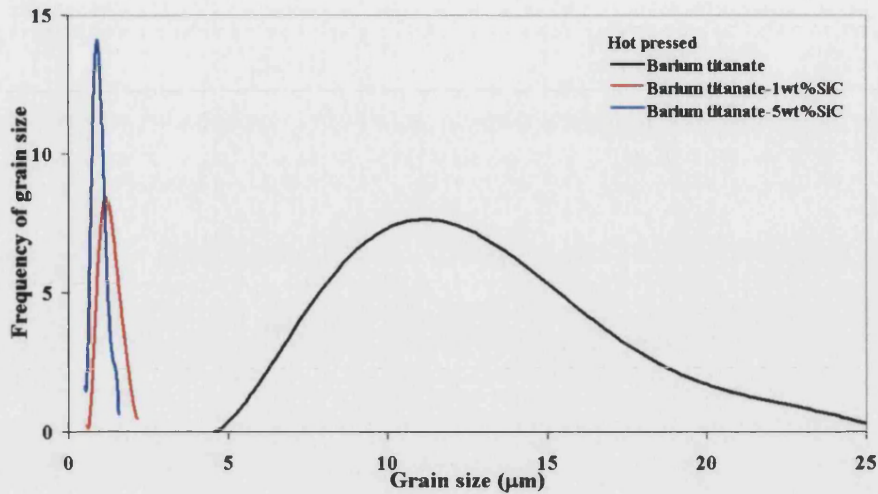
Figure 5.83: Grain size distributions for hot pressed barium titanate monolith

and composites indicating no bimodal grain distributions.

Similar analysis was conducted on the particle size distribution for the silver composites. The trend was difficult to observe due to the small number of particles analysed, typically in the region of 50-200. For the silver (oxide) composites all the samples appeared to have single distributions centred around 4 μm. The higher silver content composites appeared to have a broader range of sizes. The results for the composites produced using silver nitrate were the same, in that no bimodal distribution was observed. In this case the distributions were centred about 3 μm. This difference in average silver particle size may be due to the different starting materials, as the silver oxide powder has a larger particle or agglomerate size in comparison to the silver nitrate powder.

5.1.g.iii   *Particle location*

5.1.g.iii.a   Particle location in barium titanate-silicon carbide composites

Insufficient silicon carbide particles were observed under the optical microscope or the SEM to make an estimate of the silicon carbide particle size after sintering. In fact, these particles were not seen in their original state. The possible reaction products of these particles were observed as silicon rich areas during X-ray mapping of the composites, see Figure 5.84. The presence of silicon was conclusively observed in the 15wt% silicon carbide samples, Figure 5.85, however, the low carbon content suggests the silicon carbide is no longer in its original form. From the dispersed nature of the silicon shown by the X-ray map image it is suggested that the silicon has formed a secondary phase. It is thought that this second phase may have become glassy in behaviour and flowed between the barium titanate grains during sintering.
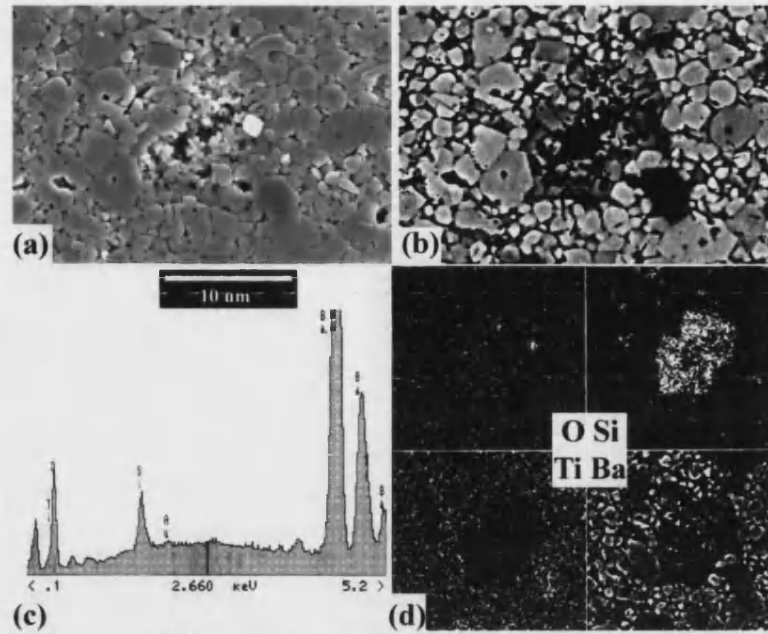
Figure 5.84: Barium titanate-3wt% silicon carbide (a) secondary electron image, (b) back-scattered electron image, (c) X-ray diffraction pattern for the central region and (d) X-ray elemental maps showing the presence and location of silicon.
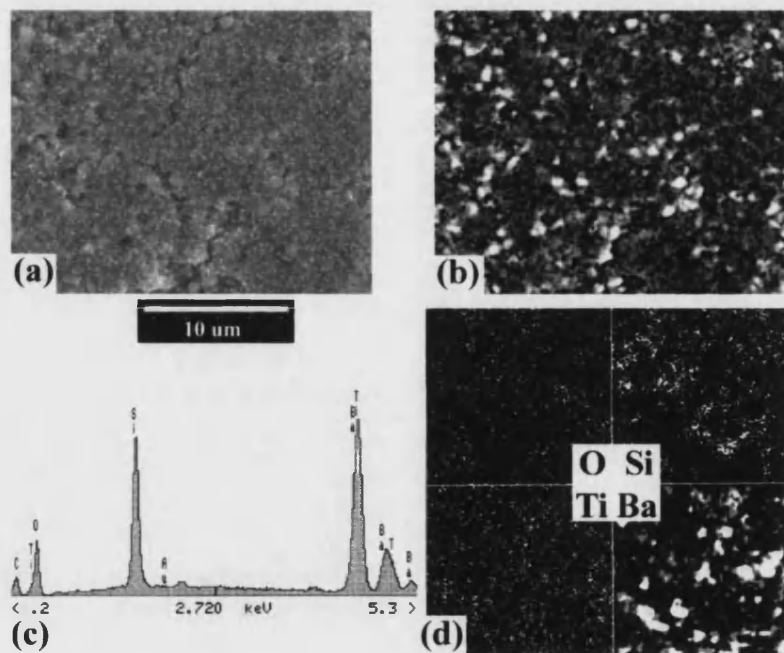
Figure 5.85: Barium titanate-15wt% silicon carbide (a) secondary electron image, (b) back-scattered electron image, (c) X-ray diffraction pattern and (d) X-ray elemental maps indicating the presence of silicon but not as discrete particles.

Silicon was also observed in the hot pressed composites, but not as discrete particles, Figure 5.86.
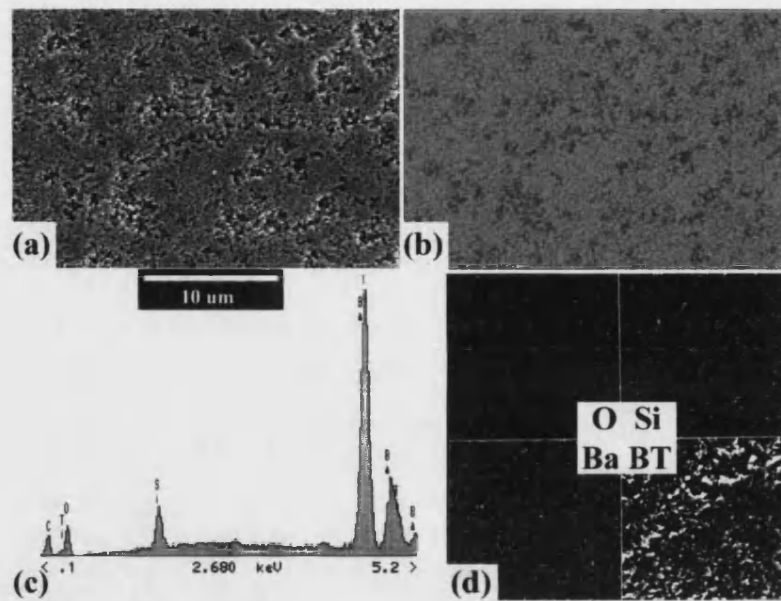
Figure 5.86: Hot pressed barium titanate-5wt% silicon carbide (a) secondary electron image,

(b) back-scattered electron image, (c) X-ray diffraction pattern indicating presence of

silicon and (d) X-ray elemental maps of the same area.

5.1.g.iii.b   Particle location in barium titanate-silver (oxide) composites

The silver particles could be observed easily using secondary electrons, but the back-scattered image had greater contrast, with the silver particles showing up as bright regions as can be seen in Figure 5.87.
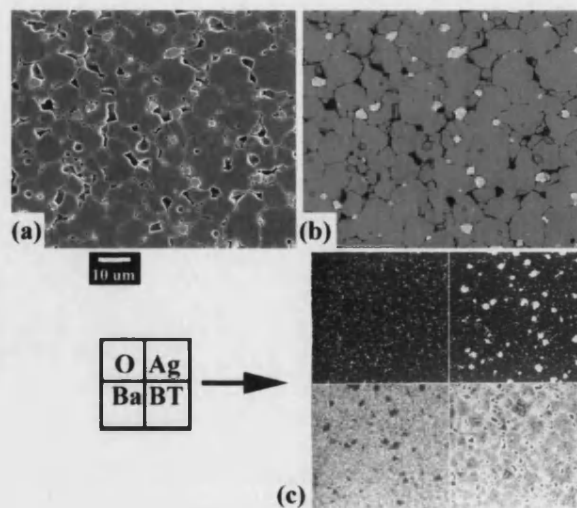
Figure 5.87: Barium titanate-4.7wt% silver (a) secondary electron image, (b) back-scattered

electron image and (c) X-ray elemental maps showing the good phase contrast and location

of silver particles (bright regions). Silver oxide derived metal.

The location of the silver particles changes as the proportion of silver increases, see Figure 5.88. At higher silver contents the proportion of silver at the grain boundaries increases. While the large silver particles (>1 μm) are located in between the grains, the smaller particles were observed to be within the grains.
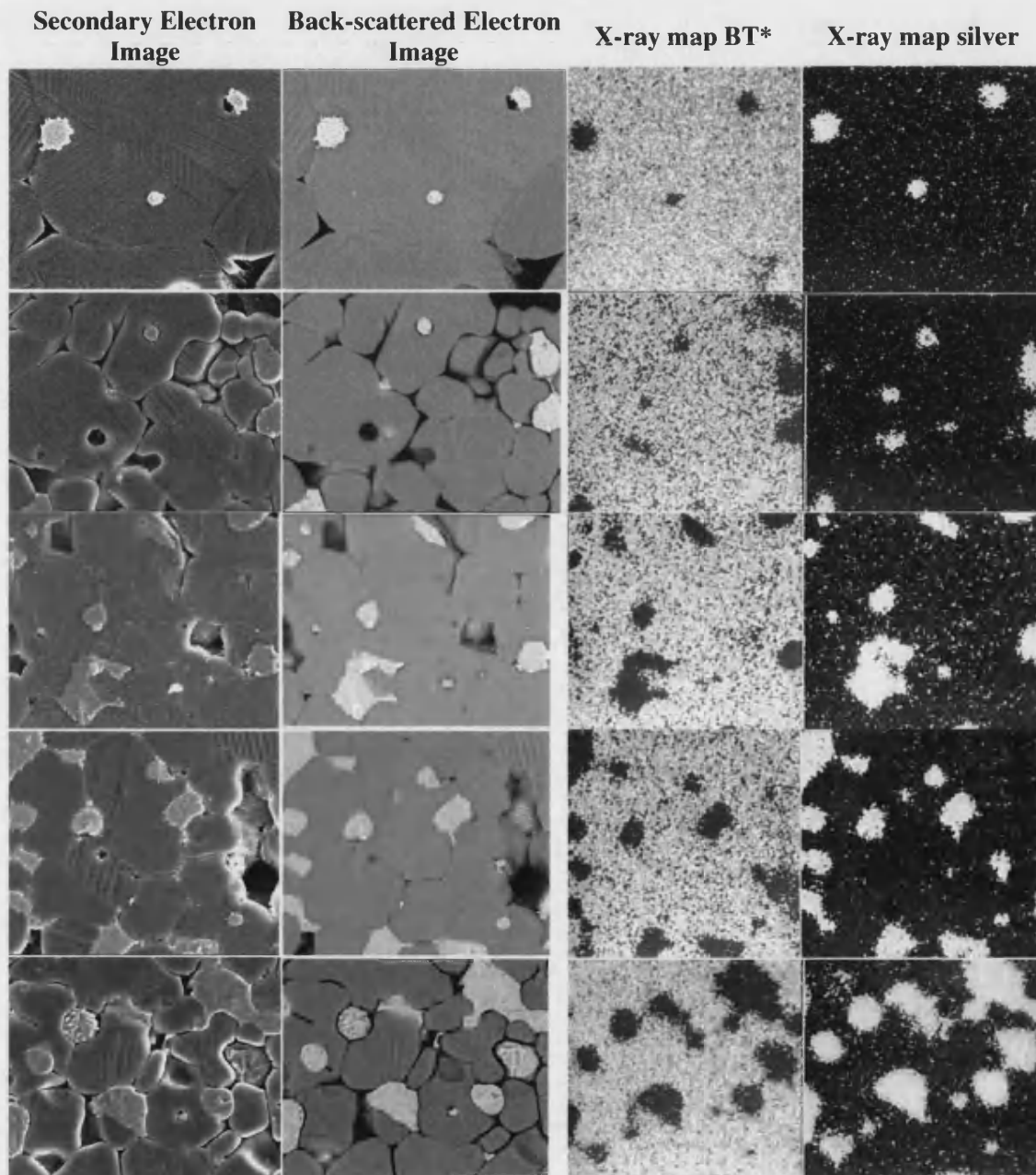
Figure 5.88: (a) Secondary electron image, (b) back-scattered electron image and (c) X-ray elemental maps for barium titanate-1.9, 4.7, 9.3, 14 and 18.6wt% silver composites. Image width is approximately 15 μm and BT* is the combined elemental maps of barium and titanium. Silver oxide derived metal.

5.1.g.iii.c   Particle location in barium titanate-silver (nitrate) composites

As with the silver (oxide) composites, the larger particles were located intergranularly and smaller particles situated within the grains, Figure 5.89. The observation of silver particles within grains and at grain boundaries has been reported by Chen[70].
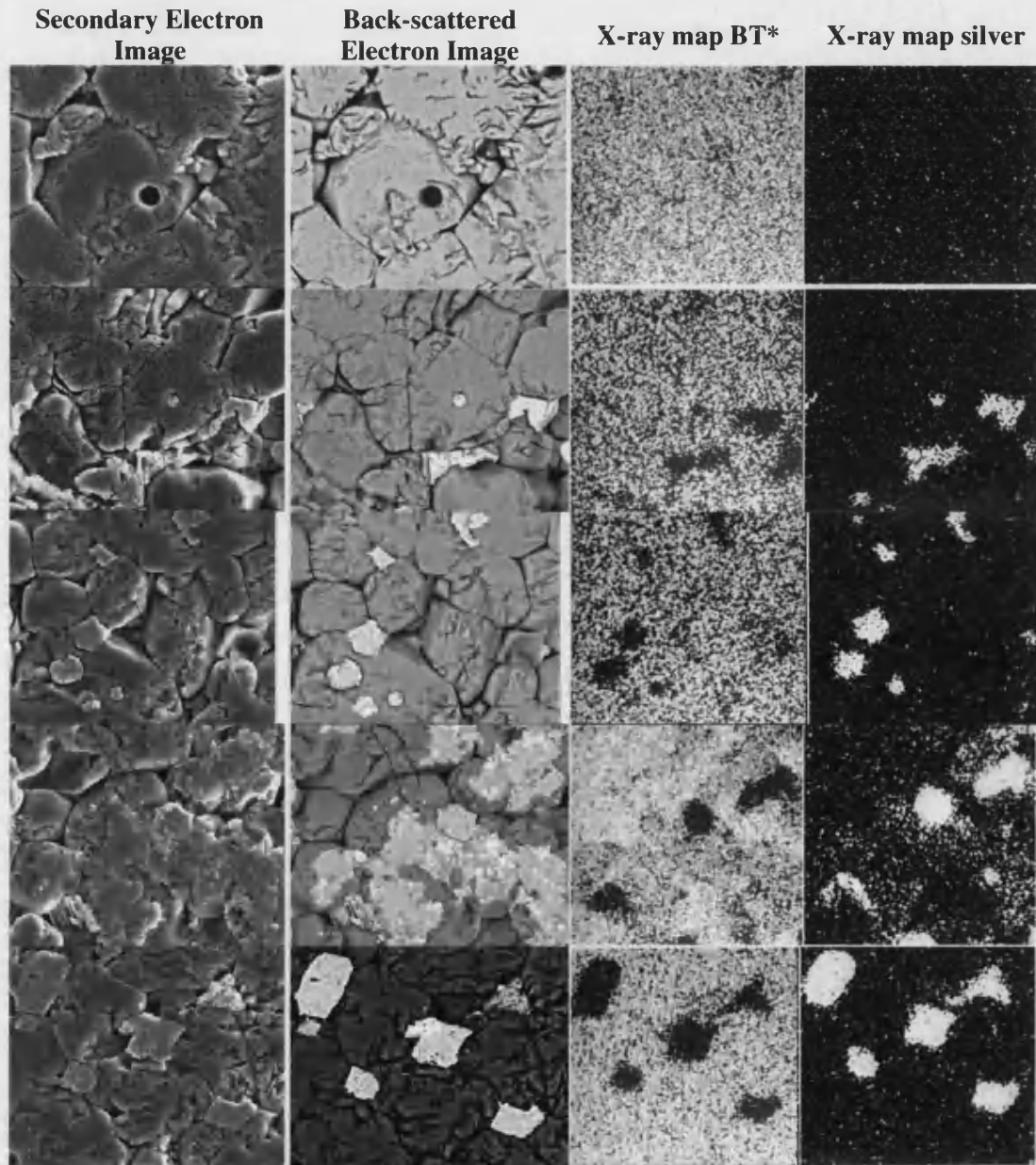
Figure 5.89: (a) Secondary electron image, (b) back-scattered electron image and

(c) X-ray elemental maps for barium titanate-0, 3.2, 6.4, 12.7 and 19.1wt% silver

composites. Image width is approximately 15 μm and BT* is the combined elemental

maps of barium and titanium. Silver nitrate derived metal.

Porosity or 'holes' were observed in which it is believed silver particles once resided, but have since been removed by polishing or etching. This did not appear to affect the larger intergranular silver particles, but only the smaller intragranular particles, see Figure 5.90. This maybe due to the lower mechanical adhesion for the smaller particles and polishing pulls out the complete particle. The intragranular particles are generally spherical in shape to reduce the surface area to volume ratio, which is consistent with the fact that the silver is liquid at the sintering temperature.
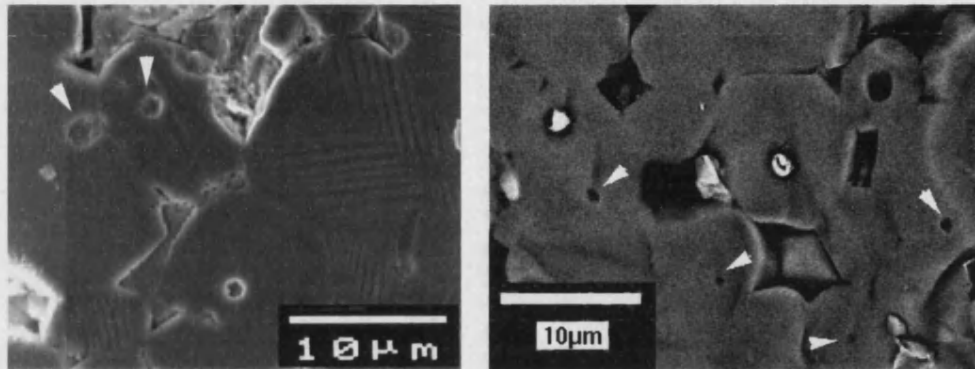
Figure 5.90: Possible silver particle loss from intragranular sites indicated by arrows.

5.1.g.iii.d   Particle location in barium titanate-5.7wt% platinum

Platinum particles appeared to reside intra- and intergranularly, Figure 5.91. As observed with the silver particles the smaller platinum particles, <1 μm, were located within the grains, whereas the larger particles were situated at the grain boundaries. X-ray diffraction analysis confirmed that the particles consisted of platinum only. The larger particles will more readily form at the grain boundary due to faster diffusion and are more effective pinning points for the grain boundary.
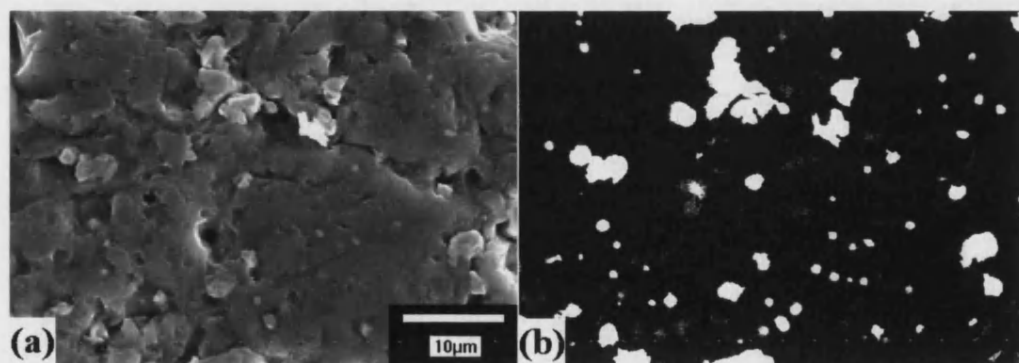
Figure 5.91: Barium titanate-5.7wt% platinum (a) secondary electron image and (b) back-scattered electron image showing intra- and intergranular platinum particle locations.

5.1.g.iv *Observation of silver depletion layer*

The extent of the silver surface depletion layer was readily observed with the use of the back-scattered imaging mode, see Figure 5.92. The silver particles show as white regions within the grey barium titanate matrix. The layer thickness was observed to be in the region of 100 μm.
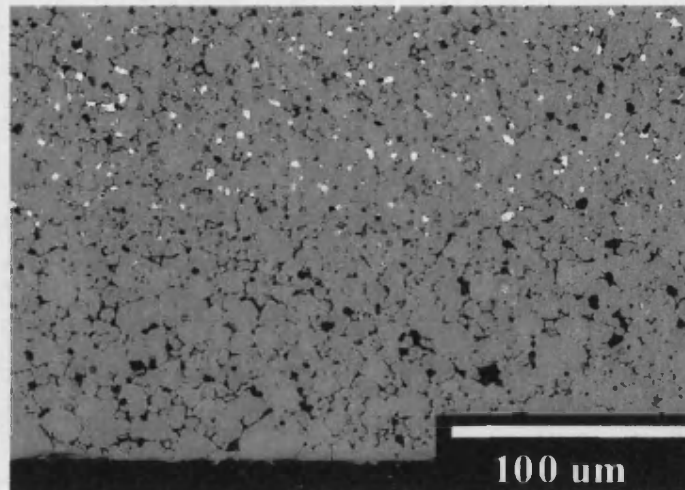
Figure 5.92: Depletion layer in barium titanate-9.3wt% silver

composite observed by using the back-scattered imaging mode.

The difference in composition between the depleted and silver rich regions may be a reason for the cracking at the interface, Figure 5.93, which was observed in the highest silver content samples. It is thought that the thermal expansion difference between the silver (28×10^{-6} °C^{-1} [48]) and the matrix (14×10^{-6} °C^{-1} [40]) produces stresses that are relieved by cracking.
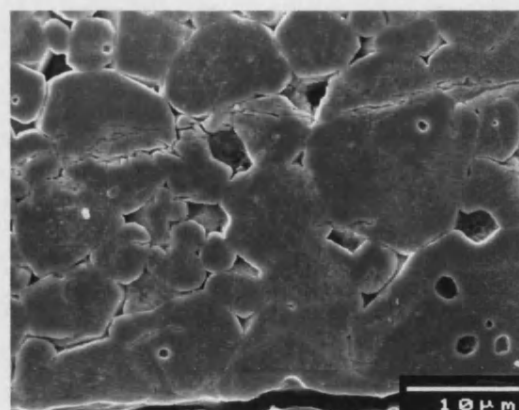
Figure 5.93: Interface cracking in barium titanate-19.1% silver

between the silver containing region and silver depleted layer.

5.1.g.v   *Observation of secondary phases*

5.1.g.v.a   Secondary phases in barium titanate-silicon carbide composites

A number of different microstructures were observed in the silicon carbide composites. Differences in barium-titanium ratio may account for the variation in brightness of the backscattered image observed between grains for a hot pressed sample, Figure 5.94.

(a)   (b)
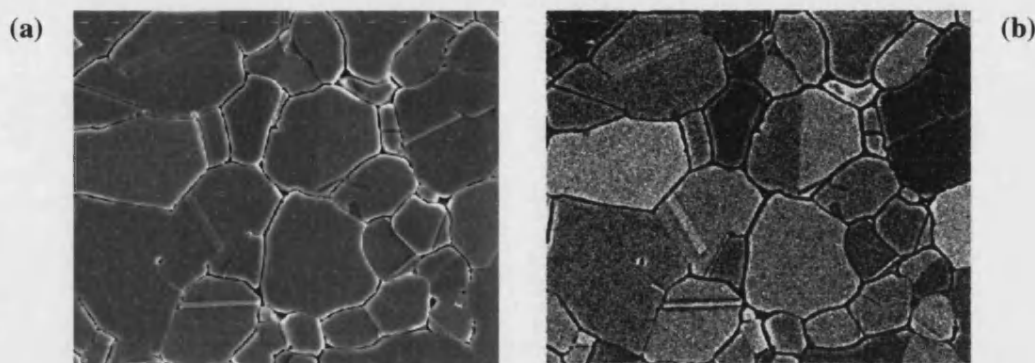
Figure 5.94: Compositional variation in hot pressed barium titanate-5wt% silicon carbide

(a) secondary electron image and (b) back-scattered electron image.

Silicon carbide particles were not observed using the SEM so it is possible that the compositional change is partly due to the solubility of silicon in the host matrix. A glassy secondary phase structure was observed when it became "squeezed out" under capillary action during thermal etching, Figure 5.95. The presence of these glassy phases indicates that the silicon carbide has been oxidised and produced a reaction phase that may influence the mechanical and electrical properties. These regions were too small to be examined by X-ray analysis for composition without the background making a significant contribution.
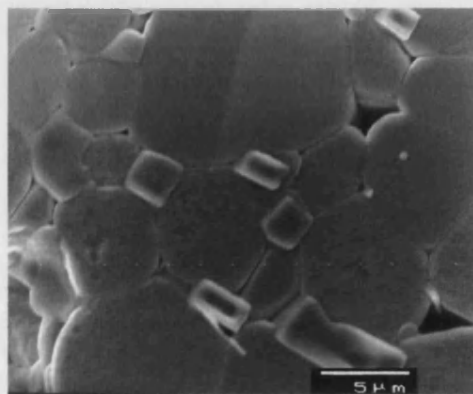
Figure 5.95: Possible glassy phase in between barium titanate grains

in pressureless sintered barium titanate-5wt% silicon carbide.

5.1.g.v.b   Secondary phases in barium titanate-silver composites

Silver, barium, titanium, carbon and oxygen peaks were detected using EDX analysis and the scanning electron microscopy of the polished samples, as shown in Figure 5.96. The carbon is due to the graphite coating applied to the samples to reduce charging effects under the application of the electron beam. No unwanted secondary phases were observed.
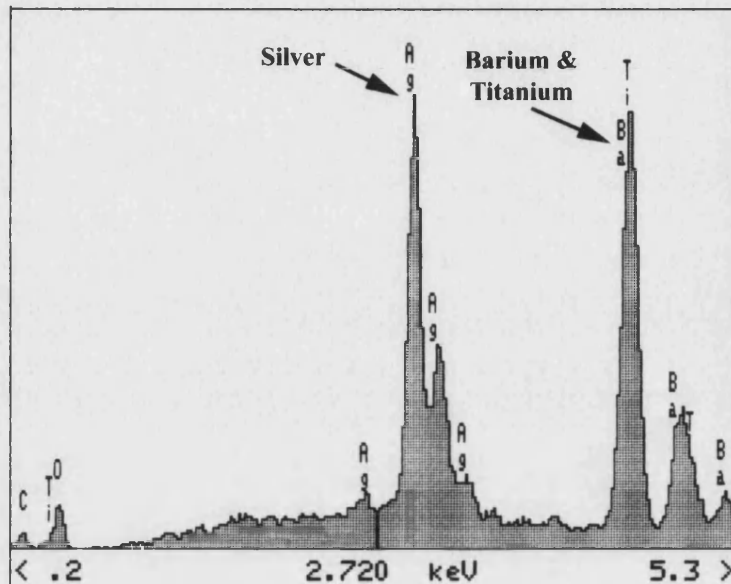
Figure 5.96: X-ray diffraction pattern for barium titanate-18.6wt% silver produced

from silver oxide. Data collected at a magnification of 300X.

Chemical etching caused the silver particles to form a "fibril" type structure as shown in Figure 5.97. These shapes are believed to occur during the chemical etching process, as the polishing, prior to etching, would be expected to remove such structures. This may be caused by the partial dissolution of the silver by the etchant and then deposition in a region of low silver content.
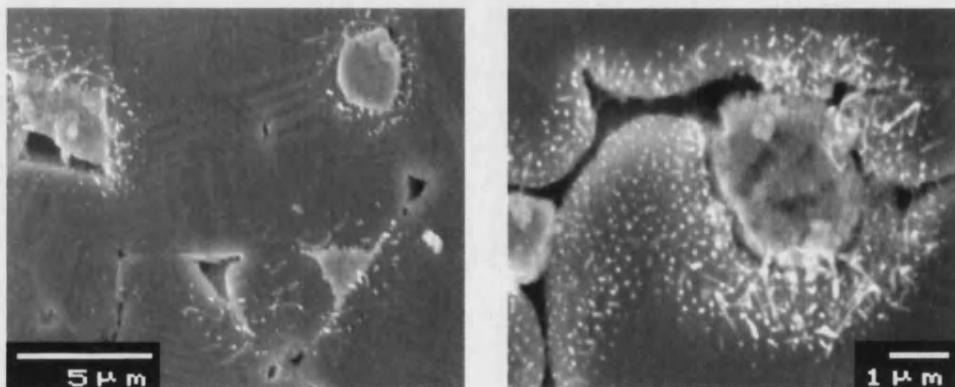
Figure 5.97: Silver "fibrils" formed during the chemical etching process.

5.1.g.v.c   Secondary phases in barium titanate-5.7wt% platinum

Silicon was detected using X-ray analysis in the barium titanate-5.7wt% platinum composite. X-ray elemental mapping was conducted to determine the location of this element, see Figure 5.98. Silicon rich areas were discovered but these were not intimately linked to any other microstructural features. The presence of silicon is unexplained, but could be due to an impurity in the starting material and would help to explain the behaviour of the composites during sintering. The silicon could be oxidised during sintering and form a glassy phase affecting the densification of the barium titanate. The starting material was not examined, as the platinum salt is highly hydroscopic.
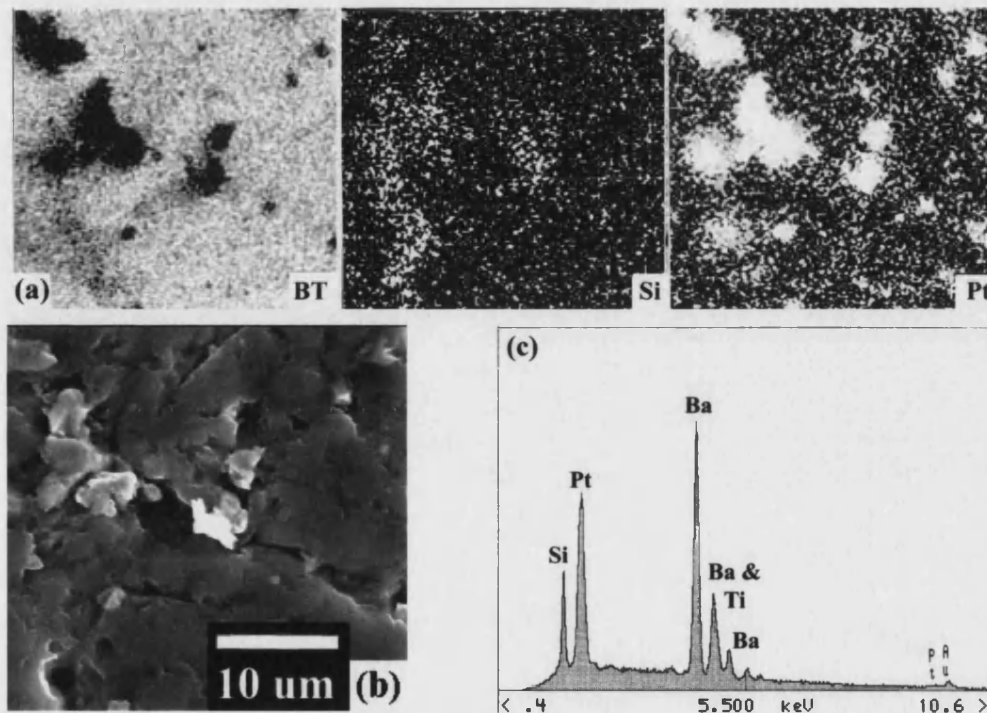
Figure 5.98: (a) X-ray map showing the location of platinum and silicon in (b) the secondary electron image and (c) the X-ray diffraction pattern indicating the presence of silicon and platinum in barium titanate-5.7wt% platinum.

5.1.g.vi   *Observation of ferroelectric domains by SEM*

The presence of domains is characteristic of a ferroelectric based piezoelectric and indicates that the material has possible uses for piezoelectric applications. Domains were frequently observed for the barium titanate monolith, Figure 5.99. The formation of a reaction phase in the composites would be expected to reduce the proportion of piezoelectric material and hence the number of domains.
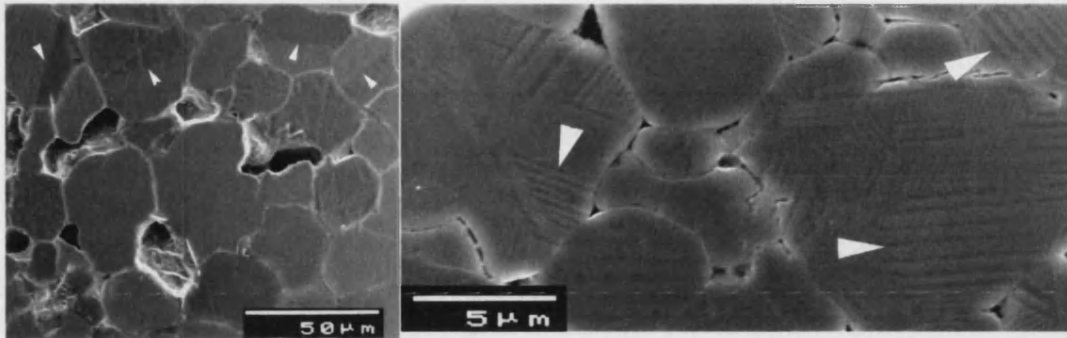
Figure 5.99: Domains in the monolithic barium titanate (white arrows indicating

domain boundary).

Fewer domains were observed in the silicon carbide containing composites, suggesting modification of the host matrix structure, Figure 5.100. This has been reported in the literature[40]. The structural change was verified by X-ray diffraction analysis, Section 5.1.a., which indicated a more cubic structure in comparison to the required tetragonal for domain formation. Although internal stresses, arising from thermal expansion coefficient mismatch, may be present in the silver composite samples the presence of domains, even at high silver contents, is promising for the piezoelectric properties, see Figure 5.101. Qualitatively the number of domains appeared to decrease as the silver fraction increased.
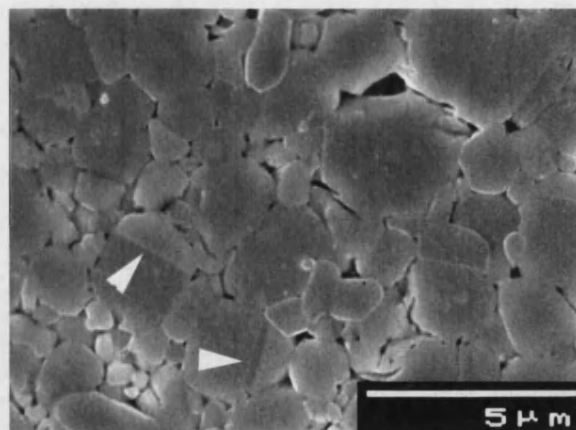
Figure 5.100: Domains indicated by white arrows in barium titanate-3wt% silicon carbide.
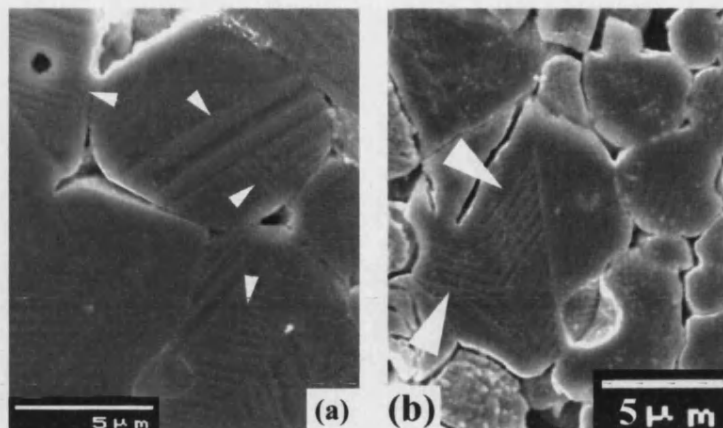
Figure 5.101: Domains in barium titanate-(a) 1.9wt% silver and (b) 18.6wt% silver composites.

5.1.h   TRANSMISSION ELECTRON MICROSCOPY

Transmission electron microscopy, TEM, was employed to investigate how the silicon carbide and silver particles influenced the domains structure in barium titanate. Additionally the grain-grain and grain-particle interfaces were examined to determine if reaction phases were present.

5.1.h.i   TEM analysis of unpoled monolithic barium titanate

Domains, in unpoled barium titanate, were observed in a simple twin configuration, as shown in Figure 5.102(a), and a 0°-90° pattern, see Figure 5.102(b). Complex domain configurations were also imaged, Figure 5.103. These grains contain domains orientated in many different directions; their interaction in an electric field will be more complicated than grains containing the simple twin configuration.
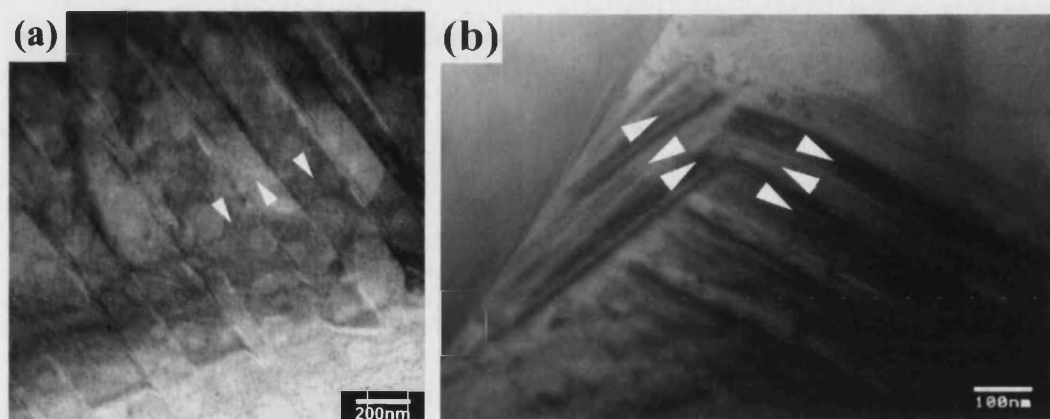
Figure 5.102: Barium titanate with (a) simple 180° domain configuration and (b) a 0°-90°

domain pattern. Arrows indicate the possible orientation of the domains.
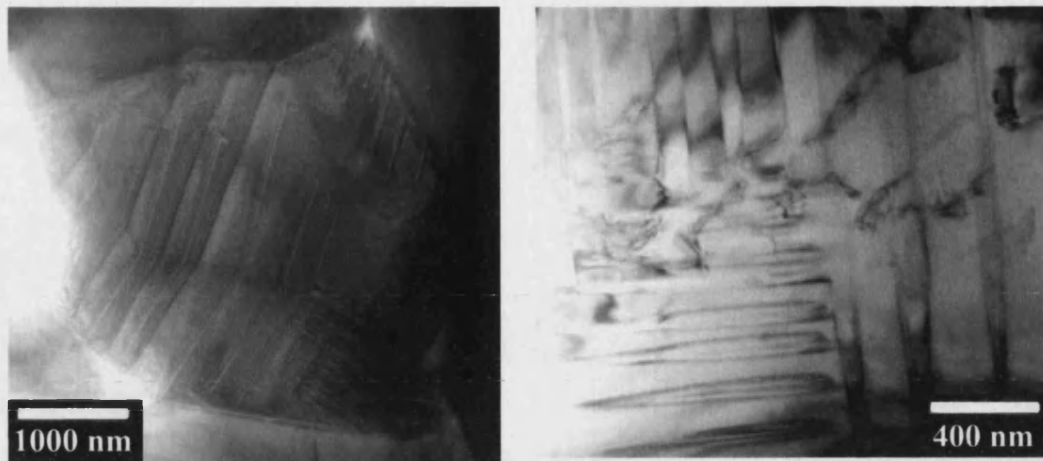
Figure 5.103: Complex domain configurations in barium titanate grains.

The high atomic mass of the barium and titanium atoms limits the thickness of viewable material by TEM, even at a high accelerating voltage, to typically a few micro-metres from the edge of the ion-milled perforated specimen. No reaction phase was expected in the monolithic ceramic; however, a glassy phase was infrequently discovered in the triple grain boundary, Figure 5.104. X-ray analysis was conducted on this region to examine its chemical composition.
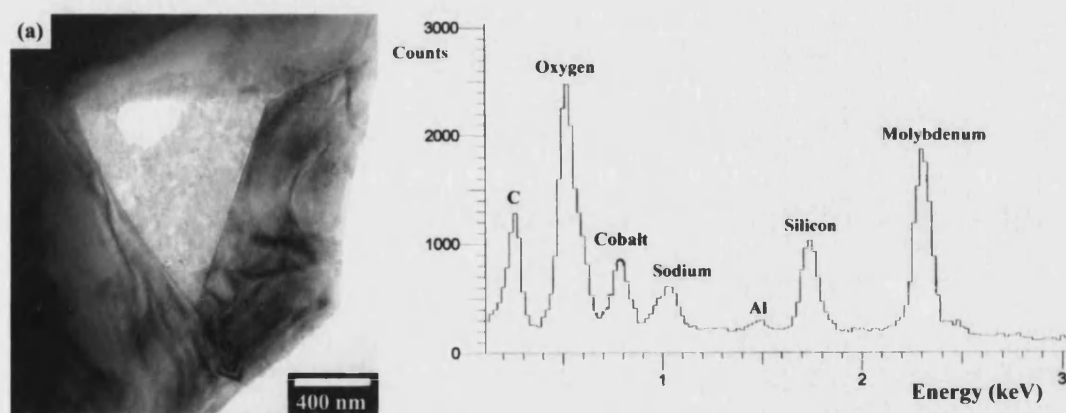
Figure 5.104: (a) triple grain junction and (b) X-ray analysis of the glassy central

region in barium titanate.

The glassy phase is rich in silicon, which originated from minor impurities in the starting powder that were too dispersed to be detected by XRD analysis and have segregated during grain growth. The carbon peak is due to the carbon film used to reduce sample charging, while the minor cobalt peak is due to electron interactions with the pole-piece (50% cobalt and 50% iron) of the microscope. The molybdenum is ascribed to contamination produced during ion-milling due the use of a molybdenum Duo-mill holder. The minor peaks of sodium and aluminium are likely to be from minor impurities in the starting powder that have been segregated to this region. This could

be confirmed with access to the manufacturer's data on the actual chemical composition of the barium titanate; although no impurities were observed from X-ray diffraction analysis. The proportion of this glassy phase is small and appears to be located solely at triple grain junctions and not at grain boundaries, unless it is too thin to observe. A clean grain boundary can be seen in Figure 5.105, showing the absence of a substantial glassy phase.
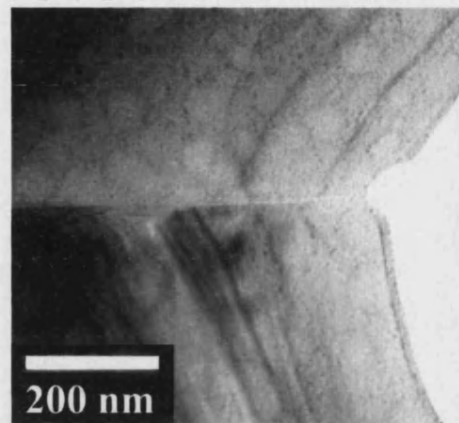
Figure 5.105: A grain boundary in monolithic barium titanate.

5.1.h.ii   *TEM analysis of barium titanate-1wt% silicon carbide composite*

Silicon carbide particles were not observed in the composite but there were a number of local stress concentrations, which appear to interact with the domain configuration, as shown in Figure 5.106. The high contrast region at the end of the domain is indicative of the large elastic stresses. It is these interactions that could benefit high field applications by pinning the domain walls.

Figure 5.106: Discontinuity of domain structure at a stress concentration.

Although actual particles were not observed, it is promising that domains, Figure 5.107, are still present indicating piezoelectric properties are possible. However, a greater amount of glassy phase material was observed in the silicon carbide composites, see Figure 5.108. This phase may be caused by the minor impurities in the silicon carbide powder, as given in the manufacturer's data, Appendix VII. Further amounts of silica could have been developed during the sintering of the composite at the high temperature, due to oxidation of the silicon carbide.
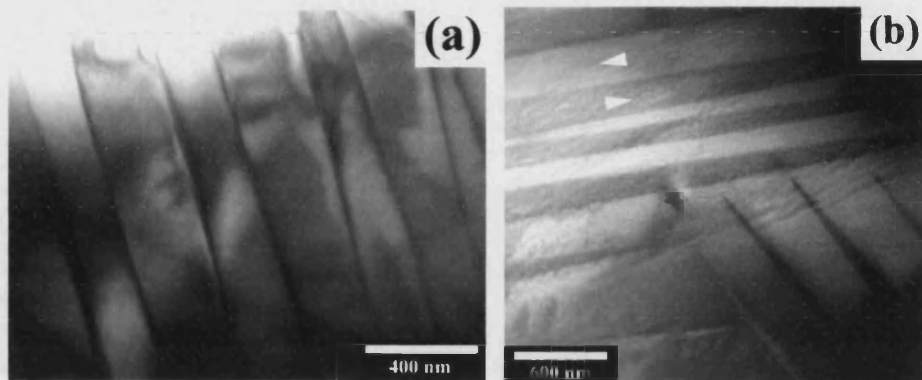
Figure 5.107: Domains observed in barium titanate-3wt% silicon carbide (a) 180° domains

and (b) two interacting sets of 180° domains.
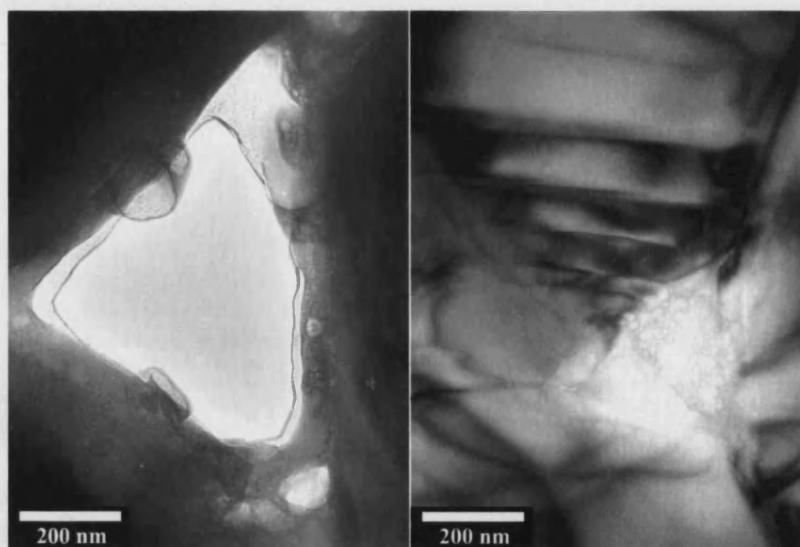
Figure 5.108: Glassy phase at grain junctions in barium titanate-silicon carbide composites.

5.1.h.iii   *TEM analysis of barium titanate-3.2wt% silver composite*

Domains and silver particles were observed in the barium titanate-5wt%silver composite, as shown in Figures 5.109 and 5.110, respectively. The nano-sized particles were confirmed as silver by X-ray analysis, see Figure 5.111, and no reaction phases were observed between the silver and the barium titanate matrix.
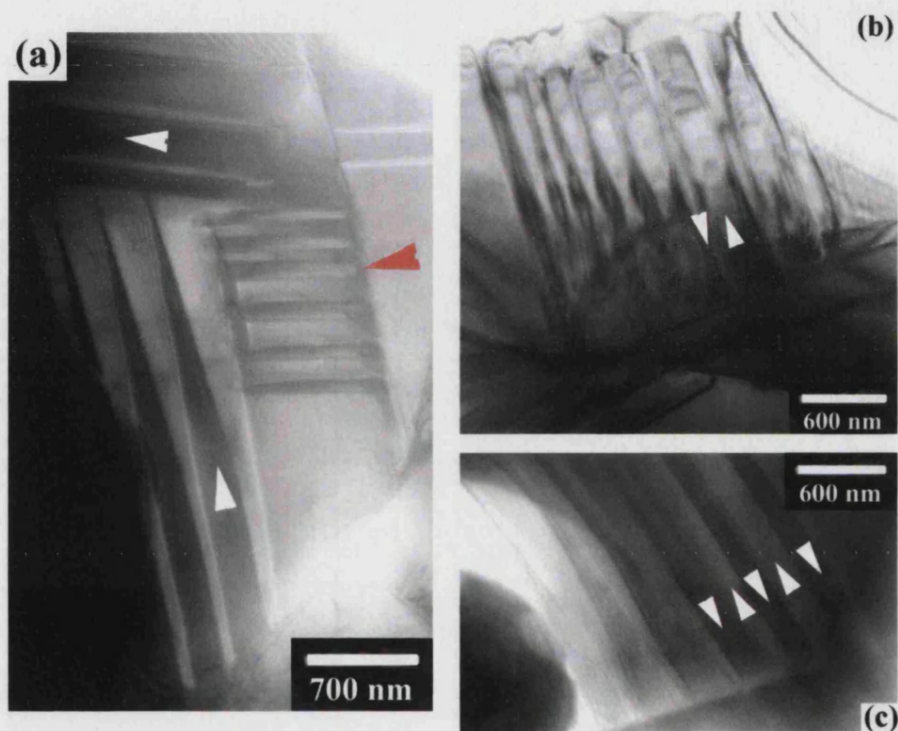
Figure 5.109: Domains (white arrows) in barium titanate-3.2wt% silver.

Red arrow indicates grain boundary.
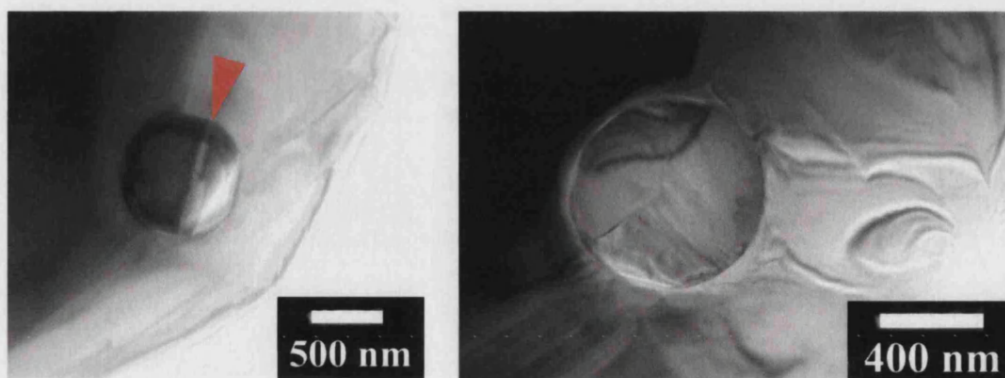
Figure 5.110: Silver particles observed in the TEM of the barium titanate-3.2wt% silver

composite showing annealing twin (indicated by red arrow).
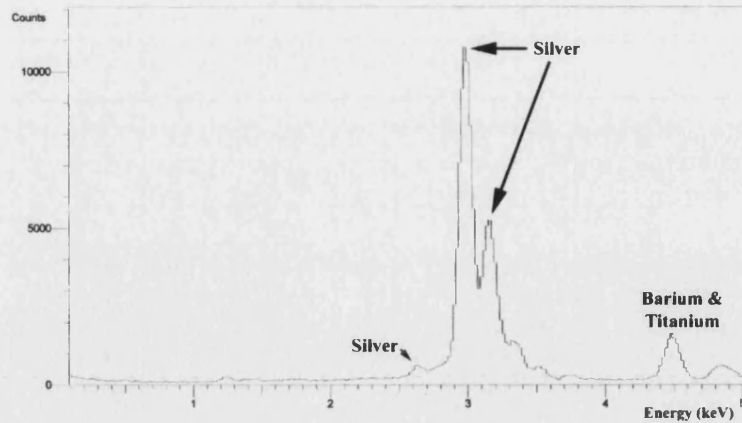
Figure 5.111: X-ray analysis of silver particle in a barium

titanate-3.2wt% silver composite sample observed using the TEM.

Due to the higher atomic weight of the silver in comparison to silicon carbide, the particles were easily observed, with improved contrast and with sample tilting domains were also observed in the barium titanate matrix, Figure 5.112. Note that at the interface of the silver and a domain, very small micro-cracks have appeared due the difference in thermal expansion coefficients. In all cases no reaction phases were observed between the silver particles and the barium titanate matrix.
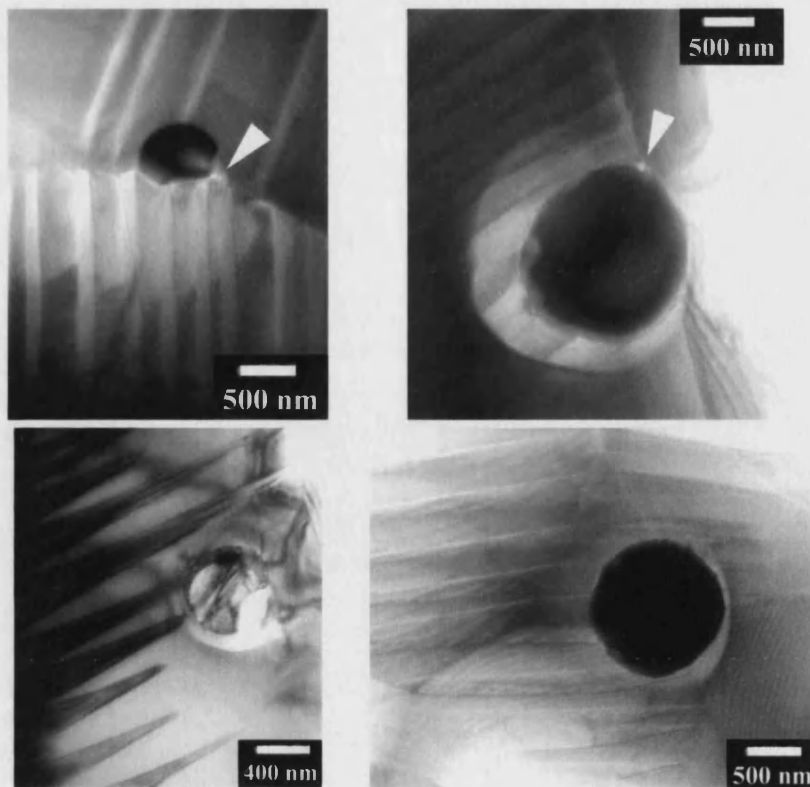
Figure 5.112: Observation of domain interaction with silver particles observed

in barium titanate-3.2wt% silver. White arrows indicate micro-cracks.

Although domains are perceived to impinge on the silver particles an applied electric field would be required to observe possible pinning events. The silver particles within the grains can be more easily examined under the higher magnification of the TEM compared to the SEM. Their size appears to be in the region of 300-1000 nm. Silver particles were also observed to interact mechanically with the matrix and introduce cracks, see Figure 5.113. These cracks and dislocations can weaken the structure mechanically but act as pinning sites for the domains, so requiring a larger electric field for domain movement in comparison to a non-defective material.
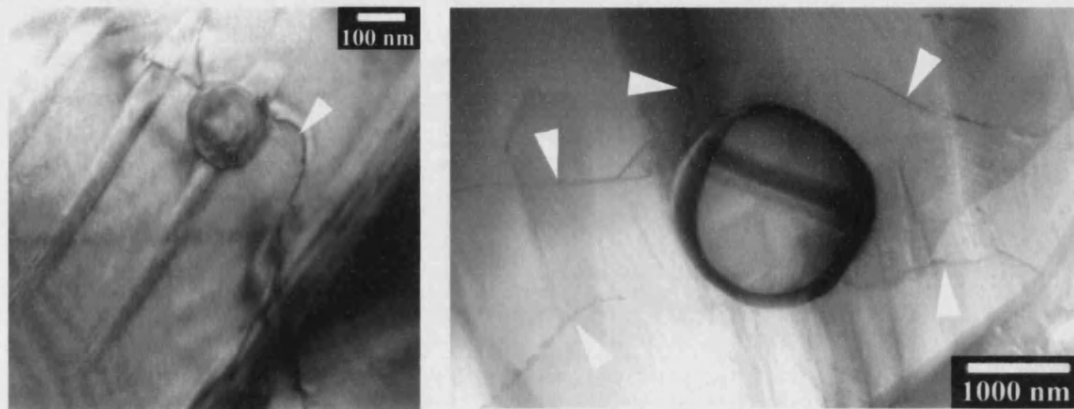
Figure 5.113: Cracking in the presence of an intragranular silver particle (white arrows

indicate cracks/dislocations) for barium titanate-3.2wt% silver.

In addition to the barium titanate, and silver particles, a glassy secondary phase was detected at some of the triple grain junctions, Figure 5.114(a). X-ray analysis of these regions, Figure 5.114(b) indicated the presence of low atomic weight elements of sulphur and phosphorus. The existence of these elements is not explained, unless segregated, as the maximum limit of sulphate impurity in the silver nitrate starting material is 0.002wt%, Appendix VII. As the glassy phase was also observed in the monolith it is likely that the glassy material is sourced from the barium titanate starting powder.
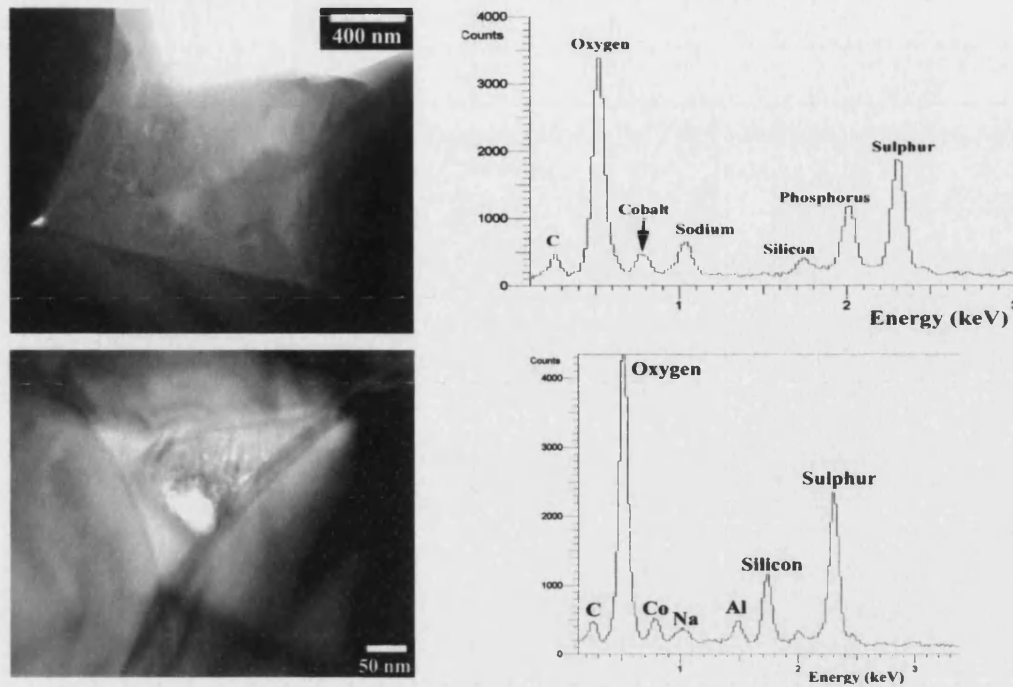
Figure 5.114: (a) Glassy secondary phase at triple grain junction and

(b) X-ray analysis for that phase, observed in barium titanate-3.2wt% silver.

5.1.i   SUMMARY OF MICROSTRUCTURAL ANALYSIS

5.1.i.i   Monolithic barium titanate

No major impurities were detected by XRD analysis in the barium titanate starting powder. The particle size was on the order of microns, but particle agglomeration was prevalent. Two peaks were observed in the sintering profile that relate to similar reported temperatures[72]. The achieved sintered density was improved by cold isostatic pressing of the green compacts and a higher sintering temperature. A glassy phase is possible above the eutectic that may be detrimental to the electrical properties, so sintering temperatures were confined to 1300°C. The glassy phase contained evidence of sulphur and silicon in its composition, which was not detected in the as received powder. The monolithic grain size was measured as approximately 10 μm and appeared to increase during the hot pressing procedure. While the pressureless sintered density was quite low (~93%) the hot pressing produced a monolithic density close to the theoretical value.

166

5.1.i.ii Barium titanate-silicon carbide composites

The addition of nano-sized silicon carbide caused the disappearance of the high temperature sintering peak, and was shown to form a reaction phase with the barium titanate matrix. X-ray analysis determined the reaction product to be $Ba_2TiSi_2O_8$, whereas thermogravimetric analysis indicated that silica might also be present from silicon carbide oxidation. The presence of this reaction phase, in hot pressed barium titanate-5vol% silicon carbide composites sintered above 1300°C, has been reported by Niihara[41]. The density achieved was affected by the particle incorporation, in that the silicon carbide hindered the densification process and reduced the grain size. Particles of silicon carbide could not be observed optically or using electron microscopy. Domains, indicative of piezoelectric properties, were observed to be present in the barium titanate-3wt% silicon carbide content composites. Domains may exist in higher silicon carbide content composites, but these samples were not examined under the TEM.

5.1.i.iii Barium titanate-silver composites

Two types of silver composites were fabricated, the first from silver oxide powder and the second from silver nitrate crystals. Silver nitrate was chosen, as it is partially soluble in ethanol and will aid dispersion of silver during powder manufacture. Both silver oxide and silver nitrate derived composites were observed to decompose to silver during the sintering cycle. Calcination of the silver (nitrate) composite powders was required to remove the gaseous decomposition products that would otherwise reduce sintering performance. The incorporation of silver oxide had little effect on the densification and reduced the barium titanate grain size. Silver, from the silver nitrate, modified the sintering kinetics, by reducing and broadening the low temperature densification peak. The silver (nitrate) composites decreased in grain size and density with the increased addition of silver. A silver surface depletion layer due to evaporation was imaged both optically and with the SEM and shown to have a depth of 50-100 μm.

The silver particle size was observed to increase as the silver content increased, with particles greater than 1-2 μm located intergranularly for both silver oxide and silver nitrate derived composites. Domains were observed to be present in these materials, with domains impinging on intragranular silver particles. Micro-cracks and dislocations were observed in the barium titanate-silver particle region, possibly due to the thermal stresses developed during processing.

5.1.i.iv   *Barium titanate-5.7wt% platinum*

Due to the expense of the starting material only a single barium titanate-platinum composition was fabricated. Thermogravimetric analysis showed platinum to be the decomposition product. However, a glassy reaction phase was produced during sintering of the composite, which is suggested to cause "slumping" of the sample. The porosity of the sintered specimens was increased compared to the monolithic material, with the particles of platinum being observed under the electron microscope, to be located intragranularly and intergranularly. The samples produced were unsuitable for extensive microstructural examination.

5.2 MECHANICAL PROPERTIES ANALYSIS

Mechanical characterisation, such as measurement of fracture strength and fracture toughness, was conducted on the monolithic barium titanate, and on the silicon carbide and silver containing composites.

5.2.a FRACTURE STRENGTH DETERMINATION

The mechanical strength of the silicon carbide and high silver content composites was expected to be relatively low, due to their high porosity, and for the hot pressed samples, due to extensive cracking from residual stresses. Additionally, the silicon carbide composites suffered from the presence of a reaction phase. The barium titanate-silicon carbide and barium titanate-silver (oxide) composites were not tested. Strength values were calculated from biaxial testing for the silver nitrate derived composites only.

Over twenty samples were tested for each barium titanate-silver formulation. The flexural strengths were calculated via equation AIV.6 (Appendix IV), and a Weibull modulus determined. The results, Figure 5.115, indicate that addition of the ductile silver causes a slight increase in the fracture strength. The strength values are comparable to the range of 65-85 MPa reported in the literature for barium titanate of 85% theoretical density[59, 167]. The Weibull modulus, however, is reduced from that expected for an advanced ceramic (10-20) to a value commonly associated with technical ceramics (5-10). These lower values correspond to a higher scatter in the results and may be caused by the high porosity.
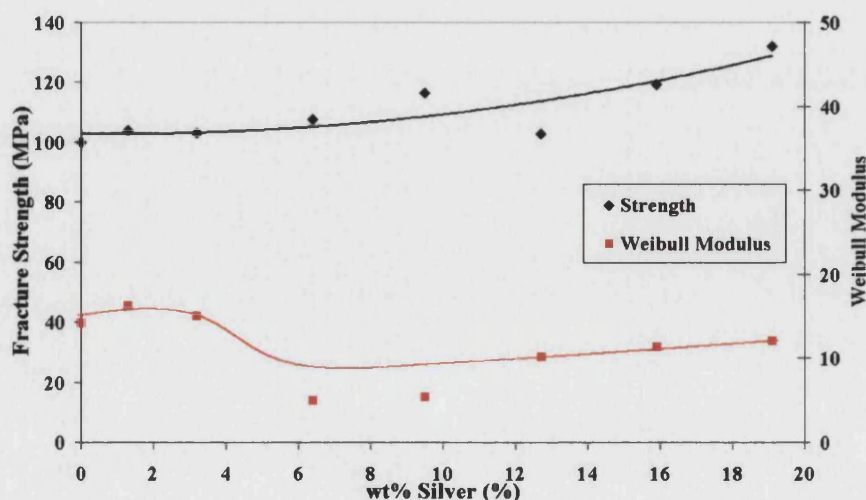
Figure 5.115: Variation of barium titanate-silver (nitrate) composite strength and

Weibull modulus with silver content.

Typically, the biaxial specimens fractured into three segments. Occasionally, especially with increase in silver content, the samples remained in one piece but cracks could be observed across the sample surface, see Figure 5.116. It is believed that ductile silver filaments, observed in the SEM (Section 5.1.g.i.c.), hold the fractured segments together to cause this effect.

(a)   **(b)**   **(c)**
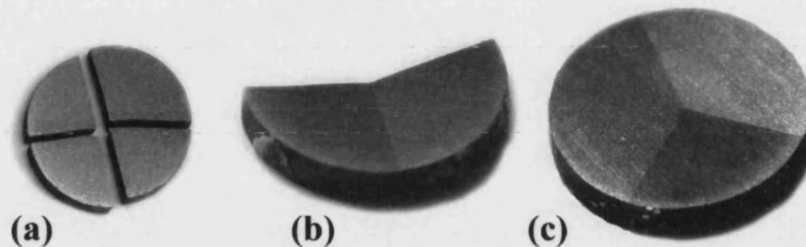
Figure 5.116: Change in sample fracture with increasing silver content (a) barium titanate-1.3wt% silver, (b) barium titanate-12.7wt% silver and (c) barium titanate-19.1wt% silver. These Indicate possible crack bridging by silver particles as silver content increases.

5.2.b   FRACTURE TOUGHNESS DETERMINATION

5.2.b.i   Fracture toughness of monolithic barium titanate

Fracture toughness of the monolith and composites was determined from the radial cracks produced during the hardness measurement process. The crack lengths were first measured optically and then from images taken using an electron microscope. Before measurement commenced, on the composites, different loads were systematically used to observe the variation in toughness under different loading conditions, see Figure 5.117.

The confidence intervals for the results are large, as expected, due to the brittle nature of the ceramic material and the large number of defects present in the porous samples. The optical results appear to give a significantly higher fracture toughness value, about 20% greater, but have a greater variability in values. The lower values recorded from electron microscopy images may be due to an underestimate of the optical crack lengths or an overestimate in the electron microscopy case. However, time dependent crack growth is a more probable cause, as the electron microscope images were taken approximately two hours after indentation. During this time slow crack growth can occur, due to atmospheric moisture aiding crack propagation, which reduces the effective toughness value recorded. Magnifications in the range of 500-2000X were used in the electron microscopy, while 200X was employed in the optical microscope. The 2 MPa.m$^{0.5}$ fracture toughness is a typical and acceptable value for barium titanate.
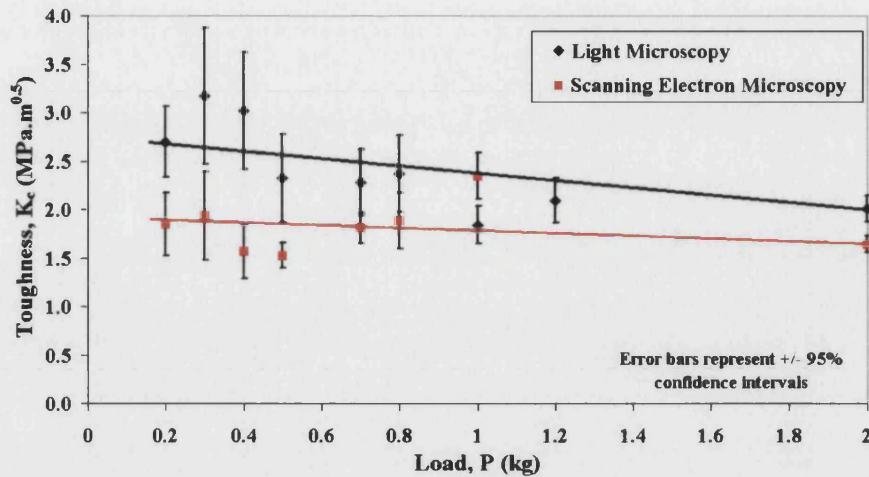
Figure 5.117: Variation of barium titanate toughness under different

loading conditions, measured optically and from SEM images.

The toughness value appears to decrease slightly with the increase in load and the difference between the optical and electron microscopy values reduces somewhat. A loading value of 1 kg was used for fracture toughness determination of the composites, with one exception, a lower load of 0.5 kg was used to reduce the generation of chips in the hot pressed specimens. Typical indents for barium titanate are shown in Figure 5.118 and are spaced out by approximately 500 μm to reduce interaction. In porous samples the cracks typically ended at surface pores, which "blunt" the crack tip and stop crack propagation. The toughness measured may simply be related to the possibility of impacting a pore, rather than the actual toughness of the material.
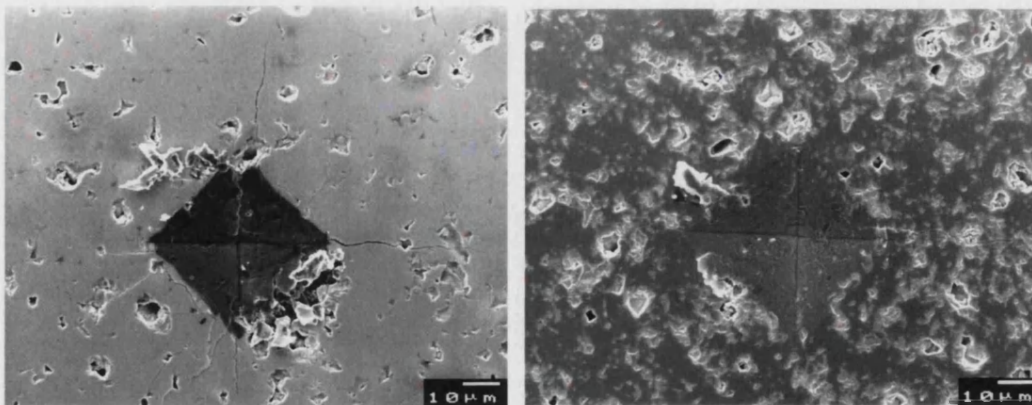
Figure 5.118: Monolithic barium titanate indented samples used for toughness

determination showing crack propagation from indent corners.

The toughness determination was also conducted on specimens produced from freeze-dried powders in order to observe the effect of a different processing technique. A compilation of the

monolithic toughness values is given in Table 5.6. The slight reduction in fracture toughness of the freeze-dried powder may be due its lower porosity that reduces the possibility of crack tips being blunted.

Table 5.6: Comparison of fracture toughness between lamp-dried

and freeze-dried barium titanate powder.

Material	Measurement technique	Toughness value ($\pm$95%CI) (MPa.m$^{0.5}$)
Lamp-dried	Optical reading	2.0 (0.2)
	SEM reading	2.3 (0.2)
Freeze-dried	Optical reading	1.6 (0.2)
	SEM reading	1.2 (0.2)

5.2.b.ii   Fracture   toughness   of   barium   titanate-silicon   carbide   composites

The fracture toughness would be expected to increase with the addition of silicon carbide particles if the particles strengthened the grain boundaries and grain interior by thermally induced residual stresses. However, as mentioned in the microstructure section, the silicon carbide was found to have reacted with the matrix and is unlikely to have a direct effect on the toughness, unless a glassy phase is present at the grain boundaries. The glassy phase observed in the TEM may strengthen or weaken the grain boundaries depending on the phase-matrix bond strength and the secondary phase strength in contrast to the monolithic grain-grain bond strength. The fracture toughness results, Figure 5.119, indicate a balance of two competing affects, that of micro-cracking/crack deflection and grain boundary weakening. At low silicon carbide contents the glassy reaction phase causes the weakening of grain boundaries and increases the crack length produced. At higher particle contents the glassy phase is still present but the thermal residual stresses of the particles, or the secondary phase produced, causes the production of micro-cracks that "blunt" the primary crack and absorb fracture energy. The higher porosity in the large silicon carbide fraction composites is an additional effect that can cause the improvement in the effective toughness, via crack blunting.
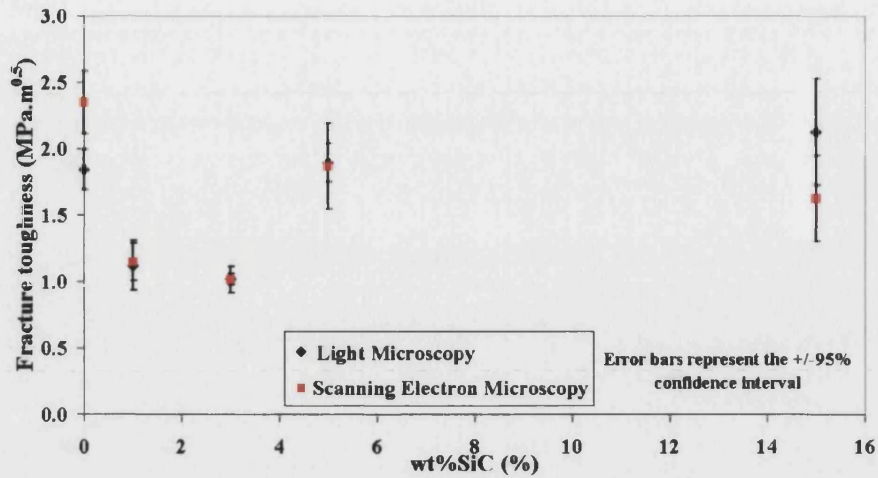
Figure 5.119: Toughness from images captured via the light and electron microscopes for pressureless sintered barium titanate-silicon carbide composites.

For the samples obtained by hot pressing a significant increase in toughness is measured for the 5wt% silicon carbide composite, see Figure 5.120. This may be due to the slightly higher porosity in these samples that led to reduced crack propagation. The value for the monolithic hot pressed sample, however, is considerably lower than the samples produced by the pressureless sintering technique. This could, again, be due to the higher porosity of the pressureless sintered samples.
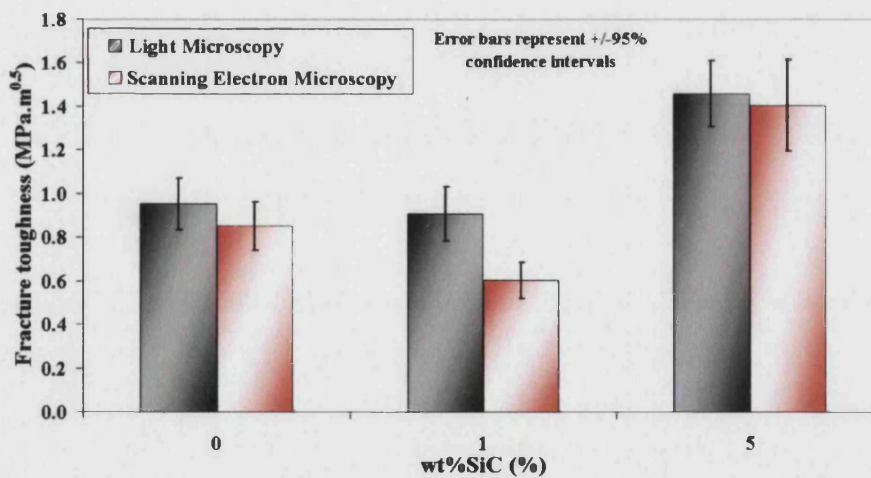
Figure 5.120: Toughness values measured for hot pressed monolithic and barium titanate-silicon carbide composites.

The hot pressed samples required a lower load, to prevent chipping adjacent to the hardness indent, than the pressureless sintered composites, as shown in Figure 5.121a. The micrograph indicates that the load was too high, since the lateral crack system grew until it intersected the surface.
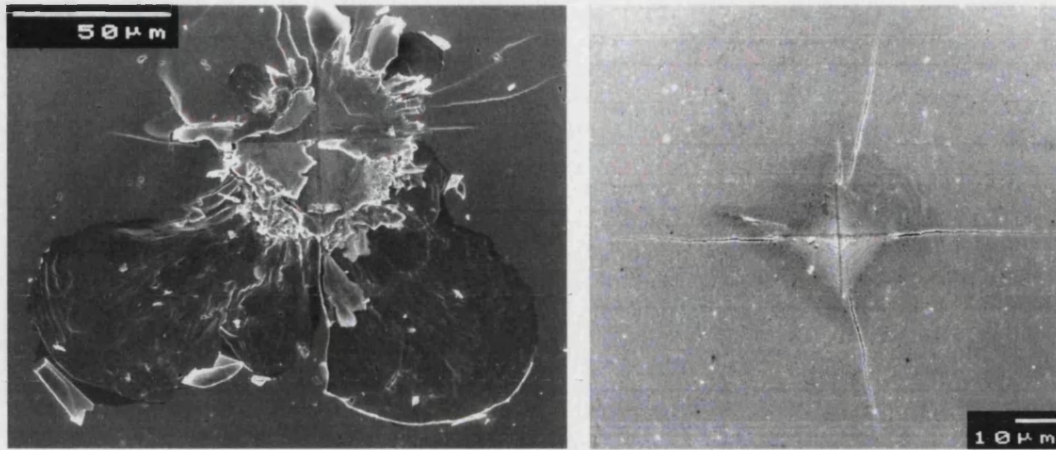
Figure 5.121: Toughness images for hot pressed (a) too heavily loaded barium titanate and

(b) correctly loaded barium titanate-1wt% silicon carbide.

5.2.b.iii   *Fracture toughness of barium titanate-silver composites*

Only the silver nitrate derived samples were tested and these showed that incorporation of silver into the barium titanate matrix caused no significant modification of the toughness from the monolithic value, see Figure 5.122. The results may indicate that the measurements are limited by processing flaws, such as porosity. The toughness may be unmodified, due to the ductile silver particles absorbing the same energy when being deformed, under crack bridging conditions, as the energy required to fracture the barium titanate matrix. The measurements acquired from SEM images are consistently lower than those attained optically. The time difference between the measurement methods may allow a certain amount of crack propagation to occur. X-ray mapping was unable to locate possible crack-bridging of silver particles.
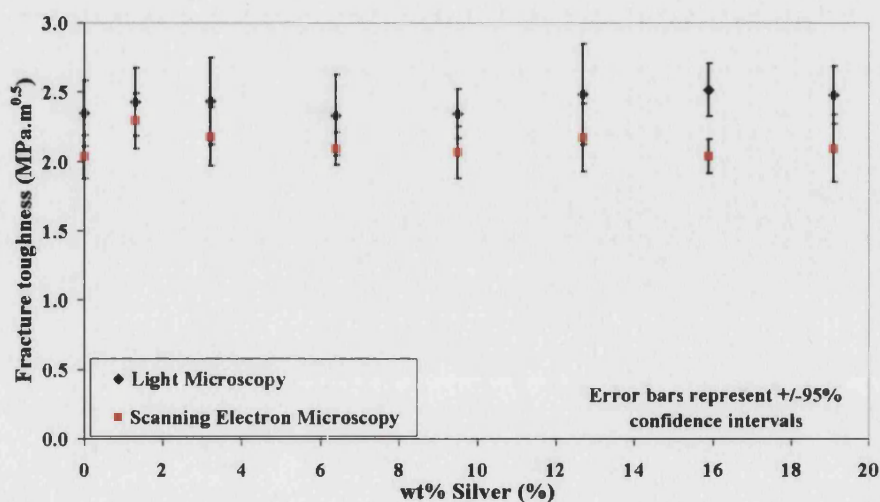
Figure 5.122: Toughness values for barium titanate-silver composites. (Nitrate derived).

5.2.c   HARDNESS DETERMINATION

5.2.c.i   Hardness of monolithic barium titanate

The effect of load on the hardness of barium titanate was determined before samples were tested. A slight decrease in the hardness value with increasing load was determined. A load value of 1 kg was chosen for hardness determination. Images of the indented samples for the monolith and composites can be seen in the fracture toughness section. The hardness value of approximately 4.1 GPa was determined for monolithic barium titanate by optical observation of the indent. This is lower than the 7 GPa reported in the literature[41], however, this reported value is for hot pressed samples and a reduction in hardness is expected due to the higher porosity of the pressureless sintered samples in this research.

Freeze-drying the powders resulted in an improved hardness as indicated in Table 5.7. It is suggested that the hardness improvement is due to the higher density in these materials, as the indent penetration is reduced, as more material is present.

Table 5.7: Hardness values for pressureless sintered monolithic

barium titanate that had been lamp-dried or freeze-dried.

Material	Measurement technique	Vickers hardness (±95%CI) (GPa)
Lamp-dried	Optical	4.1 (0.3)
	SEM	3.6 (0.2)
Freeze-dried	Optical	4.4 (0.2)
	SEM	5.3 (0.4)

5.2.c.ii   Hardness of barium titanate-silicon carbide composites

The calculated hardness values for the low volume fractions of silicon carbide added to barium titanate indicate a significant increase in hardness, Figure 5.123. However, this improvement decreases rapidly above 3wt% silicon carbide to give a hardness that is half the monolithic value when the silicon carbide fraction is 15wt%. The decrease in hardness at high silicon carbide contents is attributed due to the reduction in density of the sample, while the improvement at low silicon carbide content, even under reduced density conditions, maybe due to a thermal residual stress system with stresses counteracting the applied load. At this level of silicon carbide the

increase is sufficient to offset any decrease due to increased porosity. The reported increase in hardness with silicon carbide addition[17, 41, 77] was not observed for the hot pressed samples, Figure 5.124. An increase is proposed due to the higher hardness of the silicon carbide phase.
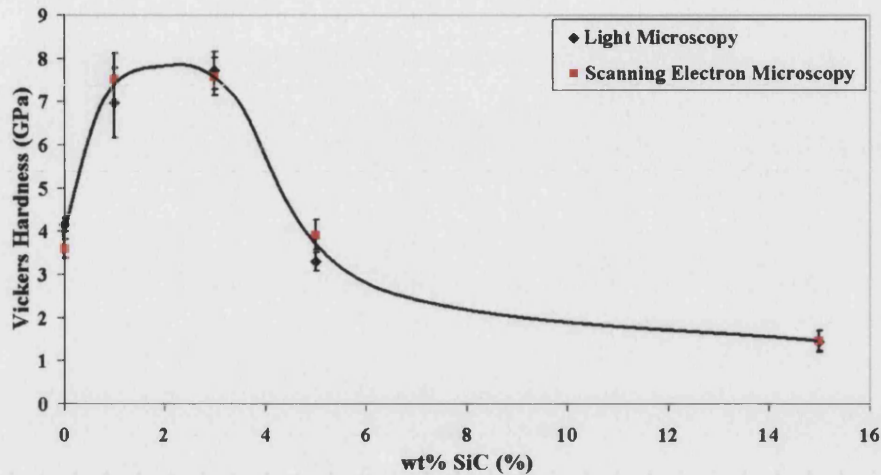
Figure 5.123: Hardness of pressureless sintered barium titanate-silicon carbide composites.

Agreement between the optical and SEM calculated hardness values was good for both the pressureless and hot pressed cases. For the hot pressed samples, there is a slight hardness increase with 1wt% silicon carbide, over the monolithic case but for the 5wt% silicon carbide composite the hardness has returned to the monolithic value, Figure 5.124. This behaviour is most likely due to the decrease in density (99% reduced to 93%) as the silicon carbide content increases. An increase from 7 GPa to 9 GPa with the addition of 5wt% silicon carbide to hot pressed barium titanate has been reported in literature[41]. The improved density on hot pressing, in comparison to the pressureless sintered samples, as expected, gives improved hardness values.
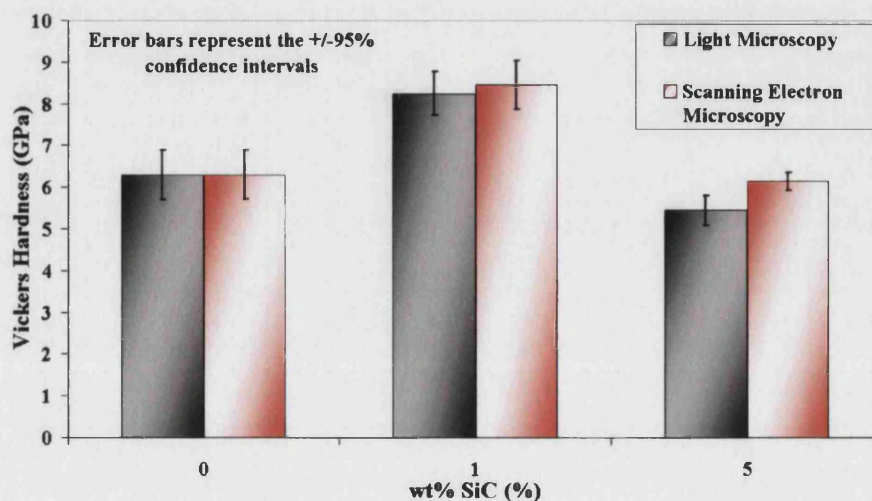
Figure 5.124: Hardness of hot pressed monolithic and barium titanate-silicon carbide composites.

5.2.c.iii   *Hardness of barium titanate-silver (nitrate) composites*

The addition of a softer material, such as silver, should reduce the composite hardness with increasing silver addition. This anticipated result was observed in the experimental measurements as shown in Figure 5.125. The actual rate of hardness decrease could well have been less if the porosity did not increase with silver content. Good agreement is observed between the light and electron microscope measurement values, suggesting minimal recovery during the measurement time period. No significant decrease in hardness was observed at low silver contents (<4wt%). Silver has a hardness of 2.5-3 GPa which suggests that the hardness decrease is greater than that expected from the rule of mixtures.
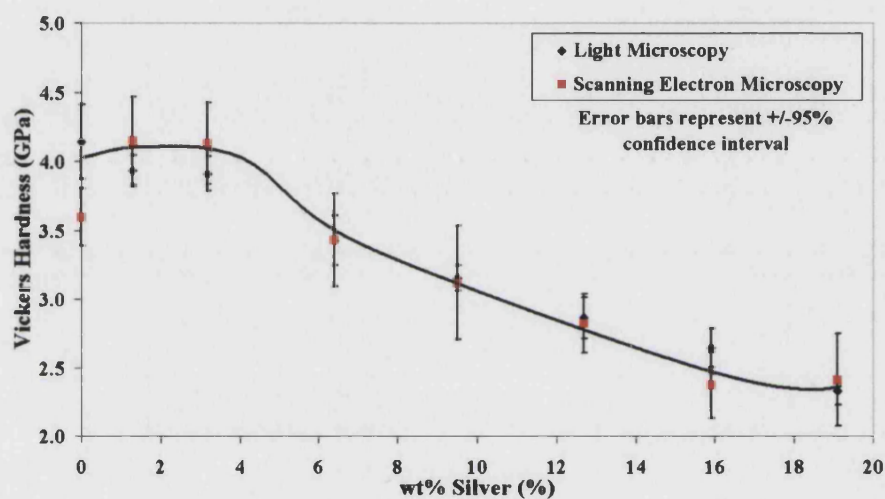
Figure 5.125: Hardness of barium titanate-silver composite showing a steady

decrease with increasing silver content above 4wt% silver. (Nitrate derived).

5.2.d   STIFFNESS DETERMINATION

Stiffness is a mechanical property related to the atomic bonding in the material. The stiffness for the materials used in this research was not measured by traditional mechanical means, as sufficient accuracy could not be achieved. Stiffness values (normal to the poling direction) were calculated from impedance data of the sample resonating in a mode normal to the poling axis using equation 5.6.

$$\text{Elastic stiffness, } 1/s_{11}^{E} = \frac{4 \, \rho \, \pi^2 l^2 f_s^2 \left(1 - \upsilon^2\right)}{2.05^2} \qquad \{5.6\}$$

Here ρ is the sample density, l the sample diameter, ν the Poisson's ratio and f_s the resonant frequency. The addition of silver gradually decreases the effective stiffness, by 25% with an addition of 16.1wt% silver, Figure 5.126. This is the expected trend for the addition of a more compliant phase. Typical values of stiffness for barium titanate and silver are ~120 GPa[168, 169] and 71 GPa[166], respectively. However, there was little difference for the silver oxide derived samples. The calculated values are consistent with those observed in the literature, which are typically 120 GPa[168, 169]. The rule of mixtures predicts a stiffness ~95 GPa with 15wt% silver. The stiffness decrease is associated with the lower density of the pressureless sintered composites. The theoretical density of the composite has been used in the calculation of the stiffness, not the actual experimental composite density.
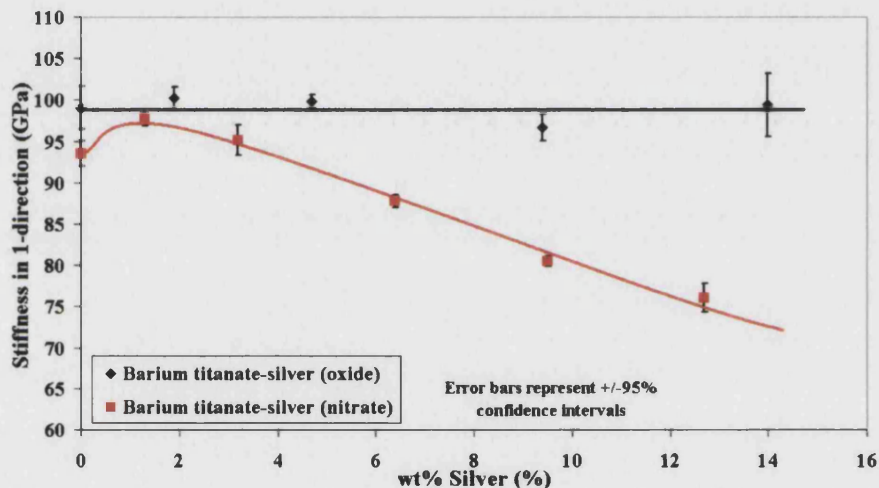
Figure 5.126: Variation of barium titanate stiffness in the 1-direction with the addition of silver.

5.2.e   SUMMARY OF MECHANICAL PROPERTIES ANALYSIS

5.2.e.i   *Monolithic barium titanate*

The monolithic barium titanate was determined to have mechanical property values similar to those reported in the literature. A comparison of property results is given in Table 5.8, which shows that the mechanical properties are typical of pressureless sintered barium titanate, but less than for the hot pressed material. The discrepancy between the literature and experimental values is largely due to the higher porosity content in the samples produced in this study, due to the different processing conditions.

Table 5.8: Comparison of the experimental and the literature mechanical

property values for monolithic barium titanate.

Property	Average experimental value (Pressureless sintered)	Literature value Pressureless sintered [Hot pressed]
Strength (MPa)	100	$65-85^{59, 167}$ [174^{41}, 145^{77}]
Toughness (MPa.m$^{0.5}$)	1.8	[0.86^{41}]
Hardness (GPa)	4.0	[6.9^{41}]
Stiffness (GPa)	96	116^{168}, 124^{169}

5.2.e.ii   Barium titanate-silicon carbide composites

Although the presence of silicon carbide initially increased hardness and reduced the grain size, the addition of silicon carbide affected all properties detrimentally when present in amounts greater than 5wt% silicon carbide. The reduction in properties above this 5wt% value may be due to the increase in porosity as the proportion of particles increases. The improvement in fracture toughness is attributed to the porosity content that causes cracks to become blunted. Improvements below 5wt% silicon carbide could be due to the formation of a glassy reaction phase improving composite density.

5.2.e.iii   Barium titanate-silver composites

The incorporation of micron-sized silver particles into the barium titanate caused no significant modification to the fracture toughness, although the density decreased with increasing silver weight fraction derived from silver nitrate. The hardness was observed to gradually decrease with silver addition, which is as would be expected from the addition of a softer secondary phase. The strength was improved by ~15% in the 19.1wt% silver composite, even with a high porosity content. These trends may change if the sintered density of the composites was unchanged from the monolithic sintered density value. The stiffness, allowing for theoretical composite density change, was reduced on silver addition, which again would be expected with the addition of a more compliant material to the matrix. The decrease, however, was significantly greater than the rule of mixtures prediction, suggesting the influence of porosity is important.

5.3 ELECTRICAL PROPERTIES ANALYSIS

Electrical testing was conducted to determine dielectric properties of the monolith and to examine the affect of particles on the composites. Piezoelectric properties were measured in order to characterise any modification of the piezoelectric nature of the electroceramic barium titanate. Additional testing was carried out into dielectric breakdown and polarisation-field behaviour to examine the performance of the composites under increasing applied electric fields.

5.3.a RELATIVE PERMITTIVITY DETERMINATION

Relative permittivity is a standard property used to characterise dielectric materials and is a measure of dipole realignment in the material under the application of an electric field.

5.3.a.i Relative permittivity of monolithic barium titanate

Both the lamp-dried and freeze-dried based ceramics showed variation in relative permittivity values of 1300-1800 (measured at 1 kHz, 1 V and room temperature) when sintered at different temperatures. These average values are in the expected range for barium titanate[18, 23, 84]. The variation was due to the small number of samples tested. The freeze-dried powder generally had an improved relative permittivity value in comparison to the lamp-dried powder, possibly due the increase in final sintered density. The density improvement can once again be used to account for the better relative permittivity values of 1690±40 achieved in the cold isostatic pressed samples.

Under an atmosphere of argon the relative permittivity was observed to increase from about 1300 to 1800. It is suggested that this is due to a moderate reduction of the barium titanate in the low oxygen content atmosphere that produces the semi-conducting non-stoichiometric phase, as reported in the literature[76].

5.3.a.ii Relative permittivity of barium titanate-silicon carbide composites

Initial composite samples had very high relative permittivity values (>30,000) in comparison to pure barium titanate (~1500) suggesting, in connection with the high dielectric loss (5.3.b.ii) that they are semi-conducting. Barium titanate having high relative permittivity is typically used in low voltage capacitors as it is lossy and therefore unsuitable at high voltages[157]. This semi-conducting behaviour can be produced by a reducing atmosphere or from reactions that reduce the oxygen

content of the barium titanate. In the pressureless sintered case, see Table 5.9, the addition of 1wt% silicon carbide appears to have little effect on the relative permittivity, while 2wt% and above significantly increases the relative permittivity in comparison to the monolithic samples. It is proposed that the silicon carbide is lost during sintering and forms a reaction phase that affects the relative permittivity by increasing the conductivity, so less charge can be stored. The considerable increase in relative permittivity is far greater than can be explained by the barium titanate being reduced during the sintering process in an inert atmosphere and remaining in a semi-conducting form on cooling. The change in the colour of the sintered materials from cream/yellow in the oxygenated state to blue/black when hot pressed confirms the reduced state of the material. The relative permittivity increases as the higher number of conducting species move under the measuring electric field and simulate a high polarisation.

Table 5.9: Relative permittivity for barium titanate-silicon

carbide composites pressureless sintered in argon.

wt% silicon carbide	0	1	2	3	5
Relative permittivity	~1800	1378	~12400	~23000	~750000

Above 1wt% silicon carbide the variation in the results was considerable. This is thought to be due to the increased probability of forming a conducting path across the sample or the presence of traps for the conducting species. A number of samples had relative permittivity values not far removed from the 1wt% silicon carbide in the 2wt% silicon carbide batch. This was not the case in higher silicon carbide composite samples.

Barium titanate-silicon carbide composites have been produced via hot pressing in the literature but electrical properties were not reported[40, 41]. From visual examination the hot pressed samples were expected, due to their black colour, to show a semi-conducting behaviour, indicating a reduced nature, and this was confirmed by the measurements. The relative permittivity for hot pressed materials was greater than 5×10^6 and re-oxidation, at lower temperatures than that mentioned in the literature ($1050°C$ [1]), reduced the value to 5×10^5 after 12 hours at approximately $400°C$. The sample became grey in colour indicating that some oxidation had occurred. The temperature of $1050°C$ was not used as samples were observed to crumble at $500°C$. This may be due to a high ramp rate of 120 °C/hr employed. Thermal stresses, however, may be sufficiently increased, during oxidation, by the presence of silicon carbide or a reaction phase to cause fracture.

5.3.a.iii   *Relative permittivity of barium titanate-silver composites*

The addition of silver into the barium titanate increased the relative permittivity, although the density was decreased, Figure 5.127. The relative permittivity increases in an approximately linear fashion for the silver (oxide) samples, giving a ~50% increase with 18wt% silver. This behaviour was similar for the silver nitrate derived samples, but an initial decrease was observed. At silver contents above 13wt% silver the increase in relative permittivity was much greater than for the silver (oxide) samples, with values up to 4000. From Figure 5.48 it can be seen that the increase in silver, derived from silver nitrate, influences the density much more than the silver produced from the silver oxide. While the increases in relative permittivity are significant, the increase is likely to be improved for composites with higher density, due to the presence of more material for polarisation.
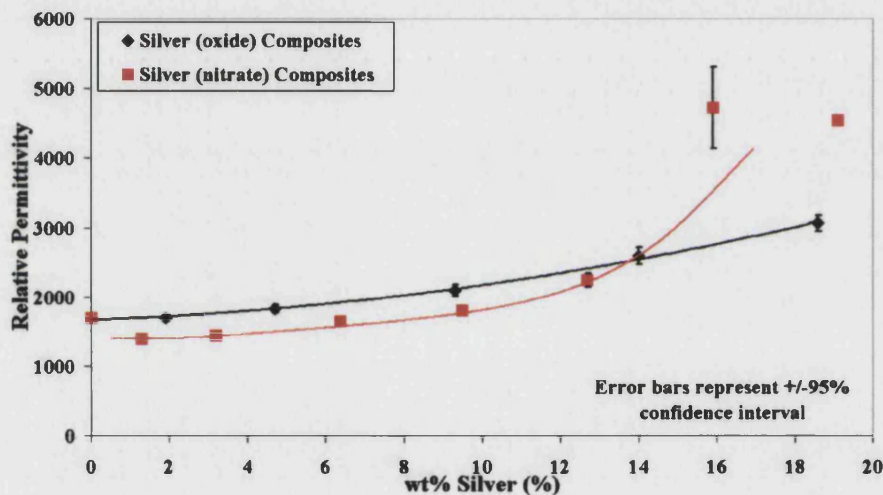
Figure 5.127: Relative permittivity for barium titanate-silver composites

(measured at 1 kHz and 1 V).

The data appear to have two trends, the first a steady increase of relative permittivity with increasing silver content. The second appears at high silver contents, giving relative permittivity values that are far greater than expected from the initial trend. The increase in relative permittivity at silver contents above 16wt% is difficult to quantify due to the large variation in results. The relative permittivity value for the 19.1wt% silver samples is an average of the data that followed the trend. Readings varied from 4000 to 100,000 and 95% confidence intervals are not shown. For the 15.9wt% silver about 25% of the measurements were greater than expected, in fact higher than 10,000, while 80% of readings were greater than 100,000 for the 19.1wt% silver samples. It is believed that these samples, with such unexpectedly high values, have silver particle distributions that have or are beginning to form a path across the sample, i.e. are near to the percolation

threshold. This explains why an increase in the silver content produces a higher proportion of samples that show this behaviour; complete percolation may be expected at ~25vol% (37wt%) silver[170-172]. A similar large variation in dielectric properties are observed in modelling results, to be discussed in Chapter 6. The increase in relative permittivity on the addition of a conductive phase, which is isolated, has been attributed to an increase of the local effective field around the phase. The experimental results are in reasonable agreement with values calculated from equation 2.9 that predicts a relative permittivity of ~2900 with a metallic volume fraction of 0.15. The relative permittivity results from barium titanate-silver (nitrate) becomes more dissimilar above ~12wt% silver. This suggests that an additional effect, possibly relating to porosity, is occurring.

5.3.a.iv *Relative permittivity of barium titanate-5.7wt% platinum*

Only limited samples were sufficiently well formed for electrical measurement, and the high porosity and reaction phase are suggested as the reasons for the low relative permittivity value of approximately 750.

5.3.a.v *Influence of poling on relative permittivity*

The effect on the relative permittivity of poling the monolithic barium titanate was examined. It has been reported for PZT in the literature that the relative permittivity increases by approximately 15% with poling[18]. The increase measured for barium titanate in this research of 1128 to 1379 is greater than the variation in the sample value of ~5%. The relative permittivity increase is attributed to alignment of 180° domains parallel to the field and relief of clamping stresses[11, 18].

5.3.b   MEASUREMENT OF DIELECTRIC LOSS

The dielectric loss was measured using a frequency of 1 kHz and a field value of 1 V at room temperature. Dielectric loss is characterised by two loss mechanisms. These are conduction loss by charge flow and the rotation of atoms in the applied AC field.

5.3.b.i *Dielectric loss of monolithic barium titanate*

Improved dielectric loss results of ~0.05 were obtained for samples sintered at a temperature of 1300°C in comparison to >0.2 for those at higher and lower temperatures. The lower the dielectric loss the less input energy is lost in the material due to non-instantaneous polarisation. The actual loss values measured were high in comparison to the literature value of <0.02[128] for uni-axially

pressed samples. In general the freeze-dried powders give reduced loss, while the materials consolidated at 150 MPa gave results (~0.014) that surpass the freeze-dried powder. This appears to indicate that the density of the material is important in producing a low loss value. No significant change was recorded between sintering the monolith in an atmosphere of air or argon.

5.3.b.ii   Dielectric loss of barium titanate-silicon carbide composites

Table 5.10 shows the dielectric loss results for the barium titanate-silicon carbide composites. Measurement was not possible using the high silicon carbide content samples due to their high conductivity.

Table 5.10: Dielectric loss for the cold iso-statically pressed and

pressureless sintered barium titanate-silicon carbide composites.

wt% silicon carbide	0	1	3	5
Dielectric loss	0.014	0.008	Immeasurable	Immeasurable

The addition of 1wt% silicon carbide caused a reduction in the dielectric loss in comparison to the monolith for the uni-axially pressed samples. This result is also observed when a higher green compact forming pressure is employed. The beneficial result from silicon carbide addition appears to be restricted to this silicon carbide content. The low loss may be caused by the formation of a reaction phase, or the solubility of phases into the barium titanate. The dielectric loss of the hot pressed samples was not measurable before and after oxidation heat treatment, due to the conducting nature of the material. It is inferred, from this, that while a high relative permittivity is beneficial other properties can be detrimentally affected.

5.3.b.iii   Dielectric loss of barium titanate-silver composites

The modification of the dielectric loss by incorporation of silver is shown in Figure 5.128. The addition of silver does not modify the dielectric loss until a weight fraction above 16wt% is reached. Above this silver level some samples became conducting, presumably due to an interconnecting path of silver. The presence of the conducting silver may counteract electron scattering from defects, such as pores, and as such the overall loss is unaffected. The 95% confidence interval for the 19.1wt% silver composite was ~±0.1. Generally the silver nitrate

derived specimens have a similar behaviour to those derived from silver oxide. Performance may be enhanced if the density of the composites can be improved.
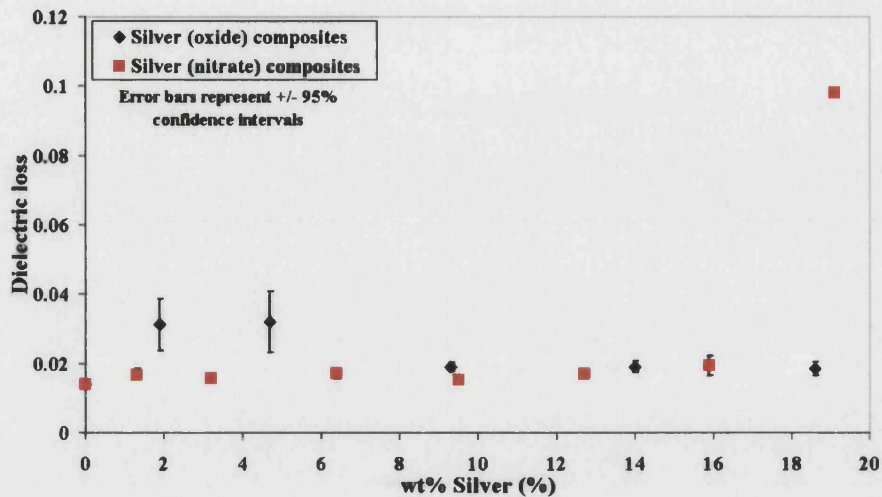
Figure 5.128: Dielectric loss for barium titanate-silver composites

derived from silver oxide and silver nitrate powders.

5.3.b.iv   Dielectric loss of barium titanate-5.7wt% platinum

A value of 0.09 was determined for the dielectric loss of the platinum samples. This high value is thought to be due to the low density of the samples and the possible presence of a secondary phase.

5.3.c   MEASUREMENT OF PIEZOELECTRIC COEFFICIENTS

The calibration of the Take Control PM25 Piezometer was undertaken using a standard material supplied with the equipment. The piezoelectric coefficient, d_{33}, of this hard lead zirconate titanate (PZT) standard sample was measured as 328 pC/N, which is well within the measurement error ($\pm 2\%$) of the equipment when compared with the quoted value of 330 pC/N.

A corona poling facility was constructed to allow research into the piezoelectric effect. Before the effect of composite composition on the piezoelectric coefficients (d_{33} & d_{31}) was examined, poling trials were performed to determine optimum conditions of temperature, time, and field voltage that would produce a reasonably consistent d_{33} value for monolithic barium titanate.

5.3.c.i   Poling equipment characterisation

Characterisation of the poling rig was undertaken using specially produced small disc samples in order that a large number of measurements could be quickly carried out and spatial effects of the electric field examined. The 'micro-disks' of 5 mm diameter were re-used a number of times and de-poled in between runs using a temperature of 150°C (300 °C/hr) for two hours. The samples were tested after de-poling to ensure the piezoelectric coefficient had fallen into the range 0-5 pC/N.

5.3.c.i.a   Influence of sample position on poling performance

The micro-disks were placed throughout the chamber of the poling rig, as indicated in Chapter 4. This allowed the spatial variation of the applied electric field to be studied. An electric potential difference of 12.5 kV was generated between the needle and base (a distance of 3.5 cm as used in literature[148, 173]) and the temperature controller was set to 145°C. After a poling time of 15 minutes at this temperature the samples were cooled to below 50°C before the field was removed. The test was conducted three times with the same micro-disks being placed in different positions. A typical result for the piezoelectric coefficient distribution is given in Figure 5.129.
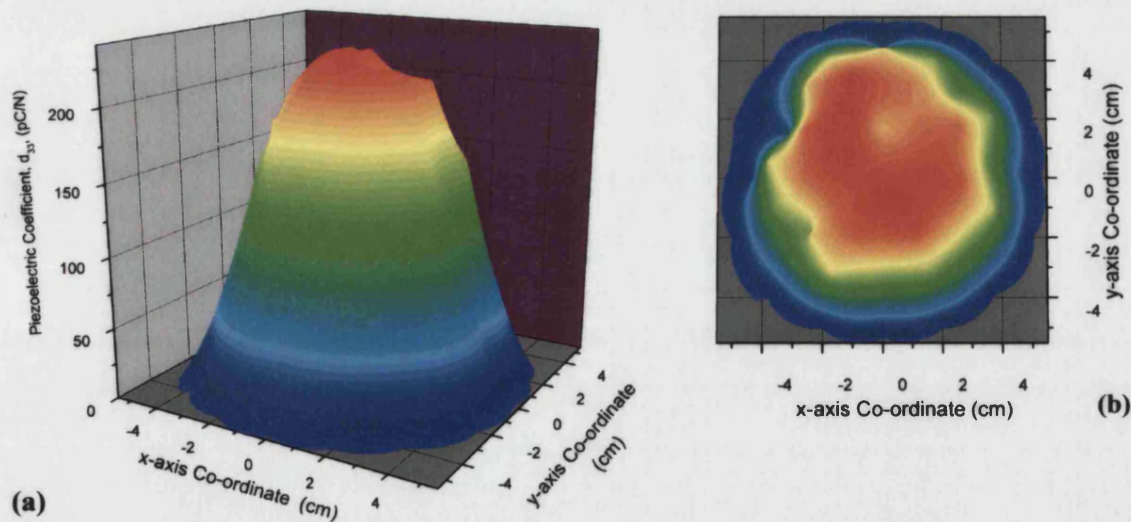
Figure 5.129: Piezoelectric coefficient, d_{33}, variation with spatial position in the poling rig, represented (a) three-dimensionally and (b) in plan view.

The results suggest that efficient poling of the samples is achieved within a radius approximately equal to the needle-base distance from the needle-base axis. The d_{33} reduces rapidly outside this region, so samples to be poled must be within this area. The perpendicular piezoelectric coefficient, d_{31}, was measured and a similar result attained as shown in Figure 5.130.
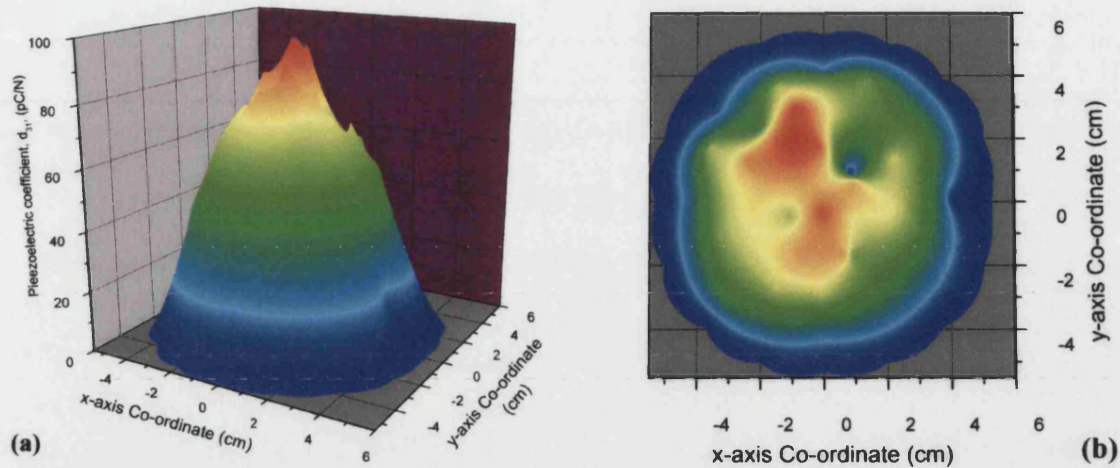
Figure 5.130: Piezoelectric coefficient, d_{31}, variation with spatial position in the poling rig, represented (a) three-dimensionally and (b) in plan view.

5.3.c.i.b   Influence of temperature and time on sample poling performance

Samples were placed in the area delineated in 5.3.c.i.a. and the poling temperature varied under a constant electric potential of 12.5 kV (needle-base distance of 3.5 cm). Samples were held at the poling temperature for various times before being *immediately* removed and d_{33} measured. The results for "controller" temperatures from room temperature to the maximum 145°C are indicated in Figure 5.131. The actual temperature of the samples will be lower as the thermocouple for the temperature controller is situated in the aluminium base. The difference in temperature between that set on the controller and that experienced by the sample was measured using a K-type thermocouple, the results are shown in Table 5.11.
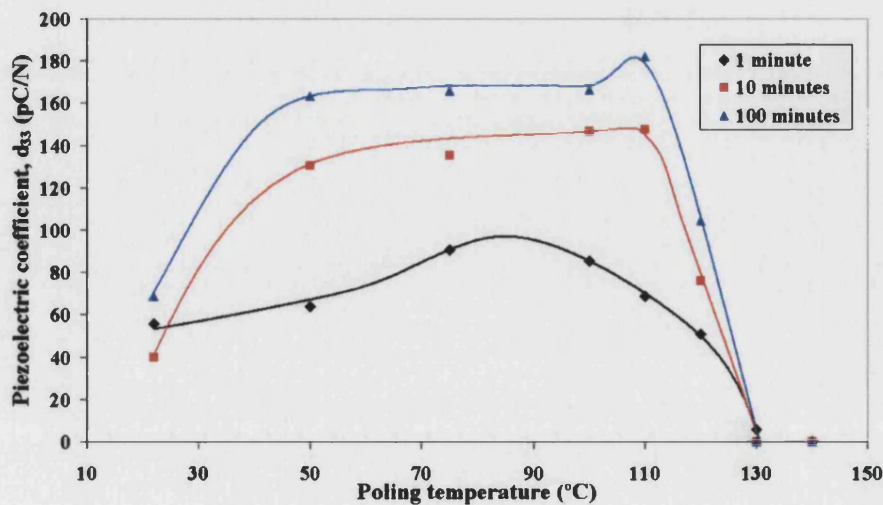
Figure 5.131: Variation of piezoelectric coefficient, d_{33}, with poling temperature and time held at this temperature and under the applied electric field.

Table 5.11: Temperature difference between that set on controller and that experienced by the top and bottom surfaces of the sample within the poling chamber.

Controller Temperature (°C)	100	110	145
Temperature of sample bottom surface (°C)	87	103	135
Temperature of sample top surface (°C)	79	94	128

As expected, at higher temperature, more thermal energy allows a greater amount of domain movement. Both a higher temperature and longer times within the field generates a higher piezoelectric coefficient. It appears that poling is not accomplished if the samples are heated to 130°C or above, even when left within the electric field for 100 minutes, due to the barium titanate having a cubic structure and is non-piezoelectric at this temperature as highlighted in Chapter 2, Section 2.2.b.i.

Samples were held under the poling voltage as the temperature fell to below 50°C from a variety of temperatures in order to investigate if the domain configuration formed at higher temperatures could be frozen in. The measurements of d_{33}, see Figure 5.132, indicates that an improved d_{33} value can be achieved by using a poling temperature greater than 120°C, which increases d_{33} gradually; below this temperature the change is much greater.
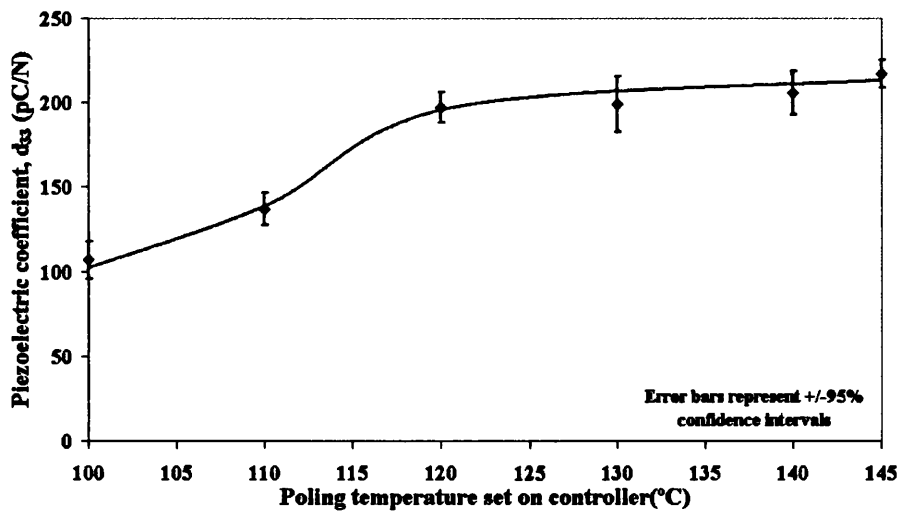
Figure 5.132: Variation of d_{33} for samples cooled to below 50°C from various poling controller temperatures.

With the samples placed in the immediate vicinity of the needle-base axis, and by using a sufficient dwell time of 15 minutes at 145°C, piezoelectric values can be recorded that are similar to the 149 pC/N reported in the literature[168].

5.3.c.i.c Influence of poling voltage and ageing on poling performance

Different poling voltages were assessed and the piezoelectric coefficients measured directly after poling and subsequently after 24 hours. A poling controller temperature of 130°C was used and samples were allowed to cool to below 70°C after a dwell time of 10 minutes. The results of using different voltage to needle-base ratios are shown in Figure 5.133.
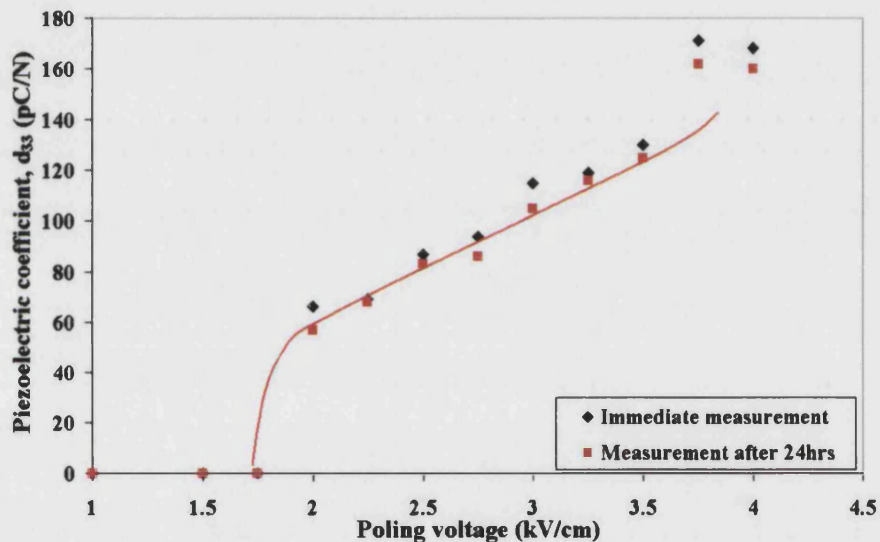
Figure 5.133: Variation of piezoelectric coefficient with applied poling

voltage for monolithic barium titanate.

Fields below 1.75 kV/cm (needle potential to needle height ratio) did not pole the barium titanate samples, while the piezoelectric coefficient increased gradually above 2 kV/cm. Above 3.75 kV/cm a considerable increase is observed, but still higher fields produced no net benefit, suggesting saturation of the switched domains. A disadvantage of high field levels, especially at high temperature, is the potential for electrical discharge between the sample and needle, Figure 5.134(a). This did not prevent poling of the sample, but can lead to detrimental effects, as black damage marks were observed on the sample sides, as in Figure 5.134(b). Electrons travelling across the sample during discharge cause the higher conductivity black marks or "tracking". The formation of these paths decreases the charge that may be built up on the top surface of the sample

and therefore the effective field for sample poling is reduced. Discharge occurs at the sample edge, as the electric field is more concentrated in this region, due to the small radius of curvature.
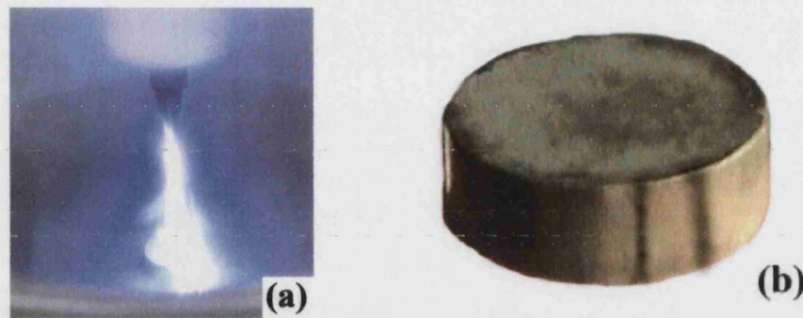
Figure 5.134: (a) Discharge from needle during poling and (b) effect of

discharge on the sample surface showing black marks.

Measurement after a 24 hour period revealed a drop in the piezoelectric coefficient between 5 and 10%, Figure 5.133. This drop is expected as domains that are not strongly aligned in the poled direction gradually return, with time, to a random orientation under the influence of thermal energy and stress. The majority of the reduction occurs in the first 24 hours after poling, with the ageing rate being defined as the percentage change in d_{33} per time decade.

The voltage employed for poling of the composite was as high as possible without allowing discharge to take place. In most cases one or two discharges occurred before the system settled down. When testing disc samples, typically of 12 mm in diameter, a slight difference in the piezoelectric value measured at the sample edge to that at the centre was observed. This edge effect was about 5-10 pC/N for the barium titanate samples and is discussed in more detail below for PZT.

5.3.c.i.d   Influence of sample on piezoelectric coefficient measurement

The different piezoelectric coefficient obtained at the edge of the sample in comparison to that at the centre was investigated. Large lead zirconate titanate (PZT-5H) discs, as large discs of barium titanate were not available, were poled using the procedure mentioned in Chapter 4. The results, shown in Figure 5.135, revealed higher d_{33} values at the sample edge than the centre.
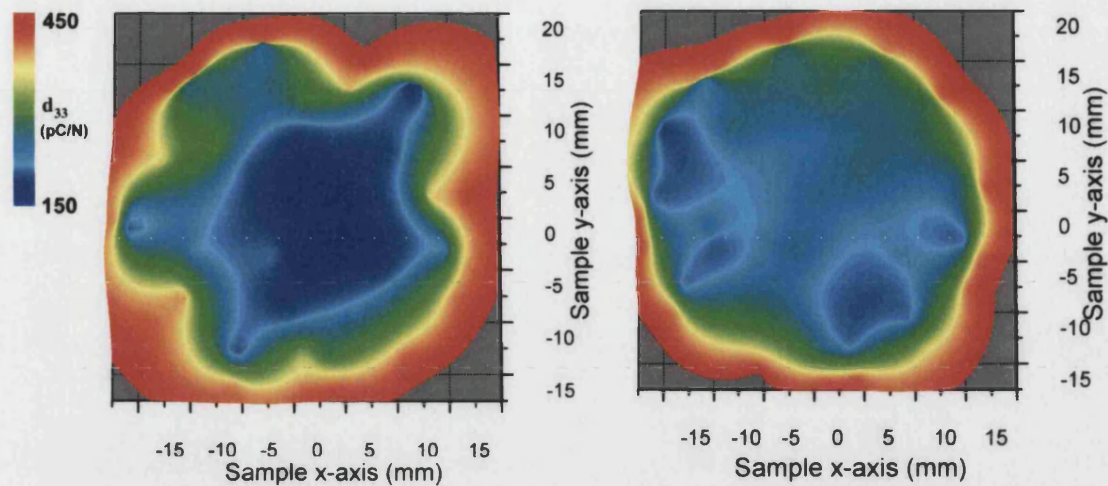
Figure 5.135: Variation in piezoelectric coefficient over two different large PZT discs. Red indicates a higher piezoelectric coefficient with respect to blue.

The difference between the sample centre and edge is due to the non-uniform poling electric field. Figure 5.136 shows that a higher voltage is observed at the sample edge as the small radius of curvature concentrates the charge. Care is needed when applying the electric field as a non-uniform field can result if the needle is unsymmetrical or off centre.

Figure 5.136: Arrows indicating non-uniform electric field at sample edge.

It is also noted that different d_{33} values at the edge in comparison to the centre can result, as the force is applied from a point source, even though the charge is collected from the whole sample. The measured value will be affected by the presence of defects, such as pores and cracks, and their placement in the sample, see Figure 5.137. The d_{33} measurements were carried out at the centre of each sample to reduce edge effects.
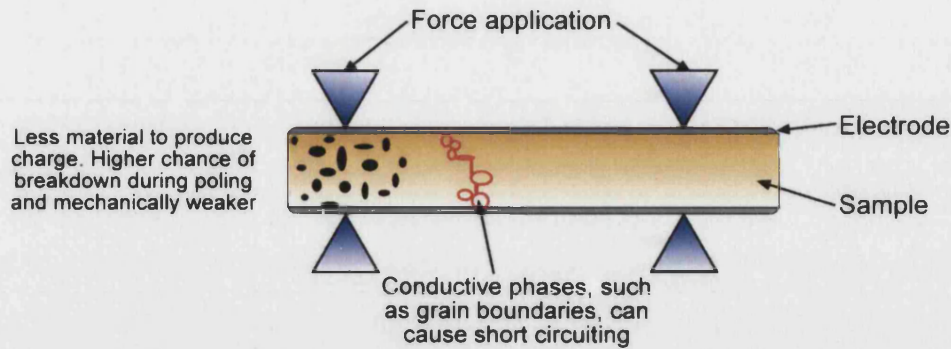
Figure 5.137: Effect of sample defects on the measured value of the piezoelectric coefficient.

5.3.c.ii   *Poling performance of barium titanate-silicon carbide composites*

Figure 5.138 shows the increase in d_{33} as a function of poling voltage and the requirement for a minimum poling voltage before domain orientation will occur. The activation barrier of 1.75 kV/cm mentioned for the monolith was used as the base voltage for the composite samples, as poling was expected to be more difficult due to possible domain pinning in the silicon carbide composites.
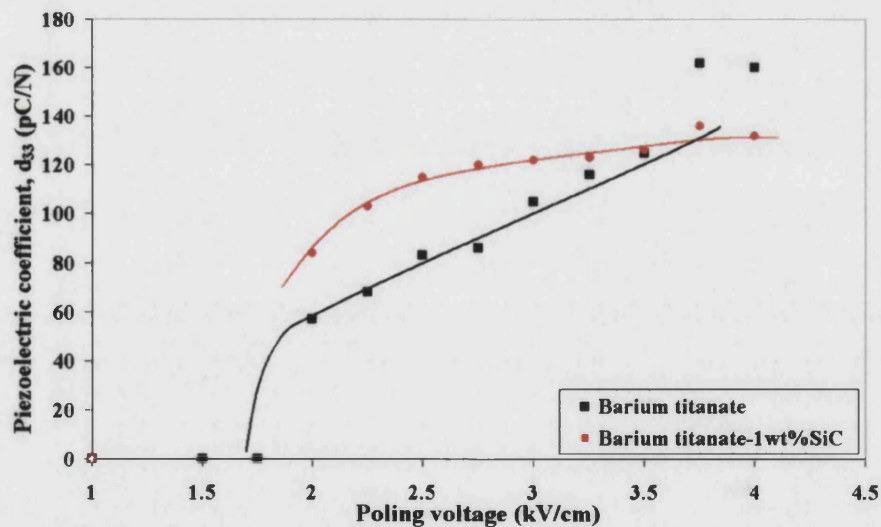
Figure 5.138: Effect of poling voltage on the d_{33} value for barium titanate

and barium titanate-1wt% silicon carbide.

The composite had an improved starting d_{33} value, however, at higher voltages the value changed less than for the monolith. A saturation value was observed for an applied voltage of 3.5 kV/cm. The d_{33} value of ~130 pC/N achieved with this voltage is less than that for the fully poled barium

titanate (typically between 150 and 190 pC/N depending on composition and fabrication). The improved d_{33} value at low applied voltages, in comparison to the monolith, could be caused by the porosity reducing the clamping of domains under the poling field. The reduction in poling efficiency, at high fields, with the addition of silicon carbide may be explained by the presence of a non-piezoelectric reaction phase that reduces the amount of material that can contribute to the piezoelectric coefficient. However, if this were the case the effect should also occur at lower poling voltages. It is interesting to note that both composite and monolith require the same poling voltage for saturation, suggesting a common process. If pinning of domain walls was occurring the piezoelectric coefficient would be expected to be low until the applied poling field exceeds the pinning energy. This does not occur suggesting pinning is not present in this composite type. Composites with higher silicon carbide contents could not be poled due to their conductive nature.

5.3.c.iii Poling performance of barium titanate-silver (oxide) composites

A drop in the piezoelectric coefficient was detected with a small addition of silver to barium titanate as shown in Figure 5.139. Incorporation of additional silver reduced the d_{33} value further but in a more gradual manner, with the expectation of a zero value being reached above 20wt% silver.
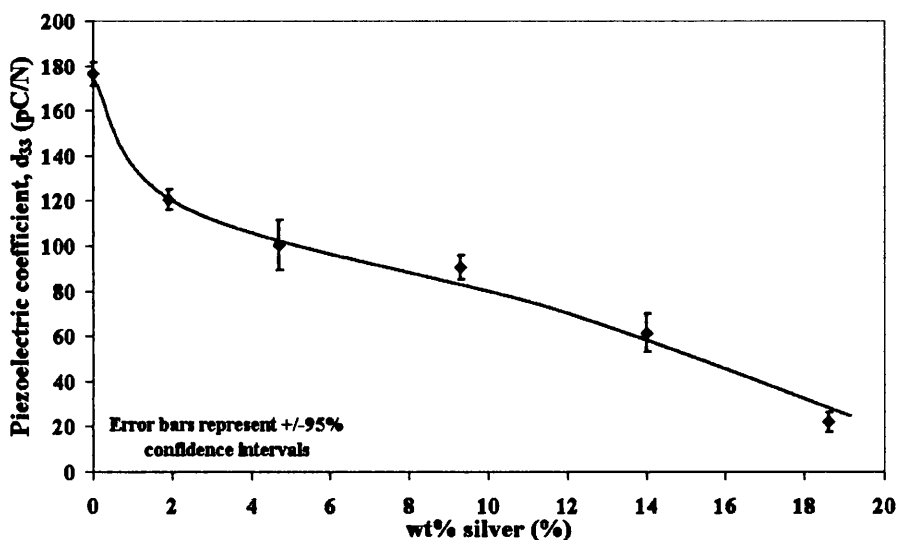
Figure 5.139: The piezoelectric coefficient for different barium titanate-silver

compositions (derived from silver oxide).

A reduction of the piezoelectric coefficient with the addition of a non-piezoelectric phase is expected from the rule of mixtures. The predicted piezoelectric coefficient from the rule of mixtures for barium titanate-20wt% silver is approximately 150 pC/N. The decrease in the d_{33} value is, however, more severe as incorporation of the silver not only reduces the amount of piezoelectric phase that can contribute to the d_{33} value, but also causes difficulties in poling of the composites. Silver is highly conductive and its addition is likely to increase the conductivity of the sample and therefore affect the charge build-up necessary for domain reorientation. Conductivity phenomena (the inverse of resistivity) are reported in Section 5.3.d.

5.3.c.iv   *Poling performance of barium titanate-silver (nitrate) composites*

Similar results to the silver oxide derived samples were recorded for the composites manufactured from silver nitrate, as shown in Figure 5.140. No sharp drop for small silver addition was observed in this case, instead a gradual decrease with increasing silver fraction was measured. The d_{33} value had reduced to zero in the 19.1wt% silver composite, as the sample was too conductive to be poled.
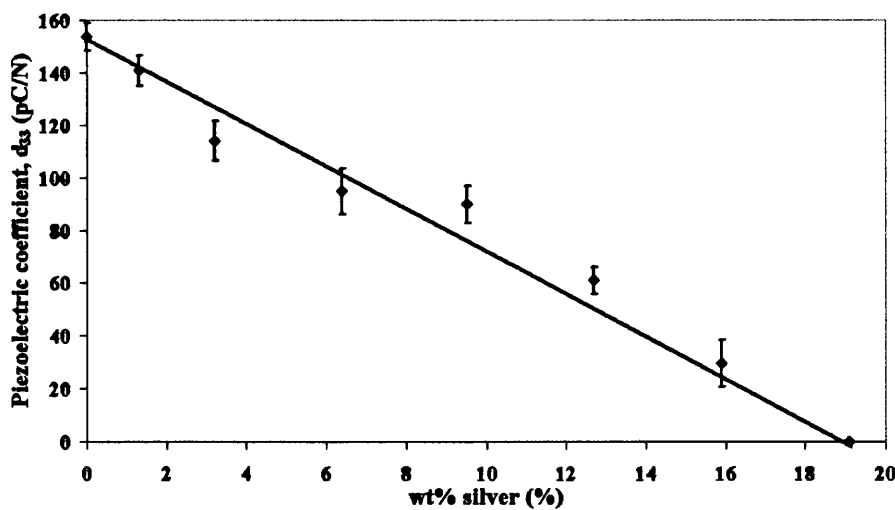
Figure 5.140: The piezoelectric coefficient, d_{33}, for different barium titanate-silver compositions (derived from silver nitrate).

Measurement of the perpendicular piezoelectric coefficient, d_{31}, indicated a similar trend as for the d_{33}, Figure 5.141. As expected, the measured d_{33} value was much greater than the d_{31} value.
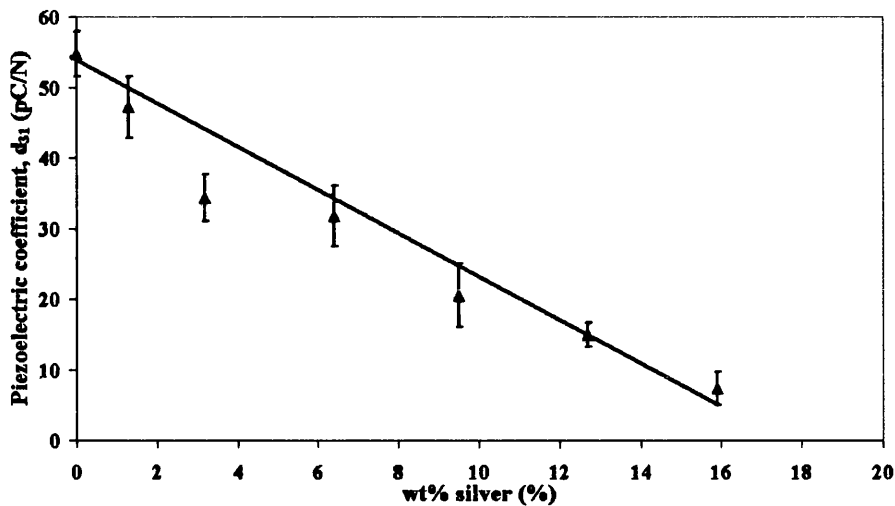
Figure 5.141: The piezoelectric coefficient, d_{31}, for different barium titanate-silver

compositions (derived from silver nitrate).

5.3.d   RESISTIVITY DETERMINATION

Resistivity was investigated by measuring the sample resistance, dimensions and applying equation 2.13. The resistance of the sample was determined on a LCR meter that was calibrated (within 5% of the value stated) with known resistor values. The resistivity is the inverse of the conductivity and is a useful screening parameter to determine a material's behaviour as a dielectric. A composite that is too conductive (low resistivity value) will not be able to be poled as the sample loses its dielectric (capacitive) behaviour.

5.3.d.i   Resistivity of monolithic barium titanate

The lower density produced by uni-axial pressing gave a resistivity of 0.16 MΩ.m, which was considerably less than the 0.82 MΩ.m achieved in the cold isostatic pressed samples (both sintered at 1300°C). In general a higher sintering temperature reduced the sample resistivity, while improved processing, such as freeze-drying increases the uni-axial value to 0.52 MΩ.m. The reduction of resistivity with sintering temperature may be due to the formation of a more conductive reaction phase, such as a glassy liquid phase above the eutectic. The 95% confidence intervals in all cases were ~±50 kΩ.m

5.3.d.ii   Resistivity of barium titanate-silicon carbide composites

Table 5.12 shows the results of resistivity versus silicon carbide content. The incorporation of silicon carbide causes a reduction in the resistivity in comparison to the monolith. This would be expected if the particles were reacting to form a phase that increased the conductivity of electrons or increased the motion of ionic charges over small distances. The composites have become substantially conductive with 5wt% silicon carbide. The attempted re-oxidation of the hot pressed 5wt% silicon carbide increased the resistivity from $\sim 1 \times 10^{-7}$ MΩ.m to $\sim 1 \times 10^{-5}$ MΩ.m. These composite samples are substantially conductive even after heat treatment.

Table 5.12: Resistivity for barium titanate-silicon carbide composites.

wt% silicon carbide	0	1	2	3	5
Resistivity (MΩ.m)	0.8	0.8	0.1	4×10^{-6}	1.5×10^{-7}

5.3.d.iii   Resistivity of barium titanate-silver composites

Figure 5.143 shows the resistivity values obtained for composites derived from silver oxide and silver nitrate. A large initial reduction in resistivity occurred in the silver (oxide) samples for a small addition of silver, while the reduction is gradual for the silver (nitrate) composites. The resistivity reduction with high silver addition is less in the silver (oxide) samples than the silver (nitrate) samples, which may be related to the higher density of the silver (oxide) composites. The rate of resistivity decrease increases at 13wt% silver ($\sim$7.6vol% silver) for the silver nitrate derived composites. A dramatic decrease in resistivity has been reported to occur in a region called the percolation threshold, which occurs at a second phase volume fraction of approximately 0.25 (assuming equal particle size and shape). This may be reduced if the second phase is significantly smaller in particle size than the matrix, as the particles become segregated at the grain boundaries, as seen in Section 5.1.g.iii.b & c. It is not known whether the observed resistivity change is at this threshold, as samples with higher silver contents were not suitable for testing due to their high porosity content. Silver has a resistivity of 1.6×10^{-14} MΩ.m, so a decrease of many orders is certainly possible at higher silver contents.
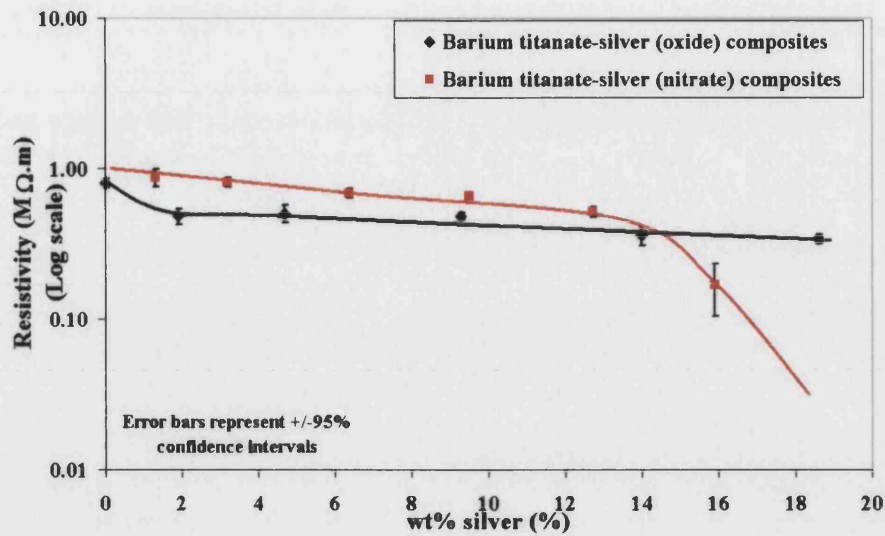
Figure 5.142: Resistivity for silver oxide and silver nitrate derived composites

showing a decrease with silver content.

5.3.d.iv   *Resistivity of barium titanate-5.7wt% platinum*

The addition of 5.7wt% platinum into a barium titanate matrix reduced the resistivity to 0.27 $M\Omega$.m from 0.8 $M\Omega$.m. This is a considerably greater decrease than occurred for a similar weight fraction addition of silver, suggesting that the platinum particles may be segregated at the grain boundaries or an additional conducting phase was present.

5.3.e   IMPEDANCE ANALYSIS

Impedance analysis was employed to determine the coupling coefficient, K_{eff}, and the mechanical quality factor, Q_m. No significant change was observed in the value obtained when the same sample was tested under different ambient temperature and humidity conditions.

5.3.e.i   *Impedance analysis of monolithic barium titanate*

Impedance measurements were carried out on unpoled barium titanate samples and the same samples 24 hours after poling. This process was carried out to observe the effect of the poling voltage value. Figure 5.143 shows the impedance results of this trial. A linear response in impedance is observed for the un-poled sample, indicating it is capacitive. For poled samples, the minimum impedance corresponds to the radial resonance, which reduces as the sample becomes increasingly poled.

197
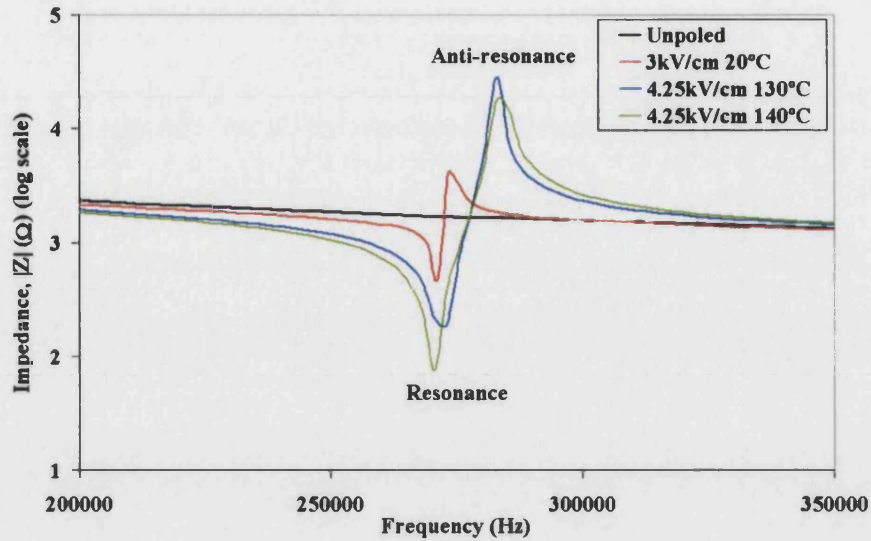
Figure 5.143: Resonant and anti-resonant peaks for un-poled and poled barium titanate.

Peaks corresponding to additional harmonics of the radial resonance and overtones, such as vibrational modes in the thickness dimension are not shown. The results confirm that increasing the poling voltage affects the material and that the higher temperature of 140°C is beneficial. Domain orientation is maximised by using a controller temperature of 140°C and a poling voltage greater than 3.75 kV/cm, Section 5.3.c.

Practical measurements of the radial frequency for uni-axially and cold isostatically pressed monolithic samples showed that the resonant peak is in the 264-270 kHz region (for a sample radius of ~6 mm) for both manufacturing processes. The calculated radial resonant frequency based on equation 2.33 and using theoretical barium titanate density of 6020 kg.m^{-3} was approximately 60 kHz lower than the measured frequency, which is likely to be due to the ~7% porosity of the samples. Recalculation, see Table 5.13, with a density lower than the theoretical, showed that porosity is not the only reason for the higher experimental resonant frequency as at 80% theoretical density the radial frequency is still 40 kHz lower. This is assuming that the stiffness of the material is unchanged, however, this may not be the case.

The effective coupling coefficient, K_{eff}, was calculated using equation 2.35 and gave an average of 0.23 for the uni-axial pressed samples, and 0.25 for the cold isostatically pressed samples. The results suggest that there is a slight improvement of coupling in the cold isostatically pressed samples, due to the enhanced density. An effective coupling coefficient of ~0.32-0.35 has been reported in the literature[22, 120, 174].

Table 5.13: Estimated radial frequency mode with different porosity values and assuming constant compliance coefficient of 8.6×10^{-12} m^2N^{-1}.

Density (% of theoretical)	F_{radial} (kHz)
100	209
90	220
80	234

Equation 2.15 allowed calculation of the mechanical quality factor, Q_m. No significant difference between the uni-axially pressed and cold-isostatically pressed mechanical quality factors was observed, the average for each being ~180 (± 50). The considerable variation in the values is thought to be due to microstructural differences, including porosity. A value of 400 has been reported for Q_m[168], indicating that these composites fall short by a considerable margin.

5.3.e.ii   *Impedance analysis of barium titanate-silver (oxide) composites*

Silver (oxide) composites were tested using the impedance analysis equipment and the results are given in Figure 5.144.
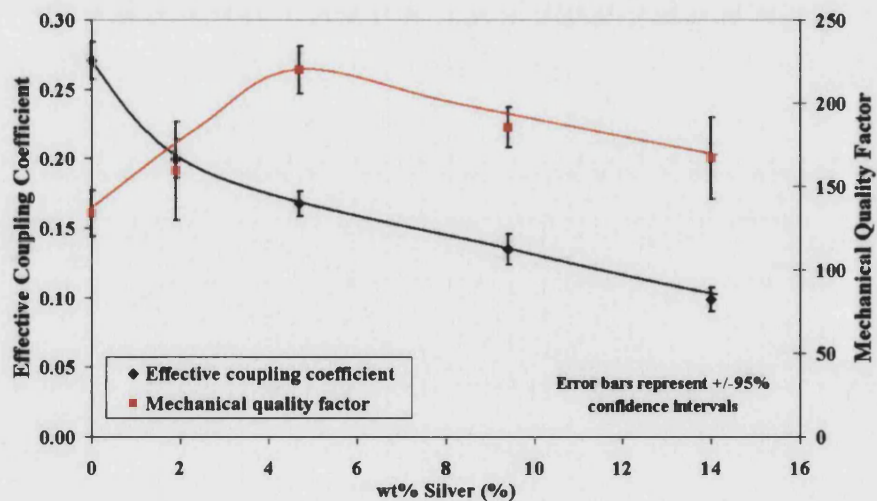
Figure 5.144: Impedance analysis of barium titanate-silver (oxide) composites showing the effective coupling coefficient and the mechanical quality factor.

A reduction of the effective coupling coefficient occurs with the increase in the silver content. The reduction may in part be due to the reduced amount of piezoelectric phase (higher porosity) or elastic deformation of silver particles absorbing energy by mechanical loss. There appears to be no clear increase or decrease in the mechanical quality factor, which suggests the increase due to the effective coupling coefficient decrease balances the increase due to a higher sample capacitance and $|Z_{max}|$. The value of the mechanical quality factor is lower than 400 reported in literature[168], but comparable to the monolith value.

5.3.e.iii   *Impedance analysis of barium titanate-silver (nitrate) composites*

The trend for the effective coupling coefficient is similar to that for the silver oxide derived composites, as shown in Figure 5.145. The mechanical quality factor is observed to increase to a plateau with the addition of silver. The mechanical quality factor values are more reasonable in the composites than for the monolith, with some samples reaching values approaching 330. It appears that the addition of silver is beneficial to the mechanical quality factor but reduces the coupling coefficient, due to the reduced poling efficiency. The coupling coefficient is improved with poling as shown by the greater difference in anti-resonant and resonant frequencies in Figure 5.143.
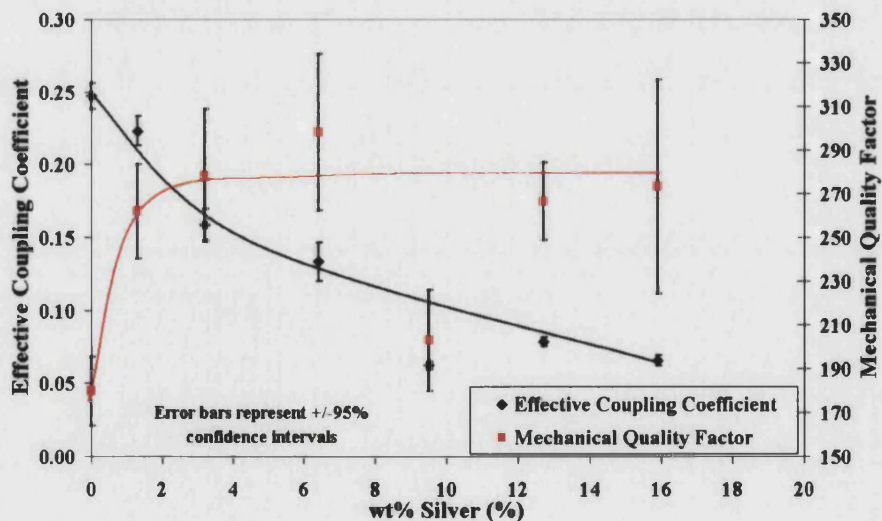
Figure 5.145: Impedance analysis results for barium titanate-silver (nitrate) composites

showing the effective coupling coefficient and the mechanical quality factor.

5.3.f   MEASUREMENT OF DIELECTRIC BREAKDOWN OF BARIUM TITANATE-SILVER (NITRATE) COMPOSITES

The dielectric breakdown voltage is the maximum electric field in which the specimen can operate. The measurement is related to the volume of material under test, as a smaller volume is less likely to contain a critical defect that may help cause breakdown at a certain applied voltage. This makes it similar to the mechanical strength in that the volume of the tested sample is significant, and as such Weibull statistics can be applied. Only the silver nitrate derived samples were tested, as they had good resistivities over a range of compositions and a sufficient number of samples were available. The average breakdown voltage and Weibull modulus are indicated in Figure 5.146.

The monolithic breakdown strength is slightly higher than expected from the literature, which reports 7.4 kV/mm for barium titanate[59, 152]. The results show a reduction in the breakdown strength as the silver content increases. This is expected as silver is conductive and aids conduction of charge through the material. At high volume fractions the particles become sufficiently close that conduction occurs at all voltages and a dielectric strength cannot be obtained. The low Weibull modulus shows the materials have a high variability, which is typical of ceramics.
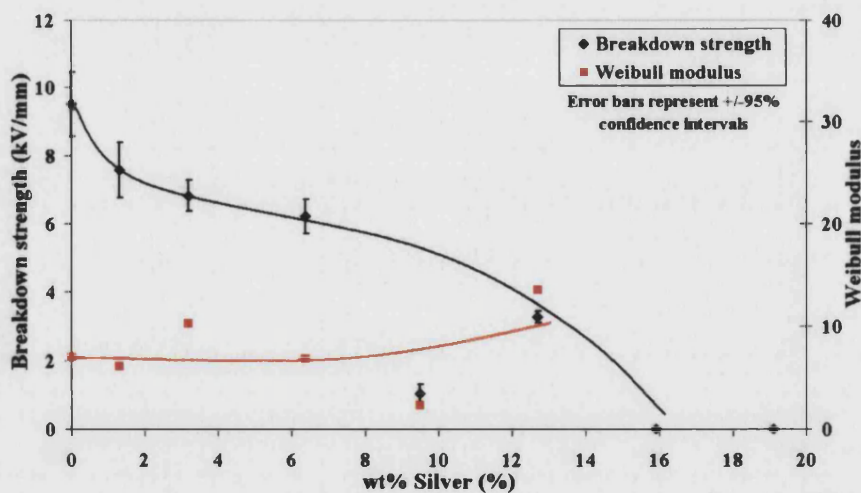
Figure 5.146: Reduction in breakdown voltage for silver nitrate derived composites

with increasing silver content and Weibull modulus showing typical ceramic variability.

(Tested at 22.6°C).

At low silver content the breakdown event was dramatic due to the high voltage that was discharged through the sample. The flow of charge inevitably produced a physical hole though the

sample, Figure 5.147(a), and produced sufficient heat to melt the material and produce globules on
cooling, see Figure 5.147(b).
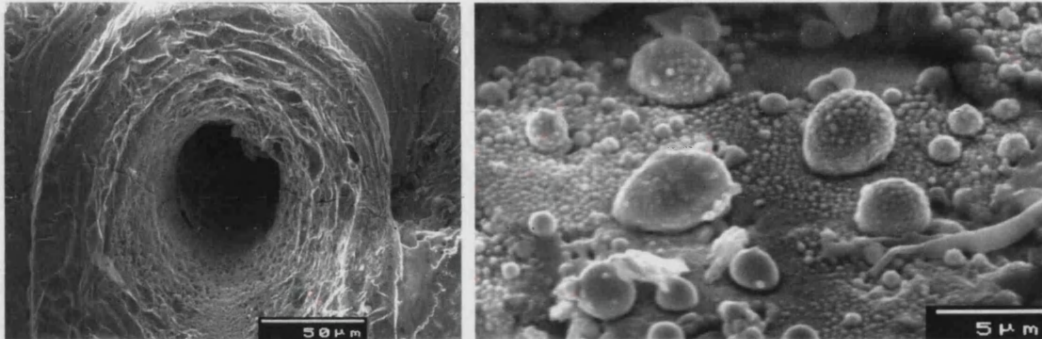
Figure 5.147: (a) Typical breakdown hole surrounded by (b) cooled molten globules of material.

Breakdown within the electrode rather than at the edge of the electrode increased in occurrence as
the silver content increased. The positions of the breakdown events are shown in Figure 5.148,
with an example of each type.
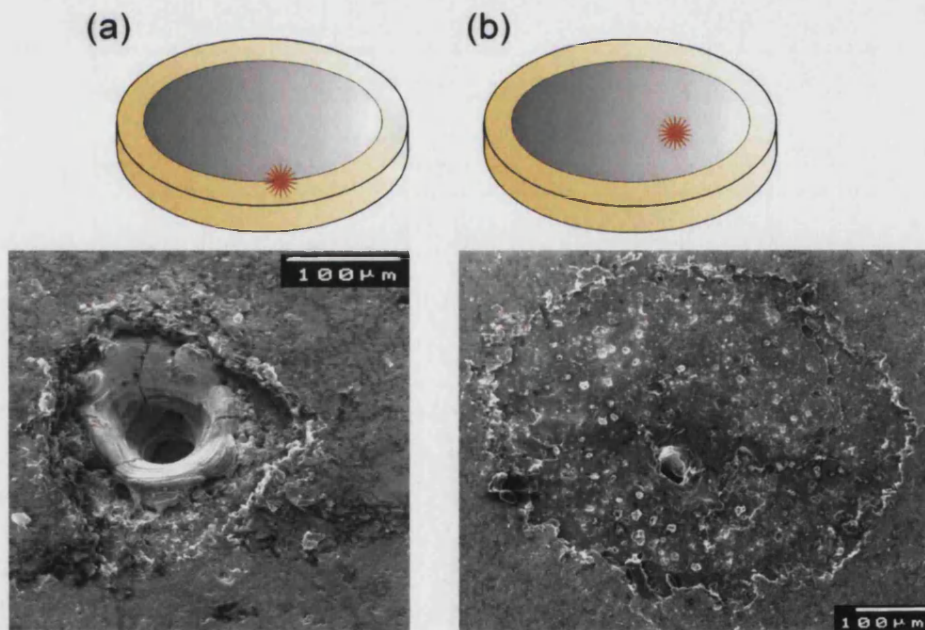
Figure 5.148: Position of breakdown event in (a) monolith and barium titanate-silver composites
below 6.4wt% silver and (b) above 6.4wt% silver.

The change in breakdown position relates to the resistance of the material to breakdown. If the
resistance is high the field builds up so that the sharp radius of the electrode edge concentrates the
field to cause breakdown. When the resistance of the material is lower (silver present) this field is

still present but the sample starts to conduct between the electrodes before a sufficiently high field
for breakdown forms at the electrode edge.

A figure of merit can be used to determine whether the decrease in the dielectric breakdown
strength outweighs the increase in the sample relative permittivity with the increase in silver
content. A capacitor requires a high relative permittivity to store a large amount of charge but must
also be able to withstand a large electric field. The capacitance, C, is simply the charge stored by
the device, Q, divided by the voltage across the device, V. As the capacitance is also related to the
sample dimensions, equation 2.7, the charge stored is directly proportional to the electric field, E,
with the proportionality constant given by the sample area, A, multiplied by sample relative
permittivity, ε_r, as indicated in equation 5.7.

$$Q = \varepsilon_r AE \qquad\qquad \{5.7\}$$

Therefore the maximum charge stored by a capacitor of fixed dimensions is the relative
permittivity multiplied by the maximum field the material can resist (the breakdown strength).
Figure 5.149 indicates the figure of merit, $\varepsilon_r.E_{Max}$, calculated for the silver composites.
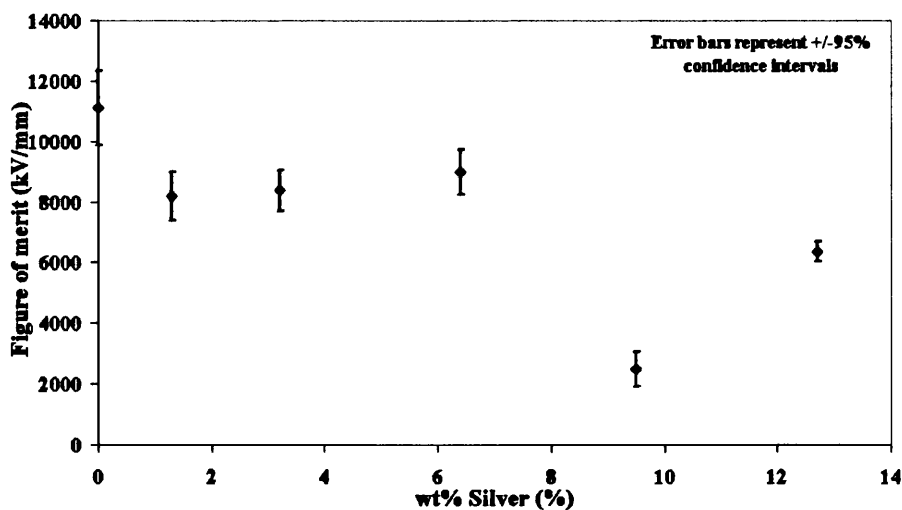
Figure 5.149: Figure of merit for barium titanate-silver (nitrate) composites

as a capacitor material.

It appears that the reduction in breakdown strength, or the rise in relative permittivity is not
sufficiently strong, to improve the figure of merit, by the addition of silver. Although, there may

be an opportunity for these composites as a high relative permittivity material used under a low electric field. This behaviour may be modified if the sample density could be improved.

5.3.g   POLARISATION-FIELD ANALYSIS

Figure 5.150 shows the change in polarisation with increasing applied field for monolithic barium titanate. As the electric field increases in strength the polarisation increases to a saturation level (and maximum polarisation), indicated by the low gradient behaviour. This should be horizontal, however, pick-up in the current cable occurred, due to the proximity of the high voltage cable. On complete removal of the electric field the polarisation decreases, but does not return to the original un-polarised state. This non-zero polarisation is the remanant polarisation and is due to the pinning of domains by oxygen vacancies and defects. Reversal of the electric field direction reduces the energy barrier to domain motion and the polarisation returns to zero under an electric field strength termed the coercive field. Increasing the electric field above this value produces polarisation in the opposite direction to before, and a remanant polarisation on electric field removal. The behaviour shown in Figure 5.150 is similar to that shown in Appendix II (Figure AII.42). The area of the polarisation loop gives the hysteretic loss.
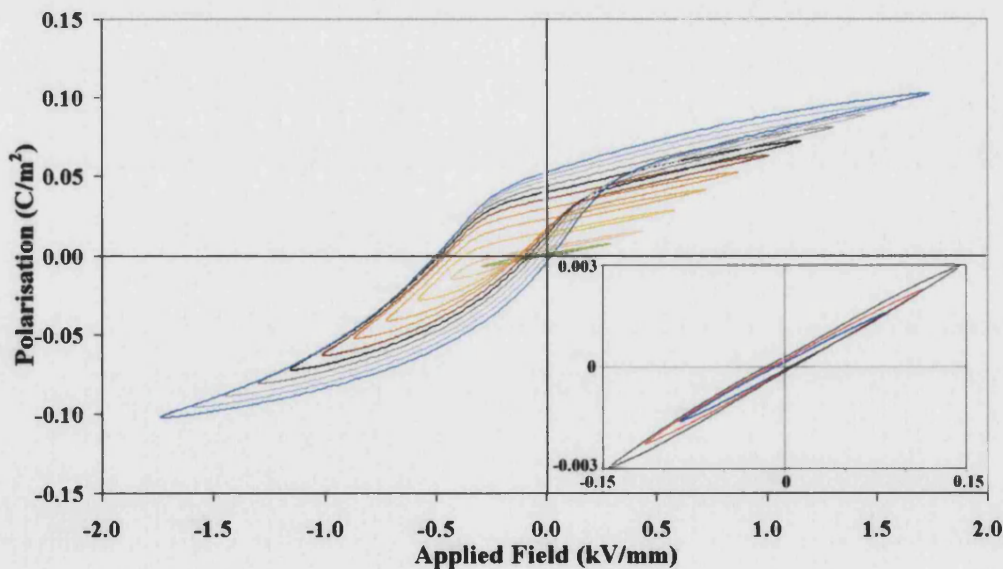
Figure 5.150: Polarisation-Field behaviour for monolithic barium titanate showing

the hysteresis loop shape and size under various applied voltages.

The inset indicates the behaviour under low electric fields.

It is observed that the loops are generally elliptical at low electric fields (typically <0.5 kV/mm), see insert in Figure 5.150, and broaden into the characteristic hysteretic shape at higher fields. The polarisation-field loop is comparable to that reported in the literature[175] with a polarisation of ~0.12 Cm^{-2} for a field level of 2 $kVmm^{-1}$.

To compare the different composite compositions, Figures 5.151, 5.152 and 5.153 have been constructed to show the change in loop behaviour under an applied field of ~2 kV/mm. The graphs above show that with the addition of silicon carbide and silver particles there is an increase in the maximum polarisation achieved for the same field, and a broadening of the loop, signifying greater hysteresis loss. The 1.9wt% silver and 9.3wt% silver composites, from silver oxide, have nearly circular hysteresis loops indicating the samples are similar to resistors rather than capacitors. These samples where not tested at any higher fields than those indicated in order that sample breakdown would not destroy the sensitive equipment. The increase in the coercive field with increasing particle content suggests that domains are become increasingly pinned, as a higher reverse voltage is required to de-pole the material.
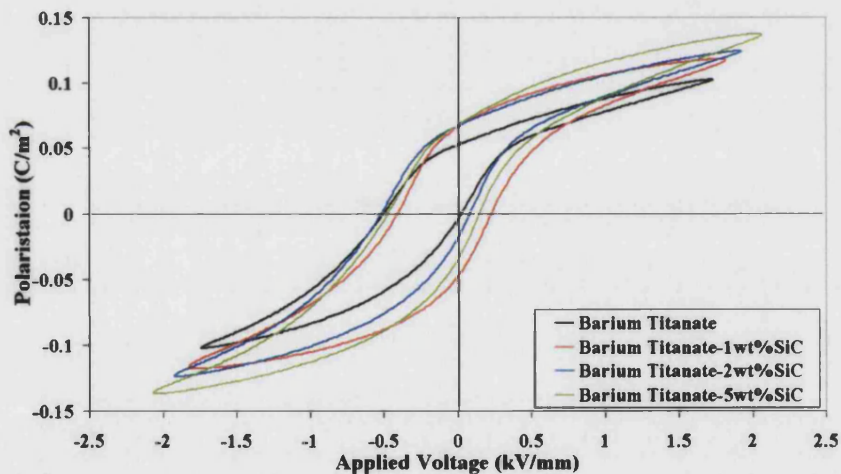
Figure 5.151: Polarisation-field behaviour of barium titanate-silicon carbide composites.
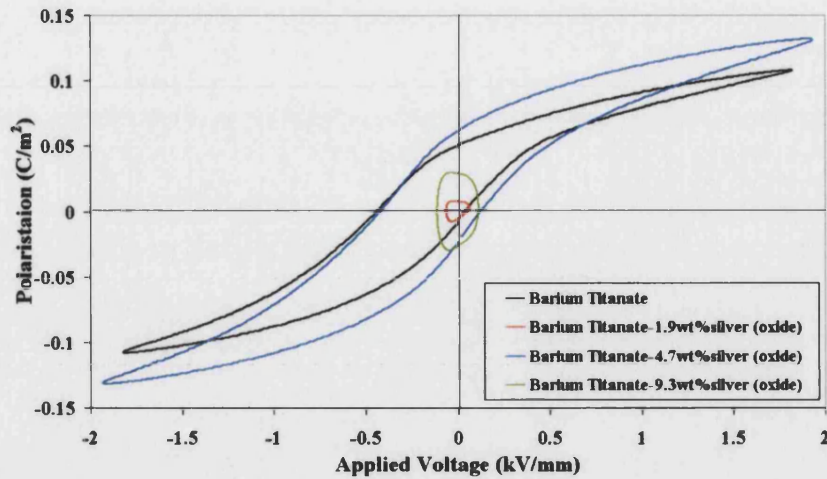
Figure 5.152: Polarisation-field behaviour of barium titanate and barium titanate-silver
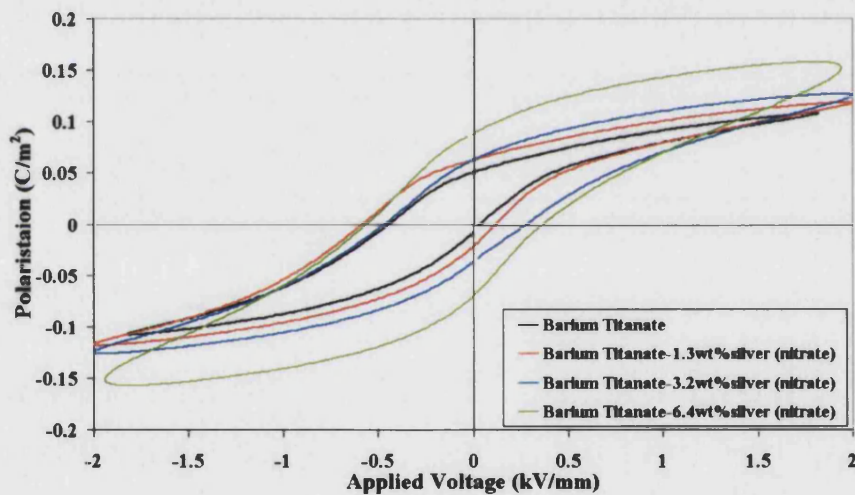
(oxide) composites.

Figure 5.153: Polarisation-field behaviour of barium titanate and barium titanate-silver

(nitrate) composites.

Many different parameters can be calculated from the polarisation-field behaviour and these parameters can vary with the electric field. Table 5.14 shows the values calculated for various properties at an electric field level of 1.5 kV/mm. Additional results for the coercive field at an electric field level 0.05 kV/mm are also given.

Table 5.14: Calculated property responses for an applied electric field amplitude of 1.5 kV/mm (high field). Low field is 0.05 kV/mm.

Property		BT	BT-SiC (wt%)		BT-Ag (oxide) (wt%)		BT-Ag (nitrate) (wt%)		
			1	5	4.7	9.3	1.3	3.2	6.4
Maximum polarisation (C/m^2)		0.095	0.107	0.115	0.107	-	0.086	0.102	0.126
Remanant polarisation (C/m^2)		0.025	0.052	0.040	0.028	-	0.026	0.035	0.056
Coercive field (kV/mm)	Low field	0.005	0.016	0.005	0.004	0.026	0.003	0.004	0.003
	High field	0.23	0.30	0.28	0.24	-	0.30	0.31	0.35
Hysteresis loss (Jm^{-3})		7.2×10^4	1.2×10^5	1.1×10^5	9.2×10^4	-	7.5×10^4	1.2×10^5	1.8×10^5

5.3.g.i   *Maximum polarisation*

The maximum polarisation attained increases as the, silicon carbide and silver, particle content increases. This may be due to an increase in the number of dipoles influenced by the field or porosity could reduce the stress clamping domains. This is analogous to the saturation magnetisation that is directly related to the number of dipoles per unit volume and the elementary dipole strength[33].

5.3.g.ii   *Remanant polarisation*

The increase of the remanant polarisation with the addition of both silicon carbide and silver particles suggests that once the domains have become orientated with the field they have been unable to switch back. Pinning of the domains may cause this behaviour, suggesting that the addition of particles has been successful in affecting the polarisation-field characteristics. This could be caused by a change in oxidation state of the barium titanate in the silicon carbide composites that increases oxygen vacancies that act as pinning centres. For the barium titanate-silver composites the small (<1 µm) intragranularly located silver particles could act as pinning centres.

5.3.g.ii   Coercive field

Under low applied fields the coercive field is unchanged, unless the material is resistive, in which case the coercive field is considerably increased. The low field value corresponds to the field necessary to cause domain wall motion. With a high field the coercive value is increased and with the incorporation of silicon carbide or silver particles it also increases. This indicates that domain motion at low field has become more difficult in these composites. At higher fields it becomes more difficult to switch the domains back to a non-polarised position.

5.3.g.iii   Hysteresis loss

From the curves in Figures 5.151, 5.152, and 5.153 the increase in hysteresis loss is expected with the addition of both silicon carbide and silver particles, with a doubling for barium titanate-6.4wt% silver (nitrate) from the monolithic value. The increase in loss is undesirable as the energy lost is converted to heat that can cause a degradation of properties, especially under high drive. However, devices would not usually be used in situations where total reversal of polarisation is required. Typically, poled materials are employed in low field applications, where the losses are small, such as under the electric field response shown in the insert of Figure 5.150. The high loss indicates a material that requires more energy to depolarise and is similar to the difference between hard (large magnetisation-force loop) and soft (small magnetisation-force loop) magnetic materials[176]. Hard magnetic materials are produced by the precipitation of carbide particles, which are effective in obstructing magnetic domain wall motion[176].

5.3.h   SUMMARY OF ELECTRICAL PROPERTIES ANALYSIS

5.3.h.i   Barium titanate-silicon carbide composites

The addition of silicon carbide did not enhance the overall electrical properties of barium titanate. While the relative permittivity increased dramatically, as semi-conducting when oxygen deficient, the material had a high dielectric loss and low resistivity that made poling difficult and the composition unsuitable for piezoelectric applications. Polarisation-field analysis suggests that the domains observed in the electron microscope undergo motion under the high applied electric field, which is greater than that used in poling.

5.3.h.ii   Barium titanate-silver composites

The barium titanate-silver composites show more promise than those using silicon carbide as the relative permittivity is improved without the formation of a semi-conducting material and higher dielectric loss. However, the silver particles are conducting and result in a decrease in the resistivity of 50% with 10wt% silver. The dielectric loss was unaffected by silver addition, until the content caused the possibility of conducting networks. The silver particles, being non-piezoelectric, are detrimental to the piezoelectric coefficient, such as d_{33}. Improvements may be achievable for the figure of merit by improving the composite density, as the high porosity decreases the relative permittivity and breakdown strength. With the increase in the remanant polarisation and coercive field the domains may have become pinned by the silver particles.

5.3.h.iii   Barium titanate-5.7wt% platinum

The addition of platinum reduced the resistivity to a greater extent, with a smaller weight fraction, than the silver. This is thought to have been due to the higher segregation of platinum particles to the grain boundary, due to their small size. The samples had a low density and high conductivity that made them unsuitable for electrical characterisation.

6 COMPUTATIONAL MODELLING

6.1 INTRODUCTION

In recent years modelling of materials and processes has become more popular as the average computer performance increases making the results more reliable and reducing computation time. For example the modelling of electrical properties, in particular common transport phenomena in disordered materials, have been studied[171]. In this work modelling is undertaken to evaluate the dielectric response of a virtual dielectric material as a function of simulated metallic particle content. The dielectric material is modelled by a random array of resistors and capacitors and the results compared with previously reported modelling results[177] and the actual behaviour of fabricated samples.

6.2 MODELLING TECHNIQUES

The model consists of producing a network from two different electrical elements, resistors and capacitors, and examining how this structure behaves when stimulated. The dielectric properties of dielectric materials and not the piezoelectric response are modelled. In the literature the matrix has consisted of randomly dispersed resistors and "holes" or "blanks". The intention was to examine critical behaviour in disordered materials, such as polymer gels and sintered powders[178]. This type of structure can be visualised in two dimensions as a large array of squares. The array size is assumed to be sufficiently large that boundary effects are negligible. A fraction of the squares (coloured red) represent resistors, while white squares indicate no component present, Figure 6.1.
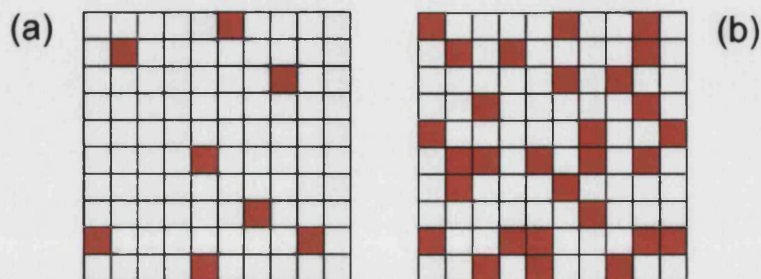
Figure 6.1: Representation of a large array of squares coloured red (resistor) and

white (hole) for (a) low resistor content and (b) high resistor content.

The coloured square distribution is assumed to be random and that they do not attract or repel blank squares or other coloured squares. A "cluster" is defined as a group of neighbouring coloured squares with at least one side in common. The number and properties of these clusters is addressed by percolation theory[170]. Percolation occurs when one cluster traverses the whole system either by extending from the top row to the bottom row or spanning the system vertically and horizontally[179].

As the proportion of one of the components increases, a critical point is reached in which a percolating cluster is formed. The volume fraction of that constituent at which this event occurs is called the percolation threshold, p_c. This is the minimum component proportion necessary for the first percolation path to appear across the system[170, 180]. For an array of resistors this threshold corresponds to a large change in the conductivity, typically of a few orders of magnitude[125]. A similar result is observed in physical systems that consist of conducting and insulating phases[125, 181]. For a detailed discussion of percolation the reader is referred to Stauffer[170] and in particular chapter five of the paper by Clerc[182], which relates specifically to electrical modelling with resistors and capacitors.

This section is concerned with the change in relative permittivity; conductivity and phase angle as compositional changes are introduced into a resistor-capacitor, R-C, network. It is intended to represent the electrical properties of a conductor (resistor)-dielectric (capacitor) composite material. Systems have been studied theoretically[125] and experimentally[112, 122, 124, 125, 183, 184]. Simulations have been conducted by digitising actual two-dimensional and three-dimensional systems and calculating electrical properties of the network produced[185]. Electrical properties have also been simulated on random R-C networks produced manually or via algorithms[177, 186-188]. A number of different techniques have been used to obtain the electrical properties from these computational models, such as Gaussian elimination[170, 177, 185, 186] and star-triangle[186-188].

The star-triangle method applies a sequence of transformations to the components in the R-C two-dimensional lattice resulting in a reduction of the lattice to a single component that has the same conductance as the original entire lattice[186]. This method is computationally more efficient than the Gaussian elimination technique, but is restricted to certain well-behaved two-dimensional lattices[186]. Gaussian elimination involves the simultaneous solution of all the node voltages of the lattice, which are given by Kirchoff's laws[186]. These laws being:

i. The current flowing into a node in a circuit must equal the current flowing out of that node.

ii. For any closed loop path around a circuit the sum of the voltage gains and voltage drops equals zero.

The following sections deal with the methods used to produce two-dimensional and three-dimensional resistor-capacitor networks, their solution for electrical properties and comparison with the results published in the literature.

6.3 NETWORK COMPOSITION

In general, the published work has been concerned with the properties of resistor only systems, with compositions close to the percolation threshold[170, 171, 178, 179]. In this research the construction of a R-C network with simulated properties that represent a dielectric material are of interest. In the networks constructed in this work, conductors are represented by 1 kΩ resistors and dielectric regions by 1 nF capacitors. A 1 GΩ resistor shunts each capacitor in order that the DC floating nodes do not cause errors when the network is solved. Square arrays of resistors and capacitors (with shunts) were constructed of the required size (total number of resistors components). The top and bottom of the network were defined as electrodes by placing wires across the component ends, as shown in Figure 6.2. One electrode edge was connected to ground, whilst the other was linked to an AC power source (50 V) through a 100 MΩ resistor. This resistor was used to provide a constant current of 5×10^{-7} A. The voltage across the network was measured using a terminal between the top electrode and the external resistor, as shown in Figure 6.2.
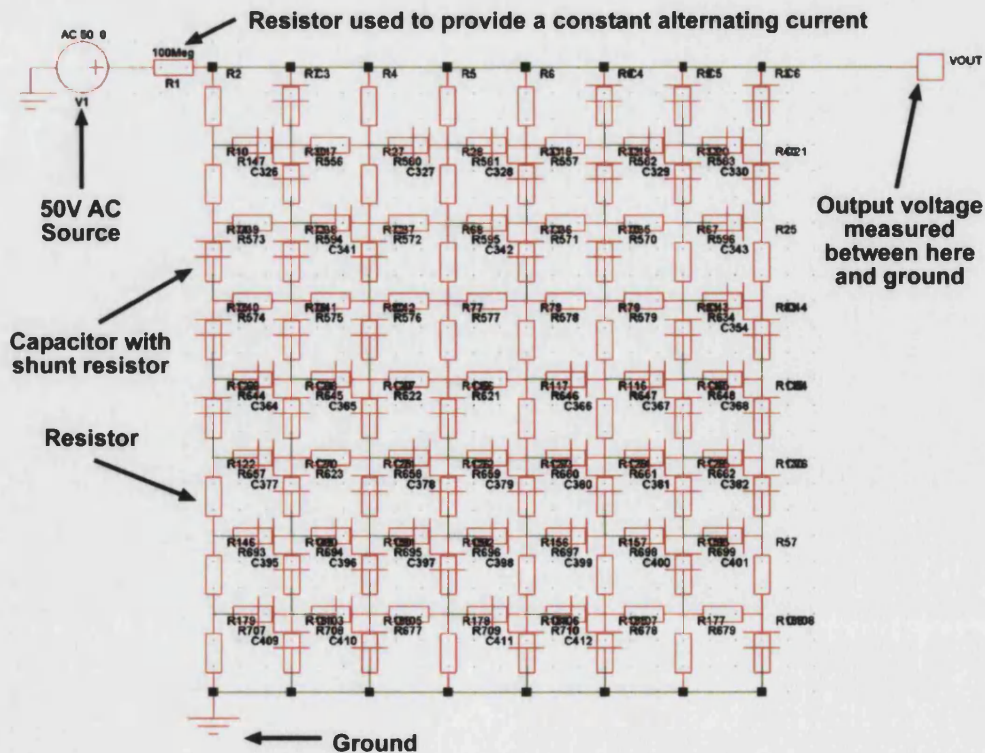
Figure 6.2: Representation of an 8x8 network circuit diagram.

Initially, small sized systems were produced by manually constructing the circuit diagram. The component type, resistor or capacitor, to be inserted was randomly determined by rolling a 10-sided dice, as described in more detail in Section 6.5. All components were positioned and the required links between components were added before the system response was analysed. Practically, only small systems could be built by this method due to its time consuming nature. Larger arrays could be constructed by joining small arrays together, but each would consist of a repeating pattern of components in a non-random circuit structure.

In order to reduce the time in constructing a random R-C network a Matlab macro was written so that square arrays of any size and composition could be produced. This macro and the associated batch files are located in Appendix II. The macro was used to produce various R-C systems in order to determine a suitable resistors-capacitors ratio to represent a dielectric material. Simulations were conducted on systems containing approximately 4 to 96% capacitors, in steps of 4%. The actual percentage of capacitors will vary due to the random nature of the network composition. 128 runs were carried out at each composition using a square matrix with a side length of 16 components (16x16 – as used in the literature). A similar procedure was conducted for three-dimensional cubic networks with a side length of 16 components. The three-dimensional circuit creation macro is in Appendix II.

Fixed R-C ratio networks were produced for comparison with reported results, these having a composition of 60%R-40%C, 50%R-50%C and 40%R-60%C [177, 187]. A specific capacitor (or resistor) fraction for the random R-C network was chosen to represent a model dielectric material, which was then used for the following analysis,

i. **Array size**

It has been reported that the same principal characteristics are observed between small and large arrays[177]. Two and three-dimensional networks of increasing size were simulated to examine this, Section 6.4.

ii. **Effect of resistor and capacitor defects**

Components (resistors and capacitors) of various values were incorporated into a matrix with a composition that represents a dielectric material. This is discussed in more detail in Section 6.8.

6.4 NETWORK SIZE

The limit to the network size is the time that is required by the computer software to generate and solve it. As the general computing performance of the machines available to researchers has increased with time, so have the size of the networks. For square networks in two-dimensions the number of components in the network is twice the square of the side length. However, this does not take into account the number of shunts present, which depends on the number of capacitors. Results in the literature have quoted the matrix size in terms of the number of components[177, 188], however, in this research the side length of the matrix is used.

Once a composition for the model dielectric network had been chosen various sized networks were simulated to observe changes in dielectric response. The square matrix side lengths constructed in two-dimensions were 4, 8, 16, 32, 64, 128 and 256. The networks were solved on standard Windows PCs (450 MHz-1.9 GHz CPU, 64 Mb-1 Gb RAM) and it is envisaged that larger networks can be solved with more resources. Larger networks of a side length of 512 components were produced, however, the resources available to solve the file were insufficient. Twenty five runs at each network size were simulated. The results for the R-C network sizes of 16 and 64 components were compared with reported results[177, 187].

In the three-dimensional case the number of components, n_{comp}, (ignoring the 1 GΩ shunts) is given by equation 6.1. The structure of the three-dimensional array is given in Appendix V.

$$n_{comp} = 2a^2(a+1) + a(a^2 - 1)$$ {6.1}

While cubic network side lengths up to 64 components were produced (4, 8, 16 and 32 components), only arrays up the side length of 32 components could be solved. Again 25 runs at each size were simulated to examine the influence of the network size.

6.5 NETWORK PRODUCTION

The circuits generated were originally two-dimensional arrays of components, however, real materials are three-dimensional. For this reason, a three-dimensional model was constructed and compared with the two-dimensional model.

6.5.a   TWO-DIMENSIONAL NETWORK PRODUCTION

Preliminary networks were constructed by rolling a 10-sided dice and using the random numbers generated to decide whether the component to be placed in the circuit was a resistor or a capacitor. The desired R-C ratio was decided by assigning the dice numbers to either a resistor or a capacitor. For instance, to produce a 50:50 R-C network the numbers 0-4 corresponded to resistors and 5-9 to capacitors. With this in mind the network was constructed from its top left corner and all the vertical components added first, Figure 6.3(a). The horizontal elements were then added, Figure 6.3(b).
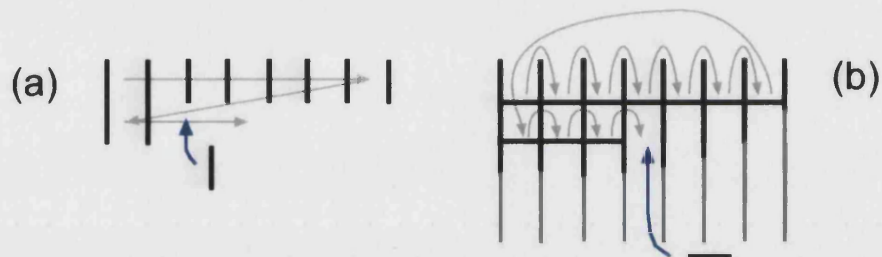
Figure 6.3: Network construction by placement of (a) vertical components first

and then (b) horizontal components.

This method limited the change in percentage of capacitors (and resistors) to steps of 10% and is time consuming, typically taking five hours to produce a square network with a side length of 16 components. As manual construction of the networks was inefficient, a faster method was required. The circuit simulation software used in this work can read circuits that are stored in a special format within a text file. Files in this format were produced by running a macro written in Matlab. The basic file structure used and details of how the network was constructed by the Matlab macro is given in Appendix V.

The circuit is made up of two important parts, the components and the nodes. The nodes determine how the components are linked together. The Matlab constructed circuit was built in a similar fashion as the ones done by hand, in that the matrix size sets the values of the nodes. This is only possible with the presence of the shunt resistors. The presence of these resistors means that every bond (a bond connects two nodes) has a resistor. Knowing the size of the network and how the components are sequentially added to the network the node values can be deduced. The macro inserts capacitors or resistors randomly between these nodes.

6.5.b   THREE-DIMENSIONAL NETWORK PRODUCTION

A benefit of producing the network via a Matlab script is that a three-dimensional cubic array could be generated, which would be practically impossible if manually constructed, due to the high density of components. Figure 6.4 shows a representation of both the two-dimensional and three-dimensional networks.
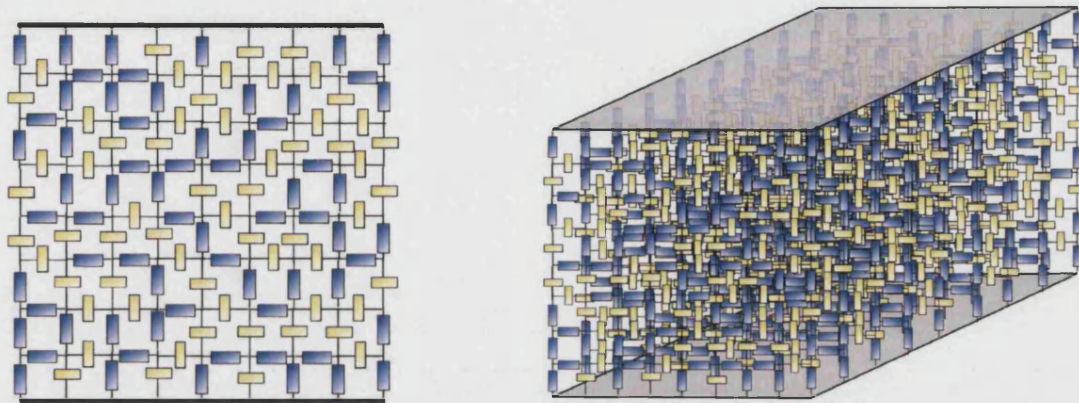
Figure 6.4: Representation of (a) two-dimensional and (b) three-dimensional networks.

The capacitors are represent in yellow and resistors in blue.

The three-dimensional network was constructed by joining the required number of two-dimensional layers together using an "adhesive" layer. Figure 6.5 shows the method used to connect two adjacent two-dimensional layers in the "adhesive" layer. The node values are again predictable once the matrix size and the way the components are sequentially added to the network are known.
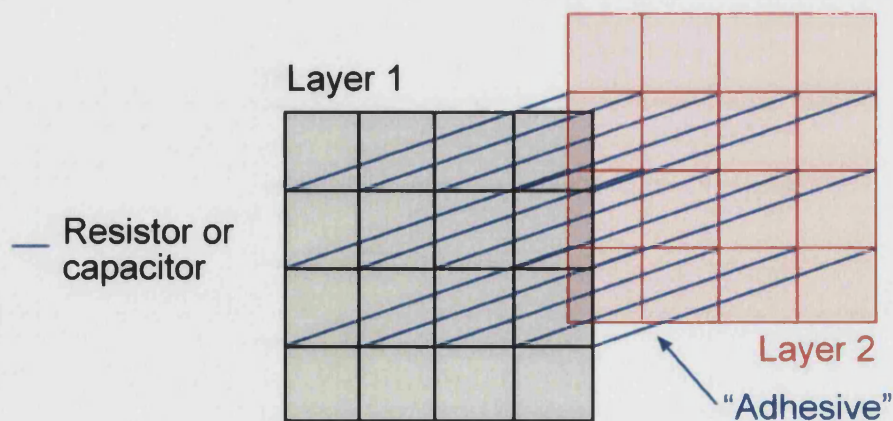
Figure 6.5: The method of connection between two adjacent two-dimensional

layers used in the "adhesive" layer.

The main script, in Appendix V, prompts the user for the required variables as for the two-dimensional case. A sub-macro is then run in which the first two-dimensional layer is generated, after which a second sub-macro creates the "adhesive" layer before the first sub-macro is repeated, then the second, and so on. This continues until the required network depth has been generated. Both sub-macros can be found in Appendix V.

6.6 NETWORK OUTPUT PARAMETERS

After the circuit has been constructed the software solves the simulation. The software used in this work was SIMetrix 3.1, which uses a simulation algorithm from SPICE (Simulation Program (with) Integrated Circuit Emphasis) version 3f.5. The program simulates the behaviour of the circuit over the range of frequencies chosen for the analysis type. Output files can also be created that contain the real and imaginary parts of the voltage (V_{OUT}) and the network phase angle for each stimulus frequency. V_{OUT} is the voltage across the R-C network. The file generated by the Matlab macro can be read into SIMetrix and solved as for a manually drawn circuit. A SIMetrix script (Appendix V) was written to maximise the use of computer resources in solving multiple simulations.

The electrical properties of the circuit, in terms of relative permittivity and conductivity, can be obtained using the properties of the complex impedance, Z^*. This parameter can be split into its real impedance, Z', and imaginary impedance, Z'', parts, as shown in equation 6.2. i is the square root of minus one ($i = \sqrt{-1}$).

$$Z^* = Z' + iZ'' \hspace{3cm} \{6.2\}$$

The complex admittance, Y^*, is the inverse of the complex impedance, Z^* and has real, Y', and imaginary, Y'', parts. These parts are related to the conductivity, σ, and capacitance, C, via equations 6.3 and 6.4 [182], where ω ($=2\pi f$) is the angular frequency of the stimulus.

$$Y' = \sigma \hspace{3cm} \{6.3\}$$

$$Y'' = \omega C \hspace{3cm} \{6.4\}$$

6.6.a   NETWORK CONDUCTIVITY

The conductivity, σ, of the network at a certain applied voltage can be calculated from the relationship given in equation 6.5.

$$\sigma = \frac{t}{RA} \qquad \{6.5\}$$

In two-dimensions the cross-sectional area, A, is simply the matrix size, a. The sample thickness, t, is also equal to a, as it is a square array. R is the resistance, which from Ohm's law is equal to the voltage divided by the current. The current has been set to 5×10^{-7} A by the large external resistor of 100 MΩ (as shown in Figure 6.2) and as such,

$$\sigma = \frac{5 \times 10^{-7}}{real(V_{OUT})} \qquad \{6.6\}$$

V_{OUT} is the voltage measured across the network. In three-dimensions the network has a cross-sectional area of a^2 and this is taken into account when calculating the conductivity.

6.6.b   NETWORK REAL RELATIVE PERMITTIVITY

The imaginary part of the admittance, Y", is proportional to the imaginary part of the inverse voltage, V_{OUT}. Thus from equation 6.4,

$$Y'' = \omega\, C \propto imag\left(\frac{1}{V_{OUT}}\right) \qquad \{6.7\}$$

The real part of the relative permittivity can now be calculated using the relationship given previously, equation 4.15, which states the capacitance is proportional to the relative permittivity.

$$\varepsilon' \propto \frac{imag\left(\dfrac{1}{V_{OUT}}\right)}{\omega} \qquad \{6.8\}$$

6.6.c   NETWORK IMAGINARY RELATIVE PERMITTIVITY

The real part of the admittance, Y', is proportional to the real part of the inverse voltage, V_{OUT}. The imaginary part of relative permittivity is related to the conductivity by equation 6.9:

$$\varepsilon'' \omega \propto \sigma \propto real\left(\frac{1}{V_{OUT}}\right) \tag{6.9}$$

As such the imaginary relative permittivity is simply proportional to the real($1/V_{OUT}$) divided by the frequency.

6.6.d   NETWORK PHASE ANGLE

The phase angle, a measure of the lag of voltage behind the current, is obtained directly from the SIMetrix simulation. For a resistor the phase angle is 0° (the stimulus voltage and current response are in phase), while a capacitor has a value of -90° (the current leads the voltage).

6.7 POWER LAW ZONE

It has been reported that threshold theory predicts that above the percolation limit a region exists where increasing the conductive phase content produces a power law increase in the electrical conductivity and relative permittivity[125]. This effect has been observed experimentally in a tungsten-silica system[125]. In two-dimensions, the percolation threshold is at a conductive phase fraction of 0.5 [170, 179, 182] for a system where the constituents are of equal size. In three-dimensions, it is approximately 0.248 [171, 178, 182]. However, the percolation threshold value can vary in practice, depending on the size of the constituent phases, as shown in Figure 6.6.
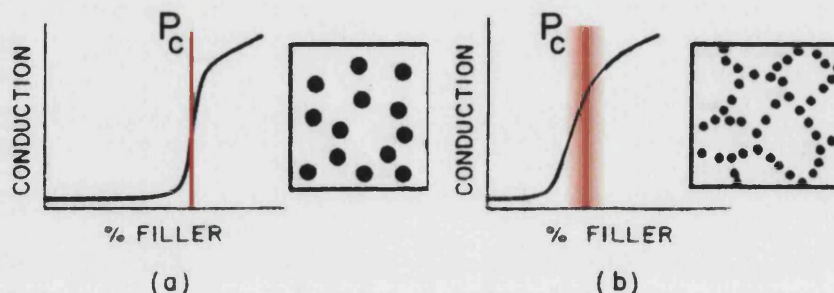
Figure 6.6: Variation of percolation threshold, P_c, with (a) similar and

(b) different sized particles[181].

As the particle sizes become more dissimilar the threshold moves to lower proportions. This occurs as the smaller conductor particles become segregated at the grain boundaries[181]. The threshold also depends on the aspect ratio of the filler[124], for example a value of ~0.75vol% graphite in polypropylene has been reported as the percolation threshold due to the high aspect ratio of the graphite fibres[183].

Power law regions have been observed in simulated dielectric results[177]. It has been reported that the complex conductivity, $\sigma*$, and permittivity, $\varepsilon*$, for a dielectric composed of a random microscopic network of purely dielectric and purely conductive material, follows equation 6.10 and 6.11 [177].

$$\sigma*(\omega) = (i\omega\varepsilon\varepsilon_0)^\alpha \sigma^{(1-\alpha)} \propto (i\omega)^\alpha \qquad \{6.10\}^{177}$$

$$\varepsilon*(\omega) = \frac{\sigma*(\omega)}{i\omega\varepsilon_0} \propto (i\omega)^{(\alpha-1)} \qquad \{6.11\}^{177}$$

An interpretation of the power law exponent, α, is that it represents the proportion of capacitive material and may be useful in the characterisation of the networks produced[177].

6.8 DEFECT INCLUSION IN A REPRESENTATIVE DIELECTRIC NETWORK

With the use of the Matlab script it became possible to incorporate a random distribution of components having desired properties, such as high or low resistance, into the resistor-capacitor network. Networks, 256 of each, were constructed with resistor defect fractions of 0, 0.02, 0.05, 0.10 0.15, 0.20, 0.25 and 0.30. These fractions were chosen for comparison with the measured relative permittivity of the barium titanate-silver composites fabricated with 0, 0.02, 0.05, 0.10 0.15, 0.20, 0.25wt% $AgNO_3$. The resistor defect values used where 1 $\mu\Omega$, 10 Ω, 1 kΩ, 1 MΩ and 1 GΩ. Networks containing the same fractions of a capacitive defect were also solved in order to examine the effect of a dielectric inclusion on the electrical properties. The capacitor defect values used were 1 μF, 1 nF, 1 pF. Three-dimensional networks containing the same defect values and fractions as above have also been produced and solved.

6.9 COMPUTATIONAL MODELLING RESULTS

6.9.a INTRODUCTION

The behaviour of a dielectric with applied electric field frequency is dependent on the dipole response. Modelling has been employed to assess the effect of using a simple resistor-capacitor network to examine the dielectric properties of simulated materials over a range of frequencies. A standard matrix composition (R:C) that was intended to represent a dielectric material was decided upon before the influence of network size was examined. Finally the effects of resistive and capacitive "defects" were simulated and compared with the literature and experimental results. The results reported in this section are those obtained on circuits produced using Matlab software.

6.9.b INFLUENCE OF NETWORK COMPOSITION ON NETWORK PERFORMANCE

6.9.b.i Two-dimensional network composition results

For the two-dimensional case 128 runs were performed on a 16 component side length matrix (512 components) over a range of resistor contents. The resistor percentage is the number of 1 kΩ resistors multiplied by one hundred and then divided by the total number of resistors (including the 1 GΩ shunts). The results of various network compositions on phase angle, relative permittivity and conductivity are presented in Figure 6.7 for an AC stimulus of 1 kHz.

The graphs are composed of more than one series as different behaviours in the relative permittivity, conductivity and phase angle were observed for the same composition. The trend of phase angle, relative permittivity and conductivity at low resistor contents (trend 1 in Figure 6.7a) are different to that at high resistor contents (trend 2 in Figure 6.7a). These behaviours corresponded to the network behaving in a capacitive (trend 1) or conductive (trend 2) manner and have been reported by Bouamrane[187]. The term "separation" is used to indicate that for the same composition some of the random networks behaved resistively, while some were capacitive. Additional behaviours were observed when analysing the phase angle results. Trend 3 and 4 are results that did not correspond to either capacitive (trend 1) or conductive (trend 2) behaviours. The four trends (1-4) are given in Table 6.1 and relate to the frequency behaviour given in Figure 6.8(d).

Table 6.1: Behaviour of the phase angle indicating the four trends observed in Figure 6.8(d).

Trend	Behaviour
1	*Capacitive* – The response for all frequencies is capacitive.
2	*Conductive* - The response for all frequencies is resistive.
3	*Low-High* – The frequency response changes from capacitive to resistive as the frequency increases.
4	*High-Low* - The frequency response changes from resistive to capacitive as the frequency increases.

These "separated" results can be averaged, but the response observed may be important, so the difference is highlighted in this work. This behaviour has been observed as a larger error in practical resistivity results with increasing silver content, Section 5.3.d. This occurs as some of the samples are conducting (conductive path between electrodes) while others are still capacitive (no conductive path between electrodes) at certain silver contents. The plots in Figure 6.7 indicate that the response of the two-dimensional network varies with the resistor-capacitor ratio. Figure 6.7(a) reveals that at a low fraction of resistors the network behaviour is capacitive (phase angle of -90°), as would be expected. At a high resistor content the response is resistive as indicated by a phase angle of 0°. In between these two cases the imaginary relative permittivity and conductivity increase gradually and a peak in the real relative permittivity is observed, Figure 6.7(b). This real relative permittivity peak appears to correspond to the 50:50 composition, which is the percolation threshold value in the two-dimensional case.
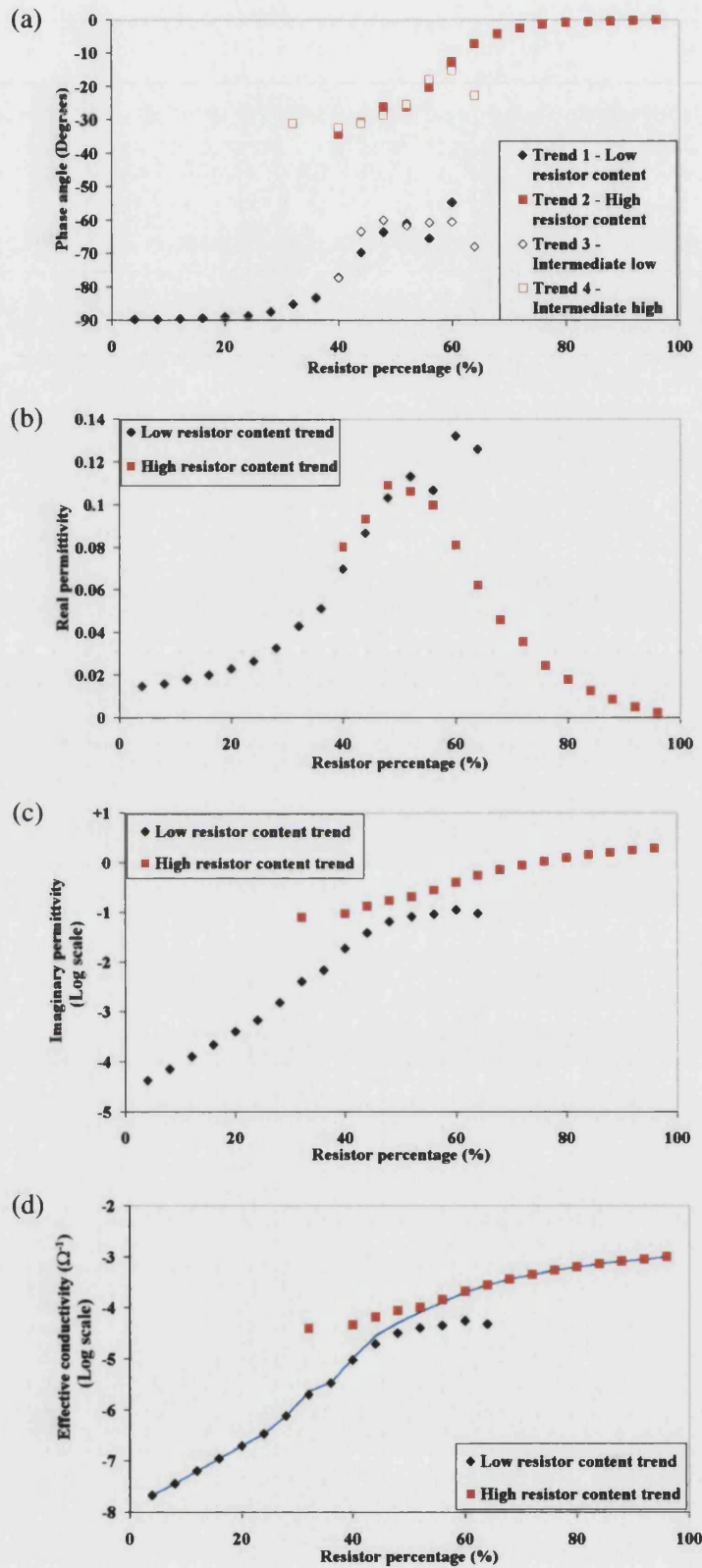
Figure 6.7: Influence of increasing resistor content on a two-dimensional network showing

(a) variation of phase angle, (b) peak in the real relative permittivity and steady increase of

(c) imaginary relative permittivity and (d) conductivity at a frequency of 1 kHz.

The separation in the capacitive and conductive results can be observed more easily when the frequency behaviour of the network at certain compositions is considered. Figure 6.8 shows the relative permittivity, conductivity and phase angle versus frequency for a range of resistor contents. For the real relative permittivity, Figure 6.8(a), the low frequency behaviour value is higher than that at high frequency. At low frequencies the resistors act as short circuits, while at high frequency the resistors act as open circuits and the response is limited by the capacitors. The low frequency real relative permittivity is greater than that at high frequency as the resistors (short circuits) link parallel capacitors.

Separation behaviour is observed in the 40% and 60% resistors content networks at high frequency, Figure 6.8(a). If the resistor content is low (20%R – the behaviour is capacitive, i.e. trend 1) or high (80%R – the behaviour is conductive, i.e. trend 2) a separation of the results is not observed. The frequency response below ~100 Hz is due to the 1 GΩ resistors that shunt the capacitors and a reduced imaginary relative permittivity would be expected if they were not present. A peak in the imaginary relative permittivity, Figure 6.8(b), is due to the frequency relating to the time constant (~1/RC) of the circuit and disappears at high resistor contents due to the non-zero DC conductivity of the network. The graphs show that at 40% resistors a proportion of the networks have become conducting (40*), as indicated in Figure 6.8(c) where the low frequency conductivity is tending towards that of a 1 kΩ resistor ($10^{-3}\Omega^{-1}$), while the rest are capacitive (40). The separation is observed at low frequency for the imaginary relative permittivity and conductivity. The complexity in the separation is highlighted by Figure 6.8(d) that shows the phase angle behaviours of the network compositions with frequency. The four possible trends, as mentioned in Table 6.1, of phase angle with frequency are shown by the 60% resistor simulation. The network structure that produces trends three and four are not known.

For the relative permittivity and conductivity a well-defined behaviour is observed by modelling, regardless of composition, at a frequency of ~100,000 Hz. This well-defined region has been reported to follow a power law behaviour, which is discussed later.

Separation in results (capacitive and resistive behaviour at fixed composition) has been observed in experimental electrical property results where larger property variations occurred as the silver content increased, see Section 5.3.d. This was for compositions where the weight fraction of silver was ~20% (~10vol%).

Figure 6.8: Change in (a) real relative permittivity, (b) imaginary relative permittivity, (c) conductivity and (d) phase angle with frequency for certain resistor-capacitor ratios (two-dimensional) showing the trends as in Table 6.1, with trend 2 (*), trend 3 (-) and trend 4 (/). The legend indicates the percentage of resistors.

The number of simulated networks producing a conducting behaviour increased with the percentage of resistors in the network. Figure 6.9 shows the proportion of non-conducting simulation runs as resistor content increases. Networks began to show conducting tendencies at 40% resistors and by 60% resistors all networks were conducting. A conducting behaviour is undesirable for simulating a dielectric (capacitive) material. This effect occurs, as with the random placement of components it is possible that a conducting network will be formed, below the expected percolation threshold, across the finite size of the network.
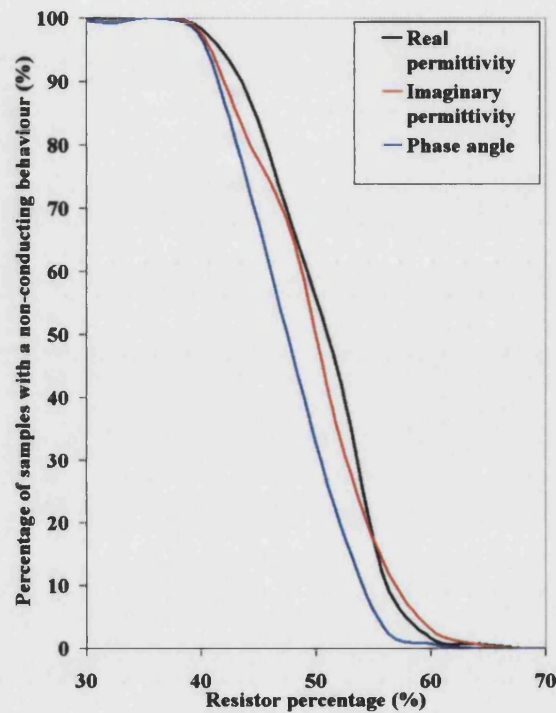
Figure 6.9: Percentage of two-dimensional networks of non-conducting

behaviour in the compositional range of 30-70% resistors.

From these results, in order to simulate a capacitive material, such as barium titanate, a resistor-capacitor ratio of 30:70 was chosen to reduce the possibility of completely conducting networks occurring due to the finite network size.

6.9.b.ii   *Three-dimensional network composition results*

In the three-dimensional case 128 simulations were run with a network side length of 16 components. The response at 1 kHz is shown for the phase angle, permittivities and conductivity in Figure 6.10. As in the two-dimensional case separation was observed.
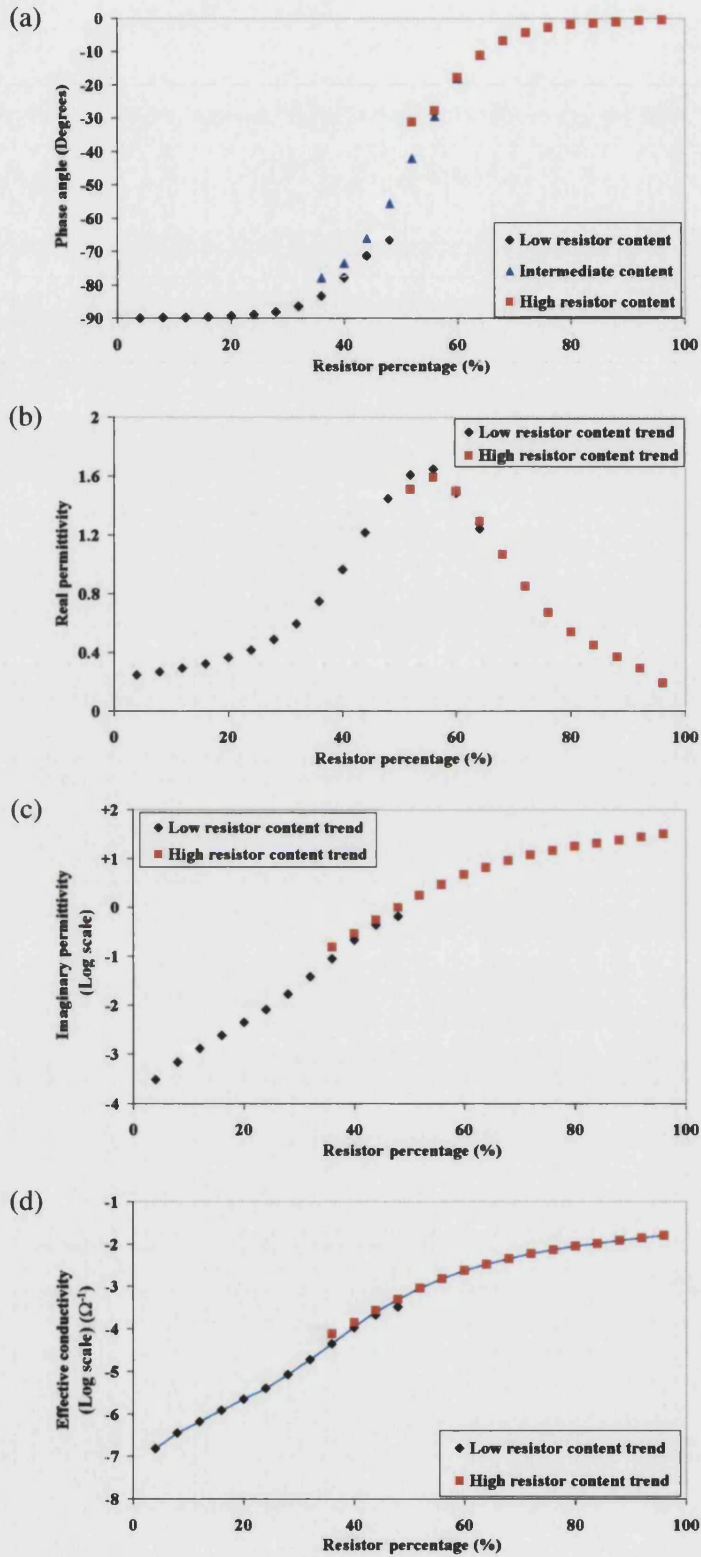
Figure 6.10: Influence of increasing resistor content on a three-dimensional network showing

(a) variation of phase angle, (b) peak in the real relative permittivity and steady increase of

(c) imaginary relative permittivity and (d) conductivity at a frequency of 1 kHz.

The results are similar to the two-dimensional case, which is unexpected as the percolation threshold is at approximately 25% second phase content in three-dimensions. An explanation for this is lacking, but there are some differences in the results. The low-high behaviour (trend three in Figure 6.7a) is not present, and the phase angle results are more continuous in the three-dimensional case, as observed by comparing Figures 6.6(a) and 6.9(a). A clearer trend is also observed for the real, and imaginary, permittivities, as well as the conductivity. It is noted that both the real and imaginary relative permittivity and conductivity are displaced to higher values in the three-dimensional case, when compared to the two-dimensional results, see Figures 6.7(b), 6.10(b), 6.7(c), 6.10(c), 6.7(d) and 6.10(d).

The behaviour of the relative permittivity, conductivity and phase angle with frequency were plotted, Figure 6.11, as with the two-dimensional results. Unlike the two-dimensional real relative permittivity result, no high frequency separation is observed for the 40%R content, Figure 6.11(a), however, it is present in the imaginary relative permittivity and conductivity plots at low frequency.

The phase angle results, Figure 6.11(d), show a rotational symmetry between the capacitive and conductive responses at complementary resistor contents. For example the 20%R and 80%R responses are similar when one is rotated by 180° and overlaid on the other, similarly for the 40%R* and 60%R* trends. The loss of trend 3 in the three-dimensional case suggests that it is an artefact of the two-dimensional network. The similarity between the two-dimensional and three-dimensional simulations indicates that it may be possible to obtain results using the two-dimensional model that are sufficiently close to the three-dimensional case, but with the benefit of larger networks (reduced dispersion of results). As with the two-dimensional relative permittivity and conductivity results, uniform behaviour, regardless of network composition, is observed at a frequency of ~100,000 Hz.
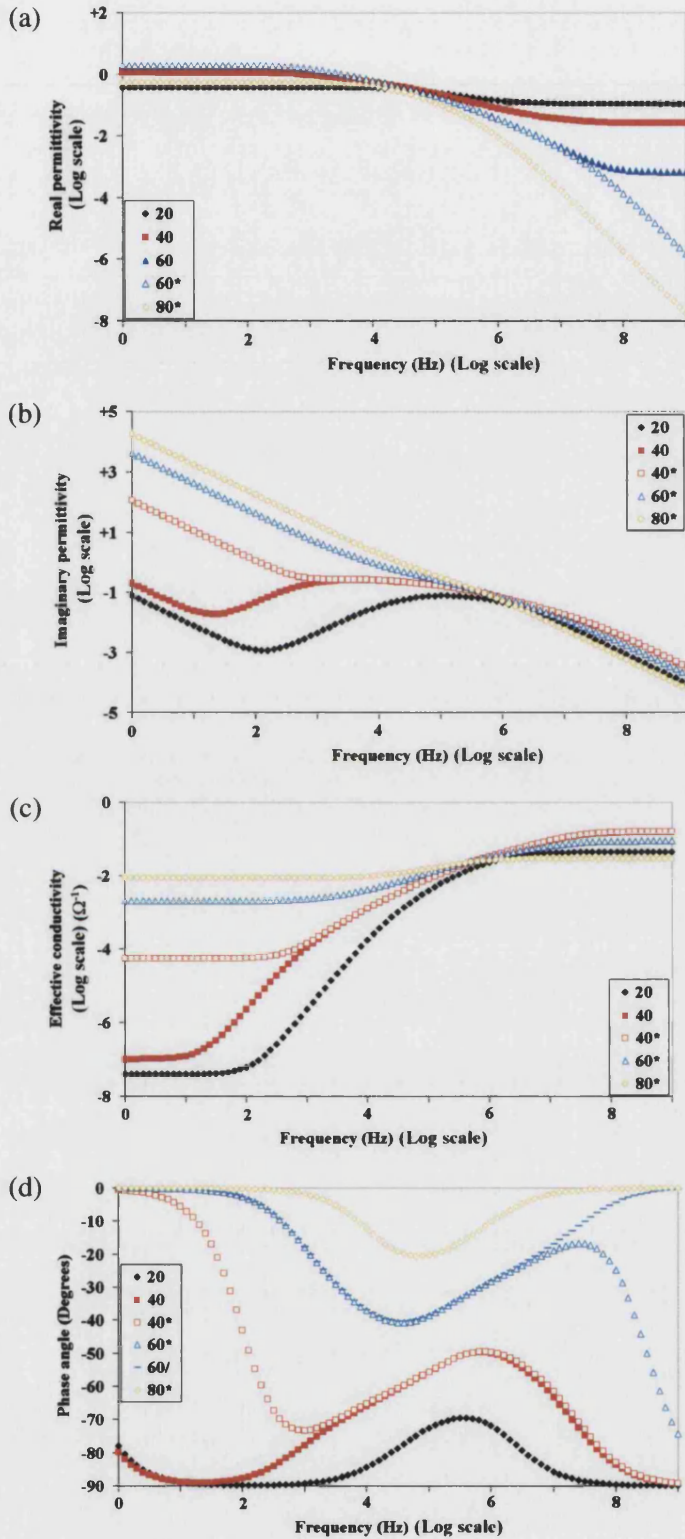
Figure 6.11: Variation in (a) real relative permittivity, (b) imaginary relative permittivity, (c)
conductivity and (d) phase angle with frequency for specific resistor-capacitor ratios showing trend
2 (*) and trend 4 (/). The legend indicates the percentage of resistors for each series.

As in the two-dimensional case, the number of networks that had a non-conducting behaviour were plotted against network composition, Figure 6.12. The figure shows that the percentage of networks with conducting behaviour for imaginary and phase angle are identical, as the series overlap. In terms of the real relative permittivity the majority of simulation results were conductive for networks of >60%R, while this is the case >45%R for the imaginary and phase angle response. This infers that the imaginary and phase angle response is more sensitive to the network non-conducting behaviour. At a resistor content of 70% all the simulation results were conductive. The results are significantly different from those in two-dimensions, Figure 6.9, where the proportion of conducting networks is similar for relative permittivity (real and imaginary) and phase angle.
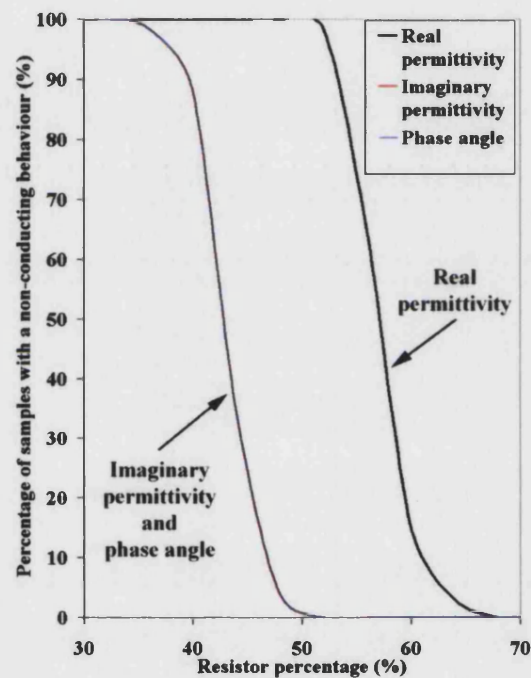
Figure 6.12: Percentage of three-dimensional simulations

with non-conducting behaviour.

As the percolation threshold, in this three-dimensional case, appears to be at the 50:50 resistor-capacitor ratio a 30%:70% composition was also chosen for use as the matrix material in further three-dimensional studies, as was the case for the two-dimensional networks.

6.9.b.iii   *Comparison of results with reported results*

6.9.b.iii.a   Two-dimensions

To obtain a comparison of the frequency response of relative permittivity, conductivity and phase angle, with reported results on similar two-dimensional networks[177], networks (two-dimensional) were produced that had resistor:capacitor of 60:40, 50:50 and 40:60. The results simulated by a Matlab-Simetrix method for the real and imaginary permittivities as a function of frequency are given in Figures 6.12 and 6.13. The data plotted is for all 256 simulations at each R:C ratio and shows the dispersion of results due to the random construction of the networks. Conductivity versus frequency results are shown in Figure 6.15 and phase angle in Figure 6.16. Real and imaginary permittivities and phase angle are compared with results adapted from reported literature[177]. The reported[188] conductivity response from the Star-Delta simulation technique is used for comparison of network conductivity, Figure 6.15(d).
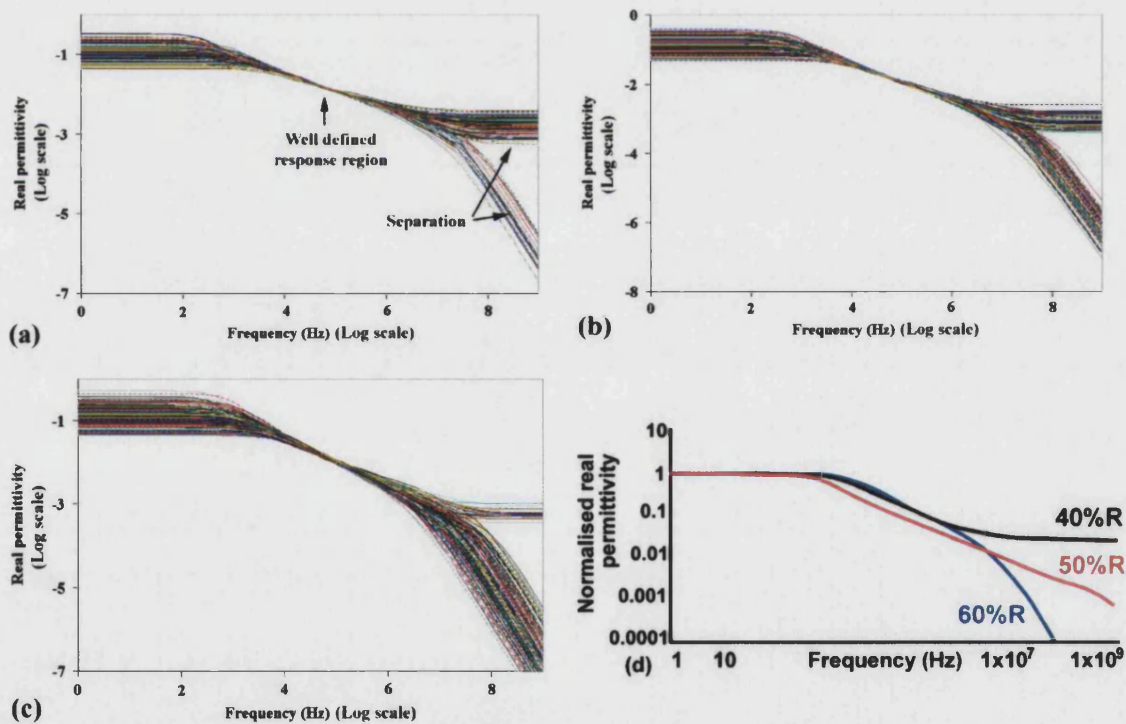
Figure 6.13: Variation of real relative permittivity with frequency for resistor-capacitor ratios of (a) 40%R:60%C, (b) 50%R:50%C, (c) 60%R:40%C and (d) the literature[177] (two-dimensional).

As the frequency increases, the real relative permittivity is unaffected until the loss peak frequency is reached when a linear decrease occurs to a lower plateau. At low frequencies the resistors act as short circuits, while at high frequency the resistors act as open circuits and the response is limited by the capacitors. The low frequency real relative permittivity is greater than that at high

frequency as the resistors (short circuits) link parallel capacitors. Separation of non-conductive (forms a plateau) and conductive (relative permittivity continues decreasing) networks is observed at high frequency only. Even though significant dispersion is observed at low and high frequency a well defined response is shown at a frequency ~100,000 Hz; this is discussed later. The literature result, Figure 6.13(d), shows the overall trend of the majority of networks at a specific composition. With a majority of capacitors a double plateau trend is observed (Figure 6.13(d)-40%R compare with Figure 6.13(a)), while with a majority of resistors the high frequency response is conducting (Figure 6.13(d)-60%R compare with Figure 6.13(c)).

Ignoring the imaginary relative permittivity behaviour below 100 Hz, which is due to the 1 GΩ shunts, a loss peak is observed at ~1000 Hz in all cases, Figure 6.14. Separation is shown at low frequency and the well-defined imaginary relative permittivity response is observed at a frequency of ~100,000 Hz. The peak in the imaginary relative permittivity is observed less often at high resistor contents due to the non-zero DC conductivity of the network[177]. Comparison with the literature, Figure 6.14(d), indicates that the frequency response of the imaginary relative permittivity is in good agreement with the response simulated in this work.
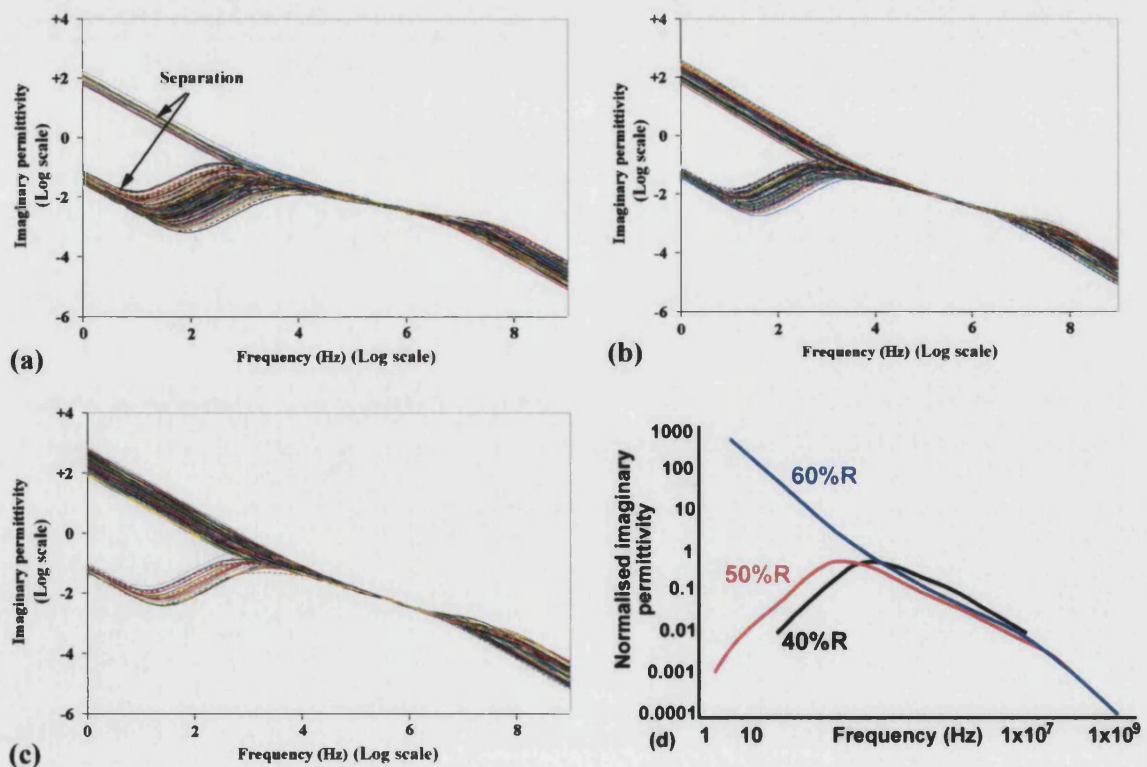
Figure 6.14: Variation of imaginary relative permittivity with frequency for resistor-capacitor ratios of (a) 40%R:60%C, (b) 50%R:50%C, (c) 60%R:40%C and (d) the literature[177] (two-dimensional).

The conductivity results from simulations in this work (Figure 6.15(a),(b) and (c)) are in good agreement with those reported using the Star-Delta transformation technique (Figure 6.15(d)), especially at high frequency. The discrepancies in the 40%R:60%C and 50%R:50%C ratios is respectively due to the 1 GΩ shunts and plotting an average of the results.
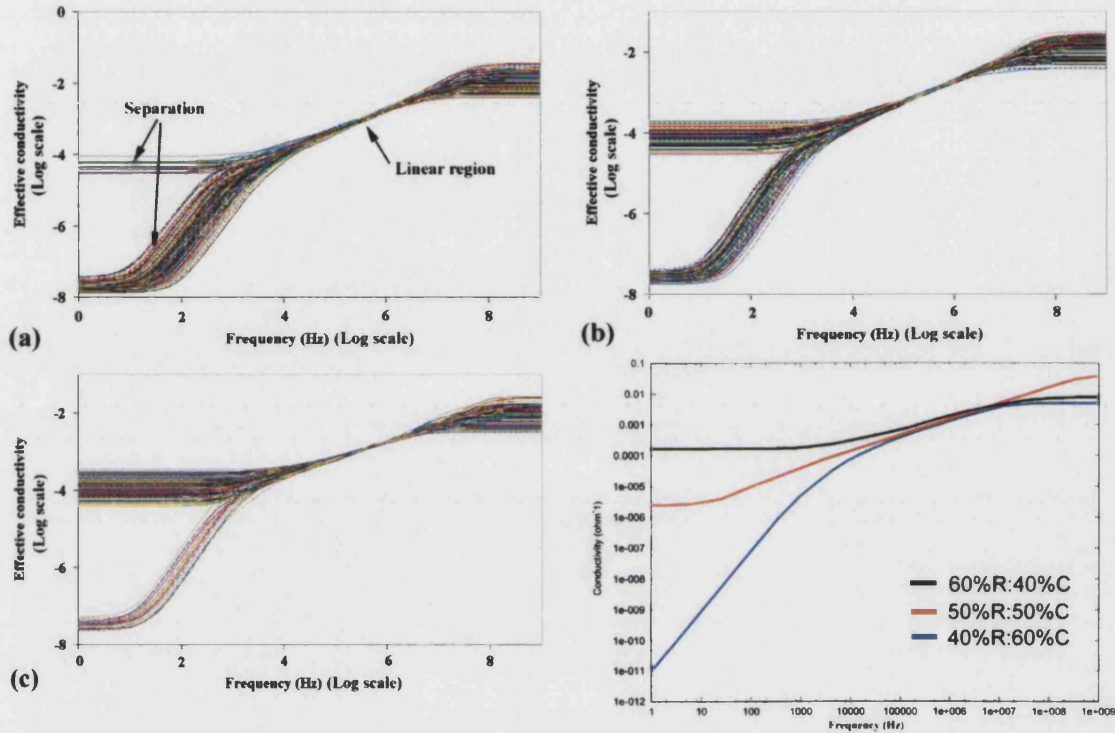
Figure 6.15: Variation of conductivity with frequency for resistor-capacitor ratios of

(a) 40%R:60%C, (b) 50%R:50%C, (c) 60%R:40%C and (d) Star-Delta technique result[188]

(two-dimensional).

The phase angle graphs in Figure 6.16 indicate the separation, once more, that occurs as the percentage of resistors in the network is modified. The amount of separation is shown by the density of the plots, and indicates that ~10% do not follow the majority of simulations at the 40%R:60%C and 60%R:40%C compositions. The separation is close to 50:50 in the 50%R:50%C situation as expected at the percolation threshold. The literature (Figure 6.16(d)) has reported the phase angle response with frequency and shows the network behaviour more clearly than that reported in this work. The overall trend is still observed, at low resistor content (Figure 6.16(a)-40%R) capacitive behaviour is shown by the high density of data at a phase angle of –90°. At high resistor content (Figure 6.16(c)-60%R) conductive behaviour is observed by the higher density of data at a phase angle of ~0°. At the intermediate network composition (Figure 6.16(b)-50%R), there are four different trends shown, as detailed in Table 6.1. The literature result (Figure

6.16(d)), however, reports that at low frequency the phase angle response is capacitive and changes to the conductive trend at high frequency. This difference is unexplained, however, the plateau at a frequency of ~100,000 Hz exists in both.
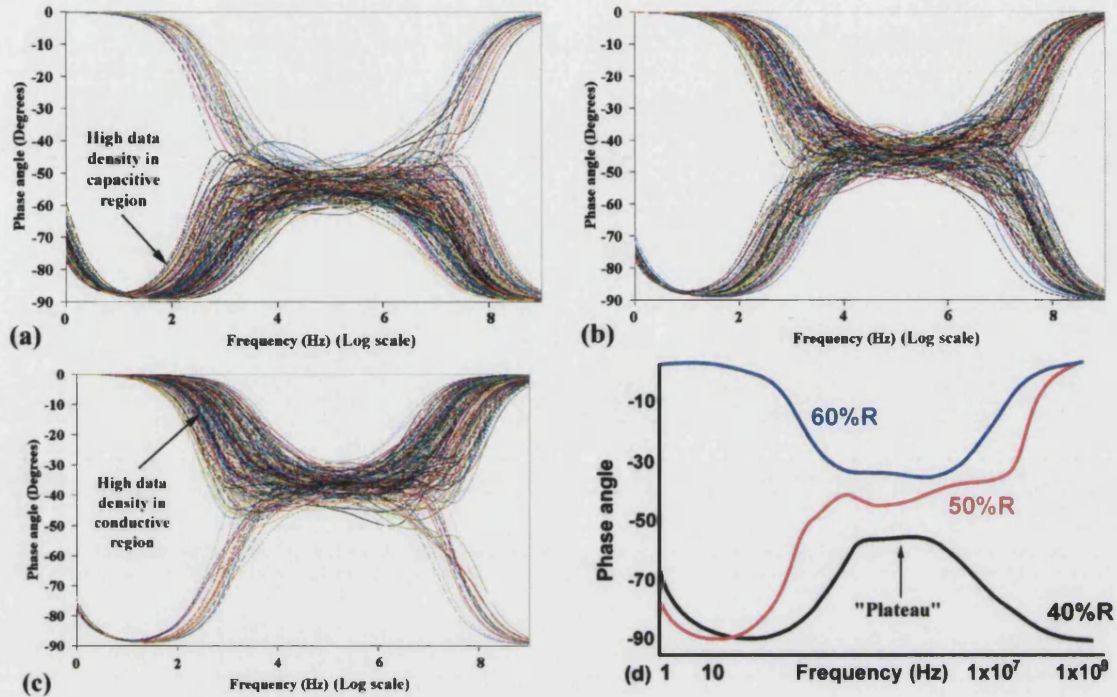
Figure 6.16: Variation of phase angle with frequency for resistor-capacitor ratios of (a) 40%R:60%C, (b) 50%R:50%C and (c) 60%R:40%C, (d) the literature[177] (two-dimensional).

It has been reported in the literature[177] that the linear region in the relative permittivity and conductivity response follows a power law relationship dependent on the network composition. The suggested format for this relationship is that given in equation 6.12., where σ^* is the complex conductivity of the network and ω the frequency of the stimulating field. The parameter α is the fraction of capacitors in the network.

$$\sigma^*(\omega) \propto (i\omega)^\alpha \qquad \{6.12\}^{177}$$

To ascertain if this power law relationship exists in the results modelled in this study a trend line was fitted to the conductivity data in the frequency range 1×10^3-1×10^7 Hz, as this corresponded to the linear region of the conductivity-frequency graph, such as that highlighted in Figure 6.15. The gradient, α, of a power law trend line fitted to the conductivity versus frequency plot for the various network compositions are given in Table 6.2.

Table 6.2: Fraction of capacitors, α, for three different two-dimensional network compositions.

Network type (%R:%C)	α
60:40	0.399
50:50	0.487
40:60	0.594

The calculated values for α propose that the simulated results in this study follow the power law relationship in the frequency response range 1×10^3-1×10^7 Hz, as observed in the literature[177]. This is additional confirmation that the results produced by the modelling technique are in good agreement with that previously published. It is noted, however, that only those results that followed the required capacitive or conductive trend were used.

6.9.b.iii.b   Three-dimensions

To compare with the two-dimensional results, three-dimensional networks with the same compositions (60%R:40%C, 50%R:50%C and 40%R:60%C) and network side length (16 components) were simulated. Results are presented in the following figures; real relative permittivity in Figure 6.17, imaginary relative permittivity in Figure 6.18, conductivity in Figure 6.19 and phase angle in Figure 6.20.

For the real relative permittivity the three-dimensional results are about a magnitude higher than the two-dimensional results due to the larger number of capacitor elements. At low frequencies the resistors act as short circuits, while at high frequency the resistors act as open circuits and the response is limited by the capacitors. The low frequency real relative permittivity is greater than that at high frequency as the resistors (short circuits) link parallel capacitors. Separation into conductive and capacitive trends does not occur until the 60%R:40%C composition, Figure 6.17c. This suggests that the formation of a conductive network is not as easy in the three-dimensional case, which is unexpected as the probability of forming a conducting path across a random network of equal side length in two-dimensions and three-dimensions is the same. It is noted that the power law region is better defined than in the two-dimensional results.
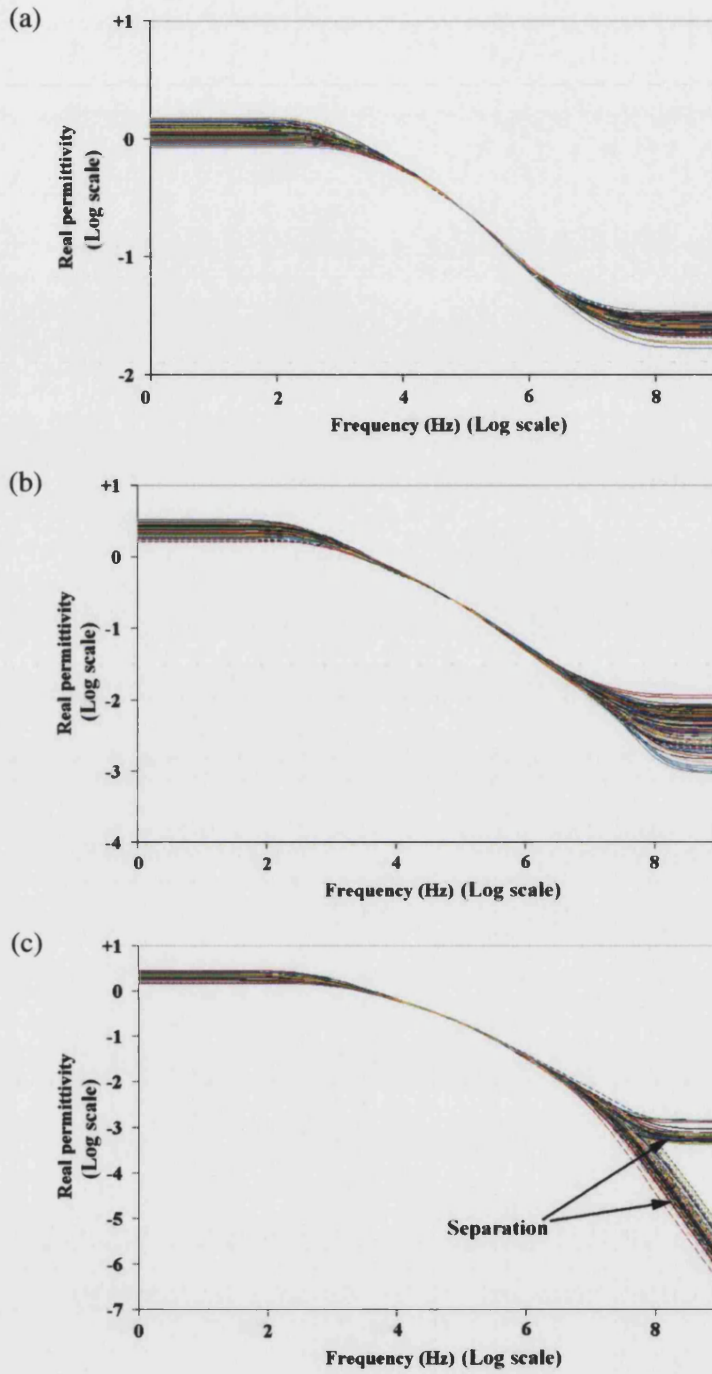
Figure 6.17: Variation of real relative permittivity with frequency for resistor-capacitor ratios of (a)
40%R:60%C, (b) 50%R:50%C and (c) 60%R:40%C for three-dimensional networks.
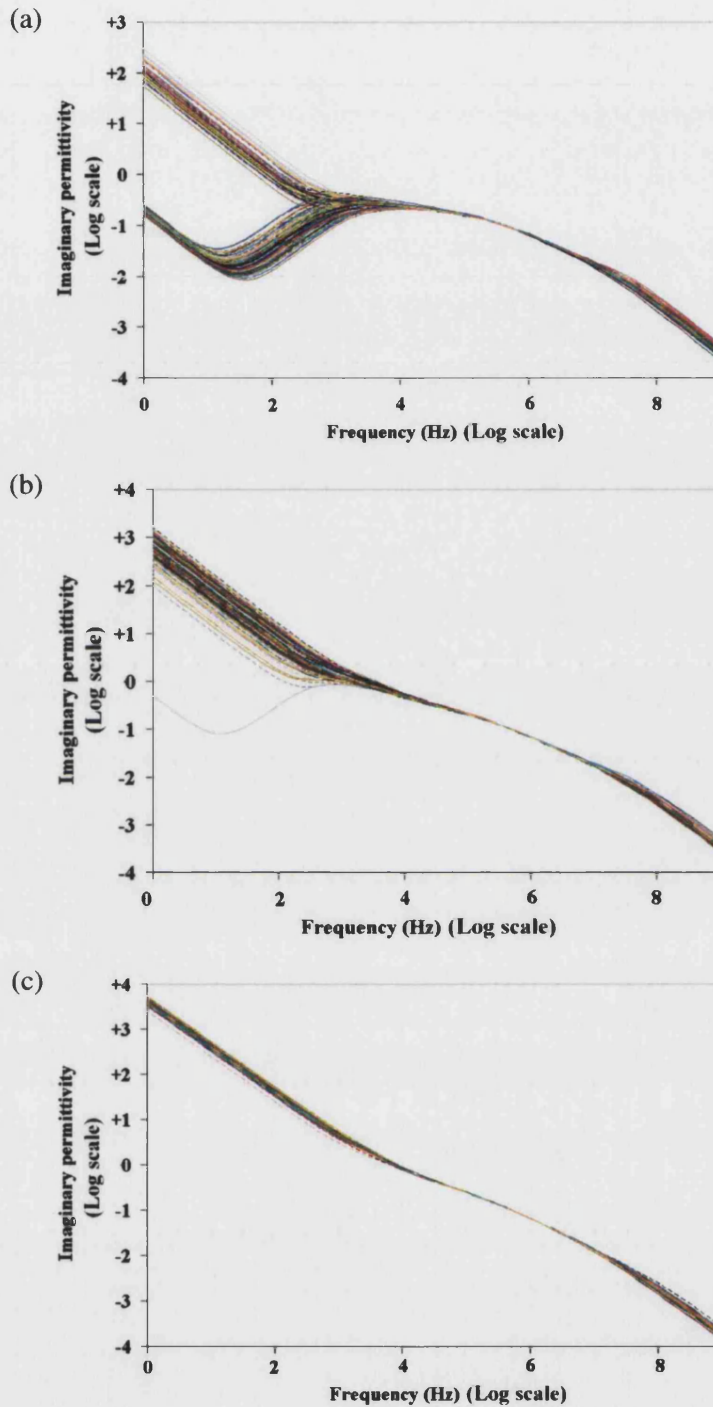
Figure 6.18: Variation of imaginary relative permittivity with frequency for resistor-capacitor ratios of (a) 40%R:60%C, (b) 50%R:50%C and (c) 60%R:40%C for three-dimensional networks.

For the imaginary relative permittivity the low frequency separation is observed, as for the two-dimensional case, except there is no capacitive trend in the 60%R:40%C, which is expected for a composition above the percolation threshold. The magnitude is once again greater than the two-dimensional case by a factor of ~10, otherwise the results are in good agreement.

As with the imaginary relative permittivity the conductivity has no separation occurring in the
60%R:40%C composition (Figure 6.19c). The trends are once again a factor of 10 higher, even
though the third-dimension of the network has been taken into account in the calculation. The
power law region is well defined, but appears to occur at a slightly higher frequency than in the
two-dimensional case.
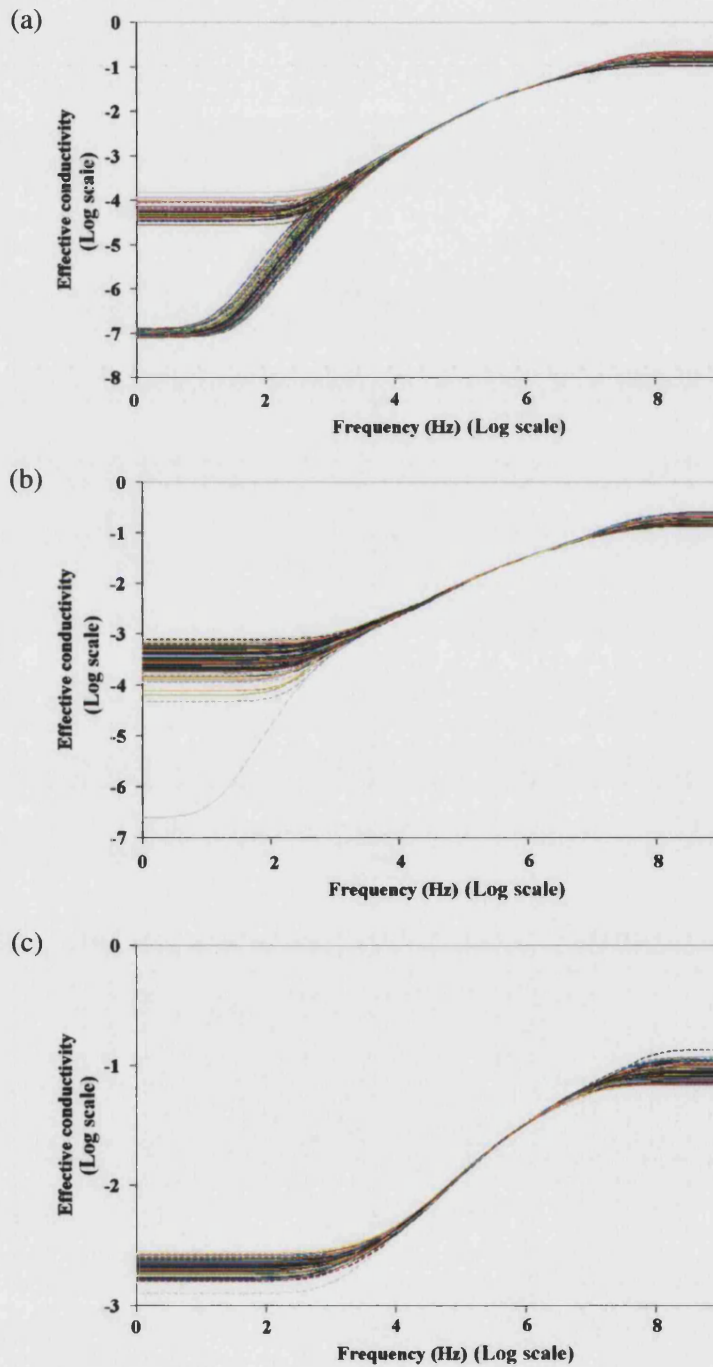
Figure 6.19: Variation of conductivity with frequency for resistor-capacitor ratios of (a)
40%R:60%C, (b) 50%R:50%C and (c) 60%R:40%C for three-dimensional networks.

Comparison of the two- and three-dimensional phase angle results shows significant differences in the response. The high frequency conductive trend is missing in the 40%R:60%C (Figure 6.20(a)) and 50%R:50%C (Figure 6.20(b)) compositions, whereas the low frequency capacitive trend is missing in the 60%R:40%C (Figure 6.20(c)) composition. The phase angle plateau in the three-dimensional case is not as well defined as in the two-dimensional case.
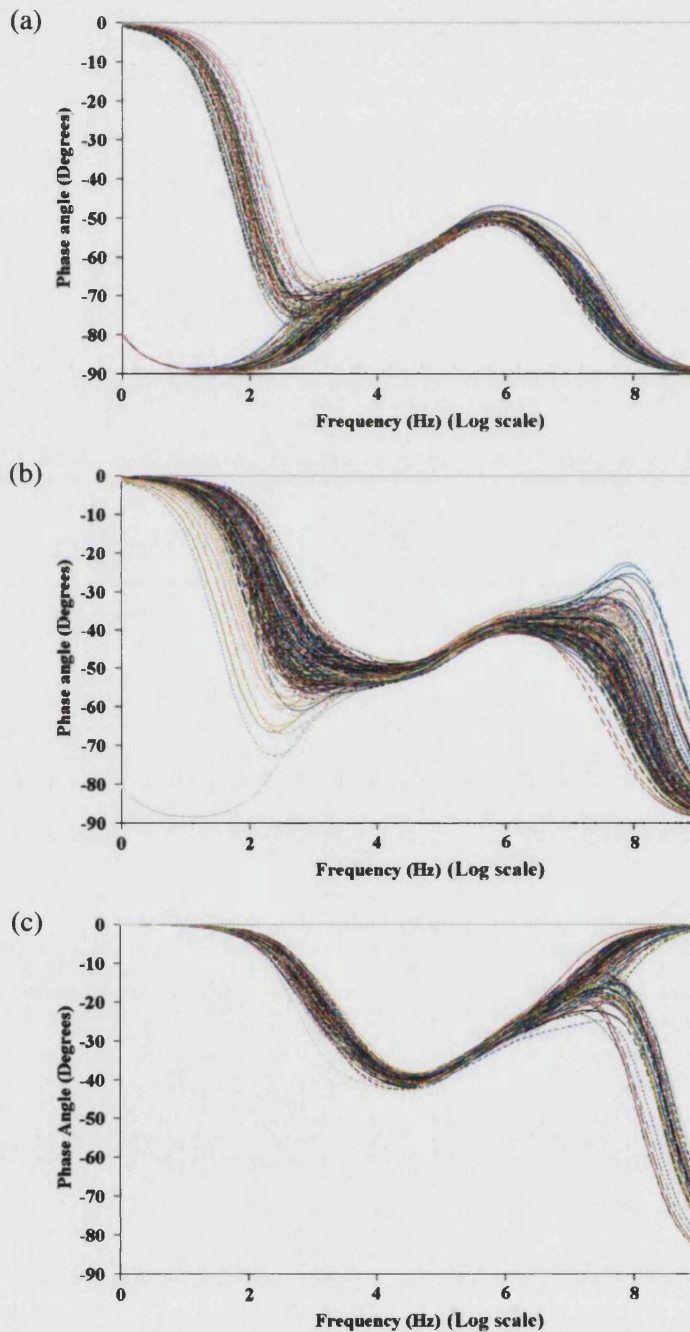
Figure 6.20: Variation of phase angle with frequency for resistor-capacitor ratios of (a) 40%R:60%C, (b) 50%R:50%C and (c) 60%R:40%C for three-dimensional networks.

The fraction of capacitors, α, was calculated from the power law region of conductivity for the three-dimension case and the results are given in Table 6.3. The frequency range in this case was reduced to 5×10^3-1×10^6 Hz as the linear region is less broad than in the two-dimensional situation, even though the dispersion of results is less.

Table 6.3: Fraction of capacitors, α, calculated from the power law region of conductivity versus frequency for three-dimensional networks of various compositions.

Network type (%R:%C)	α
60:40	0.429
50:50	0.573
40:60	0.750

The calculated α value for the three-dimensional networks is higher than that expected from the two-dimensional results. A reason for the higher α value could be that the network fabrication program does not produce the intended resistor-capacitor ratio. This was studied by determining the number of capacitors, and hence resistors, in the network and comparing this value to the intended number set during network construction. Variation was observed to exist, but with three-dimensional network above a side length of 8 components, it is minimal. The remaining possibility is that the arrangement of components in the network, for a fixed composition, in some way affects the result in the three-dimensional case. So far it has not been possible to view the three-dimensional networks to determine the influence of component arrangement.

6.9.c   INFLUENCE OF NETWORK SIZE ON NETWORK PERFORMANCE

Different sized networks were produced using a Matlab macro (Appendix V) and a 30:70 resistor-capacitor composition was used to determine the optimum network, in terms of size and time to solve, to obtain the best results. This network size, thus determined in the two-dimensional and three-dimensional cases, was then used for further study.

6.9.c.i   Two-dimensional 30%R:70%C network size results

The results, Figure 6.21, indicate that for network sizes above a side length of 128 components there is no significant modification of the response behaviour. The standard deviation is plotted in order to represent the dispersion of the results that were observed in 6.9.b.iii.
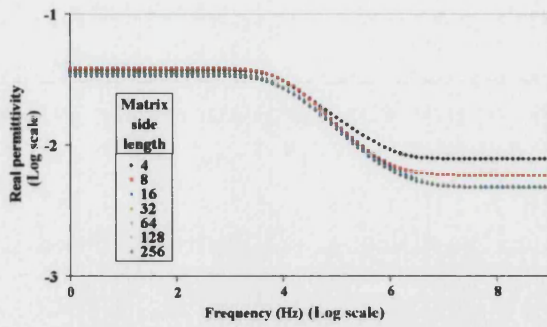
(a) Average real relative permittivity
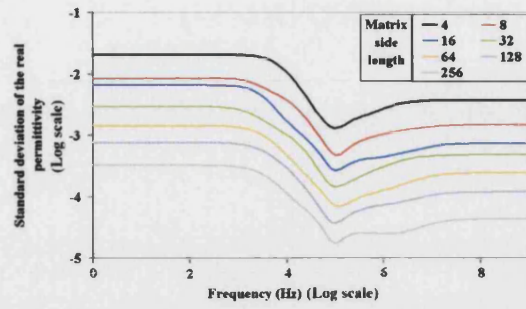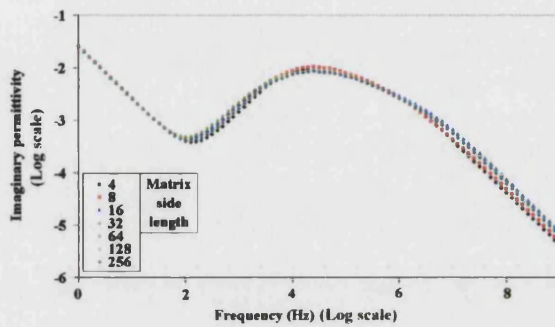
(b) Standard deviation of real permittivity

(c) Average imaginary relative permittivity
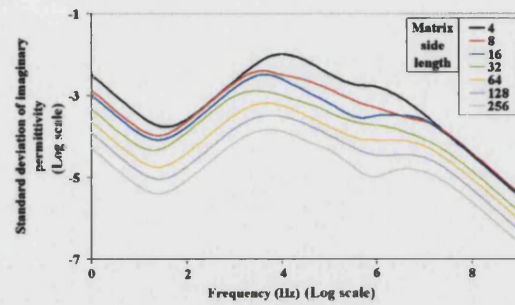
(d) Standard deviation of imaginary permittivity
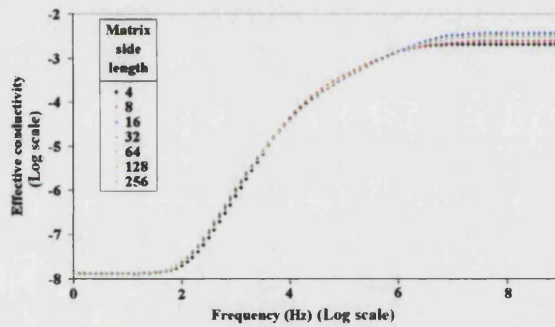
(e) Average conductivity
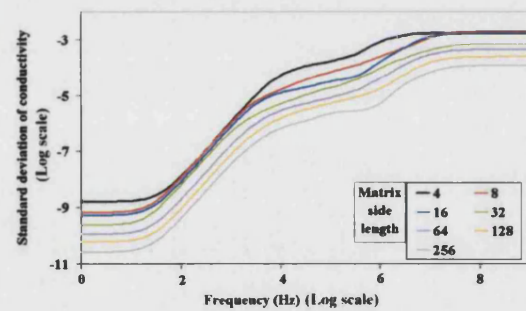
(f) Standard deviation of conductivity
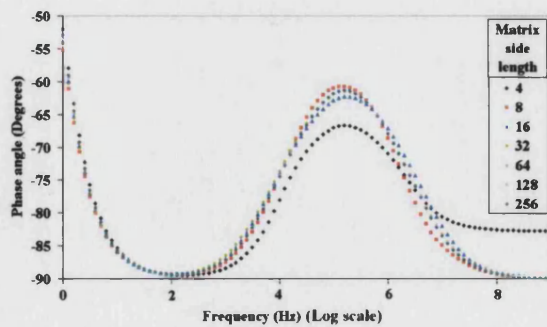
(g) Average phase angle
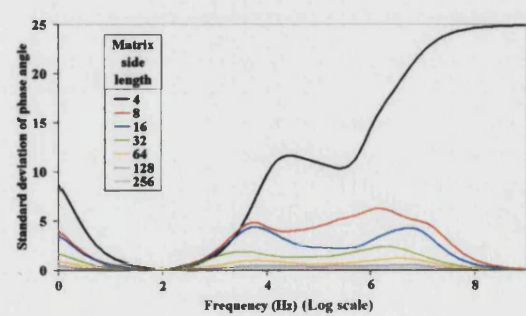
(h) Standard deviation of phase angle

Figure 6.21: Variation of relative permittivity (real (a) and imaginary (c)), conductivity (e) and phase angle (g) with frequency for different two-dimensional 30%R:70%C network sizes. The standard deviations are also shown, which indicate the variation in the responses (b, d, f, h).

The graphs (right hand side of Figure 6.21) show that the standard deviation decreases with increasing network size. This behaviour is expected as the likelihood of a critical component path being created is reduced as the network size increases, similarly for real materials. The dispersion is also observed when testing real materials as a variance in the measured value, due to minor compositional and structural variations in the samples.

At low frequencies the resistors act as short circuits, while at high frequency the resistors act as open circuits and the response is limited by the capacitors. By modifying the network composition the likelihood of a resistor or capacitor continuous link between the electrodes varies. The low frequency real relative permittivity is greater than that at high frequency as the resistors (short circuits) link parallel capacitors. No significant change in the behaviour for relative permittivity, conductivity and phase angle above a threshold network side length of 128 components was observed. The standard deviation, however, continues to decrease as the network size increases for all parameters.

Unpublished work by Bouaurane[187] reported conductivity results of different sized square networks with a 60%C:40%R composition as shown in Figure 6.22. It is observed that networks above a side length of 45 components show no significant change in response with frequency. A network side length of 128 components is used in the further two-dimensional modelling simulations.
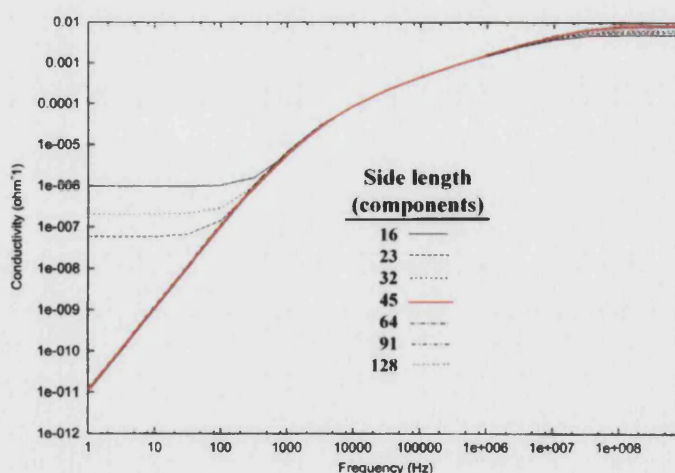
Figure 6.22: Influence of square network size on the conductivity-frequency

response of a 60%C:40%R network. Above a two-dimensional network side

length of 45 components no major response change is observed.

6.9.c.ii   *Three-dimensional 30%R:70%C network size results*

The three-dimensional (cubic) results up to a network side length of 32 components, see Figure
6.23, were similar to the two-dimensional situation as larger network sizes were required to reduce
the standard deviation of the results. No threshold size was reached with the network sizes
simulated as shown by the lack of overlap of data over the simulated frequency range in the real
relative permittivity results, Figure 6.23(a). The SIMetrix programme was unable to solve (or the
solution time was extremely long) networks of side length equal to 64 components. Solving
simulations of networks with a side length of 32 components took approximately 7000 seconds for
each run; therefore a network with a side length of 16 components (simulation time ~120 seconds)
was used in further modelling. As the three-dimensional networks have thickness the conductivity
results are "normalised" by dividing the conductivity, obtained in the same method for two-
dimensional networks, by the number of components forming the side length of the network.
Figures 6.22(e) and (g) shows that with networks of side lengths of 4 and 8 a significant conductive
behaviour appears to exist, as the low frequency conductivity increases and the phase angle is
greater than $-90°$. This also corresponds to the particularly high standard deviation for these 4 and
8 component side length networks, Figures 6.22(f) and (h). It is suggested that these networks are
of insufficient size and the formation of a resistor chain across the network is likely.

(a) Average real relative permittivity

(b) Standard deviation of real permittivity

(c) Average imaginary relative permittivity

(d) Standard deviation of imaginary permittivity

(e) Average conductivity

(f) Standard deviation of conductivity

(g) Average phase angle

(h) Standard deviation of phase angle
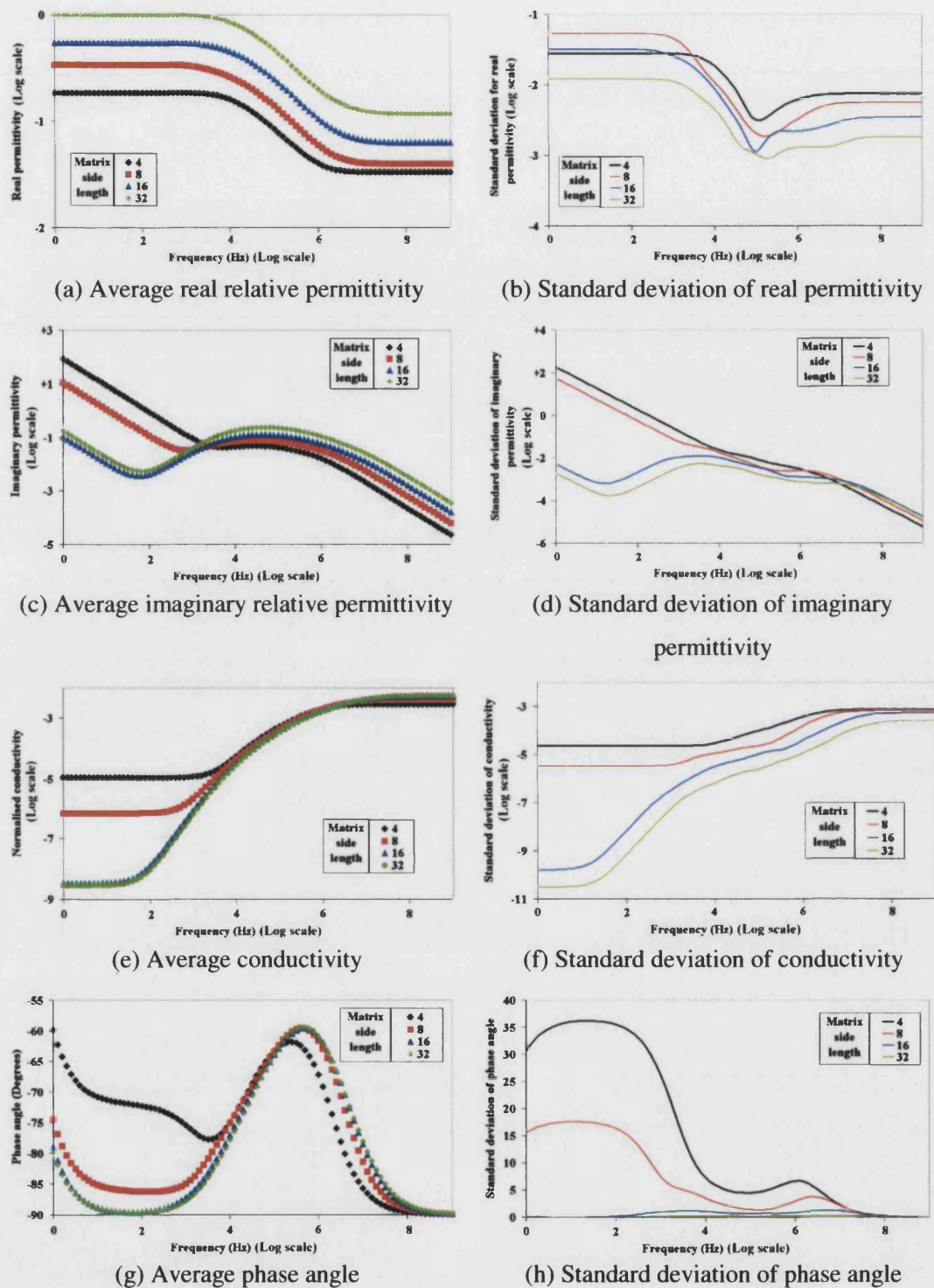
Figure 6.23: Variation of relative permittivity (real (a) and imaginary (c)), conductivity (e) and phase angle (g) with frequency for different three-dimensional network sizes. The standard deviations are also shown, which indicate the variation in the responses (b, d, f, h).

6.9.c.ii.a   Actual resistor-capacitor ratio

To determine the actual resistor-capacitor ratio for the networks produced using the Matlab macro, the components were counted in all the networks used for the size simulations. The variation in R:C was greater in the small networks as the addition of a single component had a proportionally high effect on the ratio outcome. The reduction in response variation was observed to be greater in the three-dimensional system, than for the two-dimensional case, due to the higher number of components. A network size of 64 components is required to reduce the disparity to a low level for the two-dimensional network, while a cube side length of more than 16 components is suitable in the three-dimensional case.
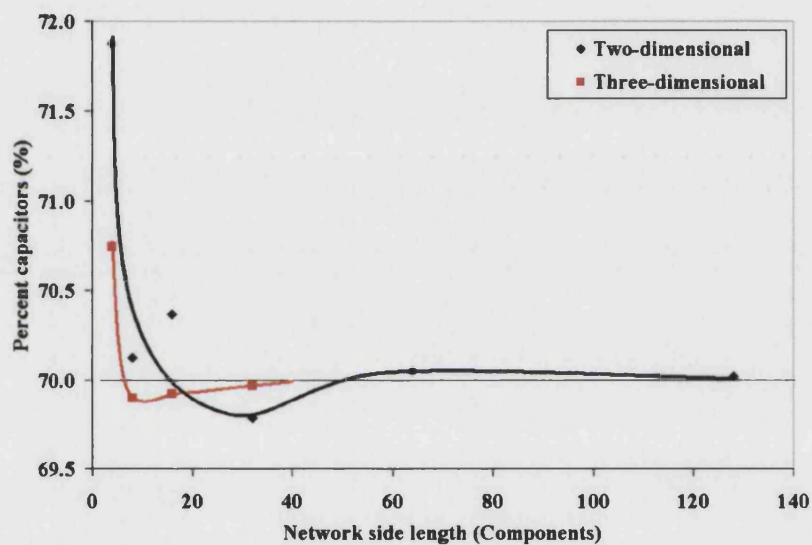
Figure 6.24: Actual percentage of capacitors in two and three-dimensional

networks depending on network side length.

6.9.d   INFLUENCE OF DEFECT INCLUSIONS ON THE PERFORMANCE OF TWO-DIMENSIONAL NETWORKS

Resistive and capacitive components were added to the 30%Resistor:70%Capacitor network that has been chosen to represent a dielectric material. Networks with a side length of 128 components were simulated and the change in relative permittivity, conductivity and phase angle examined. This is in order to simulate the presence of conducting (resistors) or insulating (capacitors) on these properties of the 30%R:70%C network.

6.9.d.i   *Effect of resistor inclusions (two-dimensional)*

Resistive components of 1 μΩ, 10 Ω, 1 kΩ, 1 MΩ and 1 GΩ values were added in volume
fractions of 0.02, 0.05, 0.10, 0.15, 0.20, 0.25 and 0.30 to the 30%R:70%R network in a random
fashion. The results for a 15vol% addition of the various resistor types are shown in Figure 6.25.
This gives a total resistor content of 41% (30+70*0.15). This percentage was chosen as it is below
the percolation threshold and reduces the number of separation responses to <3%.

The real relative permittivity response with the addition of lower resistance inclusions (1 μΩ and
10 Ω) than the matrix shows an increase in the relative permittivity, Figure 6.25(a). As the addition
of 1 kΩ resistors has the same low frequency response this is proposed to be purely due to
connection of more capacitors. The high frequency permittivity is greater than that for the
unmodified network for the 1 μΩ resistor inclusion, while the 1 kΩ response is reduced. This
response was also the result observed practically with the addition of silver particles (low
resistance) to the dielectric matrix barium titanate (30%R:70%C) reported in Section 5.3.

(a) Real relative permittivity

(b) Imaginary relative permittivity

(c) Conductivity
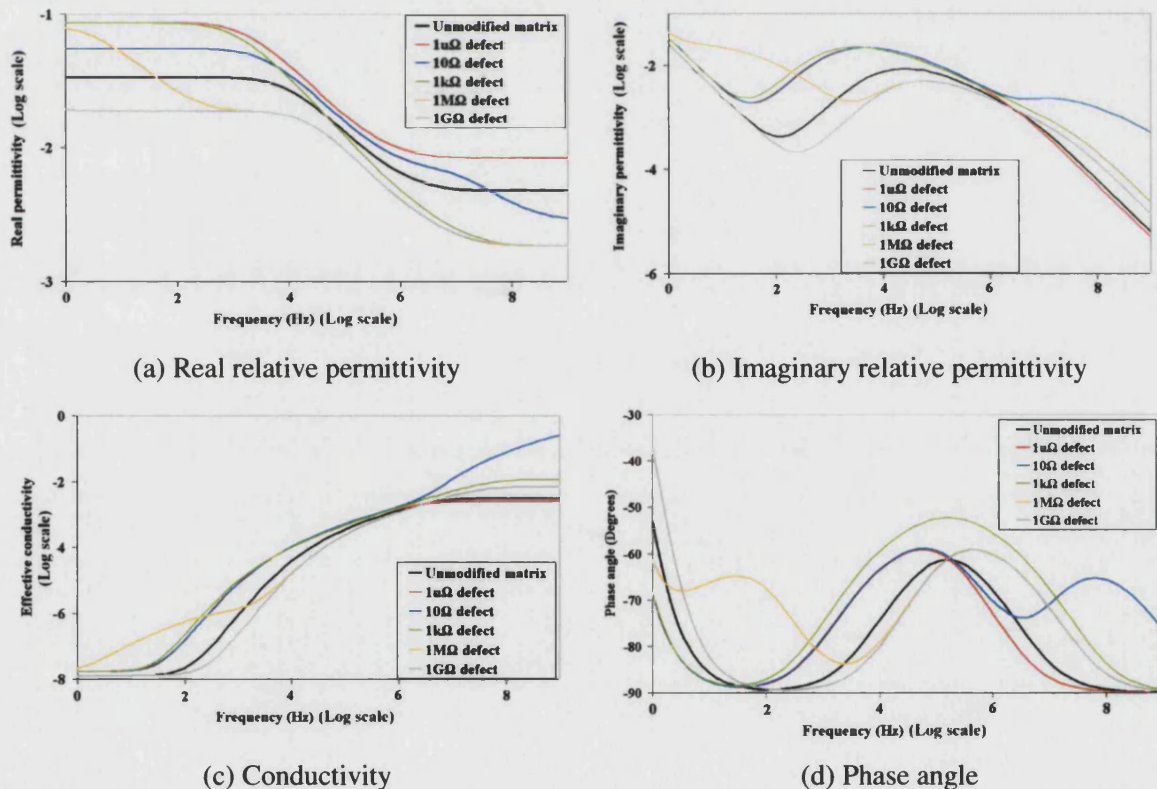
(d) Phase angle

Figure 6.25: Effect of various resistor defect values at 15vol% on the (a) real relative permittivity,
(b) imaginary relative permittivity, (c) conductivity and (d) phase angle with frequency.

(Two-dimensional network).

For all the parameters there is a significant change in the response for the 10 Ω and 1 MΩ resistor types at high and low frequency respectively. This change may be due to the interaction of the component values at certain frequency values, where the time constant of the resistor and capacitor component pair is similar to the applied stimulus frequency. This would also account for the change in the imaginary peak position, Figure 6.25(b). When only one resistor type is present, as in the reference 30%R:70%R network, there will be a single frequency at which the capacitor conductance is identical to the resistor conductance. The admittance of the resistor is independent of frequency while that of the capacitor increases with frequency. This is represented in Figure 6.26 as 'Resistor 1' and the 'Capacitor' that interact at the frequency f_2.
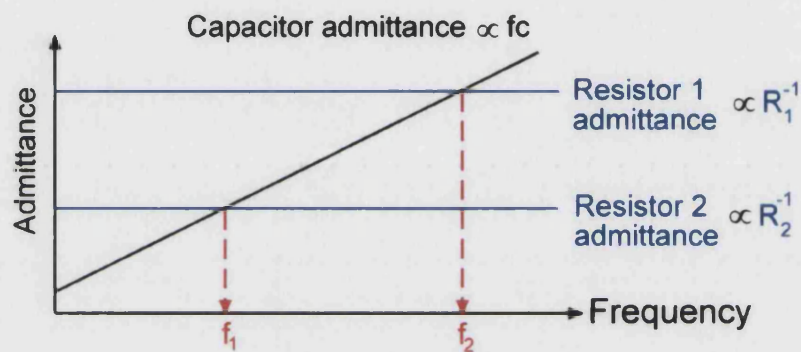
Figure 6.26: Frequency response of capacitors and resistors indicating

frequencies at which conductivity responses overlap.

If another resistor of lower value, Resistor 2, is added, an additional interaction occurs at a lower frequency, f_1. As such, there will be two interaction frequencies for the networks containing defects, these are given in Table 6.4. The time constant, τ, is calculated using equation 6.13, where R and C are the values of the resistor and capacitor respectively.

$$\tau = \frac{1}{2\pi RC} \qquad \{6.13\}$$

Table 6.4: Time constants for networks containing various resistor values.

Resistor 1 value (Ω)	Resistor 2 value (Ω)	Capacitor value (F)	Time constant for resistor 1 (Hz)	Time constant for resistor 2 (Hz)
10^3	10^{-6}	10^{-9}	1.6×10^5	1.6×10^{14}
10^3	10^1	10^{-9}	1.6×10^5	1.6×10^7
10^3	10^3	10^{-9}	1.6×10^5	1.6×10^5
10^3	10^6	10^{-9}	1.6×10^5	1.6×10^2
10^3	10^9	10^{-9}	1.6×10^5	1.6×10^{-1}

This interaction is observed at the frequency at which the phase angle "plateau" occurs. The primary phase angle plateau occurs at ~160 kHz due to the 1 kΩ base network resistors. With the presence of 10 Ω resistors an additional plateau is observed at ~16 MHz. This proposition fits the trend in the data of the primary plateau, which is close to 100 kHz. The proportion of the capacitors affects the height of the plateaux. These calculated time constants are for a single parallel RC circuit, however, in these networks there are many possible combinations of resistors and capacitors.

6.9.d.ii   Effect of capacitor inclusions (two-dimensional)

Capacitive components of 1 μF, 1 nF and 1 pF values were randomly added, to simulate insulating defects, in volume fractions of 0.02, 0.055, 0.10, 0.15, 0.20, 0.25 and 0.30 to the base network. The results for a 15vol% addition of the various capacitor types are shown in Figure 6.27. This capacitor content was chosen to allow comparison with the properties changes with the resistive inclusion content of 15vol%.

The addition of a small capacitor value (e.g. 1 pF) caused the real relative permittivity to be reduced and the addition of a high capacitance value (e.g. 1 μF) causes the real relative permittivity to increase. This is the expected outcome, as the relative permittivity is proportional to the capacitance of the sample. From the time constants the phase angle plateaux would be expected at 160 Hz, 160 kHz and 16 MHz, however only a single plateau at ~100 kHz, which shifts to slightly higher and lower frequencies, is observed. The reasons for this shift and the loss of the phase angle plateaux are not clear, but may be related to low proportion of capacitor defects.

(a) Real relative permittivity

(b) Imaginary relative permittivity

(c) Conductivity
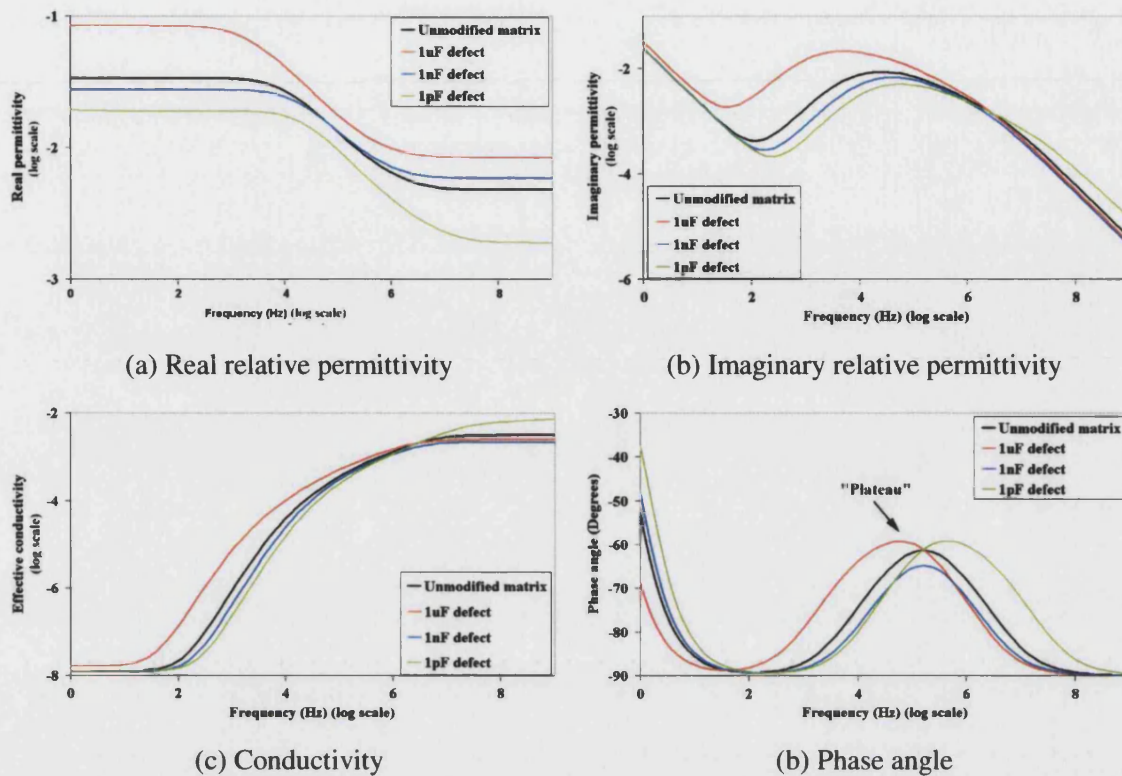
(b) Phase angle

Figure 6.27: Effect of various capacitor defect values at 15vol% on the (a) real relative permittivity,

(b) imaginary relative permittivity, (c) conductivity and (d) phase angle with frequency.

(Two-dimensional network).

6.9.e   INFLUENCE OF DEFECT INCLUSIONS ON THE PERFORMANCE OF THREE-DIMENSIONAL NETWORKS

Using a basic 30%C:70%R three-dimensional network composition with a side length of 16 components, resistive and capacitive components were added to simulate the influence of these defects on the relative permittivity, conductivity and phase angle of the network.

6.9.e.i   Effect of resistor inclusions (three-dimensional)

Resistive components of 1 μΩ, 10 Ω, 1 kΩ, 1 MΩ and 1 GΩ values were added in volume fractions of 0.02, 0.05, 0.10, 0.15, 0.20, 0.25 and 0.30 to the base network in a random fashion. The results for a 15vol% addition of the various resistor types are shown in Figure 6.28. The trends of relative permittivity, conductivity and phase angle were similar to the two-dimensional case but the two-dimensional networks had real relative permittivity responses that where more dispersed. The three-dimensional real and imaginary permittivities (Figures 6.26(a&b)) were also

approximately a magnitude greater than in the two-dimensional case (Figures 6.23(a&b)). The conductivity (Figures 6.23(c) and 6.26(c)) are in good agreement, while there is more low frequency dispersion of the phase angle in the two-dimensional case (Figures 6.23(d) and 6.26(d)).

(a) Real relative permittivity

(b) Imaginary relative permittivity

(c) Conductivity
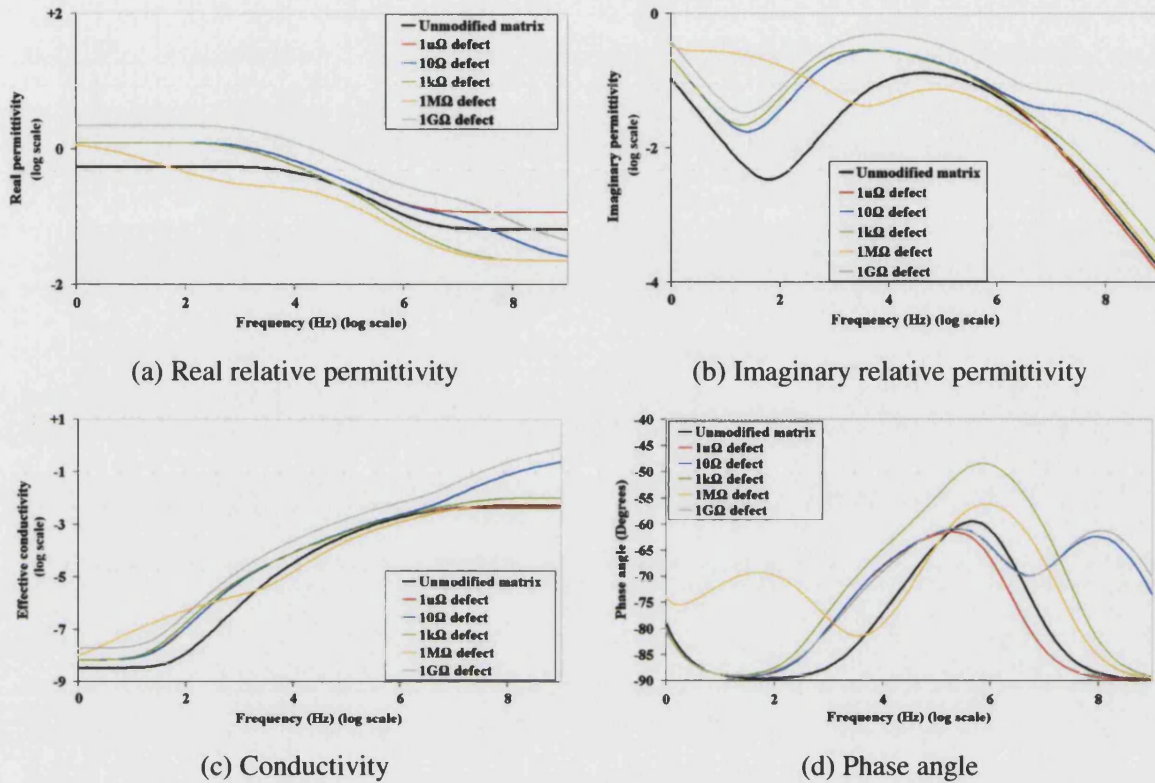
(d) Phase angle

Figure 6.28: Effect of various resistor defect values at 15vol% on the (a) real relative permittivity, (b) imaginary relative permittivity, (c) conductivity and (d) phase angle with frequency for three-dimensional networks.

6.9.e.ii   *Effect of capacitor inclusions (three-dimensional)*

Capacitive components of 1 μF, 1 nF and 1 pF values were added in volume fractions of 0.02, 0.05, 0.10, 0.15, 0.20, 0.25 and 0.30 to the base network in a random fashion. The results for a 15vol% addition of the various capacitor types are shown in Figure 6.29. As with the two-dimensional case the incorporation of a smaller capacitor value causes a decrease in the relative permittivity. This response is expected as the overall capacitance of the sample is reduced. As with the addition of resistors (Figure 6.28), in three-dimensions (Figure 6.27(a&b)) the relative permittivity plots are a magnitude higher than in two-dimensions (Figure 6.27(a&b)). There appears to be an anomaly at a frequency of ~100 Hz for the addition of 1 μF capacitors, however, the overall frequency response is that expected. The reason for this anomaly is unknown, especially when it exists in so many simulations (average of 256 simulations).

(a) Real relative permittivity

(b) Imaginary relative permittivity

(c) Conductivity
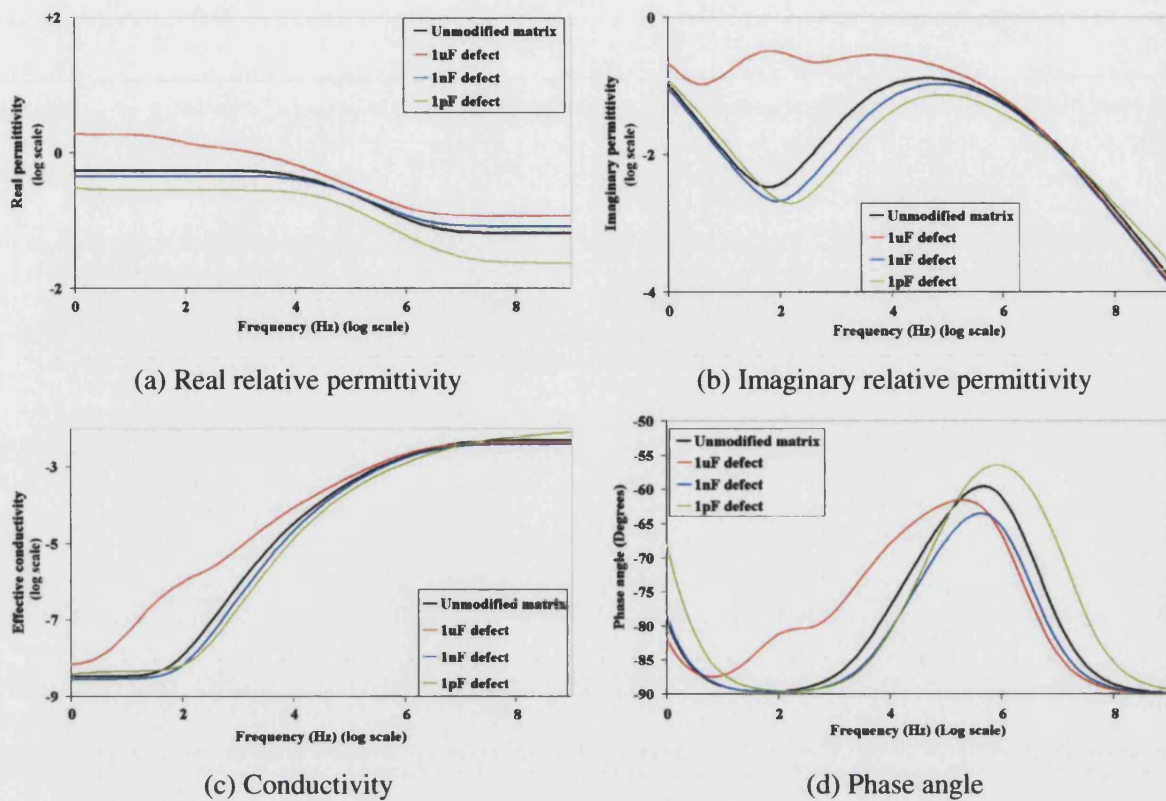
(d) Phase angle

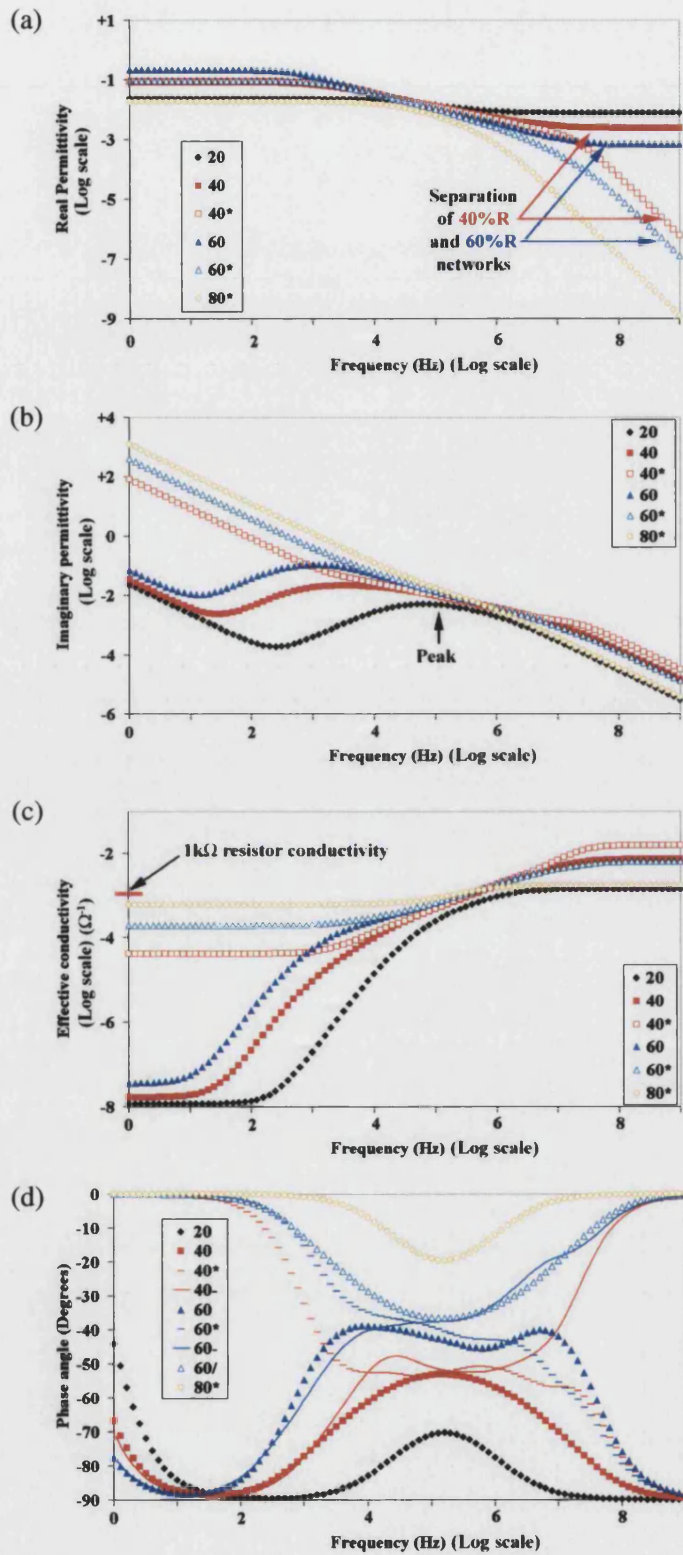Figure 6.29: Effect of various capacitor defect values at 15vol% on the (a) real relative permittivity, (b) imaginary relative permittivity, (c) conductivity and (d) phase angle with frequency

for three-dimensional networks.

The response from the three-dimensional networks is in good agreement with those of the two-dimensional simulations.

6.9.f   INFLUENCE OF INCLUSIONS ON NETWORK POWER LAW REGION RESPONSE

A power law relationship between conductivity and frequency of these R-C networks has been reported[177] to occur at a frequency ~100,000 Hz, with the capacitor volume fraction, α, being the exponent, equation 6.12. The power law equation has been fitted to the averaged conductivity response over the frequency range of 1×10^4 to 1×10^6 Hz for the 15vol% resistor and capacitor defect included networks in two- and three-dimensions, the results are given in Table 6.5. The expected value (in brackets) is that calculated for the capacitor content in the binary 1 kΩ-1 nF network.

Table 6.5: α values calculated from power law trend lines for two- and three-dimensional networks with the addition of 15vol% resistive and capacitive components from conductivity data in the frequency range of 1×10^4-1×10^6 Hz. Parentheses indicate the expected result, which is the actual capacitor content.

Inclusion type	Two-dimensional	Three-dimensional
None (30%R:70%C)	0.752 (~0.700)	0.874
1μΩ	0.578	0.707
10Ω	0.598	0.720
1kΩ	0.602 (~0.595)	0.704
1MΩ	0.904	0.950
1GΩ	0.914	0.727
1μF	0.581	0.706
1nF	0.816 (~0.910)	0.945
1pF	0.913	0.975

The highlighted rows in Table 6.5 show simple compositional differences of the base 30%R:70%C network with an additional 15vol% of 1 kΩ resistors or 15vol% 1 pF capacitors. In two-dimensions the α value for the base network is higher than expected, while the values are close to the expected 0.595 value for 1 μΩ, 10 Ω and 1 kΩ defects. With large resistor values (1 MΩ and 1 GΩ) the α values are considerably higher than expected. With capacitive defects, only the 1 pF defect result is close to the expected value, while that for the 1 μF defect is very low. A better fit with the power law equation may be achieved by choosing a different frequency range. A fixed frequency range was chosen in this analysis to assess the usefulness of the power law region in determining the network composition in two- and three-dimensions.

The calculated α-values in three-dimensions are always higher than the expected values for resistive and capacitive defects (except for the 1 μF). Even though visually the differences in conductivity for the various defects are small in the expected power law region (Figures 6.26(c) and 6.27(c)) the fitting of a trend line suggests that the power law equation is not valid in three-dimensions. This may be due to a reduction in the size of the power law region.

6.9.g   SIMULATION TIMES

The time taken to solve simulations is important. Large networks will give a response that is less dependent on the arrangement of the individual components, but these take much longer to solve. The variation in the response has been shown for network size modification, see Section 6.9.c, and shows that the standard deviation is reduced with a larger network size. The computational time increased considerably as the network size increased, typically ~0.3 s and 240 s for two-dimensional network size of 8 and 64 components respectively. Adding the third dimension increased the simulation time to 17.3 s for a cube side length of 8 components.

6.9.h   COMPARISON OF MODELLING RESULTS WITH EXPERIMENTAL RESULTS

To compare the simulated real relative permittivity values with experimental measurements from monolithic and barium titanate-silver composites the capacitance was determined over a frequency range of $1-1\times10^6$ Hz at various temperatures (186°C, 242°C and 310°C as used by Hirose *et al*[115]). The increased temperature was required to increase the conductivity of the barium titanate into a range that could be determined by the equipment. The calculated relative permittivity results at the different temperatures for the barium titanate monolith are shown in Figure 6.30.
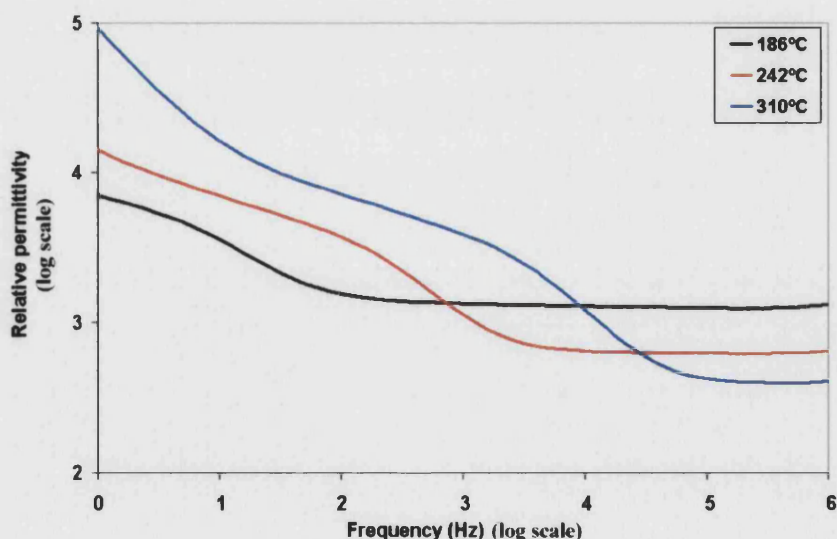
Figure 6.30: Relative permittivity versus frequency for barium titanate measured at

temperatures of 186°C, 242°C and 310°C.

The relative permittivity as a function of frequency and temperature follows a behaviour that is similar to that reported in the literature, Figure 6.31. A rapid decrease in relative permittivity is

observed at ~10 Hz and 186°C. This response shifts to higher frequencies as the temperature is increased. The high frequency relative permittivity decreases at higher temperatures as the bulk permittivity decreases, which is also the reason for the shift to higher frequency of the rapid decrease between the plateaux.
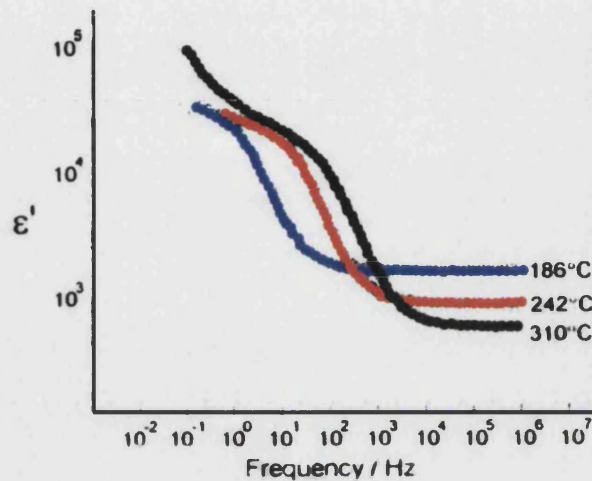
Figure 6.31: Frequency dependence of real relative permittivity for

barium titanate at 186°C, 242°C and 310°C [115].

The response appears comparable to simulated results where a real relative permittivity decrease is observed between a low and high frequency plateau, for example, Figure 6.21(a). The low frequency behaviour is thought to be due to the grain boundaries, while the bulk and grain boundaries determine the response at high frequency[115]. A simple equivalent circuit consisting of two parallel resistor-capacitor elements has been used to represent the behaviour in Figure 6.31 by the authors[115].

Barium titanate-silver composites containing different silver contents were also tested in order to compare the simulated response of the random 30%R:70%C network containing resistive defects of lower resistance than the matrix. The frequency, f, at which the permittivity and AC conductivity are a fractional power of frequency occurs when the admittance of the capacitors in the network $(2\pi fC)$ is comparable to admittance of the resistors, as in equation 6.14.

$$\sigma_{particle} = 2\pi f C_{matrix} \qquad \{6.14\}$$

Here $\sigma_{particle}$ is the conductivity of the particle inclusion and C_{matrix} is the matrix capacitance, which is related to the relative permittivity by equation 2.17. Using a silver conductivity of 6.2×10^7 Ω^-

^{1}.m^{-1} and a barium titanate relative permittivity of 1500, the calculated frequency is ~10^{15} Hz. This is with a silver volume fraction of 0.1, however, the silver content has a minor effect. This frequency is considerably higher than can be experimentally measured using the equipment used in this study. To observe the modelled interaction in the measurement frequency range (1 MHz and below) a particle material must have a conductivity below ~10^{-2} Ω^{-1}.m^{-1}.

The network models demonstrated (Figure 6.25(a)) that the incorporation of a less resistive phase increases the relative permittivity. Experimentally, Figure 6.32, increasing the silver content caused an increase in the measured relative permittivity, which has been observed in the simulated results, Figure 6.33.
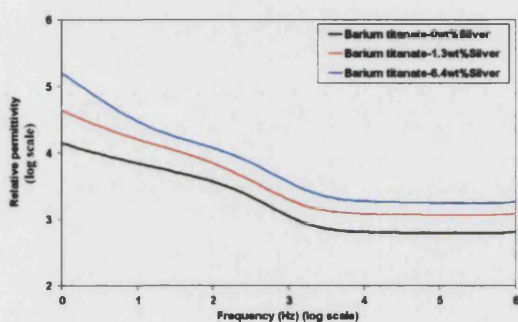
Figure 6.32: Increase in relative permittivity with addition of silver to barium titanate at a temperature of 242°C over a frequency range of 1 Hz-1 MHz.
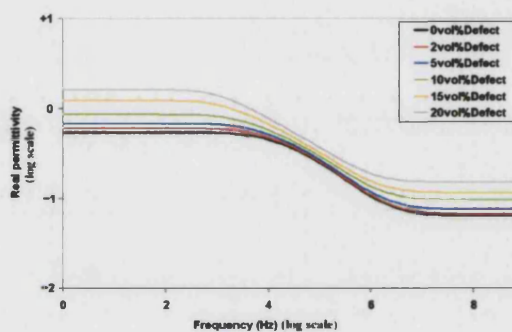
Figure 6.33: Increase in relative permittivity with increasing 1 µΩ resistor defect content in a 30%R:70%C matrix as a function of frequency. (16 component length cube).

Figure 6.33 shows that with the addition of 5% 1 µΩ resistors into the 30%R:70%C matrix a relative permittivity increase of ~24% is achieved at 1 kHz. At room temperature and 1 kHz the practical relative permittivity increase with 6.4wt% silver was <10%. The difference is due to the measurement of different response phenomena in the samples. The high frequency experimental real relative permittivity (>10^4 Hz) corresponds to the low frequency region in the modelled work. The low frequency experimental response (<10^2 Hz) is due to the charge build-up on the sample electrodes. A relative permittivity plateau would be expected if only the grain boundary response was observed[19]. The reduction in permittivity in the 10^2-10^4 Hz frequency range is the change from grain boundary response to the grain interior and grain boundary response[115]. The drop in modelled relative permittivity at ~10^4 Hz is not observed experimentally as the frequency is beyond the capability of the equipment (frequency range is limited to 10^{-4} to 10^7 Hz). The use of higher frequency or modelling with more resistive particles, such as silicon carbide, would allow observation of the modelling results in the experimental frequency range.

Figures 6.34 and 6.35 compare the experimental and simulated conductivity, while Figures 6.36 and 6.37 are the behaviours of the phase angle in each case. The high frequency experimental conductivity ($>10^4$ Hz) corresponds to the low frequency modelled response. The rapid increase in the modelled conductivity at ~100 Hz is observed at ~10^5 Hz in the practical case. Based on the previous calculation using equation 6.14 this rapid increase at 10^5 Hz cannot be due to the AC conductivity of the capacitive barium titanate matrix being comparable to that of the silver particles. To bring this expected response into the measured frequency range the conductive phase should have a conductivity of ~10^{-2} Ω^{-1}.m^{-1}. It is proposed that the structural feature responsible for the experimental conductivity results is a skin of altered material on the surface of the barium titanate grains. This altered material may be formed by partial solubility of silver into the barium titanate. The low frequency experimental conductivity (10^2 Hz) increases due to a reduction in the ionic charge build up at the electrodes.
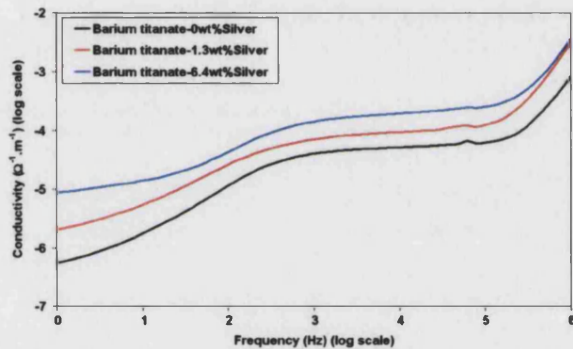
Figure 6.34: Increase in conductivity with addition of silver to barium titanate at a temperature of 242°C over a frequency range of 1 Hz-1 MHz.
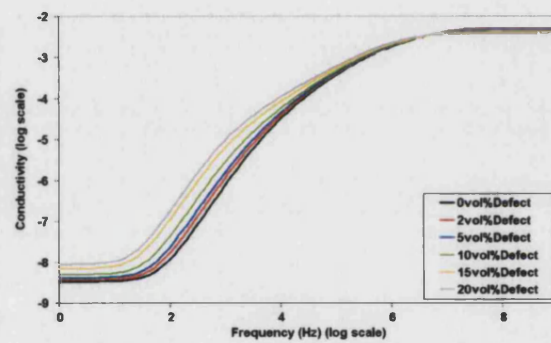
Figure 6.35: Increase in conductivity with increasing 1 $\mu\Omega$ resistor defect content in a 30%R:70%C matrix as a function of frequency. (16 component length cube).

Comparison of the experimental, Figure 6.36, and simulated, Figure 6.37, phase angle results indicates that at high and low frequency the respective response is capacitive. As the silver content increases the low frequency side of the phase angle peak is observed to increase due to the higher proportion of conductive particles (phase angle ~-60°) that influences the ionic charge carriers. The phase angle peak of the simulated results shifts to lower frequencies with increasing inclusion content, however, this frequency range is not observed in the practical results. The experimental phase angle peak at a frequency ~900 Hz is not expected to change with silver addition. The change suggests that the barium titanate has a "skin" of conductive material that is increasing the phase angle. This could be due to the formation of a conductive "skin" on the barium titanate grains due to limited interdiffusion of the silver into the barium titanate.
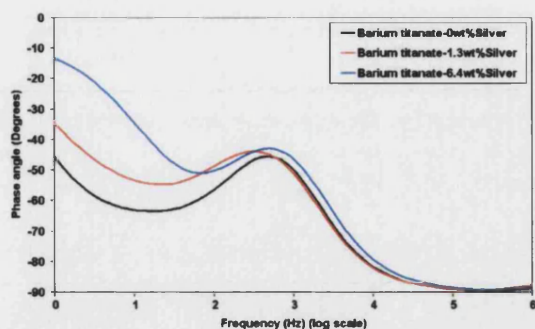
Figure 6.36: Change in phase angle with addition of silver to barium titanate at a temperature of 242°C over a frequency range of 1 Hz-1 MHz.
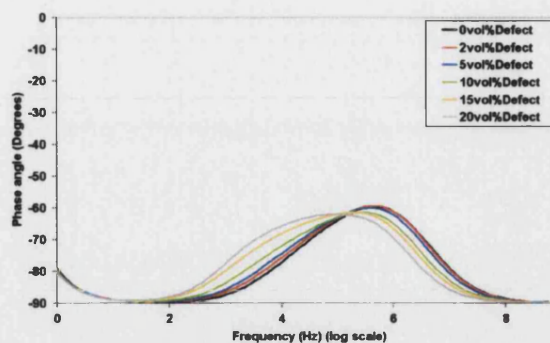
Figure 6.37: Change in phase angle with increasing 1 μΩ resistor defect content in a 30%R:70%C matrix as a function of frequency. (16 components side length cube).

6.9.i   SUMMARY

The computational modelling has predicted a number of key points and the research can be summarised as below:

a) A methodology has been developed to generate and analyse random two- and three-dimensional resistor-capacitor networks. The two-dimensional networks produced are comparable to those solved by the Star-Delta transformation technique[188] and by the use of Simetrix[177].

b) A threshold network size of 128 components was observed for the two-dimensional situation, while no such threshold was seen in the three-dimensional network responses. The extensive computing time in the three-dimensional case meant that networks of only 16 components could be solved in the time available.

c) Separation of the results was observed, which has been mentioned by previous researchers[187], however, the separation in the phase angle appears to be more complex than that observed in the relative permittivity or conductivity responses. This probability of separation may be related to the number of conducting and non-conducting samples observed in the experimental resistivity results, which showed a high degree of scatter. It was observed that at high silver contents a number of samples still remained capacitive, as the silver had not formed a conducting path between the electrodes.

d) The general response of two-dimensional and three-dimensional networks is similar, except that the size of the power law region is reduced in the three-dimensional case.

e) The power law was valid for most two-dimensional defect models, but failed to predict the composition in three-dimensional networks.

f) An increase in relative permittivity was observed with the incorporation of a lower resistance inclusion (1 $\mu\Omega$) in the simulated dielectric matrix at low frequency (1 kHz). This response was found in both the two- and three-dimensional networks; it was also found experimentally, as discussed in Section 6.9.h.

g) The two-dimensional modelling results suggest that at 1 kHz the addition of resistors as defects into a dielectric increases the conductivity if the resistors are of lower value than those forming the dielectric, otherwise the conductivity is decreased. This is expected as the lower resistor value defects will allow easier charge transfer between the electrodes. The result, however, in three-dimensions is not as clear as the conductivity appears to increase with the addition of any resistor value. The addition of smaller value defect capacitance caused a decrease in the conductivity (at 1 kHz) for both network dimensional types.

h) The incorporation of resistive defects into the dielectric model broadened the plateau/peak in the phase angle, and in some cases introduced an additional peak; thought to be due to the additional time constant relating to the defect value. Capacitive defects produced only small peak height and width changes in the phase angle.

i) Two-dimensional networks appear to have a response sufficiently similar to the three-dimensional case and allow larger networks of smaller response variation to be studied. The complication of using a three-dimensional network may not, therefore, be essential for studying dielectric properties of resistor-capacitor networks.

j) Heating monolithic and barium titanate-silver composites to 242°C has shown that there is agreement of the relative permittivity trend with increasing content of a less resistive phase in both simulated and practical results. Unexpected conductivity behaviour was observed at frequencies much lower than the predicted silver-barium titanate interaction, which may be due to a high conductivity skin on the barium titanate grains.

k) Finally, the computational modelling provides a method of assessing the relative permittivity, conductivity and phase angle changes with frequency and network composition. The network composition can be varied to simulate the addition of resistive or capacitive defects and also the distribution of these phases within the network.

7 GENERAL DISCUSSION

7.1 INTRODUCTION

This chapter is a summary of microstructural observations, together with the mechanical and electrical property analysis for the fabricated composites. Lastly, the results from the computational modelling are compared with experimental measurements.

7.2 MONOLITHIC BARIUM TITANATE

7.2.a MICROSTRUCTURAL ANALYSIS

The barium titanate starting powder had a particle size of 1 μm, but formed agglomerates up to 25 μm in size, and contained no major impurities as observed from X-ray diffraction analysis. Sintering of the pure barium titanate starting powder produced samples with a density comparable with that reported by other researchers[60]. This density, 93%, could be improved to ~99% through hot pressing. While hot pressing is occasionally[40, 41] used, it was employed to a limited extent in this work, as the technique is expensive and requires difficult post-sintering sample preparation. The monolithic barium titanate hot pressed sample was observed to be of a black/blue colour, which indicates that the material is in a chemically reduced state with a low resistivity[32, 76]. Barium titanate in an oxidised state has a yellow/cream colour[32, 189].

Dilatometry indicated two sintering peaks at 1170°C and 1300°C, as expected from the literature[72]. X-ray diffraction analysis did not detect any unexpected crystalline second phases when barium titanate was sintered below 1320°C. The monolithic grain size of 9.5±0.4 μm is comparable to other studies of barium titanate[70]. Hot pressing increased the grain size to 12.7±0.5 μm, suggesting that grain growth had occurred, which was not reported in the literature[1, 41, 76]. The intragranular fracture mode observed here for the monolithic barium titanate has been reported in the literature[41, 69, 144]. Domains were observed using electron microscopy (SEM and TEM) and indicated that the material should have piezoelectric behaviour when poled. It was decided that the barium titanate samples produced were suitable as reference materials for the composite samples and were similar to samples produced elsewhere.

7.2.b   MECHANICAL PROPERTIES

The measured strength of 100 MPa and the fracture toughness, ~2 MPa.m$^{0.5}$, are typical values for barium titanate, especially for pressureless sintered, rather than hot pressed samples[41]. The pressureless sintered hardness value of 4 GPa is in agreement with the reported hot pressed value of 6.9 GPa [41]. This value is comparable with the 6 GPa that was measured in this research for a hot pressed sample. Hot pressed samples had a lower toughness of 0.9 MPa.m$^{0.5}$ when compared with the pressureless sintered samples. This suggests that the toughness of the pressureless sintered samples benefits from the presence of finer grain size and pores that reduce crack propagation by decreasing crack tip stress. The stiffness (in 1-direction) value of ~100 GPa is in agreement with the 116 GPa quoted in the literature[168].

7.2.c   ELECTRICAL PROPERTIES

Relative permittivity measurement of monolithic barium titanate gave a value of 1500, which is within the reported range of 950-1740[18, 23, 84]. The dielectric loss value of ~0.01 is comparable with the literature value of 0.007[23]. The resistivity value of 0.8 MΩ.m indicates that monolithic barium titanate is insulating. Barium titanate was corona poled using a temperature of 130°C and a potential greater than 7.5 kV with a tip height of 2 cm. Domain alignment achieved saturation when samples where cooled in the field. Piezoelectric coefficient measurements confirmed that domain reorientation occurred under the poling field with d_{33} and d_{31} values of ~170 pC/N and ~-55 pC/N, respectively. These values are in agreement with the literature[168]. Impedance analysis of poled barium titanate samples showed a coupling coefficient of ~0.25, which is lower than the ~0.35 given in literature[22]. This could be due to the high porosity of the pressureless sintered samples. The dielectric breakdown result (9.5 kV/mm) was comparable with the literature (7.4 kV/mm)[152], however, decreasing the porosity by hot pressing would be beneficial by reducing the tendency of internal breakdown initiation inside pores. The polarisation-field loops were similar to those in the literature, with a polarisation of ~0.12 Cm^{-2} for a field level of 2 kVmm^{-1} [175].

7.3 BARIUM TITANATE-SILICON CARBIDE COMPOSITE

7.3.a   MICROSTRUCTURAL ANALYSIS

The particle size of the silicon carbide was determined to be approximately 200nm, but agglomeration of these particles was observed to occur. The addition of the silicon carbide to the barium titanate, even at a mass fraction under 5%, was observed to reduce the density and grain

size of the sintered composite in comparison to the monolith. This suggests that the presence of the silicon carbide inhibits diffusion during sintering and any liquid phases that are formed have a minor effect. A glassy phase was observed by TEM analysis to be present at grain junctions. Dilatometry confirmed that the sintering rate was affected, with the loss of the higher temperature sintering rate peak (1300°C) observed for the barium titanate. X-ray diffraction analysis indicated that a chemical reaction occurs between the barium titanate and the silica layer present on the silicon carbide, equation 7.1. The reaction phase reduces the proportion of dielectric material and may increase the conductivity of the composite.

$$2BaTiO_3 \,_{(s)} + 2SiO_2 \,_{(l)} \rightarrow Ba_2TiSi_2O_8 \,_{(s)} + TiO_2 \,_{(s)} \qquad \{7.1\}$$
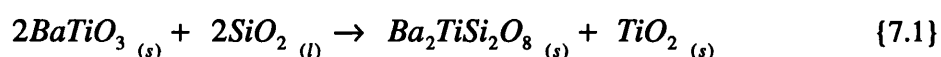
This reaction phase was reported by Niihara[41] to be present in hot pressed barium titanate-silicon carbide, however, its influence on electrical properties was not discussed. With the addition of silicon carbide the grain size was observed to reduce from ~50 μm to ~5 μm, indicating that the particles influence the diffusion of the sintering species. The formation of a reaction phase having a lower melting point may enhance liquid phase sintering, however, the particles could be pinning grain boundaries due to high interface bond strength. SEM and TEM analysis of barium titanate-silicon carbide samples, however, failed to observe the original silicon carbide particles, presumably as they had completely reacted.

The fracture mode was observed to change from intragranular to intergranular with silicon carbide addition. The change could be caused by grain boundary weakening by the presence of a glassy phase. For barium titanate-silicon carbide the fracture has been reported to be intragranular[3]. Domains were observed using electron microscopy in composites with 1-3wt% silicon carbide indicating that piezoelectric properties may be realised if these domains could become aligned.

7.3.b   MECHANICAL PROPERTIES

Mechanical testing of the barium titanate-silicon carbide composites was limited due to the significant decrease of the composite density. Measurement of the fracture toughness of pressureless sintered composites indicated an initial decrease (1.0 MPa.m$^{0.5}$) before returning to the original monolith value (2.0 MPa.m$^{0.5}$) above 5% silicon carbide content. This behaviour is likely to be caused by the high porosity in these composites rather than by direct influence of the silicon carbide particles. The hot pressed samples showed an increased toughness to ~1.4 MPa.m$^{0.5}$ (from ~1.0 MPa.m$^{0.5}$) with 5wt% silicon carbide content. This is similar to the 0.33 MPa.m$^{0.5}$ increase reported by Niihara[41]. Crack deflection and grain boundary strengthening by silicon carbide

particles is not proposed as silicon carbide particles that could interact with cracks were not observed. As expected, the hardness was lower than the hot pressed value in the literature, due to the higher porosity. The reported increasing trend of hardness with silicon carbide content by Niihara[41] for hot pressed composites was not observed. For the pressureless sintered composites addition of 2wt% silicon carbide doubled the monolithic hardness value to ~7.5 GPa, possibly due to grain size reduction with minor porosity increase. For higher silicon carbide contents, however, the hardness was reduced, due to increased porosity.

7.3.c ELECTRICAL PROPERTIES

The electrical properties of barium titanate-silicon carbide are not present in the literature, which is unexpected since the main use of barium titanate is as a dielectric material. One aim of this research was to measure the electrical properties of the composite and determine if it is suitable as a dual structural and dielectric material. Permittivity and dielectric loss values indicated, and confirmed by resistivity calculations, that the composite had become semi-conducting due the reducing atmosphere during sintering. Subsequent annealing in an oxidising atmosphere was ineffective in producing significant oxidisation, unlike that reported in the literature[1]. This was a disadvantage as poling became ineffective above 3wt% silicon carbide and as such the use of the composite for piezoelectric application is inadvisable. The high dielectric loss of the composites was confirmed by polarisation-field analysis. Even with a possible increase in mechanical properties as reported by Niihara[41] the material has poor dielectric properties so failing in its primary application as an electroceramic. No benefit would be gained from using barium titanate-silicon carbide as a structural ceramic as better materials, such as alumina, are available.

7.4 BARIUM TITANATE-SILVER COMPOSITE

7.4.a MICROSTRUCTURAL ANALYSIS

Both the silver oxide powder and silver nitrate solution method produced barium titanate-silver composites with no reaction phases between the components. Both the silver oxide and silver nitrate containing powders were observed to have decomposed on heating using thermogravimetric analysis. A higher than expected decomposition temperature (above 400°C) was recorded for the silver nitrate. X-ray diffraction analysis of powders calcined at 300°C indicated the presence of silver and complete decomposition of both compounds to silver during sintering was confirmed by X-ray diffraction analysis. Dilatometry indicated that the addition of silver reduced the

temperature at which sintering began. However, the overall percent shrinkage was generally unaffected by low silver contents. It is suggested that the silver does not aid the densification process, as there is negligible solubility between the silver and barium titanate. The final sintered density was observed to be independent of silver content for the silver (oxide) samples, however, silver loss, and diffusion inhibition by the silver, may explain the density reduction with the silver (nitrate) composites. Silver loss due to capillary action of the molten silver at the sintering temperature was observed at the sample surface. This loss did not appear to extend into the sample core, but formed a depletion layer of ~50-100 µm depth, similar to that reported by Chen[47].

Image analysis of polished composite cross-sections showed that large silver particles (>1 µm) where situated at grain boundaries, while those particles <1 µm tended to reside within the grains. It is these smaller particles that may interact with domain wall motion and influence the piezoelectric properties. The intergranular silver particles have potential for composite toughening by crack-bridging. The grain size was observed to decrease with increasing silver content, with a 50% grain size reduction obtained with the addition of 18wt% silver in both composite types. The silver particle size in the sintered composites increased with increasing silver content in both types, but by differing amounts. In the silver (oxide) composites a ~30% increase in silver particle size was measured in comparison to a 100% increase for the barium titanate-silver (nitrate), both with silver contents near 18wt%. The increase in particle size indicates that agglomeration of the silver is taking place under the sintering conditions due to its molten state and that the original silver (nitrate) particles are smaller than the silver (oxide) particles. Agglomeration of second phase particles may be hindered if particles with a higher melting point are used.

Domain walls were observed to impinge on silver particles, but in the absence of an electric field it is not known whether the motion of the domains will be affected. Electron microscopy revealed the spherical nature of intragranular silver particles and that intergranular silver particles conformed to the grain shape. No reaction phases were observed at the barium titanate-silver interface and the ductility of the particles may allow crack-bridging to operate.

7.4.b   MECHANICAL PROPERTIES

Incorporation of silver into barium titanate increased the strength of the composites from 100 MPa to 120 MPa. Samples with high silver contents were observed not to fracture completely, this being proposed to be due to the presence of silver filaments bridging the fracture surfaces. This mechanism would be expected to improve the fracture toughness. However, incorporation of silver did not significantly improve the fracture toughness as determined by indentation. This could be a result of the increasing porosity with higher silver (nitrate) contents. The hardness decreased, by

about 40% to 2.5 GPa with 19wt% silver, as expected for the incorporation of a mechanically softer phase. The hardness reduction was greater than expected from the rule of mixtures. The stiffness was calculated from impedance analysis data and indicated two different trends depending on the starting silver compound. With the silver (oxide) composites no change in stiffness was determined as the silver content increased. The silver (nitrate) composites showed a decrease in stiffness with silver content. The reason for this difference is unclear as no major microstructural variations between the two composites types were observed, however, this trend is similar to that observed for the composite densities.

7.4.c   ELECTRICAL PROPERTIES

At low silver contents the benefits to the relative permittivity were small, however, with 10wt% silver a significant increase to ~4800, from ~1800, was observed. This increase is suggested to be due to the silver particles acting as electrodes within the barium titanate and increasing the local electric field, thereby activating a greater amount of charge. While the conductivity of the samples increased with silver content the samples could still be poled as the dielectric barium titanate matrix was continuous. The piezoelectric coefficients decreased linearly with increasing silver additions. The reduction in d_{33} was greater than was expected from the rule of mixtures with the incorporation of a non-piezoelectric phase. The dielectric loss had no significant relationship with silver content.

The coupling coefficient was observed to decrease for both the silver (oxide) and silver (nitrate) composites. The reduction was faster with the silver (nitrate) samples, with a value below 0.1 measured for a composition of 9.5wt% silver, while this value was not reached until a weight fraction of 14% in the silver (oxide) samples. No improvement of the mechanical quality factor was observed but it is noted that the large error bars may prevent determination of minor changes. Both the coupling coefficient and mechanical quality factor were lower than values reported in the literature. As expected from the reduction in resistivity with increasing silver content the dielectric breakdown voltage was decreased. A figure of merit was calculated to take into account the changes in permittivity and dielectric behaviour of the silver composites. This was observed to decrease with increasing silver content. Increasing the composite density would allow an improved figure of merit to be achieved by increasing the permittivity and dielectric breakdown strength. Polarisation-field analysis indicated that the addition of low silver content increases the remanant polarisation in comparison to barium titanate. The coercive field was increased, suggesting that the silver particles may be reducing the ability of the domains to move under the application of an electric field.

7.5 BARIUM TITANATE-PLATINUM COMPOSITE

X-ray diffraction analysis of the sintered composite showed that the platinum compound had decomposed to platinum; however, a secondary phase (of unknown composition) was also present. The presence of the platinum or secondary phase hindered the densification of the composite, by inhibiting diffusion of sintering species, as indicated by the low shrinkage of 4.4% (in comparison to the monolithic value of 17.0%). The high melting temperature of the platinum may increase the grain keying of the barium titanate particles in comparison to the silver, which is molten at the sintering temperature. Thermogravimetric analysis, TGA, showed that the platinum compound decomposed when heat treated, but required a higher temperature (above 500°C) than the silver nitrate (450°C from TGA, 300°C in literature[47, 49]). As with the barium titanate-silver composites the small platinum particles (<1 μm) were located intragranularly. Particle agglomeration during sintering is reduced due to the higher melting temperature of the platinum in comparison to the silver. Samples were not suitable for observation of domains due to the high porosity.

7.6 COMPUTATIONAL MODELLING

A random network of resistors and capacitors was constructed to examine the change in dielectric properties with composition as a function of frequency. In order to simulate a dielectric material a composition with 30%resistors and 70%capacitors was chosen. Two-dimensional networks with specific resistor-capacitor ratios compared favourably with literature results[177]. Three-dimensional networks with the same composition had similar properties. Analysis of the network size indicated that square (cubic) networks were required to have a side length of 128 (above 32) components to reduce variation in the results.

Networks in two-dimensions and three-dimensions where constructed to determine the effect of incorporating either resistive, or capacitive, components into the dielectric material over a 1 Hz to 1 GHz frequency range. By increasing the proportion of resistive components the 1 kHz real permittivity response could be increased. Increasing the capacitive proportion reduced the low frequency permittivity value, but increased the high frequency value. The results from two-dimensional and three-dimensional modelling were similar. Analysis of the power law region in general allowed the proportion of capacitors to be determined but with the addition of resistive or capacitive components the values were no longer those expected.

The experimental results of the general permittivity-frequency relationship observed from high frequency impedance analysis of both monolithic and silver composite samples agreed well with the low relative permittivity plateaux observed from modelling. The frequency dependence of conductivity and phase angle of the barium titanate-silver composites also showed reasonable agreement. The comparable experimental and modelled dielectric results, with the addition of low resistivity inclusions into a dielectric matrix, indicate that computational modelling has potential for the design, investigation and engineering of dielectric composite structures.

8 CONCLUSIONS AND FUTURE WORK

The aim of the research presented in this thesis was to fabricate barium titanate particulate-based composites and develop an understanding of their influence on microstructure, mechanical and electrical properties. In addition to manufacturing a range of piezoelectric composites, modelling of a dielectric material containing conductive inclusions was undertaken with comparisons of simulated results with experimental results.

8.1 CONCLUSIONS

8.1.a BARIUM TITANATE-SILICON CARBIDE COMPOSITES

I. A reaction phase between the nano-sized silicon carbide and barium titanate matrix was observed and identified as barium titanate silicate, $Ba_2TiSi_2O_8$. The proposed reaction mechanisms is,

$$2BaTiO_{3(s)} + 2SiO_{2(l)} \rightarrow Ba_2TiSi_2O_{8(s)} + TiO_{2(s)}$$
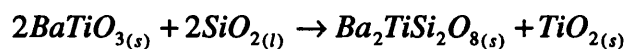
II. Barium titanate under the sintering conditions was chemically reduced to a semi-conducting state with a resistivity of 4 Ω.m when 3wt% silicon carbide was added. This reduces the poling efficiency of the composites.

III. Re-oxidation of the sintered composite had little effect and caused sample cracking to become pronounced in the hot pressed samples.

IV. Silicon carbide addition caused the removal of the 1300°C peak in the sintering rate.

V. The monolithic grain size (~50 μm) was reduced by approximately ten times with the presence of silicon carbide, indicating that silicon carbide is a good grain size modifier at low contents.

VI. The fracture mode of barium titanate changed from intragranular to intergranular on addition of silicon carbide.

VII. An initial decrease in toughness (to ~1.0 MPa.m$^{0.5}$ from ~2.0 MPa.m$^{0.5}$) with increasing silicon carbide content was observed below 5wt% silicon carbide. This is suggested to be caused by thermal residual stresses generated by the silicon carbide reaction phase and possible crystallographic transformations of the barium titanate. Above the 5wt% silicon carbide content the toughness was similar to the monolithic value of 2.0 MPa.m$^{0.5}$ possibly due to the high porosity causing stress dissipation at the crack tip.

VIII. A small amount of silicon carbide addition increased the hardness of barium titanate.

8.1.b   BARIUM TITANATE-SILVER COMPOSITES

I. No reaction occurred between the barium titanate and silver particles as observed by X-ray analysis employed with the transmission electron microscope, TEM.

II. A high silver content (>6wt%) inhibits the densification of barium titanate, due to the poor solubility of sintering species in the intergranular silver. A grain size decrease of 50% was observed for an addition of 18wt% silver to barium titanate.

III. Silver particles sized below 1 μm were located within the grains had domains attached to them.

IV. The strength of barium titanate can be improved with the addition of silver particles. A silver content of 10wt% increased the strength from 100 MPa to 110 MPa.

V. No significant change in fracture toughness was observed with the addition of silver, suggesting that any beneficial crack-bridging by the silver inclusions is minimal.

VI. The permittivity was significantly increased with the addition of over 10wt% silver, with no corresponding increase in dielectric loss. The monolithic permittivity value, ~1500, increased to ~3000 with 15wt% silver.

VII. Although conductivity increased with silver content, poling was still achieved and the piezoelectric coefficients, d_{33} and d_{31}, were observed to decrease linearly with increasing silver content. The increased conductivity reduced the dielectric breakdown strength.

VIII. The incorporation of silver increased the coercive field and remanant polarisation of barium titanate.

8.1.c   BARIUM TITANATE-PLATINUM COMPOSITE

I. The use of the hydrogen hexachloroplatinate(IV) was found to be unsuitable for the manufacture of barium titanate particulate composites due to the formation of a glassy phase and the inhibition of the densification process. Calcination of the starting powder did not prevent the formation of a secondary phase.

8.1.d   COMPUTATIONAL MODELLING

I. Two- and, for the first time, three-dimensional networks of random resistors and capacitors have been successfully constructed and modelled. The frequency response of permittivity, conductivity and phase angle was simulated.

II. The two-dimensional simulated results of the frequency response of permittivity, conductivity and phase angle were comparable to that reported in the literature. Results from simulating three-dimensional networks were similar to the two-dimensional percolation results.

III.   The addition of low resistance defects was observed to increase the real permittivity of a random R-C dielectric network, as observed experimentally.

IV.   The scatter in the simulated network results is similar to the dispersion in the experimental resistivity results, indicating the random structure of the material. The region of low scatter may indicate regimes with materials of more consistent properties.

V.   The modelled frequency behaviour for permittivity, conductivity and phase angle of a resistor-capacitor random network containing low resistance inclusions was compared to results observed for silver loaded barium titanate (at elevated temperature). The high frequency experimental results corresponded to the low frequency modelled results. A change in the conductivity for the barium titanate-silver composites in the measured frequency range (<1 MHz) was unexpected and is proposed to be due to a conductive "skin" on the barium titanate grains.

VI.   The random R-C network models provide a novel method of predicting the electrical response of ferroelectric materials with a heterogeneous structure.

8.2 FUTURE WORK

I. In this research, barium titanate was employed as the piezoelectric matrix material. However, alternative piezoelectric materials, such as lead zirconate titanate (PZT), that have higher piezoelectric coefficients may be used. A requirement, for the material, is that reactions that detrimentally influence the dielectric and piezoelectric properties of the matrix should not occur between the composite constituents. Unreactive inclusions may enhance the relatively low strength of electroceramics (by crack deflection and grain boundary strengthening) and either improve or have no overall effect on the permittivity (internal electrode effect with metallic particles). Data on particle loaded PZT has been reported[12-14] but a full characterisation of the microstructural, mechanical and electrical properties has yet to be carried out.

II. The metallic particles used as inclusions could be investigated further. The silver appears not to react with the barium titanate, however, it agglomerates under the processing conditions. Other methods of producing platinum or other metallic particles could be researched. Nano-sized particles (<0.1 μm) have attracted considerable interest and could be used. A range of metals are now becoming commercially available as nano-sized particles. If the production of these particles does not require the decomposition of a starting material during the fabrication process then benefits of reduced secondary phase

formation may be achieved. However, uniform dispersion and the breakdown of particle agglomerates is required. It is considered that nano-sized particles would mainly be of benefit for high field applications where the particles, situated within grains, could restrict the movement of domains. This is analogous to the effective obstruction of magnetic domain wall motion by tungsten and chromium carbide precipitate particles in magnetic steel materials[176].

III. Domains in the barium titanate were observed to interact with the silver particles. A more detailed study could be conducted on the interaction of the domains with the silver particles fabricated in the barium titanate-silver composites. Samples could have an electric field applied intermittently to cause domain motion during TEM observation. The field levels required for domain wall motion could then be compared with those required by the monolith to determine the optimum particles types.

IV. Complex responses, such as electromagnetostrictive, may be achieved by the use of magnetostrictive particles in a piezoelectric matrix. Under the application of a magnetic field the particles exert a strain on the piezoelectric composite, which in turn generates a surface charge, hence coupling magnetic and electric fields[190].

V. Many of the properties characterised in this research were adversely affected due to the increasing porosity with higher silver contents. Sintering optimisation of barium titanate-silver composites is likely to improve the density and thus the electrical properties that depend on density, such as the capacitor figure of merit, coupling coefficient and mechanical quality factor.

VI. The small three-dimensional network size may be the reason for their simulated results corresponding closely to the two-dimensional network results. Computational modelling could be improved for the three-dimensional case with the use of larger networks.

VII. Modelling in this research consisted of point defects in a dielectric matrix. Networks could be made more complex by creating groups of components that could represent the different parts of a material, such as grain boundary and grain bulk. This could allow investigation of inclusions having different aspect ratios, such as fibres. The components types added to the reference matrix could be extended to include inductors and semi-conductors

9 REFERENCES

1. HWANG, H. J., UEDA, S. & NIIHARA, K., 'Grain boundary controlled mechanical and dielectric properties of $BaTiO_3$-based nanocomposite', *Ceram. Trans.*, 1994, **44**, 399-408

2. KOMERNENI, S., 'Nanocomposites', *J. Mat. Chem.*, 1992, **2** (12), 1219-30

3. STERNITZKE, M., 'Review: Structural ceramic nanocomposites', *J. Eur. Ceram. Soc*, 1997, **17**, 1061-82

4. NIIHARA, K., NAKAHARI, A., SEKINO, T. & HIRANO, T., 'Supertough and strong ceramics by nanodispersions', *Proc. 3rd Jpn. Int. SAMPE Symp.*, Dec 7-10 1993, 2074-2080

5. NIIHARA, K & NAKAHIRA, A., 'Particulate strengthened oxide ceramics-nanocomposites', *Advanced structural inorganic composites Ed. Vincenzini, P., Elsevier*, 1990, 637-644

6. ROY, R., ROY, R. A. & ROY, D.M., 'Alternative prospectives on "Quasi-crystallinity" non-uniformity and nanocomposites', *Mat. Letter*, 1986, **4** (8,9), 323-28

7. SUZUKI, T. S., SAKKA, Y., MOVITA, K. & HIRAGA, K., 'Enhanced superplasticity in a alumina-containing zirconia prepared by colloidal processing', *Scripta Materialia*, 2000, **43**, 705-10

8. TUAN, W., LIN, M. & WU, H., 'Preparation of Al_2O_3/Ni composites by pressureless sintering in H_2', *Ceram. Int.*, 1995, **21**, 221-25

9. OH, S-T., SEKINO, T. & NIIHARA, K., 'Fabrication and mechanical properties of 5vol% copper dispersed alumina nanocomposite', *J. Eur. Ceram. Soc.*, 1998, **18**, 31-37

10. FERRONI, F.P. & PEZZOTTI, G., 'Evidence for bulk residual stress strengthening in Al_2O_3/SiC nanocomposites', *J. Am. Ceram. Soc*, 2002, **85** (8), 2033-8

11. TAJIMA, K., HWANG, H. J., SANDO, M. & NIIHARA, K., 'PZT nanocomposites reinforced by small amount of oxides', *J. Eur. Ceram. Soc., Electroceramics VI 1998, Switzerland, Elsevier*, 1999, **19**, 1179

12. HWANG, H. J., SANDO, M., TORIYAMA, M. & NIIHARA, K., 'Effect of secondary phase dispersion on mechanical and piezoelectric properties of PZT-based nanocomposites', *IEEE Int. Symp. on Applications of Ferroelectrics*, 1996, 373-75

13. TAJIMA, K., HWANG, H., SANDO, M. & NIIHARA, K., 'Electric-field-induced crack growth behaviour in PZT/Al_2O_3 composites', *J. Am. Ceram. Soc.*, 2000, **83** (1), 651-53

14. PEARCE, D. & BUTTON, T., 'Processing and properties of silver/PZT composites', 'http://www.fmg.bham.ac.uk/papers/pzt/Ag-pzt/agpzt.htm', 26/02/03

15. HWANG, H.J., TAJIMA, K., SANDO, M., TORIYAMA, M. & NIIHARA, K., 'Fatigue behaviour of PZT-based nanocomposites with fine platinum particles', *J. Am. Ceram. Soc.*, 1998, **81** (12), 3325-8

16. NAGAI, T., HWANG, H., YASUOKA, M., SANDO, M. & NIIHARA, K., 'Preparation of barium titanate-dispersed-magnesia nanocomposite', *J. Am. Ceram. Soc.*, 1998, **81** (2), 425-28

17. TIAN, L., ZHOU, Y. & LEI, T.C., 'Mechanical properties of $Al_2O_3+ZrO_2+$Nano-SiCp ceramic composite', *Ceram. Int.*, 1996, **22**, 451-56

18. JONA, F. & SHIRANE, G., 'Ferroelectric crystals', *Dover Publications Inc, New York*, 1993

19. BHALLA, A.S., GUO, R. & ROY, R., 'The perovskite structure – A review of its role in ceramic science and technology', *Mat. Res. Innovat.*, 2000, **4**, 3-26

20. FINK, D. & CARROLL, J.M., 'Standard handbook for electrical engineers', *McGraw-Hill Book Company, London*, 1968, 10th Edn., Sec4-382

21. ROSEN, C. Z., HIREMATH, B. V. & NEWNHAM, R (Ed), 'Piezoelectricity: Key papers in physics', *Am. Inst. of Physics*, 1992, **5**, 4, 13, 119, 157, 285

22. HAERTLING, G.H., 'Ferroelectric ceramics: History and Technology', *J. Am. Ceram. Soc.*, 1999, **82** (4), 797-818

23. MOULSON, A. J. & HERBERT, J. M., 'Electroceramics – Materials, Properties & Applications', *Chapman & Hall*, 1990

24. Qinetiq Nanomaterials Ltd, 'http://www.nano.qinetiq.com/02_products_materials/', 26/02/03

25. PADMANABHAN, K., 'Mechanical properties of nanostructured materials', *Met. Sci. & Eng.*, 2001, **A304-6**, 200-5

26. RUDOLPH, S., 'Melting points of ceramics', 'http://www.a-m.de/englisch/lexikon/schmelzpunkte.htm', 26/02/03

27. NAGAI, T., HWANG, H., YASUOKA, M., SANDO, M. & NIIHARA, K., 'Dielectric properties of Pb(Zr, Ti)O_3-dispersed MgO nanocomposite', *Jpn. J. Appl. Physics*, 1998, **37**, 3377-81

28. NAGAI, T., HWANG, H., YASUOKA, M., SANDO, M. & NIIHARA, K., 'Piezoelectric dispersed ceramic nanocomposite', *J. Korean Physical Soc.*, 1998, **32**, S1271-73

29. KOVALENKO, L.L., 'Semiconducting barium titanate doped with oxygen free compounds', *J. Eur. Ceram. Soc., Electroceramics VI 1998, Switzerland, Elsevier*, 1999, **19**, 965

30. LAARZ, E., CARLSSON, M., VIVIEN, B., JOHNSSON, M., NYGREN, M. & BERGSTROM, L., 'Collodial processing of Al_2O_3-based composites reinforced with TiC and TiC particulates, whiskers and nanoparticles', *J. Eur. Ceram. Soc.*, 2001, **21**, 1027-35

31. HWANG, H.J., NAGAI, T., SANDO, M., TORIYAMA, M. & NIIHARA, K., 'Fabrication of piezoelectric particle-dispersed ceramic nanocomposite', *J. Eur. Ceram. Soc., Electroceramics VI 1998, Switzerland, Elsevier*, 1999, **19**, 993

32. NAGAI, T., HWANG, H., SANDO, M. & NIIHARA, K., 'Preparation of ceramic nanocomposite with perovskite dispersiod', *Mat. Res. Soc. Symp. Proc.*, 1997, 375-80

33. KINGERY, W.D., 'Introduction to ceramics', *J. Wiley & Sons Inc*, 1976

34. TODD, R. I., 'Alumina/SiC nanocomposites – big things from small packages', *21ˢᵗ century ceramics Ed. Thompson, D. P. & Mondal, H., IOM*, 1996, **55**, 225-248

35. KOH, Y-H., KIM, H-W., & KIM, H-E., 'Microstructural evolution and mechanical properties of Si₃N₄-SiC (nanocomposites) –Si₃N₄ (whiskers) composites', *J. Mat. Res.*, 2000, **15** (2), 364-68

36. BORSA, C., JIAO, S., TODD, R. & BROOK, R., 'Processing and properties of Al₂O₃/SiC nanocomposites', *J. Microscopy*, 1995, **77** (3), 305-12

37. SCHMID, H., ALSAN, M., ASSMANN, S., NAB, R. & SCHMIDT, H., 'Microstructural characterisation of Al₂O₃-SiC nanocomposites', *J. Eur. Ceram. Soc.*, 1998, **18**, 39-49

38. ANYA, C. & ROBERTS, S., 'Pressureless sintering and elastic constants of Al₂O₃-SiC "nanocomposite" ', *J. Eur. Ceram. Soc.*, 1997, **17**, 565-73

39. DENG, Z-Y., SHI, J-L., ZHANG, Y-F., JIANG, D-Y. & GUO, J-K., 'Pinning effect of SiC particles on mechanical properties of Al₂O₃-SiC ceramic matrix composites', *J. Eur. Ceram. Soc.*, 1998, **18**, 501-08

40. HWANG, H., SEKINO, T., OTA, K. & NIIHARA, K., 'Perovskite-type BaTiO₃ ceramics containing particulate SiC: Part I-Structure variation and phase transformation', *J. Mat. Sci.*, 1996, **31**, 4617-24

41. HWANG, H. & NIIHARA, K., 'Perovskite-type BaTiO₃ ceramics containing particulate SiC: Part II-Microstructure and mechanical properties', *J. Mat. Sci.*, 1998, **33**, 549-558

42. WILHELM, M. & WRUSS, W., 'Influence of annealing on the mechanical properties of SiC-Si composites with sub-micron SiC microstructures', *J. Eur. Ceram. Soc.*, 2000, **20**, 1205-13

43. FERKEL, H. & MORDIKE, B.L., 'Magnesium strengthened by SiC nanoparticles', *Mat. Sci. & Eng*, 2001, **A298**, 193-9

44. LIN, Y-J. & CHEN, L-J., 'Oxidation of SiC powders in SiC/Alumina/Zirconia compacts', *Ceram. Int.*, 2000, **26**, 593-8

45. NARUSHIMA, T., GOTO, T., IGUCHI, Y. & HIRAI, T, 'High-temperature active oxidation of chemically vapor-deposited silicon carbide in an Ar-O₂ atmosphere', *J. Am. Ceram. Soc.*, 1991, **74** (10), 2583-6

46. CHOU, W. & TUAN, W., 'Toughening and strengthening of alumina with silver inclusions', *J. Eur. Ceram. Soc.*, 1995, **15**, 291-95

47. CHEN, C-Y. & TUAN, W., 'Evaporation of silver during co-firing with barium titanate', *J. Am. Ceram. Soc.*, 2000, **83** (7), 1693-98

48. HWANG, H., WATARI, K., SANDO, M., TORIYAMA, M. & NIIHARA, K., 'Low temperature sintering and high strength Pb(Zr,Ti)O$_3$-matrix composites incorporating silver particles', *J. Am. Ceram. Soc.*, 1997, **80** (3), 791-93

49. CHEN, C-Y. & TUAN, W-H., 'Effect of silver on the sintering and grain-growth behaviour of barium titanate', *J. Am. Ceram. Soc.*, 2000, **83** (12), 2988-92

50. HWANG, H.J., YASUOKA, M., SANDO, M., TORIYAMA, M. & NIIHARA, K., 'Fabrication, sinterability, and mechanical properties of lead zirconate titanate/silver composites', *J. Am. Ceram. Soc.*, 1999, **82** (9), 2417-22

51. LALANDE, J., SCHEPPOKAT, S., JANSSEN, R. & CLAUSSEN, N., 'Toughening of alumina/zirconia ceramic composites with silver particles', *J. Eur. Ceram. Soc.*, 2002, **22**, 2165-71

52. SUK, M-J., MIN, K.H., KIM, Y.D. & MOON, I-H., 'Synthesis of Al$_2$O$_3$/Cu nanocomposite by dispersion and reduction of copper oxide', *Advances in powder metallurgy & particulate materials 2001, pt9: Composites, laser fabrication, mechanical alloying, nanocrystalline materials, aluminium compiled by ALSEN, W.B. & KASSAM, S.*, 9-42

53. HWANG, H.J., TORIYAMA, M., SEKINO, T. & NIIHARA, K., 'In-situ fabrication of ceramic/metal nanocomposites by reduction reaction in barium titanate-metal oxide systems', *J. Eur. Ceram. Soc.*, 1998, **18**, 2193-99

54. CHEN, R.Z. & TUAN, W.H., 'Interfacial fracture energy of Al$_2$O$_3$/Ni nanocomposites', *J. Mat. Sci. Lett.*, 2001, **20**, 2029-30

55. SLINKINA, M.V., VOLOSENTSEVA, L.I. & SEGALLA, A.G., 'Diffusion and solubility of silver in various ceramics based on lead zirconate-titanate', *Inorganic materials*, 1993, **29** (3), 456-9

56. LIDE, D.R., 'CRC handbook of chemistry and physics', 86th Edition, 5-7

57. Applied Epi, 'http://www.appliedepi.com/components/mbesources.htm', 26/02/03

58. ERNST, F., KIENZLE, O. & RUHLE, M., 'Structure and composition of grain boundaries in ceramics', *J. Eur. Ceram. Soc.*, 1999, **19**, 665-73

59. WEISS, E. & BELL, A., 'A Comparison of the electrical and mechanical strengths of conventional and flux-sintered barium titanate-based dielectrics', *Brit. Ceram. Proc.*, 1992, **49**, 229-39

60. LIM, M-H., CHOU, J-F. & LU, H-Y., 'The rate-determining mechanism in the sintering of undoped non-stoichiometric barium titanate', *J. Eur. Ceram. Soc.*, 2000, **20**, 517-26

61. LEE, J-K., HOMG, K-S. & JANG, J-W., 'Roles of Ba/Ti ratios in the dielectric properties of BaTiO$_3$ ceramics', *J. Am. Ceram. Soc.*, 2001, **84** (9), 2001-6

62. VOLTZKE, D. & ABICHT, H-P., 'The influence of different additives and the mode of their addition on the sintering behaviour and the properties of semiconducting barium titanate ceramics', *Solid State Sciences*, 2000, **2** (1), 149-59

63. STEARNS, L., ZHAO, J. & HARMER, M., 'Processing and microstructure development in Al₂O₃-SiC "nanocomposites" ', *J. Eur. Ceram. Soc.*, 1992, **10**, 473-77

64. MAEKAWA, K., NAKADA, Y. & KIMURA, T., 'Origins of hindrance in densification of Ag/Al₂O₃ composites', *J. Mat. Sci.*, 2002, **37**, 397-410

65. BAMBA, N., CHOA, Y., SEKINO, T. & NIIHARA, K., 'Effects of nano-sized silicon carbide particulate on microstructure and ionic conductivity for 8mol % yttria stabilised zirconia based nanocomposites', *Solid State Ionics III*, 1998, (1-2), 171-179

66. YONG, J-F., CHOA, Y-H., SINGH, J. & NIIHARA, K. 'Fabrication and mechanical properties of Si₃N₄/SiC nanocomposite with pressureless sintering and sinter-post-hiping', *J. Ceram. Soc. Jpn.*, Oct 98, 951-57

67. SURYANARAYANAN, R., YER, I. & SASTRY, S.M.L., 'Consolidation of nanoparticles-development of a micromechanistic model', *Acta Mater.*, 1999, **47** (10), 3079-98

68. WANG, H., GAO, L. & GUO, J., 'The effect of nanoscale SiC particles on the microstructure of Al₂O₃ ceramics', *Ceram. Int.*, 2000, **26**, 391-96

69. POHANKA, R., RICE, R. & WALKER, B., 'Effect of internal stress on the strength of BaTiO₃', *J. Am. Ceram. Soc.*, 1976, **59** (1-2), 71-74

70. CHEN, C. & TUAN, W., 'Mechanical and dielectric properties of BaTiO₃/Ag composites', *Mat. Sci. Lett.*, 1999, **18**, 353-54

71. CHEN, R. & TUAN, W., 'Pressureless sintering of Al₂O₃/Ni nanocomposites', *J. Eur. Ceram. Soc.*, 1999, **19**, 463-8

72. SAUCY, C., REANEY, I. & BELL, A., 'Microstructure and electromechanical properties of BaTiO₃-ZrO₂ "Core-shell" ceramics', *Brit. Ceram. Proc.*, 1993, **51**, 29-52

73. GACHIGI, K., KUMAR, U. & DOUGHERTY, J., 'Grain size effects in barium titanate', *Proc. 8ᵗʰ IEEE Int. Symp. on Application of Ferroelectrics*, 1992, 492-5

74. WANG, S-F. & DAYTON, G., 'Dielectric properties of fine-grained barium titanate X7R materials', *J. Am. Ceram. Soc.*, 1999, **82** (10), 2677-82

75. ZHAO, J., STEARNS, I., HARMER, M., CHAN, H., MILLER, G. & COOK, R., 'Mechanical behaviour of alumina-silicon carbide "nanocomposite", *J. Am. Ceram. Soc.*, 1993, **76** (2), 503-10

76. HWANG, H. & NIIHARA, K., 'Fabrication of surface barrier layer capacitor on BaTiO₃-based composite containing particulate SiC', *J. Mat. Res.*, 1998, **13** (10), 2866-70

77. HWANG, H., NAKAHIRA, A., SEKINO, T. & NIIHARA, K., 'Mechanical property and fracture behaviour of BaTiO₃-based nanocomposites', *Transcip. J. Jpn. Soc. Powder Powder Metall.*, 1994, **10**, 1175-80

78. OHJI, T. & NIIHARA, K., 'Comments on "Physical limitations of the inherent toughness and strength in ceramic-ceramic and ceramic-metal nanocomposites', *J. Ceram. Soc. Jpn.*, 1996, **104** (6), 581-82

79. GAO, L., WANG, H., HONG, J., MIYAMOTO, H., MIYAMOTO, K., NISHIKAMA, Y. & TORRE, S., 'Mechanical properties and microstructure of nano-SiC-Al₂O₃ composites densified by spark plasma sintering', *J. Eur. Ceram. Soc.*, 1999, **19**, 609-13

80. LUAN, W., GAO, L. & GUO, J., 'Size effect on dielectric properties of fine-grained BaTiO₃ ceramics', *Ceram. Int.*, 1999, **25**, 727-29

81. WINN, A. & TODD, R., 'Microstructural requirements for alumina-SiC nanocomposites', *Brit. Ceram. Trans.*, 1999, **98** (5), 219-24

82. HWANG, H., NAGAI, T., OHJI, T., SANDO, M., TORIYAMA, M. & NIIHARA, K., 'Curie temperature anomaly in lead zirconate titanate/silver composite', *J. Am. Ceram. Soc.*, 1998, **81** (3), 709-12

83. HWANG, H. & NIIHARA, K., 'Subcritical crack growth phenomenon and fractography of barium titanate and barium-titanate-based composite', *Transip. Scripta Metallurgica et Materialia*, 1997, **36** (2), 183-87

84. ARLT, G., HENNINGS, D. & DE WITH, G., 'Dielectric properties of fine-grained barium titanate ceramics', *American Institute of Phys. J. Appl. Phys.*, 15 Aug 1985, **58** (4), 1619-25

85. LEE, B-K., CHUNG, S-Y. & KANG, S-J., 'Necessary conditions for the formation of {111} twins in barium titanate', *J. Am. Ceram. Soc.*, 2000, **88** (1), 2858-60

86. FRANKLIN, S. & RAND, B., 'Reactions of silicon and carbon in reducing atmosphere', *Eng. with Ceram., Ed. Lee, W. & Derby, B., Brit. Ceram. Proc.*, 1999, **59**, 243-254

87. SHIMOO, T., OKAMURA, K. & TOYODA, F., 'Thermal stability of SiO₂-coated SiC fiber (Hi-Nicalon) under argon atmosphere', *J. Mat. Sci.*, 2000, **35**, 3811-6

88. ARBOGAST, D.F., FOSTER, M.C., PHOTINOS, P.J., NIELSON, R.M. & ABRAHAMS, S.C., 'Fresnoite, Ba_2TiSi_2O_7: A New Ferroelectric Mineral', 'http://www.aps.org/BAPS MAR98/abs/S2225005.html', 26/02/03

89. Fresnoite Mineral Data, 'webmineral.com/data/Fresnoite.shtml', 26/02/03

90. SENZ, S., GRAFF, A., BLUM, W., HERSE, D. & ABICHT, H-P., 'Orientation relationships of reactively grown Ba₆Ti₁₇O₄₀ and Ba₂TiSi₂O₈ on BaTiO₃ (001) determined by X-ray diffraction', *J. Am. Ceram. Soc.*, 1998, **81** (5), 1317-21

91. FELGNER, K-H., MULLER, T., LANGHAMMER, H.T. & ABICHT, H-P., 'Investigations on the liquid phase in barium titanate ceramics with silica additions', *J. Eur. Ceram. Soc.*, 2001, **21**, 1657-60

92. BROOK, R. & MACKENZIE, R., 'Nanocomposite Materials', *Materials World*, Jan 93, 27-30

93. EVANS, A., 'Perspective on the development of high toughness ceramics', *J. Am. Ceram. Soc.*, 1990, **73** (2), 187-206

94. OHJI, T., JEONG, Y-K., CHOA, Y-H. & NIIHARA, K., 'Strengthening and toughening mechanisms of ceramic nanocomposites', *J. Am. Ceram. Soc.*, 1998, **81** (6), 1453-60

95. CAIN, M., STEWART, M. & GEE, M., 'Mechanical and elastic strength measurements for piezoelectric ceramics: Technical measurement notes', *NPL report CMMT(A)99*, 1998

96. SHANG, J.K. & TAN, Y., 'A maximum strain criterion for electric-field-induced fatigue crack propagation in ferroelectric ceramics', *Mat. Sci. & Eng. A*, 2001, 301, 131-9

97. PEZZOTTI, G., NISHIDA, T. & SAKAI, M., 'Physical limitations of the inherent toughness and strength in ceramic-ceramic and ceramic-metal nanocomposites', *J. Ceram. Soc. Jpn.*, 1995, 103, 901-09

98. FANG, T., HSEIH, H-L. & SHIAU, F-S., 'Effect of pore morphology and grain size on the dielectric properties and tetragonal-cubic phase transition of high-purity barium titanate', *J. Am. Ceram. Soc.*, 1993, 76 (5), 1205-11

99. HOLK, R. & PROVENZANO, V., 'Bounds on the strength of a model nanocomposite', *Nanostructured materials*, 1997, 8 (3), 289-300

100. BORSA, C., FERREIRA, H. & KIMINAMI, R., 'Liquid phase sintering of Al_2O_3-SiC nanocomposites', *J. Eur. Ceram. Soc.*, 1999, 19, 615-21

101. HYAGA, H., HAYASHI, Y., SEKINO, T. & NIIHARA, K., 'Fabrication process and electrical properties of $BaTiO_3$/Ni nanocomposite', *Nanostructured Materials*, 1997, 9, 547-50

102. DE WITH, G. & WAYEMANS, H.H.M., 'Ball-on-ring test revisited', *J. Am. Ceram. Soc.*, 1989, 72 (8), 1538-41

103. SEO, S. & KISHIMOTO, A., 'Effect of polarization treatment on bending strength of barium titanate/zirconia composite', *J. Eur. Ceram. Soc.*, 2000, 20, 2427-2431

104. CHUNG, H-T., SHIN, B-C. & KIM, H-G., 'Grain-size dependence of electrically induced microcracking in ferroelectric ceramics', *J. Am. Ceram. Soc.*, 1989, 72 (2), 327-29

105. DERE, H., EVANS, A., ODETTE, G., MEHRABIAN, R., HECHT, R. & EMILIAN, M., 'Ductile reinforcement toughening of γ-TiAl: Effects of debonding and ductility', *Acta Metallurgica Materialia*, 1990, 38 (8), 1491-1502

106. ZHOU, J., LI, L., GUI, Z., ZHANG, X. & BARBER, D., 'Sol-gel derived $BaTiO_3$ thin films with embedded silver nanoparticles: Preparation and dielectric properties', *Nanostructured materials*, 1997, 8 (3), 321-28

107. W. R. CALLISTER: 'Materials science and Engineering: An introduction', J. Wiley & Sons Inc., Chichester, 1994, 646-94

108. TAYA, M., HAYASHI, S., KOBAYASHI, A. & YOON, H., 'Toughening of a particulate-reinforced ceramic-matrix composite by thermal residual stress', *J. Am. Ceram. Soc.*, 1990, 73 (5), 1382-91

109. ANSTIS, G.R., CHANTIKUL, P., LAWN, B.R. & MARSHALL, D.B., 'A critical evaluation of indentation techniques for measuring fracture toughness: I, direct crack measurements', *J. Am. Ceram. Soc.*, 64 (9), 533-538

110. OKAZAKI, K. & IGARASHI, H., 'Importance of microstructure in electronic ceramics', *Ceramic microstructure '76*, 564-83

111. ASMANI, M., KERMEL, C., LERICHE, A. & OURAK, M., 'Influence of porosity on Young's modulus and Poisson's ratio in alumina ceramics', *J. Eur. Ceram. Soc.*, 2001, **21**, 1081-6

112. ALDRICH, D.E., FAN, Z. & MUMMERY, P., 'Processing, microstructure, and physical properties of interpenetrating Al$_2$O$_3$/Ni composites', *Mat. Sci. & Tech.*, 2000, **16**, 747

113. University of Connecticut, 'Dielectric behaviour and ferroelectricity', 'http://www.ims.uconn.edu/~alpay/201/Dielectric.pdf', 26/2/03

114. BELL, A. J. & MOULSON, A. J., 'The effect of grain size on the dielectric properties of barium titanate ceramics', *Brit. Ceram. Soc.*, 1985, **36**, 57-66

115. HIROSE, N & WEST, A. R., 'Impedance spectroscopy of undoped BaTiO$_3$ ceramics', *J. Am. Ceram. Soc.*, 1996, **79** (6), 1633-41

116. BELL, A., MOULSON, A. & CROSS, L., 'The effect of grain size on the permittivity of BaTiO$_3$', *Ferroelectrics*, 1984, **54**, 147-50

117. ARLT, G. & PEUSENS, H., 'The dielectric constant of coarse grained BaTiO$_3$ ceramics', *Ferroelectrics*, 1983, **48**, 213-24

118. LEE, M-H, HALLIYAL, A & NEWNHAM, R. E., 'Poling of co-precipitated lead titanate-epoxy 0-3 piezoelectric composite', *J. Am. Ceram. Soc.*, 1989, **72** (6), 986-90

119. KOUMOTO, K., TAGAWA, H., NAKANO, T., TAKEDA, S. & YANAGIDA, H., 'TEM observation of the grain boundaries in semiconducting barium titanate thick films', *Jpn. J. Appl. Physics*, 1984, **23** (5), L305-307

120. NAGAI, T., HWANG, H., YASUOKA, M., SANDO, M. & NIIHARA, K., 'Ceramic nanocomposites with perovskite-type ferroelectric dispersiod', *Key Eng. Mat.*, 1999, **161-63**, 509-512

121. EMOTO, H. & HOJO, J., 'Sintering and dielectric properties of BaTiO$_3$-Ni composite ceramics', *J. Ceram. Soc. Jpn.*, 1992, **100** (4), 555-9

122. KWON, S., SHIN, F. & TSUI, W., 'Dielectric constant of silver-thermosetting polyester composites', *J. Mat. Sci.*, 1984, **19**, 4093-8

123. ABELES, B., SHENG, P., COTTS, M.D. & ARIE, Y., 'Structural and electrical properties of granular metal films', *J. Adv. Phys.*, **24**, 1975, 407-460

124. CHEN, I. G. & JOHNSON, W. B., 'Alternating-current electrical properties of random metal-insulator composites', *J. Mat. Sci.*, 1991, **26**, 1565-76

125. TEPPAR, T. & BERGER, S., 'Correlation between microstructure and electrical properties of tungsten-silica nanocomposites', *Nanostructured Materials*, 1999, **11** (7), 895-907

126. CONDER, R., PONTON, C. & MARQUIS, P., 'Processing of alumina/silicon carbide nanocomposites', *Nanoceramics, Ed. Freer, R., Brit. Ceram. Proc.*, 1993, **51**, 105-17

127. ARLT, G., 'The role of domain walls on the dielectric, elastic and piezoelectric properties of ferroelectrics ceramics', *Ferroelectrics*, 1987, **76**, 451-58

128. WU, K. & SCHULZE, W., 'Effect of AC Field level on the aging of the dielectric response of polycrystalline $BaTiO_3$', *J. Am. Ceram. Soc.*, 1992, **75** (12), 3385-89

129. HALL, D., 'Rayleigh behaviour and the threshold field in ferroelectric ceramics', *Ferroelectrics*, 1999, **223**, 319-328

130. HALL, D.A. & STEVENSON, P.F., 'High field dielectric behaviour of ferroelectric ceramics', *Ferroelectrics*, 1999, **228**, 139-58

131. HALL, D.A., 'Review: Non-linearity in piezoelectric ceramics', *J. Mat. Sci.*, 2001, **36**, 4575-4601

132. TAKEUCHI, T., BETOURNE, E., TABUCHI, M., KAGEYAMA, H., KOBAYASHI, Y., COATS, A., MORRISON, F., SINCLAIR, D. & WEST, A., 'Dielectric properties of spark plasma-sintered $BaTiO_3$, *J. Mat. Sci.*, 1999, **34**, 917-24

133. CABALLERO, A., VILLEGAS, M., FERNANDEZ, J., VIVIANI, M., BUSCAGLIA, M. & LEONI, M., 'Effect of humidity on the electrical response of porous $BaTiO_3$ ceramics', *J. Mat. Sci. Lett.*, 1999, **18**, 1297-9

134. DEXTER, 'Domain theory', 'www.dextermag.com/domain_theory.htm', 26/02/03

135. ZIVKOVIC, L., STOJANOVIC, B., PAVLOVIC, V., NIKOLIC, Z. & MARINLOVIC, B., 'SEM investigation of domain structure in (Ba, Ca, Pb)TiO_3', *J. Eur. Ceram. Soc., Electroceramics VI 1998, Switzerland, Elsevier*, 1999, **19**, 1085

136. DENNIS, M., 'Transmission electron microscopy of ferroelectric domains in $BaTiO_3$', Thesis, Sept 1972, Pennsylvania State University

137. HU, H-L. & CHEN, L-Q., 'Three dimensional computer simulation of ferroelectric domain formation', *J. Am. Ceram. Soc.*, 1998, **81** (3), 492-500

138. COOK, W.R., 'Domain Twinning in barium titanate ceramics', *J. Am. Ceram. Soc.*, 1956, **39** (1), 17-19

139. OGAWA, T., 'Domain structure of ferroelectric ceramics', *Ceram. Int.*, 2000, **26**, 383-90

140. MORENO, J., GUIU, F., MEREDITH, M., REECE, M., ALFORD, N. & PENN, S., 'Anisotropic and cyclic mechanical properties of piezoelectrics –compression testing', *J. Eur. Ceram. Soc., Electroceramics VI 1998, Switzerland, Elsevier*, 1999, **19**, 1321

141. ZHU, T. & YANG, W., 'Toughness variation of ferroelectrics by polarisation switch under non-uniform electric field', *Acta Materialia*, 1997, **45** (11), 4695-4702

142. WANG, H. & SINGH, R. N., 'Crack propagation in piezoelectric ceramics: effect of applied electric fields', *J. Appl. Phys.*, 1 June 1997, **81** (11), 7471-79

143. MORRISON, F.D., SINCLAIR, D.C. & WEST, A.R., 'Characterisation of lanthanum doped barium titanate ceramics using impedance spectroscopy', *J. Am. Ceram. Soc.*, 2001, **84** (3), 531-8

144. MESCHKE, F., KOLLECK, A. & SCHNEIDER, A., 'R-Curve behaviour of BaTiO$_3$ due to stress-induced ferroelectric domain switching', *J. Eur. Ceram. Soc.*, 1997, **17**, 1143-49

145. VILLEGAS, M., CABALLERO, A.C., MOURE, C., DURAN, P., FERNANDEZ, J.F. & NEWNHAM, R.E., 'Influence of processing parameters on the sintering and electrical properties of Pb(Zn$_{1/3}$Nb$_{2/3}$)O$_3$-based ceramics', *J. Am. Ceram. Soc.*, 2000, **83** (1), 141-46

146. UCHINO, K. & HIROSE, S., 'Loss mechanisms in piezoelectrics: How to measure different losses separately', *IEEE Transactions on Ultrasonics, Ferroelectrics and frequency control*, 2001, **43** (1), 307

147. SHERRIT, D., VAN NICE, D., GRAHAM, J., MUKHERJEE, B. & WIEDERICK, H., 'Domain wall motion in piezoelectric materials under high stress', *Proc. Int. Soc. for the Applications of Ferroelectrics*, 1992, 167-70

148. WALLER, D. & SAFARI, A., 'Corona poling of PZT ceramics and flexible piezoelectric composites', *Ferroelectrics*, 1988, **87**, 189-95

149. SESSLER, G., 'Poling and properties of polarisation of ferroelectric polymers and composites', *Key Eng. Mat.*, 1994, **92-93**, 249-74

150. BATLLO, F., BEAUGER, A., NIEPCE, J. & SCHOULER, E., 'Solid state chemistry and dielectric behaviour in BaTiO$_3$ for multilayer ceramic capacitors', *Brit. Ceram. Proc.*, 1989, **41**, 117-26

151. HENNINGS, D.F.K., 'Dielectric materials for sintering in reducing atmospheres', *J. Eur. Ceram. Soc.*, 2001, **21**, 1637-42

152. SHIN, B-C. & KIM, H-G., 'Partial discharge, microcracking and breakdown in BaTiO$_3$ ceramics', *Ferroelectrics*, 1988, **77**, 161-166

153. WAANDERS, J. W., 'Piezoelectric ceramics – Properties and application', *Phillips*, 1991

154. *European standard prEN 50324-2:1999E Piezoelectric properties of ceramic materials and components; Part 2: methods of measurement and properties – low power*, 1999

155. METLOV, K., 'Representability of the domain wall motion in random potentials by the Preisach model', *Physica B*, 2000, **275**, 164-7

156. CAIN, M. G. & STEWART, M., 'Measurement good practice guide No. 33: Piezoelectric resonance', *NPL*, Teddington, 2001

157. BOWEN, C.R., LOPEZ-PRIETO, M., MAHON, S. & LOWRIE, F., 'Impedance spectroscopy of piezoelectric actuators', *Scripta Materialia*, 2000, **42** (8), 813-18

158. SMITH, R.C. & OUNAIES, Z., 'A domain wall model for hysteresis in piezoelectric materials', ICASE Report no. 99-52, 1999

159. RAPRA Technology Ltd., 'Particle size analysis – The laser diffraction technique', www.azom.com/details.asp?ArticleID=1528', 26/02/03

160. ALLEN, T., 'Particle Size Measurement', *Chapman & Hall*, 1968

161. XUE, J., WANG, J. & WAN, D., 'Nanosized Barium titanate powder by mechanical activation', *J. Am. Ceram. Soc.*, 2000, **83** (1), 232-34

162. SHETTY, D.K., ROSENFIELD, A.R., DUCKWORTH, W.H. & HELD, P.R., 'A Biaxial-flexure test for evaluating ceramic strengths', *J. Am. Ceram. Soc.*, 1983, **66** (1), 36-42

163. ERHART, J. & BURIANOVA, L., 'What is really measured on a d_{33}-meter?', *J. Eur. Ceram. Soc.*, 2001, **21**, 1413-5

164. CAIN, M. G., STEWART, M. & HALL, D.A., 'Ferroelectric Hysteresis: Measurement & Analysis', NPL report CMMT(A)152, 1999

165. CAS 26023-84-7, *Aldrich, England*, 2003

166. Metals handbook: Properties and selection of metals, 8th Ed., *Am. Soc. for Metals, Metals Park, Ohio, USA*, 1961, 1

167. BLAMEY, J.M. & PARRY, T.V., 'Strength and toughness of barium titanate ceramics', *J. Mat. Sci.*, 1993, **28**, 4988-93

168. NEAR C., 'Properties of Morgan Electro ceramic ceramics', *Technical Publication TP-226*, 2003

169. Properties of Piezo Material Barium titanate, http://www.efunda.com, 19/03/03

170. STAUFFER, D., 'Introduction to percolation theory', *Taylor & Francis, London and Philadelphia*, 1985

171. SAHIMI, M., HUGHES, B.D., SCRIVEN, L.E. & DAVIS, H.T., 'Critical exponent of percolation conductivity by finite-size scaling', *J. Phys. C: Solid State Phys.*, 1983, **16**, L521-7

172. GINGOLD, D.B. & LOBB, C.J., 'Percolative conduction in three dimensions', *Phys. Rev. B.*, 1990, **42** (13), 8220-8224

173. WALLER, D., TIGBAL & SAFARI, A, 'Poling of PZT ceramics and flexible piezoelectric composites by corona discharge techniques', *J. Am. Ceram. Soc.*, 1989, **72** (2), 322-24

174. JAFFE, B., COOK, W.R. & JAFFE, H., 'Non-metallic solids: Vol. 3: Piezoelectric ceramics', Ed. Roberts, J.P. & Popper, P., *Academic Press, London*, 1971

175. NOWOTNY, J., 'Electronic ceramic materials', *Trans Tech Publications, Switzerland-Germany-UK-USA*, 1992

176. CALLISTER, W.D., 'Materials science and engineering, An introduction', *John Wiley & Sons, Inc., New York*, 2000, 688-693

177. ALMOND, D. & VAINES, B., 'The dielectric properties of random R-C networks as an explanation of the 'universal' power law dielectric response of solids', *J. Phys. Condens. Matter*, 1999, **11**, 9081-93

178. CRACIUM, F., GALASSI, C. & RONCARI, E., 'Experimental evidence for similar critical behaviour of elastic modulus and electric conductivity in porous ceramic materials', *Europhysics Lett.*, 1998, **41** (1), 55-60

179. HU, C-K, 'Universal scaling functions for percolation models', *Proc. Natl. Sci. Counc. Roc.(A)*, 1999, **23** (3), 331-47

180. www.seas.smu.edu/~jll/pm/01ch1.pdf, 19/03/03

181. NEWNHAM, R.E., 'Composite electroceramics', *Ferroelectrics*, 1986, **86**, 1-32

182. CLERC, J.P., GIRAUD, G., LAUGIER, J.M. & LUCK, J.M., 'The electrical conductivity of binary disordered systems, percolation clusters, fractals and related models', *Advances in physics*, 1990, **39** (3), 191-309

183. CHEN, X-M., SHEN, J-W. & HUANG, W-Y., 'Novel electrically conductive polypropylene/graphite nanocomposites', *J. Mat. Sci. Lett.*, 2002, **21**, 213-4

184. TEPPER, T. & BERGER, S., 'Dielectric permittivity and electrical conductivity of tungsten-silica nanocomposites', *Mat. Sci. & Eng.*, 2001, **C15**, 195-7

185. COVERDALE, R.T., JENNINGS, H.M. & GORBOCZI, E.J., 'An improved model for simulating impedance spectroscopy', *Computational materials*, 1995, **3**, 465-74

186. FRANK, D.J. & LOBB, G.J., 'Highly efficient algorithm for percolative transport studies in two dimensions', *Phys. Rev. B*, 1988, **37** (7), 302-7

187. BOUAMRANE, R., 'Dielectric properties of random R-C networks', Unpublished work

188. BOUAMRANE, R. & ALMOND, D.P., 'The 'emergent scaling' phenomenon and the dielectric properties of random R-C networks', Unpublished work (Private communication).

189. CLARK, I., MARQUIS. F. & SINCLAIR, D., 'The influence of grain boundary impedance on the p-type conductivity of undoped $BaTiO_3$ ceramics', *J. Eur. Ceram. Soc.*, 2002, **22**, 579-583

190. MAHAJAN, R.P., PATANKAR, K.K., KOTHALE, M.B. & PATIL, S.A., 'Conductivity, dielectric behaviour and magnetoelectric effect in copper ferrite-barium titanate composites', *Bull. Mater. Sci.*, 2000, **23** (4), 273-279

APPENDICES

APPENDIX I: PROPERTIES OF RESEARCH RELATED MATERIALS

Barium titanate, BaTiO₃

Colour: Yellow (Oxidised) – dark blue/black (Reduced)[1]

Bonding: Ionic

Crystal Structure: Tetragonal at room temperature[2]

Density (gcm⁻³): 5.8[3]

Young's Modulus (GPa): 67[3]

Curie Temperature (°C): 120[4]

Relative Permittivity

Single crystal values: 230 (polar direction) and 4770 (perpendicular)[2]

Polycrystalline prediction: 1740 (Lichtenecker relationship)[2]

Measured: 1500[4], ε_{11}=1900, ε_{33}=1600[2]

Quality factor: 140[2]

Coupling factors[2, 3]: k_{31}=0.2, k_{33}=0.5, k_{15}=0.5, k_p=0.38, k_{31}=0.21, k_{33}=0.49, k_{15}=0.44

Piezoelectric coefficients[2, 4, 5] **(pC/N):** d_{31}=-56, -79, d_{33}=150, 190, 191, d_{15}=270

Maximum polarisation (C/m²): 0.15[2]

Thermal expansion coefficient (x10⁻⁶ m.°C⁻¹): 14[6]

Silicon Carbide, SiC

Colour: Dark grey

Crystal structure: α-SiC is hexagonal, β-SiC is cubic diamond

Bonding: Covalent

Density (gcm⁻³): 3.2[7]

Thermal expansion Coefficient (x10⁻⁶ m.°C⁻¹): 4.6-5.7[8]

Poisson's Ratio: 0.183-0.192[7]

Young's Modulus (GPa): 700[7] (single crystal), 410[1, 7]

Tensile strength (MPa): 34-137[7]

Electrical resistivity (μΩ.m): 1x10⁴ [7]

Oxidation: Passive oxidation due to a dense silica surface layer, which changes to active oxidation by silicon oxide gas formation at high temperature. Transition temperature decreases as oxygen partial pressure reduced (1350°C-2.5Pa, 1550°C-123Pa)[8]. The silica layer can be removed by a hydrofluoric acid etch, however re-oxidation occurs during sintering[9].

UF45 particle size (nm): 240[9], 200[10]

Lead zirconate titanate, PZT

Young's modulus (GPa): 78[11]

Poisson's ratio: 0.37[11]

Silver

Crystal structure: Face-centred cubic[14]

Density (g/cm^3): 10.5[12, 13]

Poisson's ratio: 0.38[11], 0.37[14]

Young's modulus (GPa): 75[11], 71[14]

Melting point (°C): 961.8[12], 960.8[14]

Electrical resistivity ($\mu\Omega$.cm): 1.63[12], 1.59[14]

Hardness (GPa): 2.5-3

Thermal expansion coefficient (x10^{-6} m.°C^{-1}): 19.68[14]

Vapour pressure (mm Hg): 0.1/1190°C, 1/1360°C (volatisation greater under oxidising atmosphere)[14]

Tensile strength (MPa): 125.5[14]

Platinum

Crystal structure: Face-centred cubic

Density (g/cm^3): 21.4[12, 14, 15]

Poisson's ratio: 0.39[12, 14]

Young's modulus (GPa): 171[12], 146.9[14]

Melting point (°C): 1768.4[12, 14]

Electrical resistivity ($\mu\Omega$.cm): 9.85[12], 9.83[14]

Vapour pressure (mm Hg): 1.1x10^{-6}/1500°C[14]

Tensile strength (MPa): 137.9[14]

References

1. HWANG, H. & NIIHARA, K., 'Fabrication of surface barrier layer capacitor on BaTiO$_3$-based composite containing particulate SiC', *J. Mat. Res.*, 1998, **13** (10), 2866-70

2. MOULSON, A. J. & HERBERT, J. M., 'Electroceramics – Materials, Properties & Applications', *Chapman & Hall*, 1990

3. MEMSnet, 'http://www.memsnet.org/material/bariumtitanatebatio3bulk/', 27/02/03

4. FINK, D. & CARROLL, J.M., 'Standard handbook for electrical engineers', *McGraw-Hill Book Company, London*, 1968, 10th Edn., Sec4-382

5. OGAWA, T., 'Domain structure of ferroelectric ceramics', *Ceram. Int.*, 2000, **26**, 383-90

6. HWANG, H., SEKINO, T., OTA, K. & NIIHARA, K., 'Perovskite-type $BaTiO_3$ ceramics containing particulate SiC: Part I-Structure variation and phase transformation', *J. Mat. Sci.*, 1996, **31**, 4617-24

7. MEMSnet, 'http://www.memsnet.org/material/siliconcarbidesicbulk/', 27/02/03

8. LIN, Y-J. & CHEN, L-J., 'Oxidation of SiC powders in SiC/Alumina/Zirconia compacts', *Ceram. Int.*, 2000, **26**, 593-8

9. WILHELM, M. & WRUSS, W., 'Influence of annealing on the mechanical properties of SiC-Si composites with sub-micron SiC microstructures', *J. Eur. Ceram. Soc.*, 2000, **20**, 1205-13

10. OHJI, T., JEONG, Y-K., CHOA, Y-H. & NIIHARA, K., 'Strengthening and toughening mechanisms of ceramic nanocomposites', *J. Am. Ceram. Soc.*, 1998, **81** (6), 1453-60

11. HWANG, H., NAGAI, T., OHJI, T., SANDO, M., TORIYAMA, M. & NIIHARA, K., 'Curie temperature anomaly in lead zirconate titanate/silver composite', *J. Am. Ceram. Soc.*, 1998, **81** (3), 709-12

12. Alfa Aesar, 'Johnson Matthey 2002-03 Catalogue: Research chemicals, metals and materials', 2002, 968 & 993

13. MEMSnet, 'http://www.memsnet.org/material/silveragbulk/', 27/02/03

14. Metals handbook: Properties and selection of metals, 8th Ed., *Am. Soc. for Metals, Metals Park, Ohio, USA*, 1961, 1

15. MEMSnet, 'http://www.memsnet.org/material/platinumptbulk/', 27/02/03

APPENDIX II: ADDITIONAL LITERATURE INFORMATION

AII.1   PIEZOELECTRICITY

In crystallography, elements of symmetry are used to define different crystal classes and point groups. These elements are;

   i.   centre of symmetry,

  ii.   axis of rotation,

 iii.   mirror plane.

Using this method all crystals can be classified into one of 32 point groups, that are subdivided into seven crystal systems. Out of the 32 possible point groups 21 have a non-centro symmetric crystal structure[1]. The other eleven classes cannot possess polar properties as, under a uniform stress, the centre of symmetry brings about a compensation of the relative charge displacements in the lattice.

Under an electric field these centro-symmetric crystals will change shape but the strain remains unchanged if the field direction is reversed. The strain produced is proportional to the square of the applied electric field, and the behaviour is called electrostriction, which occurs in all substances, as shown in Figure AII.1[2]. Positive electrostriction is where a crystal elongates in its polarisation direction and contracts perpendicular to this direction. This behaviour is due to ions shifting from symmetrical positions that depend on lattice spacing[2].
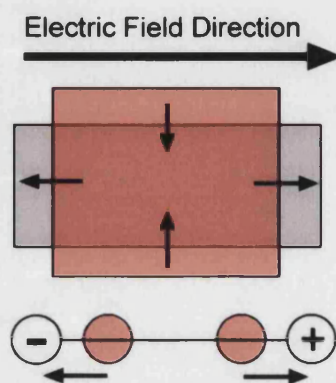
Figure AII.1: The positive electrostriction effect.

The 21 non-centro-symmetric classes have one or more polar axes, with the exception of the cubic class 432, which has other symmetry elements that combine to exclude polarisation. Of these 21, 10 can show spontaneous polarisation, that is a permanent internal dipole moment, and are termed ferroelectric[1, 3]. These are also pyroelectric materials and contain a permanent polarisation within a given temperature range[3]. A limited number of pyroelectric materials can have the following properties:

Ferroelectricity (proposed in 1912[3])

In a ferroelectric, the application of an electric field changes the direction of spontaneous polarisation and the material demonstrates polarisation reorientation[1-4], Figure AII.2a. The spontaneous electric dipole alignment is by their mutual interaction and occurs at a temperature at which the randomising effects of thermal energy are overcome and the dipoles line up in parallel arrays.

Piezoelasticity

The spontaneous polarisation direction is changed by mechanical stress[1], Figure AII.2b.
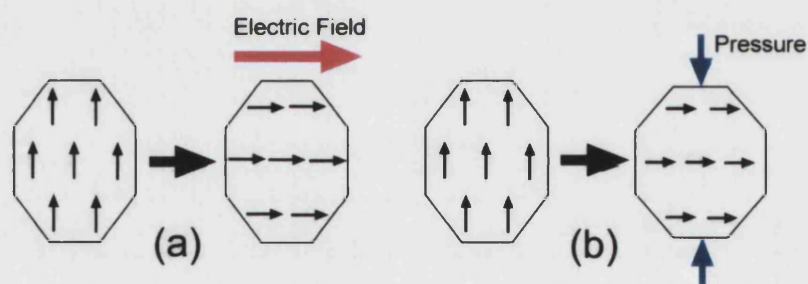
Figure AII.2: Schematic showing (a) ferroelectricity, which is polarisation orientation by application of an electric field and (b) piezoelectricity, which is polarisation orientation by the application of pressure.

Ferroelectricity is not predictable from crystal structure[1]. In 1921 ferroelectricity was discovered in Rochelle salt and it was not until 1944 that ferroelectricity was discovered in minerals with the perovskite structure[3, 5]. Calcium titanate, $CaTiO_3$, was the first perovskite structure to be discovered. There are more than 60 ferroelectric compounds with the perovskite structure[6] that have the general chemical formula ABO_3, including titanates (such as barium titanate, $BaTiO_3$), zirconates, niobates, tantalates and stannates[7].

AII.2   DENSIFICATION

The density of the final sintered ceramic composite depends on the powder fabrication, powder consolidation, liquid phases, inclusions, temperature and time. Uniform powder pressing is important, as density variation can cause warping of samples[8]. In general a process called solid state sintering occurs to densify ceramic powders. This requires the transport of atomic species of the matrix to reduce the proportion of voids present. To aid this process it is beneficial to produce a green compact of the highest density possible so that the solid particles are in intimate contact. Powder consolidation is generally undertaken by pressing the powder particles together. In some cases the particles, especially second phase metallics, may undergo plastic deformation during the consolidation process. The morphology and size of both the matrix and the second phase powder particles can affect this densification. A greater green density is achieved by a broad particle size distribution as the smaller particles can fit in the interstices of the large particles, Figure AII.3.
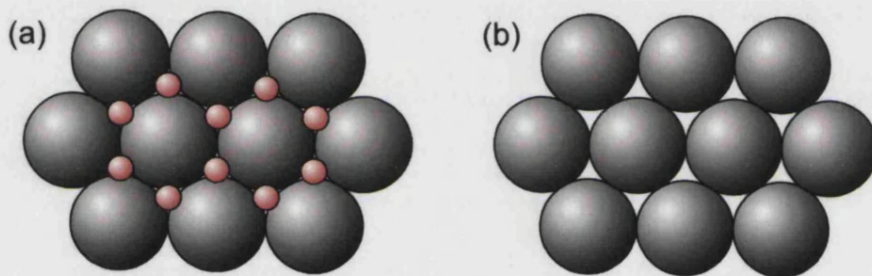
Figure AII.3: The effect of particle size on ideal green density packing for

(a) different particle size and (b) equal particle size.

Phases that have a high aspect ratio, such as fibres, are difficult to pack, unless aligned, Figure AII.4, so the green density can be reduced[9] in comparison to powders.
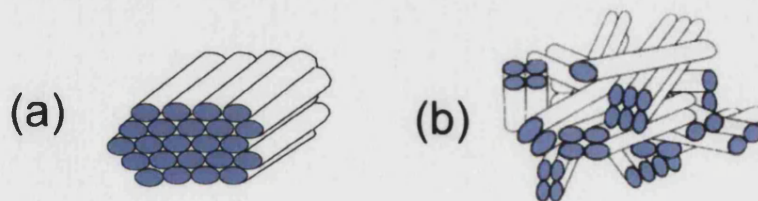
Figure AII.4: Packing of (a) aligned fibres and (b) randomly orientation fibres.

Before firing individual grains are separated by 25-60% porosity[8], depending on the efficiency of consolidation. It is desirable to eliminate as much of this porosity as possible to improve the composite properties (see Sections 2.4 and 2.5 for the effect of porosity on the mechanical and electrical properties, respectively). Under the influence of temperature the vacancies within the

material have sufficient energy to move by diffusion. Diffusion occurs due to a difference in free energy or chemical potential between two areas[8]. Atoms are more loosely bound at the surface of the particle than those in the bulk, so they move more readily over the surface.

The driving force for solid state sintering is the reduction of surface area (energy) by the decrease in the amount of solid-vapour interfaces. Usually this proceeds with the formation/extension of a new/current, lower energy, solid-solid interface. The positive curvature of the particle surface has a larger vapour pressure than the region of negative curvature at the "neck" in between the particles[8]. Material is transferred to the "neck" under this pressure gradient.

The particles become closer as material migrates from the solid-solid interface (grain boundary) to the neck area, changing the shape and size of local pores. Diffusion is greater from the grain boundary than from the bulk due to the higher disorder[8]. This method of densification continues up-to about 10% porosity, after which the densification rate is reduced by rapid grain growth, caused by secondary re-crystallisation. The sintering rate decreases when the pores become isolated from grain boundaries as the diffusion distance is greater and bulk diffusion is slower. Additives can be added to prevent/slowdown the grain boundary migration and so allow pore elimination[8].

While grain boundary and surface diffusion are important at low temperature, volume diffusion can occur at higher temperatures leading to the occurrence of compositional changes. Conventionally the volume shrinkage is about 35%, while 12-15% linear shrinkage is observed[8].

Even high purity (99% pure) ceramics can have a glass-like grain boundary layer. This amorphous material has a random structure and the distance of individual diffusion jumps can cover a range of values, many of which can be smaller than the solid atom-atom jumps. At high temperature this phase is likely to be a liquid and accelerates sintering due to a higher diffusion rate. This can produce higher density ceramics, however, the glass phase can reduce the mechanical strength if it is weak. A number of microstructural modifications can occur due to the presence of a liquid phase during sintering[10];

i.   matrix grain growth;
ii. formation of residual crystalline or glassy phases;
iii. formation of elongated, platelet and abnormally sized grains;
iv. heterogeneous distribution of a secondary phase.

The liquid, or glass-like, phase present on the particles may be due to a non-stoichiometric starting composition of the constituent composite powders. This may have been caused by the processing method, which may produce differently composed micro-regions[11].

According to sintering theory the densification rate is related to grain size through the following proportion, equation AII.1.

$$Densification \ rate \ \propto \ (grain \ size)^{-n} \qquad \{AII.1\}^{9, \ 12},$$

where n is 3 for lattice diffusion and 4 for grain boundary diffusion[9, 12].

The compacted particles in the green state coalesce and grow to form grains by the diffusion process mentioned earlier. In general increasing the sinter dwell time enables longer diffusion paths that produce larger grains[11]. The growth of large grains at the expense of smaller ones by long-range diffusion is called Oswald ripening[13]. Previously a stagnation grain size was mentioned in regard to the presence of a secondary phase. This stagnated grain size, G_s, can be predicted by Zener's formula[13], when the particle pinning force equals the thermodynamic driving force, equation AII.2.

$$G_s = \frac{\phi}{V_f} \qquad \{AII.2\}^{14-16},$$

where ϕ is the particle diameter and V_f is the particle volume fraction. This model assumes that the grain boundaries are randomly located, but in practice they have been observed to take positions that preferentially pass through particles[17] in order to minimise grain boundary energy.

AII.3   THEORETICAL STRENGTH OF MATERIALS

The theoretical tensile strength is estimated from the work required to generate the new fracture surfaces in a homogeneous flaw free solid. The energy to create the new surfaces is provided by the relaxation energy of the broken bonds. If the stress at which fracture begins is, σ_m, and the new unit cross-sectional area surface energy is 2γ and Hooke's law is observed, then this leads to Griffith's equation, equation AII.3. The parameter a is the atomic spacing.

$$\sigma_m \approx \sqrt{\frac{2 \gamma E_{Young}}{a}} \approx \frac{E_{Young}}{10} \qquad \{AII.3\}^8$$

Practical values of strength are far smaller ($\sim E_{Young}/100$) due to the presence of flaws that concentrate stress. Under these conditions only a small volume of the material reaches the theoretical stress even though the average applied stress is low. Under conditions of an atomically sharp crack tip and crack size of 2c, equation AII.3 becomes:

$$\sigma_f = \sqrt{\frac{E_{Young} \gamma}{2c}} \qquad \{AII.4\}^8$$

For a fracture strength, σ_f, of $\sim$100 MPa and a typical E_{Young} and γ of 100 GPa and 4.5 J/m^2, respectively, a typical flaw has a length in the region of 10 μm. This is consistent with pores as fracture initiators in commercial barium titanate[18].

AII.4   WEIBULL STATISTICS

An important consequence of this flaw initiation theory is that the strength of brittle solids is statistical in nature, depending on the probability that under the applied stress there is a flaw capable of initiating fracture. As such, testing a smaller volume of the sample can provide better results (high strength) due to the lower probability of a critical flaw being present[8]. Brittle fracture may be controlled by reducing either the production (lower stress concentration) or propagation (tougher material) of cracks.

This variability in strength is taken into account by the Weibull survival probability function $P_s(\sigma)$, equation AII.5, that assumes the risk of fracture is proportional to a function of stress, σ, and sample volume, V.

$$P_s(\sigma) = \exp\left(\frac{-V}{V_0}\right)\left(\frac{\sigma}{\sigma_0}\right)^m \qquad \{AII.5\}^8,$$

where σ_0 is the characteristic strength, V_0 a normalising constant and m is the Weibull modulus, which is related to the homogeneity of the flaws present in the material. A plot of ln(ln(1/Ps)) versus ln(σ) has a slope equal to m.

AII.5   PRIMARY TOUGHENING MECHANISMS

A number of primary toughening mechanisms based on energy dissipation may be employed[19-24]:

i.   **Transformation toughening**

A good example is zirconia where a crystallographic phase change (tetragonal to monoclinic) causes residual compressive stress ahead of the crack, shielding the crack tip from an applied load, Figure AII.5.
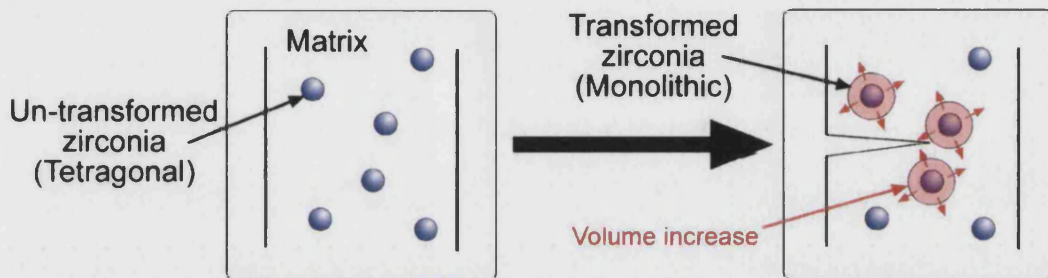
Figure AII.5: Crack removes transformation restraint of tetragonal zirconia.

ii.   **Micro-crack toughening**

Fracture occurs along the lowest energy paths in regions of local residual tension. The toughness change is detected when a passing macro-crack activates micro-cracks, Figure AII.6. The material ahead of the micro-cracks is degraded, which can be detrimental to strength if they are larger than other defects[25]. Micro-cracking is beneficial for toughness as the increase in new surface area absorbs energy. The internal stress that causes micro-cracking can result from a number of causes, such as phase transformation, thermal expansion anisotropy, thermal shock or electric stress from high fields[26].
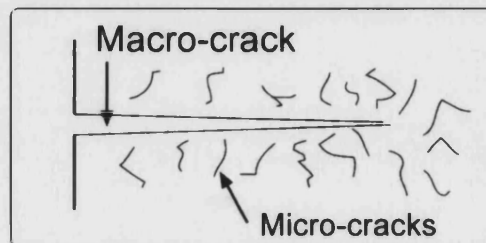
Figure AII.6: Micro-cracks formed by residual tension in matrix and passing macro-crack.

iii. **Twinning**

This diffusionless shear stress induced transformation is where a region of the crystal becomes a reflection of a neighbouring region about the twin plane, see Figure AII.7. This process reduces stress by causing deformation in such away that the twinned grain takes on a shape that is more stable in respect to neighbouring grains.

Twinning plane
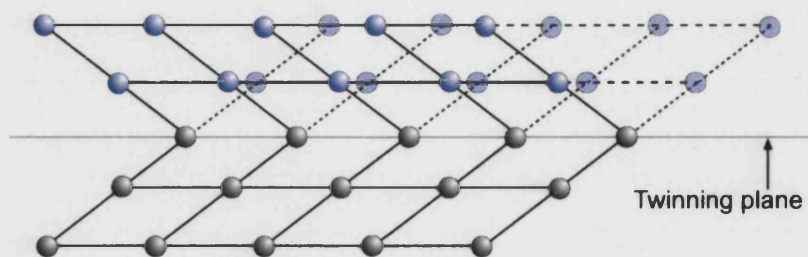
Figure AII.7: Arrangement of atoms on either side of a twin interface.

iv. **Crack bridging**

This requires a high aspect ratio second phase, such as whiskers or fibres, or one that is ductile, that will join the fracture surfaces together, Figure AII.8. Crazing in polymers is an example of this phenomenon[27]. The incorporation of 30%vol nano-particles (0.1 μm) is anticipated to increase the toughness by 10% due to this process[22]. Brittle inclusions with a similar toughness to the matrix require either residual stresses or weak interfaces, ideally both, to have a beneficial effect. The low fracture energy interfaces lead to crack deflection and possible frictional sliding losses[23]. The ductility of metals permits ligaments to remain and contribute to increased toughness through plastic deformation after the crack has passed, Figure AII.8.
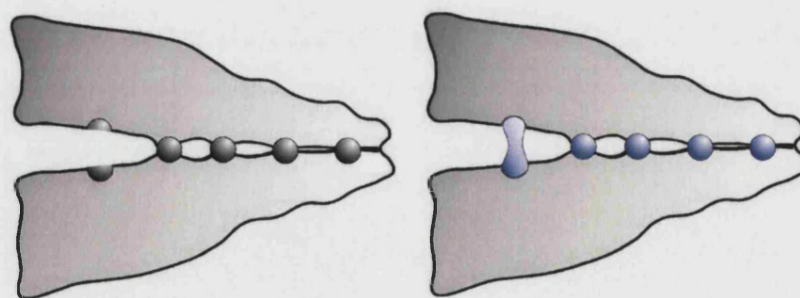
Figure AII.8: Schematic showing crack bridging and possible plastic deformation

with ductile particles.

v. **Crack deflection**

This is due to low fracture energy interfaces or residual stresses[28]. Toughening results from a diminishing of the stress intensity at the crack tip. The benefits depend on the shape, volume fraction and interparticle spacing of the reinforcement. It has been reported that a 10-70% improvement in toughness may be achievable with particle volume fractions in the range of 0.1-0.3[29]. The direction of crack deflection depends on the mismatch of thermal expansion coefficients or the Young's modulus of the two phases. A second phase with a higher thermal expansion coefficient, or modulus, produces a tangential compressive strain near the particle interface that diverts the crack around the particle[28]. The crack can be deflected to adjacent particles due to the presence of a tensile stress between particles and in doing so expends energy creating additional crack surfaces, Figure AII.9.
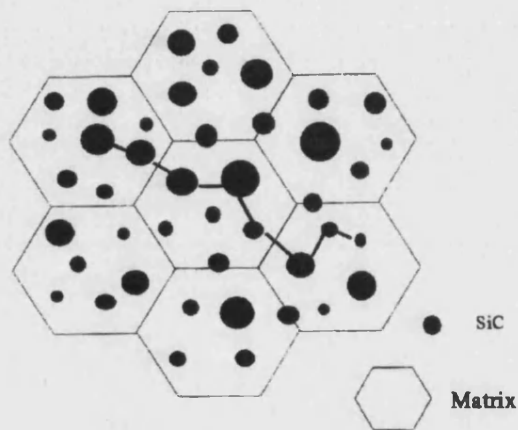
Figure AII.9: Diagrammatic representation of crack deflection[30].

AII.6   SECONDARY TOUGHENING MECHANISMS

Secondary toughening mechanisms include,

i. **Residual stresses**[29]

Matrix thermal expansion coefficient anisotropy and/or differences in the matrix-inclusion expansion coefficient can lead to residual stresses in the material once cooled from the sintering temperature. This may enhance micro-cracking, crack deflection or change the fracture mode. Residual stresses are discussed in more detail in AII.7 and Section 2.4.d.

ii. Fracture mode[29]

In general the grain boundary is weaker than the grains and if a crack is forced through a stronger region, such as the grain bulk, it may expend more energy. The fracture mode is considered in more detail in Section AII.7.

iii. Grain size[29]

With a reduction in grain size both the residual stresses and fracture mode may be affected. A decrease in grain size can improve the toughness by increasing the crack distance required for failure.

iv. Domain switching

This is only applicable in ferroelectric ceramics. Domain reorientation in the stress field of a crack tip can provide the requisite energy adsorption mechanism for enhanced fracture toughness. The mechanism differs from transformation toughening, as there is no change in the crystal structure, only a reorientation of the domains within the process zone[31]. The upper boundary for increasing the toughness through this mechanism, in comparison to no switching, has been reported to be 10%[32]. This phenomenon is considered to be rare as it occurs in the 10-50 μm grain size range only[33].

It has also been observed that the fracture toughness can be improved by applying an electric field to a piezoelectric ceramic. This is believed to modify the internal stress system by domain movement and increases the toughness, by relieving internal stress, along the field direction[34, 35].

Toughness is associated with a complex mechanism with many possible factors and the incorporation of inclusions can increase the complexity. Wahi[36] suggested equation AII.6, for the mode one fracture toughness, K_{1c}, in composites that contain brittle particles in a ceramic matrix.

$$K_{1c}^2 \approx 2\left\{\left(\Delta E_{Young} . \upsilon_{matrix} + \Delta \upsilon . E_{Young\ matrix}\right) V_p + E_{Young\ matrix} \upsilon_{matrix}\right\} \qquad \{\text{AII.6}\}^{36},$$

where Δ represents the differences in particle-matrix values for the Young's modulus, E_{Young}, and Poisson's ratio, υ. V_p is the particle volume fraction. An improvement in the toughness, K_{1c}, can also enhance the strength, σ_f, due to the relationship given in equation AII.7.

$$\sigma_f = \frac{K_{1c}}{Y \sqrt{\pi c}} \qquad \{\text{AII.7}\}^{37,\ 38},$$

where c is the critical flaw size and Y is a geometrical constant that depends on the sample profile, commonly approximated to unity.

The possible toughening mechanisms have been reported by Sternitze[19] and are summarised in Table AII.1.

Table AII.1: Reported mechanisms for enhanced toughening in nano-composites[19].

Mechanism	Comment
Zener grain boundary pinning	Reduced matrix grain size
Dislocation networks	Refined microstructure
Flaw size reduction	Strength increase
Crack healing	Annealed strength increase
Crack deflection	Cracks deflected at particles
Crack bowing	Difficult to verify experimentally
Thermal expansion mismatch	Fracture mode change possible, local compressive stresses may strengthen grain boundary
Average internal stress	Average matrix stress is tensile if the matrix has larger thermal expansion coefficient

AII.7 RESIDUAL STRESS

A fundamental phenomenon in polycrystalline materials and composites is the development of residual stresses. Stresses are developed due to the differences in the coefficient of thermal expansion, CTE, between the matrix and the second phase particles[14]. These residual stresses are generated during cooling of the ceramic[30]. Any internal stresses that are formed during firing are removed by the diffusion processes[39]. Residual stresses can be generated in the monolithic polycrystalline material due to anisotropic CTE in the crystals[8], such as in alumina[14, 40]. This can be a source of grain boundary failure, especially at triple points, Figure AII.10a[41]. Cracking due to restraint from surrounding grains[8] may not completely relieve the stresses developed.
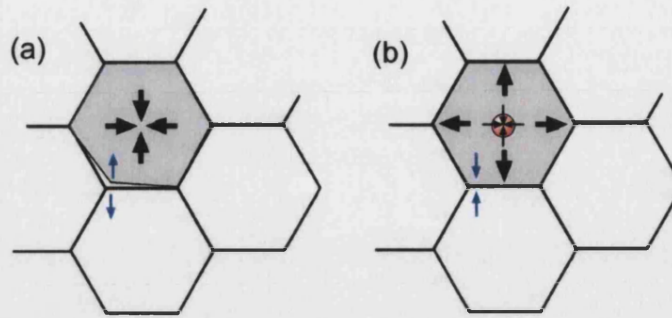
Figure AII.10: (a) Monolithic thermal expansion anisotropy micro-crack and

(b) particle stress field inhibiting micro-crack formation in particulate composite[41].

The addition of a secondary phase, of lower thermal expansion coefficient, can reduce this anisotropy[14] due to generation of a compressive stress field, Figure AII.10b, which prevents crack formation. The Selsing model, shown in equation AII.8, gives the relationship between the thermally generated residual stresses, $\sigma_{thermal}$, and the difference in the CTE values, $\Delta\alpha$.

$$\sigma_{thermal} = \frac{\Delta\alpha\Delta T}{\left[\dfrac{1+\upsilon_m}{2E_m}\right] + \left[\dfrac{1-2\upsilon_p}{E_p}\right]} \qquad \{AII.8\}^{[42]},$$

where ΔT is the change in temperature during cooling, ν_m and ν_p are the Poisson's ratios of the matrix and particles respectively, while E_m and E_p are Young's Moduli.

Examination of these residual stresses shows that in a system where the matrix has the greater CTE a general tensile stress is set-up in the matrix[14, 19, 29, 39] and the particles are compressed. Detailed calculations of matrix and particle stresses can be found in the literature[43, 44]. Superimposed upon this stress system are local tensile hoop and radial compressive stresses, Figure AII.11.
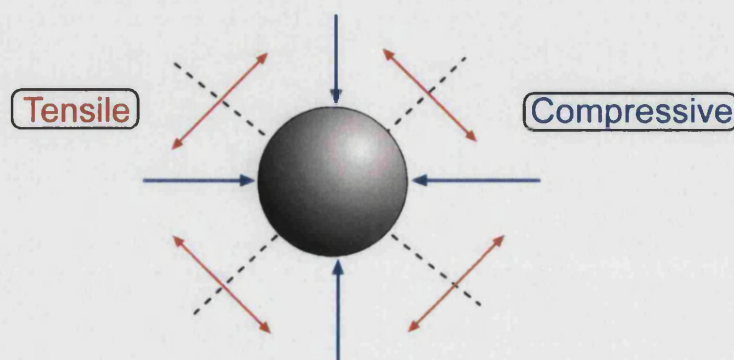
Figure AII.11: Tensile and compressive stresses generated in matrix surrounding

a particle of lower thermal expansion coefficient than the matrix.

Micro-cracking by the tensile stress is prevented if the particles are smaller than the critical particle size[40]. Estimation of the size and inclusion volume fraction effects on the radial and tangential stresses has been undertaken[44] and is summarised in Figure AII.12. Figure AII.12(a) shows that the radial and tangential stresses decrease with distance from the matrix-particle interface. Increasing the inclusion size causes the radial and tangential stresses to increase, whereas increasing the volume fraction of inclusions increases the radial stress, but decreases the tangential stress, Figure AII.12(b).
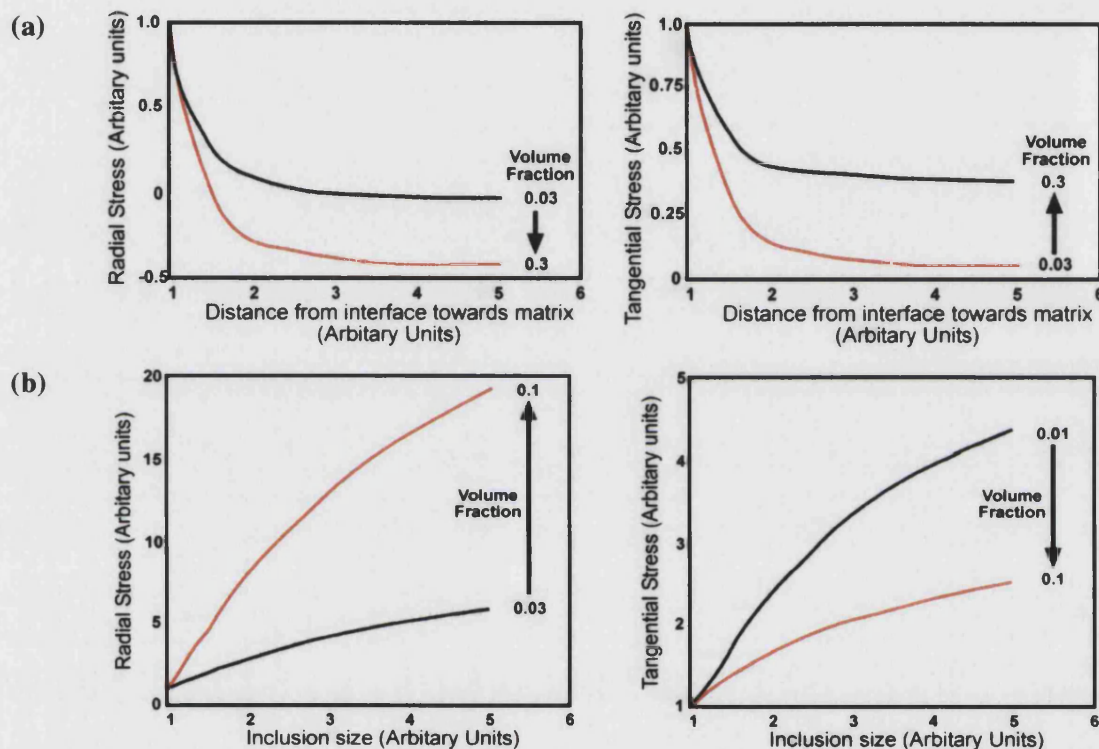
Figure AII.12: (a) Radial stress decrease and tangential stress increase with increased particle volume fraction and (b) effect of inclusion size on the stress at a fixed distance from interface[44]

Figure AII.13 gives an example of the stress distribution between two silicon carbide particles in the Al_2O_3-5vol% silicon carbide system. The result has been confirmed by strain contour observation under the Transmission Electron Microscope, TEM[30].
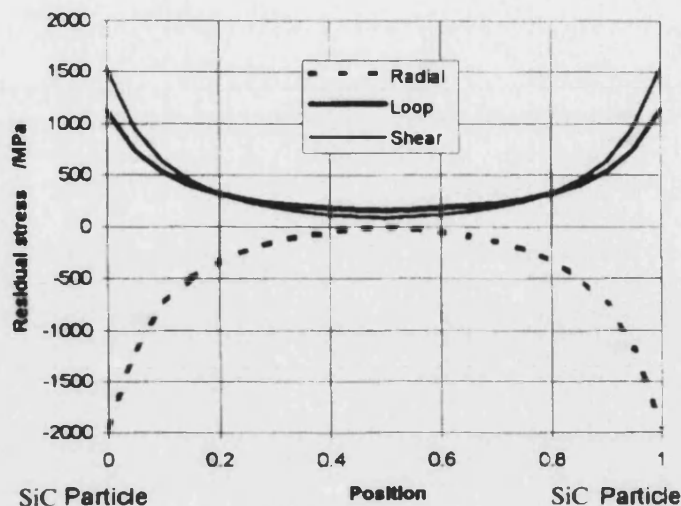
Figure AII.13: Calculated stress distribution for Al_2O_3-5vol% silicon carbide[30].

Predictions for the critical inclusion size that causes micro-cracking have also been reported, Figure AII.14. Inclusions larger than the critical size cause spontaneous micro-cracking, which agrees with observed results[44]. As the difference between the particle and matrix coefficients of thermal expansion increases the critical inclusion size will decrease.
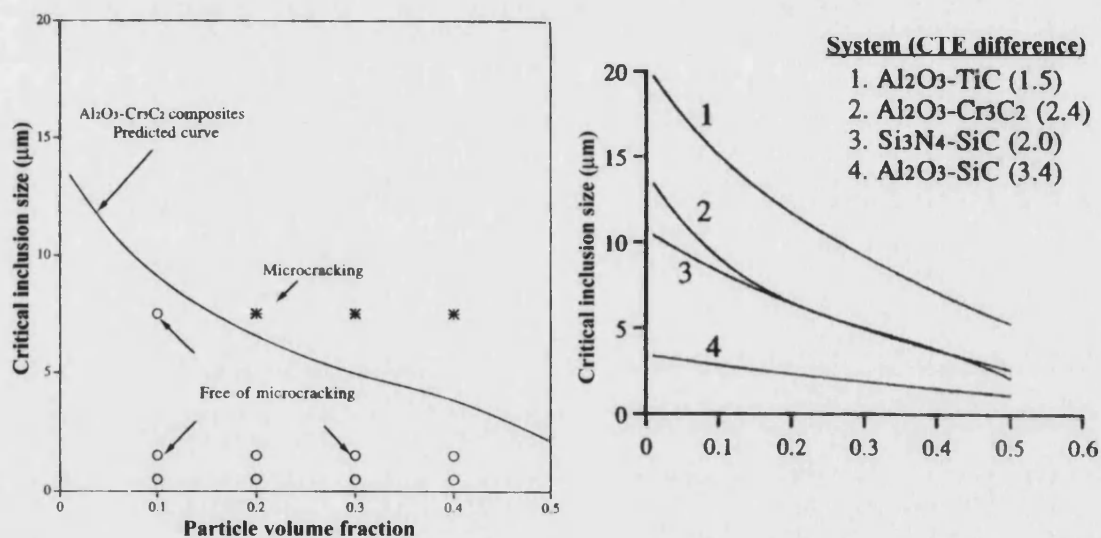
Figure AII.14: Predictions of critical inclusion size that cause micro-cracking[44].

While crack deflection is a possibility, the high radial compressive stresses generated by adjacent particles can cause crack pinning[45]. Overall these compressive stresses have two functions, that of increasing pinning effects and increasing interfacial bonding. Apart from the possibility of internal stress from thermal mismatch another condition is created by crystal transformation during cooling from the sintering temperature[42, 46]. The large change of the barium titanate cell dimensions as the temperature decreases, indicating that the formation of domains may be affected by the stress.

Transmission electron microscope examination of barium titanate has indicated that the internal stress levels can be such that domains are not generated[47, 48]. The generation of residual stresses due to thermal expansion mismatch between the particles and matrix can influence the phase transformation. For example, a pseudo-cubic structure is generated, rather than tetragonal, with silicon carbide in barium titanate[49].

Internal stress can be generated by domain re-orientation, a process that may develop micro-cracks if the matrix is unable to accommodate the stress produced[26]. Internal stresses can be relieved by twinning[50, 51] (the reported domain reorientation stress in PZT is <10 MPa[52]), smaller grains, pores and flaws or even a grain boundary phase[42] and thermal processes, such as annealing[30, 53]. It has, however, been suggested that the stresses are only partially relieved by annealing as slow bulk diffusion inhibits stress alleviation[45]. However, annealing may also eliminate dislocations by allowing them sufficient thermal energy to move short distances to crack tips encouraging crack healing, but only in the composite, as internal stresses from thermal mismatch are present[30].

An important consequence of a fluctuating stress field is the ability to deflect cracks, and crack formation may also be enhanced[54]. Other toughening mechanisms, such as particle bridging, can occur as grain boundary diffusion relaxes internal stresses at intergranular particles more so than intragranular particles[54]. Intergranular particle stresses can also be relieved by elastic accommodation and grain boundary sliding[45].

AII.8   RELATIVE PERMITTIVITY

The relative permittivity, or dielectric constant, of a material describes the dielectric displacement induced when it is excited by an electric field[1, 2, 8]. Ferroelectrics are generally characterised by a high relative permittivity of 200-10,000, while typical insulators have values of $5-100^3$. The application of an electromotive force, such as an electric field, to an ideal dielectric material causes no long-range charge transport, only limited local rearrangement, forming dipoles[1]. Conductors contain no dipoles due to their small resistance[4]. Relative permittivity is a measure of the electric dipoles present within the material and their ability to realign in response to an electric field[4]. The process of dipole formation or alignment in an electric field is called polarisation[55]. There are a number of different polarisation types[1], which are described below and illustrated in Figure AII.15.

i.   **Atomic/electronic**

This polarisation type is present in all materials as it is due to electron displacement. The minimum contribution is estimated at 0.09 C/m^{2}[2].

ii. **Ionic**

This is caused by relative movement of cations and anions in the lattice. The maximum contribution is estimated to be 0.17 C/m^2 [2].

iii. **Dipolar**

Orientation of molecules by the electric field causes this polarisation type.

iv. **Space charge**

Space charge polarisation is caused by charge diffusion under an electric field and is limited by potential barriers generated by charge build up.
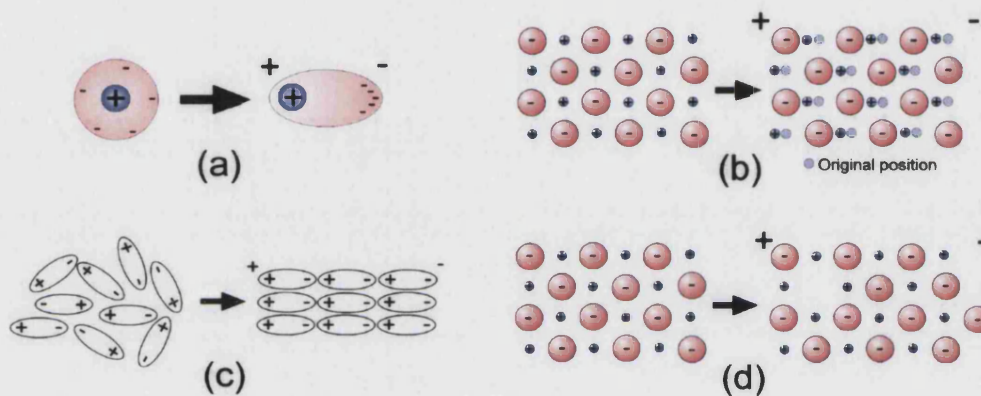
Figure AII.15: Polarisation types (a) atomic/electronic, (b) ionic, (c) dipolar and (d) space charge.

These different polarisation mechanisms produce a relative permittivity that is related to the driving frequency of the electric field, Figure AII.16. Abrupt changes in the relative permittivity occur when the frequency exceeds the rate at which a polarisation type can operate. Resonance is observed in the ionic and atomic polarisation mechanisms. Apart from these abrupt changes the relative permittivity is virtually independent of frequency[56].

In an ideal capacitor the electric charge would adjust to the voltage change instantaneously. In practice charge has inertia and a new charge distribution takes time to be established[1]. The current, with time, in an ideal dielectric drops to zero, or a dc conductivity value for real materials[8]. Once the relaxation time for a particular polarisation type, which is the inverse of the minimum reorientation time, is exceeded, by the applied frequency, the dipole can no longer keep up and stops contributing to the relative permittivity, generating the abrupt changes in Figure AII.16[56]. Electronic/atomic and ionic charge build-up is much slower in comparison to the slower dipole orientation and space charge polarisation types. Relative permittivity is also dependent on temperature as the polarisation processes are thermally activated.
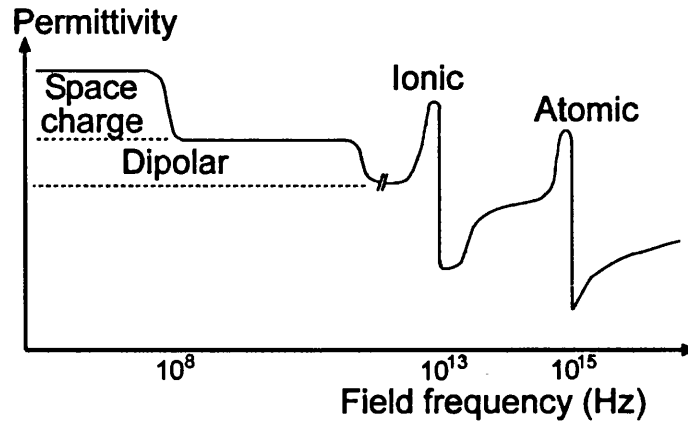
Figure AII.16: Relationship between relative permittivity and frequency

showing the influence of the polarisation types[56].

The absolute permittivity, ε, of units Fm^{-1}, is defined as:

$$\varepsilon = \frac{D}{E}$$
{AII.9},

where D is the electric flux density produced by the application of an electric field, E, to a substance. However the permittivity of a material is commonly stated as a relative value, ε_r, as given by equation AII.10.

$$\varepsilon_r = \frac{\varepsilon}{\varepsilon_0}$$
{AII.10}

Here ε_0 is the free space value, i.e. the permittivity of a vacuum, which is a constant equal to $8.854 \times 10^{-12}\ Fm^{-1}$.

The relative permittivity is related to the physical properties of a sample and its electrical capacitance such as in a parallel plate capacitor, Figure AII.17. Capacitance is the ratio of the stored charge on the electrodes, Q, to the potential difference between them, V.
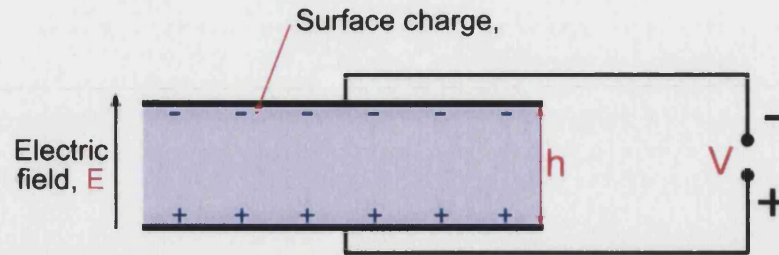
Figure AII.17: Surface charge generated in parallel plate capacitor.

Application of the capacitance-charge relationship and the insertion of a dielectric medium causes polarisation of the material with a relative permittivity given by equation AII.11. The polarisation charge density on the dielectric surface compensates for a fraction of the total charge density carried by the plates, which is reduced[1, 8].

$$\varepsilon_r = \frac{C\,h}{A\,\varepsilon_0} \qquad \{AII.11\}$$

A is the cross-sectional area of the dielectric medium and h the distance between the plates. The relative permittivity can be calculated by measuring the capacitance, C, of a sample of known dimensions. When used as a capacitor material the intent is to suppress ferroelectric and piezoelectric properties, which reduce the charge storage capacity[3].

AII.9   GRAIN SIZE AND RELATIVE PERMITTIVITY

A marked change in the relative permittivity with grain size has been reported by many researchers[1, 21, 48, 57-62]. The general trend is shown in Figure AII.18, whereby a peak is present around a grain size of 1 μm [62].
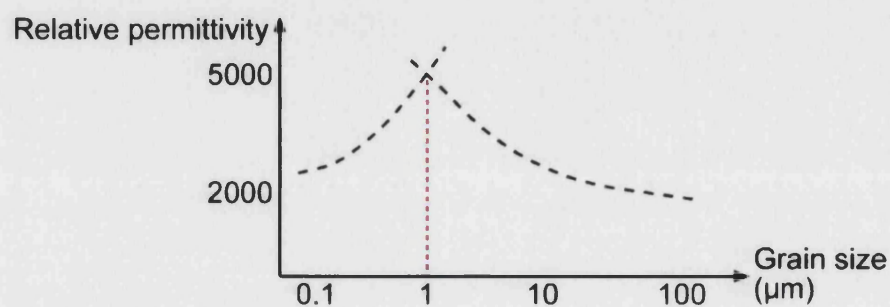
Figure AII.18: Grain size effect on the relative permittivity of barium titanate.

These measured results cannot be explained by averaging the single crystal values[48]. In the case above the relative permittivity appears to follow the trend described by equation AII.12 for grain sizes above 1 μm.

$$\varepsilon_r = 1000 + \frac{3200}{d_s} \qquad \{AII.12\}^{62},$$

where d_w is the domain size, which is approximately equal to the square root of the grain size[60]. The basic form, equation 2.8, has the first term as the volume term (value of 1000), which is constant, whereas the second term depends on the 90° domain walls within the grains of the material[63]. It is proposed that the domain wall vibration contribution increases with decreasing grain size[62]. Figure AII.19 represents a summary of the results from reports[1, 48, 59, 60] that show the effect of different grain sizes on the temperature-relative permittivity relationship.
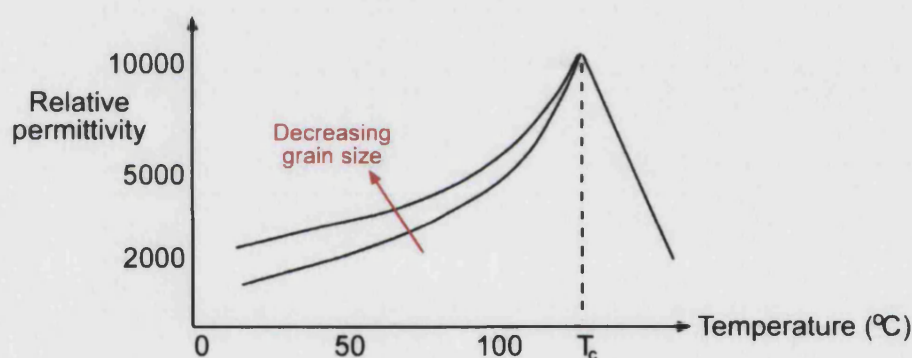
Figure AII.19: Effect of grain size on the relative permittivity trend with temperature.

The principal justification for this trend appears to be focussed upon the internal stress in fine-grained systems[1, 48, 58, 60]. Devonshire's phenomenological theory* shows that a stress increase is accompanied by a relative permittivity rise[64], irrespective of any domain contribution. A relative permittivity increase has been observed for PZT under the application of a stress parallel to the direction of the applied electric field[65]. This suggests that as the grain size is reduced, the internal stress is unrelieved by domain formation and reaches a critical value at a grain size of approximately 1 μm[58]. It is suggested that the grains are too small for domains to exist as the domain width, which is inversely proportional to the grain size, would be too great[48]. It would

---

* Devonshire's approach consists of expanding the free energy of the cubic crystal in terms of strains and polarisations and using crystal properties to determine coefficients. It is capable of explaining the dielectric, piezoelectric and elastic behaviour of the crystal at any temperature by means of a single free energy polynomial involving a limited number of terms[2].

appear that the reduction of grain size is key to the change in relative permittivity and it has been proposed that the grain surface and structure below 400 nm are more important to relative permittivity than indicated from previous theories, which rely on grain boundary effects[59].

AII.10 DOMAINS

In 1907 Pierre Weiss postulated the presence of domains in magnetic materials[66] and similar assumptions can be applied to postulate ferroelectric domains. Figure AII.20 is a simplified schematic structure of a ferroelectric crystal of chemical formula A^+B^- and simple square lattice. The B^- ions have two minimum positions of energy that are separated by an energy barrier. As such, these ions always lie closer to one of two adjacent A^+ ions than the other. The A-B pair represents a dipole and spontaneous polarisation is represented by the dipoles aligning in the same direction[2].
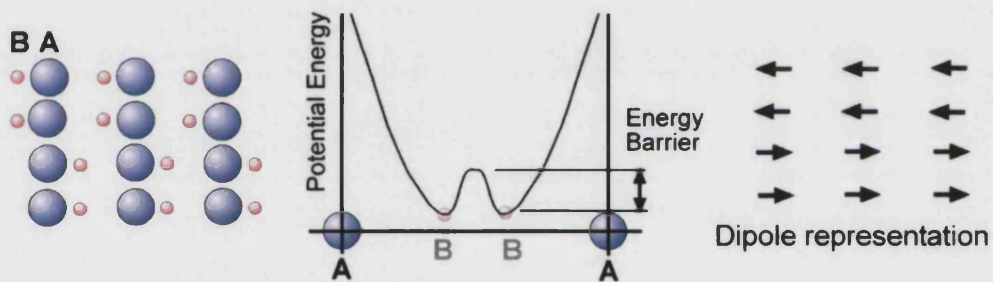
Figure AII.20: Schematic of the A-B crystal structure, potential energy

variation between A^+ ions and the representation of dipoles[2].

As the temperature increases thermal motion of lattice ions changes the potential energy curve, making the distribution of B-ions symmetrical with respect to A-ions[2], Figure AII.21. No dipoles are present and this would be analogous to barium titanate above the Curie temperature.
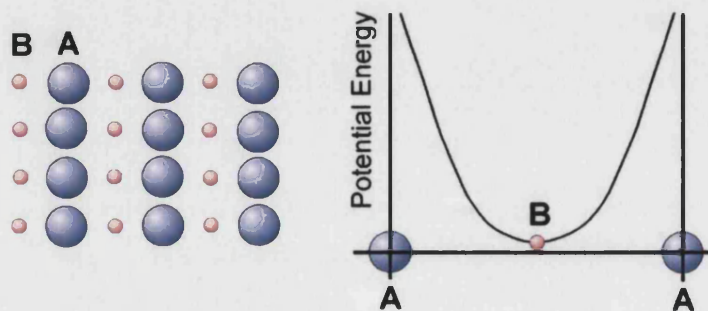
Figure AII.21: Symmetric ion distribution and modified potential energy

distribution for the A-B crystal structure at elevated temperature[2].

Ferroelectric materials are characterised by a domain structure generated by the minimisation of the internal energy through local charge displacement, i.e. spontaneous polarisation. In barium titanate the domain structure is formed during the cubic to tetragonal crystal transformation[67]. Domains are regions of "homogenous" polarisation[68]. With the onset of polarisation a surface charge density is generated and an accompanying depolarisation field[1]. Polarisation in the same direction occurs if the resulting polarisation from neighbouring dipoles exerts a sufficiently large force on a dipole[8]. As a ferroelectric ceramic cools from above its Curie temperature it will contract. Since all the crystal orientations within the polycrystalline ceramic are randomly aligned this contraction will be isotropic. However, individual crystals will favour anisotropic contraction according to their domain orientation. These two systems lead to the ferroelectric material forming many, seemingly randomly oriented domains. Twinning is the formation of these domains to balance the domain wall energy, elastic and electric field energy, Figure AII.22. Domains are separated by twin boundaries that are regions of polarisation transition that are configured by the polarisation orientation of adjacent domains[68]. In a perfectly insulating crystal no charge is accumulated on the walls. In real materials charge on the wall is compensated by material conduction and the walls can be 'locked' in place[1].
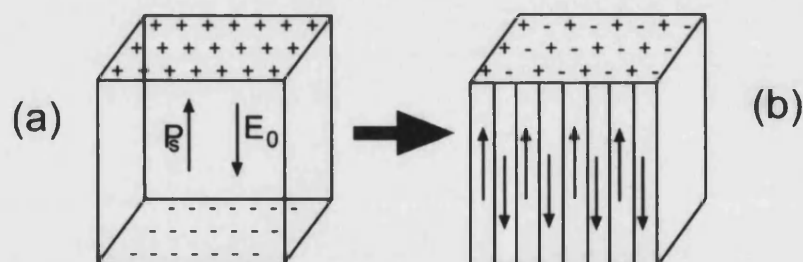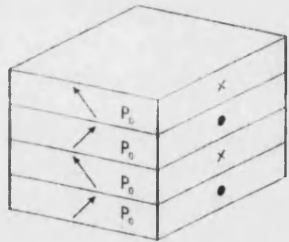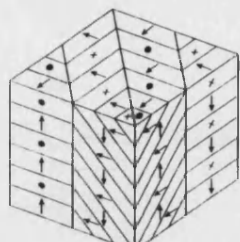
Figure AII.22: (a) Charge associated with spontaneous polarisation, P_S, and electric field generated, E_0, (b) formation of 180° domains to minimise electrostatic energy[1].

New domains can be nucleated by pores, inclusions, grain boundaries, surfaces, cracks and dislocations[68]. The critical nucleus size of aligned domains has been calculated as 70 nm by 16 nm for 180° domains[69]. An equilibrium domain configuration is established only if sufficient time is allowed for wall mobility. It has been suggested that the domain pattern is different in coarse grains in comparison to fine grains. This can affect the average polarisation of the grain, P_{grain}, as highlighted in Table AII.2, P_0 is the polarisation of the single crystal[51]. It appears that the average grain polarisation is reduced for the coarse grained structure, suggesting a reduced relative permittivity value.

Table AII.2: Reduction of the single crystal polarisation value, P_0, with grain size[51].

Fine grain domain pattern		Coarse grain domain pattern	
	$P_{grain} = \dfrac{P_0}{\sqrt{2}}$		$P_{grain} = \dfrac{P_0 \sqrt{2}}{3}$

The domain pattern generated depends on the electrical and mechanical stress conditions[70]. Twinning causes a banded structure to form, Figure AII.23(b), from a simple lamellar configuration, Figure AII.23(a).
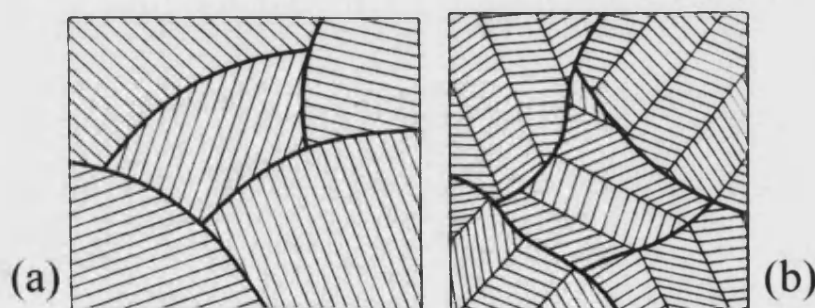
Figure AII.23: (a) Simple lamellar twinning and (b) banded twin structure in polycrystalline piezoelectric materials[70].

There are two types of domain, known as 90° and 180° domains[62, 68], and these are shown in Figure AII.24. For the 90° domains the c-axis of each twin is mutually perpendicular, whilst they are parallel and have opposite polarity in the 180° domains[71, 72].
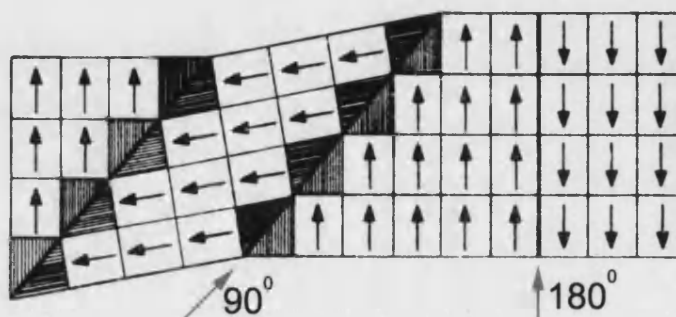
Figure AII.24: Physical representation of 90° domains and thinner 180° domains[2].

308

Clamping by adjacent grains, however, can hinder the formation of a domain configuration. As the tetragonal structure is anisotropic, a change of domain direction by 90° will require a change in shape. This is different to magnetic domains, which are not related to crystal structure but to electron configuration. A magnetic domain wall consists of a rotation of electron spins whilst an electric domain is one of varying structure. The domain wall width will depend on the type of domain boundary and a 180° domain wall width of 8 nm has been reported[68] (~10 nm [1], 1.4 nm [73]). The 90° domain boundary is greater in size than a 180° domain boundary as there is crystallographic change, as shown in Figure AII.24 [2]. 90° domain widths have been reported down to 50 nm [48]. Wall energies of the order of 10 mJ/m² have been reported[1] (7 mJ/m² [2], 42 mJ/m² [73]).

A number of reports suggest that the spontaneous domain size produced is related to the grain size[60, 70, 74], by equation AII.13, which is shown graphically in Figure AII.25.

$$Domain\ Size\ \propto\ \sqrt{Grain\ size} \qquad\qquad \{AII.13\}^{74}$$

As reported in Section 2.3.b, the addition of second phase particles can reduce the grain size and therefore the associated domain size.
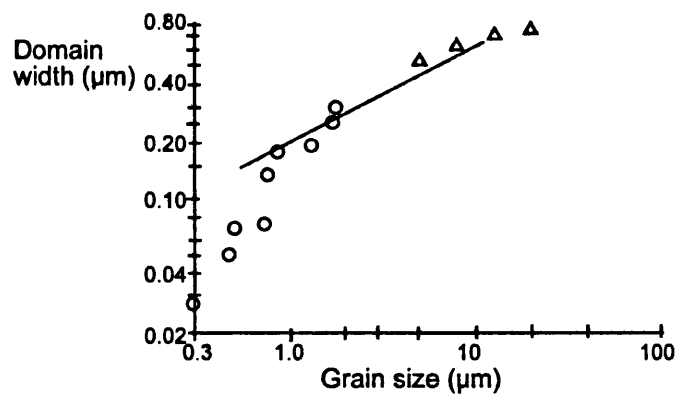
Figure AII.25: Change in domain width with grain size[60, 70, 74].

The complex domain structure in large grains is a disadvantage in cases where it is required to drive a domain boundary through a grain using an external field[62]. Deformation of the dielectric material can influence the domain structure as cooperative twinning in adjacent grains can relieve stress. A sufficiently high internal stress can maintain the materials shape by inhibiting domain motion and also their formation, Figure AII.26.
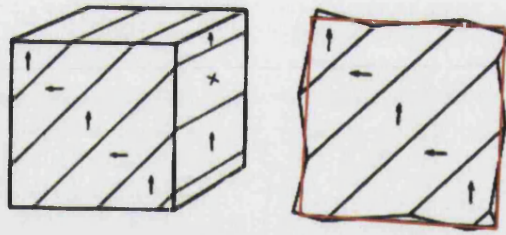
Figure AII.26: Clamped grain domain configuration (left)

and deformation in the free grain (right).

The energy balance indicated by Figure AII.27 has been proposed to account for the lack of twins below a certain grain size. The available elastic strain energy is below a critical value in small grains so that the high domain wall energy prevents their formation[70]. Note that surface grains would be expected to twin differently compared to bulk grains due to reduced clamping stresses. The presence of the domains influences the relative permittivity and the piezoelectric coupling factors[75].
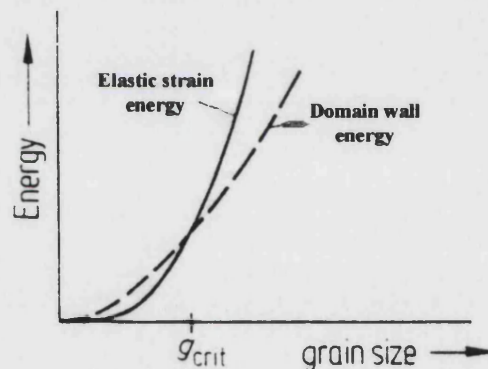
Figure AII.27: Elastic strain energy and domain wall energy increase with grain size[70].

AII.11   POLING AND DOMAIN ORIENTATION

A ferroelectric polycrystalline material has no overall polarisation as the domains are randomly orientated, Figure AII.28. A process termed "poling" is necessary to align the unit cell dipoles within the material. Poling requires the reversal of individual 180° domains and rotation of 90° domains[76]. Polarisation is only allowed along certain directions depending on the crystallographic class, so not all of the domains will be precisely aligned to the poling direction but will be as close as the crystal orientation permits if given sufficient energy and time.
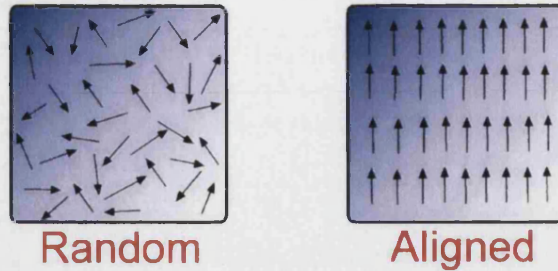
Figure AII.28: Representation of random and aligned domain states in a piezoelectric ceramic.

The greater the number of polarisable directions available the closer the polar axes can align to the poling field and increase the piezoelectric properties. In polycrystalline piezoelectrics the maximum attainable polarisation can be given as a fraction of the single crystal value. For a tetragonal perovskite there are six polar directions giving a fraction of 0.83. In practice the value is limited by internal strains that inhibit 90° domain reorientation. Almost complete reversal of 180° domain occurs[1]. The intention of poling is to cause as many domains as possible to be aligned in the poling direction[76]. Domains can be switched (90° domains rotated while 180° domains reversed) by electrical fields[75].

A meta-stable state of alignment can be induced by application of thermal energy and an electric field. The combination of high field and temperature causes domain reorientation and the ceramic develops a polar direction[1]. Depending on the poling conditions the amount of reorientation can vary. Commercial poling operations involve heating components in oil baths in which electric fields in the region of kilovolts per millimetre are generated. The induced poled state can be destroyed by heat, high electric fields or intense mechanical stress that transform the domains back to their original random state.

AII.12 DOMAIN PINNING

Domain mobility leads to difficulties in producing uniform and consistent materials[8] as the motion is energetically lossy, leading to a non-linear response with field application[51]. Pinning of ferroelectric domains is analogous to the restraining of magnetic domains. Wall motion, required for a domain to grow, can be influenced by the presence of entities that make such movement more difficult. There are two types of pinning entity[77, 78];

i. **Strong**

   Powerful centres, small number required, such as inclusions. Reversible bowing of domain wall between centres occurs before breakaway from the pinning entity.

ii. **Weak**

Large number of small centres, typically atomic defects, such as oxygen vacancies and dopant ions. The domain wall remains relatively planar.

The second type can explain the difference between the soft and hard piezoelectric materials. Soft PZT has few defects/dopants[51] while the hard PZT has many. Isolated secondary phase regions can act as a pinning point by reducing the domain wall energy when it is intersected, Figure AII.29. The wall becomes attracted to these inclusions due to reduction in the energy of the system.
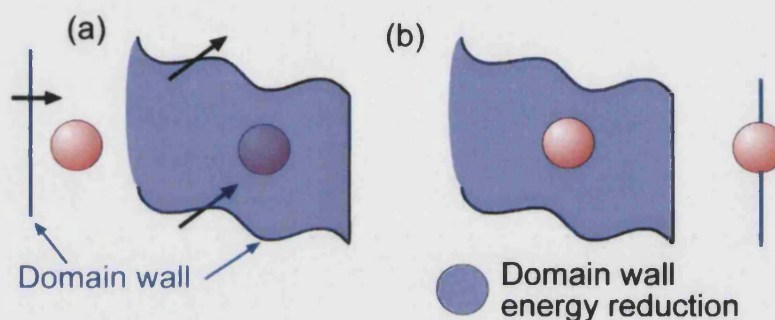
Figure AII.29: (a) Domain wall energy higher than in (b) where the wall

(in blue) intersects an inclusion (in red).

Examples of these pinning species include oxides, carbides, pores and cracks[78, 79]. Under repeated application of an electric field the domains become pinned at these potential energy minima. Higher fields are then required for escape, to overcome the potential energy barriers[78]. The Preisach model for magnetic pinning is relevant in this situation, as the pinning field varies with position[80], Figure AII.30.
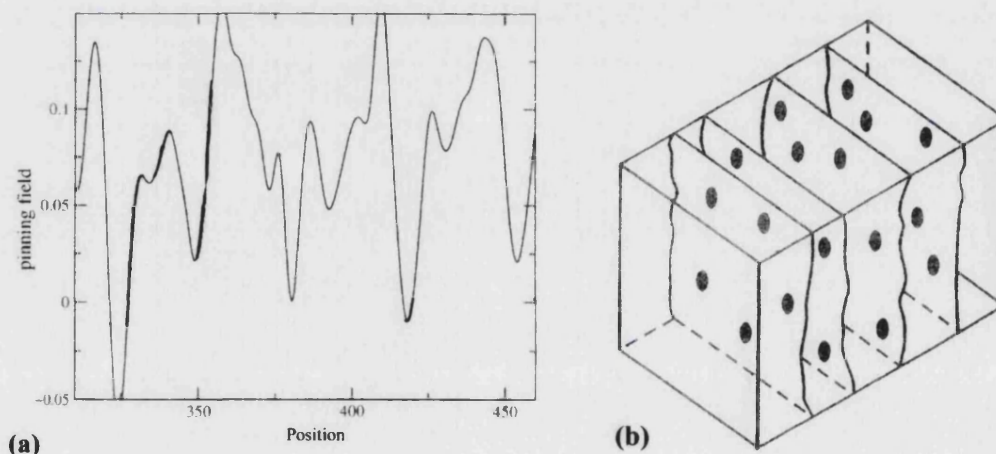
Figure AII.30: (a) Potential energy versus position describes a (b) pinning field for the

movement of a domain wall[80].

The variation of relative permittivity at low fields occurs where the same pinning field influences the domain motion. In the Rayleigh region translation across these pinning fields occurs[81]. The energy required to surmount the pins has been simulated using a normal distribution of pinning energies. The domains can obtain energy from thermal activation to overcome the barriers. It is suggested that the mean pinning energy is 1.2×10^{-19} J with a standard deviation of 1.8×10^{-20} J [78].

AII.13   DIELECTRIC LOSS

Dielectric loss is related to non-instantaneous polarisation due to the inertia of charges and absorption of electrical energy by the dielectric[56]. Polarisation is time-dependent as a new charge distribution will take time to be established. The final static charge distribution forms after the instantaneous atomic and ionic polarisations, δ, Figure AII.31[1].
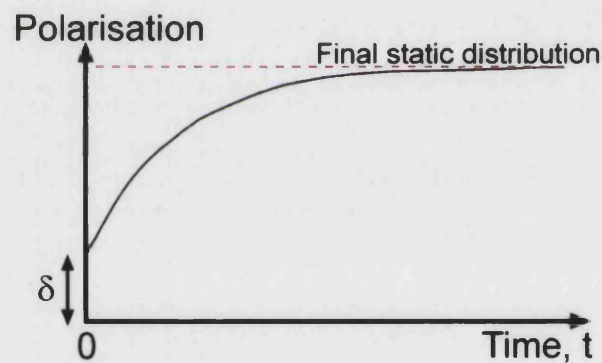
Figure AII.31: Time-dependent polarisation[1].

In the case of piezoelectric materials there is an additional mechanism related to domain wall motion[82]. Below 1 GHz the major loss mechanism is the DC conductivity associated with charge carrier movement[83]. Ferroelectrics are normally characterised by a loss in the range 0.1-7%[3]. Other loss mechanisms include dipole reorientation[4] and ion jumping[8]. Ion vibration and deformation losses are only expected above 10 GHz[8].

Dielectric loss is given by the loss tangent, which is the imaginary relative permittivity divided by the real relative permittivity at that frequency. In AC circuits there is a phase shift corresponding to a time lag between the applied voltage and the induced current[8]. A peak is observed in the loss on a frequency spectrum, when the relaxation frequency of the dipoles is equal to the applied field period[4, 8]. Techniques can analyse the loss of a dielectric material in terms of energy loss in the electrical to mechanical conversion, commonly called the coupling coefficient, K_{eff}, and

mechanical quality factor, Q_m. These parameters can be determined from impedance analysis, Section 2.5.g.

Dielectric loss is important as the loss mechanisms, especially when subjected to high alternating fields, can result in self-heating that can result in the degradation of properties. Electrical and mechanical cycling can cause irreversible microstructural damage, such as crack formation, and reversible damage, such as domain reorientation[52].

It has been proposed that the dielectric loss would be reduced with smaller grain sizes, as they will have a lower spontaneous polarisation than large grains. Therefore, less energy is required to rotate the dipoles under an electric field[59]. It has also been suggested that domain wall motion may be mostly non-hysteretic[21]. Figure AII.32 indicates the results for a reduction in grain size for different applied fields. A similar rapid rise in loss, as occurs for relative permittivity, is observed at high fields[84, 85].
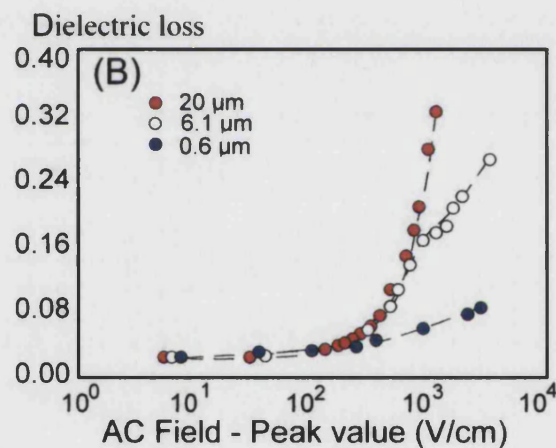
Figure AII.32: Behaviour of dielectric loss with field and grain size[84].

It has been proposed that the increase in loss with higher fields is the result of lossy ferroelectric domain wall motion[81]. To improve the range and usefulness for high field applications it would be beneficial to delay or eliminate this rapid increase in loss at high electric fields, which in this case can be achieved by a reduced grain size. Low loss at the device utilisation frequency is required for device efficiency and reliability[56].

AII.14   PIEZOELECTRICITY II

Piezoelectricity was discovered in Rochelle salt (Potassium Sodium Tartrate) in 1880 by Jacques and Pierre Curie[3]. Piezoelectricity is one property of a group of dielectric materials called ferroelectrics. These materials are characterised by having a domain structure that can be modified by an electric field. The piezoelectric effect is manifest as a spontaneous electric polarisation across the opposite faces of a volume of material when under an applied stress. The magnitude of the polarity is directly proportional to the mechanical stress applied to it. The converse is also true, i.e. the application of an electric field causes strain in a volume of piezoelectric material. There are two different cases of piezoelectric behaviour[86]:

i.   Centres of the positive and negative charges are non-symmetric with the unit cell planes under no applied pressure. This is the case in barium titanate, where there is spontaneous polarisation.

ii.   The dipole moments are only induced by application of pressure on the crystal, such as occurs in quartz.

On the macroscopic scale all the unit cell dipoles align in a single crystal to form a single domain. For a polycrystalline solid of randomly orientated grains and domains there is no overall piezoelectric effect due to cancellation and alignment is only localised[1]. Therefore, these materials need to be poled (AII.11 and Section 2.5.a.ix).

A number of the materials that demonstrate the piezoelectric effect have been extensively researched and used over the past 100 years. Quartz was the first commercial piezoelectric material and is used extensively in the form of single crystals. Single crystal piezoelectric ceramics have improved piezoelectric properties in comparison to their polycrystalline counterparts. However, single crystal ceramics are expensive and time consuming to produce, and can only be manufactured in certain simple geometries. The high cost and simple shapes restrict single crystal piezoelectric ceramics to high value/performance applications.

Polycrystalline ceramics are relatively cheap to produce, in a variety of shapes and sizes, using conventional ceramic procedures. Despite inferior properties, polycrystalline piezoelectric ceramics are used in the majority of applications due to their low cost and ease of manufacture. In order to take advantage of the piezoelectric effect in polycrystalline ferroelectric materials, they need to be poled. This is the process of aligning all the domains, and hence dipoles, so the piezoelectric properties of each domain will reinforce one another and lead to a net, bulk effect.

Piezoelectricity can be summarised as "an electrical polarisation arising from anisotropy in some non-centro symmetric crystals when subjected to mechanical stress".

AII.14.a Piezoelectric notation

There are a number of different parameters that can be measured and relationships given to distinguish piezoelectric materials[87]. In the direct piezoelectric effect (generator) the application of a stress produces a polarisation in the piezoelectric material. This induces a charge on the sample electrodes, with a dielectric displacement, D, given by equation AII.14.

$$D = e\varepsilon_t \qquad \{AII.14\}$$

Here e is the piezoelectric modulus and ε_t the strain tensor. This represents only the dielectric displacement caused by the mechanical deformation. The piezoelectric, however, is also a dielectric, permittivity of ε, and as such there is an additional displacement due to the electric field generated, E. As such the dielectric displacement becomes that given by equation AII.15.

$$D = e\varepsilon_t + \varepsilon E \qquad \{AII.15\}$$

The indirect effect can be similarly represented as the application of a voltage produces an electric field, E, through the piezoelectric material. If the material is clamped a stress, σ_T, given by equation AII.16, is generated that opposes the field.

$$\sigma_T = -Ee \qquad \{AII.16\}$$

This represents only the elastic stress due to the electric field, however the material is also an elastic solid that obeys Hooke's Law. As such equation AII.16 becomes equation AII.17.

$$\sigma_T = C^E \varepsilon_t - Ee \qquad \{AII.17\},$$

where C^E is the elastic stiffness under constant electric field, ε_t the strain. This is the case under an applied voltage (motor effect).

Both equations (AII.15 and AII.17) can be derived from the electric enthalpy density, H, equation AII.18.

$$H = \sigma_T \varepsilon_t - DE \qquad \{AII.18\}$$

$\sigma_T \varepsilon_t$ is effectively the elastic energy and DE the piezoelectric energy component. For a linear piezoelectric material, H is given by equation AII.19.

$$H = \frac{C^E \varepsilon_t^2}{2} - eE\varepsilon_t - \frac{\varepsilon E^2}{2} \qquad \{AII.19\}$$

The direct piezoelectric effect is given by equation AII.20 and the indirect effect by equation AII.21.

$$\frac{dH}{dE} = -D \qquad \{AII.20\}$$

$$\frac{dH}{d\varepsilon_t} = \sigma_T \qquad \{AII.21\}$$

AII.15 RESISTIVITY

Resistivity, ρ, is a geometrically independent value of the materials resistance to the flow of electrons. It is related to the electrical resistance of the material, R, the sample thickness, l, and the sample cross-sectional area, A, as shown in equation AII.22.

$$\rho = \frac{RA}{l} \qquad \{AII.22\}$$

The resistivity is equal to the reciprocal of the conductivity, σ. The conductivity is an inherent property determined by the number of charge carriers, their velocity and the charge they carry. The resistivity of a pure substance is dependent on its electronic band structure and the three basic behaviours (metal, semiconductor and insulator) are illustrated in Figure AII.33.
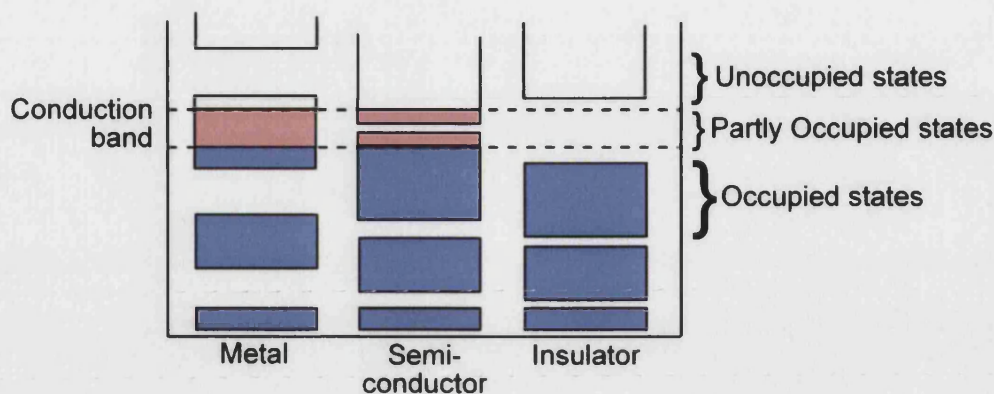
Figure AII.33: Electronic band structure for metal, semi-conductor and insulator materials[8].

In metals, the presence of a continuous finite concentration of electrons in the conduction band gives low resistivity, for example copper has a resistivity of 1.7×10^{-8} Ω.m. For a semiconductor the composition and temperature affect the concentration of charge carriers. Silicon carbide is a semiconductor and has a resistivity of 0.1 Ω.m. In an insulator, such as alumina (resistivity greater than 10^{12} Ω.m), the energy gap between the conduction band and valence band is sufficiently large that there are no electrons available for conduction. Conductivity, when it is present in insulators, is due to ionic movements and the energy barrier for this depends on the temperature and species involved. The application of an electric potential, however, can make ion diffusion in a direction parallel to the field easier, Figure AII.34.
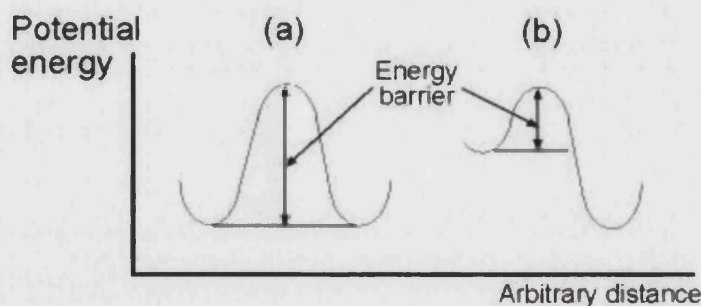
Figure AII.34: Potential energy barrier for ionic diffusion (a) without and

(b) with an applied field[8].

A.15.a.i   *Effect of particles on resistivity*

The presence of non-conducting particles, particularly those situated at the grain boundaries, impedes the diffusion of oxygen vacancies and the lattice diffusion becomes rate determining[45]. The incorporation of metallic particles is expected to decrease the resistivity, due to the easy

electron transport through the second phase, if present as a continuum. Before this stage is reached, however, it has been reported that there is a narrow compositional transition stage over which the electrical conductivity changes by orders of magnitude[83]. This transitional behaviour is generally described as the percolation phenomenon with the critical composition termed the percolation threshold. Figure AII.35 represents the three resistivity regimes that can occur with a binary metal-dielectric system[88].
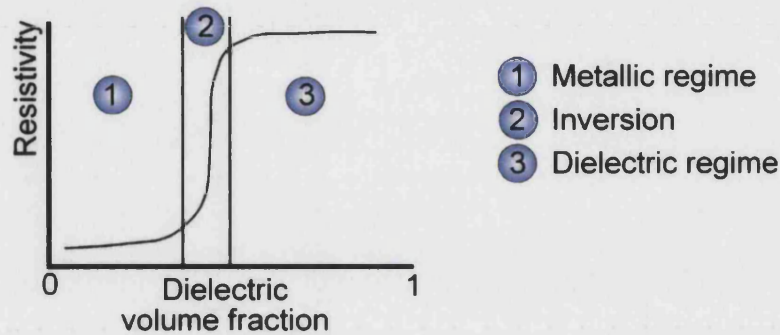
Figure AII.35: Change in resistivity with dielectric volume fraction in a metallic matrix.

In the metallic regime the large volume fraction of metal grains form a metallic continuum with dielectric inclusions. In this compositional range electron transfer properties are unaffected, however, the electron scattering at the dielectric inclusions affects the mean free path. The gradual increase in resistivity is due to the increased conduction path length caused by the intervening inclusions. The third regime is an inversion of the first, i.e. a dielectric continuum with isolated metallic particles; conduction is due to electron-hole/ionic transport. In between these regimes is the transition region where the inversion occurs. At a critical composition inclusions become interconnected and the resistivity is due to percolation along a metallic maze and electron tunnelling between close but isolated particles.

The transition can be affected by the relative particle sizes of the two constituents, as shown in Figure AII.36. If both particle types are of similar size they will tend to be uniformly located throughout the composite. The percolation threshold is well defined at a specific volume fraction of metallic filler. If the filler is of a smaller particle size it becomes segregated at grain boundaries, so a smaller volume fraction is required for percolation. The beginning of the rapid increase in conductivity is at a lower volume fraction of metal and the transition is broader[65].
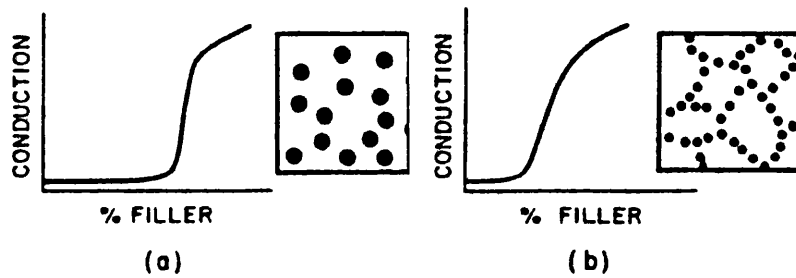
Figure AII.36: Effect of metallic filler particle size on the resistivity transition regime[65].

AII.16 DIELECTRIC STRENGTH

The dielectric strength of a substance is the magnitude of the electric field required to produce an electrical breakdown[4, 56]. One or more of the following mechanisms[89] can cause breakdown in an insulator.

AII.16.a Intrinsic strength

As the voltage across the insulator increases the current produced gradually rises as the barrier to charge motion decreases. This occurs until a saturation current is reached, above which the current will rapidly increase, initiating breakdown. Breakdown can produce localised melting and a breakdown channel through the sample that renders the sample unusable[8]. The intrinsic strength of a dielectric is of the order of 0.1 MV/mm and can be reduced by the presence of defects and electrode effects[8].

AII.16.b Thermal breakdown

A flowing current generates heat, through Joule heating, and dielectric losses further raise the sample temperature. If the rate of heat generation is faster than the rate of heat loss, then the increase in temperature can raise dielectric losses and increase the conductivity by exciting electrons into the conduction band[4]. This in turn reinforces the cycle and eventually leads to a thermal "run-away" effect and breakdown. Thermal "run-away" proceeds by an avalanche effect, where electrons liberate additional electrons by collisions[8].

AII.16.c Discharge mechanism

The presence of porosity can concentrate the applied electric field by two to three times[90] and corona discharge ("lightning") within the pore can initiate the thermal breakdown mechanism. The high localised fields can excite electrons into the conduction band to initiate the discharge. A field

greater than 10 MV/mm is required to generate this effect[55].

AII.16.d   Influences on dielectric strength

It has been reported that a wide range of factors influence the dielectric strength; these are mentioned below[89].

i.   Material homogeneity

Certain regions of the material can be more susceptible to dielectric breakdown due to the concentration of secondary phases, impurities or porosity. It has been suggested that the grain boundaries have little effect in comparison to the porosity[91]. Pores cause a local variation of the electric field and lower both mechanical and electrical strength[8]. Weibull statistics are often employed for analysis of the dielectric strength data[90].

ii.   Sample dimensions and geometry

Edge effects and sample thickness have been reported to influence the dielectric strength. A strength improvement is observed with thinner samples, as the probability of a critical defect being present is reduced[8]. As the magnitude of the electric field is proportional to the inverse of the radius of curvature, sharper edges aid breakdown at a lower field[92].

iii.   Electrode arrangement

Initiation of breakdown commonly occurs at the electrode even though the average measured field is low[8]. The stress amplification at electrode discontinuities has been confirmed by modelling and suggests the electric field is four to six times that of the applied field. This stress enhancement does not penetrate into the bulk to any appreciable extent, and can be significantly reduced by oil immersion[89].

iv.   Environmental conditions

The dielectric strength is reduced at elevated temperatures, as conductivity in the material is higher[8, 91]. The presence of dust and water on the sample surface can concentrate the electric field due to the higher radius of curvature[92]. The breakdown strength of air is 3 kV/mm [92, 93] so it is generally recommended that the dielectric breakdown test be undertaken with the sample immersed in oil[89].

v.   Time

The chance of breakdown is increased as the voltage application time increases due to the build-up of charge on surfaces and at defects[8].

AII.17   IMPEDANCE ANALYSIS

Most solids freely vibrate at a frequency determined by their shape, size, stiffness and density. For the same stiffness and density, smaller systems have a faster periodic motion, which may be approximated by sine waves, i.e. the oscillations describe simple harmonic motion[94]. The free vibration of an object is affected by its stiffness and those with a higher Young's modulus allow sound to travel between the boundaries faster so the vibrational frequency is higher. The acoustic resonant frequency, $f_{acoustic}$, is given by equation AII.23.

$$f_{acoustic} = \frac{C_m}{2\pi \, L} \qquad\qquad \{\text{AII.23}\}^{[94]},$$

where C_m is the speed of sound in that material and L is the acoustic length. An external force can be used to drive a freely oscillating system and at a certain frequency a maximum amplitude is observed. For piezoelectric materials the electromechanical coupling between the electric field and the strain allows resonance to be induced by electrical AC excitation. Electrical impedance is an indication of current flow, which is proportional to the functional response, or charge generation[94]. Impedance analysis, investigates the vibration of the material in relation to the frequency of an applied field. Figure AII.37 shows a chart of impedance, |Z|, versus applied frequency, f.
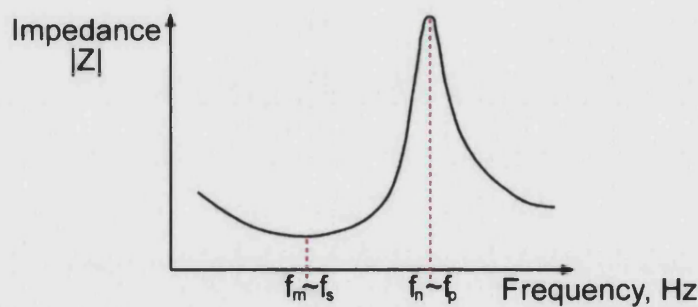
Figure AII.37: Representation of the impedance-frequency plot[95].

f_m and f_n are respectively the minimum and maximum impedance frequencies generated. In the simplified case the series resonant frequency, f_s, is approximately equal to f_m, while the parallel resonant frequency, f_p, can be approximated by f_n. The material is inductive from f_m to f_n and capacitive outside this range[95]. At low frequency the sample vibrates in phase with the applied voltage and the impedance decreases linearly as $1/\omega C$. At the mechanical resonance, f_m, the AC voltage is exactly in phase with the physical vibration. Minimum impedance occurs as the high strain levels cause large charge displacements, and thus high current levels. The sample dimensions match a strain amplitude wavelength and there is a net charge transfer into and out of

the sample during one complete cycle. Internal losses and the resistance of leads and electrodes govern the value of the minimum impedance. This is represented by the series resonant frequency, f_s. Above this frequency the phase difference between applied voltage and the mechanical vibration grows to a maximum (180°) at f_n. Physical vibration is nearly completely suppressed as the generated voltage output is in anti-phase with the applied voltage and current is almost prevented from flowing[78, 96]. Due to the strain symmetry there is an equal mixture of tensile and compressive regions and little net charge is developed[94].

Different material dimensions will be in resonance/anti-resonance at different frequencies[97], these are the modes of vibration[94], Figure AII.38. As the applied frequency increases, the object passes through modes associated with the longest dimension through to the shortest dimension of the object. In practice, devices, such as sensors, are used well below their resonant frequencies so that they have sufficient time to react to the stimulus[98]. The parameters that are calculated from impedance measurement data are given in Section 2.5.g.
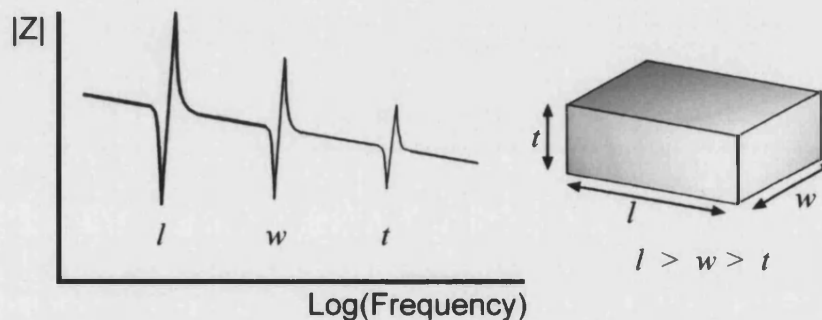
Figure AII.38: Impedance-frequency plot indicating the relative positions of the resonant peaks corresponding to (l) length, (w) width and (t) thickness modes.

AII.18 POLARISATION-FIELD ANALYSIS

Hysteresis in the broad sense is the retardation of an effect behind the cause of the effect. For piezoelectric materials hysteresis is typically attributed to the impediment of domain wall movement by pinning centres inherent in the material[99]. This behaviour is analogous to magnetic hysteresis where wall motion can be obstructed by carbide precipitates that enhance the coercivity[56]. Hysteretic domain wall motion has been previously mentioned as a loss mechanism at low fields. The degree of hysteresis and non-linear effects increase as the drive voltage is raised[99]. It has been suggested that the reversible domain wall motion (bowing) is micro-hysteresis, while at high fields the wall movement for extended distance[99] and domain switching is macro-hysteresis[81].

With the domain walls moving a considerable distance, the pinning centres are overcome and the process becomes irreversible[99]. The hysteresis behaviour can be characterised by measuring the polarisation, P, produced under the application of an electric field, E. Figure AII.39 indicates the polarisation-field behaviour of four different components.
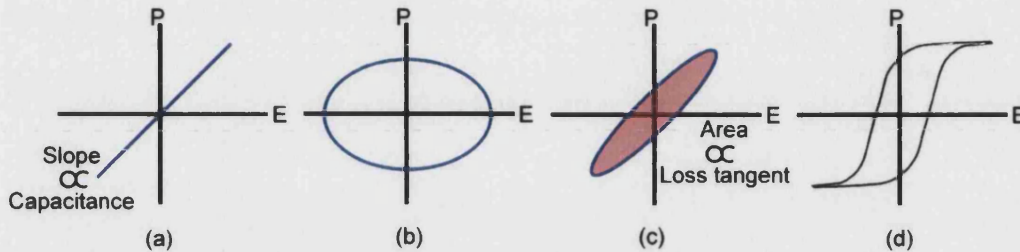
Figure AII.39: Polarisation-electric field plots for (a) an ideal capacitor, (b) an ideal resistor,

(c) a lossy capacitor and (d) a ferroelectric[100].

The loop for an ideal capacitor is a linear relationship between polarisation and electric field. The gradient of the line is proportional to the capacitance as the current leads the voltage by 90°. Therefore the charge (integral of current with time) is in phase with the voltage. For an ideal resistor the voltage and current are in phase and the behaviour describes an ellipse. Combining the previous two components produces a lossy capacitor with a loop area proportional to the loss tangent, and a gradient related to the capacitance. A ferroelectric has a more complex loop as the change in polarisation state is coupled with a polarisation strain. For these materials the polarisation-field loop is characterised by the reference points of coercive field, saturation and remanant polarisations[100], as shown in Figure AII.40.
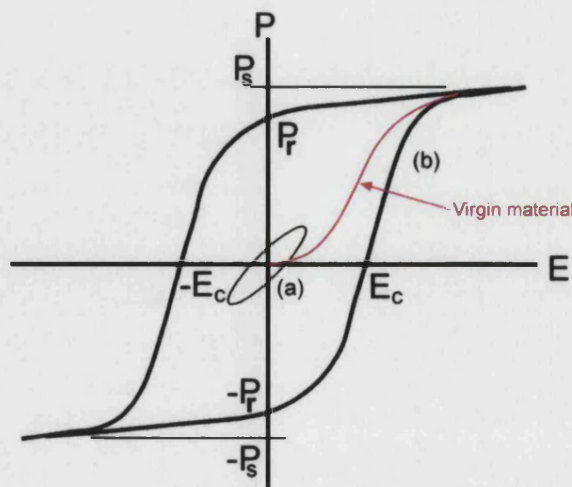
Figure AII.40: Ferroelectric polarisation-field loop behaviour at (a) low and (b) high field.

Behaviour shown in red is for an initially unpoled material.

The coercive field, E_c, is the electric field required to reduce the polarisation to zero from the polarised state. The saturation polarisation, P_s, is the maximum polarisation attained by the applied electric field and corresponds to all the possible dipoles being aligned in the field direction. The remanant polarisation, P_r, is the polarisation of the material after the electric field has been removed. A high P_r indicates a large internal polarisability, strain and electromechanical coupling factor[3].

For an unpoled sample increasing the electric field causes domain walls to move and those domains orientated in the direction of the applied field grow at the expense of anti-parallel domains. At higher fields the polarisation increases more rapidly due to domain switching[8]. This continues until a saturation polarisation, P_s, is reached where all the possible domains have grown to their maximum size and all domains of like-orientation are aligned in the poling direction.

When the field strength is decreased the polarisation will also decrease, but there remains a remanant polarisation, P_r, in the ceramic when the field has been removed. This occurs because there is insufficient thermal energy available for the domains to pass pinning centres and return to their original equilibrium positions. Additional energy input is required, by the application of a field of opposite polarity, to move the domains to their original state[8]. With a remanant polarisation the ceramic will exhibit a piezoelectric effect as a higher proportion of the dipoles are aligned in one direction. Application of the electric field in the opposite direction causes the domains to switch back until there is no remanant polarisation. The electric field required to produce this effect is called the coercive field, $-E_c$. Further increase of the field will align domains in the opposite direction, by nucleation and growth of anti-parallel domains[2], and lead to a minima in polarisation, $-P_s$. This is where the alignment of the domains is saturated in the opposite direction to the original. A reduction of the field to zero will again produce remanant polarisation, $-P_r$, and will require the coercive field, E_c, to obtain zero polarisation in the sample. Increasing the field strength above E_c will again align domains until maximum polarisation, P_s, is again reached. Repeated cycling of the same field will produce similar loops.

The coercive field value varies in practice from 50-200 V/mm, while thermodynamic theory predicts a value of about 10 kV/mm. The low experimental value has been suggested to be due to the domains leaving the metastable state (anti-parallel to field) to a stable state, parallel to the field, before the metastable state becomes completely unstable[2]. An additional possibility is "back-switching" of domains after the field has been removed from the completely polarised material. This consists of the creation of a few small domains that are anti-parallel to the majority of domains. Reduction of sample energy by closing flux is the drive for this process. Reversal of the

field causes these domains, which are now parallel to the applied field, to immediately grow, Figure AII.41, thus reducing the field strength required for polarisation reversal[2].
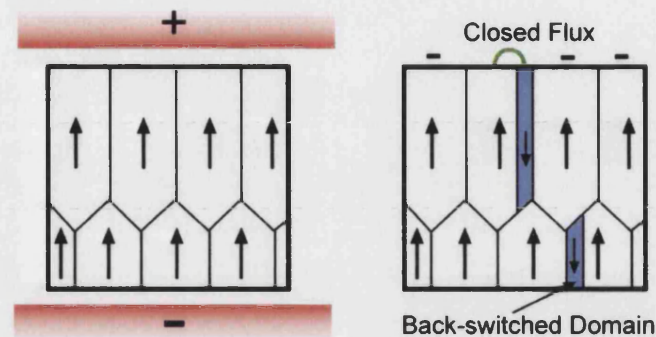
Figure AII.41: Illustration of domain back-switching with domains

(a) under field and (b) field removed.

The polarisation-field loop can be asymmetric, with a shift along the electric field axis, due to the presence of an internal bias field that is generated in the direction of the first poling field to be applied[101]. The polarisation-field loop can also be affected by electrode edge effects[2]. It has been suggested that this asymmetry increases under aging due to a domain stabilisation process[3, 84]. Table AII.3 displays the difference in maximum polarisation and coercive field between a single crystal and the polycrystalline solid of barium titanate. The increase in the coercive field for polycrystalline materials demonstrates the greater difficulty in driving domain walls attached to grain boundaries.

Table AII.3: Maximum polarisation and coercive field for single crystal

and polycrystalline barium titanate[1].

Property	Single crystal	Polycrystalline ceramic
Maximum polarisation (C/m^2)	0.27	0.15
Coercive field (kV/mm)	0.1	1.8

AII.18.a   Grain size and polarisation-field behaviour

In large grain ceramics switching requires the generation of complicated domain boundaries that are driven by the external field through the grain. The situation is different for fine grains where there is a simple domain configuration, or none at all, for single domain particles. Figure AII.42

shows the polarisation-field results for a fine-grained (<10 μm) and a coarse-grained barium titanate[62].
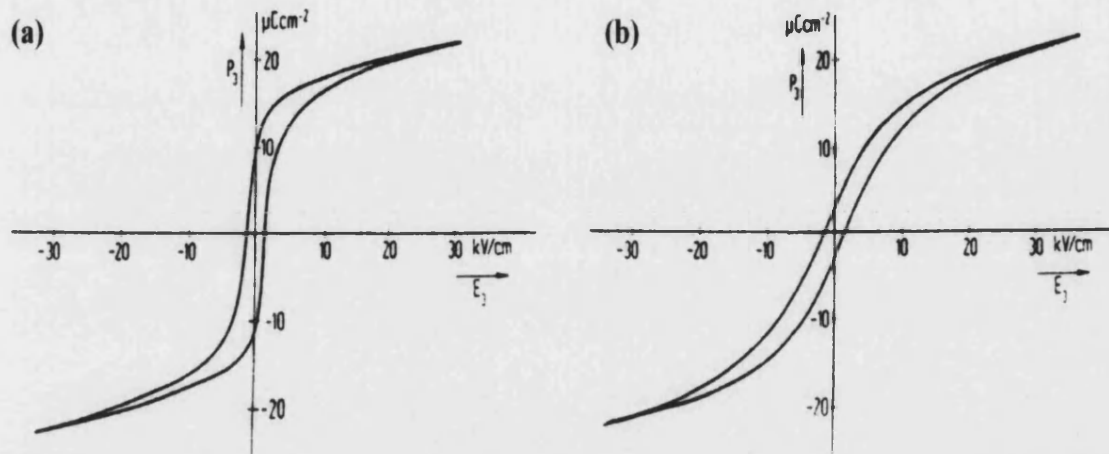
Figure AII.42: Polarisation-field loops for (a) coarse and (b) fine grained barium titanate[62].

In the fine-grained structure the reversible energy generated via the electric field and internal elastic stress energy is negligible below a polarisation of 11 $\mu C/m^2$. The slanted fine-grained loop is a result of increasing internal stress as the domains are unable to orient without inducing stress[62].

AII.18.b   Temperature and polarisation-field behaviour

Temperature affects the polarisation-field loop by reducing the electric field required for domain movement. The coercive field is reduced as the temperature is increased, until at T_c there is no hysteresis. At low temperature a large coercive field is required as the domain configuration is "frozen in"[8].

AII.19   REFERENCES

1. MOULSON, A. J. & HERBERT, J. M., 'Electroceramics – Materials, Properties & Applications', *Chapman & Hall*, 1990

2. JONA, F. & SHIRANE, G., 'Ferroelectric crystals', *Dover Publications Inc, New York*, 1993

3. HAERTLING, G.H., 'Ferroelectric ceramics: History and Technology', *J. Am. Ceram. Soc.*, 1999, **82** (4), 797-818

4. University of Connecticut, 'Dielectric behaviour and ferroelectricity', 'http://www.ims.uconn.edu/~alpay/201/Dielectric.pdf', 26/2/03

5. BHALLA, A.S., GUO, R. & ROY, R., 'The perovskite structure – A review of its role in ceramic science and technology', *Mat. Res. Innovat.*, 2000, **4**, 3-26

6. ROSEN, C. Z., HIREMATH, B. V. & NEWNHAM, R (Ed), 'Piezoelectricity: Key papers in physics', *Am. Inst. of Physics*, 1992, **5**, 4, 13, 119, 157, 285

7. FINK, D. & CARROLL, J.M., 'Standard handbook for electrical engineers', *McGraw-Hill Book Company, London*, 1968, 10th Edn., Sec4-382

8. KINGERY, W.D., 'Introduction to ceramics', *J. Wiley & Sons Inc*, 1976

9. STEARNS, L., ZHAO, J. & HARMER, M., 'Processing and microstructure development in Al_2O_3-SiC "nanocomposites" ', *J. Eur. Ceram. Soc.*, 1992, **10**, 473-77

10. BORSA, C., FERREIRA, H. & KIMINAMI, R., 'Liquid phase sintering of Al_2O_3-SiC nanocomposites', *J. Eur. Ceram. Soc.*, 1999, **19**, 615-21

11. VOLTZKE, D. & ABICHT, H-P., 'The influence of different additives and the mode of their addition on the sintering behaviour and the properties of semiconducting barium titanate ceramics', *Solid State Sciences*, 2000, **2** (1), 149-59

12. TIAN, L., ZHOU, Y. & LEI, T.C., 'Mechanical properties of Al_2O_3+ZrO_2+Nano-SiCp ceramic composite', *Ceramics International*, 1996, **22**, 451-56

13. FAN, D., CHEN, L-Q. & CHEN, S-P., 'Numerical simulation of Zener pinning with growing second phase particles', *J. Am. Ceram. Soc.*, 1998, **81** (3), 526-32

14. TODD, R. I., 'Alumina/SiC nanocomposites – big things from small packages', *21st century ceramics Ed. Thompson, D. P. & Mondal, H.*, IOM, 1996, **55**, 225-248

15. BORSA, C., JIAO, S., TODD, R. & BROOK, R., 'Processing and properties of Al_2O_3/SiC nanocomposites', *J. Microscopy*, 1995, **77** (3), 305-12

16. HOLK, R. & PROVENZANO, V., 'Bounds on the strength of a model nanocomposite', *Nanostructured materials*, 1997, **8** (3), 289-300

17. WINN, A. & TODD, R., 'Microstructural requirements for alumina-SiC nanocomposites', *Brit. Ceram. Trans.*, 1999, **98** (5), 219-24

18. POHANKA, R., RICE, R. & WALKER, B., 'Effect of internal stress on the strength of $BaTiO_3$', *J. Am. Ceram. Soc.*, 1976, **59** (1-2), 71-74

19. STERNITZKE, M., 'Review: Structural ceramic nanocomposites', *J. Eur. Ceram. Soc*, 1997, **17**, 1061-82

20. SCHMID, H., ALSAN, M., ASSMANN, S., NAB, R. & SCHMIDT, H., 'Microstructural characterisation of Al_2O_3-SiC nanocomposites', *J. Eur. Ceram. Soc.*, 1998, **18**, 39-49

21. CONDER, R., PONTON, C. & MARQUIS, P., 'Processing of alumina/silicon carbide nanocomposites', *Nanoceramics, Ed. Freer, R., Brit. Ceram. Proc.*, 1993, **51**, 105-17

22. OHJI, T. & NIIHARA, K., 'Comments on "Physical limitations of the inherent toughness and strength in ceramic-ceramic and ceramic-metal nanocomposites', *J. Ceram. Soc. Jpn.*, 1996, **104** (6), 581-82

23. EVANS, A., 'Perspective on the development of high toughness ceramics', *J. Am. Ceram. Soc.*, 1990, **73** (2), 187-206

24. MISHRA, R.S. & MUKHERJEE, A.K., 'Processing of high hardness-high toughness alumina matrix nanocomposites', *Mat. Sci. & Eng.*, 2001, **A301**, 97-101

25. TUAN, W., LIN, M. & WU, H., 'Preparation of Al_2O_3/Ni composites by pressureless sintering in H_2', *Ceram. Int.*, 1995, **21**, 221-25

26. CHUNG, H-T., SHIN, B-C. & KIM, H-G., 'Grain-size dependence of electrically induced microcracking in ferroelectric ceramics', *J. Am. Ceram. Soc.*, 1989, **72** (2), 327-29

27. PEZZOTTI, G., NISHIDA, T. & SAKAI, M., 'Physical limitations of the inherent toughness and strength in ceramic-ceramic and ceramic-metal nanocomposites', *J. Ceram. Soc. Jpn.*, 1995, **103**, 901-09

28. FABER, K. & EVANS, A., 'Crack deflection processes-I: Theory', *Acta Metallurgica*, 1983, **31** (4), 565-76

29. TAYA, M., HAYASHI, S., KOBAYASHI, A. & YOON, H., 'Toughening of a particulate-reinforced ceramic-matrix composite by thermal residual stress', *J. Am. Ceram. Soc.*, 1990, **73** (5), 1382-91

30. LUO, J. & STEVENS, R., 'The role of residual stress on the mechanical properties of Al_2O_3-5%volSiC nano-composition', *J. Eur. Ceram. Soc.*, 1997, **17**, 1565-72

31. VIRKAR, A.V. & MATSUMOTO, R.L.K., 'Ferroelectric domain switching as a toughening mechanism in tetragonal zirconia', *J. Am. Ceram. Soc.*, 1986, **69** (10), c224-26

32. REECE, M.J. & GUIU, F., 'Estimation of toughening produced by ferroelectric/ ferroelastic domain switching', *J. Eur. Ceram. Soc.*, 2001, **21**, 1433-6

33. HWANG, H., NAKAHIRA, A., SEKINO, T. & NIIHARA, K., 'Mechanical property and fracture behaviour of $BaTiO_3$-based nanocomposites', *Transcip. J. Jpn. Soc. Powder Powder Metall.*, 1994, **10**, 1175-80

34. NAGAI, T., HWANG, H., YASUOKA, M., SANDO, M. & NIIHARA, K., 'Preparation of barium titanate-dispersed-magnesia nanocomposite', *J. Am. Ceram. Soc.*, 1998, **81** (2), 425-28

35. SCHNEIDER, G. & HEYER, V., 'Influence of the electric field on Vickers indentation crack growth in $BaTiO_3$', *J. Eur. Ceram. Soc., Electroceramics VI 1998, Switzerland, Elsevier*, 1999, **19**, 1299

36. WAHI, R. P. & ILSCHNER, B, 'Fracture behaviour of composites based on Al_2O_3-TiC', *J. Mat. Sci.*, 1980, **15**, 875

37. YONG, J-F., CHOA, Y-H., SINGH, J. & NIIHARA, K. 'Fabrication and mechanical properties of Si₃N₄/SiC nanocomposite with pressureless sintering and sinter-post-hiping', *J. Ceram. Soc. Jpn.*, Oct 98, 951-57

38. MUNRO, R. & FREIMAN, S.W., 'Correlation of fracture toughness and strength', *J. Am. Ceram. Soc.*, 1999, 82 (8), 2246-8

39. BROOK, R. & MACKENZIE, R., 'Nanocomposite Materials', *Materials World*, Jan 93, 27-30

40. KOMERNENI, S., 'Nanocomposites', *J. Mat. Chem.*, 1992, 2 (12), 1219-30

41. FERRONI, F.P. & PEZZOTTI, G., 'Evidence for bulk residual stress strengthening in Al₂O₃/SiC nanocomposites', *J. Am. Ceram. Soc*, 2002, 85 (8), 2033-8

42. HWANG, H., NAGAI, T., OHJI, T., SANDO, M., TORIYAMA, M. & NIIHARA, K., 'Curie temperature anomaly in lead zirconate titanate/silver composite', *J. Am. Ceram. Soc.*, 1998, 81 (3), 709-12

43. VEZZOLI, G., CHEN, M. & CASLAVSKY, J., 'New high dielectric strength materials: micro/nanocomposites of suspended Au clusters in SiO₂/SiO₂-Al₂O₃-Li₂O gels', *Ceram. Int.*, 1997, 23, 105-108

44. LIU, D-M. & WINN, E.J., 'Microstresses in particulate-reinforced brittle composites', *J. Mat. Sci.*, 2001, 36, 3487-3495

45. HWANG, H. & NIIHARA, K., 'Fabrication of surface barrier layer capacitor on BaTiO₃-based composite containing particulate SiC', *J. Mat. Res.*, 1998, 13 (10), 2866-70

46. OKASAKI, K., 'Mechanical behaviour of ferroelectric ceramics', *Ceram. Bul.*, 1984, 63 (9), 1150-1157

47. HWANG, H., SEKINO, T., OTA, K. & NIIHARA, K., 'Perovskite-type BaTiO₃ ceramics containing particulate SiC: Part I-Structure variation and phase transformation', *J. Mat. Sci.*, 1996, 31, 4617-24

48. BELL, A. J. & MOULSON, A. J., 'The effect of grain size on the dielectric properties of barium titanate ceramics', *Brit. Ceram. Soc.*, 1985, 36, 57-66

49. HWANG, H. J., UEDA, S. & NIIHARA, K., 'Grain boundary controlled mechanical and dielectric properties of BaTiO₃-based nanocomposite', *Ceram. Trans.*, 1994, 44, 399-408

50. BELL, A., MOULSON, A. & CROSS, L., 'The effect of grain size on the permittivity of BaTiO₃', *Ferroelectrics*, 1984, 54, 147-50

51. HALL, D.A., 'Review: Non-linearity in piezoelectric ceramics', *J. Mat. Sci.*, 2001, 36, 4575-4601

52. MORENO, J., GUIU, F., MEREDITH, M., REECE, M., ALFORD, N. & PENN, S., 'Anisotropic and cyclic mechanical properties of piezoelectrics –compression testing', *J. Eur. Ceram. Soc., Electroceramics VI 1998, Switzerland, Elsevier*, 1999, 19, 1321

53. CHOU, I. A., CHAN, H. M. & HARMER, M. P., 'Machining-induced surface residual stress behaviour in Al_2O_3-SiC nanocomposites', *J. Am. Ceram. Soc.*, 1996, **79** (9), 2403-9

54. OHJI, T., JEONG, Y-K., CHOA, Y-H. & NIIHARA, K., 'Strengthening and toughening mechanisms of ceramic nanocomposites', *J. Am. Ceram. Soc.*, 1998, **81** (6), 1453-60

55. University of Virginia, 'Introduction to materials science, Chapter 19, Electrical properties', 'www.people.virginia.edu/~lz2n/mse209/Chapter19-p3.pdf', 26/02/03

56. W. R. CALLISTER: 'Materials science and Engineering: An introduction', J. Wiley & Sons Inc., Chichester, 1994, 646-94

57. NAGAI, T., HWANG, H., SANDO, M. & NIIHARA, K., 'Preparation of ceramic nanocomposite with perovskite dispersiod', *Mat. Res. Soc. Symp. Proc.*, 1997, 375-80

58. GACHIGI, K., KUMAR, U. & DOUGHERTY, J., 'Grain size effects in barium titanate', *Proc. 8th IEEE Int. Symp. on Application of Ferroelectrics*, 1992, 492-5

59. LUAN, W., GAO, L. & GUO, J., 'Size effect on dielectric properties of fine-grained $BaTiO_3$ ceramics', *Ceram. Int.*, 1999, **25**, 727-29

60. ARLT, G., HENNINGS, D. & DE WITH, G., 'Dielectric properties of fine-grained barium titanate ceramics', *American Institute of Phys. J. Appl. Phys.*, 15 Aug 1985, **58** (4), 1619-25

61. FANG, T., HSEIH, H-L. & SHIAU, F-S., 'Effect of pore morphology and grain size on the dielectric properties and tetragonal-cubic phase transition of high-purity barium titanate', *J. Am. Ceram. Soc.*, 1993, **76** (5), 1205-11

62. ARLT, G., 'The role of domain walls on the dielectric, elastic and piezoelectric properties of ferroelectrics ceramics', *Ferroelectrics*, 1987, **76**, 451-58

63. ARLT, G. & PEUSENS, H., 'The dielectric constant of coarse grained $BaTiO_3$ ceramics', *Ferroelectrics*, 1983, **48**, 213-24

64. SHERRIT, D., VAN NICE, D., GRAHAM, J., MUKHERJEE, B. & WIEDERICK, H., 'Domain wall motion in piezoelectric materials under high stress', *Proc. Int. Soc. for the Applications of Ferroelectrics*, 1992, 167-70

65. NEWNHAM, R.E., 'Composite electroceramics', *Ferroelectrics*, 1986, **86**, 1-32

66. DEXTER, 'Domain theory', 'www.dextermag.com/domain_theory.htm', 26/02/03

67. ZIVKOVIC, L., STOJANOVIC, B., PAVLOVIC, V., NIKOLIC, Z. & MARINLOVIC, B., 'SEM investigation of domain structure in (Ba, Ca, Pb)TiO_3', *J. Eur. Ceram. Soc., Electroceramics VI 1998, Switzerland, Elsevier*, 1999, **19**, 1085

68. DENNIS, M., 'Transmission electron microscopy of ferroelectric domains in $BaTiO_3$', Thesis, Sept 1972, Pennsylvania State University

69. MILLER, R.C. & WEINREICH, G., 'Mechanism for the sidewise motion of 180° domain walls in barium titanate', *Phys. Rev.*, 1960, **117**, 1460

70. ARLT, G., 'Review: Twinning in ferroelectric and ferroelastic ceramics; stress relief', *J. Mat. Sci.*, 1990, **25**, 2655-66

71. HU, H-L. & CHEN, L-Q., 'Three dimensional computer simulation of ferroelectric domain formation', *J. Am. Ceram. Soc.*, 1998, **81** (3), 492-500

72. COOK, W.R., 'Domain Twinning in barium titanate ceramics', *J. Am. Ceram. Soc.*, 1956, **39** (1), 17-19

73. 'Domains', 'www.mems.rice.edu/~stenner/Images/DW.html', 11/03/02

74. CAO, W. & RANDALL, C., 'Grain size and domain size relations in bulk ceramic ferroelectric materials', *J. Phys. Chem. Solids*, 1996, **57** (10), 1499-1505

75. OGAWA, T., 'Domain structure of ferroelectric ceramics', *Ceram. Int.*, 2000, **26**, 383-90

76. SAYER, M., JUDD, B., El-ASSAL, K. & PARSAD, E., 'Poling of piezoelectric ceramics', *J. Canadian Ceram. Soc.*, 1981, **50**, 23-28

77. SKONSKI, R. & COEY, J.M.D., 'Permanent magnetism', *Inst. Phys. Pub., Bristol & Philadelphia*, 1999, 182-6 & 266-7

78. JOSEPH, E., Private communication, *Qinetiq*, July 2002

79. JILES, D., 'Introduction to magnetism and magnetic materials', 2nd Ed., *Chapman & Hall*, 1998, 184-7

80. METLOV, K., 'Representability of the domain wall motion in random potentials by the Preisach model', *Physica B*, 2000, **275**, 164-7

81. HALL, D.A. & STEVENSON, P.F., 'High field dielectric behaviour of ferroelectric ceramics', *Ferroelectrics*, 1999, **228**, 139-58

82. ARLT, G. 'Ferroelectrics – domains and losses', *Brit. Ceram. Proc.: Electroceramics Ed. Moulson, A.J., Binner, J. & Morrell, R.*, Proc. 41, Feb 89, 109-116

83. CHEN, I. G. & JOHNSON, W. B., 'Alternating-current electrical properties of random metal-insulator composites', *J. Mat. Sci.*, 1991, **26**, 1565-76

84. WU, K. & SCHULZE, W., 'Effect of AC Field level on the aging of the dielectric response of polycrystalline $BaTiO_3$', *J. Am. Ceram. Soc.*, 1992, **75** (12), 3385-89

85. MORRISON, F.D., SINCLAIR, D.C. & WEST, A.R., 'Characterisation of lanthanum doped barium titanate ceramics using impedance spectroscopy', *J. Am. Ceram. Soc.*, 2001, **84** (3), 531-8

86. NOWOTNY, J., 'Electronic ceramic materials', *Transtech Publishing, UK*, 1992

87. WANG, H. & SINGH, R. N., 'Crack propagation in piezoelectric ceramics: effect of applied electric fields', *J. Appl. Phys.*, 1 June 1997, **81** (11), 7471-79

88. ABELES, B., SHENG, P., COTTS, M.D. & ARIE, Y., 'Structural and electrical properties of granular metal films', *J. Adv. Phys.*, **24**, 1975, 407-460

89. CAIN, M., STEWART, M. & GEE, M., 'Mechanical and elastic strength measurements for piezoelectric ceramics: Technical measurement notes', *NPL report CMMT(A)99*, 1998

90. WEISS, E. & BELL, A., 'A Comparison of the electrical and mechanical strengths of conventional and flux-sintered barium titanate-based dielectrics', *Brit. Ceram. Proc.*, 1992, **49**, 229-39

91. SHIN, B-C. & KIM, H-G., 'Partial discharge, microcracking and breakdown in BaTiO$_3$ ceramics', *Ferroelectrics*, 1988, **77**, 161-166

92. LUX, J., 'Corona', 'home.earthlink.net/~jimlux/hv/corona.htm', 26/02/03

93. ELERY, G., 'Electric field to produce spark in air (Dielectric breakdown)', 'hypertextbook.com/facts/2000/AliceHong.shtml', 26/02/03

94. CAIN, M. G. & STEWART, M., 'Measurement good practice guide No. 33: Piezoelectric resonance', *NPL*, Teddington, 2001

95. WAANDERS, J. W., 'Piezoelectric ceramics – Properties and application', *Phillips*, 1991

96. UCHINO, K. & HIROSE, S., 'Loss mechanisms in piezoelectrics: How to measure different losses separately', *IEEE Transactions on Ultrasonics, Ferroelectrics and frequency control*, 2001, **43** (1), 307

97. BOSER, O., 'Electromechanical resonance in ceramic capacitors and evaluation of the piezoelectric materials' properties', *Advanced Ceramic Materials*, 1987, **12** (2), 167-72

98. HOLMES, J., PEARCE, D. & BUTTON, T., 'Novel piezoelectric structures for sensor applications', *J. Eur. Ceram. Soc.*, 2000, **20**, 2701-4

99. SMITH, R.C. & OUNAIES, Z., 'A domain wall model for hysteresis in piezoelectric materials', ICASE Report no. 99-52, 1999

100. STEWART, M., CAIN, M.G. & HALL, D.A., 'Ferroelectric Hysteresis: Measurement & Analysis', NPL report CMMT(A)152, 1999

101. OKAZAKI, K. & IGARASHI, H., 'Importance of microstructure in electronic ceramics', *Ceramic microstructure '76*, 564-83

APPENDIX III: COMPOSITE FABRICATION

AIII.1 POWDER PREPARATION

While traditional clay based materials require minimal processing before use, technical ceramics require considerable processing. High purity and controlled particle size are generally required to ensure that the end product is reliable and has the required surface finish with minimal post-sintering machining. To achieve these requirements numerous methods have been devised to produce the powders. Popular methods include precipitation of components from the reaction of two solutions and mixed oxide compounding. It has been suggested that the mixed oxide procedure is no longer appropriate and that wet chemical methods, with a shorter diffusion distance for the reacting ions, finer particle sizes and a high degree of chemical homogeneity are more suitable[1]. The disadvantage of wet chemical methods, however, are agglomeration of particles[1]. This appendix gives some background information on the possible techniques used for manufacturing barium titanate matrix. There is also information on the finishing techniques used to prepare the samples for microstructural, mechanical and electrical characterisation.

Barium titanate powder is formed by reacting stoichiometric amounts of the base chemicals titania (TiO_2) and barium carbonate ($BaCO_3$). The barium carbonate decomposes when heated with the evolution of carbon dioxide, and the product, barium oxide, reacts with the titania. The initial powders must be fine and well mixed to ensure that the reaction is uniform and goes to completion. A white/cream powder is produced that can be used to form the specimen required. Additives, however, are typically incorporated and these can include the following.

  i.   Binders – such as Polyvinyl Alcohol (PVA), to increase the green density and compact strength[2, 3].
  ii.   Lubricants – to improve pressing behaviour and increase green compact strength.
  iii. Sintering additives – to reduce the sintering temperature or inhibit grain growth.
  iv.   Dispersants – to ensure uniform distribution of the particles in suspensions.

AIII.1.a   POWDER DISPERSION

The size and distribution of particles, dispersion of additives and the breakdown of agglomerates influence the preparation of powders ready for pressing into the specimen shape. Dry powder

routes can produce large agglomerates that result in significant crack-like voids, which form due to differential sintering. Soft agglomerates are either formed by spontaneous particle attraction (van der Waals forces) or particle cohesion due to surface tension effects (absorbed atmospheric water)[4]. A number of techniques have been devised to reduce particle agglomeration and improve dispersion of additives[5], such as:

i.   **Precipitation** – Precipitation of the barium titanate in a suspension of silicon carbide.

ii. **Vibration** – The powder is ultrasonically vibrated in suspension to break-up agglomerates and improve dispersion[6-9].

iii. **pH** – The pH of the powder suspension is modified so that zeta potentials will cause dispersion of the particles, Figure AIII.1. The isoelectric point is the pH at which the particles have zero charge and is approximately four for silicon carbide. By using a pH far different from this value, the particles will have the same charge and repel one another[10, 11].

iv. **Dispersants** – The addition of dispersants, which are chemicals that commonly affect the zeta potentials, can be used. This method may be undesirable, however in some cases, as the dispersant is generally organic and as such can leave carbon deposits behind after sintering. A commonly used dispersant is Dispex A40 a polyphosphate[6, 9, 12].
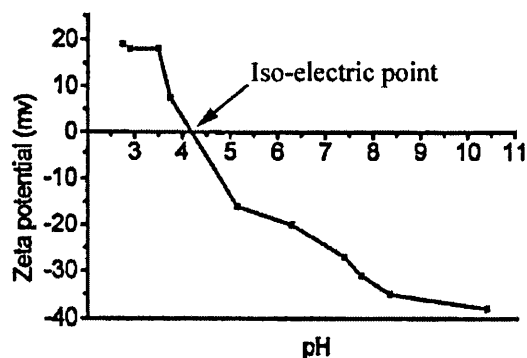
Figure AIII.1: Relationship between zeta potential and pH for silicon carbide[5].

AIII.1.b PARTICLE MIXING AND MILLING

Milling is carried out in either the dry or wet state to control the particle size and distribution of the powder. The dry powder and any additives are placed in a container with milling media for dry mixing and milling[13]. The container is generally polymeric, such as polyethylene[14, 15] or ceramic, such as zirconia. The milling media can be metal pellets, but more often sintered ceramic pellets are used due to the lower wear rates and to reduce contamination, which will also increase with milling time[15]. The container is sealed and rotated at a speed that causes the media to impact on the particles and break up agglomerates. The extent of the milling will depend on the time, media size and energy provided to the media.

Wet milling is similar to dry milling except that a liquid medium is used to aid the dispersion of the particles. The liquid medium may be organic, such as methanol[7] and ethanol[15], or water[16]. Organic solvents can be advantageous compared to water, as they offer a range of vapour pressures, giving a range of evaporation rates[10]. A faster rate of evaporation can reduce agglomeration of particles. The choice of medium depends on:

i. the powder being milled, as reactions may occur,

ii. the behaviour of the mix under drying. Certain powder-medium combinations may promote the formation of agglomerates.

iii. the economic cost.

iv. environmental concerns[10]. Organic solvents are expensive, more detrimental to the environment and have more implications for health and safety.

An aqueous medium has been reported as being undesirable since hard particles are produced[8]. Methanol is recommended as the best organic medium due to lower volume sedimentation in comparison to other solvents[8]. The use of an organic medium can eliminate the presence of –OH groups that form bonds between particles, so reducing the aggregate strength[17]. The most important milling processes are ball and attrition milling.

AIII.1.b.i   *Ball milling*

Ball milling, see Figure AIII.2, is a simple and cheap method of mixing the powders, however, it does suffer from long process times. The technique involves imparting potential energy to the grinding media, which is subsequently transformed into the kinetic energy used to break-up the powders. The rotation speed in ball milling is kept sufficiently low to ensure that the milling media drop from the top of the container, instead of being "stuck" to the container sides due to the inertial forces. Table AIII.1 summarises the process variables as reported in the literature.
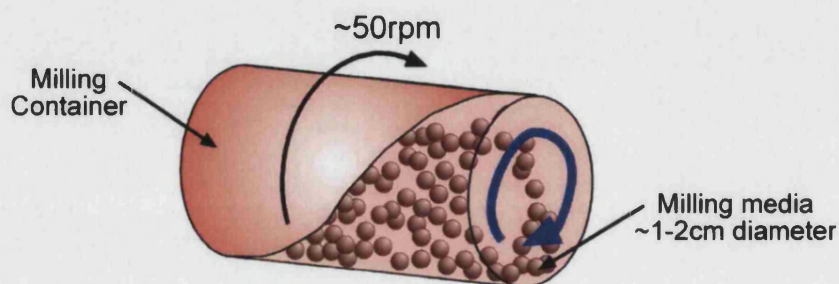
Figure AIII.2: Ball milling schematic indicating rotation speed and media size.

Table AIII.1: Reported ball-milling parameters.

System	Medium	Media type	Time (hr)	Reference
Al_2O_3/ SiC	Methanol	-	-	7
Al_2O_3/ SiC	Ethanol	Alumina	6-12	15
MgO/ $BaTiO_3$	n-Butyl alcohol	Zirconia	16	18
$BaTiO_3$	Methanol	-	-	2
$BaTiO_3$/ SiC	Ethanol	Zirconia	24	14, 19
$BaTiO_3$/ Ag	Deionised water	Zirconia	4	20

AIII.1.b.ii   *Attrition milling*

While ball milling is the traditional process for the mixing of powders, either in the dry or wet states, higher energy techniques are required to produce smaller particle sizes. Smaller particles are more resistant to fracture as they are protected from impact by larger particles. More energy is required to cause particle fracture because of the lower probability of large flaws being present to aid particle breakage as the particle size decreases. Attrition milling, Figure AIII.3, involves the use of a ceramic tree arrangement that imparts energy to the milling media, which are generally smaller in size than those used in the ball mill. Attrition milling uses higher rotational speeds (500 rpm[21]), compared to ball milling, to convey greater energy to the media. The media in turn impacts other media elements crushing the powder in the collision. The greater energy of the impacts and the more numerous impact events cause an increase in temperature and the milling container requires water-cooling. The container is typically made of a low wear rate material, such as alumina or zirconia, to reduce contamination.
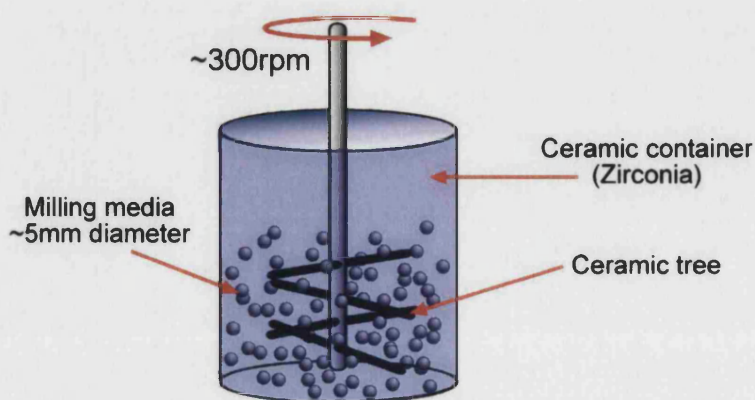
Figure AIII.3: Attrition milling schematic.

Ceramic systems that have been attrition milled are reported in Table AIII.2. In addition to a finer final particle size, attrition milling benefits from a shorter processing time when compared to ball milling[9].

Table AIII.2: Reported attrition milling parameters.

System	Medium	Media type	Time (hr)	Reference
Al_2O_3/ SiC	Distilled water	Zirconia	1.5	3
Al_2O_3/ SiC	Deionised water	Zirconia	2	6, 9
$BaTiO_3$	Ethanol	-	5	21
$BaTiO_3$	Ethanol	Polyurethane coated steel balls	2	22
Al_2O_3/ Ag	Ethanol	-	4	23

AIII.1.c   POWDER DRYING

If the milling or mixing process has involved a liquid medium this needs to be removed in order to produce the dry powder used for consolidation. The careful removal of the liquid is critical to avoid generation of agglomerates, as surface tension typically causes the particles to aggregate. Hard agglomerates can result from fast drying rates at high temperatures[24]. A number of drying techniques have been reported:

i.   **Oven** – While economical and simple, impurities and inhomogeneities can result from the use of a drying oven, and heavy agglomeration can occur[17].

ii.   **Infrared lamp** – High temperatures can produce agglomerates so the height of the lamp needs to be adjusted as the liquid evaporates[8].

iii.   **Freeze-drying** – This is a common method[6, 9, 24] due to the low degree of agglomeration and also results in a material of high green and sintered densities[24]. Freeze-drying is the optimal procedure for aqueous solutions. The short time to freeze the ceramic slurry suppresses agglomerate formation and avoids segregation. The powder is subsequently treated by converting the frozen water directly to water vapour[17]. This method, however, requires slightly more complex equipment, is slow and therefore relatively expensive.

AIII.1.d   POWDER SIEVING AND CALCINATION

AIII.1.d.i   Sieving

Sieving of the dried powder after milling is intended to break-up soft agglomerates and ensure that the particle size used is suitable for consolidation. This process can be carried out before or after calcination. Table AIII.3 gives the types of sieve that have been employed in literature.

Table AIII.3: Sieve sizes used in the preparation of various composite systems.

System	Sieve size (μm)	References
MgO/ BaTiO₃	110	18
Al₂O₃/ SiC	150, 180	3, 6
BaTiO₃/ SiC	320	19
BaTiO₃	~74	22
PZT/ Ag	320	13
BaTiO₃/ Ag	100	25

AIII.1.d.ii   Calcination

Calcination causes the powder constituents to interact by inter-diffusion of their ions and reduces the extent of diffusion that must occur during sintering[26]. An elevated temperature is required to supply the necessary thermal energy to allow diffusion of the ionic constituents. Table AIII.4 provides a summary of the calcination temperatures reported in the literature for various composite systems.

Table AIII.4: Calcination temperatures used in the preparation of various ceramic-inclusion systems.

System	Calcination temperature (°C)	Reference
Al₂O₃/ SiC	600	6
BaTiO₃/ Ag	300, 3hr (AgNO₃ decomposition)	25, 27
MgO/ BaTiO₃	800, 30min	18
Al₂O₃/ Ni	500, Hydrogen (NiNO₃ decomposition)	28

Dried powders are usually calcined, however, the green compacts may also be treated[24]. Calcination is also beneficial in burning out organic dispersants[24] and other organic additives that may have been added to improve milling or pressing. If they are not removed the final sinter density could be reduced by the formation of gaseous reaction phases that cause bloating of the sample if the gas is unable to escape. This is exacerbated where a liquid sintering phase forms and encapsulates the gases released to form bubbles. Calcination can also cause the required decomposition of constituents so that the products are located homogeneously in the final state from the powder preparation method. This is generally the case for the reduction of some metal oxides to form the base metal, such as silver from silver oxide. The decomposition may, otherwise, be conducted at the sintering temperature.

Ball milling is cheap and easy to carry out, however, attrition milling produces a smaller particle size and has a shorter process time. Once the powders have been dried and sieved, and if necessary calcined, they are consolidation into the required shape before being sintered.

AIII.2   POWDER CONSOLIDATION

The dried powders prepared by milling require consolidation into a green compact before sintering. This improves diffusion during the sintering process as the distance between powder particles is reduced. Consolidation also reduces the total shrinkage during sintering so improving the dimensional tolerance of the sample. The extent to which the particles pack together is determined by a number of factors:

i.   **Particle size distribution** – A broad particle size distribution allows an enhanced packing efficiency, as the smaller particles are able to occupy the interstitial sites of the larger particles.

ii.   **Particle shape** – Although the particles will have a lower aspect ratio than fibres their packing can be reduced if the particles are of an irregular shape, Figure AIII.4.

(a)   (b)
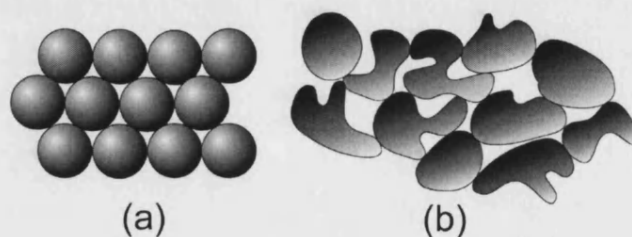
Figure AIII.4: Packing of particles that are (a) spherical and (b) irregular in shape.

iii. **Particle ductility** – A higher green density can be achieved if the particles deform under the applied pressure. This is particularly likely in metallic systems.

iv. **Pressing pressure** – A higher forming pressure will cause increased deformation and a higher green state density. This may be achieved by exceeding the yield stress of the particle, which increases the particle surface contact area. It has been reported that pressures above 7 MPa have little beneficial effect on the bulk density achieved[29], Figure AIII.5.
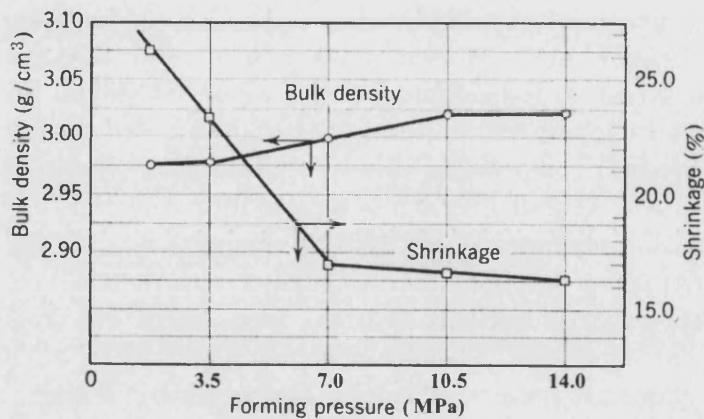
Figure AIII.5: Effect of forming pressure on bulk density of BeO[29].

v. **Time** – Increasing the forming time will allow particles to rearrange under the applied stress, this is similar to the process of creep.

vi. **Temperature** – Increasing the temperature during the forming process will allow the particles to yield more, under the stress, and increase particle contact.

vii. **Agglomeration** – Densification under pressure can be inhibited in localised regions by the presence of agglomeration, as discussed in Appendix II.

AIII.2.a   METHODS OF POWDER PRESSING

There are a number of different methods for applying pressure to produce a dense and strong green compact. In addition to increasing the green strength of the compact, a greater compaction results in a lower firing shrinkage to achieve the same final density[29]. This makes control of the sintering process simpler and leads to less warping and fewer defects. The following pressing techniques have been described in the literature.

i.   Uni-axial

The powder is pressed with a die made of hardened steel that may be polished to reduce friction. The actual material used for die construction will depend on the powder material and the die life required. The pressure is applied only along one axis of the sample, Figure AIII.6. This method suffers from a varying pressure distribution through the compact, as material in the centre of the sample is stationary, while material near the die punch can move a considerable distance, see Figure AIII.7(a). Maximum resistance to compaction comes from wall friction[29]. The extent of this pressure distribution depends on the aspect ratio of the die, thinner longer samples have a greater variation, Figure AIII.7(b). The pressure variation can manifest itself as cracks that propagate along the interface between regions of different densities. Problems can be reduced with the introduction of lubricants and binders[29]. A green compact may be formed uni-axially and the pressure distribution more uniformly distributed by cold iso-static pressing[7, 30, 31].

ii.   Cold isostatic pressing

This technique benefits from a better pressure distribution through the compact by applying the pressure equally over the whole sample, Figure AIII.6. The uniform densification reduces sample warping during the firing process, but requires a more complex sample consolidation process. The sample must be encased in a rubber sheath to protect the powder from the fluid through which the pressure is applied. The flexible moulds are vacuum-sealed and submerged in the fluid (composed of glycerine, hydraulic oil, water and rust inhibitor) within the pressure chamber. The fluid transfers the pressure to the mould surfaces and then after decompression the part is ejected from the mould.
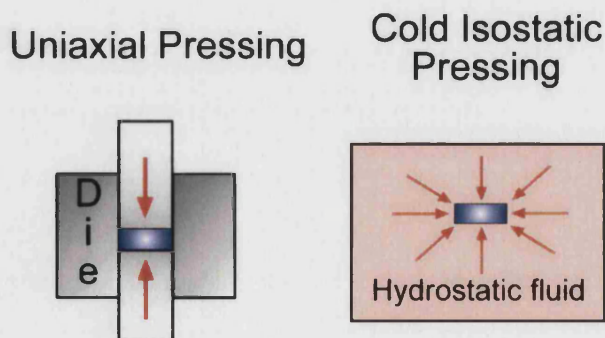
Figure AIII.6: Schematics of uni-axial and cold isostatic pressing.
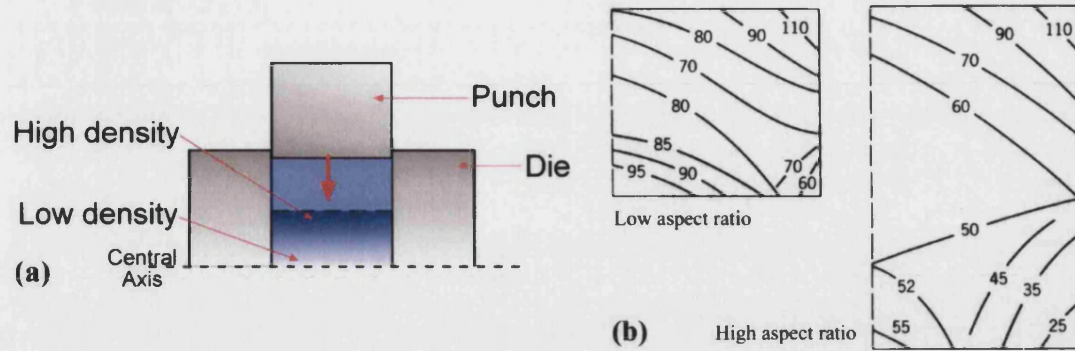
Figure AIII.7: (a) Uni-axial pressing density variation and (b) compacting powder pressure distribution in cylindrical dies of low and high aspect ratio (pressing from one end). Lines of constant pressure (in psi) are shown[29].

AIII.2.b   UNI-AXIAL PRESSING PARAMETERS

Table AIII.5 lists some systems that have been manufactured by the uni-axial pressing method. The pressing pressure is low, typically about 50 MPa, in order to fabricate samples of sufficient green strength for handling.

Table AIII.5: Reported uni-axial pressures.

System	Pressure (MPa)	Reference
Al_2O_3/ SiC	42, 20	7, 9
PZT/ Ag	40	13, 30
Al_2O_3/ Ag	56	23
Al_2O_3/ Ni	18	31
$BaTiO_3$	100	22

AIII.2.c   COLD ISOSTATIC PRESSING PARAMETERS

In cold isostatic pressing the desired sample shape can be initially formed by uni-axial pressing, using a relatively low pressure, before cold isostatic pressing increases the green strength and density. The pressure used in the uni-axial press is sufficient to form a green compact that can be handled easily. Reported pressures during cold isostatic pressing for a number of systems are given in Table AIII.6.

Table AIII.6: Reported cold isostatic pressures.

System	Pressure (MPa)	Reference
Al_2O_3/ SiC	350, 140	7, 9
PZT/ Ag	200	13, 30
Al_2O_3/ Ni	250	31

AIII.3   SINTERING

A high temperature is required to supply sufficient thermal energy so that diffusion, driven by differences in chemical potential, can occur at a desirable rate. The net effect is the reduction in the solid-gas surface area and an increase in solid-solid 'grain' boundaries. The sintering process may be combined with forming the sample shape, by hot pressing, as discussed later. Classical sintering, called "pressureless sintering", is simply the heating of the sample at atmospheric pressure to a high temperature, typically above 1000°C, in order to enable and accelerate diffusion. Increasing the sintering temperature and time can improve the sample density and enlarge the grain size[32]. The atmosphere in which the samples are heated may be controlled to influence the properties of the sintered material. Static[18, 33-37] or flowing[7, 15] atmospheres may be employed depending on the material requirements. To prevent the formation of reaction phases, by the oxidation of constituents at the elevated temperature, atmospheres of argon or nitrogen may be used. Nitrogen has been reported to give a better final ceramic density than argon, and this is believed to be due to its higher diffusion rate[9]. An atmosphere, such as hydrogen, may also be used to instigate reduction of a compound to produce a desired second phase. Another method for atmosphere control is to cover the samples to create a controlled micro-atmosphere[8]. This is often done in the sintering of PZT with loose PZT to ensure that loss of lead is minimal.

An additional factor, apart from the temperature and sintering atmosphere, is the support used for the samples[24]. A powder bed is used so that the samples are less likely to become attached to a flat support as the contact area is reduced. This also allows the atmosphere to surround the sample completely. The bedding material must not react with the sample, so one of the sample constituents may be used, such as silicon carbide for the alumina-silicon carbide system[3, 8, 9] or a completely different material, such as zirconia for the $BaTiO_3$-silver system[20]. A coarse silicon carbide powder bed (120 grit) has been reported to allow better effusion of possible reaction gases from the sample and improve the final sinter density in comparison to a finer powder bed (600 grit)[9]. Table AIII.7 tabulates some of the reported sintering parameters, indicating a sintering temperature of 1300°C is suitable for barium titanate.

Table AIII.7: Reported pressureless sintering parameters in composite systems.

System	Temperature (°C)	Time (hr)	Atmosphere	Reference
Al_2O_3	1450	2	Nitrogen	7
Al_2O_3/ SiC	1775	4	Nitrogen	7
MgO/ PZT	1100-1150	2	$PbZrO_3$ controlled	38
$BaTiO_3$/ ZrO_2	1300-1320	2	Air	39
$BaTiO_3$/ Ag	1290	2	Air	20, 25
$BaTiO_3$/ Ni	1300	-	-	40

Other sintering methods have been designed to give particular benefits, such as a high heating rate to control low temperature diffusion, or sintering at a lower temperature to prevent the formation of reaction phases. A technique called Pulse Electric Current Sintering (PECS)[41] and spark-plasma sintering (SPS)[11, 42] apparently lower the sintering temperature[41] and have a high heating rate by generating a plasma discharge between the particles. The discharges have also been reported to purify and activate the particle surface[11]. Currently, however, these techniques are in their infancy and the present research is concerned with the effects of the secondary phase inclusions on the properties, not the method of production.

AIII.4   HOT PRESSING

Hot pressing methods have the advantage of sintering the material at the same time as it undergoes consolidation. This is equivalent to uni-axial pressing at an elevated temperature, increasing the particle interaction and enhancing the degree of densification. The external pressure aids pore removal whilst diffusion is improved due to the high temperature[43]. This method is reported to remove large pores caused by non-uniform mixing of the ceramic powder[29]. During hot pressing consolidation is accelerated, and as it takes place at a much lower temperature, compared to conventional sintering, extraneous reactions, that would occur at higher temperatures, are suppressed. The die material is typically graphite[18, 41, 44] as the high pressure and elevated temperatures cause a metallic die to deform. A graphitic die, however, produces a reducing environment and consequently a post-sintering oxidation of the sample may be required. Table AIII.8 details the variables that have been published for different hot pressed monolithic and particulate composite systems.

Table AIII.8: Reported hot pressing variables.

System	Temperature (°C)	Pressure (MPa)	Time (hr)/ atmosphere	Reference
Al_2O_3	1400, 1400	50, 50	0.5/ Nitrogen, 1/ vacuum	7, 8
Al_2O_3/ SiC	1600-1800, 1550-1700, 1640, 1700	30, 25, 50, 25	-/ Nitrogen, 1/ Argon, 1/ Nitrogen, 1/ Argon	3, 6-8, 45
MgO/ SiC	1700-1900	30	-/ Nitrogen	45
MgO/ SiC	1700-1800	30	-/ Nitrogen	46
MgO/ BaTiO_3	1350	40	-/ Nitrogen	18, 34
MgO/ BaTiO_3	1350	30	1/ -	41
$BaTiO_3$	1300, 1100-1400, 1050-1150	-, 30, 30	-, 1/ Argon, -	19, 44, 47
$BaTiO_3$/ SiC	1100-1400, 1300	30	1/ Argon	14, 48

Hot pressing generally uses a lower temperature than that required for pressureless sintering. For this reason metal-strengthened composites are normally hot pressed in order to reduce particle coarsening[49]. The application of pressure at elevated temperature allows the rearrangement and plastic yielding of metallic and non-metallic particles[50]. While hot pressing produces better quality samples, with higher density and fewer defects, it is expensive and a graphite mould lasts only for a limited number of process cycles. For this reason uni-axial and cold isostatic pressing may be used in combination to produce suitable samples.

AIII.5 ANNEALING

After the sintering heat treatment, it may be necessary to modify the oxygen content and possibly relieve internal stresses within the sintered sample[34]. This is generally the case for materials that have been sintered in a reducing atmosphere to prevent high temperature oxidation of a component or to instigate a required chemical reaction. The annealing process is conducted at a temperature below the original sintering temperature to reduce the amount of grain growth. Some annealing

processes may be used to control the final grain structure. Reported annealing parameters are given in Table AIII.9.

Table AIII.9: Reported annealing parameters.

System	Temperature (°C)	Time (hr)/ Atmosphere	Reason for annealing	Reference
Al_2O_3	1500	-/ Argon-1%Hydrogen	Possible stress relief	3
Al_2O_3/ SiC	1700, 1700-1800	-/ Nitrogen, -/ Argon-1%Hydrogen	Possible stress relief and prevent oxidation	3, 8
MgO/ $BaTiO_3$	1250, 1300	8/ Air, 8/ Air	Possible stress relief and crack healing	18, 39
$BaTiO_3$	900-1300	10-30/ Air	Grain size control	34
$BaTiO_3$/ SiC	1000	1-6/ Air	Re-oxidation of matrix	41

AIII.6 POST-SINTERING PREPARATION

The surface of sintered ceramics generally requires some preparation to produce samples for testing. This may consist of machining the sample into the required shape for mechanical testing, such as for the 3-point bend test, or simply polishing to remove surface roughness in preparation for electrical testing. The reported procedures for sample preparation for microscopy, mechanical and electrical characterisations are given below.

AIII.6.a SURFACE PREPARATION FOR LIGHT AND ELECTRON MICROSCOPY

Reported surface finishes for the preparation of samples for analysis by optical and electron microscopy are summarised in Table AIII.10. A surface finish of 1 μm is suitable for microscopic analysis of samples.

Table AIII.10: Reported surface finishes for optical and electron microscopy analysis.

System	Final finish (μm)	Reference
$Al_2O_3/$ SiC	1, 1, 3, 1, 6, 1, 1	7, 8, 3, 5, 11, 49
$Al_2O_3/$ Ni	0.05	31
$Al_2O_3/$ Ag	0.05	23
PZT/ Ag	0.05	13, 51
$BaTiO_3$	1, 0.25	52, 53

AIII.6.a.i   *Etching*

Etching of the polished surface of the sample is generally required for microscopy to improve the contrast between the grain and the grain boundaries. A freshly polished sample will be sufficiently flat that the incident light is reflected equally from all parts and no features can be distinguished, Figure AIII.8(a). The etching process affects the grain boundary more than the bulk so that an increased contrast is produced. Thermal and chemical techniques are the two methods used for etching.

A.6.a.i.a   Thermal Etching

The use of elevated temperature, during thermal etching, allows the atoms that are more loosely bound at the grain boundary to diffuse and move to positions of lower energy. The sharp grain corners become rounded, scattering light more efficiently, and appear darker, Figure AIII.8(b). A thermal etch temperature ~200°C below the sintering temperature has been recommended for barium titanate[22].

(a)   Grain Boundary   Highlighted grain boundary   (b)
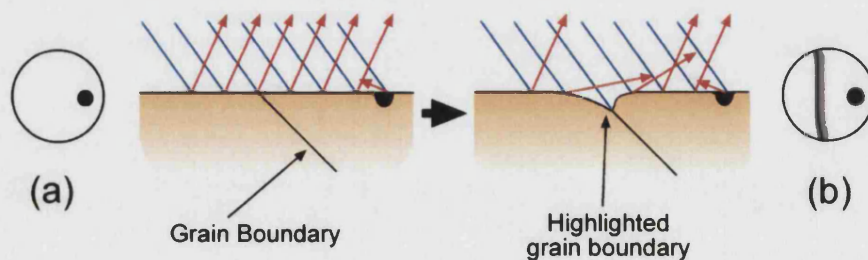
Figure AIII.8: Incident light reflected from (a) a freshly polished surface and

(b) an etched surface showing contrasting features.

A.6.a.i.b   Chemical etching

This technique is similar to thermal etching, but involves the removal of the more loosely bound grain boundary atoms using aggressive chemicals. In some cases etching rates of individual grains can be dissimilar, due to their composition or crystal alignment, causing additional contrast. Chemical etching can be used to specifically attack one of the composite constituents and highlight the location of this phase. This technique, however, can suffer from unwanted localised etching and exaggerated grain boundary widths[9]. This can be caused by chemical inhomogeneity of the sample or by etchant that becomes trapped in pores and is poorly rinsed away.

Table AIII.11 shows some of the variables used for the thermal and chemical etching of different ceramics. These etching methods can be employed to highlight the domain structure in piezoelectric ceramics. In microstructures where the grains are less than one micron in diameter, the grains can be completely eliminated from the surface, by chemical etching, before the domains emerge[54].

Table AIII.11: Reported (a) thermal and (b) chemical etching variables.

(a) Thermal etching				
System	Temperature (°C)	Time (min)	Atmosphere	Reference
Al_2O_3	1350	-	Air	7, 8
Al_2O_3/ SiC	1450	60	Vacuum	3
Al_2O_3/ SiC	1450	-	Argon	7, 8
Al_2O_3/ SiC	1550	15	Flowing argon	15
Al_2O_3/ SiC	1400-1600	-	Nitrogen	5
Al_2O_3/ SiC	1400	90	Vacuum, Argon	9
$BaTiO_3$	1200	30	Air	55

(b) Chemical etching				
System	Etchant	Time (min)	Other	Reference
Al_2O_3/ SiC	Orthophosphoric acid	-	250°C	9
$BaTiO_3$	HCl/ HF dilute solution	1-2	-	52, 56
$BaTiO_3$	5%HCl solution	-	-	53
$BaTiO_3$/ Ag	HCl/ HF dilute solution	-	-	20, 25, 27

It has been reported that the thermal etching of $Al_2O_3/$ SiC leads to oxidation of the silicon carbide while the chemical etch left the particle intact[9]. Thermal etching of a ceramic-metal composite is likely to remove the metal on the surface if the vapour pressure of the metal is high at the etching temperature.

AIII.6.b   SURFACE PREPARATION FOR MECHANICAL TESTING

The reported surface finishes for samples required to undergo mechanical testing are summarised in Table AIII.12. The considerable range of surface finishes used relates to the different test methods subsequently employed. A high surface finish, below 3 μm, is suggested to minimise fracture initiation at surface flaws.

Table AIII.12: Reported surface preparations for mechanical testing.

System	Final finish (μm)	Reference
BaTiO₃/ SiC	50, 30	43, 57
Al₂O₃/ SiC	1, 6, 3, 25, 6, 35	3, 7, 11, 15, 58, 59
Al₂O₃/ ZrO₂/ Ag	3	60
BaTiO₃	1	55
PZT/ Ag	0.5	13, 51
PZT/ Pt	0.5	61
Al₂O₃/ Ni	45	31
Al₂O₃/ Ag	45	23

AIII.6.c   SURFACE PREPARATION FOR ELECTRICAL TESTING

The European standard, for determining the piezoelectric properties of ceramics, suggests that the average roughness, before electroding the specimen, should be less than 1 μm and surfaces should be parallel within 50 μm of the sample length[62]. The actual planarity, however, of tested samples has not been reported in literature. Table AIII.13 shows some reported surface finishes used to produce samples for electrical characterisation. A surface finish similar to that required for microscopy and mechanical characterisation appears suitable.

Table AIII.13: Reported surface finishes for electrical measurement testing.

System	Final finish (μm)	Reference
PZT/ Ag	0.5	63
BaTiO$_3$	1, 1	21, 64
Al$_2$O$_3$/ SiC	6	65
PZT/ Al$_2$O$_3$	35	66

AIII.7   ELECTRODING

Electroding involves the production of a suitable electrode contact on the sample to ensure good electrical conductivity when testing. The most documented electroding metal used is silver, while others metals have also been used, which include gold[48, 67-69], platinum[65, 70, 71] and indium[41, 69, 72]. Alternative application techniques have been employed, such as sputtering[48, 70, 71], but in general a paste is either applied manually or screen-printed. Table AIII.14 indicates the range of conditions used for baking a silver coating.

Table AIII.14: Reported silver electroding parameters.

Temperature (°C)	Time (Min)	Reference
750	-	73
350	15	65
350	60	74
600	Few minutes	35, 61
600	10	47, 66, 75
600	30	40

AIII.8   POLING

AIII.8.a   INTRODUCTION

As discussed in Chapter 2 and Appendix II, poling of polycrystalline electroceramics is required to align the domains and generate a material that has useful functional properties. The basic technique involves application of a sufficiently high static potential difference across the sample that causes the dipoles to be re-oriented. In general thermal energy is also supplied so that the

dipole re-orientation is faster. A higher field will be required for ceramics containing domain walls that need to overcome the energy barriers of pinning centres[76]. A common industrial poling technique is the oil bath method, however, corona poling is useful on a laboratory scale.

AIII.8.b OIL BATH POLING

The samples for poling are directly connected to a voltage and immersed in high breakdown strength oil, contained in an oil bath. The oil prevents breakdown, which would occur if air were between the voltage electrodes under the applied field. By heating the oil to a required temperature, heat is transferred to the sample. While this method is used successfully in commercial poling applications it is quite hazardous on the laboratory scale due to high voltages and the presence of high temperature oil. Variables of 120°C, 30 kV/cm for 30 minutes have been reported for the poling of PZT/ Al_2O_3 in silicone oil[66].

AIII.8.c CORONA POLING

An alternative to the oil bath poling method is the application of a potential over the sample in a non-contact technique called corona poling, Figure AIII.9.
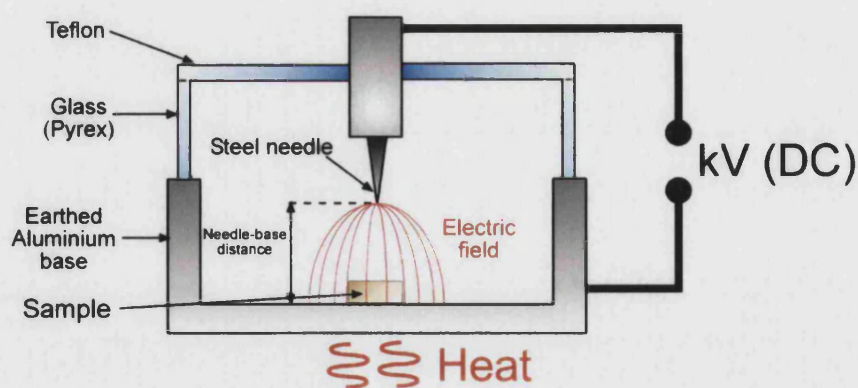
Figure AIII.9: Corona poling set-up.

The corona technique, in comparison to the oil bath method, has the additional variables of height, number and geometry of the needles. It has been reported, however, that the degree of poling is independent of the number and geometrical placements of the electrode needles[77].

As in the oil bath method the sample is heated and an electric field is generated across the electrodes. In corona poling, however, the sample is not in contact with the top electrode and is placed on a base plate. This has advantages for commercial manufacturing as the process can be

adapted to process samples continuously[77]. The actual area in which the sample can be poled increases with electrode height provided the voltage increases proportionally[77]. For a single electrode point the maximum diameter for effective poling is approximately twice the needle-base height[77]. The low breakdown strength of the air limits the fields generated, to values much lower than for the oil bath poling method. The air atmosphere needs to be of low humidity to reduce unwanted discharge. However, it has been reported that charging and poling can continue in spite of limited area breakdown events[78].

It has been reported that for saturation poling of PZT the voltage to needle-sample separation ratio must be greater then 3.5[79]. The degree of poling (measured by the piezoelectric coefficient) has a non-linear increase with applied voltage, Figure AIII.10.
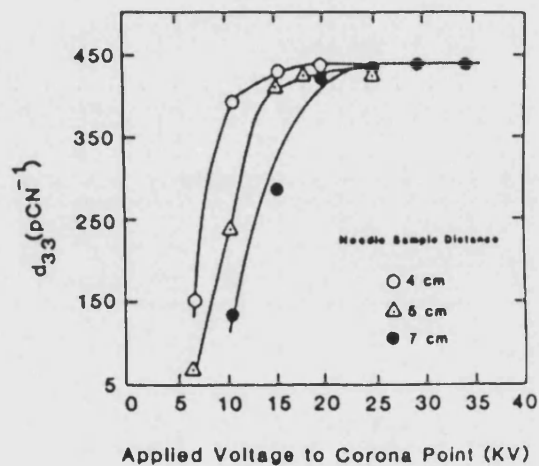
Figure AIII.10: Variation of piezoelectric coefficient with applied voltage for different needle-sample separations (80°C)[79].

PZT can be poled by the corona technique; a temperature of 80°C and a voltage of 6 kV/cm for five minutes has been reported to be sufficient[77].

AIII.9 REFERENCES

1. HENNINGS, D., 'Review of chemical preparation routes for barium titanate', *Brit. Ceram. Proc: Electroceramics, Ed. Moulson, A.J., Binner, J., Morrell, R.*, Feb 89, **41**, 1-10

2. CONDER, R., PONTON, C. & MARQUIS, P., 'Processing of alumina/silicon carbide nanocomposites', *Nanoceramics, Ed. Freer, R., Brit. Ceram. Proc.*, 1993, **51**, 105-17

3. BORSA, C., JIAO, S., TODD, R. & BROOK, R., 'Processing and properties of Al$_2$O$_3$/SiC nanocomposites', *J. Microscopy*, 1995, **77** (3), 305-12

4. LANGE, F.F., DAVIS, B.I. & AKSAY, I.A., 'Processing-related fracture origins: III, differential sintering of ZrO$_2$ agglomerates in Al$_2$O$_3$/ZrO$_2$ composite', *J. Am. Ceram. Soc.*, 1983, **66** (6), 407-08

5. WANG, H., GAO, L. & GUO, J., 'The effect of nanoscale SiC particles on the microstructure of Al$_2$O$_3$ ceramics', *Ceram. Int.*, 2000, **26**, 391-96

6. WINN, A. & TODD, R., 'Microstructural requirements for alumina-SiC nanocomposites', *Brit. Ceram. Trans.*, 1999, **98** (5), 219-24

7. ZHAO, J., STEARNS, L., HARMER, M., CHAN, H., Miller, G. & COOK, R., 'Mechanical behaviour of alumina-silicon carbide "nanocomposite", *J. Am. Ceram. Soc.*, 1993, **76** (2), 503-10

8. STEARNS, L., ZHAO, J. & HARMER, M., 'Processing and microstructure development in Al$_2$O$_3$-SiC "nanocomposites" ', *J. Eur. Ceram. Soc.*, 1992, **10**, 473-77

9. ANYA, C. & ROBERTS, S., 'Pressureless sintering and elastic constants of Al$_2$O$_3$-SiC "nanocomposite" ', *J. Eur. Ceram. Soc.*, 1997, **17**, 565-73

10. BLANCOLOPEZ, M.C., RAND, B. & RILEY, F.L., 'The isoelectric point of BaTiO$_3$', *J. Eur. Ceram. Soc.*, 2000, **20**, 107-118

11. GAO, L., WANG, H., HONG, J., MIYAMOTO, H., MIYAMOTO, K., NISHIKAMA, Y. & TORRE, S., 'Mechanical properties and microstructure of nano-SiC-Al$_2$O$_3$ composites densified by spark plasma sintering', *J. Eur. Ceram. Soc.*, 1999, **19**, 609-13

12. LAARZ, E., CARLSSON, M., VIVIEN, B., JOHNSSON, M., NYGREN, M. & BERGSTROM, L., 'Collodial processing of Al$_2$O$_3$-based composites reinforced with TiC and TiC particulates, whiskers and nanoparticles', *J. Eur. Ceram. Soc.*, 2001, **21**, 1027-35

13. HWANG, H., WATARI, K., SANDO, M., TORIYAMA, M. & NIIHARA, K., 'Low temperature sintering and high strength Pb(Zr,Ti)O$_3$-matrix composites incorporating silver particles', *J. Am. Ceram. Soc.*, 1997, **80** (3), 791-93

14. HWANG, H., SEKINO, T., OTA, K. & NIIHARA, K., 'Perovskite-type BaTiO$_3$ ceramics containing particulate SiC: Part I-Structure variation and phase transformation', *J. Mat. Sci.*, 1996, **31**, 4617-24

15. JEONG, Y-K., NAKAHIRA, A., MORGAN, P.E.D. & NIIHARA, K., 'Effect of milling conditions on the strength of alumina-silicon carbide nanoparticles', *J. Am. Ceram. Soc.*, 1997, **80** (5), 1307-09

16. SCHMID, H., ALSAN, M., ASSMANN, S., NAB, R. & SCHMIDT, H., 'Microstructural characterisation of Al_2O_3-SiC nanocomposites', *J. Eur. Ceram. Soc.*, 1998, **18**, 39-49

17. LUAN, W., GAO, L. & GUO, J-K., 'Study on drying stage of nanoscale powder preparation', *Nanostructured Materials*, 1998, **10**, 1119-25

18. NAGAI, T., HWANG, H., YASUOKA, M., SANDO, M. & NIIHARA, K., 'Preparation of barium titanate-dispersed-magnesia nanocomposite', *J. Am. Ceram. Soc.*, 1998, **81** (2), 425-28

19. HWANG, H. J., UEDA, S. & NIIHARA, K., 'Grain boundary controlled mechanical and dielectric properties of $BaTiO_3$-based nanocomposite', *Ceram. Trans.*, 1994, **44**, 399-408

20. CHEN, C. & TUAN, W., 'Mechanical and dielectric properties of $BaTiO_3$/Ag composites', *Mat. Sci. Lett.*, 1999, **18**, 353-54

21. ENG, L.M., GUNTHERODT, H.J., SCHNEIDER, G.A., KOPKE, U. & SALDANA, J.M., 'Nanoscale reconstruction of surface crystallography from 3-dimensional polarisation distribution in ferroelectric $BaTiO_3$ ceramics', *Science*, June 18 1998

22. LIM, M-H., CHOU, J-F. & LU, H-Y., 'The rate-determining mechanism in the sintering of undoped non-stoichiometric barium titanate', *J. Eur. Ceram. Soc.*, 2000, **20**, 517-26

23. CHOU, W. & TUAN, W., 'Toughening and strengthening of alumina with silver inclusions', *J. Eur. Ceram. Soc.*, 1995, **15**, 291-95

24. STERNITZKE, M., 'Review: Structural ceramic nanocomposites', *J. Eur. Ceram. Soc*, 1997, **17**, 1061-82

25. CHEN, C-Y. & TUAN, W-H., 'Effect of silver on the sintering and grain-growth behaviour of barium titanate', *J. Am. Ceram. Soc.*, 2000, **83** (12), 2988-92

26. MOULSON, A. J. & HERBERT, J. M., 'Electroceramics – Materials, Properties & Applications', *Chapman & Hall*, 1990

27. CHEN, C-Y. & TUAN, W., 'Evaporation of silver during co-firing with barium titanate', *J. Am. Ceram. Soc.*, 2000, **83** (7), 1693-98

28. CHEN, R.Z. & TUAN, W.H., 'Interfacial fracture energy of Al_2O_3/Ni nanocomposites', *J. Mat. Sci. Lett.*, 2001, **20**, 2029-30

29. KINGERY, W.D., 'Introduction to ceramics', *J. Wiley & Sons Inc*, 1976

30. HAERTLING, G.H., 'Ferroelectric ceramics: History and Technology', *J. Am. Ceram. Soc.*, 1999, **82** (4), 797-818

31. HWANG, H.J., NAGAI, T., SANDO, M., TORIYAMA, M. & NIIHARA, K., 'Fabrication of piezoelectric particle-dispersed ceramic nanocomposite', *J. Eur. Ceram. Soc., Electroceramics VI 1998, Switzerland, Elsevier*, 1999, **19**, 993

32. HWANG, H. & NIIHARA, K., 'Perovskite-type BaTiO$_3$ ceramics containing particulate SiC: Part II-Microstructure and mechanical properties', *J. Mat. Sci.*, 1998, 33, 549-558

33. HWANG, H. J., SANDO, M., TORIYAMA, M. & NIIHARA, K., 'Effect of secondary phase dispersion on mechanical and piezoelectric properties of PZT-based nanocomposites', *IEEE Int. Symp. on Applications of Ferroelectrics*, 1996, 373-75

34. NAGAI, T., HWANG, H., SANDO, M. & NIIHARA, K., 'Preparation of ceramic nanocomposite with perovskite dispersiod', *Mat. Res. Soc. Symp. Proc.*, 1997, 375-80

35. TODD, R. I., 'Alumina/SiC nanocomposites – big things from small packages', *21st century ceramics Ed. Thompson, D. P. & Mondal, H., IOM*, 1996, 55, 225-248

36. BAMBA, N., CHOA, Y., SEKINO, T. & NIIHARA, K., 'Effects of nano-sized silicon carbide particulate on microstructure and ionic conductivity for 8mol % yttria stabilised zirconia based nanocomposites', *Solid State Ionics III*, 1998, (1-2), 171-179

37. OH, S-T., SEKINO, T. & NIIHARA, K., 'Fabrication and mechanical properties of 5vol% copper dispersed alumina nanocomposite', *J. Eur. Ceram. Soc.*, 1998, 18, 31-37

38. NAGAI, T., HWANG, H., YASUOKA, M., SANDO, M. & NIIHARA, K., 'Dielectric properties of Pb(Zr, Ti)O$_3$-dispersed MgO nanocomposite', *Jpn. J. Appl. Physics*, 1998, 37, 3377-81

39. SAUCY, C., REANEY, I. & BELL, A., 'Microstructure and electromechanical properties of BaTiO$_3$-ZrO$_2$ "Core-shell" ceramics', *Brit. Ceram. Proc.*, 1993, 51, 29-52

40. EMOTO, H. & HOJO, J., 'Sintering and dielectric properties of BaTiO$_3$-Ni composite ceramics', *J. Ceram. Soc. Jpn.*, 1992, 100 (4), 555-9

41. YONG, J-F., CHOA, Y-H., SINGH, J. & NIIHARA, K. 'Fabrication and mechanical properties of Si$_3$N$_4$/SiC nanocomposite with pressureless sintering and sinter-post-hiping', *J. Ceram. Soc. Jpn.*, Oct 98, 951-57

42. TAKEUCHI, T., BETOURNE, E., TABUCHI, M., KAGEYAMA, H., KOBAYASHI, Y., COATS, A., MORRISON, F., SINCLAIR, D. & WEST, A., 'Dielectric properties of spark plasma-sintered BaTiO$_3$, *J. Mat. Sci.*, 1999, 34, 917-24

43. POHANKA, R., RICE, R. & WALKER, B., 'Effect of internal stress on the strength of BaTiO$_3$', *J. Am. Ceram. Soc.*, 1976, 59 (1-2), 71-74

44. SURYANARAYANAN, R., YER, I. & SASTRY, S.M.L., 'Consolidation of nanoparticles-development of a micromechanistic model', *Acta Materialia*, 1999, 47 (10), 3079-98

45. NIIHARA, K & NAKAHIRA, A., 'Particulate strengthened oxide ceramics-nanocomposites', *Advanced structural inorganic composites Ed. Vincenzini, P., Elsevier*, 1990, 637-644

46. KOMERNENI, S., 'Nanocomposites', *J. Mat. Chem.*, 1992, 2 (12), 1219-30

47. LUAN, W., GAO, L. & GUO, J., 'Size effect on dielectric properties of fine-grained BaTiO$_3$ ceramics', *Ceram. Int.*, 1999, 25, 727-29

48. HWANG, H. & NIIHARA, K., 'Fabrication of surface barrier layer capacitor on BaTiO$_3$-based composite containing particulate SiC', *J. Mat. Res.*, 1998, **13** (10), 2866-70

49. CHEN, R. & TUAN, W., 'Pressureless sintering of Al$_2$O$_3$/Ni nanocomposites', *J. Eur. Ceram. Soc.*, 1999, **19**, 463-8

50. TUAN, W., LIN, M. & WU, H., 'Preparation of Al$_2$O$_3$/Ni composites by pressureless sintering in H$_2$', *Ceram. Int.*, 1995, **21**, 221-25

51. HWANG, H.J., YASUOKA, M., SANDO, M., TORIYAMA, M. & NIIHARA, K., 'Fabrication, sinterability, and mechanical properties of lead zirconate titanate/silver composites', *J. Am. Ceram. Soc.*, 1999, **82** (9), 2417-22

52. KULCSAR, F., 'A Microstructure study of Barium titanate ceramics, *J. Am. Ceram. Soc.*, 1956, **39** (1), 13-17

53. PAIK, U. & HACKLEY, V.A., 'Influence of solids concentration on the isoelectric point of aqueous barium titanate', *J. Am. Ceram. Soc.*, 2000, **83** (10), 2381-4

54. ARLT, G., HENNINGS, D. & DE WITH, G., 'Dielectric properties of fine-grained barium titanate ceramics', *Am. Inst. Phys. J. Appl. Phys.*, 15 Aug 1985, **58** (4), 1619-25

55. MESCHKE, F., KOLLECK, A. & SCHNEIDER, A., 'R-Curve behaviour of BaTiO$_3$ due to stress-induced ferroelectric domain switching', *J. Eur. Ceram. Soc.*, 1997, **17**, 1143-49

56. CHUNG, H-T., SHIN, B-C. & KIM, H-G., 'Grain-size dependence of electrically induced microcracking in ferroelectric ceramics', *J. Am. Ceram. Soc.*, 1989, **72** (2), 327-29

57. HWANG, H. & NIIHARA, K., 'Subcritical crack growth phenomenon and fractography of barium titanate and barium-titanate-based composite', *Transcript. Scripta Metallurgica et Materialia*, 1997, **36** (2), 183-87

58. CHOU, I. A., CHAN, H. M. & HARMER, M. P., 'Machining-induced surface residual stress behaviour in Al$_2$O$_3$-SiC nanocomposites', *J. Am. Ceram. Soc.*, 1996, **79** (9), 2403-9

59. SMITH, S.M., SCATTERGOOD, R.O., SINGH, J.P. & KARASEK, K., 'Effect of silica and processing environment on the toughness of alumina composites', *Am. Ceram. Soc. Comm.*, 1989, **72** (7), 1252-5

60. LALANDE, J., SCHEPPOKAT, S., JANSSEN, R. & CLAUSSEN, N., 'Toughening of alumina/zirconia ceramic composites with silver particles', *J. Eur. Ceram. Soc.*, 2002, **22**, 2165-71

61. HWANG, H.J., TAJIMA, K., SANDO, M., TORIYAMA, M. & NIIHARA, K., 'Fatigue behaviour of PZT-based nanocomposites with fine platinum particles', *J. Am. Ceram. Soc.*, 1998, **81** (12), 3325-8

62. *European standard prEN 50324-2:1999E Piezoelectric properties of ceramic materials and components; Part 2: methods of measurement and properties – low power*, 1999

63. HWANG, H., NAGAI, T., OHJI, T., SANDO, M., TORIYAMA, M. & NIIHARA, K., 'Curie temperature anomaly in lead zirconate titanate/silver composite', *J. Am. Ceram. Soc.*, 1998, **81** (3), 709-12

64. FANG, T., HSEIH, H-L. & SHIAU, F-S., 'Effect of pore morphology and grain size on the dielectric properties and tetragonal-cubic phase transition of high-purity barium titanate', *J. Am. Ceram. Soc.*, 1993, **76** (5), 1205-11

65. WANG, X. & XIAO, P., 'Non-destructive characterisation of alumina/silicon carbide nanocomposite using impedance spectroscopy', *J. Eur. Ceram. Soc.*, 2000, **20**, 2591-9

66. TAJIMA, K., HWANG, H., SANDO, M. & NIIHARA, K., 'Electric-field-induced crack growth behaviour in PZT/Al$_2$O$_3$ composites', *J. Am. Ceram. Soc.*, 2000, **83** (1), 651-53

67. ZHOU, J., LI, L., GUI, Z., ZHANG, X. & BARBER, D.J., 'Sol-Gel derived BaTiO$_3$ thin films with embedded silver nanoparticles: Preparation and dielectric properties', Nanostructured materials, 1997, **8** (3), 321-328

68. CHEN, I. G. & JOHNSON, W. B., 'Alternating-current electrical properties of random metal-insulator composites', *J. Mat. Sci.*, 1991, **26**, 1565-76

69. MORRISON, F.D., SINCLAIR, D.C. & WEST, A.R., 'Characterisation of lanthanum doped barium titanate ceramics using impedance spectroscopy', *J. Am. Ceram. Soc.*, 2001, **84** (3), 531-8

70. SHIN, B-C. & KIM, H-G., 'Partial discharge, microcracking and breakdown in BaTiO$_3$ ceramics', *Ferroelectrics*, 1988, **77**, 161-166

71. WANG, S-F., YANG, T.C.K., WANG, Y-R. & KUROMITSU, Y., 'Effect of glass composition on the densification and dielectric properties of BaTiO$_3$ ceramics', *Ceram. Int.*, 2001, **27**, 157-62

72. HIROSE, N & WEST, A. R., 'Impedance spectroscopy of undoped BaTiO$_3$ ceramics', *J. Am. Ceram. Soc.*, 1996, **79** (6), 1633-41

73. WANG, S-F. & DAYTON, G., 'Dielectric properties of fine-grained barium titanate X7R materials', *J. Am. Ceram. Soc.*, 1999, **82** (10), 2677-82

74. HALDER, N., CHATTOPADHYAY, D., DAS SHARMA, A., SAHA, D., SEN, A. & MAITI, H.S., 'Effect of sintering atmosphere on the dielectric properties of barium titanate based capacitor', *Mat. Res. Bull.*, 2001, **36**, 905-13

75. NAGAI, T., HWANG, H., YASUOKA, M., SANDO, M. & NIIHARA, K., 'Ceramic nanocomposites with perovskite-type ferroelectric dispersiod', *Key Eng. Mat.*, 1999, **161-63**, 509-512

76. SAYER, M., JUDD, B., El-ASSAL, K. & PARSAD, E., 'Poling of piezoelectric ceramics', *J. Canadian Ceram. Soc.*, 1981, **50**, 23-28

77. WALLER, D. & SAFARI, A., 'Corona poling of PZT ceramics and flexible piezoelectric composites', *Ferroelectrics*, 1988, **87**, 189-95

78. SESSLER, G., 'Poling and properties of polarisation of ferroelectric polymers and composites', *Key Eng. Mat.*, 1994, **92-93**, 249-74

79. WALLER, D., TIGBAL & SAFARI, A., 'Poling of PZT ceramics and flexible piezoelectric composites by corona discharge techniques', *J. Am. Ceram. Soc.*, 1989, **72** (2), 322-24

80. PEARCE, D. & BUTTON, T., 'Processing and properties of silver/PZT composites', 'http://www.fmg.bham.ac.uk/papers/pzt/Ag-pzt/agpzt.htm', 26/02/03

APPENDIX IV: CHARACTERISATION TECHNIQUES

AIV.1   X-RAY ANALYSIS

The X-ray diffraction, XRD, technique is used to identify the crystallographic phases present in ceramic materials by comparing the diffraction pattern of the experimental material with standard data. Figure AIV.1 shows the schematic of typical X-ray diffraction equipment indicating the production of X-rays by bombarding a copper target with high energy electrons.
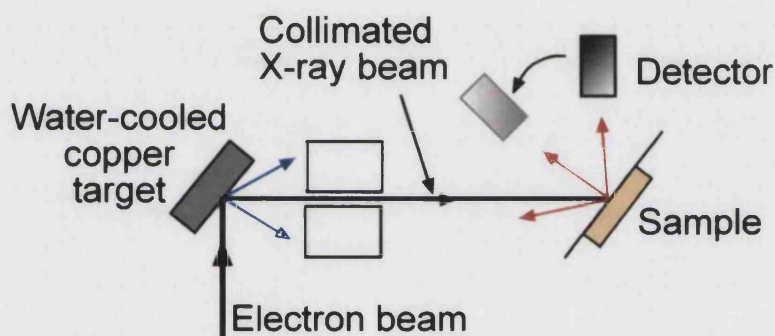
Figure AIV.1: X-ray diffraction equipment schematic showing X-ray beam

generation and position of sample and X-ray beam detector.

The incident beam of X-rays is scattered by the electrons associated with each atom or ion of the sample that lies within the beams path. Constructive interference of the scattered rays occurs when Bragg's law, equation AIV.1, is satisfied, as illustrated in Figure AIV.2. The n parameter is an integer, λ the wavelength of the incident radiation, d the lattice spacing and θ is the angle of reflection from the plane of atoms.

$$n\lambda \;=\; 2d\sin\theta \tag{AIV.1}$$
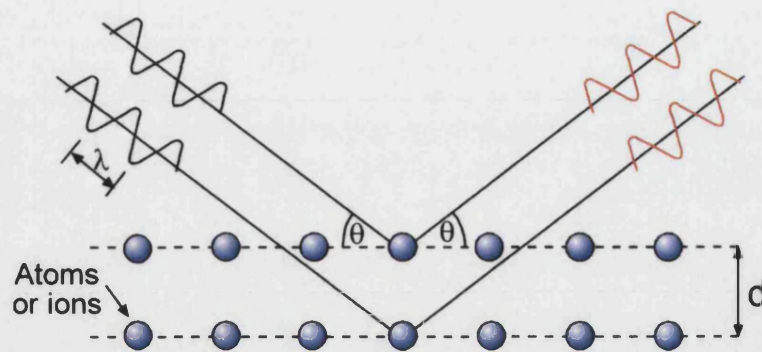
Figure AIV.2: Diffraction of incident X-ray beam by planes of atoms.

An X-ray diffraction pattern consists of a plot of the relative intensity versus the diffraction angle, 2θ, of the diffracted X-rays, as shown in Figure AIV.3. In addition to identifying the phases present the relative quantities of crystal phases can be determined from the characteristic peak intensities.
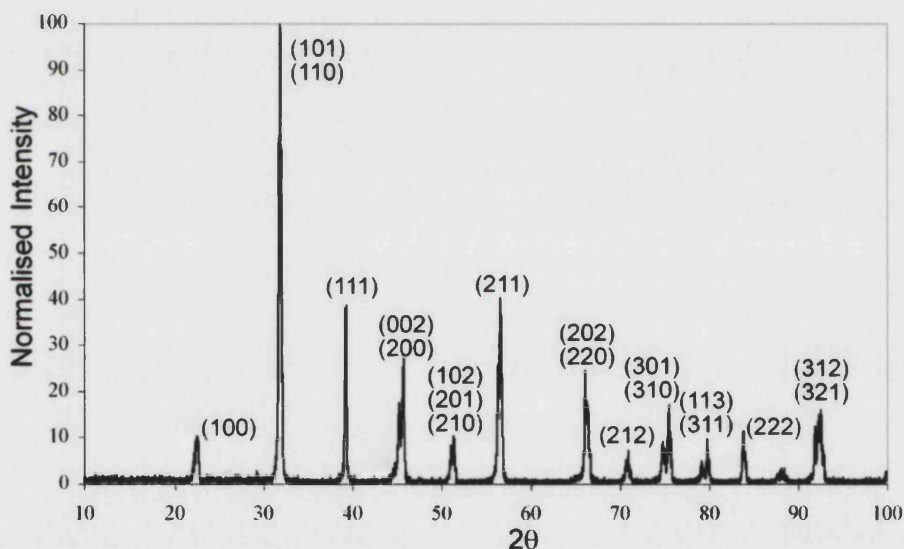
Figure AIV.3: A typical XRD plot (tetragonal barium titanate).

For X-ray diffraction analysis the powdered or solid specimen is placed in an aluminium sample holder (Phillips Standard sample holder) and pressed, in the case of powder, to ensure the specimen surface remains flat and level. The holder is positioned in the X-ray beam to obtain maximum sample exposure. The X-rays collide with the sample and are reflected from the crystal planes that are present. Each reflection corresponds to a specific plane within the crystal.

Each phase within the sample irradiated by the X-ray beam will produce a diffraction pattern that is independent of the other phases present[1, 2]. If the absorption of the phase is known then the

intensity is proportional to the amount of the phase present[2]. The overall absorption coefficient of a material can be calculated from the individual absorption coefficients of the elements that make up the material. It is recommended that the particle size is small enough for extinction and micro-absorption effects to be negligible in order to increase the signal to noise ratio[2]. Extinction is the reduction in intensity through reflections causing interference and absorption from lower and higher planes in the crystal, see Figure AIV.4. The loss is greatest in a perfect crystal, while the effect is reduced in actual crystals as they are imperfect[1, 2].
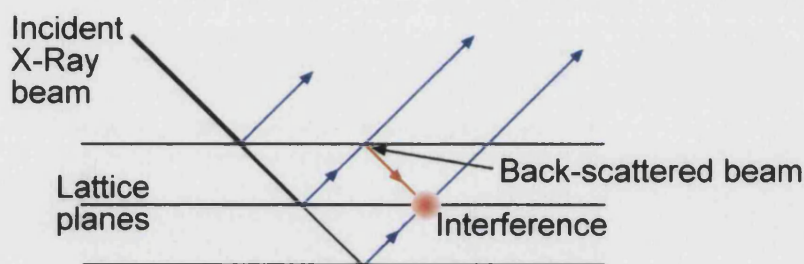
Figure AIV.4: Extinction in a perfect crystal due to interference between

back-scattered and diffracted X-ray beams.

Micro-absorption is the direct absorption of the incident radiation by the particle, the larger the particle the greater the energy loss and a broader intensity peak is produced. A 25% improvement of intensity may be achieved by reducing the particle size from the 15-50 μm range to below 5 μm [2]. The intensity of the incident beam and that of the diffracted beam are both diminished by the material surrounding the lattice planes, which diffract the beam[1].

In a system of two components with equal absorption coefficients a linear relationship exists between the intensities of the peaks corresponding to each component. If one component is increased by a specific percentage then the intensity peak of the other component will drop by the same amount. A non-linear relationship results where the absorption coefficients are dissimilar[2]. If the background counting rate is appreciable the uncertainty in the net characteristic peak height is greater, so a higher number of counts, and a slower scan speed is required to increase the accuracy of the measurement.

AIV.2   THERMOGRAVIMETRIC ANALYSIS

Thermogravimetric analysis, TGA, is commonly used to investigate the decomposition or oxidation of materials, such as polymers. The sample is heated in air (or another atmosphere) and the change in mass is recorded. When a sample decomposes and a gas is evolved a mass decrease is recorded,

while production of an oxide layer gives an increase in mass. An example of a TGA trace is illustrated in Figure AIV.5, where the material mass loss at T_D, may be due to decomposition, while the weight loss at 100°C can be assigned to the elimination of water.
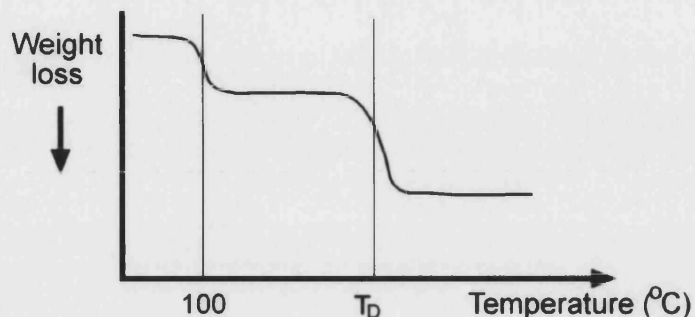
Figure AIV.5: TGA of a material that has mass loss at T_D, possibly due to

decomposition, while the weight loss at 100°C is the elimination of water.

AIV.3   SINTERING RATE DETERMINATION

The rate of sintering is commonly determined by measuring the shrinkage of the specimen during the sintering heat treatment[4, 5]. The rate is calculated by determining the gradient of the shrinkage versus time plot. A peak in the sintering rate is typically observed when this rate is plotted against the sintering temperature, Figure AIV.6(a). Knowledge of this temperature is useful in a technical context as it allows optimisation of firing conditions. The peak in the sintering rate can be modified by the addition of secondary phases. These phases may lower the temperature of the peak by forming a liquid phase that allows faster diffusion, as shown in Figure AIV.6(b).
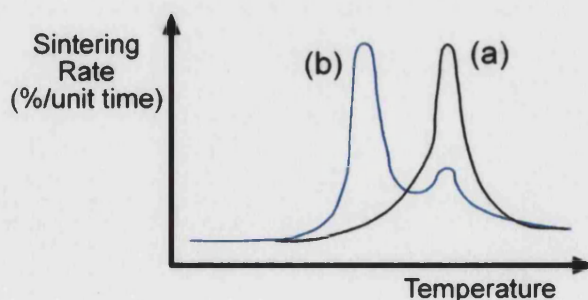
Figure AIV.6: Representative sintering rate-temperature plot for (a) an unmodified powder and

(b) a powder that has been modified to lower the temperature of the sintering rate peak.

Accurate measurements of sample shrinkage can be obtained using a dilatometer, Figure AIV.7. The dilatometer is a furnace with a Linearly Variable Displacement Transducer (LVDT) to

measure the sample displacement as a function of temperature. The sample is placed in a holder and the furnace follows the required heating profile and the connected LVDT measures the change in length of the sample.
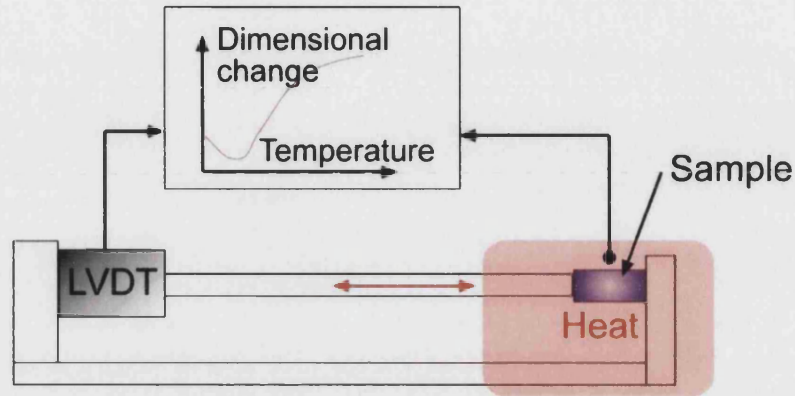
LVDT = Linearly Variable Displacement Transducer

Figure AIV.7: Schematic of dilatometer equipment showing the position of

the LVDT and sample in relation to the hot zone of the furnace.

AIV.4   DENSITY MEASUREMENT

AIV.4.a   Theoretical density

The estimated density of a binary composite can be obtained from equation AIV.2 if the porosity of the sample is assumed to be negligible[6], where ψ is the weight percentage of ceramic or filler and ρ the density.

$$Theoretical\ density = \frac{\psi_{ceramic} + \psi_{filler}}{\left(\dfrac{\psi_{ceramic}}{\rho_{ceramic}}\right) + \left(\dfrac{\psi_{filler}}{\rho_{filler}}\right)} \qquad \{AIV.2\}$$

AIV.4.b   Experimental density

Determination of the sample density is important as porosity affects electrical and mechanical properties. The simplest method for the determination of the sample density is to use the geometric method, equation AIV.3, in which the mass and sample dimensions are measured. This method is

only practical for samples of a constant cross-section, low surface roughness and those that are sufficiently strong to survive the handling.

$$Density \ (g.cm^{-3}) \ = \ \frac{Mass \ (g)}{Thickness \ (cm) \ . \ Cross-Sectional \ area \ (cm^2)} \qquad \{AIV.3\}$$

Higher accuracy can be obtained using Archimedes method, a buoyancy technique. Archimedes Principle states that the buoyant force on a submerged object is equal to the weight of the fluid that is displaced by the object. The procedure followed, to obtain the density of sintered samples, is given below with mass measurements taken using a Sartorius density determination kit and a Sartorius balance (Sartorius AG, Germany). The material must not dissolve in the liquid medium, which makes it unsuitable for the green compact density determination of barium titanate.

Archimedes density measurement procedure.

i. The dry mass of the sample is measured, ϕ_{dry}.

ii. The sample is then boiled in distilled water for thirty minutes to fill open pores with water.

iii. The sample is left in the water while the water temperature returns to room temperature.

iv. The weight of the saturated sample suspended in water, is measured, ϕ_{sat}.

v. The sample is removed from the water and any excess water removed before being re-measured to give the impregnated mass, ϕ_{impreg}.

vi. Sample density and porosity calculated using equations AIV.4 and AIV.5.

The sample volume is given by the difference between ϕ_{sat} and ϕ_{impreg}, while the difference between ϕ_{impreg} and ϕ_{dry} gives the open pore volume[7]. The bulk density is the mass per unit volume of the specimen including all pores, accessible and inaccessible from the surface by an immersion liquid. The bulk density of the sample is calculated using equation AIV.4, while the porosity (both open and closed) is given by equation AIV.5. ρ_{Bat} is the theoretical density of barium titanate (5.95 gcm^{-3}) or composite and ρ_{H2O} is the density of water at the measurement temperature, in this case taken as 1 gcm^{-3} *.

$$Bulk \ density \ = \ \rho_{H_2O} \left(\frac{\phi_{dry}}{\phi_{impreg} - \phi_{sat}} \right) \qquad \{AIV.4\}$$

---

* The change in the density of water is negligible around room temperature, at 15°C it has a density of 0.9991 gcm^{-3}, while at 20°C it is 0.9982 gcm^{-3}.

$$Porosity\ (\%) = 100 \left[1 - \left(\frac{Bulk\ density}{\rho_{Bat}} \right) \right] \qquad \{AIV.5\}$$

AIV.5 SCANNING ELECTRON MICROSCOPY

The Scanning Electron Microscope, SEM, has a greater depth of field in comparison with the light microscope; due to the method by which the image is obtained from a narrow beam of electrons that has a smaller wavelength than light. The SEM is one of the most versatile instruments available for observing features on the microscopic scale, such as particle size[8]. Disadvantages of electron microscopy include cost, the need for sample coating, higher maintenance and working in a vacuum environment. In brief, the SEM involves the production of an electron beam, which systematically scans the surface of a specimen and mainly produces secondary electrons and X-rays from interactions with the atoms present. These signals are rastered to produce an image of the sample surface from the different detectors, these being,

i. **Secondary electron detector**

Electrons that escape from the sample after collision are collected to produce a topographical image.

ii. **Back scattered electron detector**

High energy electrons that rebound from the sample nearly parallel to the primary electron beam are collected by two semi-circular semiconductor sensors. The signal from this device displays the compositional (atomic number dependent) contrast of the sample. In order to observe a purely compositional contrast, unaltered by topographical effects, the specimen surface needs to be flat.

iii. **X-ray detector**

The energy of the primary electron beam is sufficient to knock electrons from the atomic shells of the elements in the sample. When the empty site is filled by an electron from a higher energy level a characteristic X-ray is emitted. The X-ray has the energy difference of the two energy levels in the atom. Each element yields a characteristic spectral fingerprint. The energy dispersive detector separates the emitted X-rays according to energy, resulting in a plot of X-ray counts versus X-ray energy. The spectral peaks correspond to specific elements and the relative intensities can be

used to determine the relative concentrations of the elements present. Elemental mapping of the sample is possible as the beam scans the sample. The detector is protected from the microscope vacuum by a window transparent to X-rays of very thin beryllium. Absorption by the window decreases the sensitivity of the detector to low energy X-rays (those below sodium). In the absence of the window elements of atomic number down to boron can be detected.

It is necessary to coat non-conducting or poorly conducting materials with a conductor to avoid the build up of local electrical charges. The coating material is usually gold[9], but as this element strongly absorbs X-rays the X-ray diffraction pattern from the sample can be distorted and generate large gold peaks on the diffraction pattern which may overlay the specimen peaks of interest. Gold can be replaced by the less absorbing, but conductive, lighter element carbon, to reduce interaction with the sample peaks.

AIV.6   TRANSMISSION ELECTRON MICROSCOPY

Information can be obtained from samples that are thin enough to allow electrons to pass through. The advantage of TEM is the ability to observe full morphological, crystallographic and micro-analytical information[10]. However, the technique suffers from complex and time-consuming sample preparation, small specimen analysis area and a vacuum working environment.

Electrons are produced in the same way as for the SEM, but higher electron energies are achieved by using a larger accelerating voltage. Transmitted electrons are focused on to a fluorescent screen either as a diffraction pattern of the specimen or one of several types of image, such as bright or dark field, depending on which electron beams are allowed to pass through the aperture in the back focal plane of the objective lens. The imaging modes are:

i.   **Bright field**

This is the conventional imaging mode in which the aperture is centred on the transmitted (undiffracted) beam. In this mode the crystalline areas appear dark on a bright background.

ii.   **Dark field**

The aperture is centred on a certain diffraction beam so that only those electrons corresponding to this beam contribute to the image. In this case the crystals are bright on a dark background.

The diffraction pattern and associated bright field and dark field images can be viewed directly on a fluorescent screen, recorded on photographic film or captured using a charge-coupled device (CCD) camera and recorded on a computer.

X-ray energy dispersive analysis is also possible in the TEM with the advantage that the thinner specimens provide higher spatial resolution in comparison to the SEM, where the X-rays are collected from the bulk volume of about 1 µm diameter, as illustrated in Figure AIV.8. The illuminated volume in the TEM is a little greater than the beam area multiplied by the specimen thickness and can be of the order of nanometres.
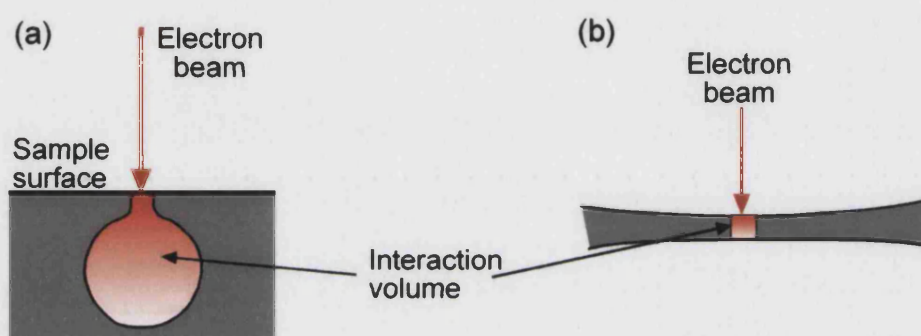
Figure AIV.8: Volume of material that produces X-rays in (a) SEM and (b) TEM.

The ideal TEM specimen is thin with parallel sides to avoid gross thickness contrast variations. The sample needs to be stable under vacuum and storage, representative of the bulk material and unchanged by preparation. Complex sample preparation, following the general procedure given below, is required to produce the thin samples.

i.   The sintered disc specimen was ground to a thickness between one and two millimetres using 600 grit and 1200 grit emery paper.

ii.   A 3 mm core drill was used to grind out a 3 mm diameter primary TEM specimen.

iii.   These discs were subsequently ground to a thickness of 150-200 µm using 1200 grit paper.

iv.   A VCR Group dimpler (Model D500i, VCR Group Inc., USA) was used to reduce the disc centre thickness to 5-10 µm, generating a sample as illustrated in Figure AIV.9(a).

v.   Ion beam thinning was conducted on both sides of the sample simultaneously using a Gatan Dual Ion mill thinner model 600 (England). Argon was used as the ionised gas, under a voltage of 4 kV, to sputter material from the specimen that was orientated at an angle of 10°. Ion milling for more than 50 hours was required to create a small perforation in the sample, Figure AIV.9(b). The thickness of the region around the perforation should be sufficiently thin for electron beam penetration.

vi.   To reduce sample charging a thin layer of carbon[9] was applied with a Carbon coating machine model 12E6 (Edwards High Vacuum Ltd. England). Gold is unsuitable as a coating material for TEM specimens as it readily absorbs electrons and reduces the effectiveness of X-ray energy dispersive analysis.

Figure AIV.9: Representation of (a) dimpled and (b) ion milled TEM specimens.

AIV.7   STRENGTH DETERMINATION

A popular method for the determination of fracture strength is the three-point bend test with a crosshead speed of 0.5 mm/min and rectangular specimens of the ceramic system to be tested[11-19]. However, only a small volume of material is stressed, which increases the sampling error[20]. Biaxial testing of disc samples increases the volume tested and removes the presence of two sample edges that can give rise to premature failure in brittle materials. It also has the advantage of requiring minimum sample shaping. In the biaxial test a disc shaped sample is loaded in bending from the top and bottom disc faces[20]. There are three different loading point geometries possible, namely:

i.   Ball-on-ring

ii.   Piston-3-ball

iii.   Ring-on-ring

The ball-on-ring method, used in this work, is suitable for testing the ceramic strength with axisymmetric bending of the disk and requires minimal alignment[21]. A schematic is shown in Figure AIV.10(a). The bending stress reduces from the centre of the sample outwards to the edge, with the overhang having a negligible effect on the stress distribution within the ring support[20, 21]. The low stress at the sample edges reduces the possibility of premature failure due to edge defects.
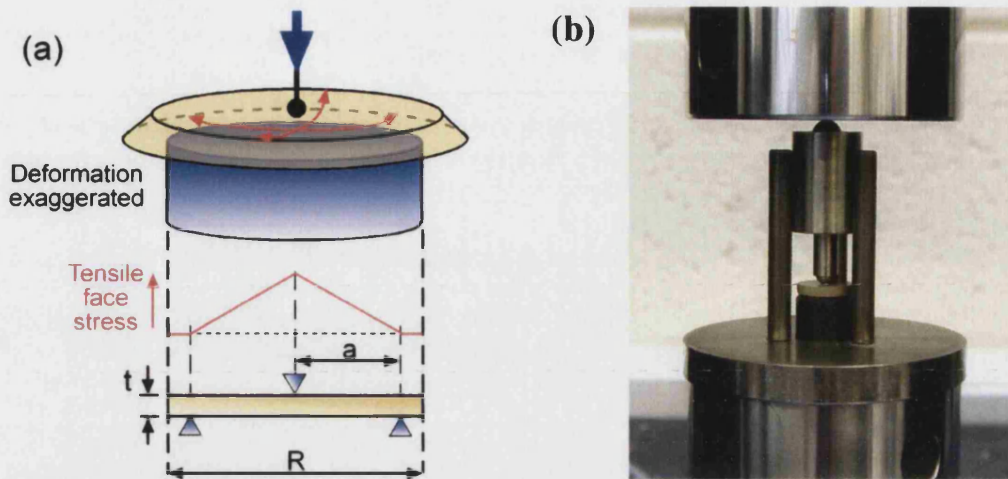
Figure AIV.10: Ball-on-ring (a) loading schematic and (b) practical test device.

Sample failure is detected as a sharp drop in the load-displacement curve[20] and fracture strength, $S_{biaxial}$, values are calculated via equation AIV.6.

$$S_{biaxial} = \frac{3P(1-\upsilon)}{4\pi\ t^2}\left\{1+2\left[\ln\left(\frac{a}{b}\right)\right]+\left[\frac{(1-\upsilon)\ a^2}{(1+\upsilon)R^2}\right]\left[1-\left(\frac{b^2}{2a^2}\right)\right]\right\} \qquad \{AIV.6\}^{22}$$

Here P is the failure load (in Newtons), t is the thickness of the disc (in millimetres), a is the support point radius (in millimetres), b is the radius of uniform loading at the centre (in millimetres), R the disc radius (in millimetres) and υ is the Poisson's ratio for the material. For this research the value of a was 5.2mm, b was taken to be t/3 [22] and υ was assumed to be 0.33.

The values obtained for strength were analysed using Weibull statistics. This involves assigning each sample a probability value in accordance with a ranking estimator. For N samples, numbered from 1 to i the ranking estimator, RE, is given by equation AIV.7 [20].

$$RE_i = \frac{i-0.5}{N} \qquad \{AIV.7\}^{20}$$

The ranked data results are plotted on a log-log graph with ordinate, Y_i, and abscissa, x_i, as described below;

$$y_i = \ln\left(\ln\left[\frac{1}{1-REi}\right]\right) \qquad \{AIV.8\}^{20}$$

$$x_i = \ln(S_{biaxial}) \qquad \{AIV.9\}^{20}$$

The regression line has a gradient m, the Weibull modulus, which is a measure of the spread of results, and a y-axis intercept that corresponds to the characteristic failure strength. Materials that have large scatter, such as refractories, have low Weibull moduli values in comparison to metals that have low scatter and a Weibull modulus nearer 30. A high Weibull modulus, however, may arise from failure being dominated by large sample defects of consistent size, such as pores[20].

AIV.8 TOUGHNESS DETERMINATION

Many techniques have been devised to estimate the resistance of a material to crack propagation, such as Vickers indentation, Knoop indentation and Controlled Surface Flaw[11, 13, 23]. The methods rely on applying a controlled indent to the material and measuring the extension of the crack produced. The characteristic radial traces on the surface provide a record of crack growth readily amenable to direct post-indentation measurement. Vickers indention is a common technique in which the load is applied to the material through the use of a diamond shaped indentor. Figure AIV.11 shows the two crack systems that are generated by the Vickers indent.
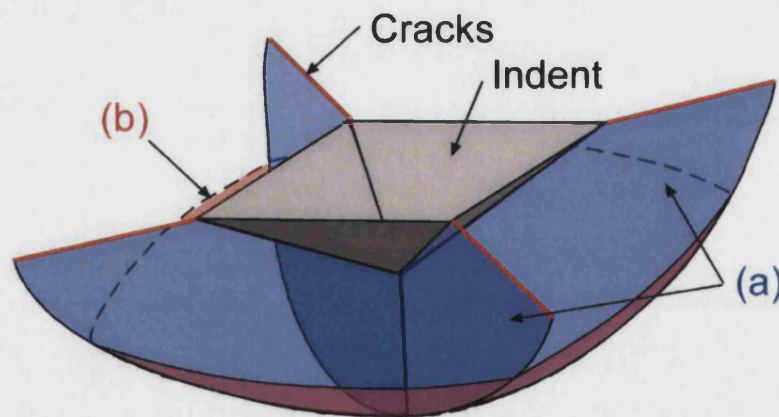
Figure AIV.11: The (a) radial/median and (b) lateral crack systems produced by a Vickers indent.

The lateral cracks spread outward from the deformation zone, beneath the indention surface, and may interact with the radial system under heavy loading. In this case the crack turns upwards to intersect the surface, producing chips. Measurement of crack length is recommended to be undertaken below this load level[24].

If cracks are produced then an estimate of the fracture toughness, K_c, at mechanical equilibrium, can be calculated via equation AIV.10.

$$K_c = C_v \left(\frac{E_{Young}}{H_v} \right)^{1/2} \left(\frac{P_v}{c_0^{3/2}} \right)$$

{AIV.10}[24],

where C_v is a material-independent constant for Vickers radial cracks (taken as 0.016 [25]), E_{Young} the Young's modulus of the material (in N/m^2), H_v its hardness in N/m^2, P_v the load applied (in Newtons) and c_0 the instantaneous half crack length on load removal (in metres). For simplicity the Young's modulus was assumed to be 100 GPa for monolithic and composite samples. Slow crack growth can occur after the load is removed and then c_0 becomes c. The crack size should, therefore, be measured directly after indentation, otherwise the calculated toughness will be less than the true K_c value[24].

AIV.9   MEASUREMENT OF PIEZOELECTRIC COEFFICIENTS

The piezoelectric coefficient, d_{33}, is the charge per unit force (C/N) measured in the poled direction of the sample. The disc samples are suitable for measurement as the lateral dimensions are at least twice the sample thickness[26]. The d_{31} coefficient is the charge per unit force in the orthogonal directions for a disc. In this work the charge per unit force was measured with a Take Control Piezometer System PM25, Figure AIV.12. This device applies an oscillating force of 0.1 N at 97 Hz and measures the charge generated by the sample. A frequency of 97 Hz is chosen such that it is not affected by the 50 Hz mains frequency and is lower than the resonant frequency of the sample[26]. A schematic of the piezometer device is given in Figure AIV.13, showing the force application arm, which also collects the charge generated in d_{33} measurement mode.
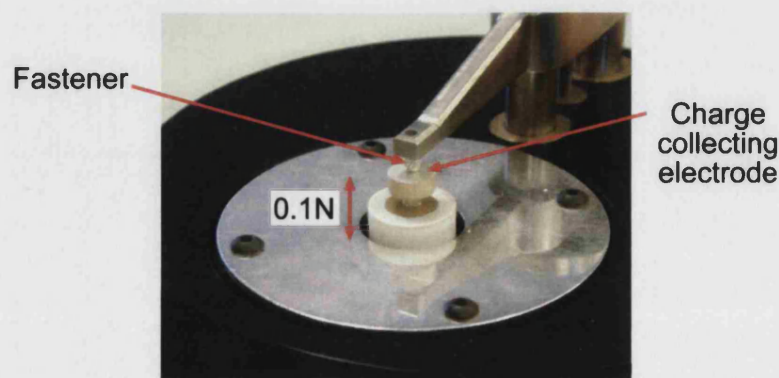
Figure AIV.12: Take Control Piezometer System PM25 for determination of d_{33}.
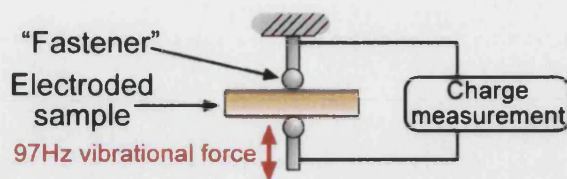
Figure AIV.13: Schematic diagram of piezometer used for d_{33} determination.

The piezometer displays the value of d_{33}, in pC/N. The specimen may be tested with or without electrodes, however, electrodes improve the charge flow over the surface and increase the measurement response to the applied stress[26]. The force is applied using a small set (5mm diameter) of "fasteners" and these are placed at the centre of the specimen. A measurement error of two percent has been reported for this instrument[26]. The calibration of the PM25 piezometer was undertaken using the PZT reference sample supplied with the device that is reported to have a d_{33} of 330 pC/N.

In addition to d_{33}, two measurements of d_{31} were taken at 90° to each other. In this case the sample is rotated such that the force is applied perpendicular to the poling direction using insulating fasteners. Care was taken to align the disc vertically with the fasteners to reduce misfit between the fasteners and the sample. The charge generated by the d_{31} coefficient was then measured using additional electrodes. The measurements of the monolithic and composite d_{33} and d_{31} piezoelectric coefficients were carried out at least 24 hours after poling to enable the rapid ageing in this time period to stabilise[27, 28].

AIV.10   POLARISATION-FIELD ANALYSIS

Polarisation-Field, PE, analysis requires the application of an electric field to a sample while measuring the current response of the material. These measurements were carried out at the National Physical Laboratory, NPL, using a modular Polarisation-Strain-Electric Field (PSE) system (a device listing is given in Table AIV.1). A schematic diagram of the system is shown in Figure AIV.19, indicating the principal parts. The control PC is used to set the experimental variables, such as input voltage for the function generator, and also acquires the response data from the digital storage scope. The input signal voltage is amplified and the displacement and current through the sample are measured and passed to a digital storage scope.
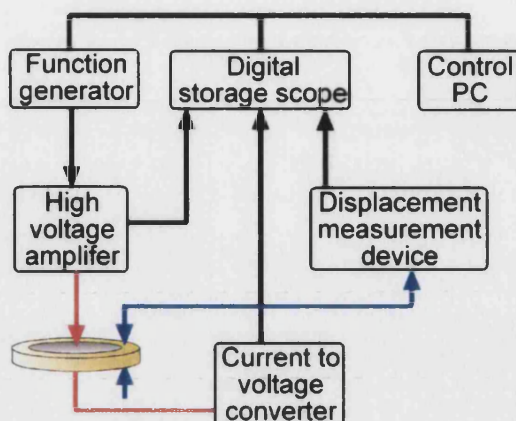
Figure AIV.14: Schematic of PSE hysteresis measurement equipment[29].

Table AIV.1: Polarisation-Strain-Field Device list

Function	Type
Function generator	HP33120A
	Thurlby Thandar TG1304
	PC analog output card
Current-to-voltage converter	Keithley 428
	Stanford Research SR570
	Virtual earth 741 op amp
Displacement measurement system	MTI Fotonic 2000 fibre optic
High voltage amplifier	TREK
	Chevin Research HVA1B
Data Acquisition	Gould Datasys 840 DSO
	Tektronix DSO TDS 420
	PC Data acquisition board with LabView driver

The specimen is held between two electrodes, to which a potential difference is applied, Figure AIV.20(a). The top of one of these electrodes serves as the bottom half of a capacitor that is used to measure the displacement of the sample, as shown in Figure AIV.20(b). The displacement measurement equipment is sensitive to current and was disconnected in case sample breakdown occurred causing flashover in this capacitor.
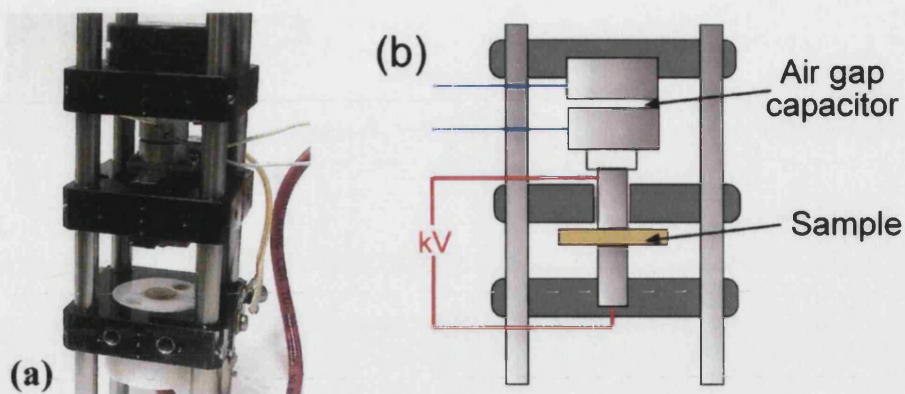
Figure AIV.15: (a) The PSE specimen holder and (b) a schematic.

The control PC recorded the voltage and current that were subsequently interpreted using a Labview based software supplied by NPL. This software can be used to view and analyse the parameters, which can then be exported for display in Excel. The parameters obtained during the test are given in Table AIV.2.

Table AIV.2: Polarisation-Strain-Field Parameters

Parameter name (units)	Comment
E_0 (kV/mm)	Field amplitude, calculated as the applied voltage divided by the specimen thickness.
P_0 (Cm^{-2})	Polarisation amplitude, calculated by equation AIV.11. This is necessary as in practise the actual value of polarisation is not known, since only changes in charge are measured. The polarisation at zero field strength may not be zero, as it could represent the positive or negative remnant polarisation. The maximum and minimum polarisation values are assumed to be equal. $$P_0 = \left|P_{max}\right| = \left|P_{min}\right| \qquad \{AIV.11\}$$
$P_r(1)$ (Cm^{-2})	Positive remnant polarisation.
$P_r(2)$ (Cm^{-2})	Negative remnant polarisation.
$E_c(1)$ (kV/mm)	Coercive field (negative)
$E_c(2)$ (kV/mm)	Coercive field (positive)
E_i (kV/mm)	The hysteresis loop may shift along the electric field axis due to ageing effects, this is quantified by the E_i parameter, equation AIV.12. This is commonly called the internal bias. $$E_i = \frac{E_c(1) + E_c(2)}{2} \qquad \{AIV.12\}$$
U_H	Hysteresis loss, this is the area of the Polarisation-Electric field loop.
E_{ps1}	Real permittivity, calculated from equation AIV.13. $$E_{ps1} = \sqrt{\left(\frac{P}{\varepsilon_0 E}\right)^2 - E_{ps2}^2} \qquad \{AIV.13\}$$
E_{ps2}	Imaginary permittivity is given by equation AIV.14. $$E_{ps2} = \frac{U_H}{\pi\,\varepsilon_0 E_0^2} \qquad \{AIV.14\}$$
Diel loss	Dielectric loss tangent is the imaginary permittivity divided by the real permittivity.
S_0 (ppm)	Induced strain amplitude, calculated as the induced displacement divided by sample thickness.
d_1 (pm/V)	Real piezoelectric strain coefficient
d_2 (pm/V)	Imaginary piezoelectric strain coefficient
Piezoloss	Piezoelectric loss tangent is simply d_2 divided by d_1.

AIV.11 REFERENCES

1. CULLITY, D.B.D., 'Elements of X-ray diffraction', 2nd Ed., *Addison-Wesley Publishing company Inc*, 1978

2. KLUG, H.P. & ALEXANDER, L.E., 'X-ray diffraction procedures for polycrystalline and amorphous materials', 2nd Ed., *John Wiley & Sons, New York, London*, 1974

3. RAPRA Technology Ltd., 'Particle size analysis – The laser diffraction technique', www.azom.com/details.asp?ArticleID=1528', 26/02/03

4. SAUCY, C., REANEY, I. & BELL, A., 'Microstructure and electromechanical properties of $BaTiO_3$-ZrO_2 "Core-shell" ceramics', *Brit. Ceram. Proc.*, 1993, **51**, 29-52

5. VOLTZKE, D. & ABICHT, H-P., 'The influence of different additives and the mode of their addition on the sintering behaviour and the properties of semiconducting barium titanate ceramics', *Solid State Sciences*, 2000, **2** (1) 149-59

6. HUANG, C-L., WENG, M-H., LION, C-T. & WU, C-C., 'Low temperature sintering and microwave dielectric properties of $Ba_2Ti_9O_{20}$ ceramic using glass additions', *Mat. Res. Bul.*, 2000, **35**, 2445-56

7. KINGERY, W.D., 'Introduction to ceramics', *J. Wiley & Sons Inc*, 1976

8. HWANG, H., SEKINO, T., OTA, K. & NIIHARA, K., 'Perovskite-type $BaTiO_3$ ceramics containing particulate SiC: Part I-Structure variation and phase transformation', *J. Mat. Sci.*, 1996, **31**, 4617-24

9. BORSA, C., FERREIRA, H. & KIMINAMI, R., 'Liquid phase sintering of Al_2O_3-SiC nanocomposites', *J. Eur. Ceram. Soc.*, 1999, **19**, 615-21

10. WILLIAMS, D.B. & CARTER, C.B., 'Transmission Electron Microscopy - A textbook for material science', *Plenum Press, New York and London*, 1996

11. HWANG, H. & NIIHARA, K., 'Perovskite-type $BaTiO_3$ ceramics containing particulate SiC: Part II-Microstructure and mechanical properties', *J. Mat. Sci.*, 1998, **33**, 549-558

12. NAGAI, T., HWANG, H., YASUOKA, M., SANDO, M. & NIIHARA, K., 'Preparation of barium titanate-dispersed-magnesia nanocomposite', *J. Am. Ceram. Soc.*, 1998, **81**(2), 425-28

13. HWANG, H. J., SANDO, M., TORIYAMA, M. & NIIHARA, K., 'Effect of secondary phase dispersion on mechanical and piezoelectric properties of PZT-based nanocomposites', *IEEE Int. Symp. on Applications of Ferroelectrics*, 1996, 373-75

14. TIAN, L., ZHOU, Y. & LEI, T.C., 'Mechanical properties of Al_2O_3+ZrO_2+Nano-SiCp ceramic composite', *Ceram. Int.*, 1996, **22**, 451-56

15. WILHELM, M. & WRUSS, W., 'Influence of annealing on the mechanical properties of SiC-Si composites with sub-micron SiC microstructures', *J. Eur. Ceram. Soc.*, 2000, **20**, 1205-13

16. GAO, L., WANG, H., HONG, J., MIYAMOTO, H., MIYAMOTO, K., NISHIKAMA, Y. & TORRE, S., 'Mechanical properties and microstructure of nano-SiC-Al_2O_3 composites densified by spark plasma sintering', *J. Eur. Ceram. Soc.*, 1999, **19**, 609-13

17. OH, S-T., SEKINO, T. & NIIHARA, K., 'Fabrication and mechanical properties of 5vol% copper dispersed alumina nanocomposite', *J. Eur. Ceram. Soc.*, 1998, **18**, 31-37

18. CHOU, W. & TUAN, W., 'Toughening and strengthening of alumina with silver inclusions', *J. Eur. Ceram. Soc.*, 1995, **15**, 291-95

19. DENG, Z-Y., SHI, J-L., ZHANG, Y-F., JIANG, D-Y. & GUO, J-K., 'Pinning effect of SiC particles on mechanical properties of Al_2O_3-SiC ceramic matrix composites', *J. Eur. Ceram. Soc.*, 1998, **18**, 501-08

20. CAIN, M., STEWART, M. & GEE, M., 'Mechanical and elastic strength measurements for piezoelectric ceramics: Technical measurement notes', *NPL report CMMT(A)99*, 1998

21. SHETTY, D.K., ROSENFIELD, A.R., DUCKWORTH, W.H. & HELD, P.R., 'A Biaxial-flexure test for evaluating ceramic strengths', *J. Am. Ceram. Soc.*, 1983, **66** (1), 36-42

22. DE WITH, G. & WAYEMANS, H.H.M., 'Ball-on-ring test revisited', *J. Am. Ceram. Soc.*, 1989, **72** (8), 1538-41

23. KOMERNENI, S., 'Nanocomposites', *J. Mat. Chem.*, 1992, **2** (12), 1219-30

24. ANSTIS, G.R., CHANTIKUL, P., LAWN, B.R. & MARSHALL, D.B., 'A critical evaluation of indentation techniques for measuring fracture toughness: I, direct crack measurements', *J. Am. Ceram. Soc.*, **64** (9), 533-538

25. TUAN, W.H & WU, J.M., 'Effect of microstructure on the hardness and fracture toughness of $YBa_2Cu_3O_{7-x}$/Ag composite', *J. Mat. Sci.*, 1993, **28**, 1415-20

26. ERHART, J. & BURIANOVA, L., 'What is really measured on a d_{33}-meter?', *J. Eur. Ceram. Soc.*, 2001, **21**, 1413-5

27. LEE, M-H, HALLIYAL, A & NEWNHAM, R. E., 'Poling of co-precipitated lead titanate-epoxy 0-3 piezoelectric composite', *J. Am. Ceram. Soc.*, 1989, **72** (6), 986-90

28. ROSEN, C. Z., HIREMATH, B. V. & NEWNHAM, R (Ed), 'Piezoelectricity: Key papers in physics', *Am. Inst. Phys.*, 1992, **5**, 4, 13, 119, 157, 285

29. CAIN, M. G., STEWART, M. & HALL, D.A., 'Ferroelectric Hysteresis: Measurement & Analysis', NPL report CMMT(A)152, 1999

APPENDIX V

Matlab files used for computational modelling:

multi.m – Batch production script

netmain.m – Two-dimensional resistor-capacitor network script

net3main.m – Three-dimensional resistor-capacitor network structure script

network3d1a.m – Two-dimensional resistor-capacitor layer script

network3d2a.m – Three-dimensional "adhesive" layer script

Simetrix macro used for computational modelling

Matlab

Table AV.1 shows the basic file structure used in the SiMetrix circuit simulator for specifying network component types and connections. This file was generated by Matlab.

Table AV.1: Basic file structure used in the SiMetrix circuit simulator.

File row text (header, body, footer)	Annotation
*	Comment – filename, information
V1 R1_N 0 AC 50 0	Sets variables of voltage source. {source_name, node_1, node_2, source_type, voltage, phase} source_name is V1, there is only one source in these circuits. node_1 is the negative end of resistor 1 (R1). node_2 is earth (0). source_type is "AC" as AC analysis is required in comparison to a DC voltage. voltage of 50 has been used in all simulations. The phase has been set to 0 in all simulations.
R1 VOUT R1_N 100Meg	The external resistor. {resistor_name, node_1, node_2, resistor_value} Resistor (R1) of 100 MΩ is connected between the VOUT terminal and a node (R1_N) representing the negative pin of this resistor.
R2 VOUT R2_N 1k C1 VOUT R3_P 1n R3 VOUT R3_P 1G : :	The rest of the network
.ac dec 10 1 1G	Analysis type variables {analysis_type, spacing_of_analysis_point, number_of_points, start_frequency, end_frequency} All analysis has been AC with a ten (10) points logarithmically spaced in each frequency decade (dec). The analysis begins at 1 Hz (1) and finishes at 1 GHz (1G).
.keep /nov /noi VOUT	Saves VOUT information in a data file without the current (/noi) and voltage (/nov) values at each node.

Network construction

Figure AV.I shows the beginning of a network construction, highlighting the components and nodes. The actual Matlab script is later in this appendix, but the general procedure is given below.
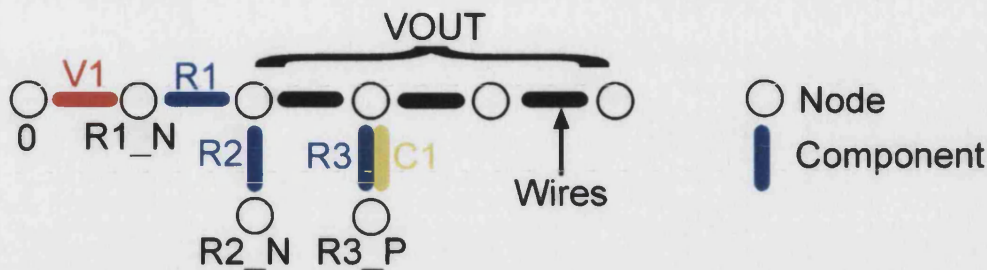
Figure AV.I: Component and node names at the beginning of network construction.

1. Prompt user for matrix size, a, and percentage of resistors required, j.

2. Set all other variables to zero, except resistor number, r (=2), and capacitor number, c (=1).

3. Add header

4. Define various variables, including row variable s.

5. Generate random number between 0 and 99.

6. If first row (s≤1) insert component with node_1=VOUT

7. If last row (s≥a^2-a) insert component with node_2=0

8. Otherwise insert component with node_1 and node_2 determined by formulae.

9. The component inserted is determined by the random number and the j variable. If the random number is greater than j a capacitor is inserted otherwise a resistor is added.

10. This continues over all the positions in the matrix x-y, where x and y are defined by a.

multi.m: Matlab script to produce 256 files using the netmain.m Matlab macro.

```
%script multi.m
clear all
a = 16;
b = 0;
j = 30;
%open file
fid = fopen('a-b-j-1.net','w');
netmain
status = fclose(fid);
%file closed
%open file
fid = fopen('a-b-j-2.net','w');
netmain
status = fclose(fid);
%file closed
:
:
%open file
```

```
fid = fopen('a-b-j-255.net','w');
netmain
status = fclose(fid);
%file closed
%open file
fid = fopen('a-b-j-256.net','w');
netmain
status = fclose(fid);
%file closed
%end
```

netmain.m: Script to produce two-dimensional random resistor-capacitor networks

```
%script file netmain.m
%to produce the central part of the netlist for Simetrix
r=2;      %start resistor number at 2
c=1;      %start capacitor number at 1
d=0;    %set random number variable to zero
e=0;    %set break point variable to zero
s=0;    %set vertical node variable to zero
z=0;    %set vertical mod N-P variable to zero
u=0;    %set vertical N-P variable 1 to zero
v=0;    %set vertical N-P variable 2 to zero
t=0;    %set horizontal first node variable to zero
f=0;    %set horizontal mod N-P variable to zero
g=0;    %set horizontal N-P variable to zero
h=0;    %set horizontal N-P variable to zero
%header
fprintf(fid, ['*\n']);
fprintf(fid, ['V1 R1_N 0  AC 50  0\n']);
fprintf(fid, ['R1 VOUT R1_N 100Meg\n']);
%construct vertical components
for y = 0:a-1   %y is down
    for x = 0:a    %x is across
%define s
s = (x+2)+(y-1).*(a+1);
%define z
z = mod((x+y),2);
if (z == 0)
    u = '_P';
    v = '_N';
else
    u = '_N';
    v = '_P';
end
%define rnd number and break point
d = fix(100*rand);
e = (((100-b)*j)/100)+b;
%loop to produce top and bottom contacts
%general format of line X{r} X{s}{u} X{r}{v} value
if(s <= 1)
    %top contact
    if (d < b) %defects
    fprintf(fid, ['R' num2str(r) ' VOUT R' num2str(r) (v) ' 1k\n']);
    r = r+1;
    elseif(d >= e) %capacitor addition
    fprintf(fid, ['R' num2str(r) ' VOUT R' num2str(r) (v) ' 1G\n']);
    fprintf(fid, ['C' num2str(c) ' VOUT R' num2str(r) (v) ' 1n\n']);
    r = r+1;
    c = c+1;
    else   %resistors
    fprintf(fid, ['R' num2str(r) ' VOUT R' num2str(r) (v) ' 1k\n']);
    r = r+1;
    end
elseif(s >= -a+a^2)
```

```
%bottom ground
if (d < b)  %defects
fprintf(fid, ['R' num2str(r) ' R' num2str(s) (u) ' 0 1k\n']);
r = r+1;
elseif(d >= e)  %capacitor addition
fprintf(fid, ['R' num2str(r) ' R' num2str(s) (u) ' 0 1G\n']);
fprintf(fid, ['C' num2str(c) ' R' num2str(s) (u) ' 0 1n\n']);
r = r+1;
c = c+1;
else  %resistors
fprintf(fid, ['R' num2str(r) ' R' num2str(s) (u) ' 0 1k\n']);
r = r+1;
end
else
   %bulk of material
   if (d < b)  %defects
   fprintf(fid, ['R' num2str(r) ' R' num2str(s) (u) ' R' num2str(r) (v) ' 1k\n']);
   r = r+1;
   elseif(d >= e)  %capacitor addition
   fprintf(fid, ['R' num2str(r) ' R' num2str(s) (u) ' R' num2str(r) (v) ' 1G\n']);
   fprintf(fid, ['C' num2str(c) ' R' num2str(s) (u) ' R' num2str(r) (v) ' 1n\n']);
   r = r+1;
   c = c+1;
   else  %resistors
   fprintf(fid, ['R' num2str(r) ' R' num2str(s) (u) ' R' num2str(r) (v) ' 1k\n']);
   r = r+1;
   end
end
%end of loop to produce top and bottom contacts
end %x
end %y
%construct horizontal components no loop required
%define t
t = r+a+1-(a+1)^2;  %calculates first node point
for y = 0:a-2   %y is rows
   for x = 0:a-1    %x is columns
%define f
f = mod((x+y),2);
if (f == 0)
    g = '_N';
    h = '_P';
else
    g = '_P';
    h = '_N';
end
w = mod(t,(a+1));
d = fix(100*rand);
e = (((100-b)*j)/100)+b;
if (d < b)  %defects
fprintf(fid, ['R' num2str(r) ' R' num2str(t) (g) ' R' num2str(t+1) (h) ' 1k\n']);
r = r+1;
t = t+1;
   if (w == 0)      %to shift t value to next row
      t = t+1;
   end
elseif (d >= e)  %capacitor addition
fprintf(fid, ['R' num2str(r) ' R' num2str(t) (g) ' R' num2str(t+1) (h) ' 1G\n']);
fprintf(fid, ['C' num2str(c) ' R' num2str(t) (g) ' R' num2str(t+1) (h) ' 1n\n']);
r = r+1;
c = c+1;
t = t+1;
   if (w == 0)      %to shift t value to next row
      t = t+1;
   end
else  %resistors
fprintf(fid, ['R' num2str(r) ' R' num2str(t) (g) ' R' num2str(t+1) (h) ' 1k\n']);
```

```
r = r+1;
t = t+1;
    if (w == 0)      %to shift t value to next row
        t = t+1;
    end
end
end %x
end %y
%footer
fprintf(fid, ['\n']);
fprintf(fid, ['.ac dec 10 1 1G\n']);
fprintf(fid, ['.keep /nov /noi VOUT\n']);
%end
```

net3main.m: Script to produce the structure of three-dimensional random resistor-capacitor networks

```
% script file net3main.m
o=0; %set depth production loop to zero
r=2;      %start resistor number at 2
c=1;      %start capacitor number at 1
%header
fprintf(fid, ['*\n']);
fprintf(fid, ['V1 R1_N 0 AC 50 0\n']);
fprintf(fid, ['R1 VOUT R1_N 100Meg\n']);
for o = 1:a        %depth
run network3d1a
fprintf(fid, ['\n']);
run network3d2a
fprintf(fid, ['\n']);
end
%end depth production loop
%add capping depth layer
network3d1a;
%footer
fprintf(fid, ['\n']);
fprintf(fid, ['.ac dec 10 1 1G\n']);
fprintf(fid, ['.keep /nov /noi VOUT\n']);
%end
```

network3d1a.m: Script to produce the two-dimensional random resistor-capacitor layers in the construction of the three-dimensional networks

```
%script file network3d1a.m
d=0;    %set random number variable to zero
e=0;    %set break point variable to zero
s=0;    %set vertical node variable to zero
z=0;    %set vertical mod N-P variable to zero
u=0;    %set vertical N-P variable 1 to zero
v=0;    %set vertical N-P variable 2 to zero
t=0;    %set horizontal first node variable to zero
f=0;    %set horizontal mod N-P variable to zero
g=0;    %set horizontal N-P variable to zero
h=0;    %set horizontal N-P variable to zero
q=0;      %set layer dependence of s variable to zero
%construct vertical components
for y = 0:a-1  %y is down
    for x = 0:a    %x is across
%define s and q
s = (x+2)+(y-1).*(a+1);
q = (r-(a+1));
%define z
```

```
z = mod((x+y),2);
if (z == 0)
    u = '_P';
    v = '_N';
else
    u = '_N';
    v = '_P';
end
%define rnd number and break point
d = fix(100*rand);
e = (((100-b)*j)/100)+b;
%loop to produce top and bottom contacts
%general format of line X{r} X{s}{u} X{r}{v} value
if(s <= 1)
    %top contact
    if (d < b)  %defects
    fprintf(fid, ['R' num2str(r) ' VOUT R' num2str(r) (v) ' 1k\n']);
    r = r+1;
    elseif(d >= e)  %capacitor addition
    fprintf(fid, ['R' num2str(r) ' VOUT R' num2str(r) (v) ' 1G\n']);
    fprintf(fid, ['C' num2str(c) ' VOUT R' num2str(r) (v) ' 1n\n']);
    r = r+1;
    c = c+1;
    else   %resistors
    fprintf(fid, ['R' num2str(r) ' VOUT R' num2str(r) (v) ' 1k\n']);
    r = r+1;
    end
elseif(s >= -a+a^2)
    %bottom ground
    if (d < b)  %defects
    fprintf(fid, ['R' num2str(r) ' R' num2str(q) (u) ' 0 1k\n']);
    r = r+1;
    elseif(d >= e)  %capacitor addition
    fprintf(fid, ['R' num2str(r) ' R' num2str(q) (u) ' 0 1G\n']);
    fprintf(fid, ['C' num2str(c) ' R' num2str(q) (u) ' 0 1n\n']);
    r = r+1;
    c = c+1;
    else   %resistors
    fprintf(fid, ['R' num2str(r) ' R' num2str(q) (u) ' 0 1k\n']);
    r = r+1;
    end
else
    %bulk of material
    if (d < b)  %defects
    fprintf(fid, ['R' num2str(r) ' R' num2str(q) (u) ' R' num2str(r) (v) ' 1k\n']);
    r = r+1;
    elseif(d >= e)  %capacitor addition
    fprintf(fid, ['R' num2str(r) ' R' num2str(q) (u) ' R' num2str(r) (v) ' 1G\n']);
    fprintf(fid, ['C' num2str(c) ' R' num2str(q) (u) ' R' num2str(r) (v) ' 1n\n']);
    r = r+1;
    c = c+1;
    else   %resistors
    fprintf(fid, ['R' num2str(r) ' R' num2str(q) (u) ' R' num2str(r) (v) ' 1k\n']);
    r = r+1;
    end
end
%end of loop to produce top and bottom contacts
end %x
end %y
%construct horizontal components no loop required
%define t
t = r+a+1-(a+1)^2;  %calculates first node point
for y = 0:a-2   %y is rows
    for x = 0:a-1    %x is columns
%define f
f = mod((x+y),2);
```

```
if (f == 0)
    g = '_N';
    h = '_P';
else
    g = '_P';
    h = '_N';
end
w = mod(t,(a+1));
d = fix(100*rand);
e = (((100-b)*j)/100)+b;
if (d < b)  %defects
fprintf(fid, ['R' num2str(r) ' R' num2str(t) (g) ' R' num2str(t+1) (h) ' 1k\n']);
r = r+1;
t = t+1;
    if (w == 0)        %to shift t value to next row
        t = t+1;
    end
elseif (d >= e)  %capacitor addition
fprintf(fid, ['R' num2str(r) ' R' num2str(t) (g) ' R' num2str(t+1) (h) ' 1G\n']);
fprintf(fid, ['C' num2str(c) ' R' num2str(t) (g) ' R' num2str(t+1) (h) ' 1n\n']);
r = r+1;
c = c+1;
t = t+1;
    if (w == 0)        %to shift t value to next row
        t = t+1;
    end
else    %resistors
fprintf(fid, ['R' num2str(r) ' R' num2str(t) (g) ' R' num2str(t+1) (h) ' 1k\n']);
r = r+1;
t = t+1;
    if (w == 0)        %to shift t value to next row
        t = t+1;
    end
end
end %x
end %y
%end
```

network3d2a.m: Script to produce the "adhesive" random resistor-capacitor layers in the construction of the three-dimensional networks

```
%script file network3d2a.m
d=0;   %set random number variable to zero
e=0;   %set break point variable to zero
i=0;      %set depth mod N-P variable to zero
k=0;      %set depth N-P variable 1 to zero
l=0;      %set depth N-P variable 2 to zero
m=0;   %set depth previous layer node variable to zero
n=0;      %set depth next layer node variable to zero
%construct depth components
%define m and n numbers
m = (r-2*a*a);
n = (r+(a*a)-1);
for y = 0:a-2   %y is down
    for x = 0:a    %x is across
%define i
i = mod((x+y),2);
if (i == 0)
    k = '_N';
    l = '_P';
else
    k = '_P';
    l = '_N';
end
```

```
%define rnd no and break point
d = fix(100*rand);
e = (((100-b)*j)/100)+b;
%loop to produce adhesive layer
%general format of line X{r} X{s}{u} X{r}{v} value
if (d < b)  %defects
        fprintf(fid, ['R' num2str(r) ' R' num2str(m) (k) ' R' num2str(n) (l) ' 1k\n']);
        r = r+1;
        m = m+1;
        n = n+1;
elseif(d >= e)  %capacitor addition
        fprintf(fid, ['R' num2str(r) ' R' num2str(m) (k) ' R' num2str(n) (l) ' 1G\n']);
        fprintf(fid, ['C' num2str(c) ' R' num2str(m) (k) ' R' num2str(n) (l) ' 1n\n']);
        r = r+1;
        c = c+1;
        m = m+1;
        n = n+1;
else    %resistors
        fprintf(fid, ['R' num2str(r) ' R' num2str(m) (k) ' R' num2str(n) (l) ' 1k\n']);
        r = r+1;
        m = m+1;
        n = n+1;
end
end %x
end %y
%end
```

Simetrix script: To maximise the simulation time on the computers.

```
run /file ./b/a-b-j-1.net ./b/a-b-j-1.dat
show /file ./b/real/reala-b-j-1.txt real(1/vout)
show /file ./b/imag/imaga-b-j-1.txt imag(1/vout)
show /file ./b/ph/pha-b-j-1.txt ph(vout)
echo 1

run /file ./b/a-b-j-2.net ./b/a-b-j-2.dat
show /file ./b/real/reala-b-j-2.txt real(1/vout)
show /file ./b/imag/imaga-b-j-2.txt imag(1/vout)
show /file ./b/ph/pha-b-j-2.txt ph(vout)
echo 2

run /file ./b/a-b-j-3.net ./b/a-b-j-3.dat
show /file ./b/real/reala-b-j-3.txt real(1/vout)
show /file ./b/imag/imaga-b-j-3.txt imag(1/vout)
show /file ./b/ph/pha-b-j-3.txt ph(vout)
echo 3
:
:
run /file ./b/a-b-j-255.net ./b/a-b-j-255.dat
show /file ./b/real/reala-b-j-255.txt real(1/vout)
show /file ./b/imag/imaga-b-j-255.txt imag(1/vout)
show /file ./b/ph/pha-b-j-255.txt ph(vout)
echo 255

run /file ./b/a-b-j-256.net ./b/a-b-j-256.dat
show /file ./b/real/reala-b-j-256.txt real(1/vout)
show /file ./b/imag/imaga-b-j-256.txt imag(1/vout)
show /file ./b/ph/pha-b-j-256.txt ph(vout)
echo 256
```

APPENDIX VI

X-Ray Diffraction Analysis Reference Data

04-0756, Silicon Carbide, SiC.

04-0783, Silver, Ag.

05-0626 Tetragonal Barium Titanate, $BaTiO_3$.

06-0363, Silver Nitrate, $AgNO_3$.

12-0793, Silver Oxide, Ag_2O.

14-0654 Silicon Dioxide, SiO_2.

21-1276 Titania (Rutile), TiO_2.

22-0513 Barium Titanium Silicate, $Ba_2TiSi_2O_8$.

26-0178 Tetragonal Barium Oxide, BaO.

26-0339, Silver Carbonate, Ag_2CO_3.

31-0174 Cubic Barium Titanate, $BaTiO_3$.

43-1038, Silver Oxide, AgO

Theoretical composite density calculation

04-0756, Silicon Carbide, SiC.

4- 756   JCPDS-ICDD Copyright (c) 1995   PDF-2 Sets 1-45 database   Rad.= 1.54060 Quality:

	2-theta	Int.	h k l
alpha-SiC	34.062*	50	1 0 7
	34.467*	20	0 1 11
	34.882*	20	1 0 13
Silicon Carbide	35.452*	30	1 0 16
	35.744*	100	0 1 17
Rad: CuKa1 Lambda: 1.54050 Filter: d-sp:	36.191*	20	1 0 19
Cutoff: Int: I/Icor:	37.121	10	1 0 22
Ref: Thibault, Am. Mineral., 33 588 (1948)	38.101*	40	1 0 25
	38.439*	30	0 1 26
	40.798	10	0 1 32
Sys: Rhombohedral (Hex) S.G.: R3m (160)			
a: 3.073 b: c: 128.17 A: C: 41.7084	41.584	20	1 0 34
A: B: C: Z: 51 mp:	41.989	20	0 1 35
Ref: Ibid.	44.600	10	0 1 41
	45.790	10	1 0 43
Dx: 3.240 Dm: 3.218 SS/FOM: F30=3(.064,138)	53.888	<10	1 0 58
ea: nwB: ey: Sign: 2V:	54.233	10	0 1 59
Ref:	55.660	10	1 0 61
	57.559	<10	1 0 64
CAS no.: 409-21-2. % composition: Si 69.64, C 29.91, Al 0.05, Fe 0.20, Ca	59.599	50	1 0 67
0.16, Mg <0.01. Polytype 51R, formerly type V.	60.026	50	0 1 68
*FeKalpha radiation and Geiger-counter X-ray spectrometer.			
PSC: hR34. Mwt: 40.10. Volume[CD]: 1048.20.	61.345	<10	1 0 70
	63.687	<10	1 1 27
	65.186	20	1 1 33
	66.229	20	1 1 36
	70.785	10	2 0 2

2-theta	Int.	h k l	2-theta	Int.	h k l	2-theta	Int.	h k l
72.033	50	2 0 17	104.991	20	0 0132	141.467	<10	0 2124
72.675	10	0 1 86	108.024	<10	0 2 94	144.413	<10	1 0151
73.330	10	1 1 54	109.716	10	1 0127	146.232	20	0 2127
75.374	10	2 0 32	110.766	10	1 2 50	148.171	20	3 0 69
76.084	10	2 0 35	115.066	<10	1 2 59	156.351	<10	3 0 75
79.079	<10	2 0 44	116.471	<10	1 0133			
85.017	10	0 2 58	118.140	<10	2 1 64			
85.950	<10	1 0103	120.104	10	1 0136			
88.898	10	1 0106	120.781	40	3 0 6			
89.934	10	0 1107	121.702	<10	3 0 15			
92.094	<10	2 0 71	126.138	20	2 1 76			
95.578	10	2 0 77	126.929	20	1 2 77			
100.762	10	1 2 14	132.677	<10	0 2118			
101.460	20	2 1 19	133.943	50	2 0119			
103.040	10	1 0121	135.591	<10	3 0 54			

Strong lines: 2.51/X   2.63/5   1.55/5   1.54/5   1.31/5   0.84/5   2.36/4   0.89/4

04-0783, Silver, Ag.

4- 783   JCPDS-ICDD Copyright (c) 1995   PDF-2 Sets 1-45 database   Quality: i

	d A	Int.	h k l
Ag	2.359	100	1 1 1
	2.044	40	2 0 0
Silver	1.445	25	2 2 0
	1.231	26	3 1 1
Silver-3C, syn	1.1796	12	2 2 2
Rad: CuKa1 Lambda: 1.54056 Filter: Ni d-sp:			
Cutoff: Int: Diffractometer I/Icor: 5.20	1.0215	4	4 0 0
Ref: Swanson, Tatge, Natl. Bur. Stand. (U.S.), Circ. 539, 1 23 (1953)	0.9375	15	3 3 1
	0.9137	12	4 2 0
	0.8341	13	4 2 2
Sys: Cubic S.G.: Fm3m (225)			
a: 4.0862 b: c: A: C:			
A: B: C: Z: 4 mp: 960.6 deg.			
Ref: Ibid.			
Dx: 10.50 Dm: 10.50 SS/FOM: F9=65(.015,9)			
ea: nwB: 0.181 ey: Sign: 2V:			
Ref: Winchell, Elements of Optical Mineralogy, II 17			
Color: Light gray metallic			
Pattern taken at 27 C. Sample obtained from Johnson Matthey Company, Ltd. CAS			
no.: 7440-22-4. Spectrographic analysis indicated faint traces of Ca, Fe and			
Cu. Purity >99.999%. Opaque mineral optical data on specimen from Great Bear			
Lake, Canada: RR2Re=94.1, Disp.=16, VHN100=55-63, Color values .314, .321,			
94.2, Ref.: IMA Commission on Ore Microscopy QDF. Cu type. Gold group, gold			
subgroup. PSC: cP4. Mwt: 107.87. Volume[CD]: 68.23.			

Strong lines: 2.36/X   2.04/4   1.23/3   1.45/3   0.94/2   0.83/1   1.18/1   0.91/1

05-0626 Tetragonal Barium Titanate, BaTiO₃.

```
5- 626              JCPDS-ICDD Copyright (c) 1995   PDF-2 Sets 1-45 database      Rad.= 1.54060  Quality: *
```

		2-theta	Int.	h k l
BaTiO₃		22.039	12	0 0 1
		22.263	25	1 0 0
Barium Titanium Oxide		31.498	100	1 0 1
		31.647	*	1 1 0
		38.888	46	1 1 1
Rad: CuKa1 Lambda: 1.5405 Filter: Ni d-sp:		44.856	12	0 0 2
Cutoff: Int: Diffractometer I/Icor: 8.343		45.378	37	2 0 0
Ref: Swanson, Fuyat, Natl. Bur. Stand. (U.S.), Circ. 539, 3 45 (1954)		50.614	6	1 0 2
		50.978	8	2 0 1
Sys: Tetragonal S.G.: P4mm (99)		51.100	7	2 1 0
a: 3.994 b: c: 4.038 A: C: 1.0110				
A: B: C: Z: 1 mp:		55.955	15	1 1 2
Ref: Ibid.		56.253	35	2 1 1
		65.755	12	2 0 2
Dx: 6.012 Dm: SS/FOM: F30=19(.049,32)		66.123	10	2 2 0
		70.359	5	2 1 2
ea: nwB: ey: Sign: 2V:		70.663	2	3 0 0
Ref:		74.336	5	1 0 3
		75.094	7	3 0 1
Color: Colorless		75.164	9	3 1 0
X-ray pattern at 26 C. Sample from National Lead Company. CAS no.:		78.768	3	1 1 3
12047-27-7. Annealed at 1400 C in MgO. Spectroscopic analysis: <0.1% Bi, Sr;		79.472	5	3 1 1
<0.01% Al, Ca, Fe, Mg, Pb, Si; <0.001% Mn, Sn. Inverts to cubic form at 120 C.		83.492	7	2 2 2
Merck Index, 8th Ed., p. 122. PSC: tP5. Plus 10 additional reflections. Mwt:		86.966	1	2 0 3
233.23. Volume[CD]: 64.41.		87.287	1	[3 0 2]
		88.069	1	3 2 0

2-theta	Int.	h k l	2-theta	Int.	h k l	2-theta	Int.	h k l
91.586	7	2 1 3	103.869	1	1 0 4	108.946	1	3 0 3
92.060	12	3 1 2	104.502	1	2 2 3	109.733	5	4 1 1
92.328	12	3 2 1	104.991	1	3 2 2	113.556	2	3 1 3
99.495	1	0 0 4	105.362	1	4 1 0	114.362	2	3 3 1
100.984	2	4 0 0	108.256	3	1 1 4	117.506	3	2 0 4

Strong lines: 2.83/X 2.31/5 2.00/4 1.63/4 3.99/3 1.64/2 4.03/1 2.02/1

06-0363, Silver Nitrate, AgNO₃.

```
6- 363              JCPDS-ICDD Copyright (c) 1995   PDF-2 Sets 1-45 database      Quality: i
```

		d A	Int.	h k l
AgNO₃		4.53	55	1 1 1
		4.10	55	1 0 2
Silver Nitrate		3.67	60	0 2 0
		3.58	6	1 1 2
		3.45	10	0 2 1
Rad: CuKa1 Lambda: 1.5405 Filter: Ni d-sp:		3.16	12	2 1 0
Cutoff: Int: Diffractometer I/Icor:		3.09	8	1 2 1
Ref: Swanson et al., Natl. Bur. Stand. (U.S.), Circ. 539, 5 59 (1955)		3.01	100	2 1 1
		2.806	40	1 1 3
Sys: Orthorhombic S.G.: Pbca (61)		2.733	55	1 2 2
a: 6.995 b: 7.328 c: 10.118 A: C:				
A: B: C: Z: 8 mp:		2.678	4	2 1 2
Ref: Lindley, Woodward, J. Chem. Soc. A, 123 (1966)		2.531	45	2 2 0
		2.482	4	0 2 3
Dx: 4.351 Dm: SS/FOM: F30=28(.017,63)		2.305	35	2 1 3
		2.249	30	1 3 1
ea: 1.731 nwB: 1.741 ey: ~1.788 Sign: + 2V: ~60 deg.		2.170	12	3 1 1
Ref: Ibid.		2.118	12	3 0 2
		2.082	30	0 2 4
Color: Colorless		1.965	16	2 3 1
X-ray pattern at 26 C. Sample from Johnson Matthey Company, Ltd. CAS no.:		1.904	10	1 3 3
7761-88-8. Spectroscopic analysis: <0.01% Mg, Cu; <0.001% Fe, Ca; <0.0001% Na.		1.879	16	1 1 5
Hexagonal AgNO3 is also reported. Merck Index, 8th Ed., p. 948. C.D. Cell:		1.855	20	1 1 3
a=7.328, b=10.118, c=6.995, a/b=0.7243, c/b=0.6913. PSC: oP40. Mwt: 169.87.		1.833	20	3 2 2
Volume[CD]: 518.64.		1.789	4	2 2 4
		1.747	10	1 4 1

d A	Int.	h k l	d A	Int.	h k l	d A	Int.	h k l
1.721	12	2 3 3	1.578	8	4 2 0	1.4230	6	2 3 5
1.703	20	2 1 5	1.508	8	3 3 3	1.4065	<1	4 3 1
1.676	16	4 1 1	1.496	12	3 1 5	1.3893	4	1 1 7
1.663	8	3 3 1	1.4835	10	0 4 4	1.3855	4	3 4 2
1.639	6	1 0 6	1.4381	10	4 0 4	1.3483	4	5 0 2

Strong lines: 3.01/X 3.67/6 4.53/6 4.10/6 2.73/6 2.53/5 2.81/4 2.31/4

12-0793, Silver Oxide, Ag₂O.

12-793	JCPDS-ICDD Copyright (c) 1995	PDF-2 Sets 1-45 database	Quality: i

	d A	Int.	h k l
Ag₂O			
	3.348	4	1 1 0
Silver Oxide	2.734	100	1 1 1
	2.367	35	2 0 0
	1.674	18	2 2 0
	1.427	12	3 1 1
Rad: CuKa1 Lambda: 1.54056 Filter: Ni d-sp:			
Cutoff: Int: Diffractometer I/Icor: 5.60	1.367	6	2 2 2
Ref: Natl. Bur. Stand. (U.S.) Monogr. 25, 1 45 (1962)	1.184	<1	4 0 0
	1.086	4	3 3 1
	1.059	2	4 2 0
Sys: Cubic S.G.: Pn3m (224)	0.9667	2	4 2 2
a: 4.736 b: c: A: C:			
A: B: C: Z: 2 mp:	0.9115	2	5 1 1
Ref: Ibid.			
Dx: 7.245 Dm: SS/FOM: F11=35(.016,20)			
ea: nwB: ey: Sign: 2V:			
Ref:			

Color: Dark brown
Pattern at 25 C. Sample was obtained from Fisher Scientific Company,
Washington, D.C., USA. CAS no.: 20667-12-3. Heated between 250 C and 280 C to
sharpen the pattern. Their spectroscopic analysis showed 0.001-0.01% Fe, Mg,
Pb and Si. Merck Index, 8th Ed., 948. Ag2O type. PSC: cP6. Mwt: 231.74.
Volume[CD]: 106.23.

14-0654 Silicon Dioxide, SiO₂.

14-654	JCPDS-ICDD Copyright (c) 1995	PDF-2 Sets 1-45 database	Rad.= 1.54060 Quality:

	2-theta	Int.	h k l
SiO₂			
	14.274	8	0 0 1
Silicon Oxide	20.258	4	-1 2 1
	25.956	30	0 3 1
Coesite, syn	28.871	100	0 4 0
	32.412	8	0 4 1
Rad: CuKa Lambda: 1.5418 Filter: Ni d-sp:			
Cutoff: Int: Diffractometer I/Icor:	33.280	10	-1 3 2
Ref: Keat, Norton Company, Worcester, Massachussetts, USA, Private Communication	38.611	4	-1 4 2
	39.312	8	0 5 1
	41.385	4	-2 4 2
	44.600	6	-1 5 2
Sys: Monoclinic S.G.: P21/a (14)			
a: 7.17 b: 12.38 c: 7.17 A: C:	49.498	4	0 3 3
A: B: 120.00 C: Z: 16 mp:	50.978	8	2 0 2
Ref: Zoltai, Buerger, Z. Kristallogr., Kristallgeom., Kristallphys., Kristallchem.,	53.547	12	-3 1 4
111 129	53.888	10	-1 7 1
Dx: 2.90 Dm: 3.01 SS/FOM: F25=2(.113,101)	55.296	2	-3 2 4
ea: 1.599 nwB: ey: 1.604 Sign: + 2V: 54 deg.	58.357	6	-1 7 2
Ref: Dana's System of Mineralogy, 7th Ed., I 668	59.812	10	0 8 0
	61.753	4	-1 8 1
Color: Colorless	65.808	2	-1 8 2
Synthetic material. O2Si type. C.D. Cell: a=7.170, b=12.380, c=7.170,	66.282	4	-2 7 3
beta=120.00, a/b=0.5792, c/b=0.5792, S.G.=P21/n (14). PSC: mP48. Mwt: 60.08.			
Volume[CD]: 551.18.	69.879	12	2 3 3
	71.340	2	-3 6 4
	73.662	6	-2 9 1
	77.103	4	-5 1 5
	82.267	6	-2 8 4

Strong lines: 3.09/X 3.43/3 1.71/1 1.35/1 2.69/1 1.70/1 1.55/1 6.20/1

21-1276 Titania (Rutile), TiO$_2$.

21-1276	JCPDS-ICDD Copyright (c) 1995	PDF-2 Sets 1-45 database	Rad.= 1.54060 Quality: *

	2-theta	Int.	h k l
TiO$_2$	27.447	100	1 1 0
	36.086	50	1 0 1
Titanium Oxide	39.188	8	2 0 0
	41.226	25	1 1 1
Rutile, syn	44.052	10	2 1 0
Rad: CuKa1 Lambda: 1.54056 Filter: Mono. d-sp:	54.323	60	2 1 1
Cutoff: Int: Diffractometer I/Icor: 3.40	56.642	20	2 2 0
Ref: Natl. Bur. Stand. (U.S.) Monogr. 25, 7 83 (1969)	62.742	10	0 0 2
	64.040	10	3 1 0
	65.480	2	2 2 1
Sys: Tetragonal S.G.: P42/mnm (136)			
a: 4.5933 b: c: 2.9592 A: C: .6442	69.010	20	3 0 1
A: B: C: Z: 2 mp:	69.790	12	1 1 2
Ref: Ibid.	72.410	2	3 1 1
	[74.411]	1	[3 2 0]
Dx: 4.25 Dm: 4.23 SS/FOM: F30=107(.009,32)	76.510	4	2 0 2
ea: 2.9467 nwB: 2.6505 ey: Sign: + 2V:	79.822	2	2 1 2
Ref: Dana's System of Mineralogy, 7th Ed., I 575	82.335	6	3 2 1
	84.260	4	4 0 0
Color: Reddish brown	87.464	2	4 1 0
Pattern taken at 25 C. Sample obtained from National Lead Co., South Amboy,	89.557	8	2 2 2
New Jersey, USA. No impurity over 0.001%. Two other polymorphs anatase			
(tetragonal) and brookite (orthorhombic) converted to rutile on heating above	90.708	4	3 3 0
700 C. Optical data on specimen from Dana's System of Mineralogy, 7th	95.275	6	4 1 1
Ed., I 555. Opaque mineral optical data on specimen from Sweden:	96.017	6	3 1 2
R3R%=20.3, Disp.=Std., VHN100=1132-1187, Ref.: IMA Commission on Ore	97.177	4	4 2 0
Microscopy QDF. Pattern reviewed by Syvinski, W., McCarthy, G., North Dakota	[98.514]	<1	[3 3 1]
State University, Fargo, North Dakota, USA, ICDD Grant-in-Aid (1990).			
Agrees well with experimental and calculated patterns. Additional weak			
reflections [indicated by brackets] were observed. O2Ti type. Rutile group,			
rutile subgroup. Also called: titania. W used as internal standard. PSC:			
tP6. Validated by calculated pattern. Mwt: 79.90. Volume[CD]: 62.43.			

2-theta	Int.	h k l	2-theta	Int.	h k l	2-theta	Int.	h k l
105.099	2	4 2 1	120.059	8	2 1 3	140.052	12	5 2 1
106.019	2	1 0 3	122.788	8	4 3 1	143.116	2	4 4 0
109.406	2	1 1 3	123.660	8	3 3 2	155.070	2	5 3 0
116.227	4	4 0 2	131.847	6	4 2 2			
117.527	4	5 1 0	136.549	8	3 0 3			

Strong lines: 3.25/X 1.69/6 2.49/5 2.19/3 1.62/2 1.36/2 1.35/1 0.82/1

22-0513 Barium Titanium Silicate, Ba$_2$TiSi$_2$O$_8$.

```
22-513              JCPDS-ICDD Copyright (c) 1995    PDF-2 Sets 1-45 database    Rad.= 1.54060  Quality: *
```

		2-theta	Int.	h k l
Ba TiSi O 2 2 8		14.679	5	1 1 0
		16.972	14	0 0 1
Barium Titanium Silicate		20.801	8	2 0 0
		22.508	12	1 1 1
Fresnoite, syn		23.292	20	2 1 0
Rad: CuKal Lambda: 1.54056 Filter: Mono. d-sp:		26.989	45	2 0 1
Cutoff: Int: Diffractometer I/Icor: 4.20		28.995	100	2 1 1
Ref: Natl. Bur. Stand. (U.S.) Monogr. 25, 9 19 (1971)		29.585	10	2 2 0
		33.191	25	3 1 0
		34.372	20	0 0 2
Sys: Tetragonal S.G.: P4bm (100)				
a: 8.5291 b: c: 5.2110 A: C: .6110		37.523	8	3 1 1
A: B: C: Z: 2 mp:		38.034	2	3 2 0
Ref: Ibid.		40.548	6	2 0 2
		41.969	20	2 1 2
Dx: 4.44 Dm: 4.43 SS/FOM: F30=52(.014,41)		42.340	4	4 0 0
ea: 1.765 nwB: 1.775 ey: Sign: - 2V:		43.716	16	4 1 0
Ref: Alfors et al., Am. Mineral., 50 314 (1965)		45.092	10	3 3 0
		46.011	6	2 2 2
Color: Colorless		47.256	15	4 1 1
Pattern taken at 25 C. The sample was prepared at NBS, Gaithersburg, Maryland,		47.649	6	4 2 0
USA, by C.R. Robbins. PSC: tP26. To replace 10-197. Mwt: 506.73.				
Volume[CD]: 379.08.		48.541	20	3 1 2
		52.166	2	3 2 2
		52.618	3	0 0 3
		55.008	1	1 1 3
		55.660	2	4 0 2

2-theta	Int.	h k l	2-theta	Int.	h k l	2-theta	Int.	h k l
56.783	9	4 1 2	76.401	3	2 0 4	95.311	1	0 0 5
57.207	5	2 0 3	77.348	2	2 1 4	95.960	3	7 4 1
57.903	11	3 3 2	79.480	2	5 1 3	96.280	2	8 2 0
58.341	11	2 1 3	80.022	2	6 2 2	97.177	1	1 1 5
60.082	2	4 2 2	80.199	1	2 2 4	99.060	1	2 0 5
61.103	6	5 2 1	80.982	2	5 4 2	99.940	2	5 2 4
61.463	5	4 4 0	82.105	4	3 1 4			
63.570	3	5 3 0	82.327	5	5 2 3			
65.610	3	6 0 0	83.821	1	6 4 1			
66.330	3	5 3 1	84.760	2	6 3 2			
66.661	2	6 1 0	86.995	2	5 3 3			
68.323	2	6 0 1	87.721	1	4 0 4			
69.371	2	5 2 2	88.663	2	4 1 4			
70.754	5	4 1 3	88.918	2	6 0 3			
71.754	3	3 3 3	89.578	2	3 3 4			
72.352	4	4 4 2	91.476	1	4 2 4			
72.481	4	0 0 4	92.227	1	6 5 1			
73.283	4	5 4 1	92.642	2	6 2 3			
74.309	3	5 3 2	93.565	3	5 4 3			
76.264	3	6 0 2	95.047	1	8 0 1			

```
Strong lines: 3.08/X  3.30/5  2.70/3  3.82/2  2.61/2  2.15/2  1.87/2  2.07/2
```

26-0178 Tetragonal Barium Oxide, BaO.

```
26-178              JCPDS-ICDD Copyright (c) 1995    PDF-2 Sets 1-45 database    Rad.= 1.54060  Quality: i
```

		2-theta	Int.	h k l
BaO		28.401	50	0 0 1
		29.073	50	1 1 0
Barium Oxide		35.337	65	1 0 1
		41.167	100	1 1 1
		41.685	5	2 0 0
Rad: MoKal Lambda: 0.70930 Filter: Mono. d-sp:				
Cutoff: Int: Densitometer I/Icor:		51.223	15	2 0 1
Ref: Liu, L.-g, J. Appl. Phys., 42 3702 (1971)		55.697	20	2 1 1
		60.546	25	2 2 0
		62.965	20	1 0 2
Sys: Tetragonal S.G.: P4/mmm (129)		68.311	20	3 1 0
a: 4.332 b: c: 3.135 A: C: .7237				
A: B: C: Z: 2 mp:		75.586	20	3 1 1
Ref: Ibid.		78.459	<5	2 1 2
Dx: 8.655 Dm: SS/FOM: F12=31(.023,17)				
ea: nwB: ey: Sign: 2V:				
Ref:				
CAS no.: 1304-28-5. Pressure at approximately 290 kbar. PSC: tP4. Mwt:				
153.33. Volume[CD]: 58.83.				

```
Strong lines: 2.19/X  2.54/7  3.14/5  3.07/5  1.53/3  1.65/2  1.48/2  1.37/2
```

26-0339, Silver Carbonate, Ag₂CO₃.

```
26-339          JCPDS-ICDD Copyright (c) 1995   PDF-2 Sets 1-45 database      Rad.= 1.54060  Quality: *
```

2-theta	Int.	h k l
18.277	15	1 0 0
18.547	35	0 2 0
20.543	30	1 1 0
26.111	2	-1 2 0
27.404	3	0 0 1
28.986	8	0 1 1
32.594	60	-1 0 1
33.666	100	-1 3 0
35.009	6	1 1 1
37.073	2	2 0 0
37.686	11	0 4 0
37.752	13	-1 2 1
38.252	8	2 1 0
38.749	14	1 2 1
39.582	35	0 3 1
41.765	11	2 2 0
44.347	10	1 3 1
45.888	2	-2 0 1
46.917	6	-2 1 1
47.072	9	2 3 0
47.516	4	2 0 1
48.514	6	2 1 1
50.644	3	-1 4 1
51.378	13	1 5 0
53.854	3	-2 4 0

Ag₂CO₃

Silver Carbonate

```
Rad: CuKa1      Lambda: 1.540598      Filter: Mono.       d-sp: Diff.
Cutoff:         Int: Diffractometer   I/Icor:
Ref: Natl. Bur. Stand. (U.S.) Monogr. 25, 13 36 (1976)
```

```
Sys: Monoclinic           S.G.: P21 (4)
a: 4.8510       b: 9.544      c: 3.2533       A: 0.5083    C: 0.3409
A:              B: 91.96      C:              Z: 2         mp:
Ref: Ibid.

Dx: 6.083    Dm:           SS/FOM: F30=54(.014,39)
```

```
ea:          nwB:          ey:          Sign:    2V:
Ref:
```

```
CAS no.: 534-16-7.  The sample was prepared by precipitation, adding K2CO3 to
AgNO3 solution.  Major impurities: 0.001 to 0.01% Al and Si; 0.001 to 0.001%
Ca, Cu Pe, and Mg.  Pattern at 25 C.  W used as internal standard.  PSC: mP12.
To replace 12-766.  Mwt: 275.75.  Volume[CD]: 150.53.
```

2-theta	Int.	h k l	2-theta	Int.	h k l	2-theta	Int.	h k l
54.653	9	-2 3 1	61.481	3	1 1 2			
55.807	6	0 5 1	63.300	<1	-3 0 1			
56.066	10	2 3 1	64.030	<1	1 2 2			
56.555	6	0 0 2	64.179	1	-3 1 1			
56.936	1	3 0 0	64.628	2	3 3 0			
57.915	9	0 6 0	65.289	1	3 0 1			
60.112	2	-1 1 2	66.123	1	3 1 1			
60.459	3	3 2 0	66.817	5	-1 3 2			
60.634	3	1 0 2						
61.300	2	1 6 0						

Strong lines: 2.66/X 2.75/6 4.78/4 2.28/4 4.32/3 4.85/2 2.32/1 2.38/1

31-0174 Cubic Barium Titanate, BaTiO₃.

```
31-174          JCPDS-ICDD Copyright (c) 1995   PDF-2 Sets 1-45 database       Quality: *
```

d A	Int.	h k l
4.04	14	1 0 0
2.85	100	1 1 0
2.328	30	1 1 1
2.016	35	2 0 0
1.803	10	2 1 0
1.6445	25	2 1 1
1.4250	15	2 2 0
1.3440	5	3 0 0
1.2740	15	3 1 0
1.2160	5	3 1 1
1.1634	4	2 2 2

BaTiO₃

Barium Titanium Oxide

```
Rad: CuKa      Lambda: 1.5418      Filter: Ni      d-sp:
Cutoff:        Int: Diffractometer  I/Icor:
Ref: Naka, S. et al., Bull. Chem. Soc. Jpn., 47 1168 (1974)
```

```
Sys: Cubic              S.G.:
a: 4.031       b:          c:          A:          C:
A:             B:          C:          Z:          mp:
Ref: Naka, S., Private Communication, (1976)

Dx:           Dm:          SS/FOM: F11=40(.025,11)
```

```
ea:          nwB:          ey:          Sign:    2V:
Ref:
```

```
Sample was prepared by hydrolysis of titanium tetraisopropoxide in aqueous
solution of barium hydroxide and has submicron size of particles.  Absorbs
about 6% of OH and alcoholic radicals.  Metastable form.  It changes to stable
tetragonal form above 800 C.  Mwt: 233.23.  Volume[CD]: 65.50.
```

Strong lines: 2.85/X 2.02/4 2.33/3 1.64/3 1.43/2 1.27/2 4.04/1 1.80/1

43-1038, Silver Oxide, AgO.

```
43-1038          JCPDS-ICDD Copyright (c) 1995   PDF-2 Sets 1-45 database       Quality: C
```

		d A	Int.	h k l
AgO		5.588	1	1 0 0
		2.957	2	1 1 0
Silver Oxide		2.902	<1	0 1 1
		2.794	50	2 0 0
		2.771	100	-1 1 1

Rad: CuKa1	Lambda: 1.54056	Filter: Mono.	d-sp: Calculated
Cutoff: 15.0	Int: Calculated	I/Icor: 6.00	

Ref: Grier, D., McCarthy, G., North Dakota State University, Fargo, North Dakota, USA, ICDD Grant-in-Aid, (1991)

Sys: Monoclinic		S.G.: P21/c (14)			
a: 5.8592	b: 3.4842	c: 5.4995	A: 1.6816	C: 1.5784	
A:	B: 107.506	C:	Z: 4	mp:	

Ref: Ibid.

Dx: 7.684   Dm: SS/FOM: F30=216(.004,37)

ea:	nwB:	ey:	Sign:	2V:	

Ref:

Peak height intensities. Calculation of diffractometer peak intensities done with MICRO-POWD v. 2.2 (D. Smith and K. Smith) using default instrument broadening function (NBS Table), diffracted beam monochromator polarization correction, and atomic scattering factors corrected for anomalous dispersion. Cell parameters from Jansen, M., Fischer, P., J. Less-Common Met., 137 123-131 (1988). Atomic positions from same source: Ag(1) in 2c, Ag(2) in 2a, O in 4e with x=0.2959, y=0.3452, z=0.2221. Anisotropic thermal parameters also from Jansen: Ag(1), U(1,1)=0.0096, U(2,2)=0.0076, U(3,3)=0.0099, U(1,2)=0.0001, U(1,3)=0.0043, U(2,3)=-0.0003; Ag(2), U(1,1)=0.0127, U(2,2)=0.0204, U(3,3)=0.0209, U(1,2)=-0.0055, U(1,3)=0.0039, U(2,3)=-0.0003; O, U(1,1)=0.0133, U(2,2)=0.0124, U(3,3)=0.0124, U(1,2)=0.0002, U(1,3)=0.0044, U(2,3)=0.0011. Intensity threshold for <1=0.1%. AgO type. PSC: mP8. Mwt: 123.87. Volume[CD]: 107.07.

d A	Int.	h k l
2.708	1	-1 0 2
2.622	35	0 0 2
2.416	86	1 1 1
2.286	36	-2 0 2
2.204	<1	-2 1 1
2.180	<1	2 1 0
2.138	1	1 0 2, -1 1 2
2.095	<1	0 1 2
1.9112	<1	-2 1 2
1.8631	<1	2 1 1, 3 0 0
1.8231	<1	1 1 2
1.7946	<1	-3 0 2
1.7421	10	0 2 0
1.7016	23	-3 1 1
1.6769	12	2 0 2
1.6533	<1	0 2 1
1.6426	<1	3 1 0
1.6279	<1	-1 2 1
1.6222	19	-1 1 3
1.5532	<1	-2 1 3

d A	Int.	h k l	d A	Int.	h k l	d A	Int.	h k l
1.4859	<1	-2 2 1	1.1470	<1	-3 2 3	0.9876	2	1 2 4
1.4783	13	2 2 0	1.1429	2	-4 0 4	0.9811	2	-1 3 3
1.4651	<1	-1 2 2	1.1256	5	-1 3 1	0.9750	1	-6 0 2
1.4609	11	3 1 1	1.1065	4	-5 1 1	0.9695	<1	-5 2 1
1.4511	12	0 2 2	1.1025	5	4 0 2, -4 2 2	0.9674	<1	0 3 3
1.4233	5	-4 0 2	1.0975	3	1 3 1	0.9565	<1	-4 1 5
1.4098	9	1 1 3	1.0898	4	4 2 0	0.9556	2	-4 2 4
1.3965	13	4 0 0, -3 1 3	1.0859	2	-4 1 4	0.9424	3	1 1 5
1.3855	9	-2 2 2	1.0753	<1	-2 3 1	0.9417	3	3 3 1
1.3716	<1	-1 0 4	1.0693	4	2 0 4, -2 2 4	0.9319	3	4 2 2
1.3672	<1	2 2 1	1.0645	4	3 1 3	0.9313	2	6 0 0
1.3539	4	-2 0 4	1.0527	3	-5 1 3	0.9276	3	1 3 3
1.3496	2	-4 1 1	1.0495	2	2 2 3	0.9253	2	-1 2 5, 4 1 3
1.3176	<1	-4 1 2	1.0476	3	0 2 4	0.9237	2	-3 3 3
1.3112	4	0 0 4	1.0422	3	-1 1 5	0.9165	1	-2 0 6
1.2723	<1	3 2 0	1.0243	<1	-3 2 4	0.9155	<1	-6 1 3
1.2620	<1	-2 1 4	1.0145	3	-3 1 5, -5 0 4	0.9115	2	2 2 4
1.2340	<1	0 2 3	1.0044	<1	0 1 5	0.9026	<1	-3 0 6
1.2081	5	2 2 2	0.9978	2	-3 3 1	0.8973	1	-6 0 4
1.1821	<1	3 2 1	0.9892	3	5 1 1			

Strong lines: 2.77/X 2.42/9 2.79/5 2.29/4 2.62/4 1.70/2 1.62/2 1.48/1

Composite density calculation

Matrix density (g/cm^3) = ρ_m

Particle density (g/cm^3) = ρ_p

Mass percent of particle present (%) = m_p

Total mass of sample = 100g

As such,

Volume of matrix, $V_m = \dfrac{100 - m_p}{\rho_m}$

Volume of particles, $V_p = \dfrac{m_p}{\rho_p}$

Composite volume, $V_t = V_m + V_p$

Therefore composite theoretical density, $\rho_c = \dfrac{100}{V_t}$

For example, with $\rho_{BaTiO3} = 5.95$g/cm^3, $\rho_{Ag} = 10.5$g/cm^3 and for an m_p of 10% the ρ_c is 6.22g/cm^3.

APPENDIX VII

397

Health & Safety Data Sheets

Barium Titanate

Silicon Carbide

Silicon Carbide (Lonza UF45 composition)

Silver Oxide

Silver Nitrate

Hydrogen hexachloroplatinate(IV)

Barium titanate, BaTiO₃

I   PRODUCT IDENTIFICATION

Trade Name:	Barium Titanate	Synonym:	Barium Titanate
Formula:	$BaTiO_3$	Chemical Family:	Metal Titanate
Calc. Molecular Weight:	233.24	CAS #: 12047-27-7	

II   HAZARDOUS INGREDIENTS

Component	CAS #	%	TLV	OSHA PEL
Barium Titanate	12047-27-7	99.9	0.5 mg/m³ (as Ba)	0.5 mg/m³ (As Ba)
Barium Oxide (BaO)	1304-28-5	NA	0.5 mg/m³	0.5 mg/m³
Titanium Oxide (TiO₂)	13463-67-7	NA	10 mg/m³	15 mg/m³

III   PHYSICAL DATA

Boiling Point (°C):	No Data	Melting Point:	1654 °C
Density:	5.95	Vapor Pressure:	N/A
% Volatile by Volume:	N/A	Reaction with H₂O:	N/A
Appearance and Odor:	White powder, pieces or pressed parts, odorless.	Solubility in H₂O:	Insoluble
Other Comments:	This material has inert or nuisance dust limits of 5 mg/m³ respirable dust.		

IV   FIRE AND EXPLOSION HAZARDS DATA

Flash Point (Method used): N/A
Special Fire Fighting Procedures: Use self-contained breathing apparatus to avoid dust generated during fire fighting.

Autoignition Temp (°C): No data
Flammable Limits: Upper: Non-flammable   Lower: No data

Extinguishing Media: Nonflammable. This material is not combustible nor will it support combustion.
Unusual Fire and Explosion Hazards: Non-flammable.

V   HEALTH HAZARD INFORMATION

Toxicity Data: No data.
Toxic Hazard Rate for Barium Titanate: Unknown. Animal experiments show low toxicity.

Toxic Hazard Rate for Titanium Compounds: This material is considered physiologically inert. There are no reported cases where titanium compounds have caused intoxication.

HMIS Rating: Health: 2   Flammability: 0   Reactivity: 0P   ersonal Protection: E
Routes of Entry: Inhalation? Yes   Skin? Yes   Ingestion? Yes

Effects of Over Exposure (acute and chronic):

Inhalation: Barium compounds may cause local irritation to the nose, throat, and mucous membranes. Long term exposure to Barium compounds can lead to baritosis, a benign pneumoconiosis.

Dermal/Eye Contact: A moderate irritant to the eyes and skin. Prolonged skin contact may cause dermatitis.

Other: Barium poisoning is virtually unknown in industry, although the potential exists when the soluble forms are used. When ingested or given orally, the soluble, ionized barium compounds exert a profound effect on all muscles and especially smooth muscles. The heart rate is slowed and may stop in systole. Other effects are increased intestinal peristalsis, vascular construction, bladder contraction, and increased voluntary muscle tension.

Medical Conditions Generally Aggravated By Exposure: Inhalation may aggravate pre-existing disorders.
Carcinogenicity: None   **NTP?** No   **IARC Monographs?** No   **OSHA Regulated?** No

EMERGENCY AND FIRST AID PROCEDURES:

EYES: Immediately flush eyes with lukewarm water for at least 15 minutes. Seek emergency medical attention.
SKIN: Wash affected area with soap and water. Seek medical attention.
INHALATION: Remove victim to fresh air. Seek medical attention
INGESTION: DO NOT induce vomiting. Seek medical attention immediately.

VI   REACTIVITY DATA

Stability: Stable
Incompatibility (Material to Avoid): Acids
Conditions Contributing to Instability: None known

Conditions to Avoid: None known
Hazardous Decomposition Products: Thermal and Other: Ba fumes upon thermal decomposition
Hazardous Polymerization: Will not occur

VII   SPILL OR LEAK PROCEDURES

Steps to Be Taken in Case Material Is Released or Spilled: Try to keep material dry and away from acid. Sweep or scoop up spilled material. Handle with adequate ventilation. For nuisance dust, see OSHA 29 CFR 1910-94.

Ventilation: See CFR 1910-1000 (air contaminates). Respirators may be a requirement. '

Waste Disposal Method: Waste containing more than 0.2% soluble Barium is hazardous. This material may contain more than 0.2% soluble Barium if the pH is low. It can be rendered nonhazardous by mixing with excess sulfate to form insoluble barium sulfate. Dispose of in accordance with Local, State, and Federal regulations.

VIII   SPECIAL PROTECTION INFORMATION

Respiratory Protection (Specify Type): Wear a NIOSH-approved is required if TLV and PEL exposure limits are exceeded.
Ventilation: Local Exhaust: Recommended.   **Mechanical:** Recommended
Special: N/A   **Other:** N/A

Protective Gloves: Protective gloves required.   **Eye Protection:** Safety glasses required.
Other Protective Equipment: None necessary.

IX   SPECIAL PRECAUTIONS

Other Handling and Storage Conditions:

•Keep container closed.
•Store in a cool, dry place, and away from acids.
•Wash thoroughly after handling.

Transportation Requirements:

DOT Class: N.C.
UN Number: 1564
IMCO Class: 6.1

Silicon carbide, SiC

Synonyms: carbon silicide, betarundum, crystolon.
Molecular formula: Si C
CAS No: 409212
EC No: 2069918

Physical data

Appearance: grey crystalline powder
Melting point:
Boiling point:
Vapour density:
Vapour pressure:
Specific gravity: 3.21
Flash point:
Explosion limits:
Autoignition temperature:

Stability

Stable. Incompatible with strong oxidizing agents.

Toxicology

Skin and eye irritant. May be harmful by inhalation or ingestion. R36/37. Typical OEL 5-10 mg/m3.

Personal protection

Avoid breathing dust. Use safety glasses and suitable ventilation.

This information was last updated on January 21, 1998. We have tried to make it as accurate and useful as possible, but can take no responsibility for its use, misuse, or accuracy. We have not verified this information, and cannot guarantee that it is up-to-date.

Silicon Carbide (Lonza UF45 composition)

LONZA-Werke GmbH
Waldshut

Konstanzer Straße 15
Postfach 1643
D-7890 Waldshut-Tiengen 1
Telefon 07751/82-0
Telex 792243
Telefax 07751/92182

LONZA

Qualitätszeugnis

18 APR 1994

For 11.04.1994

CBL Ceramics

Our Contract No.: 3025/4

Material/Product: Silicon Carbide UF
SiC grade UF- 45

Chemical Analysis

Lot-No.:		1259
BET	m²/g	43,7
total SiC %		91,75
free C	%	0,03
free Si	%	0,08
O	%	4,28
Al	%	0,04
Fe	%	0,02
Ti	%	< 0,01
Ca	%	< 0,01
Mg	%	< 0,01
Na	%	< 0,03
pH		5,6

Nach DIN 50049, Punkt 2.3.

LONZA-Werke GmbH / Keramik

Silver Oxide

HEALTH AND SAFETY INFORMATION

Product Silver oxide

Hazard Class NR UN No CAS No 20067-12-3

BDH Product Codes 30090

PHYSICAL DATA

Description Black powder

M Pt(deg C) 300d   B Pt(deg C) n/a   Specific Gravity n/a

Solubility in water Immiscible or insoluble

Vapour pressure n/a mmHg at Deg.C
Vapour density n/a (air = 1)

FIRE AND EXPLOSION HAZARD Not applicable

Flash point(deg C) n/a
Explosive limits (%): lower n/a, upper
Auto-ignition temperature(deg C) n/a

Firefighting measures Not applicable

HEALTH HAZARD May be harmful if ingested in quantity or if inhaled as dust. May irritate eyes or skin.

Toxicity data no data

Carcinogenicity No evidence of carcinogenic properties
Mutagenicity/Teratogenicity No evidence of mutagenic or teratogenic effects
Exposure limits not assigned (Long-term, 8 hour TWA)

FIRST AID

Eyes   Irrigate thoroughly with water. If discomfort persists obtain medical attention.
Lungs   Remove from exposure
Skin   Wash off thoroughly with soap and water.
Mouth   Wash out mouth thoroughly with water. In severe cases obtain medical attention.

REACTIVE HAZARDS

Stability Stable

Reaction None
with water

Other known hazards

Forms explosive compounds with ammonia and hydrazine. Can react vigorously or violently with magnesium, sulphides, nitroalkanes, alkali metals. See 'Handbook of Reactive Chemical Hazards', Bretherick, Butterworths, for details.

Avoid contact with: Water (no)   Acids (no)   Bases (no)
Oxidisers (no)   Combustibles (yes)

SPILLAGE DISPOSAL

Precautions Wear appropriate protective clothing

Mix with sand, transfer carefully to container and arrange removal by disposal company. Wash site of spillage thoroughly with water and detergent.

For large spillages liquids should be contained with sand or earth and both liquids and solids transferred to salvage containers. Any residues should be treated as for small spillages.
If material has entered surface drains it may be necessary to inform local authorities, including fire services if flammable.

PROTECTIVE MEASURES as appropriate to quantity handled

Respirator   Dust respirator
Ventilation   Not applicable
Gloves   Rubber or plastic
Eye protection   Goggles or face shield
Other measures   Plastic apron, sleeves, boots if handling large quantities

STORAGE AND HANDLING

Special requirements
None

Silver Nitrate

1. Identification of the substance/preparation and of the company/undertaking

Identification of the product

Catalogue No: 10233   ID No.: 1023300

Product name: **Silver nitrate AnalaR**

Manufacturer/supplier identification

Company: Merck Eurolab Ltd, Merck House, Poole, Dorset, England, BH15 1TD
                        Telephone : 01202 669700   Telefax : 01202 665599

Emergency telephone No.: 01202 669700

2. Composition/information on ingredients

Chemical characterization

Inorganic salt

Product name: Silver nitrate

CAS number: 7761-88-8   EC-No.: 231-853-9

3. Hazards identification

Causes burns. Very toxic to aquatic organisms, may cause long-term adverse effects in the aquatic environment.

4. First aid measures

Eye contact: Irrigate thoroughly with water for at least 10 minutes. OBTAIN MEDICAL ATTENTION.
Inhalation: Remove from exposure, rest and keep warm. In severe cases obtain medical attention.
Skin contact: Wash off skin thoroughly with water. Remove contaminated clothing and wash before re-use. In severe cases, OBTAIN MEDICAL ATTENTION.
Ingestion: Wash out mouth thoroughly with water and give plenty of water to drink. OBTAIN

5. Fire-fighting measures

Special risks:

May ignite combustible material. May evolve toxic fumes in fire.

Suitable extinguishing media:

Water spray

6. Accidental release measures

Wear appropriate protective clothing.
If local regulations permit, transfer spillage into containers of water, stir to dissolve or suspend and run to waste, diluting greatly with running water. Otherwise mix with wet sand, transfer to container and arrange removal by disposal company. As contact with any oxidant can render organic matter (paper, wood, textiles) dangerously combustible, wash area of spillage and contaminated clothing thoroughly with water.
For large spillages liquids should be contained with sand or earth and both liquids and solids transferred to salvage containers. Any residues should be treated as for small spillages.

7. Handling and storage

Handling:

Avoid generation of dusts. Change contaminated clothing. Application of skin- protective barrier cream recommended. Wash hands after working with substance. Do not empty into drains.

Storage:

Store at room temperature (15 to 25°C recommended). Keep well closed and protected from direct sunlight and moisture. Store away from combustible materials.

8. Exposure controls/personal protection

As appropriate to the situation and the quantity handled. Engineering methods to control or prevent exposure are preferred. Methods could include process enclosure or mechanical ventilation.

Respirator: Dust respirator required when dusts are generated.
Ventilation: Extraction hood
Gloves: Rubber or plastic
Eye Protection: Goggles or face-shield
Other Precautions: Plastic apron, sleeves, boots - if handling large quantities

9. Physical and chemical properties

Form:	solid
Colour:	colourless to white
Odour:	odourless
Melting temperature	212°C
Boiling temperature	444°C
Density(g/ml)	4.33
pH value	5.4 - 6.4 (100g/l H2O)
Solubility in water	2,150 g/l (20°C)
Flash point	Not applicable

10. Stability and reactivity

light-sensitive.

Substances to be avoided
nonmetals, organic substances, alkali hydroxides, acetylidene, acetylene, aldehydes, nitriles, ammonia/alcohols, ammonium compounds, combustible substances, hydrazine and derivatives, carbides, organic nitro compounds, magnesium in powder form (with water), alcohols.

Hazardous decomposition products: nitrous gases.

11. Toxicological Information

The following applies to soluble silver compounds: only slightly absorbed via the gastrointestinal tract. Strong irritations after contact with eyes and skin. The following applies to practically insoluble silver compounds: long-term inhalation or ingestion can result in a persistent discoloration (grey to blue) of the skin and mucous membranes (argyria).

Further data

LD50 50 mg/kg oral, mouse.

No evidence of carcinogenic properties. Evidence of reproductive effects.

12. Ecological information

The following applies to silver compounds in general: biological effects: silver ions toxic for aquatic organisms; bacteria: Ps. putida toxic from 0.006 mg/l up; protozoa: U. parduczi toxic from 0.1 mg/l up;

arthropods: D. daphnia EC50: 0.004 mg/l; algae: M. aeruginosa toxic from 0.0007 mg/l up; Sc. quadricauda toxic from 0.009 mg/l up

The following applies to nitrates in general: may contribute to the eutrophication of water supplies. Hazard for drinking water. Fish: LC50 > 500 mg/l.

13. Disposal considerations

Chemical residues are generally classified as special waste, and as such are covered by regulations which vary according to location. Contact your local waste disposal authority for advice, or pass to a chemical disposal company. Rinse out empty containers thoroughly before returning for recycling.

14. Transport information

UN-No.: 1493

IMO: 5.1/1493

IATA: 1493

Correct technical name: SILVER NITRATE

ADR/RID: 5.1,22'(b)

IMDG class: 5.1

Packaging group: II

Packaging group: II

15. Regulatory information

Labelling according to EC directives

Symbol: C N   Corrosive. Dangerous for the environment.

R-phrases: R34-50/53

Causes burns. Very toxic to aquatic organisms, may cause long-term adverse effects in the aquatic environment.

S-phrases: S26-45-60-61

In case of contact with eyes, rinse immediately with plenty of water and seek medical advice. In case of accident or if you feel unwell, seek medical advice immediately (show the label where possible). This material and its container must be disposed of as hazardous waste. Avoid release to the environment. Refer to special instructions/Safety data sheets.

EC-No.: 231-853-9

Local Regulations

U.K. Transport Category 2

Within the UK, the use of this material must be assessed under the Control of Substances Hazardous to Health (COSHH) regulations.

Silver nitrate 'AnalaR'

AgNO₃	M.W.169.87
Minimum assay (on dried material)	99.8%
Maximum Limits of Impurities	
Solution in water	Passes test
Chloride (Cl)	0.0005%
Sulphate (SO₄)	0.002%
Cadmium (Cd)	0.0001%
Copper (Cu)	0.0002%
Iron (Fe)	0.0002%
Lead (Pb)	0.001%
Nickel (Ni)	0.0005%
Zinc (Zn)	0.0001%
Substances not precipitated by hydrochloric acid (as sulphates)	0.01%

Also complies with BS 6376: Part 2: 1984 (ISO 6353/2-1983) and the corresponding ACS specification

Hydrogen hexachloroplatinate (IV)

1 Identification of substance

Product details

Trade name: *Dihydrogen hexachloroplatinate (IV) hexahydrate*

Stock number: 36259

Manufacturer/Supplier: Alfa Aesar, Johnson Matthey PLC,
Orchard Road, Royston, Hertfordshire, SG8 5HE, England

Informing department: Health, Safety and Enviromental Department, Tel:(0044) 176 3253 000
E-mail:gcat@matthey.com www.alfa-chemcat.com Fax:(0044) 176 3253 668

Emergency information: During normal hours the Health, Safety and Environmental Department. After normal hours call Chemtrec at (800) 424-9300.

2 Composition/Data on components:

Chemical characterization:
Designation: (CAS#)

dihydrogen hexachloroplatinate hexahydrate
(CAS# 26023-84-7); 100%

Identification number(s):
EINECS Number:

241-010-7

3 Hazards identification

Hazard designation:

C Corrosive

Information pertaining to particular dangers for man and environment

R 34   Causes burns.
R 42/43 May cause sensitization by inhalation and skin contact.

4 First aid measures

General information: Instantly remove any clothing soiled by the product.
After inhalation: Supply fresh air and call for doctor for safety reasons.
Supply fresh air. If required, provide artificial respiration. Keep patient warm. Consult doctor if symptoms persist.
Seek immediate medical advice.

After skin contact: Instantly wash with water and soap and rinse thoroughly.
Seek immediate medical advice.

After eye contact: Rinse opened eye for several minutes under running water. Then consult doctor.
After swallowing: Seek immediate medical advice.
Information for doctor
Danger: Platinum compounds, especially platinum halogenides, are sensitizers. Sensitized persons, on re-exposure to platinum salts will show the clinical features of a Type 1 allergy: asthma and/or rhinitis and/or conjunctivitis and/or urticaria. A contact dermatitis may also occur. The symptoms of the allergic reaction to platinum salts may include any of the following: itchy red eyes, watering of the eyes, sneezing, runny nose, chest tightness, wheezing, breathlessness, cough, eczematous or urticarial (nettle rash type) skin lesions. Exposure to platinum salts in exceedingly small amounts, even below the level of physico-chmeical detection, will produce symptoms in sensitized persons. Continued exposure will give symptoms of increasing severity and can eventually lead to chronic asthma. There is a risk of anaphylactic shock occuring in sensitized persons re-encountering platinum salts. Therefore, if sensitization has developped, further exposure to platinum compounds must not be permitted.

5 Fire fighting measures

Suitable extinguishing agents: Use fire fighting measures that suit the environment.
Protective equipment: Wear self-contained breathing apparatus.
Wear full protective suit.

6 Accidental release measures

Person-related safety precautions: Wear protective equipment. Keep unprotected persons away.
Ensure adequate ventilation
Measures for environmental protection: Do not allow material to be released to the environment without proper governmental permits.
Measures for cleaning/collecting: Use neutralizing agent.
Dispose of contaminated material as waste according to item 13.
Ensure adequate ventilation.
Additional information: See Section 7 for information on safe handling
See section 8 for information on personal protection equipment.
See Section 13 for information on disposal.

7 Handling and storage

Handling
Information for safe handling: Keep containers tightly sealed.
Store in cool, dry place in tightly closed containers.
Ensure good ventilation/exhaustion at the workplace.
Prevent formation of dust.

Information about protection against explosions and fires: No special measures required.

Storage
Requirements to be met by storerooms and containers: No special requirements.
Information about storage in one common storage facility: Store away from water.
Further information about storage conditions: Keep container tightly sealed.
Store in cool, dry conditions in well sealed containers.

Store in a locked cabinet or with access restricted to technical experts or their assistants.

8 Exposure controls and personal protection

Additional information about design of technical systems: Properly operating chemical fume hood designed for hazardous chemicals and having an average face velocity of at least 100 feet per minute.

Components with critical values that require monitoring at the workplace:

Platinum metal and soluble salts (as Pt)

	mg/m3
ACGIH TLV	1 (metal); 0.002 (soluble salts)
Belgium TWA	1 (soluble salts)
Denmark TWA	1 (soluble salts)
France TWA	1 (soluble salts)
Hungary TWA	0.001; 0.002-STEL (soluble salts)
Ireland TWA	5 (metal); 0.002 (soluble salts)-Sensitizer
Netherlands TWA	1 (metal); 0.002 (soluble salts)
Switzerland TWA	1 (soluble salts)
United Kingdom TWA	5 (metal); 0.002 (soluble salts)
USA PEL (respirable)	0.002 (soluble salts)

Additional information: No data

Personal protective equipment
General protective and hygienic measures   The usual precautionary measures should be adhered to in handling the chemicals.
                                            Keep away from foodstuffs, beverages and food.
                                            Instantly remove any soiled and impregnated garments.
                                            Wash hands during breaks and at the end of the work.
                                            Avoid contact with the eyes and skin.
Breathing equipment: Use breathing protection with high concentrations.
Protection of hands: Impervious gloves
Eye protection: Safety glasses
                                            Tightly sealed safety glasses.
                                            Full face protection
                                            Face protection
Body protection: Protective work clothing.

9 Physical and chemical properties:

Form: Crystalline
Colour: Red-brown
Smell: Acidic

Change in condition
  Melting point/Melting range: 60 dec.°C
  Boiling point/Boiling range: 115 dec.°C
  Sublimation temperature / start: Not determined

Flash point: Not applicable

Ignition temperature: Not determined

Decomposition temperature: Not determined

Danger of explosion: Product is not explosive.

Critical values for explosion:
  Lower: Not determined
  Upper: Not determined

Steam pressure: Not determined

Density at 20°C   2.431 g/cm3

Solubility in / Miscibility with
  Water: Soluble

10 Stability and reactivity

Thermal decomposition / conditions to be
avoided: No decomposition if used and stored according to specifications.
Materials to be avoided: Water/moisture
                                            Acids
                                            Bases
                                            Light
Dangerous reactions: No dangerous reactions known
Dangerous products of decomposition: Hydrogen chloride (HCl)
                                            Chlorine
                                            Metal oxide

11 Toxicological information

Acute toxicity:
Primary irritant effect:
on the skin: Caustic effect on skin and mucous membranes.
                                            Irritant for skin and mucous membranes.
on the eye: Strong caustic effect.
                                            Irritant effect.
Sensitization: Sensitization possible by inhalation.
                                            Sensitization possible by skin contact.
Additional toxicological information: Swallowing will lead to a strong caustic effect on mouth and throat and to the danger of perforation of
                                            esophagus and stomach.
                                            To the best of our knowledge the acute and chronic toxicity of this substance is not fully known.

                                            No classification data on carcinogenic properties of this material is available from the EPA, IARC, NTP,
                                            OSHA or ACGIH.

12 Ecological information:

General notes: Do not allow material to be released to the environment without proper governmental permits.

13 Disposal considerations

Product:
Recommendation   Consult state, local or national regulations for proper disposal.
                                            Hand over to disposers of hazardous waste.
                                            Must be specially treated under adherence to official regulations.

Uncleaned packagings:
Recommendation: Disposal must be made according to official regulations.
Recommended cleaning agent: Water, if necessary with cleaning agent.

14 Transport information

Land transport ADR/RID and GGVS/GGVE (cross-border/domestic)

ADR/RID-GGVS/E Class: 8
Number/Letter: 16c
Kemler Number: 80
UN-Number: 2507
Label   8
Designation of goods: Chloroplatinic acid, solid

Maritime transport IMDG/GGVSea:

IMDG/GGVSea Class: 8
Page: 8140
UN Number: 2507
Packaging group: III
EMS Number: 8-06
MFAG: 700
Correct technical name: Chloroplatinic acid, solid

Air transport ICAO-TI and IATA-DGR:

ICAO/IATA Class: 8
UN/ID Number: 2507
Packaging group: III
Correct technical name: Chloroplatinic acid, solid

Publications

PANTENY, S.R., STEVENS, R. & BOWEN, C.R., 'Investigation into the processing and characterisation of piezoelectric nanocomposites ', *Key Engineering Materials*, Euro Ceramics VII, 2002, 206-2 (1-3), 1313-1316, ISBN 0-87849-882-6

PANTENY, S.R., STEVENS, R. & BOWEN, C.R., 'Piezoelectric Particulate Reinforced Nanocomposites ', *Ferroelectrics 2000 UK*, Ed. N McN Alford & E Yeatman, 2000, 75, ISBN 1 86125 135 1

Presentations

Poster

5th August 2003 – EMF2003, Cambridge, UK

9th-11th April 2002 - Congress 2002, London, UK

26th-27th March 2002 - Ferroelectrics UK 2002, Leeds, UK

10th-13th September 2001 - 7th European Ceramics Society Conference, Brugge, Belgium

15th-20th July 2001 - Chemistry of Electronic Materials, Gordon Research Conference, CT, USA

10th-14th April 2000 - Congress 2000, Cirencester, UK

Oral

16th June 2000 - "Novel piezoelectric ceramic composites", University of Bath, UK

14th May 2002 – "Piezoelectric ceramics: Particle inclusion effect on properties and modelling", University of Bath, UK